

UNIVERSITY OF CAPE TOWN
IYUNIVESITHI YASEKAPA • UNIVERSITEIT VAN KAAPSTAD

Response of composite and steel V-structures to localised air blast loading - Numerical and Experimental

Author:
Vinay Ramaswami Shekhar

Supervisors:
A/Prof. Christopher J. von Klemperer
Prof. Genevieve S. Langdon

September 15, 2023

Thesis Presented for the Degree of
DOCTOR OF PHILOSOPHY

Blast Impact and Survivability Research Unit
Department of Mechanical Engineering
Faculty of Engineering and The Built Environment
University of Cape Town

BISRU

University of Cape Town

The copyright of this thesis vests in the author. No quotation from it or information derived from it is to be published without full acknowledgement of the source. The thesis is to be used for private study or non-commercial research purposes only.

Published by the University of Cape Town (UCT) in terms of the non-exclusive license granted to UCT by the author.

University of Cape Town

Declaration

I, Vinay Ramaswami Shekhar, hereby declare that the work on which this thesis is based is my original work (except where acknowledgements indicate otherwise) and that neither the whole work nor any part of it has been, is being, or is to be submitted for another degree in this or any other university. I authorise the University to reproduce for the purpose of research either the whole or any portion of the contents in any manner whatsoever.

Signature:

Signed by candidate

Date: September 15, 2023

Abstract

This research investigated the blast performance of Glass-Fibre Reinforced Polymer (GFRP) V-structures compared to equivalent mass steel V-structures. The blast performance was measured in terms of three metrics, namely, impulse transferred, maximum mid-point deflection and permanent damage/deformation.

A series of blast experiments were performed on manufactured GFRP and steel V-structures. The GFRP V-structures were made using Vacuum Infusion (VI), using a $400\,\mathrm{g\,m^{-2}}$ woven E-glass and a Prime 20LV resin with a Low Viscosity (LV) slow hardener. The steel V-structures were manufactured by laser cutting the flat panel profiles from a sheet of 2 mm thick DOMEX-700 MC sheet and then Computer Numerical Control (CNC) bending them to the desired profile. Three panel configurations were experimentally blast tested, namely, a 105° V-angle with a 32 mm V-tip radius, a 105° V-angle with a 62 mm V-tip radius and a 120° V-angle with a 32 mm V-tip radius. Blast tests were performed by detonating PE4 charges ranging from 10 g to 40 g at a Stand-Off Distance (SOD) of 34 mm. Digital Image Correlation (DIC) was used to track the transient deformation of the V-structures, while the final deformed profile of the V-structures was determined using a 3D scanner.

A series of numerical simulations were also performed on the GFRP and steel V-structures. The simulations used quarter symmetry models to utilise the symmetry of the experimental setup. The material model parameters were obtained from a series of material tests carried out on GFRP and steel specimens. The simulations were validated against the experimental results for a number of test cases for impulse transfer, and transient and permanent deformation. The simulations were then extended to look at a range of V-tip radii, V-angles and charge masses, while the SOD was held constant.

For the steel V-structures, the blast experiments found that increasing the V-tip radius and V-angle resulted in an increase in impulse transferred as well as transient and permanent mid-point deflection. This result was confirmed when the set of V-tip radii investigated was increased in the simulations. The trends in the results for the GFRP V-structures were similar to the equivalent steel plates. The delamination and total crack length were observed to increase with an increase in V-angle and charge mass. In general, the study found that GFRP V-structures were inferior to their equivalent mass steel V-structures in terms of panel rupture threshold. The GFRP V-structures exhibited lower transient deformation, but panel rupture on the rear face was observed at a lower charge mass. No tearing or rupture was observed in the steel V-structures tested at similar charge masses.

List of publications

[1] Shekhar, V., Langdon, G., and Klemperer, C. von. "Investigation into the effect of V-tip radius on the blast performance of steel V-plates". In: *Advances in Engineering Materials, Structures and Systems: Innovations, Mechanics and Applications*. CRC Press, 2019, pp. 784–787.

[2] Langdon, G. S. and Shekhar, V. R. "The effect of the bend radius on the impulse transfer characteristics of V-hulls: Numerical simulations". *International Journal of Protective Structures* 11.1 (June 2019), pp. 69–89. DOI: 10.1177/2041419619853292.

[3] Langdon, G., Curry, A., Shekhar, V., Siddiqui, A., Murray, C., and Klemperer, C. von. "Attempts to improve on the V-hull structural design for air-blast loading applications". *ce/papers* 4.2-4 (2021), pp. 1499–1506.

[4] Shekhar, V. R., Klemperer, C. J. von, and Langdon, G. S. "The Damage and Impulse Transfer Characteristics of Flexible Steel V-Structures with Large Bend Radii". *Applied Sciences* 13.3 (2023), p. 1293.

Acknowledgements

I would like to begin by thanking all those who have helped me on this long journey towards the completion of this research project.

Firstly, to my supervisors, A/Prof. Chris von Klemperer and Prof. Genevieve Langdon. Thank you for being excellent supervisors and for your wealth of knowledge on composites and blast loading. I am grateful for the opportunities to learn from both of you and gain insights into manufacturing, analysis, and interpretation of results.

The numerical simulations performed as part of this research were conducted using facilities provided by the University of Cape Town's ICTS High-Performance Computing team: http://hpc.uct.ac.za. I would like to acknowledge the resources provided by the HPC centre that enabled the simulations to be performed. In particular, I would like to thank Andrew Lewis from the University of Cape Town's ICTS High-Performance Computing team for helping me get ANSYS LS-DYNA set up on the servers to enable me to run my simulations. I would also like to thank the Postgraduate funding office (PGFO) and the CSIR for assisting with and providing funding for this research.

To all the BISRU staff and postgraduate students, thank you for making the research environment an interesting and unique space to work in. There were many interesting conversations around the lunch table that I will fondly remember. In particular, I would like to thank Ismail Ghoor for all your help with the GFRP panel manufacture. It meant a lot to gain insights from you into the processes and approaches used to create high-quality composites. I am also grateful to the Mechanical Engineering administrative and workshop staff for all your help with the challenges around registration and the design and manufacture of the clamp frames and other components needed in the research. To Ernesto Ismail, thank you for many a good chat and your support during some rather low moments, and of course, for all the help when we taught mechanical vibrations together. To Muya Koloko, thank you for just being a good friend through some tough months and the long season of the COVID lockdown.

Lastly, to my mom and dad. Amma and Appa, thank you so much for believing in me and supporting me on this journey. I know it has been a long and challenging road and your support has meant the world to me.

Table of contents

Declaration i

Abstract ii

List of publications iii

Acknowledgements iv

Table of contents x

List of tables xii

List of figures xxiv

List of acronyms and abbreviations xxv

1 Introduction 1
- 1.1 Background and problem definition 1
- 1.2 Research questions 3
- 1.3 Hypothesis 4
- 1.4 Thesis overview 4

2 Literature review 5
- 2.1 History of Armoured Personnel Carriers and landmines 5
- 2.2 Composite materials 8
- 2.3 Manufacturing Fibre Reinforced Polymers (FRPs) 11
- 2.4 Experimental studies into the blast response of steel structures to localised air blasts from cylindrical charges 13
  - 2.4.1 Blast testing of flat and curved steel panels 13
  - 2.4.2 Blast loading of steel V-structures 15
- 2.5 Blast loading of composite structures 17
  - 2.5.1 Blast response of flat and curved FRP composite structures 17
  - 2.5.2 Response of composite V-structures to blast loading 19
- 2.6 Measurement of the transient response of blast loaded structures 20
- 2.7 Numerical simulations of blast tested structures 23
  - 2.7.1 Numerical blast modelling of metallic V-structures 25
  - 2.7.2 Numerical modelling of composite structures to dynamic and blast loads 28
- 2.8 Summary 29

3 V-structure manufacturing 31
- 3.1 Steel V-structure manufacture 31

3.2 GFRP Panel manufacture 33
3.3 Specifying the number of layers of glass-fibre 35
3.4 V-panel mould design 35
3.4.1 Male mould 36
3.4.2 Female mould 37
3.5 Final manufacturing process 39
3.6 Discussion - Manufacturing 41
3.7 Summary 41

4 Material testing 42
4.1 DOMEX-700 MC material testing 42
4.1.1 Quasistatic tensile testing 42
4.1.2 Steel material model characterisation 45
4.2 GFRP material testing 46
4.2.1 Quasistatic tensile tests 46
4.2.2 Double cantilever beam tests 49
4.3 Discussion and summary 52

5 Blast testing - Experimental design 53
5.1 Ballistic pendulums 53
5.2 Clamp frame design 55
5.3 V-structure geometry 57
5.4 Specimen preparation for high-speed imaging 57
5.5 Blast test plan 59
5.6 Discussion - Blast test design 59

6 Blast testing results - Steel 60
6.1 Impulse transfer and permanent mid-point deflection results 60
6.2 Discussion of the impulse transfer and permanent mid-point deflection results 62
6.2.1 Influence on the impulse transferred to the ballistic pendulum 62
6.2.2 Influence on the permanent mid-point deflection 63
6.3 Permanent deformation profiles 63
6.3.1 Deformation profile analysis procedure 63
6.3.2 3D scanned V-plates 65
6.3.3 Ridge profiles 65
6.3.4 Crosscut profiles 67
6.4 Discussion - Permanent deformation profiles 68
6.4.1 Influences on the 3D plate profiles 68
6.4.2 Influences on the ridge profiles 68
6.4.3 Influences on the crosscut profiles 68
6.5 Transient deformation results 69
6.5.1 Mid-point deflection time history 69
6.5.2 Ridge profiles 71

6.6 Discussion - Transient deformation results 72
6.6.1 Influence on the mid-point deflection time history 72
6.6.2 Influence on the transient ridge profiles 72
6.7 Summary 73

7 Blast testing results - GFRP 74
7.1 Impulse transfer results 74
7.2 Discussion of the impulse transfer results 76
7.3 GFRP V-structure damage results 76
7.4 Discussion of the GFRP V-structure damage results 81
7.5 Transient deformation results 81
7.5.1 Paint spalling on the GFRP V-structures 81
7.5.2 Point deflection time history 82
7.5.3 Ridge profiles 84
7.6 Discussion of the transient deformation results 86
7.7 Summary 86

8 Numerical blast simulations - Steel 88
8.1 Numerical model development 88
8.1.1 Meshing the model components 88
8.1.2 Selection of components to model 89
8.1.3 Modelling the explosive blast load 90
8.1.4 Element size, type, and formulation selection 91
8.1.5 Deformation plot visualisations 92
8.2 Numerical model validation - Steel 94
8.2.1 V-structure permanent deformed profiles - Ridge plane 94
8.2.2 V-structure permanently deformed profiles - Crosscut plane 95
8.2.3 Transient mid-point deflection 97
8.2.4 Permanent mid-point displacement 99
8.2.5 Impulse transferred 100
8.3 The influences of V-tip radius on performance metrics of the steel V-structures 101
8.3.1 The effect of V-tip radius on the simulated impulse 101
8.3.2 The influence of the V-tip radius on peak transient and permanent mid-point deflection 103
8.3.3 The effects of V-tip radius on mid-point displacement time histories 106
90° V-structures 106
105° V-structures 107
120° V-structures 107
8.3.4 The influences of the V-tip radius on the permanently deformed ridge profiles 108
90° V-structures 109
105° V-structures 109
120° V-structures 110
8.3.5 The influences of the V-tip radius on permanently deformed crosscut profiles 110

90° V-structures 111
105° V-structures 111
120° V-structures 112
8.4 The influence of the V-angle on the blast performance of steel V-structures 112
8.4.1 Effects of V-angle on impulse 113
8.4.2 Effect of V-angle on peak transient mid-point deflection 113
8.4.3 Effect of V-angle on permanent mid-point deflection 114
8.4.4 Effect of V-angle on mid-point displacement time histories 115
V-tip radius of 32 mm 115
V-tip radius of 200 mm 116
8.4.5 Effect of V-angle on the permanently deformed ridge profiles 117
V-tip radius of 32 mm 117
V-tip radius of 100 mm 118
8.4.6 Effect of V-angle on the permanently deformed crosscut profiles 119
V-tip radius of 32 mm 119
V-tip radius of 200 mm 120
8.5 Summary 120

9 Numerical blast simulations - GFRP 122
9.1 GFRP numerical blast model development 122
9.1.1 Tensile test model and GFRP material model characterisation 122
9.1.2 Delamination material model characterisation 124
9.1.3 Inclusion of damping 126
9.1.4 Numerical model specification 127
9.2 Numerical model validation - GFRP 128
9.2.1 Measured impulse 128
9.2.2 Delaminated area 128
9.2.3 Transient deflection 131
9.3 V-structure design parameters investigated 133
9.4 The effects of the V-structure design parameters on the impulse 133
9.4.1 Fibre orientation effects 134
9.4.2 V-angle effects 134
9.4.3 V-tip radius effects 135
9.5 The effects of the V-structure design parameters on the projected delaminated area 136
9.5.1 Fibre orientation effects 136
9.5.2 V-angle effects 138
9.5.3 V-tip radius effects 140
9.6 The effects of V-structure design parameters on the transient response 140
9.6.1 Fibre orientation effects 141
9.6.2 V-angle effects 143
9.6.3 V-tip radius effects 144
9.7 Summary 146

10 Discussion - V-structure blast performance **147**
10.1 Trends in the impulse transferred 147
10.2 Trends in the damage propagation 151
10.3 Comparison of the transient response 153

11 Conclusions and recommendations **155**
11.1 Conclusions 155
11.2 Recommendations 158

References **159**

A CAD drawings **A-1**

B Blast tested steel V-structure profiles - Additional figures **B-1**
B.1 Optically scanned 3D V-structure profiles B-1
B.2 Transient ridge profile data B-3

C GFRP V-structures - Supplementary photographs **C-1**

D Numerical blast simulations - Steel - Supplementary figures **D-1**
D.1 Experimental versus numerical results - Additional figures and tables D-1
D.1.1 V-structure permanent deformed profiles - Ridge plane D-1
D.1.2 V-structure permanent deformed profiles - Crosscut plane D-3
D.1.3 Transient mid-point deflection comparisons D-5
D.1.4 Permanent mid-point displacement and impulse D-7
D.2 The influences of V-tip radius on the blast performance of the steel V-structures - Supplementary tables and graphs D-8
D.2.1 V-tip radius effects on the mid-point displacement time histories D-8
D.2.2 V-tip radius effects on the permanently deformed ridge profiles D-11
D.2.3 V-tip radius effects on the permanently deformed crosscut profiles D-13
D.3 The influences of the V-angle on the blast performance of steel V-structures - Supplementary figures D-15
D.3.1 Effect of V-angle on the mid-point displacement time histories D-15
D.3.2 Effect of V-angle on the permanently deformed ridge profiles D-16
D.3.3 Effect of V-angle on the permanently deformed crosscut profiles D-17
V-tip radius of 32 mm D-17
V-tip radius of 62 mm D-18
V-tip radius of 100 mm D-19
V-tip radius of 200 mm D-21

E Numerical blast simulations - GFRP - Supplementary figures **E-1**
E.1 The Inclusion of damping E-1
E.2 The effects of the V-structure geometry on the impulse E-1
E.2.1 V-angle effects E-2
E.2.2 V-tip radius effects E-2

E.3 The effects of the V-structure geometry on the projected delaminated area E-3
E.3.1 V-tip radius effects E-4
E.3.2 Delaminated area plots - V-angle = 105° E-5
E.3.3 Delaminated area plots - V-angle = 120° E-7
E.4 The effects of V-structure geometry on the transient response E-10
E.4.1 Fibre orientation effects E-10
E.4.2 V-angle effects E-11
E.4.3 V-tip radius effects E-13

List of tables

2.1 Experiments reported by Follett [9] 19
3.1 Geometry and mass of the DOMEX-700 MC steel blast specimens 33
3.2 Manufactured panels' properties 35
3.3 Manufactured GFRP blast specimens' properties 40
4.1 Yield strength and failure strain for the steel specimens tested in the two directions at the three crosshead speeds 43
4.2 Johnson-Cook material model parameters for DOMEX-700 MC based on tensile test data 45
4.3 Effective modulus and failure strain for the GFRP specimens 46
4.4 Initiation and propagation fracture toughness values for the two fibre orientations 51
5.1 Specifications and test arrangement of the IDT vision NR4 S3 cameras 55
5.2 Summary of the experimental blast test plan 59
6.1 Impulse and final mid-point deflection versus charge mass for all steel specimens tested at a stand-off distance of 50 mm 61
6.2 Impulse and final mid-point deflection versus charge mass for DOMEX-700 MC V-structures tested at a stand-off distance of 34 mm 61
6.3 Peak and final deformation versus charge mass for DOMEX-700 MC V-structures 71
7.1 GFRP V-structure configurations and charge mass range investigated 74
7.2 Impulse versus charge mass for GFRP V-structures tested at a stand-off distance of 34 mm 75
7.3 Failure mode key used for the blast tested GFRP V-structures 77
7.4 Post blast test results for all the GFRP V-structures 79
8.1 Material model properties used for air in LS-DYNA [97] 90
8.2 Material model properties used for PE4 in LS-DYNA [99] 90
8.3 Mid-point deflection (peak and final) versus V-tip radius for the 90° DOMEX-700 MC V-structure simulations 103
8.4 Mid-point deflection (peak and final) versus V-tip radius for the 105° DOMEX-700 MC V-structure simulations 103
8.5 Mid-point deflection (peak and final) versus V-tip radius for the 120° DOMEX-700 MC V-structure simulations 104
9.1 Material properties needed for MAT_ENHANCED_COMPOSITE_DAMAGE 124
9.2 Model parameters needed for the contact card 126
9.3 Comparison of the impulse transferred results between the GFRP V-structures (numerical versus experimental) 128
9.4 Comparison of the projected delaminated area (%) between the GFRP V-structures (numerical versus experimental) 129
10.1 Comparison of the experimental impulse transferred results between the DOMEX-700 MC and GFRP V-structures 148

10.2 Impulse (in Ns) obtained from the numerical blast simulations for the DOMEX-700 MC and GFRP V-structures 148
10.3 Peak mid-point deflection (in mm) obtained from the numerical blast simulations for the DOMEX-700 MC and GFRP V-structures 153
A.1 List of manufactured parts A-1
D.1 Comparison of the impulse transferred results for selected tests (numerical versus experimental) D-7
D.2 Comparison of the mid-point displacement results for selected tests (numerical versus experimental) D-7
D.3 Simulated impulse (in Ns) versus V-tip radius for the DOMEX-700 MC V-structures D-8
E.1 Simulated impulse (in Ns) versus V-tip radius for the GFRP V-structures E-2
E.2 Projected delaminated area (%) versus V-tip radius for the GFRP V-structure simulations E-4
E.3 Peak mid-point deflection (in mm) versus V-tip radius for the GFRP V-structure simulations E-10

List of figures

1.1 Photograph of an SKPF/VKPF M/42 Armoured Personnel Carrier (APC) developed during WWII by the Swedes [4] 1
1.2 Side profile of a V-structure showing the V-tip, tip radius, V-angle and plate height 3
2.1 Photograph of a Casspir V-hulled APC [24] 7
2.2 Schematic of three different reinforcements, *i.e.* particles, flakes and fibres [29] 8
2.3 Schematic showing the differences between continuous and discontinuous fibres [28] 9
2.4 Schematic of the resin transfer moulding (RTM) process [33] 12
2.5 Blast tested flat panels tested by Jacob *et al.* [37] showing failure modes I and IIc 13
2.6 Schematic of the clamp frame, flat panel and explosive arrangement used by Jacob *et al.* [37] 14
2.7 Schematics of the V-structures tested by Chung Kim Yuen *et al.* [8] 15
2.8 Schematics of the novel V-structure tested by Langdon *et al.* [41] 16
2.9 Rupture observed for the carbon fibre structures tested by Gargano *et al.* [49] 18
2.10 Schematic of the V-structures tested by Follett [9] showing the estimated V-tip radius 19
2.11 Experimental setup showing the measuring comb used by Neuberger *et al.* [51] 20
2.12 Experimental setup showing the stereo cameras and target plate as tested by Zhao *et al.* [53] 21
2.13 Schematic of the experimental setup showing the positions of stereo cameras and the target plate as tested by Aune *et al.* [55] 22
2.14 Schematic of the side view of three 90° V-structures with bend radii of 0 mm, 40 mm and 150 mm, showing the fixed SOD and the total reduction in height [72] 26
2.15 Schematic of the experiments simulated by Wahab *et al.* [74] 27
3.1 Flat profile for a 2 mm thick DOMEX-700 MC 120° V-structure with a 32 mm V-tip radius 32
3.2 Folded profile for a 2 mm thick DOMEX-700 MC 120° V-structure with a 32 mm V-tip radius 32
3.3 Layup for the flat panel manufacture 34
3.4 Schematic of the material layup for the V-panels manufactured using a female mould 34
3.5 The resin rich area observed at the V-tip in the V-hulls manufactured by Hobson [82] 36
3.6 Photographs showing the V-panel infusion with the male mould 36
3.7 Photographs of the manufacturing issues observed when using the "male" mould 37
3.8 Photograph of the 105° female V-shaped mould with the dry material and vacuum bag fitted 37
3.9 Photographs showing the variations from the design specification observed at the V-tip and at the clamped region in the V-structures manufactured 38
4.1 DOMEX-700 MC steel quasistatic tensile test specimen geometry 42

4.2 Graphs showing the engineering stress versus engineering strain (Tensile test results, DOMEX-700 MC) 43
4.3 Graph showing the true stress versus effective plastic strain including Johnson-Cook parameters (All tensile test results, DOMEX-700 MC) 45
4.4 Photograph of a speckled GFRP tensile test specimen 46
4.5 Graph showing the GFRP tensile test results for a fibre orientation of 0°/90° including the chord line drawn through the data 47
4.6 GFRP tensile tests graphs for a fibre orientation of ±45° 48
4.7 GFRP DCB test specimen geometry and hinge block dimensions 49
4.8 Force and crack length versus load point displacement for the DCB test specimens in the two fibre orientations 50
4.9 Strain energy release rate (G_I) versus crack length for the DCB test specimens in the two fibre orientations 51
5.1 Schematic of the simple ballistic pendulum 53
5.2 Photograph of the DIC ballistic pendulum with an attached steel V-structure 54
5.3 Photograph of one of the high-speed cameras used to track the motion of the plate during the blast event (Lens cover is removed prior to testing) 54
5.4 Schematic of the clamp frame designed to mount the V-structures to the pendulums 55
5.5 Schematic of the clamp frame with a V-structure with and without the protective side shields fitted 56
5.6 Definitions of the ridge and crosscut planes and the chosen coordinate system 57
5.7 Photograph of a speckled DOMEX-700 MC steel V-structure 58
6.1 Impulse versus charge mass for the DOMEX-700 MC V-structures tested at a SOD of 34 mm 62
6.2 Mid-point deflection versus charge mass for the DOMEX-700 MC V-structures tested at a SOD of 34 mm 62
6.3 Photographs from the top view of two blast tested 105°, 32 mm V-tip radius DOMEX-700 MC V-structures 64
6.4 3D Profiles of the 105°, 32 mm V-tip radius DOMEX-700 MC V-structures tested at a SOD of 34 mm 65
6.5 Ridge profiles of the 105°, 32 mm V-tip radius DOMEX-700 MC V-structures tested at a SOD of 34 mm 66
6.6 Ridge profiles of the 105°, 62 mm V-tip radius DOMEX-700 MC V-structures tested at a SOD of 34 mm 66
6.7 Ridge profiles of the 120°, 32 mm V-tip radius DOMEX-700 MC V-structures tested at a SOD of 34 mm 66
6.8 Crosscut profiles of the 105°, 32 mm V-tip radius DOMEX-700 MC V-structures tested at a SOD of 34 mm 67
6.9 Crosscut profiles of the 105°, 62 mm V-tip radius DOMEX-700 MC V-structures tested at a SOD of 34 mm 67
6.10 Crosscut profiles of the 120°, 32 mm V-tip radius DOMEX-700 MC V-structures tested at a SOD of 34 mm 67

6.11 Mid-point deflection time history for the first 5.5 ms after the blast for the 105°, 32 mm V-tip radius DOMEX-700 MC V-structures tested at a SOD of 34 mm 69
6.12 Mid-point deflection time history for the first 5.5 ms after the blast for the 105°, 62 mm V-tip radius DOMEX-700 MC V-structures tested at a SOD of 34 mm 70
6.13 Mid-point deflection time history for the first 5.5 ms after the blast for the 120°, 32 mm V-tip radius DOMEX-700 MC V-structures tested at a SOD of 34 mm 70
6.14 The ridge profiles for a 105°, 32 mm V-tip radius DOMEX-700 MC V-structure tested with a 10 g PE4 charge at a SOD of 34 mm 71
6.15 The ridge profiles for a 105°, 62 mm V-tip radius DOMEX-700 MC V-structure tested with a 15 g PE4 charge at a SOD of 34 mm 72
6.16 The ridge profiles for a 120°, 32 mm V-tip radius DOMEX-700 MC V-structure tested with a 10 g PE4 charge at a SOD of 34 mm 72
7.1 Impulse versus charge mass for the GFRP V-structures tested at a SOD of 34 mm 76
7.2 Photograph of the back face of a ±45° GFRP V-structure tested at a charge mass of 15 g and a SOD of 34 mm 77
7.3 Photograph of the back face of a ±45° GFRP V-structure tested at a charge mass of 15 g and a SOD of 34 mm with the delaminated area drawn 77
7.4 Photographs of the failure modes identified for the blast tested GFRP V-structures 78
7.5 Photographs of the back face of three GFRP V-structures tested at a charge mass of 10 g and a SOD of 34 mm 79
7.6 Photographs of the back face of three GFRP V-structures tested at a charge mass of 15 g and a SOD of 34 mm 79
7.7 Photographs of a sectioned GFRP V-structure (120°, 34 mm V-tip radius) tested at an charge mass of 10 g with a SOD of 34 mm 80
7.8 Photographs of the spalling paint during a GFRP V-structure blast test 82
7.9 Mid-point displacement time histories for the tests done on a 105° V-structure, ±45° lay-up tested at a charge mass of 10 g and a SOD of 34 mm 82
7.10 3D profile of a V-structure showing the location of the point chosen for measuring the transient deformation of the GFRP V-structures 83
7.11 Mid-point displacement versus point displacement at 50 mm from the centre for a test performed on a 105° V-structure, ±45° lay-up tested at a charge mass of 10 g and a SOD of 34 mm 83
7.12 Point displacement time histories 50 mm from the centre for the tests done on a 105° V-structure, ±45° lay-up tested at a charge mass of 10 g and a SOD of 34 mm 83
7.13 Point displacement time histories 50 mm from the centre for the tests done on a 120° V-structure, 0°/90° lay-up tested at a charge mass of 10 g and a SOD of 34 mm 84
7.14 Ridge displacements for test one on a 105° V-structure, ±45° lay-up tested at a charge mass of 10 g and a SOD of 34 mm 85
7.15 Ridge displacements for test one on a 120° V-structure, 0°/90° lay-up tested at a charge mass of 15 g and a SOD of 34 mm 85
8.1 Going from a CAD model to a meshed component 88

8.2 Displacement time history for a central node on the clamp frame during a blast simulation of a 105°, 32 mm steel V-structure simulation at a charge mass of 20 g 89
8.3 Pressure time histories at the four corners of a 120°, 32 mm V-tip radius DOMEX-700 MC V-structure simulation with a charge mass of 20 g with insert showing pressures equalising across the plate after 0.3 ms 91
8.4 Schematic of the blast simulation of a 120°, 32 mm V-tip radius DOMEX-700 MC V-structure simulation with a charge mass of 20 g, showing the symmetry used, including the air block, the explosive charge, the clamp frames, and the bolts. 92
8.5 Equivalent plastic strain evolution for a 105° steel V-structure simulation with a 32 mm V-tip radius simulated at a charge mass of 20 g 93
8.6 Permanently deformed ridge profiles for a 105°, 32 mm V-tip radius DOMEX-700 MC V-structure at a charge mass of 15 g (numerical versus experimental) 94
8.7 Permanently deformed ridge profiles for a 105°, 62 mm V-tip radius DOMEX-700 MC V-structure at a charge mass of 20 g (numerical versus experimental) 95
8.8 Permanently deformed ridge profiles for a 120°, 32 mm V-tip radius DOMEX-700 MC V-structure at a charge mass of 20 g (numerical versus experimental) 95
8.9 Permanently deformed crosscut profiles for a 105°, 32 mm V-tip radius DOMEX-700 MC V-structure at a charge mass of 10 g (numerical versus experimental) 96
8.10 Permanently deformed crosscut profiles for a 105°, 62 mm V-tip radius DOMEX-700 MC V-structure at a charge mass of 20 g (numerical versus experimental) 96
8.11 Permanently deformed crosscut profiles for a 120°, 32 mm V-tip radius DOMEX-700 MC V-structure at a charge mass of 15 g (numerical versus experimental) 97
8.12 Mid-point deflection time history for a 105°, 32 mm V-tip radius DOMEX-700 MC V-structure at a charge mass of 20 g (numerical versus experimental) 98
8.13 Mid-point deflection time history for a 105°, 62 mm V-tip radius DOMEX-700 MC V-structure at a charge mass of 15 g (numerical versus experimental) 98
8.14 Mid-point deflection time history for a 120°, 32 mm V-tip radius DOMEX-700 MC V-structure at a charge mass of 15 g (numerical versus experimental) 99
8.15 Permanent mid-point displacement versus charge mass for the numerical simulations compared with the experimentally measured values 100
8.16 Impulse versus charge mass for the numerical simulations compared with the experimentally measured values 101
8.17 Impulse versus V-tip radius for the 90° DOMEX-700 MC V-structure simulations 102
8.18 Impulse versus V-tip radius for the 105° DOMEX-700 MC V-structure simulations 102
8.19 Impulse versus V-tip radius for the 120° DOMEX-700 MC V-structure simulations 102
8.20 Peak and final mid-point deflection versus V-tip radius for the 90° DOMEX-700 MC V-structure simulations 105
8.21 Peak and final mid-point deflection versus V-tip radius for the 105° DOMEX-700 MC V-structure simulations 105
8.22 Peak and final mid-point deflection versus V-tip radius for the 120° DOMEX-700 MC V-structure simulations 105

8.23 Mid-point deflection time histories for increasing V-tip radii for the 90° DOMEX-700 MC V-structure simulations at a charge mass of 15 g 106
8.24 Mid-point deflection time histories for increasing V-tip radii for the 105° DOMEX-700 MC V-structure simulations at a charge mass of 15 g 107
8.25 Mid-point deflection time histories for increasing V-tip radii for the 120° DOMEX-700 MC V-structure simulations at a charge mass of 10 g 108
8.26 Mid-point deflection time histories for increasing V-tip radii for the 120° DOMEX-700 MC V-structure simulations at a charge mass of 20 g 108
8.27 Permanently deformed ridge profiles for increasing V-tip radii for the 90° DOMEX-700 MC V-structure simulations at a charge mass of 15 g 109
8.28 Permanently deformed ridge profiles for increasing V-tip radii for the 105° DOMEX-700 MC V-structure simulations at a charge mass of 10 g 110
8.29 Permanently deformed ridge profiles for increasing V-tip radii for the 120° DOMEX-700 MC V-structure simulations at a charge mass of 20 g 110
8.30 Permanently deformed crosscut profiles for increasing V-tip radii for the 90° DOMEX-700 MC V-structure simulations at a charge mass of 15 g 111
8.31 Permanently deformed crosscut profiles for increasing V-tip radii for the 105° DOMEX-700 MC V-structure simulations at a charge mass of 15 g 112
8.32 Permanently deformed crosscut profiles for increasing V-tip radii for the 120° DOMEX-700 MC V-structure simulations at a charge mass of 15 g 112
8.33 Bar charts of the impulse versus the V-angle for all V-tip radii 113
8.34 Bar charts of the peak mid-point deflection versus the V-angle for all V-tip radii 114
8.35 Bar charts of the final mid-point deflection versus the V-angle for all V-tip radii 115
8.36 Mid-point deflection time histories versus the V-angle for a V-tip radius of 32 mm at all three charge masses investigated 116
8.37 Mid-point deflection time histories versus the V-angle for a V-tip radius of 200 mm at all three charge masses investigated 117
8.38 Permanently deformed ridge profiles versus the V-angle for a V-tip radius of 32 mm at all three charge masses investigated 118
8.39 Permanently deformed ridge profiles versus V-angle for a V-tip radius of 100 mm at all three charge masses investigated 119
8.40 Permanently deformed crosscut profiles versus V-angle for a V-tip radius of 32 mm at a charge mass of 15 g 120
8.41 Permanently deformed ridge profiles versus the V-angle for a V-tip radius of 200 mm at a charge mass of 20 g 120
9.1 Schematic of the quasistatic tensile test model for the GFRP specimens 123
9.2 Comparisons of the stress versus strain graphs from the simulations and experiments on the quasistatic tensile tests of the 0°/90° GFRP specimens 123
9.3 Schematic of the quasistatic DCB test model for the GFRP specimens 125
9.4 Numerical versus experimental results for the force and crack length versus load point displacement for the DCB test specimens in the ±45° fibre orientation and a crosshead speed of 2 mm min^{-1} 125

9.5 Numerical simulations with increasing amounts of damping and the experimental results for the transient response at the 50 mm point along the ridge line for a 105° 34 mm V-tip radius GFRP V-structure with a ±45° fibre orientation at a charge mass of 10 g 127
9.6 Schematic of the blast simulation of a 120°, 34 mm V-tip radius GFRP V-structure simulation showing the offset shell layers 127
9.7 Comparison of the numerical and experimental delamination for a 105° GFRP V-structure with a V-tip radius of 34 mm and a fibre orientation of 0°/90°, tested at a charge mass of 10 g 129
9.8 Comparison of the numerical and experimental delamination for a 105° GFRP V-structure with a V-tip radius of 34 mm and a fibre orientation of 0°/90°, at a charge mass of 15 g 130
9.9 Comparison of the numerical and experimental delamination for a 120° GFRP V-structure with a V-tip radius of 34 mm and a fibre orientation of 0°/90°, tested at a charge mass of 10 g 130
9.10 Comparison of the numerical and experimental delamination for a 120° GFRP V-structure with a V-tip radius of 34 mm and a fibre orientation of 0°/90°, at a charge mass of 15 g 130
9.11 Comparison of the numerical and experimental delamination for a 105° GFRP V-structure with a V-tip radius of 34 mm and a fibre orientation of ±45°, at a charge mass of 10 g 130
9.12 Comparison of the numerical and experimental delamination for a 105° GFRP V-structure with a V-tip radius of 34 mm and a fibre orientation of ±45°, tested at a charge mass of 15 g 131
9.13 Numerical versus experimental results for the mid-point deflection time history for a 105° 34 mm V-tip radius GFRP V-structure with a ±45° fibre orientation at a charge mass of 10 g 131
9.14 Numerical versus experimental results for the point deflection time history for a 105° 34 mm V-tip radius GFRP V-structure with a ±45° fibre orientation at a charge mass of 10 g 132
9.15 Numerical versus experimental results for the point deflection time history for a 120° 34 mm V-tip radius GFRP V-structure with a 0°/90° fibre orientation at a charge mass of 10 g 132
9.16 Numerical versus experimental results for the point deflection time history for a 120° 34 mm V-tip radius GFRP V-structure with a 0°/90° fibre orientation at a charge mass of 15 g 132
9.17 Numerical versus experimental results for the peak transient ridge profile for a 105° 34 mm V-tip radius GFRP V-structure with a ±45° fibre orientation at a charge mass of 10 g 133
9.18 Simulated impulse versus fibre orientation for the 105° GFRP V-structures 134
9.19 Simulated impulse versus fibre orientation for the 120° GFRP V-structures 134

9.20 Simulated impulse versus V-angle for the GFRP V-structures with a 0°/90° fibre orientation 135
9.21 Simulated impulse versus V-tip radius for the 105° GFRP V-structures with a 0°/90° fibre orientation 135
9.22 Simulated impulse versus V-tip radius for the 120° GFRP V-structures with a 0°/90° fibre orientation 136
9.23 Projected delaminated area versus fibre orientation for the 105° GFRP V-structure simulations 137
9.24 Projected delaminated area versus fibre orientation for the 120° GFRP V-structure simulations 137
9.25 Projected total delaminated area for the 105° GFRP V-structure simulations with the two fibre orientations and V-tip radii of 100 mm or 200 mm at a charge mass of 10 g 138
9.26 Projected total delaminated area for the 120° GFRP V-structure simulations with the two fibre orientations with V-tip radii of 62 mm or 200 mm at a charge mass of 15 g 138
9.27 Projected delaminated area versus V-angle for the GFRP V-structure simulations with a 0°/90° fibre orientation 139
9.28 Projected delaminated area versus V-angle for the GFRP V-structure simulations with a ±45° fibre orientation 139
9.29 Projected total delaminated area for the 105° and 120° GFRP V-structure simulations with a 200 mm V-tip radius and a ±45° fibre orientation and charge masses of 15 g and 20 g 139
9.30 Projected delaminated area versus V-tip radius for the 105° GFRP V-structure simulations with a 0°/90° fibre orientation 140
9.31 Projected delaminated area versus V-tip radius for the 120° GFRP V-structure simulations with a 0°/90° fibre orientation 140
9.32 Peak mid-point displacement versus fibre orientation for the 105° GFRP V-structure simulations 141
9.33 Peak mid-point displacement versus fibre orientation for the 120° GFRP V-structure simulations 141
9.34 Mid-point displacement time history for the 105° GFRP V-structure with 34 mm and 200 mm V-tip radii simulated at a charge mass of 10 g with the two fibre orientations 142
9.35 Peak transient ridge profiles for the 105° GFRP V-structure with 34 mm and 100 mm V-tip radii simulated at a charge mass of 10 g with the two fibre orientations 143
9.36 Peak mid-point displacement versus V-angle for the GFRP V-structures with a 0°/90° fibre orientation 143
9.37 Mid-point displacement time histories for 105° and 120° GFRP V-structure simulations with a 0°/90° fibre orientation and a 34 mm V-tip radius simulated at a charge mass of 10 g 144

9.38 Peak mid-point displacement versus V-tip radius for the 105° GFRP V-structures with a 0°/90° fibre orientation 144
9.39 Mid-point displacement time histories for 105° GFRP V-structure simulations with a 0°/90° fibre orientation simulated at a charge mass of 10 g 145
9.40 Peak transient ridge profiles for 105° GFRP V-structure simulations with a 0°/90° fibre orientation simulated at a charge mass of 10 g 145
10.1 Cumulative impulse and mid-point deflection for the 105° DOMEX-700 MC and GFRP V-structure simulations with 32 mm and 200 mm V-tip radii simulated at a charge mass of 20 g 149
10.2 Transient ridge profiles for the 105° DOMEX-700 MC and GFRP V-structure simulations with 32 mm and 200 mm V-tip radii simulated at a charge mass of 20 g 150
10.3 Plots of the permanent ridge profiles for increasing V-tip radii for the 105° DOMEX-700 MC V-structure simulations at a charge mass of 15 g 152
10.4 Plots of the permanent ridge profiles for increasing V-tip radii for the 105° DOMEX-700 MC V-structure simulations at a charge mass of 20 g 152
10.5 Projected total delaminated area for the 0°/90°, 105° GFRP V-structure simulations with increasing V-tip radii for a charge mass of 15 g 152
10.6 Projected total delaminated area for the 0°/90°, 105° GFRP V-structure simulations with increasing V-tip radii for a charge mass of 20 g 153
B.1 3D Profiles of the 105°, 32 mm V-tip radius DOMEX-700 MC V-structures tested at a SOD of 50 mm B-1
B.2 3D Profiles of the 105°, 62 mm V-tip radius DOMEX-700 MC V-structures tested at a SOD of 34 mm B-2
B.3 3D Profiles of the 120°, 32 mm V-tip radius DOMEX-700 MC V-structures tested at a SOD of 34 mm B-2
B.4 The ridge profiles for a 105°, 32 mm V-tip radius DOMEX-700 MC V-structure tested with a 15 g PE4 charge at a SOD of 34 mm B-3
B.5 The ridge profiles for a 105°, 32 mm V-tip radius DOMEX-700 MC V-structure tested with a 20 g PE4 charge at a SOD of 34 mm B-4
B.6 The ridge profiles for a 105°, 62 mm V-tip radius DOMEX-700 MC V-structure tested with a 10 g PE4 charge at a SOD of 34 mm B-4
B.7 The ridge profiles for a 120°, 32 mm V-tip radius DOMEX-700 MC V-structure tested with a 15 g PE4 charge at a SOD of 34 mm B-4
C.1 Photographs of a sectioned GFRP V-structure (105°, 34 mm V-tip radius, 0°/90° ply orientation) tested at an charge mass of 10 g with a SOD of 34 mm C-1
C.2 Photographs of a sectioned GFRP V-structure (105°, 34 mm V-tip radius, ±45° ply orientation) tested at an charge mass of 15 g with a SOD of 34 mm C-2
D.1 Permanently deformed ridge profiles for a 105° 32 mm V-tip radius DOMEX-700 MC V-structure at a charge mass of 10 g (numerical versus experimental) D-1
D.2 Permanently deformed ridge profiles for a 105° 32 mm V-tip radius DOMEX-700 MC V-structure at a charge mass of 20 g (numerical versus experimental) D-1

D.3 Permanently deformed ridge profiles for a 105° 62 mm V-tip radius DOMEX-700 MC V-structure at a charge mass of 10 g (numerical versus experimental) D-2
D.4 Permanently deformed ridge profiles for a 105° 62 mm V-tip radius DOMEX-700 MC V-structure at a charge mass of 15 g (numerical versus experimental) D-2
D.5 Permanently deformed ridge profiles for a 120° 32 mm V-tip radius DOMEX-700 MC V-structure at a charge mass of 10 g (numerical versus experimental) D-2
D.6 Permanently deformed ridge profiles for a 120° 32 mm V-tip radius DOMEX-700 MC V-structure at a charge mass of 15 g (numerical versus experimental) D-2
D.7 Permanently deformed crosscut profiles for a 105° 32 mm V-tip radius DOMEX-700 MC V-structure at a charge mass of 15 g (numerical versus experimental) D-3
D.8 Permanently deformed crosscut profiles for a 105° 32 mm V-tip radius DOMEX-700 MC V-structure at a charge mass of 20 g (numerical versus experimental) D-3
D.9 Permanently deformed crosscut profiles for a 105° 62 mm V-tip radius DOMEX-700 MC V-structure at a charge mass of 10 g (numerical versus experimental) D-3
D.10 Permanently deformed crosscut profiles for a 105° 62 mm V-tip radius DOMEX-700 MC V-structure at a charge mass of 15 g (numerical versus experimental) D-4
D.11 Permanently deformed crosscut profiles for a 120° 32 mm V-tip radius DOMEX-700 MC V-structure at a charge mass of 10 g (numerical versus experimental) D-4
D.12 Permanently deformed crosscut profiles for a 120° 32 mm V-tip radius DOMEX-700 MC V-structure at a charge mass of 20 g (numerical versus experimental) D-4
D.13 Mid-point deflection time history for a 105° 32 mm V-tip radius DOMEX-700 MC V-structure at a charge mass of 10 g (numerical versus experimental) D-5
D.14 Mid-point deflection time history for a 105° 32 mm V-tip radius DOMEX-700 MC V-structure at a charge mass of 15 g (numerical versus experimental) D-5
D.15 Mid-point deflection time history for a 105° 62 mm V-tip radius DOMEX-700 MC V-structure at a charge mass of 10 g (numerical versus experimental) D-6
D.16 Mid-point deflection time history for a 105° 62 mm V-tip radius DOMEX-700 MC V-structure at a charge mass of 20 g (numerical versus experimental) D-6
D.17 Mid-point deflection time history for a 120° 32 mm V-tip radius DOMEX-700 MC V-structure at a charge mass of 10 g (numerical versus experimental) D-6
D.18 Mid-point deflection time histories for increasing V-tip radii for the 90° DOMEX-700 MC V-structure simulations at a charge mass of 10 g D-8
D.19 Mid-point deflection time histories for increasing V-tip radii for the 90° DOMEX-700 MC V-structure simulations at a charge mass of 20 g D-9
D.20 Mid-point deflection time histories for increasing V-tip radii for the 105° DOMEX-700 MC V-structure simulations at a charge mass of 10 g D-9
D.21 Mid-point deflection time histories for increasing V-tip radii for the 105° DOMEX-700 MC V-structure simulations at a charge mass of 20 g D-10
D.22 Mid-point deflection time histories for increasing V-tip radii for the 120° DOMEX-700 MC V-structure simulations at a charge mass of 15 g D-10
D.23 Permanently deformed ridge profiles for increasing V-tip radii for the 90° DOMEX-700 MC V-structure simulation at a charge mass of 10 g D-11

D.24 Permanently deformed ridge profiles for increasing V-tip radii for the 90° DOMEX-700 MC V-structure simulation at a charge mass of 20 g D-11
D.25 Permanently deformed ridge profiles for increasing V-tip radii for the 105° DOMEX-700 MC V-structure simulation at a charge mass of 15 g D-11
D.26 Permanently deformed ridge profiles for increasing V-tip radii for the 105° DOMEX-700 MC V-structure simulation at a charge mass of 20 g D-12
D.27 Permanently deformed ridge profiles for increasing V-tip radii for the 120° DOMEX-700 MC V-structure simulation at a charge mass of 10 g D-12
D.28 Permanently deformed ridge profiles for increasing V-tip radii for the 120° DOMEX-700 MC V-structure simulation at a charge mass of 15 g D-12
D.29 Permanently deformed crosscut profiles for increasing V-tip radii for the 90° DOMEX-700 MC V-structure simulation at a charge mass of 10 g D-13
D.30 Permanently deformed crosscut profiles for increasing V-tip radii for the 90° DOMEX-700 MC V-structure simulation at a charge mass of 20 g D-13
D.31 Permanently deformed crosscut profiles for increasing V-tip radii for the 105° DOMEX-700 MC V-structure simulation at a charge mass of 10 g D-14
D.32 Permanently deformed crosscut profiles for increasing V-tip radii for the 105° DOMEX-700 MC V-structure simulation at a charge mass of 20 g D-14
D.33 Permanently deformed crosscut profiles for increasing V-tip radii for the 120° DOMEX-700 MC V-structure simulation at a charge mass of 10 g D-14
D.34 Permanently deformed crosscut profiles for increasing V-tip radii for the 120° DOMEX-700 MC V-structure simulation at a charge mass of 20 g D-15
D.35 Mid-point deflection time histories versus the V-angle for a V-tip radius of 62 mm at all three charge masses investigated D-15
D.36 Mid-point deflection time histories versus the V-angle for a V-tip radius of 100 mm at all three charge masses investigated D-16
D.37 Permanently deformed ridge profiles versus the V-angle for a V-tip radius of 62 mm at all three charge masses investigated D-16
D.38 Permanently deformed ridge profiles versus the V-angle for a V-tip radius of 200 mm at all three charge masses investigated D-17
D.39 Permanently deformed crosscut profiles versus the V-angle for a V-tip radius of 32 mm at a charge mass of 10 g D-17
D.40 Permanently deformed crosscut profiles versus the V-angle for a V-tip radius of 32 mm at a charge mass of 20 g D-18
D.41 Permanently deformed crosscut profiles versus the V-angle for a V-tip radius of 62 mm at a charge mass of 10 g D-18
D.42 Permanently deformed crosscut profiles versus the V-angle for a V-tip radius of 62 mm at a charge mass of 15 g D-19
D.43 Permanently deformed crosscut profiles versus the V-angle for a V-tip radius of 62 mm at a charge mass of 20 g D-19
D.44 Permanently deformed crosscut profiles versus the V-angle for a V-tip radius of 100 mm at a charge mass of 10 g D-20

D.45 Permanently deformed crosscut profiles versus the V-angle for a V-tip radius of 100 mm at a charge mass of 15 g D-20
D.46 Permanently deformed crosscut profiles versus the V-angle for a V-tip radius of 100 mm at a charge mass of 20 g D-20
D.47 Permanently deformed crosscut profiles versus the V-angle for a V-tip radius of 200 mm at a charge mass of 10 g D-21
D.48 Permanently deformed crosscut profiles versus the V-angle for a V-tip radius of 200 mm at a charge mass of 15 g D-21
E.1 Numerical simulations with increasing amounts of damping and the experimental results for the transient response at the 50 mm point along the ridge line for a 105° 34 mm V-tip radius GFRP V-structure with a ±45° fibre orientation at a charge mass of 15 g E-1
E.2 Simulated impulse versus V-angle for the GFRP V-structures with a ±45° fibre orientation E-2
E.3 Simulated impulse versus V-tip radius for the 105° GFRP V-structures with a ±45° fibre orientation E-3
E.4 Simulated impulse versus V-tip radius for the 120° GFRP V-structures with a ±45° fibre orientation E-3
E.5 Projected delaminated area versus V-tip radius for the 105° GFRP V-structures with a ±45° fibre orientation E-4
E.6 Projected delaminated area versus V-tip radius for the 120° GFRP V-structures with a ±45° fibre orientation E-4
E.7 Projected total delaminated area for the 0°/90° 105° GFRP V-structure simulations for a charge mass of 10 g E-5
E.8 Projected total delaminated area for the 0°/90° 105° GFRP V-structure simulations for a charge mass of 15 g E-6
E.9 Projected total delaminated area for the ±45° 105° GFRP V-structure simulations for a charge mass of 10 g E-6
E.10 Projected total delaminated area for the ±45° 105° GFRP V-structure simulations for a charge mass of 15 g E-7
E.11 Projected total delaminated area for the 0°/90° 120° GFRP V-structure simulations for a charge mass of 10 g E-8
E.12 Projected total delaminated area for the 0°/90° 120° GFRP V-structure simulations for a charge mass of 15 g E-8
E.13 Projected total delaminated area for the ±45° 120° GFRP V-structure simulations for a charge mass of 10 g E-9
E.14 Projected total delaminated area for the ±45° 120° GFRP V-structure simulations for a charge mass of 15 g E-9
E.15 Mid-point displacement time history for the 105° GFRP V-structure with 34 mm and a 200 mm V-tip radii simulated at a charge mass of 20 g with the two fibre orientations E-10

E.16 Peak mid-point displacement versus V-angle for the GFRP V-structures with a ±45° fibre orientation E-11
E.17 Mid-point displacement time histories for 105° and 120° GFRP V-structure simulations with a 0°/90° fibre orientation and a 100 mm simulated at a charge mass of 10 g E-11
E.18 Mid-point displacement time histories for 105° and 120° GFRP V-structure simulations with a 0°/90° fibre orientation and a 200 mm simulated at a charge mass of 10 g E-12
E.19 Peak transient ridge profiles for 105° and 120° GFRP V-structure simulations with a 0°/90° fibre orientation and a 34 mm simulated at a charge mass of 10 g E-12
E.20 Peak transient ridge profiles for 105° and 120° GFRP V-structure simulations with a 0°/90° fibre orientation and a 100 mm simulated at a charge mass of 10 g E-12
E.21 Peak mid-point displacement versus V-tip radius for the 105° GFRP V-structures with a ±45° fibre orientation E-13
E.22 Peak mid-point displacement versus V-tip radius for the 120° GFRP V-structures with a 0°/90° fibre orientation E-13
E.23 Peak mid-point displacement versus V-tip radius for the 120° GFRP V-structures with a ±45° fibre orientation E-13
E.24 Mid-point displacement time histories for 105° GFRP V-structure simulations with a 0°/90° fibre orientation simulated at a charge mass of 15 g E-14
E.25 Mid-point displacement time histories for 120° GFRP V-structure simulations with a 0°/90° fibre orientation simulated at a charge mass of 10 g E-14
E.26 Mid-point displacement time histories for 120° GFRP V-structure simulations with a 0°/90° fibre orientation simulated at a charge mass of 15 g E-15
E.27 Peak transient ridge profiles for 105° GFRP V-structure simulations with a 0°/90° fibre orientation simulated at a charge mass of 15 g E-15
E.28 Peak transient ridge profiles for 120° GFRP V-structure simulations with a 0°/90° fibre orientation simulated at a charge mass of 10 g E-15
E.29 Peak transient ridge profiles for 120° GFRP V-structure simulations with a 0°/90° fibre orientation simulated at a charge mass of 15 g E-16

List of acronyms and abbreviations

ALE	Arbitrary Lagrangian-Eulerian
AP-mine	Anti-Personnel mine
APC	Armoured Personnel Carrier
AT-mine	Anti-Tank mine
BISRU	Blast Impact and Survivability Research Unit
CAD	Computer-Aided Design
CET	Controlled Explosive Tube
CFRP	Carbon-Fibre Reinforced Polymer
CMC	Ceramic Matrix Composite
CNC	Computer Numerical Control
CODAM	Composite Damage Model
CZE	Cohesive Zone Element
DCB	Double Cantilever Beam
DIC	Digital Image Correlation
DMC	Dough Moulding Compound
DOB	Depth of Burial
DRU	Defence Research Unit
EOS	Equation of State
FEA	Finite Element Analysis
FRP	Fibre Reinforced Polymer
FSI	Fluid-Structure Interaction
GFRP	Glass-Fibre Reinforced Polymer
IED	Improvised Explosive Device
JWL	Jones-Wilkins-Lee
LBE	LOAD BLAST ENHANCED
LCM	Liquid Composite Moulding
LV	Low Viscosity
MBT	Modified Beam Theory
MMALE	Multi-Material Arbitrary Lagrangian-Eulerian
MMC	Metal Matrix Composite
MRAP	Mine-Resistant Ambush Protected vehicle
PE4	Plastic Explosive No. 4
PETN	Pentaerythritol Tetranitrate
RHT	Riedel–Hiermaier–Thoma
RTM	Resin Transfer Moulding
SCRIMP	Seaman Composite Resin Infusion Moulding Process
SMC	Sheet Moulding Compound

SOD	Stand-Off Distance
SPH	Smooth Particle Hydrodynamics
TNT	Trinitrotoluene
VARTM	Vacuum Assisted Resin Transfer Moulding
VI	Vacuum Infusion
WWI	World War I
WWII	World War II

Chapter 1

Introduction

1.1 Background and problem definition

Since the earliest days of war, soldiers and other military personnel have needed to be transported in combat zones. Once motorised transportation was developed, this was done with vehicles that used a standard car and truck chassis. The earliest example of a V-hulled Mine-Resistant Ambush Protected vehicles (MRAPs) dates back to World War II (WWII) with the Swedish SKPF/VKPF M/42 [1] shown in figure 1.1. These vehicles were developed to counter the threat of landmine explosions by deflecting the blast pressure wave around from the crew compartment and thus reducing the impulse imparted to the occupants and lowering the deformation of the floor. While landmines had been used in warfare since the 16th century, there was a marked increase in their usage during World War I (WWI) to combat the threat of tanks [2]. An additional threat from Improvised Explosive Devices (IEDs) to military personnel has been seen in the last two decades during the Afghanistan and Iraq wars [3]. Landmines and other forms of buried or unburied IEDs usually lead to the generation of a blast wave and also to the projection of primary and secondary fragments although this is outside the scope of the study.



Figure 1.1: Photograph of an SKPF/VKPF M/42 Armoured Personnel Carrier (APC) developed during WWII by the Swedes [4]

The early V-hulled MRAPs were developed using a standard vehicle chassis and suspension arrangement, onto which a V-hull was attached. While this reduced the cost of design and manufacture, the increase in mass affected the stability and speed of the MRAP. Later V-hulled

MRAPs utilised a monocoque chassis [5], which allowed many critical components to be moved inside the V-hull resulting in better protection in the event of a landmine explosion [5]. This approach did come with an increase in the design and manufacturing costs due to the customised layout of the chassis. Various grades of steel have been used to manufacture the V-hulls on MRAPs due to its low cost, availability, and decent ballistic protection [6]. To achieve the desired armour protection the plate thickness needed to be sufficiently large resulting in a significant increase in the total mass of the MRAP. This compromised mobility and decreased fuel efficiency which reduced its range [6]. In order to reduce the mass of these MRAPs and still retain the same levels of armament, it is necessary to change either the design of the MRAP hull or the materials used to construct the V-hull.

Fibre Reinforced Polymers (FRPs) have been extensively used in the automotive, aerospace and maritime industries due to their high strength-to-weight ratios, good corrosion resistance and design variability [6], but they have seen limited use on military personnel carriers due to incompatibilities with the existing processes used to manufacture MRAPs [6]. Glass fibres have a higher tensile strength and a lower stiffness than steel [7]; this suggests that FRP V-hulls will deform elastically prior to fibre fracture. FRPs are usually lighter than steel, which would aid in the mass reduction of the MRAP and thus improve performance, which is critical in a combat zone environment. One limitation of FRP V-hulls is that it is not possible to manufacture them with as tight a radius at the V-tip as the equivalent steel V-hulls. This might affect the ability of the structure to deflect the blast wave from a landmine or IED. Although, at the scale of a full-sized MRAP this manufacturing challenge is less likely to be significant.

The key terms used in the description of V-structures in this study are shown in figure 1.2 with labels for the V-angle, V-tip, bend radius and panel height. Previous research has been done on the blast response of steel V-structures subjected to air blasts. One of these studies looked at the effects of varying the V-angle on the mid-point deflection and impulse of DOMEX-700 MC steel V-structures [8]. It was found that decreasing the V-angle reduced the impulse transferred and lowered the permanent deflection of the V-structures but would result in an increase in the ride height of the MRAP. A few limited experiments were reported on composite V-structures by Follett [9]. The composite V-structures experienced smaller permanent deflections than the steel V-structures, although all the composites exhibited delamination, fibre failure and matrix failure on the outer surface and delamination on the inner surface [9]. No impulse transfer data was reported in the study. Due to the limited number of experiments in this study, it was not possible to draw conclusions on the performance of these V-structures compared to the equivalent mass and geometry steel counterparts. Langdon and Shekhar [10] showed using a validated numerical model on rigid V-structures that the V-tip radius, and by extension, the geometry of the V-structure was critical in controlling the impulse transferred to the V-structure.

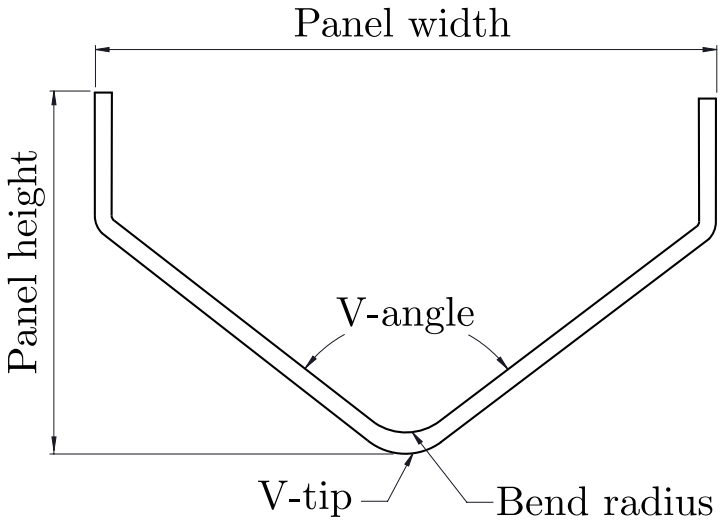

Figure 1.2: Side profile of a V-structure showing the V-tip, tip radius, V-angle and plate height

Looking at the existing body of research, it is necessary to manufacture and test a sufficiently large range of steel and GFRP V-structures with equivalent mass and geometry to characterise their blast response characteristics. Furthermore, due to the high costs of blast test experiments, it is necessary to develop numerical blast models for both the steel and GFRP V-structures. These models will allow trends in impulse, transient and permanent deformation, and deformation profiles to be determined for a range of V-structure geometries and blast loading conditions. Additionally, it is necessary to ensure that the GFRP V-structures can be manufactured with consistent V-tip radii to ensure that the deformation and impulse transferred can be accurately compared with their steel counterparts. Finally, while the effect of the V-tip radius has been studied for rigid V-structures, it has not been investigated for deformable steel and GFRP V-structures. Investigation of these effects will increase the insight into the behaviour of these V-structures with varying geometry and potentially aid in the design of V-hulled MRAPs.

1.2 Research questions

The research questions to be answered in this thesis are listed below:

1. Can GFRPs be used in place of steel in the construction of V-structures without altering the protection of the V-structures?
2. What effect does the V-tip geometry (V-angle and V-tip radius) have on impulse transfer and structural damage characteristics of GFRP and equivalent mass DOMEX-700 MC steel V-structures?
3. How does charge mass influence impulse transfer, transient deformation and damage progression in air-blast tested GFRP and equivalent mass DOMEX-700 MC steel V-structures?

1.3 Hypothesis

GFRP V-structures have a superior blast performance when compared to equivalent mass armoured steel V-structures, measured in terms of impulse transfer and structural response, for a range of air-blast loading scenarios.

1.4 Thesis overview

A literature review is provided in the Chapter 2. This includes a brief history of landmines and MRAPs, followed by a description of composite materials and the manufacture of Fibre Reinforced Polymers (FRPs). Finally, a selection of previous experimental and numerical studies performed on steel and GFRP panels with different geometries are discussed. The manufacturing of the steel and GFRP V-structures is presented next in Chapter 3. This includes the chosen V-structure geometries and the advantages and limitations of the chosen manufacturing methods.

The remaining chapters discuss the results of the various experimental testing and numerical simulations performed as part of the study. The quasistatic materials testing of steel and GFRP specimens is presented in Chapter 4. These tests were performed to gain insight into the material properties that are needed for the numerical blast models and as a check for consistency in the materials and manufacturing methods used in this study. Chapters 5 to 7 describe the design of the blast test experiments and then present and discuss the blast test results for the steel and GFRP V-structures. Included in these chapters are details of the impulse measurements, permanent deformation and damage, and the transient deformation behaviour of the V-structures. The numerical blast simulations performed on the steel and GFRP V-structures are presented in Chapters 8 and 9. These chapters start with the validation of the models with experimental results and then investigate trends in the blast performance of the V-structures when the design parameters are varied. Finally, the results of the steel and GFRP V-structures are compared with one another in Chapter 10 before the conclusions of the research and recommendations for future studies are presented in Chapter 11.

Chapter 2

Literature review

This literature review begins with a short background on landmines and APCs and aims to provide an explanation for the potential benefits of using a FRP composite V-hull on APCs. This is followed by a description of what constitutes a FRP composite material and the various manufacturing techniques available to produce these V-structures from FRPs. Next, a review of previous studies performed on steel and FRP structures subjected to localised air-blast loads is presented. A description of the techniques used to measure the transient deformation of blast loaded structures is then provided. Lastly, the published literature on the numerical modelling of blast loaded structures is detailed.

2.1 History of Armoured Personnel Carriers and landmines

Landmines can be defined as explosive devices that are either placed in the ground or fixed to objects above ground [11] and which detonate or explode when in proximity to their intended target, whether that is a person or a vehicle [12]. Landmines have been used as a means of attack since the 16th century when troops would tunnel under the position of their enemies and detonate explosives [1], while the first pressure-sensitive landmine was used during the Crimean War in the 1850s [13]. This design was copied and reused during the American Civil War and this fuse design is still in use today [13]. Landmines became an integral part of military strategy at the end of World War I (WWI) to combat the first battle tanks [2]. It is estimated that there are around 84 million landmines still buried underground, while between 2 and 5 million landmines are planted each year [12]. Additionally, approximately 12000 individuals are injured or killed each year from a landmine detonation [12].

A landmine usually contains an amount of explosive enclosed in a casing made from wood, metal or plastic and a trigger mechanism which allows the charge to be detonated [11]. Landmines can be split into two categories [12] based on the mass of explosives used and their intended target. These are Anti-Personnel mines (AP-mines) which are designed to target people and Anti-Tank mines (AT-mines) which target tanks or other armoured vehicles [14]. AP-mines can be further categorised based on their method of injury [11]. These categories are blast, fragmentation, bounding fragmentation and directional fragmentation [11, 14]. Blast mines are typically small in size and use the effect of the blast to injure the target, while fragmentation mines use the shock wave and its transmission of impulse to the fragments to propel them into the target. This increases the area of the target structure damaged in the explosion [14]. As AT-mines were developed to counter the threat of assault tanks, they are larger (and hence contain more explosive) than AP-mines [11]. An AT-mine typically contains 2 kg to 9 kg of explosive and requires a pressure of 100 kg to 300 kg to be triggered, while an AP-mine contains 10 g to 250 g

of explosives and requires a pressure of 5 kg to 50 kg to detonate [12]. While landmines are still being deployed, IEDs are becoming a more widespread threat, most notably in the recent conflicts in Iraq and Afghanistan [15]. An IED is a low-technology, home-made explosive mine, that uses either commercial or military grade explosives and is usually remotely triggered [3]. Occupants of MRAPs subjected to landmine blasts have been found to experience accelerations of up to 670 km s^{-2} [16] with injuries including fractures in the spine, feet, and elbows [17]. The reported maximum forces were found to be around 3.5 kN in the tibia and 2 kN in the spine [18]. Additional studies found that the use of a double V-hull can reduce the peak force experienced in the tibia [19], however this was not investigated as part of this study.

APCs are not a recent invention and have been used in conflicts for many centuries as a means of transporting troops onto the battlefield [20]. The development of armoured vehicles increased rapidly upon the invention of the internal combustion engine. The first major development of the APC happened at the end of World War I when the British Army commissioned an armoured vehicle based on an assault tank [20]. MRAPs are a type of APC that utilise a V-hull or armour plating to protect its occupants from exploding landmines and IEDs. V-hulled APCs have been around since the end of WWII, although the USA only started major development of MRAPs in 2006, due to the threat of IEDs [21].

Shneck [5] summarised the development of MRAPs into four categories based on the armour used and how the vehicle was designed:

- Generation 1 - Improvised kits manufactured in the field by soldiers
- Generation 2 - Kits designed and manufactured for field installation
- Generation 3 - Vehicles that use a standard chassis, onto which a mine-resistant hull was mounted
- Generation 4 - Vehicles which use a monocoque chassis which incorporated the mine-resistant hull

The SKPF/VKPF M/42 APC first used in 1944 is the earliest example of a third generation MRAP and incorporated a V-shaped hull [1], which deflected the blast wave outwards and away from the crew compartment. During the Rhodesian Bush War, there was a significant increase in the development of landmine protected APCs due to the large scale use of AT-mines as a means of attack by the guerrilla soldiers [1]. A substantial amount of development was done by the South African Defence Research Unit (DRU), who developed the Camel, which was based on a Ford F-250 chassis [1]. It had a V-shaped hull with a sharp V-angle of 43° that meant that these vehicles had a tendency to topple over, due to the high centre of gravity, while also limiting the space inside the crew compartment for personnel or equipment [1]. Pakulski *et al.* [22] found that 56% of the total accident costs from MRAP accidents came from rollovers. While these third generation MRAPs provided good protection for troops and had lower manufacturing costs, they suffered from reduced performance in the field, due to the greater mass of the vehicles [5].

Generation 4 MRAPs had excellent mine resistance and performance [20], as it was possible to move critical components inside the V-hull for better protection from a landmine or IED

explosion [1]. The main drawback of these vehicles was a greater cost of manufacture due to the custom nature of their designs [1]. The South African Casspir APC, shown in figure 2.1, was developed in 1979 and had a shallower V-angle of approximately 95° which reduced the centre of gravity and hence improved the performance of the vehicle [1]. Further development (Armour plating and engine) of the Casspir has since been performed by the DRU, although the basic design remained the same. Ramasamy *et al.* [23] investigated the effect of different modifications to the design of landmine protected vehicles on the blast protection offered by these vehicles using data from the Rhodesian bush war. In total, seventeen vehicles used during the Rhodesian war were investigated and some of the key metrics studied included the effect of the V-shaped hull, the ground clearance and the vehicle mass. Ramasamy *et al.* [23] found that all modifications resulted in a reduction of the occupants killed, while the V-shaped hull and vehicle ground clearance also resulted in a reduction in the number of vehicle occupants injured by the blast. These findings confirm the benefits of using a V-shaped hull on landmine protected vehicles as a simple way to improve their blast protection characteristics.



Figure 2.1: Photograph of a Casspir V-hulled APC [24]

In more recent years there has been an increase in the number of APCs utilising composite materials for armour protection due to their high strength-to-weight ratios [6]. The Navistar International MaxxPro was developed in 2007 and is one of the most used MRAPs by the US Army [21]. The composite armour used was bolted together to allow for easy maintenance [21]. Another MRAP that utilises composite armour is the BAE Caiman which was also developed in 2007 [21]. The BAE Caiman Light was also developed soon after and was significantly lighter than the full-sized Caiman while retaining similar blast and ballistic protection [21]. Both the Caiman and the MaxxPro utilise V-shaped hulls, although these hulls are manufactured from armoured steel, while the composite armour is simply attached to the body [21]. The MaxxPro and the Caiman have a gross mass of 19.73 t and 22.96 t respectively, with a maximum speed

of 104 km h^{-1} [21]. This means that they actually weigh significantly more and only have a slightly improved top speed compared to the Casspir APC, which has a mass of 12.58 t and a top speed of 90 km h^{-1} [25]. Additionally, the Casspir is capable of withstanding a blast from a TM-57 landmine (which contains 14 kg of TNT) [8] while the BAE Caiman is only capable of withstanding a 13 kg TNT equivalent blast [21]. This suggests that there is a need to perform experiments and further develop FRP composite V-hulls for APCs.

2.2 Composite materials

A composite can be defined as a material that is manufactured from at least two constituent materials [26–28]. The resulting composite material has more useful properties than the constituent materials [26, 28], while the constituent materials used are typically insoluble in one another [26]. Unlike metallic alloys, composites are inherently heterogeneous, with the constituent materials retaining their respective chemical and mechanical properties [28].

Composites normally contain some type of reinforcement, which may be particles, flakes or fibres, embedded in a softer material or matrix [27, 28]. Three examples of such composites are shown in figure 2.2. Particulate reinforcements include aluminium particles and silicon carbide particles, while typical examples of flake materials include glass, aluminium and silver [29]. Typical fibre reinforcement materials include glass, aramids, carbon, and boron fibres [30]. The matrix is usually polymer based, although ceramics and metals are also used [27].

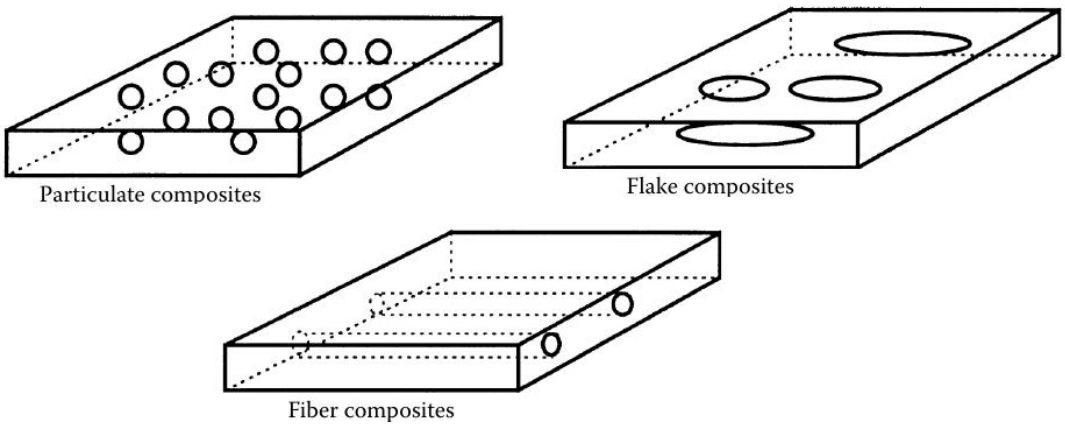

Figure 2.2: Schematic of three different reinforcements, *i.e.* particles, flakes and fibres [29]

Particulate composites are usually considered to be generally isotropic due to the random distribution of the particles in the matrix, although they tend to be weaker than continuous fibre composites [28]. Particulate composites are often less expensive to manufacture than fibre composites but contain a smaller percentage of reinforcement [28]. Flake composites have the additional benefit of a higher flexural modulus compared to particulate composites, making them more resistant to bending stresses [29]. Flake composites are also cheaper than fibre composites but can be challenging to manufacture due to difficulties in orientating the flakes in the matrix [29].

Fibre composites can be classed as either fibre-reinforced or fabric-reinforced composites [26].

Fibre-reinforced composites can be further categorised based on whether the fibres are continuous or discontinuous [26, 28]. Examples of each type of fibre are shown in figure 2.3. Continuous fibres have long aspect ratios and a preferred orientation, resulting in anisotropic mechanical properties [29]. However, discontinuous fibres have a short aspect ratio and a random orientation, which results in reduced strength and stiffness but more isotropic properties [28]. Unidirectional and helically wound fibres are examples of continuous fibre reinforcements, while whiskers and chopped fibres are examples of discontinuous fibre reinforcements [26]. Fabric-reinforced composites are made using long continuous fibres that are braided, woven or knitted [26].

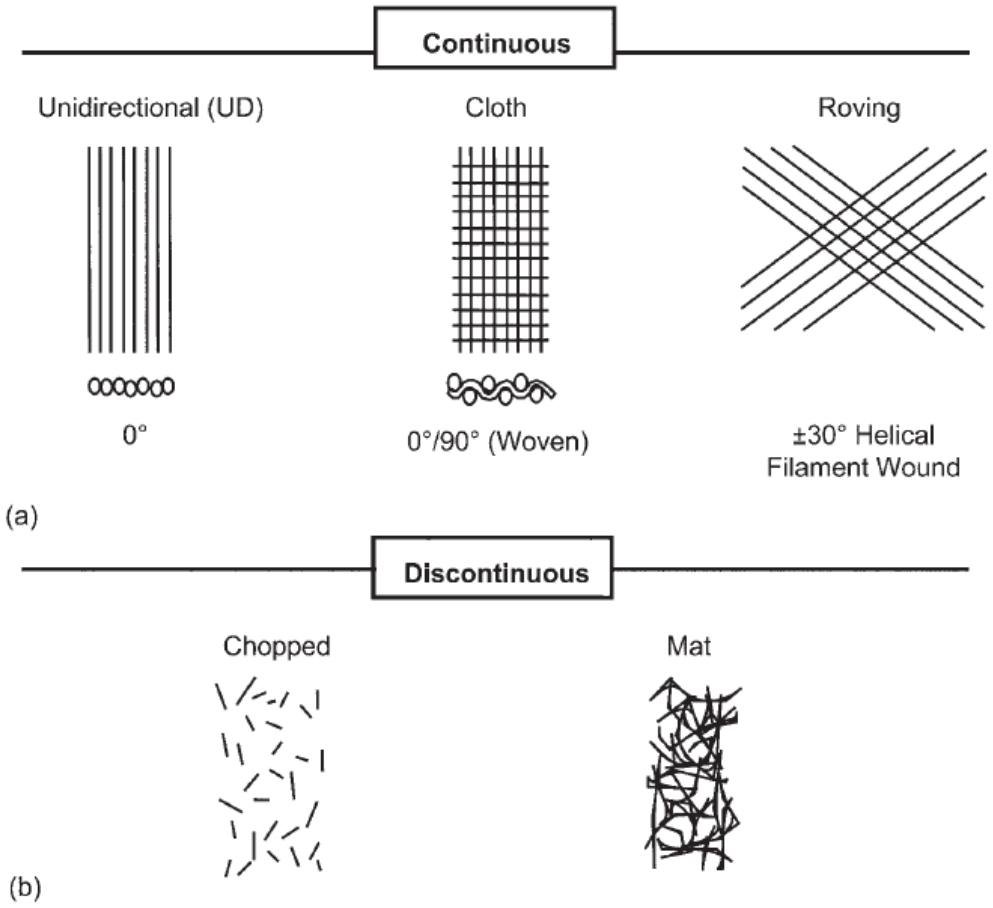

Figure 2.3: Schematic showing the differences between continuous and discontinuous fibres [28]

The matrix used in a particular composite must be chosen such that it has good adhesion with the reinforcement used. Additionally, it must have a sufficient stiffness that results in the load being distributed uniformly across the reinforcements [31]. The functions of the matrix are to hold the reinforcements in their correct orientation, to distribute the load to them and to protect the fibres from corrosion and the environment [31]. Polymer matrices are very common and can be broadly classed as either thermoset or thermoplastic. Thermoset polymers are polymers that form an insoluble and infusible solid when cured, with strong covalent bonds between the polymer chains [26, 29]. Thermoplastic polymers can be repeatedly softened using high temperatures and pressures and then reshaped using moulds or via extrusion [26, 29]. Unlike

thermoplastics, thermoset polymers cannot be reheated and reshaped due to the strong covalent bonds [29]. Examples of thermoset polymers include epoxies and polyesters while polypropylene and nylon are examples of thermoplastics [29, 31].

Fibre reinforced polymers are popular because they are relatively simple to manufacture, with high strength at relatively low cost [29]. One drawback of FRPs is their low resistance at high temperatures [31]. Metal matrices cost significantly more than polymer matrices as they need very high temperatures and pressures for processing [28, 29], although metal matrix composites (MMCs) have several advantages over FRPs. These include higher operating temperatures, better wear and fatigue resistance and higher strength and elastic stiffness [27, 29]. Typical examples of metal matrices include aluminium and titanium [29]. Similarly to metal matrices, ceramic matrices also require high temperatures and pressures for processing [28] and ceramic matrix composites (CMCs) have even higher strength and temperature resistance than MMCs, meaning that they often find use as cutting tool inserts [29]. Alumina and Calcium Alumino Silicate are typical examples of ceramic matrices [29].

Many composites are described as anisotropic. An anisotropic material is one that has different mechanical properties in all directions at a point [28]. More specifically, there are 21 independent elastic constants at a point in the 3D stiffness matrix [29]. Single lamina continuous fibre-reinforced composites are a special example of anisotropic materials, called orthotropic materials [28, 29]. A lamina is a special class of composite that is made up of one or more adjacent plies that have the same orientation and are made of the same material [26]. These materials have three mutually perpendicular planes of material symmetry, which means that loads applied in any of these three directions produce only normal strains [28, 29].

Unidirectional laminae are strong in the direction of the fibres but are very weak in the perpendicular directions as the load is taken up by the significantly weaker matrix [28]. One method to improve the strength properties in other directions is to create a laminate. When laminae are stacked in different orientations, the resulting composite is referred to as a laminate [26, 29]. The stack of plies in a particular sequence and orientation is referred to as the lay-up [26]. Each layer is identified by its location, its material and angle of orientation with respect to a reference axis [29]. A lay-up code can then be given for the composite, which is an abbreviation of the stacking sequence [26]. If the plies above and below the mid-surface are mirror images of one another, the laminate is referred to as symmetric [29]. A balanced laminate is one that contains an equal number of plies with an angle of plus and minus theta, where theta is the acute angle with respect to the reference direction [26]. If a laminate is both balanced and symmetric, then it is said to be quasi-isotropic and display near isotropic behaviour in the plane of the laminate [26].

Composites have seen limited use on MRAPs due to incompatibilities with the existing processes used to design and manufacture them with metal V-hulls [6]. One major advantage of FRPs for V-hull design is that they should be lighter than steel V-hulls. This reduction of mass would result in an improvement in the performance and mobility of the MRAPs. Finally, there have been improvements in the strength and impact resistance of composites which has resulted in an increase in their potential for use in V-hulls [6].

2.3 Manufacturing Fibre Reinforced Polymers (FRPs)

There are a number of different ways to manufacture FRP composite laminates. The method used for the manufacture of a composite is based on the type of FRP, the quality required, the allowable cost and the number of parts to be made. The manufacturing methods for FRPs using thermosetting resins can be split into three broad categories, namely, Liquid Composite Moulding (LCM), the use of resin pre-pregs, and Sheet Moulding Compound (SMC) or Dough Moulding Compound (DMC) [27]. The main objectives of the manufacturing process are to make sure that all the fibres are wetted by the resin, aligned in the correct directions and uniformly distributed [27].

The most basic techniques involve impregnating the dry fibres with low viscosity liquid resin [27]. Broadly speaking, these techniques are known as LCM. These include hand laminating, Resin Transfer Moulding (RTM), filament winding and pultrusion. Hand laminating (*i.e.* wet lay-up), is the simplest and oldest technique for manufacturing composites [32]. The main advantages of this process are that any shape can be produced and the capital costs are low, although a mould is required [27]. The limitations of wet lay-up are that the process is labour intensive and quality control is challenging [27, 32]. Furthermore, it can be difficult to accurately control the part thickness, the fibre content and the surface quality [32]. This means that wet lay-up is commonly used for low volume production or prototyping [32]. Quality can be improved through the use of vacuum bagging after the lay-up and wetting out of the dry materials. This compaction improves the fibre volume fraction and results in a part with a more consistent thickness [33].

RTM is another form of manufacturing, in which the dry fibres are placed in a mould and then the resin is injected into or drawn through the mould [33]. The process can be split up into four stages, shown in figure 2.4. The first step is the preforming stage, which involves laying dry fibres onto a mould in the shape of the final part [32]. The next step involves the infusion of resin into the mould. The last two steps are the curing and de-moulding phases [27, 32].

The basic approach of RTM involves using pressure to force the resin into the mould and infuse the dry fibres. Vacuum Assisted Resin Transfer Moulding (VARTM) is similar to RTM, except the process is vacuum driven instead of pressure driven [33]. Vacuum Infusion (VI) and Seaman Composite Resin Infusion Moulding Process (SCRIMP) are specific examples of VARTM processes that use a flexible membrane for the top half of the mould [32]. The moulds required for VARTM are lightweight and low cost and VARTM is cost-effective for mid-range production volumes. A couple of disadvantages include the possibility of void formation or resin rich or dry areas during manufacture due to air entrapment during resin impregnation and the difficulty for the resin to flow into the small gaps due to the lower pressures used that reduces the quality of the part, along with the difficulty in determining the flow rate of liquid resin through the dry products due to variations in the compression pressure [32].

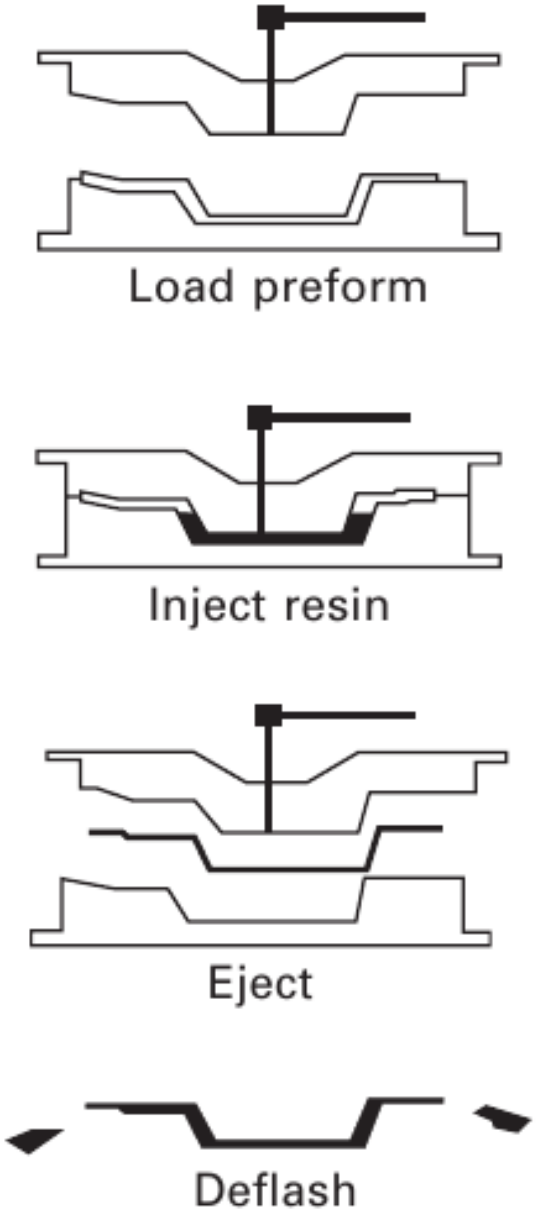

Figure 2.4: Schematic of the resin transfer moulding (RTM) process [33]

The second category of thermoset FRP manufacture involves the use of pressure and heat to consolidate pre-pregs [27]. Pre-pregs are sheets of fibres that are pre-impregnated with resin and then partially cured [27]. Layers of pre-preg are stacked in a mould and then placed in an autoclave or oven under vacuum bags at high pressures and temperatures in order to produce the final part. The mould needs to be designed to handle the high temperatures in the autoclave (and hence can be quite costly) and there is also the possibility of moisture being introduced into the resin when thawing out the pre-preg from the freezer [32]. Additionally, pre-pregs have a limited shelf life which can be costly if they are not used in the time window [32]. Pre-pregs are generally not suitable for the manufacture of MRAPs V-hulls due to their size. This would require a large autoclave to cure the panels which would be cost prohibitive.

The third category is similar to the use of pre-pregs, but instead, it uses SMC or DMC [27]. SMCs are made by combining resin containing thickening agents and particulate fillers with chopped fibres to create a slurry. The slurry is then pushed through a set of rollers to create a sheet. DMCs are similar to SMCs but the mixing is done using a blender at high shear rates, which reduces the fibre length and makes the fibre orientation more random [27]. Both SMCs and DMCs use hot press moulding to form the final shape and to cure [27]. While these manufacturing approaches can be used to produce composite structures with complex shapes, they are typically used to manufacture smaller components with a low fibre volume fraction (15-40%) and lower strength [27].

2.4 Experimental studies into the blast response of steel structures to localised air blasts from cylindrical charges

2.4.1 Blast testing of flat and curved steel panels

Several studies have been conducted on the blast performance of flat steel panels with a circular exposed area [34–36]. These studies investigated the failure modes observed in steel panels subjected to localised blast loads from cylindrical PE4 charges. Three failure modes were found. Namely, mode I - large inelastic deformation, mode II - tearing at the clamped edge, and mode III - shear failure at the clamped edge [34]. Nurick and Radford [36] extended this research by varying the explosive charge diameter. In this study, additional failure modes were identified for flat panels with a circular exposed area. Two of these failure modes were, mode II*c - partial tearing in the central area and mode IIc - capping (complete tearing in the central area of the structure) [36]. A selection of these failure modes are shown in figure 2.5.



Figure 2.5: Blast tested flat panels tested by Jacob *et al.* [37] showing failure modes I and IIc

Nurick *et al.* [38] investigated the effect of changing the shape of the explosive charge on the measured impulse and the permanent mid-point deflection of flat steel panels with a circular exposed area. Three charge shapes were considered, namely, a cylinder, a truncated cone and an inverted truncated cone while the explosive height, charge diameter, and charge mass were also varied. The Stand-Off Distance (SOD) was fixed at 14 mm for all the tests. Mode I, mode II*c, and mode IIc were observed in the experiments, matching similar findings in previous studies performed on localised blast loaded flat steel panels [34–36]. An analytical approach was used to determine the effective charge mass of each charge geometry investigated. It was found that depending on the shape, height, and diameter of the charge the shock profile varied and resulted in a different distribution of explosive energy on the structure. Using this analysis, it was found that the inverted truncated cone resulted in the highest measured impulse but the lowest permanent mid-point deflection as the load was distributed over a larger area of the target structure [38].

The blast response of flat steel panels with a quadrangular exposed area has also been extensively studied with damage and failure propagation considered in the different investigations [39, 40]. Jacob *et al.* [37] investigated the response of cold rolled, quadrangular flat mild steel panels subjected to blast loading from cylindrical Plastic Explosive No. 4 (PE4) charges. The plate thicknesses (1.6 mm to 4.0 mm), charge heights (1.8 mm to 14 mm) and charge diameters (24 mm to 64 mm) were varied, while the Stand-Off Distance (SOD) was fixed at 12 mm. The test arrangement used for the experiments is shown in figure 2.6, which was mounted onto the ballistic pendulum at the Blast Impact and Survivability Research Unit (BISRU) labs. Jacob *et al.* [37] particularly examined the effects of charge height and plate thickness on mid-point deflection and impulse transfer [37].

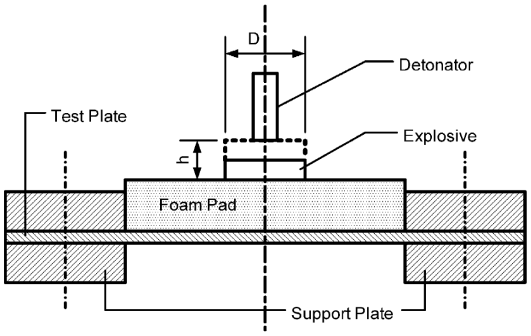

Figure 2.6: Schematic of the clamp frame, flat panel and explosive arrangement used by Jacob *et al.* [37]

Large plastic deformations were observed in all the tests, while the mid-point deflection was observed to increase as the impulse increased. Additionally, the panels exhibited thinning, followed by tearing as the impulse increased. Jacob *et al.* [37] found that, as expected, an increase in charge height (and thus an increase in charge mass for a constant charge diameter) resulted in an increase in impulse. A decrease in deflection was observed for an increase in plate thickness, while the plate aspect ratio (*i.e.* the width to thickness ratio of the panels) did not appear to influence the deformation of the panels [37].

McDonald *et al.* [40] investigated the response of high-strength armour steels to localised blast loads. In the study, four armour steels were considered with yield strengths in the range of 800 MPa to 1200 MPa. They had an exposed area of 400 mm x 400 mm and a thickness of 4 mm and were fixed to the ballistic pendulum at BISRU. Two SODs were investigated, namely, 13 mm and 25 mm, while the charge mass was varied from 40 g to 75 g. The primary aim was to determine the rupture threshold for each of the steels investigated. The armour steel with the lowest yield strength required the largest charge mass at both SODs to rupture, while the performance of the other three steels were similar at the lower SOD tested [40].

2.4.2 Blast loading of steel V-structures

The response of steel V-structures to localised blast loads has been investigated experimentally in a few key studies which considered the influences of geometric variations such as V-angle and V-structure shape, as well as effects of the SOD and charge mass used [8, 41, 42]. Chung Kim Yuen *et al.* [8] looked into the effects of the internal V-angle on the response of scaled V-structures to localised blast loading from cylindrical PE4 charges. Two manufacturing techniques (folded and welded V-structures) were also investigated. The V-tip (bend) radius was fixed at 2.0 mm for all the structures to ensure that it did not affect the V-structure performance. The V-structures were manufactured from 2.0 mm thick DOMEX-700 MC steel that was folded to V-angles of 60°, 90°, 120°, 150° and 180° (a flat structure) were tested, while the welded structures were manufactured with a V-angle of 120°. These configurations are shown in figure 2.7.

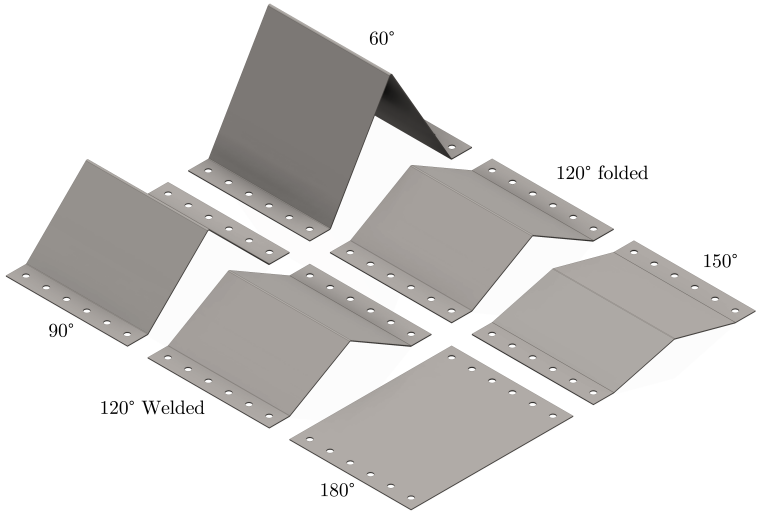

Figure 2.7: Schematics of the V-structures tested by Chung Kim Yuen *et al.* [8]

These tests were designed to reproduce a scaled version of the loading that may arise from a landmine or IED detonation under a V-hulled APC, hence the charge mass and diameter were scaled based on the dimensions and mass of a TM-57 AT-mine [43] using the Hopkinson-Cranz blast scaling provided in equation (2.1), where R is the SOD, Z is the scaled distance, and W is the scaled TNT weight parameter which is 1.3 for PE4-TNT. The width of the V-structures and SOD were scaled based on the width and ground clearance of the Casspir APC MK II [25]. These scaling laws produced a SOD of 50 mm. Additionally, the Casspir was designed to withstand a

14 kg TNT equivalent blast, which corresponded to 19 g of PE4. For the 120° V-structures, a range of stand-off distances were investigated, ranging from 18 mm to 50 mm. A SOD of 50 mm was found to produce negligible deflections and hence the SOD was reduced to 34 mm for most of the remaining tests [8].

$$Z = \frac{R}{W^{1/3}} \tag{2.1}$$

Chung Kim Yuen *et al.* [8] found that as the stand-off distance increased, the mid-point deflection decreased, due to the loading becoming less localised, but the impulse transfer was unaffected. Additionally, as expected, both mid-point deflection and impulse transferred increased as the charge mass was increased for a fixed V-angle. As the V-angle was increased the impulse transferred to the pendulum also increased and the smaller V-angles exhibited a lower mid-point deflection. Although the smaller V-angles displayed superior performance characteristics, it was also noted that the centre of gravity of a potential MRAP would be raised. Furthermore, as noted previously, on early APCs such as the Camel, the sharp V-angle of 43° limited the space within the crew compartment for troops and equipment, and increased the likelihood of the vehicle toppling over [1]. It was also noted that the welded V-structures performed significantly worse than their folded counterparts. Thus the study concluded that the best V-angle to use was a 120° folded V-structure [8]. The best performing V-structures resulted in a vehicle with a larger ride height, hence two additional approaches [41, 42] were considered as a means to reduce the centre of gravity of the MRAP. In these two studies, the V-structures were manufactured from 2.0 mm thick DOMEX-700 MC steel to allow for comparisons to be drawn with the tests performed by Chung Kim Yuen *et al.* [8].

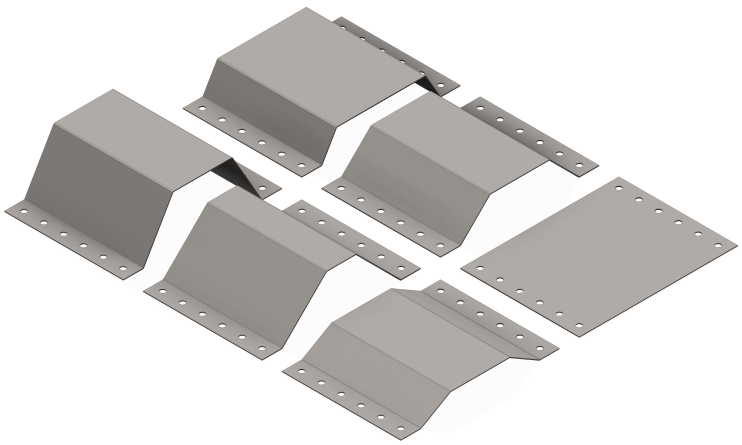

Figure 2.8: Schematics of the novel V-structure tested by Langdon *et al.* [41]

Following these experiments, Langdon *et al.* [41, 42] investigated novel V-structure designs, one of which is shown in figure 2.8, in which a portion of the "V" was cut away to reduce the height of the V-structure. The first approach involved removing the V-tip, by cutting off different ratios as shown in figure 2.8. The cut-off ratio is defined as the percentage of the height of the original V-structure that is replaced by the flat portion. Cut-off ratios of 20, 50, 75 and

100% (*i.e.* a flat structure) were investigated, with V-angles of 60°, 90°, and 120°. These shallow V-structures performed poorly when compared to the original V-structures and hence it was concluded that removing the V-tip was not a suitable technique for reducing the total height of the V-structures [41]. The second approach that was utilised involved combining a sharp and a shallow V-angle to create a compound V-angle V-structure. This meant that the sharp V-tip was still present which could deflect the blast pressure wave. In general, these novel designs also performed worse than their single V-angle counterparts in terms of impulse transfer but performed better in terms of measured permanent mid-point deflection at the V-tip [42]. Additionally, double-V or W-structures were tested. These performed poorly in terms of both metrics investigated [42].

2.5 Blast loading of composite structures

2.5.1 Blast response of flat and curved FRP composite structures

Numerous studies have investigated the response of FRPs to blast loads by considering the effects of charge mass, SOD, fibre and resin materials, and panel thickness [44–49]. Mouritz [44] reviewed multiple studies performed on blast loaded composite structures and noted that there were limited studies performed on curved, tubular, and V-shaped structures that could be considered in the review.

Comtois *et al.* [45] investigated the response of flat quasi-isotropic carbon and glass fibre laminates to blast loads from cylindrical PE4 charges. Both were made using 16 plies of pre-preg material, with the carbon fibre laminates manufactured using unidirectional sheets, and the glass fibre ones were made using woven sheets. The charge masses used were 0.5 g to 1.5 g and the SODs tested were 54 mm to 500 mm. In general, increasing the charge mass resulted in an increase in the percentage delaminated area. This matches the observations of similar research on chopped strand mat E-glass fibre composite panels tested by Franz *et al.* [50]. It was found that the amount of damage was determined by both the impulse and peak pressure and that the peak pressure experienced by the target plate was a function of the SOD [45].

Yahya *et al.* [46] also studied the effect of localised blast loading on carbon and glass fibre composite panels. In this study, the laminates were manufactured from woven pre-preg sheets, with the thickness varying from 2 mm to 12 mm. Square panels with a circular exposed area were mounted onto the ballistic pendulum at the BISRU labs, while the blast loading was created by detonating cylindrical PE4 discs. The stand-off distance was fixed at 90 mm and the mass of explosive used was between 1 g to 13 g [46]. The glass fibre composite laminates suffered from fibre breakage on the top surface and plastic deformation of the matrix at the lowest charge masses. As the explosive mass increased, fibre buckling was observed on the top surface and fibre breakage on the rear surface and along the clamped boundary although delamination was not present. The amount of fibre fracture increased significantly as the charge mass was further increased with fibre rupture observed on both the front and rear faces and through the thickness of the laminate. Furthermore, localised delamination was observed in the tests with higher charge masses. The minimal delamination was attributed to the high interlaminar fracture

toughness of the carbon fibre composite laminates. The carbon fibre panels exhibited similar failure modes to those observed for the glass fibre composite panels with additional delamination present [46].

Tekalur *et al.* [47] investigated the response of FRP composite laminates to shock loading using a shock tube and blast loading using a Controlled Explosive Tube (CET). The panels were manufactured from woven E-glass using the VARTM process. In the experiments using the shock tube, the permanent deformation of the panels was observed to increase as the applied load increased. Additionally, below a pressure of 0.6 MPa, the panels exhibited minimal delamination and no fibre failure [47]. At higher pressures, the panels experienced delamination in the centre and along the clamped boundaries followed by fibre failure on the front face. In the blast loading experiments, the panels experienced a large amount of delamination and fibre failure on the front face and no external damage on the back face [47].

Gargano *et al.* [49] tested four different woven laminate composites under blast loads from spherical PE4 charges. These were carbon-polyester, glass-polyester, carbon-vinyl ester, and glass-vinyl ester composites and were chosen due to their use in ship structures. The different laminates had between 7 and 10 layers to achieve the same thickness for all the panels tested. The exposed area was 250 mm x 250 mm, the charge masses tested were varied from 100 g to 200 g, and the SOD was varied from 0.4 m to 1.0 m. Pressure gauges were employed to capture the peak pressure from the tests, while cameras arranged in a stereoscopic configuration were used to measure the transient response. The damaged area was observed to increase with an increase in impulse, with fairly linear trends observed for two of the specimen configurations tested. The initiation points for the different failure modes in terms of impulse transferred were also presented with complete rupture being the last failure mode observed [49]. This matches the observations in studies performed on different flat composite laminates [45–47]. An example of the observed rupture is shown in figure 2.9. In general, the fibre glass laminates absorbed more energy before fibre breakage was observed, which the authors attributed to the higher strain energy density compared to their carbon fibre counterparts [49].

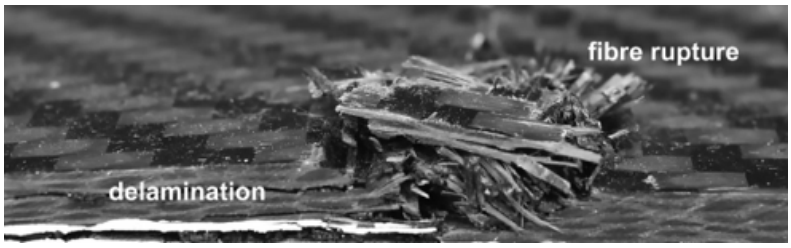

Figure 2.9: Rupture observed for the carbon fibre structures tested by Gargano *et al.* [49]

Kumar *et al.* [48] performed a series of shock tube loading experiments on curved carbon fibre composite structures. The laminates were manufactured from 32 layers of unidirectional carbon fibre. Three bend radii were tested, namely 112 mm, 305 mm and an infinite bend radius (*i.e.* a flat structure). The shock loading was created using a shock tube and high-speed imaging was used to measure the transient deformation of the structures [48]. The flat and 305 mm curved structures showed interlaminar delamination and fibre breakage on the front face. Unlike the

other two, the 112 mm curved structures showed no visible damage at lower pressures. At a pressure of 8.0 MPa they experienced large scale rupture and complete failure. Additionally, as the bend radius was reduced, the mid-point deflection of the structures decreased [48]. This suggests that structures with a smaller bend radius offer better blast protection. It is important to note that the bend radii investigated in this study were significantly larger than those proposed for the planned research on steel and GFRP V-structures.

2.5.2 Response of composite V-structures to blast loading

Follett [9] performed a series of experiments that are summarised in table 2.1, comparing the structural response of steel and composite V-structures. Follett [9] defined the SOD as the distance from the top of the hull to the top of the sand pit. The composite V-structures were manufactured from S2-glass and E-glass with a width of 666 mm and a length of 1000 mm. The V-tip radius was not reported by the author although using the schematic provided in the thesis this can be estimated to be approximately 40 mm. The impulse transferred to the test equipment was not measured in the experiments. For the composite V-structures, fibre failure, matrix failure and delamination were observed on the outer surface, while delamination was visible on the inner surface. Smaller permanent deformations were observed for the composite V-structures when compared to the steel V-structures [9].

Table 2.1: Experiments reported by Follett [9]

Material	V-angles (°)	Thickness (mm)	DOB (mm)	SOD 1 (mm)	SOD 2 (mm)	Charge mass (g)
E glass	90, 95, 101, 107	22	50	590	480	240
S2 glass	90, 95, 101, 107	22	50	590	480	240
EN8 Steel	90, 95, 101, 107	5	50	590	480	240

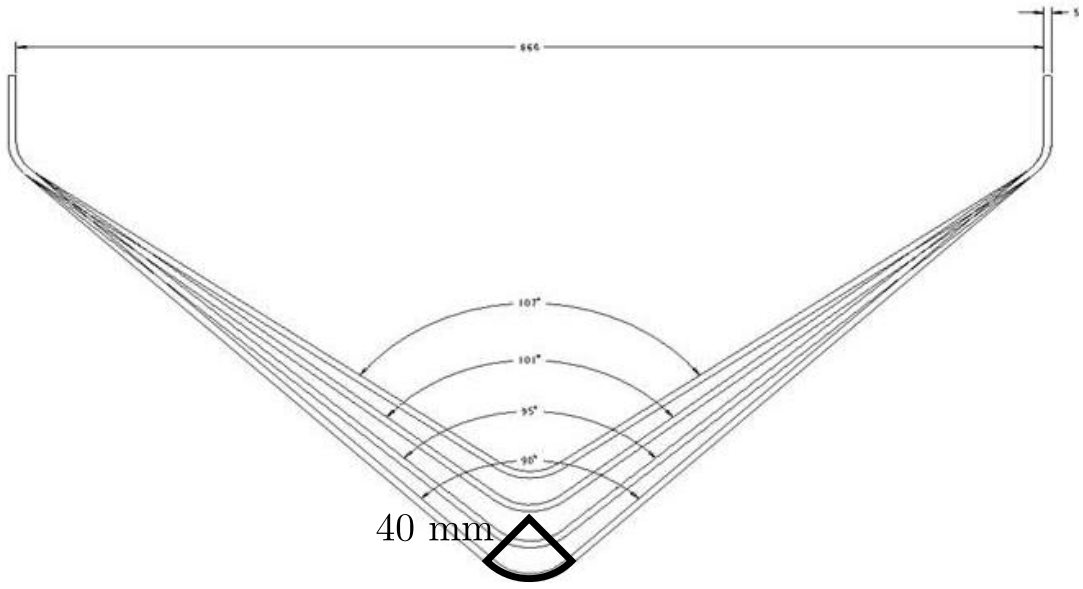

Figure 2.10: Schematic of the V-structures tested by Follett [9] showing the estimated V-tip radius

2.6 Measurement of the transient response of blast loaded structures

A number of studies have attempted to determine the transient response of metallic and FRP composite structures to blast loads. In early studies [51] metallic combs were used to measure the peak deflection during the test. While in later studies [52–56], with the improvements seen in high-speed camera technology, it became possible to track a portion of the structures and measure its displacement time history.

Neuberger *et al.* [51] investigated the response of armour steel plates with a circular exposed area to localised blast loads from spherical TNT charges ignited from their centre. The primary aim was to determine the validity of the Hopkinson scaling laws for blast loading. A measuring comb placed centrally behind the target plate was used to measure the peak mid-point deformation as shown in figure 2.11. The study found a good correlation between experimental normalised peak mid-point deflection and the numerical simulation results [51]. It should be noted that while the measuring combs are a useful tool for tracking transient deformation, they only give a single measurement point in a blast test, namely the peak deformation during the experiment.

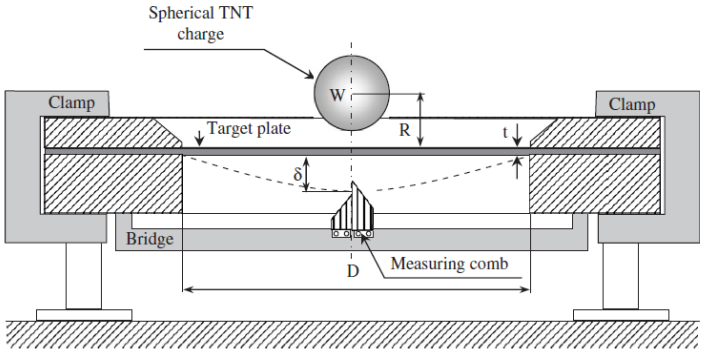

Figure 2.11: Experimental setup showing the measuring comb used by Neuberger *et al.* [51]

Tiwari *et al.* [52] employed a pair of high-speed digital cameras to measure the transient deformation of plates subjected to 1 g Pentaerythritol Tetranitrate (PETN) buried charge blast loads using Digital Image Correlation (DIC). The cameras used had a frame rate of 2083 fps and a sensor resolution of 800 × 600 pixels. In order to increase the frame rate, the resolution was lowered to 256 × 256 pixels and 128 × 128 pixels. The lower resolution resulted in smaller fields of view, namely, 150 mm × 150 mm and 75 mm × 75 mm respectively. The plates tested were manufactured from 1.6 mm thick aluminium 6061 sheets and had an exposed area of 305 mm by 356 mm. The SOD was fixed at 28.7 mm for all the tests. The authors were able to track the displacement, velocity and acceleration fields for the field of view imaged. The peak velocity was seen in the first two imaged frames and had twice the magnitude for the tests performed at the lower Depth of Burial (DOB) versus the tests performed at the higher DOB. It should be noted that an increase in frame rate would allow for a better measurement of the initial velocity of the centre of the target plates. The transient mid-point deflection was also found to be lower for the tests performed at a higher DOB. The authors were also able to generate strain maps

for the imaged area of the blast tested plates by spatially differentiating the displacement data obtained from the cameras. They reported an estimated measurement error of 0.026 mm for the out-of-plane deflection [52].

Zhao *et al.* [53, 54] extended the work performed in the previous study [52] by looking at scaling effects for buried charge explosions and looking at the transient response of the target plates. A similar setup to that used by Tiwari *et al.* [52] was used with two Vision Research Phantom V12.1 cameras in a stereo configuration as shown in figure 2.12. The plates were also made from aluminium 6061 sheet, with two different configurations considered. The smaller target plates had a thickness of 1.0 mm and a diameter of 227.6 mm, while the larger target plate had a thickness of 1.6 mm and a diameter of 355.6 mm. The charge mass, SOD, and DOB were also varied to ensure that the tests were correctly scaled. The field of view of the tests was fixed at 57 mm $\times$ 184 mm. The authors found a reasonable correlation in the shapes of the scaled mid-point displacement and velocity time histories although there were differences in the peak magnitudes. Additionally, there was a reasonable correlation in the scaled transient plate profiles obtained in terms of both peak magnitude and profile shape. The variations observed were suggested to be due to the behaviour of the sand during the tests and the lack of strain rate sensitivity in the aluminium tested.



Figure 2.12: Experimental setup showing the stereo cameras and target plate as tested by Zhao *et al.* [53]

Aune *et al.* [55] investigated the response of flat steel and aluminium plates to air-blast loading. The plates had an exposed area of 300 mm x 300 mm and a thickness of 0.8 mm and were fixed to a rigid frame that was attached to the floor. The loading was provided by detonating a 30 g spherical charge of C-4, while the SOD was varied from 125 mm to 625 mm. Additionally, a rigid target plate containing pressure transducers was used to measure the Fluid-Structure Interaction (FSI) between the explosive pressure wave and the target plates. A pair of cameras with a frame rate of 21 000 fps were used to measure the transient deformation of the rear face of the target plates as shown in figure 2.13. The authors noted that the steel plates showed primarily mode 1 failure with no tearing visible at the clamped boundaries. The transient plate response appeared to be driven by the load intensity with the elastic response decreasing as the SOD was decreased. Unlike the steel plates, the aluminium plates also showed mode II and mode II* failure at the lower SODs tested and thus DIC was not used to ensure the cameras were not damaged. As with the steel plates, a reduction in the SOD resulted in a reduction in the elastic response of the aluminium plates [55]. Problems measuring transient mid-point displacement due to paint

spalling were also reported for some of the tests conducted. Given that the planned tests will also be conducted at low SODs, a similar limited elastic rebound would be expected.

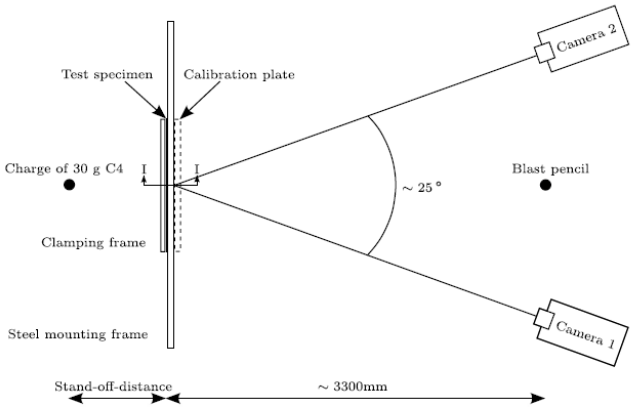

Figure 2.13: Schematic of the experimental setup showing the positions of stereo cameras and the target plate as tested by Aune *et al.* [55]

Curry and Langdon [56] used a pair of IDT vision NR4 S3 high-speed cameras mounted inside a ballistic pendulum to measure the transient response of flat 3.0 mm thick DOMEX-355MC steel plates with a 300 mm diameter circular exposed area. The loading was provided by 38 mm diameter cylindrical discs of PE4 placed at SODs of 40 mm and 50 mm with charge masses from 10 g to 50 g. The frame rate was set at 30 000 fps with a field of view of 1024 × 76 pixels. The authors noted that decreasing the SOD resulted in an increase in both the peak and permanent mid-point deflection while the peak deflection was also observed to occur earlier in time for all the charge masses investigated. The elastic vibration was found to be similar regardless of SOD or charge mass, suggesting this is primarily a function of the target plate material and geometry. It was also noted that the final deformed plate profiles varied when compared to the transient plate profiles with these variations likely due to the transient elastic behaviour of the target plates [56].

A few studies have also investigated the transient behaviour of flat composite panels [49, 57]. One such study performed by Gargano *et al.* [49] looked at the blast response of glass fibre and carbon fibre composite panels subjected to localised blast loads. Photron SAX cameras were used with a frame rate of 30 000 fps. The authors presented the plate response from the detonation to 4 ms after the detonation. This enabled them to measure the peak deformation and most of the first oscillation. A fairly linear trend was observed in the peak mid-point displacement versus the measured impulse. All four test configurations considered showed similar transient vibration behaviour in terms of the peak mid-point displacement with the glass-fibre panels having larger vibration periods. It should be noted that due to the limited number of frames recorded, there was no data available on the experimental free vibration response of the tested composite panels.

Gabriel *et al.* [57] studied the response of FRPs containing sustainable materials to uniform blast loads. The materials tested included glass fibre, flax, and jute fibres with a Prime 20 epoxy resin, and GFRPs with a Super Sap bio-based resin. The laminates were manufactured to ensure they had a nominal mass of 1 kg. The explosive loading was provided by cylindrical PE4 charges with

masses of 5 g to 11 g and placed 200 mm from the target structure. The setup used to measure the transient deformation was identical to that used by Curry and Langdon [56] although, in this study, the plates had a square exposed area with dimensions of 200 mm × 200 mm. The authors were generally able to measure the transient mid-point displacements for the GFRP panels as these typically experienced delamination. The peak displacement was found to be higher for the laminates that used a bio-based resin versus those that used the Prime 20 resin. Additionally, some data was collected for the flax fibre laminates with these showing less elastic vibration when compared to their glass fibre counterparts.

2.7 Numerical simulations of blast tested structures

There are a number of commercially available Finite Element Analysis (FEA) software packages. ABAQUS, AutoDyn, and LS-DYNA are three that have been used in previous research to simulate the response of structures to blast loads [8, 10, 58–66]. LS-DYNA was used to conduct the simulations in the research performed herein and hence this literature review focuses on the blast modelling approaches available within this software package. In LS-DYNA there are a number of approaches to model blast loads that can be considered. Tabatabaei and Volz [67] compared the three of these approaches by investigating the pressure histories and comparing the results with experimentally measured values. The first approach considered, computed the blast pressure empirically (ConWep) [68] and is known as LOAD BLAST ENHANCED (LBE). In this approach the air is not modelled using an Eulerian mesh and the loads are applied directly to the Lagrangian elements of the target structure. In the second approach, the explosive is modelled using the Multi-Material Arbitrary Lagrangian-Eulerian (MMALE) method. The air around the target structure is modelled and a part of the air is assigned with the properties of the explosive material. The explosive is allowed to detonate and the load is transferred to the target structure through the Fluid-Structure Interaction (FSI) between the detonated explosive and the plate. The third approach investigated looked at the coupling of the first two methods.

The test modelled by Tabatabaei and Volz [67] was a 36 kg spherical charge located 1.68 m from a reinforced concrete structure. Two pressure transducers placed 1.68 m and 7.42 m from the centre of the explosive were used to measure the pressure time histories. Due to computational times needed for the methods involving MMALE, the second pressure transducer time histories were not considered for these methods investigated. The key observation was that the LBE used the lowest computational time but resulted in an underestimation of the peak pressure at the closer SOD and an overestimation of the pressure at the larger SOD. The most accurate results were obtained from the MMALE approach although this did come with a significant penalty in terms of the computational time of the numerical blast simulations [67]. This does suggest that for the small SODs and localised nature of the loading used for blast tested V-structures, the MMALE approach is probably the best way to correctly capture the blast load interaction with the V-structures. Erdik *et al.* [66] numerically investigated the response of a full-scale MRAP. MMALE was used and a study was conducted on the mesh and element topology comparing the peak pressures with the ConWep approach. It was found that a greater number of Eulerian elements per Lagrangian element resulted in better predictions of the peak overpressure and

reflected impulse.

An alternative approach that can be considered for modelling the blast load is the use of Smooth Particle Hydrodynamics (SPH). Barsotti *et al.* [65] modelled the mine blast experiments performed by Anderson *et al.* [64] and compared the results obtained for the SPH model to those predicted by using an ALE approach. LS-DYNA was used in both sets of simulations. The momentum transferred to the V-structures was over-predicted by the SPH model and under-predicted by the ALE simulations. The differences were approximately 15-20% of the experimentally obtained measurements. Barsotti *et al.* [65] attributed the under-predicted impulses in the ALE simulations to material leakage through the plate. The material leakage in the simulations can be minimized through a careful selection of element sizes for the Eulerian and Lagrangian components of the simulations.

In terms of modelling the target structure and material, solid and shell elements can be used to model the structure with a number of possible material models available for both steel and composite structures. Spranghers *et al.* [69] looked at the dynamic response of flat aluminium target plates to blast loads. The authors utilised an LBE approach in LS-DYNA to model the air blast loading in the study, while the element choice and size for the target plate were varied to determine the optimal configuration to correctly capture the plate response. As expected, decreasing the element size improved the solution accuracy but increased the computational time. The solid and shell elements showed similar peak mid-point transient deformations with the shell element model slightly under-predicting the peak deformation and capturing higher vibration modes compared to solid element models. The primary advantage of the shell elements was the significant reduction in computational time compared to the same size solid elements. In the final model, the authors modelled the clamp frame using solid elements and the target plate with shell elements with a Johnson-Cook material model was used for the target plate. The boundary nodes of the target plate were tied to the clamp frame to allow forces to be transmitted between the two components. The simulations were found to fairly accurately capture the peak deformation plate profiles when compared to the experimental data. The shape of the plate profile at other timesteps also closely matched the experimental results although the simulations had a larger magnitude. This might be due to either the method chosen to model the blast load or the material model for the target plate not correctly capturing the hardening response of the plate material to the blast load [69].

A number of studies have numerically investigated the response of flat steel plates to blast loads [60, 61]. Longère *et al.* [60] investigated the response of flat steel plates to localised blast loads. ABAQUS was used to conduct the numerical simulations with the results compared with experimental results. The explosive loading was modelled using the ConWep empirical approach, while a modified Gurson microporous model developed by the author was used as the material model for the plate. This damage model enabled both plastic deformation and rupture of the steel plates to be captured by the numerical model. The various material model parameters were adjusted to investigate their effects on rupture initiation. Determining this rupture threshold in the numerical model proved to be challenging. This was attributed to the strain rates considered in the model and the use of the ConWep approach for modelling the blast

load and the limitations of this approach [60].

Mehreganian *et al.* [61] also used ABAQUS to model the response of flat steel plates to localised blast loads. Unlike Longère *et al.* [60], the authors investigated both a coupled and an uncoupled ALE approach to model the blast load. The target plates tested had thicknesses of 4.6 mm and were subjected to blast loads from cylindrical PE4 charges placed at SODs of 25 mm, 38 mm, and 50 mm. The target plates were modelled using four-node shell elements and a Johnson-Cook material model with parameters fitted to experimental data from quasistatic and intermediate strain-rate ($1\,s^{-1}$) material characterisation tests. The numerically obtained impulse was found to be close to, but always lower than, the experimentally measured values. It was also noted that the uncoupled ALE model was less accurate than the coupled ALE model when it came to the pressure-time histories. Additionally, the mid-point transient deflection was compared with the experimental measurements, with both modelling approaches over-predicting the initial peak, and a delayed time of arrival. When the maximum mid-point deflections were compared between the coupled model and the experiments, the simulation results were almost always greater than the experimentally obtained values with the variation increasing as the impulse and thus the experimental deformation increased. The maximum percentage variation observed in these results was around 10-30% depending on the test configuration [61].

2.7.1 Numerical blast modelling of metallic V-structures

Many studies [10, 58, 59, 62, 70, 71] have employed numerical approaches to investigate the interaction between V-structures and blast loading. Paykani *et al.* [58] and Saeimi-Sadigh *et al.* [59] performed numerical simulations on steel V-structures using ABAQUS. The V-structures had an internal angle of 120° and were modelled with solid tetrahedral and hexahedral elements with the mesh biased towards the centre. This was done to better capture the expected deformation in the central region of the V-structures. The blast load was modelled as a pressure load applied to the surface of the V-structures. In both studies, materials were added behind the V-structure to reduce the deformation of the V-structures. Paykani *et al.* [58] varied the choice of materials used to attenuate the displacements by considering aluminium, aluminium foam, and balsa wood as energy absorbing materials, while Saeimi-Sadigh *et al.* [59] varied the thicknesses of the materials used while also varying the thickness of the actual steel V-structures. Paykani *et al.* [58] found that aluminium foam resulted in the best improvements in terms of reducing the deformation of the V-structures, while Saeimi-Sadigh *et al.* [59] found that increasing the thickness of the V-structures resulted in the greatest reduction in permanent deformation. It is worth noting that tearing was not modelled in these studies and that the simplified pressure loading for the blast has limitations in terms of impulse transferred to the structure for near-field explosions.

Langdon and Shekhar [10] numerically investigated the effect of V-tip radius on the impulse transfer characteristics of V-structures. A quarter symmetry numerical model was developed using LS-DYNA. The model utilised the ALE solver to model the explosive detonation and the interaction of the blast pressure wave with the structure. The structures were modelled as rigid structures as initial simulations found that there was no significant effect on impulse transfer of

modelling the structures as a deformable material. The model also included the clamp frame and bolts, while the air mesh covered all the structures in the model [72]. Figure 2.14 shows the effect of increasing the bend radius on the total distance between the charge and the base of the V-structure. It can be seen that as the bend radius was increased the total distance from the explosive to the clamp frame was reduced. The study found that for all three V-angles tested, the impulse transferred increased as the bend radius was increased. At larger bend radii, the impulse transferred appeared to plateau for the 90° and 120° V-structures. An analysis of the velocity vectors and pressure histories across the structures found that the increase in impulse transfer was due to the reduced rate of pressure dissipation and the larger maximum pressures at the V-tip. This meant that if a landmine protected APC used a V-hull with a larger bend radius, the total ride height could be reduced although the impulse transfer would be greater [10].

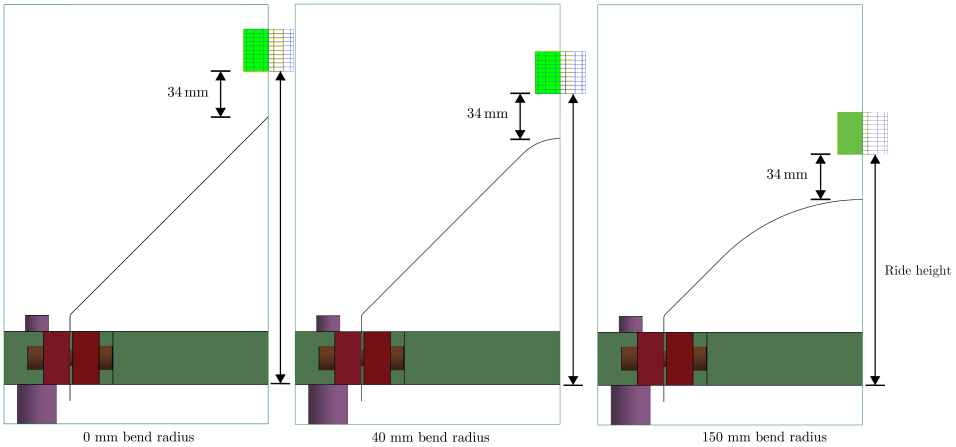

Figure 2.14: Schematic of the side view of three 90° V-structures with bend radii of 0 mm, 40 mm and 150 mm, showing the fixed SOD and the total reduction in height [72]

Markose and Rao [70, 73] used ABAQUS to model full-scaled V-hulls testing a number of parameters including the SOD, V-angle, and the eccentricity of the explosive loading. The models were validated with scaled experiments performed by Chung Kim Yuen *et al.* [8] before considering the full-scale V-hull. Solid elements were used to uniformly mesh the V-structures utilising symmetry boundary conditions where applicable. The material chosen for the full-scaled V-hulls was a mild steel and this was modelled with a Johnson-Cook material model. The authors employed an applied pressure load in a similar manner to that used in other V-structure studies [58, 59]. Again, it is worth noting that ConWep has been shown to be suitable for modelling uniformly distributed blast loads from spherical charges, while the loading from landmines is typically represented as a cylindrical disc of explosive placed at a close distance to the V-structures. This likely explains the under-predictions in deflection and impulse reported when comparing the results to previous experimental work on scaled V-structures. The study found that increasing the eccentricity of the explosive charge resulted in an increase in impulse transferred to the V-structure but, for all V-angles tested, the deflection was observed to decrease. This was expected as the blast deflection characteristics of the V-structures are reduced as the load is moved further from the centreline of the V-structure, but as the effective SOD is increasing, the load becomes less localised and thus the permanent mid-point deflection is

reduced [70].

Trajkovski *et al.* [62] used LS-DYNA to model V and U-shaped structures subjected to localised eccentric blast loads. SPH was used to model the blast load with a penalty contact approach used to model the FSI between the explosive particles and the steel structures. This was done to reduce the large computational times associated with the MMALE approach. The structures were modelled using shell elements, while the SOD was fixed at 25 mm for all the simulations. A Johnson-Cook material model was used for the PROTAC 500 armour steel. The authors observed an increase in normalised deflection for an increase in V-angle until a V-angle of 150°. This matched findings by Markose and Rao [70]. Additionally, they observed a reduction in the normalised deflection of the different shaped structures considered for an increase in the eccentricity of the explosive load. This matched the observation in previous studies for V-structures [70].

Wahab *et al.* [74] numerically investigated the response of composite steel V-structures to blast loads using ANSYS/AUTODYN. The V-structures were manufactured from composite sandwich panels with aluminium foam cores and 5 mm thick mild steel face sheets. Additional steel ribs were added to the structure as strengtheners. The experimental geometry is shown in figure 2.15. The V-angles investigated experimentally were 136° and 148° which are larger than those investigated in previous studies [8, 70]. The blast loading was provided by a 10 kg TNT equivalent charge placed at a SOD of 1 m. In the numerical model, the blast loading was modelled using an MMALE approach with the steel face sheets and stiffeners modelled with shell elements and the aluminium foam modelled with solid elements. The model was found to reasonably predict the plastic deformation, with an 11% variation in the mid-point displacement when validated against the experimentally measured values. Additional V-angles (140°, 156°, and 180° (flat plate)) and an additional charge mass (10 kg) were simulated to allow the authors to investigate the effects of the V-angle and the charge mass on the deformation of the V-structures. As expected, decreasing the V-angle was found to reduce the mid-point deflection, while increasing the charge mass resulted in an increase in the peak pressures and the mid-point deflection [74].

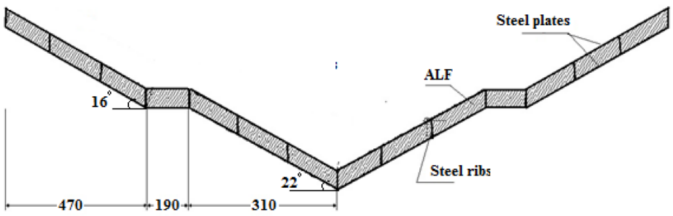

Figure 2.15: Schematic of the experiments simulated by Wahab *et al.* [74]

2.7.2 Numerical modelling of composite structures to dynamic and blast loads

Multiple studies have considered the numerical modelling of composite structures to dynamic impact and blast loads [75–80]. Forghani *et al.* [75] used LS-DYNA to model Carbon-Fibre Reinforced Polymer (CFRP) laminates subjected to impact and blast loads. The individual plies were modelled using fully-integrated shell elements and were then tied together using a tie-break interface with penalty contacts to simulate interlaminar delamination. A plasticity model with damage (MAT_PLASTICITY_WITH_DAMAGE) was chosen to model the laminate plies as it allowed for progressive damage propagation in the plies. The authors compared the material model chosen with a user-defined Composite Damage Model (CODAM) that simulated localised damage initiation and propagation. The impactor used had a hemispherical shape and a diameter of 25.4 mm, while the impact velocities were varied from $1.76\,\mathrm{m\,s^{-1}}$ to $23.19\,\mathrm{m\,s^{-1}}$. The blast tests modelled used a 50 g disc of C4 placed at a SOD of 140 mm from the target structure. The velocity of the back face of the composite panel was measured by placing an aluminium cylinder in the centre of the panel and tracking its movement. For the blast simulations, the ConWep empirical model was used to create the blast loading on the target structure. The numerical model showed good correlation with the experimentally obtained force-time histories and force-displacement histories for the impact simulations. In the blast loaded simulations, the authors provide images of the damaged plies after the simulation but no images are provided of the experimentally tested panel for comparisons to be drawn. One key takeaway is the use of tie-break contacts between the plies results in the introduction of a stiffness between the plies that needs to be adjusted for when developing these layered numerical models [75].

Dolce *et al.* [76] investigated the blast response of metallic and CFRP laminates to air-blast loads using LS-DYNA. The blast load was modelled using both a ConWep and an MMALE approach. The tests simulated target structures with an exposed area of 800 mm × 800 mm and the loading was provided by a spherical C4 charge of masses 750 g and 825 g placed 150 mm from the panels. Different thicknesses of armour steels and a 27 mm thick CFRP made from 56 layers of fibre were used as the target structure. In the numerical models, the clamp frames and bolts were also modelled with the contact between the target structure and the bolts modelled with the CONTACT_AUTOMATIC_NODES_TO_SURFACE card. The CFRP target structures were modelled with 14 layers of shell elements with 4 integration points in each layer of shell elements. The CFRP was modelled using a composites damage model (MAT_054) and the interlaminar behaviour was modelled using a tie-break contact algorithm. This is similar to the approach used by Forghani *et al.* [75]. Qualitatively, the damage propagation matched the experiments reasonably well, although the simulation under-predicted the transient deformation behaviour, suggesting that there is some additional stiffness in the numerical model [76].

Gunaryo *et al.* [79] used ConWep and SPH in LS-DYNA to model the blast loading of cylindrical TNT charges on flat GFRP laminates made from woven sheets and an epoxy resin. The GFRP specimens had thicknesses of 1.9 mm and 2.3 mm and were tested with charge masses of 60 g to 100 g at SODs of 300 mm to 1000 mm. The entire structure was modelled with encastre boundary conditions used to represent the clamped edges. Like Dolce *et al.* [76], the laminate layers

were modelled with fully integrated shell elements using a MAT_ENHANCED_COMPOSITE_DAMAGE (MAT_054) model and had an element size of 3 mm × 3 mm. Delamination was not modelled in this study with the authors using a single layer of shell elements to model the GFRP laminate. In the experiments, a mesh of sewing needles was used to measure the maximum deformation of the panels. The SPH simulations showed reasonable accuracy in terms of measuring the maximum deformation of the tested panels with a 2 mm to 3 mm under-prediction in the measurements. Additionally, at lower charge masses (typically less than 60 g), both the ConWep and SPH models showed reasonable correlation with one another and with the experimental deformation profile but at the larger charge masses, the ConWep model varied greatly from the experimentally obtained profiles [79].

Zhao *et al.* [80] tested and modelled GFRP panels subjected to near-field and contact blast loads using ANSYS-AutoDyn. An ALE method was used to model the explosive blast load and the FSI between the explosive gases and the target structures. The tested specimens had dimensions of 500 mm × 500 mm × 60 mm and were manufactured using RTM with chopped mat glass-fibre and a polyurethane resin. Two SODs were tested, namely 0 mm and 200 mm, while the charge mass was varied from 10 g to 40 g. Two pressure transducers were also placed 1 m above and below the target structures. In the near-field tests, the tested panels showed burning of the fibres on the top surface and tensile cracking on the rear surface. In the contact tests, the panels all showed through-thickness fibre rupture and with increases in the ruptured area as the charge mass was increased. In the simulations, the air was modelled as an ideal gas and the explosive gases were modelled using a Jones-Wilkins-Lee (JWL) equation of state. The air mesh was built such that the pressure at the two pressure transducer locations could be captured [80] and thus had to be significantly larger than the test area and used a fairly coarse 10 mm element size. The GFRP panels were modelled with solid hexahedral elements and also used a fairly coarse element size of 5 mm. An Riedel–Hiermaier–Thoma (RHT) damage model, typically used to model reinforced concrete structures, was used for the GFRP panels although this was not characterised in this study for the tested structures. Qualitatively, the damage observed in the simulations closely matched the damage seen for the contact blast tests. Furthermore, the blast over-pressures measured in the simulations were similar to those observed in the experiments but occurred later in time [80].

2.8 Summary

V-hulls have been used extensively in MRAPs since the 1940s to protect soldiers from the blast pressure wave created by landmines. These V-hulls have typically been manufactured from armoured steel structures. While FRP composites have been introduced to MRAPs, these have typically been used as side armour protection. With composites seeing more use in the military industry, there is a need to investigate how these FRP composites perform relative to their steel counterparts.

There is a large body of work looking at damage propagation in flat steel panels to blast loads, including their transient behaviour. These studies have considered the effects of boundary conditions, SOD, and material selection. Additionally, a number of studies have also investigated

the blast response of scaled armour steel V-structures to localised blast loads, with these studies focussing on V-structures with a sharp V-tip radius. V-tip radius effects have been studied numerically for rigid V-structures, with some trends in impulse extracted, although the influence of the V-tip radius on the deformation has not been studied.

The blast performance of flat FRP composite laminates has also been extensively investigated, including studies on the effects of the manufacturing method, the material lay-up, and the materials selected. In recent years, a selection of studies have investigated the transient behaviour of flat FRP composite laminates. Only a limited number of investigations have considered FRP V-structures, with none of these studies considering the effect of the V-tip radius of the V-structure. Additionally, no impulse or transient deformation time histories were presented in these studies. This suggests the need to investigate the blast response of both steel and FRP composite V-structures and investigate the effects of varying the V-tip radius on the damage propagation and transient response.

There exists a large body of work using numerical modelling techniques to investigate the blast performance of metallic and composite structures. A number of these studies have considered the approaches used to model the blast load and how these influence the structural deformation and the pressure-time histories. Flat steel panel studies considered the effects of the SOD, the charge mass, and the target structure geometry. Various material models have been chosen for the structures with each having different advantages when it comes to capturing the correct deflection behaviours in response to the blast loading. U and V-structures have also been studied, with studies considering the effects of SOD, explosive eccentricity, the materials used for these structures, and the effects of the V-tip radius on the measured impulse. Flat composite panels were modelled in different studies with both shell and solid elements used. A number of different damage and failure models have been implemented with each having advantages and disadvantages, with one of the major limitations being the need to tune the models to correctly reflect the structural damage seen in the experiments. Composite V-structures have not been extensively modelled in literature, suggesting that this needs further investigation to better understand their behaviour when subjected to localised blast loads.

Chapter 3

V-structure manufacturing

In this chapter, a panel refers to a structure that is produced directly from the composite manufacturing process. Specimens are produced by cutting a panel. Specimens refer to structures that are to be tested, either via quasistatic tensile tests, Double Cantilever Beam (DCB) tests, or air blast tests.

This chapter starts with a short description of the manufacturing process used to produce the DOMEX-700 MC steel V-structures and the specimen properties. Details of the process followed in the manufacturing of the Glass-Fibre Reinforced Polymer (GFRP) composite flat panels and V-panels are then provided. All GFRP panels were manufactured using Vacuum Infusion (VI). Due to the complexity surrounding the V-hull geometry, an explanation of the chosen V-tip radius and the details of the mould design procedure are provided in the next two sections. These include the two designs that were considered and the benefits and drawbacks of each design. These sections also cover the manufacturing variability of the V-panels produced by each design and what effect these might have on answering the research questions proposed in Chapter 1. Next, the final manufacturing process is described, with details of the dimensions and masses of all the manufactured blast test specimens. Finally, a chapter summary highlights the key results of the manufacturing process.

3.1 Steel V-structure manufacture

The steel V-structure specimens were all manufactured from 2 mm thick, cold-rolled, DOMEX-700 MC sheet. Three geometries were considered. These were a 105° V-structure with a 32 mm V-tip radius, a 105° V-structure with a 62 mm V-tip radius, and a 120° V-structure with a 32 mm V-tip radius. These were chosen so that the blast performance effects of V-tip radius and V-angle could be determined through experiments. The flat and folded profiles for a 120° V-structure with a 32 mm V-tip radius are shown in figures 3.1 and 3.2 respectively. The flat profiles of the specimens were laser cut and then bent into the folded profile using a CNC plate bender. The profiles of a selection of V-structures were traced and measured using image processing software to check the V-structure dimensions. It was found that there was a ± 0.5 mm variation in the V-structure width and a $\pm 1°$ variation in V-angle. Table 3.1 shows the measured mass, measured thickness, and measured V-tip radius for all the DOMEX-700 MC steel blast test specimens. The measured V-tip radius for each batch of specimens was consistent and the specimen mass and thickness were consistent for all the specimens with the same geometry.

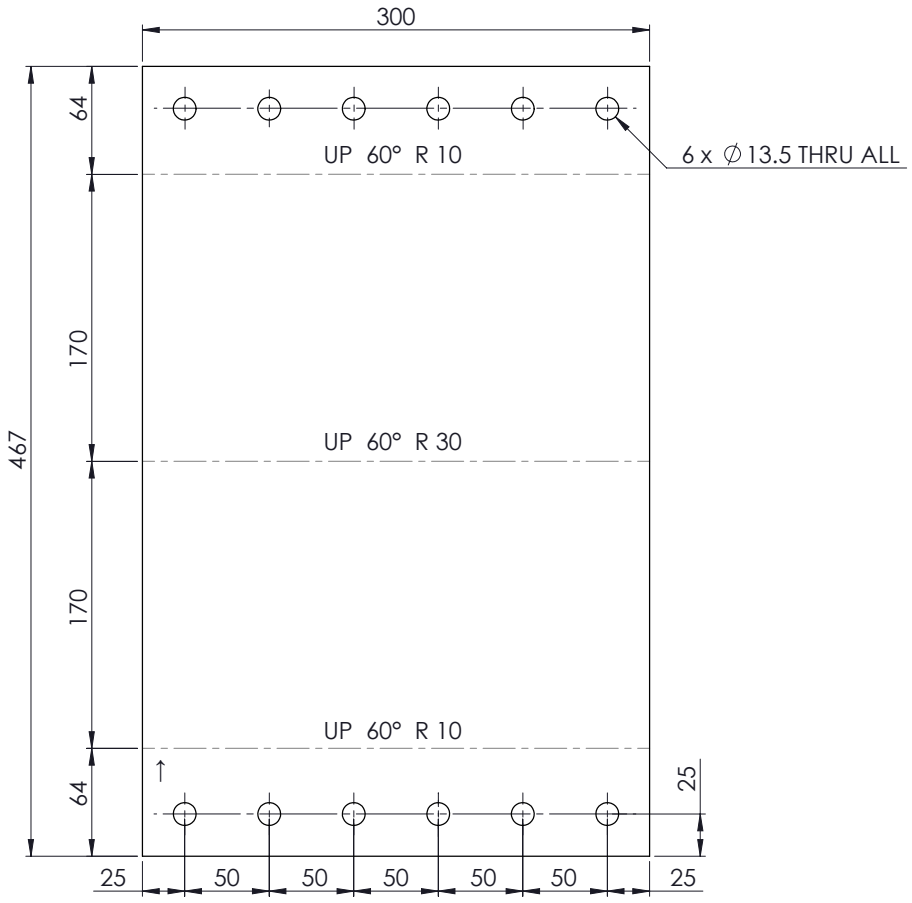

Figure 3.1: Flat profile for a 2 mm thick DOMEX-700 MC 120° V-structure with a 32 mm V-tip radius

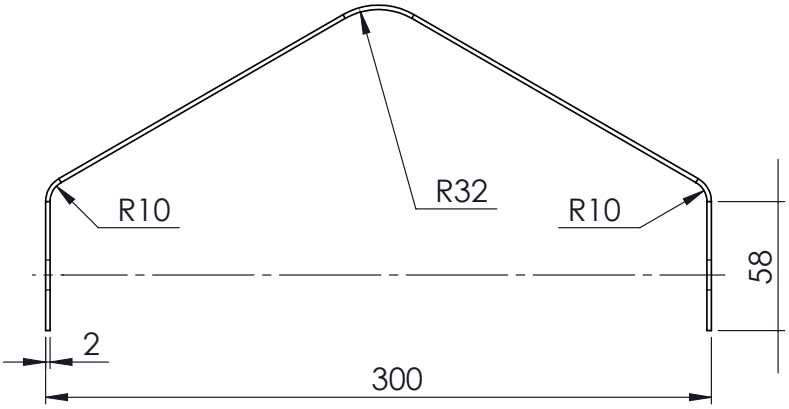

Figure 3.2: Folded profile for a 2 mm thick DOMEX-700 MC 120° V-structure with a 32 mm V-tip radius

Table 3.1: Geometry and mass of the DOMEX-700 MC steel blast specimens

	Designed values		Measured values	
Panel name	V-angle (°)	V-tip radius (mm)	Average Thickness (St. deviation) (mm)	Mass (kg)
DOMEX700_105_32_1	105	32	2.06 (0.04)	2.318
DOMEX700_105_32_2	105	32	2.04 (0.02)	2.316
DOMEX700_105_32_3	105	32	2.05 (0.03)	2.313
DOMEX700_105_32_4	105	32	2.06 (0.02)	2.323
DOMEX700_105_32_5	105	32	2.03 (0.02)	2.319
DOMEX700_105_32_6	105	32	2.04 (0.04)	2.311
DOMEX700_105_62_1	105	62	2.04 (0.03)	2.304
DOMEX700_105_62_2	105	62	2.03 (0.02)	2.301
DOMEX700_105_62_3	105	62	2.04 (0.01)	2.296
DOMEX700_105_62_4	105	62	2.03 (0.03)	2.296
DOMEX700_105_62_5	105	62	2.06 (0.03)	2.297
DOMEX700_105_62_6	105	62	2.07 (0.03)	2.303
DOMEX700_120_32_1	120	32	2.20 (0.04)	2.194
DOMEX700_120_32_2	120	32	2.20 (0.04)	2.184
DOMEX700_120_32_3	120	32	2.20 (0.04)	2.186
DOMEX700_120_32_4	120	32	2.08 (0.05)	2.193
DOMEX700_120_32_5	120	32	2.07 (0.06)	2.193
DOMEX700_120_32_6	120	32	2.06 (0.05)	2.186
DOMEX700_Flat_1	-	-	2.02 (0.01)	2.453
DOMEX700_Flat_2	-	-	2.01 (0.02)	2.452
DOMEX700_Flat_3	-	-	2.02 (0.02)	2.453
DOMEX700_Flat_4	-	-	2.02 (0.01)	2.454
DOMEX700_Flat_5	-	-	2.03 (0.02)	2.452

3.2 GFRP Panel manufacture

Vacuum Infusion was used for the manufacture of the GFRP panels. It was an appropriate choice given the panel dimensions, the number of layers of glass-fibre, and the need for consistent geometric and mechanical properties. It would not have been feasible to use hand lamination due to the panel size and thickness, and the difficulty with quality control for hand laminated parts. Prepreg manufacture would have been too expensive for this size and type of part.

The panels were manufactured using a plain weave E-glass fibre with an areal density of $400\,\mathrm{g\,m^{-2}}$ and Prime 20LV epoxy resin with a Low Viscosity (LV) slow hardener. An E-glass fibre was chosen due to its availability and lower cost compared to an S-glass fibre. Prime 20LV resin is an epoxy resin that is designed for VI processes, due to its low viscosity and good exothermic characteristics [81]. This allows for the infusion of large and thick parts before the resin starts to gel.

Before the lay-up of the dry materials, the mould surface was prepared by applying several coats

of mould release wax. This acted as a release agent to assist with the panel removal once the infusion was completed. The order of the lay-up of the dry materials began with a flow promoter layer to assist with the flow of resin across and through the panel. This was followed by a peel ply release fabric, which was also used to assist with the removal of the panel and ensure a consistent surface finish. Next, the dry layers of fibre were placed down, followed by another layer of the release fabric and the flow promoter. To ensure that each layer of material stayed in position, a small piece of masking tape was used at the corners to hold it in place. A resin feed line was fitted on one end of the panel, while a vacuum line was fitted at the other end of the panel. All the dry materials were covered with a vacuum bag that was sealed to the mould with tacky tape. The layup for a flat panel is shown in figure 3.3. A series of pleats along the edge of the vacuum bag are evident in figure 3.3. These allowed the bag to take up the 3D shape of the part and ensured a consistent tension in the bag without affecting the final part geometry. A schematic of the material lay-up for one of the V-panels is shown in figure 3.4. The dashed lines represent the folds in the mould, with each of the four panels labelled and highlighted with a black line.

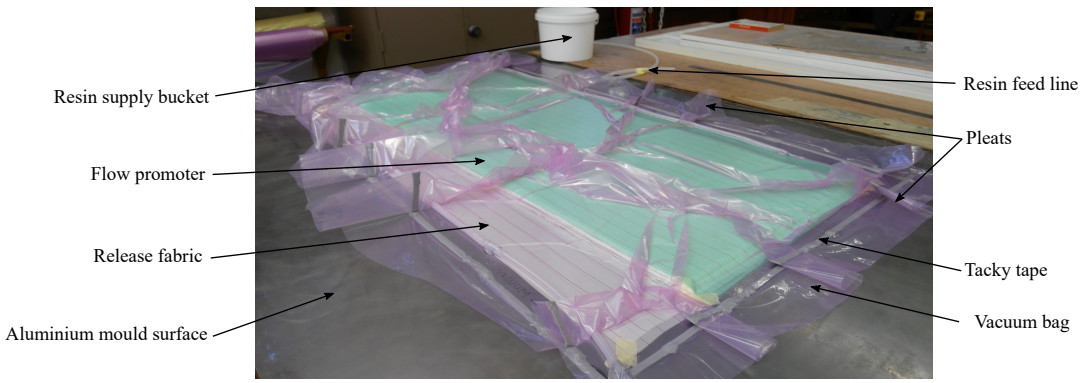

Figure 3.3: Layup for the flat panel manufacture

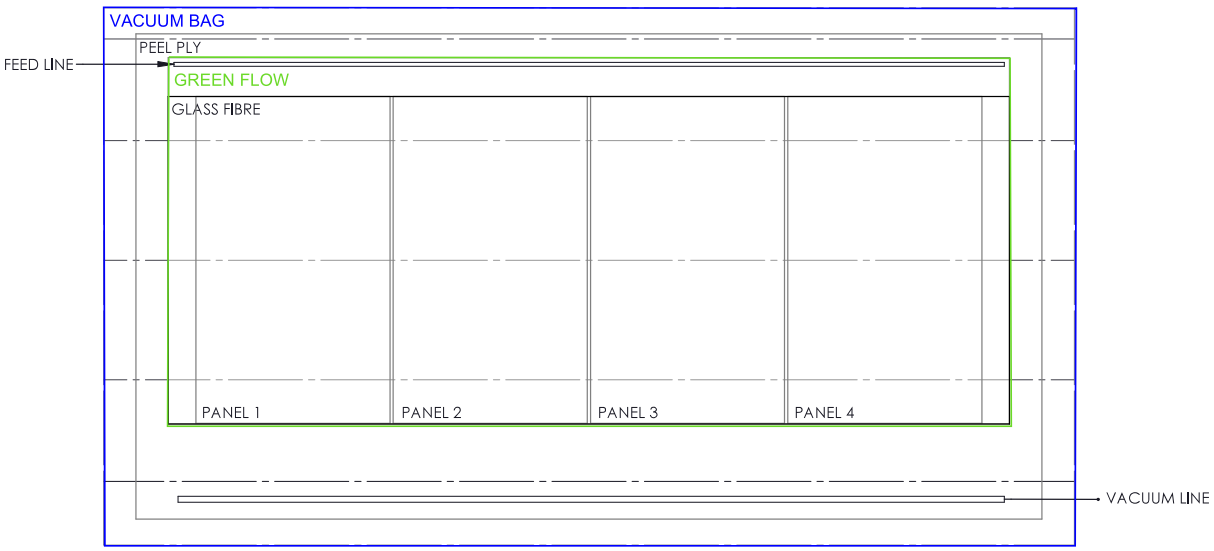

Figure 3.4: Schematic of the material layup for the V-panels manufactured using a female mould

3.3 Specifying the number of layers of glass-fibre

This study requires that the mass and the geometry of the GFRP and DOMEX-700 MC steel V-structures are equivalent, hence it is necessary to determine the number of layers of glass-fibre required to achieve this specification. The glass-fibre specimen needed to have an equivalent mass to a 2 mm DOMEX-700 MC steel specimen with the same cross-section. A previous study [82] found that 28 layers of glass fibre produced a specimen with the same area density as the steel specimen, while theoretical calculations, with a fibre volume fraction of 55% suggested that 36 layers would result in a specimen with the correct equivalent mass. Hence, it was decided that three specimens with 26, 28 and 36 layers respectively would be manufactured. The properties of the specimens and their masses are compared with a 400 mm × 400 mm × 2 mm DOMEX-700 MC steel specimen. This data is summarised in table 3.2. The density of DOMEX-700 MC is 7870 kg m^{-3} and thus the mass of a DOMEX-700 MC flat steel structure with the specified dimensions is 2.453 kg which is also the average mass of the flat steel structures. From the table, it can be seen that a GFRP specimen made from 28 layers of glass-fibre with the same dimensions has a mass of 2.566 kg. Hence it was decided that the manufactured panels for the blast test specimens should be 28 layers thick. Using 27 layers might have resulted in a mass that was closer to the steel but it would not have allowed for a symmetric laminate.

Table 3.2: Manufactured panels' properties

Panel number	Configuration	Thickness (mm)	Mass (kg)	Area (m^2)	Areal density (kg m^{-2})
1	36 layers	11.2	3.295	0.1616	20.389
2	28 layers	8.4	2.566	0.1669	15.378
3	26 layers	7,8	2.437	0.1668	14.608
Steel	DOMEX-700 MC	2.01	2.454	0.160	15.338

Two additional flat panels were manufactured and cut to size for use as tensile test specimens and DCB specimens respectively. The ASTM standard for the tensile testing of composite materials recommends a specimen thickness of 2.5 mm [83], while from the previous study, it was determined that the average thickness of a layer of infused 400 g m^{-2} E-glass was 0.32 mm. Hence, eight layers of glass-fibre were used for the tensile test panel. The ASTM standard for mode 1 (DCB) testing of composite materials, states that the DCB specimens should be between 3 mm to 5 mm thick [84]. An average thickness of 4.0 mm was selected and 12 layers of glass-fibre were used for that GFRP panel.

3.4 V-panel mould design

Two mould designs were considered for the manufacture of the GFRP V-panels, a male and a female mould. In a previous study, Hobson [82] used a female mould, as described in Chapter 2. This mould had a small bend radius of 4 mm at the V-tip of the mould, which was chosen in an attempt to match the geometry of steel V-hulls tested in a previous study [8]. The fibre layers were unable to bend tight enough to fit this radius which resulted in a resin rich area forming

at the tip during the manufacturing process, as shown in figure 3.5. This was undesirable as the panels produced did not have a uniform thickness and fibre distribution. To increase the tip radius, Hobson [82] modified the mould with an insert, but due to time constraints, this insert was poorly made. As a result, the panels manufactured had an inconsistent tip radius, which was also undesirable, as previous work shows that the V-tip radius influences the impulse transferred by a V-structure [72]. Additionally, the mould design made the laying up of the fibres, the infusion and the de-moulding challenging [82].

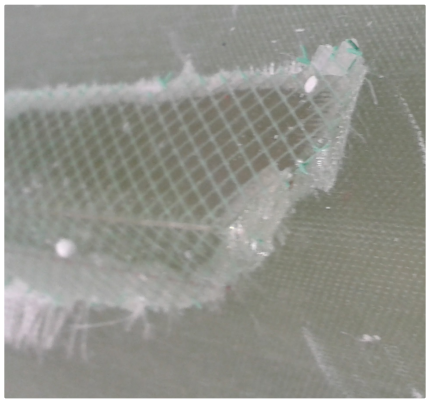

Figure 3.5: The resin rich area observed at the V-tip in the V-hulls manufactured by Hobson [82]

3.4.1 Male mould

This project first trialled a male mould to try to eliminate the issues identified in the female mould design. The design is shown in figure 3.6. This mould design simplified the lay-up of the dry material and the setting up of the vacuum bag. Additionally, the use of a centre feed placed at the V-tip assisted the infusion process as shown in figure 3.6. One of the major advantages observed in the panel produced using this mould design was the fairly consistent panel thickness. Additionally, the resin rich areas observed by Hobson [82] were not noted in this panel.



Figure 3.6: Photographs showing the V-panel infusion with the male mould

Despite these improvements gained by using the male V-mould design, the V-tip radius was

inconsistent and some fibre wrinkling was apparent. The visible wrinkling at the V-tip is shown in figure 3.7(a). A lay-up for a second trial panel was done to determine if the wrinkle at the V-tip was due to the material lay-up techniques, the centre feed line or the manufacturing technique. In this lay-up, the feed line was moved away from the centre. From figure 3.7(b), it is shown that a visible ridge was still present at the V-tip in the second process, meaning that the inconsistencies in the geometry were due to the mould design and the large number of layers of glass-fibre used. Since the blast test specimens needed to have a consistent tip radius, this approach was unsuitable. Furthermore, the wrinkling at the V-tip may have weakened the structure.



(a) Cross-section of the V-tip, showing the visible ridge and inconsistent tip radius

(b) The visible ridge in the lay-up with the dry material under vacuum

Figure 3.7: Photographs of the manufacturing issues observed when using the "male" mould

3.4.2 Female mould

A female mould was manufactured. The aluminium mould surface was bent with a 32 mm tip radius. Figure 3.8 shows the assembled 105° female V-shaped mould. The resin feed line and vacuum lines were placed on the flat surfaces of the mould on either side of the dry fibres. Similar to Hobson [82], this mould design made the layup and vacuum bagging processes more challenging, which increased the setup time. The panels manufactured with this mould were found to have a more consistent V-tip radius and hence these female moulds were used for the manufacture of the rest of the blast test panels.



Figure 3.8: Photograph of the 105° female V-shaped mould with the dry material and vacuum bag fitted

Some of the specimens cut from the V-panels produced from the female V-mould showed small inconsistencies, as shown in figure 3.9. The most common variation observed was at the curved regions on the inside of the specimens, due to the way the fibres layers were stacked when dry. It was not always possible to ensure that the layers were evenly packed in these regions, which resulted in slight thickness variations. In some cases, a small resin rich zone was formed, as shown in figure 3.9(b) and figure 3.9(c). This is not a concern in terms of the strength of the specimens as it can be seen that the fibre layers are still compacted at the V-tip. Furthermore, a detailed explanation of how this resin rich region on the inside of the V-tip was removed has been provided in Chapter 7. Figure 3.9(a) shows a typical variation observed at the V-tip for the $\pm 45°$ layup specimens where a wrinkle occurred against the mould. This was attributed to the shifting of the fibres during the layup process. It is important to note that while a wrinkle is present, this is not at the V-tip, hence it is not anticipated that it will affect the ability to answer the research questions. Furthermore, the fibre layers are still closely packed and the panel thickness does not vary significantly in this region. Hence, the panels were considered suitable for blast testing. It should be noted that these are not unusual variations found in industrial scale GFRP manufacture by VI.

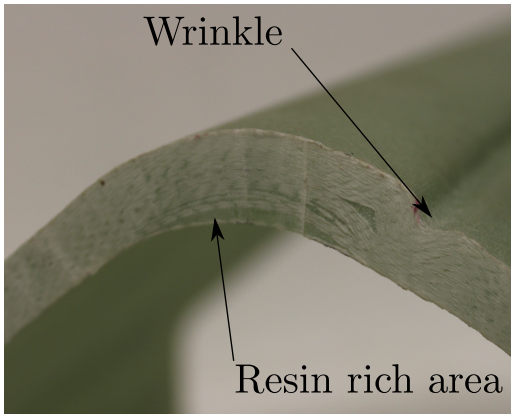

(a) 105°, $+45°/-45°$ Layup

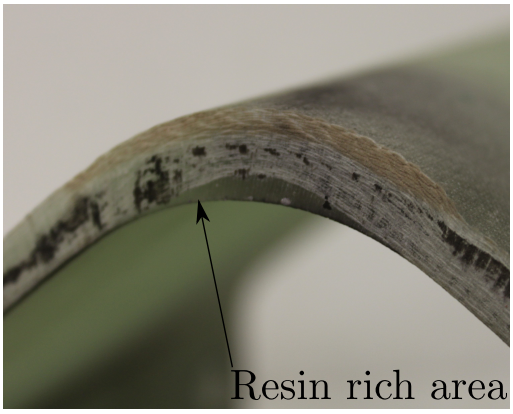

(b) 105°, 0°/90° Layup

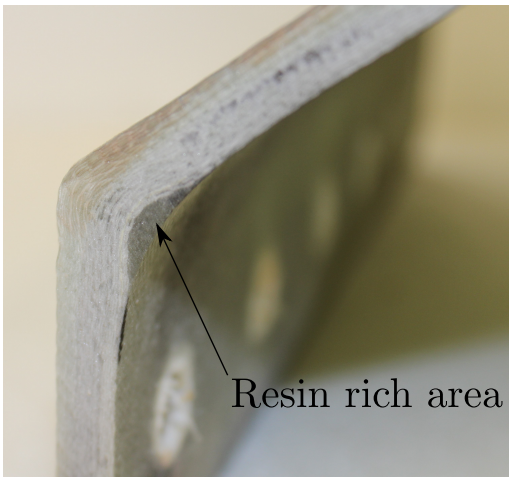

(c) 105°, 0°/90° Layup

Figure 3.9: Photographs showing the variations from the design specification observed at the V-tip and at the clamped region in the V-structures manufactured

3.5 Final manufacturing process

The blast test V-structures were manufactured in five manufacturing cycles, with each infusion process producing four specimens. Twelve specimens with a 105° V-angle and a 0°/90° lay-up were manufactured. The first set of four specimens (labelled GFRP_0-90_105_32_T#) were trial specimens manufactured using the male V-shaped mould. The next two sets of four specimens (labelled GFRP_0-90_105_32_#) were manufactured with the female 105° V-shaped mould. Following this, one set of four specimens with a 105° V-angle and a ±45° lay-up were manufactured using the same female mould. The last set of four specimens (labelled GFRP_ 0-90_120_32_#) were manufactured with a 120° V-shaped female mould.

Three flat panels were also manufactured. Eight flat blast test specimens were manufactured in a single infusion, four with a 0°/90° lay-up and four with a ±45° lay-up. Additionally, two panels were manufactured to produce specimens for material testing. The panel for tensile test specimens was made using 8 layers of glass-fibre while the panel for the Double Cantilever Beam (DCB) test specimens was made using 12 layers of glass-fibre with a non-perforated insert used to define the crack initiation point. The reasons for these choices of layers were explained in section 3.3. The details of the specimen dimensions for these two sets of tests are given in Chapter 4.

The GFRP panels were marked with the profile of the blast specimens and cut to the correct shape using a bandsaw. The V-shaped blast specimens have a projected area of 300 mm × 300 mm, while the flat specimens have an total area of 400 mm × 400 mm with an exposed area of 300 mm × 300 mm. The mounting holes were then drilled using a drill press. Further details of the blast test specimen geometry are provided in Chapter 7. Once this was done, the dimensions of each specimen were checked using a vernier caliper at 10 points across the specimen. The specimen was weighed and the V-tip radius was checked using a series of manufactured templates.

The properties of the manufactured blast test specimens are summarised in table 3.3. This shows that the masses and thicknesses of the 105° V-structures exhibited minimal variation, which suggests that the manufacturing technique was suitable. Additionally, table 3.3 shows that while the V-tip radii of the manufactured specimens are not identical to the designed values, they are consistent. Comparing the V-tip radius and specimen mass properties of both 105° and 120° GFRP V-structures, they are almost identical to their DOMEX-700 MC steel counterparts. This is a key requirement when attempting to answer the research questions and the hypothesis, as any observed differences in the blast performance of the specimens can then be attributed to the materials used for the specimens.

Table 3.3: Manufactured GFRP blast specimens' properties

Panel name	Designed values		Measured values		
	Lay-up orientation	V-angle (°)	V-tip radius (mm)	Average Thickness (St. deviation) (mm)	Mass (kg)
GFRP_0-90_105_32_T1	0°/90°	105	30-34	8.42 (0.71)	2.139
GFRP_0-90_105_32_T2	0°/90°	105	30-34	8.67 (0.88)	2.194
GFRP_0-90_105_32_T3	0°/90°	105	30-34	8.45 (0.20)	2.164
GFRP_0-90_105_32_T4	0°/90°	105	30-34	8.37 (0.31)	2.103
GFRP_0-90_105_32_1	0°/90°	105	34	8.85 (1.18)	2.301
GFRP_0-90_105_32_2	0°/90°	105	34	9.16 (1.22)	2.282
GFRP_0-90_105_32_3	0°/90°	105	34	8.99 (0.99)	2.251
GFRP_0-90_105_32_4	0°/90°	105	34	8.75 (1.13)	2.273
GFRP_0-90_105_32_5	0°/90°	105	34	9.38 (1.44)	2.302
GFRP_0-90_105_32_6	0°/90°	105	34	9.48 (1.17)	2.310
GFRP_0-90_105_32_7	0°/90°	105	34	9.23 (0.96)	2.287
GFRP_0-90_105_32_8	0°/90°	105	34	8.93 (0.57)	2.312
GFRP_45-45_105_32_1	±45°	105	34	9.06 (0.78)	2.313
GFRP_45-45_105_32_2	±45°	105	33	9.47 (1.45)	2.289
GFRP_45-45_105_32_T1	±45°	105	34	9.58 (1.23)	2.289
GFRP_45-45_105_32_T2	±45°	105	34	9.36 (1.46)	2.279
GFRP_0-90_120_32_1	0°/90°	120	32	9.04 (1.19)	2.141
GFRP_0-90_120_32_2	0°/90°	120	32	8.93 (0.85)	2.119
GFRP_0-90_120_32_3	0°/90°	120	31	8.99 (0.92)	2.144
GFRP_0-90_120_32_4	0°/90°	120	33	8.61 (0.50)	2.102
GFRP_Flat_0-90_1	0°/90°	-	-	8.36 (0.11)	2.507
GFRP_Flat_0-90_2	0°/90°	-	-	8.39 (0.19)	2.483
GFRP_Flat_0-90_3	0°/90°	-	-	8.47 (0.22)	2.511
GFRP_Flat_0-90_4	0°/90°	-	-	8.61 (0.15)	2.487
GFRP_Flat_45-45_1	±45°	-	-	8.43 (0.09)	2.463
GFRP_Flat_45-45_2	±45°	-	-	8.44 (0.12)	2.496
GFRP_Flat_45-45_3	±45°	-	-	8.62 (0.11)	2.467
GFRP_Flat_45-45_4	±45°	-	-	8.74 (0.21)	2.502

3.6 Discussion - Manufacturing

A short discussion of the key points taken from the manufacturing chapter is provided below. These focus on the advantages and limitations of the chosen manufacturing technique - VI, and the benefits of the consistent panel geometry when attempting to answer the research questions posed at the start of the thesis.

All the GFRP V-structures were manufactured using VI. The female mould used produced panels with a consistent V-tip radius of 34 mm, which was not identical to the designed value of 32 mm. This difference is small, and as it has been shown in previous studies [72], small variations in V-tip radius do not significantly affect (<1%) the impulse transfer characteristics of the V-structures. Thus it should be possible to compare the experimental blast performance of the steel and GFRP panels.

Additionally, looking at the tabulated panel properties, it can be seen that panel masses and thicknesses are also consistent for each configuration manufactured. This means that when the GFRP V-structures are tested, it should be possible to obtain repeatable results for tests performed with the same charge mass of PE4. This is important when analysing the observed failure modes and when validating the numerical blast model.

The one limitation of the female mould and VI was the resin rich area observed on the inside of GFRP V-structures at the V-tip. Although this face of the V-structure is not exposed to the blast wave, if high-speed imaging needs to be used, there is a risk of this resin-rich area breaking off during the blast test and thus any deflection of the panel in this region would be lost. Thus care needs to be taken when performing DIC with these V-structures.

3.7 Summary

This chapter detailed the manufacturing process followed for producing the steel and GFRP specimens. The GFRP specimens were made using vacuum infusion. The V-hulls were made using a female mould to provide panels with a consistent V-tip radius, which was a key requirement. The specimen masses and dimensions were recorded with the average V-tip radius being 2 mm larger for the GFRP V-structures compared to the equivalent steel V-structures. The effects of this difference have been addressed in chapter 10. Minimal variations between the steel and GFRP counterparts were observed although a resin rich area was observed at the V-tip in some of the manufactured GFRP V-structures.

Chapter 4

Material testing

Two materials were used in this research. In order to firstly confirm the consistency of these materials and secondly develop a numerical model that correctly captures the behaviour of these materials under blast loading, it was necessary to perform material property tests. For the GFRP specimens, the tests also helped confirm the consistency of the manufacturing processes chosen. This chapter presents the tests performed and the subsequent results. Following this, the process of characterising the material models used in the numerical FEA studies is provided.

4.1 DOMEX-700 MC material testing

4.1.1 Quasistatic tensile testing

Quasistatic tensile tests were performed on steel specimens designed according to the ASTM A370 [85] standard. The specimens had overall dimensions of 200 mm long and 25 mm wide, while, the gauge length and width were 80 mm and 12.5 mm, respectively. The specimen geometry is shown in figure 4.1. Specimens were laser cut in both the roll direction (direction 1) and perpendicular to the roll direction (direction 2). The width and thickness were measured at three points along the gauge length of each specimen and used to determine the average cross-sectional area of each specimen.

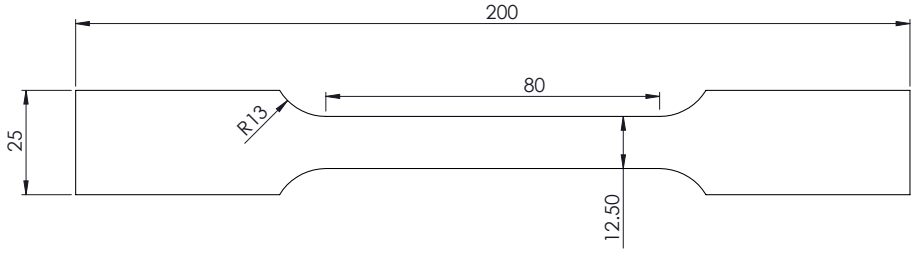

Figure 4.1: DOMEX-700 MC steel quasistatic tensile test specimen geometry

Three crosshead speeds were chosen, namely, 5 mm min^{-1}, 20 mm min^{-1}, and 100 mm min^{-1} to use the full range of speeds available with the Zwick testing machine and six specimens of each orientation were tested at each crosshead speed. The engineering stress versus the engineering strain for two crosshead speeds is shown in figure 4.2. At a crosshead speed of 5 mm min^{-1} the failure strain was 50% higher in direction 1 compared to direction 2, while at the highest crosshead speed of 100 mm min^{-1}, there was no observable difference in the failure strain in the two directions. Furthermore, there was no noticeable difference in the yield strength between the two directions regardless of the crosshead speeds. Previous studies [86] have found that DOMEX-700 MC does not experience significant rate sensitivity effects. These results are

summarised in table 4.1.

Table 4.1: Yield strength and failure strain for the steel specimens tested in the two directions at the three crosshead speeds

Direction	Crosshead Speed ($mm\,min^{-1}$)	Average yield strength (MPa)	St. deviation (MPa)	Average failure strain	Failure strain st. deviation
1	2	783.53	12.42	0.1348	0.0298
	5	806.88	5.66	0.1459	0.0105
	100	805.21	3.08	0.1365	0.0100
2	2	806.78	8.77	0.1053	0.0084
	5	792.44	12.27	0.1406	0.0227
	100	799.37	14.91	0.1290	0.0078

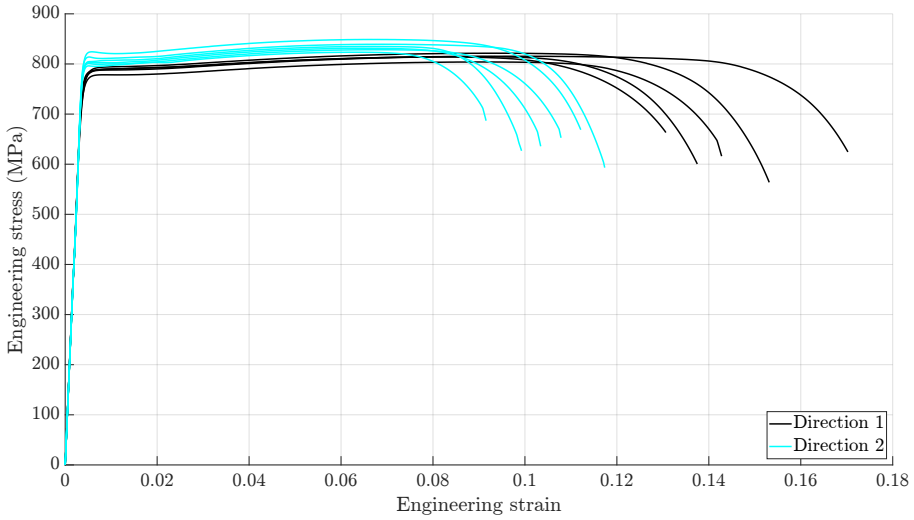

(a) Crosshead speed = $5\,mm\,min^{-1}$

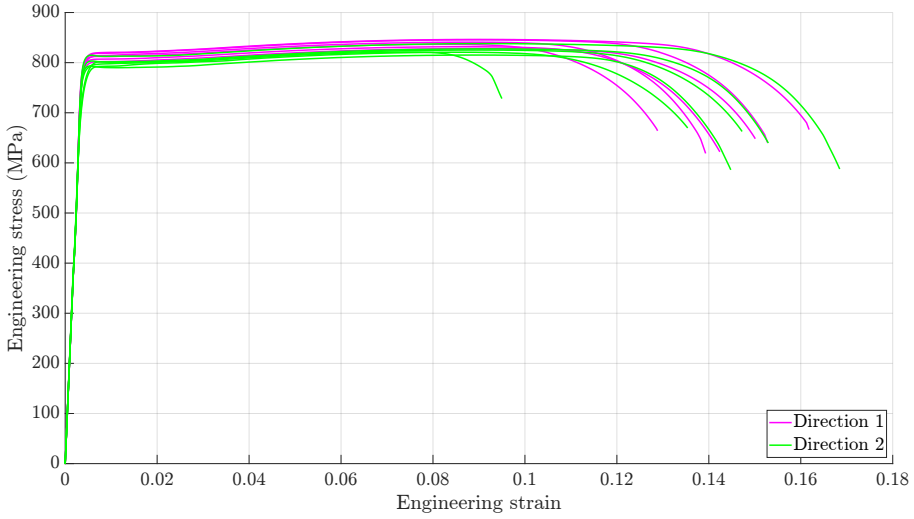

(b) Crosshead speed = $20\,mm\,min^{-1}$

Figure 4.2: Graphs showing the engineering stress versus engineering strain (Tensile test results, DOMEX-700 MC)

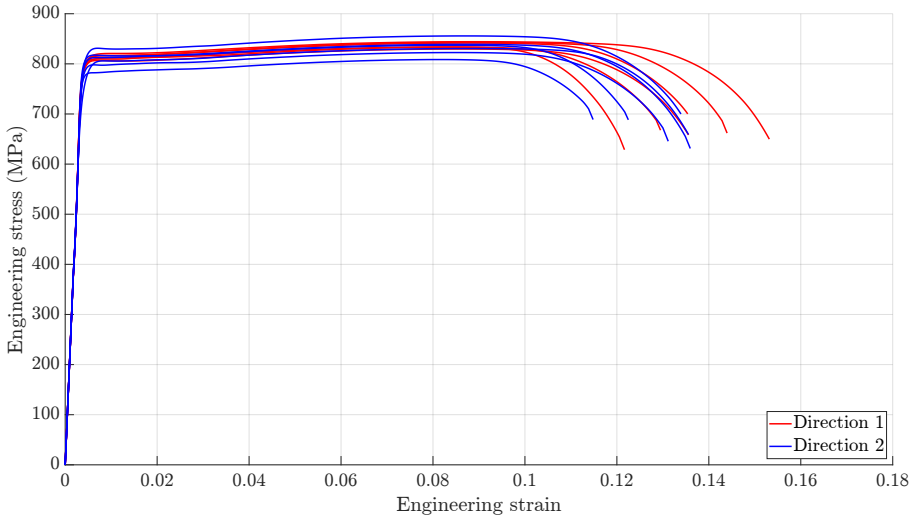

(c) Crosshead speed = 100 mm min^{-1}

Figure 4.2: Graphs showing the engineering stress versus engineering strain (Tensile test results, DOMEX-700 MC) (Cont.)

In order to fit a numerical material model to the tensile test data, the engineering stress (σ_{eng}) needs to be converted to true stress (σ_T) and the engineering strain (ϵ_{eng}) needs to be converted to true plastic strain (ϵ_T). This is done using equations (4.1) and (4.2).

$$\sigma_T = \sigma_{eng}\left(1 + \frac{\Delta u}{L_0}\right) \tag{4.1}$$

$$\epsilon_T = \ln(1 + \epsilon_{eng}) \tag{4.2}$$

$$\epsilon_{eff}^{pl} = \epsilon_T - \frac{\sigma_T}{E} \tag{4.3}$$

Where Δu is the change in length of the specimen and L_0 is the initial gauge length. The final step is to convert the true strain into effective plastic strain (ϵ_{eff}^{pl}). This is done by subtracting the elastic strain from the total strain as shown in equation (4.3). The true stress versus the effective plastic strain for all the tested specimens is shown in figure 4.3. From the data, the yield strength is within 5% for all the specimens, although there is a 30% difference in the strain at necking across all the tests. From the tensile test results, it was decided that the Johnson-Cook [87] material model could be used and that the material could be treated as isotropic.

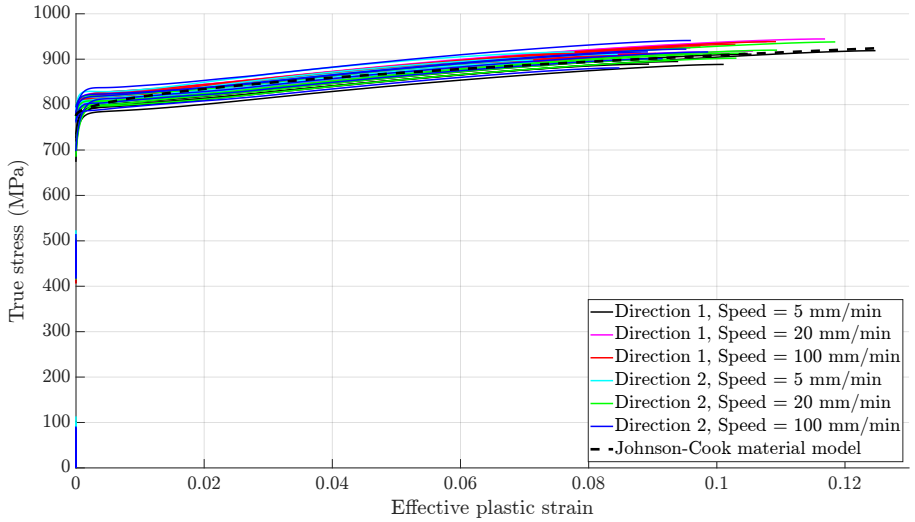

Figure 4.3: Graph showing the true stress versus effective plastic strain including Johnson-Cook parameters (All tensile test results, DOMEX-700 MC)

4.1.2 Steel material model characterisation

The Johnson-Cook [87] material model was chosen to model the DOMEX-700 MC steel in the numerical simulations. The constitutive equation for the material model is given by equation (4.4).

$$\sigma_{eq} = \left[A + B\epsilon_{eff}^{pl}\right] \times \left[1 + c\ln(\dot{\epsilon^{\star}})\right] \times \left[1 - T_m^{\star}\right] \tag{4.4}$$

$$\dot{\epsilon^{\star}} = \frac{\dot{\epsilon_p}}{\dot{\epsilon_0}} \tag{4.5}$$

$$T^{\star} = \frac{T - T_0}{T_m - T_0} \tag{4.6}$$

Where σ_{eq} is the equivalent stress, $\dot{\epsilon^{\star}}$ is the dimensionless strain rate, $\dot{\epsilon_0}$ is the reference strain rate, T is the working temperature, T_0 is the reference temperature and T_m is the melting temperature. The parameters for A, B, n, and c were varied until the black dashed curve shown in figure 4.3 was obtained for a crosshead speed of $5\,\mathrm{mm\,min^{-1}}$. The final parameters are given in table 4.2. All the experiments were conducted at room temperature, and thus the parameter m was set to 1. The strain rate was then changed to match each crosshead speed and the resulting curve compared to the experimental data. These material parameters were then used in Chapter 8 to model the blast tests.

Table 4.2: Johnson-Cook material model parameters for DOMEX-700 MC based on tensile test data

Parameter	Value
A (MPa)	770
B (MPa)	420
n	0.5
c	0.0009

4.2 GFRP material testing

4.2.1 Quasistatic tensile tests

Quasistatic tensile tests were conducted on GFRP specimens using the ASTM D3039 [83] standard. The geometry for a balanced and symmetric specimen is recommended to be rectangular with dimensions of 25 mm wide, 250 mm long, and 2.5 mm thick. The ASTM standard also recommends that emery cloth be placed between the specimen and the grips of the test equipment.

Specimens were cut with fibre orientations of 0°/90° and ±45°. The thickness and width were measured at three points along the length of each specimen and the average cross-sectional area was determined. The specimens were then painted white and speckled in black to enable DIC to be used to track their elongation during the test while the force was measured using the load cell on the Zwick tensile testing machine. An example of a speckled specimen is shown in figure 4.4. Six specimens in each fibre orientation were tested at a crosshead speed of $2\,\mathrm{mm\,min^{-1}}$.

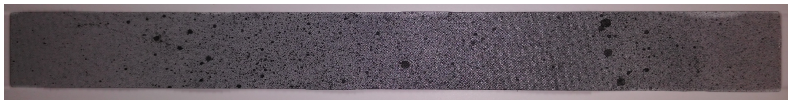

Figure 4.4: Photograph of a speckled GFRP tensile test specimen

The first set of tensile tests were performed on the 0°/90° specimens. These tests were used to obtain the elastic modulus of the glass-fibre and the failure strain for the material. The force versus extension graph for these tests is shown in figure 4.5(a). The results were converted to an engineering stress versus engineering strain graph, shown in figure 4.5(b), by dividing the force by the original cross-sectional area of each specimen and dividing the extension by the gauge length. The chord modulus was taken by drawing a straight line through the data, shown in figure 4.5(b). This was used to obtain the effective elastic modulus of the tensile test specimen. The slope of line, 18.51 GPa, is the effective elastic modulus (E_{eff}) of the specimens. The results are summarised for the two fibre orientations in table 4.3. The low standard deviation in the measured effective modulus for all the tests increases the confidence in the manufacturing method used for producing the test specimens.

Table 4.3: Effective modulus and failure strain for the GFRP specimens

Direction	Average effective modulus (GPa)	St. deviation (GPa)	Average failure strain	failure strain st. deviation
0°/90°	18.51	0.537	0.0196	0.0006
±45°	6.164	0.877	0.0802	0.0034

The next step was to determine the approximate volume fraction for all the manufactured specimens. This was done by first measuring the dry mass of the fibre-glass before each infusion and then weighing the manufactured panels after the VI process. Once the mass of glass-fibre and resin was known, the approximate volume fraction could be determined using the density

of each material. The mixed density of the Prime 20 resin (ρ_m) is provided as $1.084\,\mathrm{g\,cm^{-3}}$ or $1084\,\mathrm{kg\,m^{-3}}$ [81]. The areal density of the glass-fibre is $400\,\mathrm{g\,m^{-2}}$, while the fibres have an average thickness of 0.32 mm. The ply thickness was found by measuring the thickness of each specimen and dividing this value by the number of layers used for the specimens. Thus, the density of the glass-fibre sheets (ρ_f) is $1.710\,\mathrm{g\,cm^{-3}}$ or $1710\,\mathrm{kg\,m^{-3}}$.

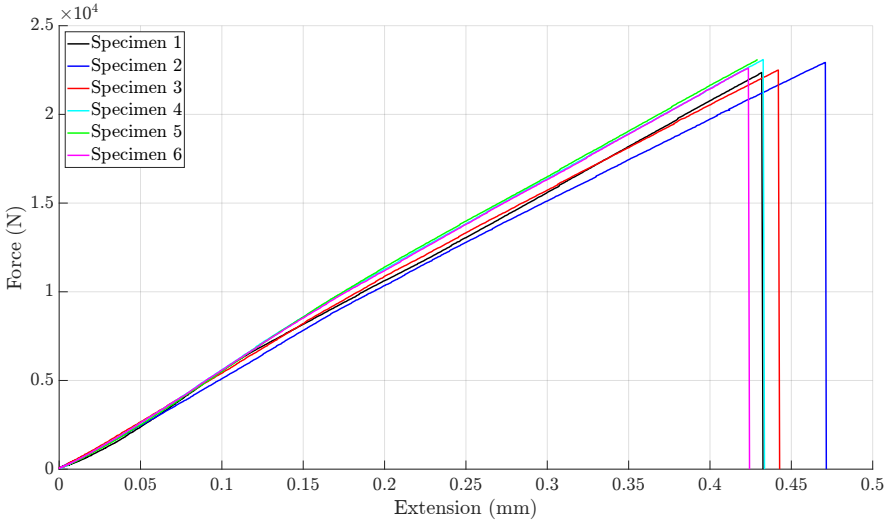

(a) Force versus extension

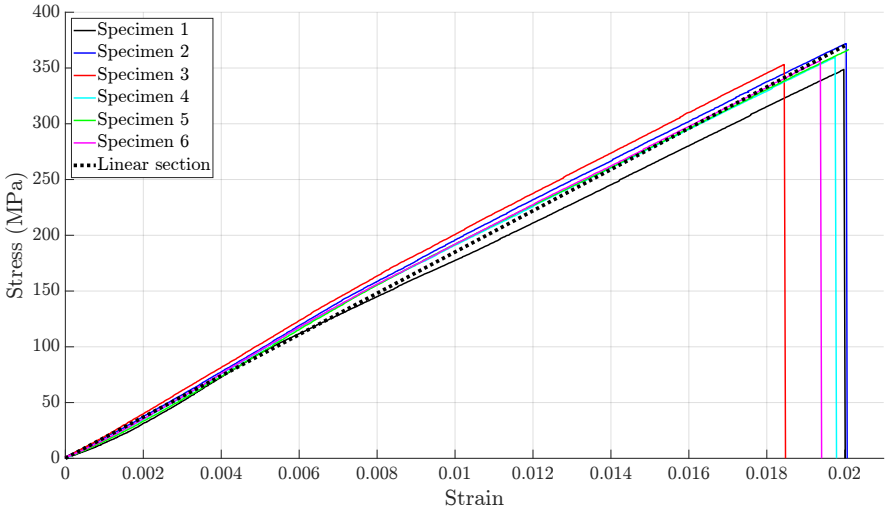

(b) Stress versus strain

Figure 4.5: Graph showing the GFRP tensile test results for a fibre orientation of 0°/90° including the chord line drawn through the data

Equation (4.7) gives the volume fraction relation for a composite material, where v_f is the fibre volume fraction, v_m is the matrix volume fraction, and v_v is the void volume fraction. The typical volume fraction for voids in a part manufactured with VI is around 8% [88]. This means that the sum of the fibre and matrix volume fractions should be 92%. Using the known masses and densities, the average fibre volume fraction was calculated as 62%, while the average matrix volume fraction was approximately calculated as 30%.

$$v_f + v_m + v_v = 1 \tag{4.7}$$

The elastic modulus for the resin (E_v) was provided as 3.5 GPa. The elastic modulus of the glass-fibre (E_f) could then be determined from equation (4.8) by setting $E_v = 0$. Hence, the elastic modulus of the glass-fibre was found to be approximately 28.15 GPa.

$$E_f \times v_f + E_m \times v_m + E_v \times v_v = E_{eff} \tag{4.8}$$

The force-extension and stress-strain results for the ±45° specimens are shown in figure 4.6. The results show that the response is fairly linear for strains below 0.008. Following this, the matrix starts to fracture as the fibres realign towards the 0° direction which results in the non-linear behaviour observed in the data. The linear part of the stress-strain graph can be used to obtain an approximate shear modulus for the material by plotting a line of best fit through the data shown in the stress-strain graph with a black dotted line. The shear modulus was found to be 6.18 GPa.

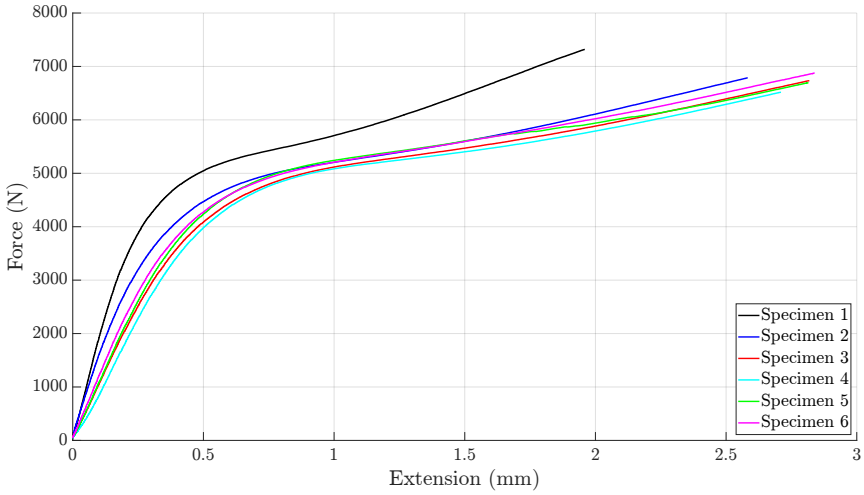

(a) Force versus extension

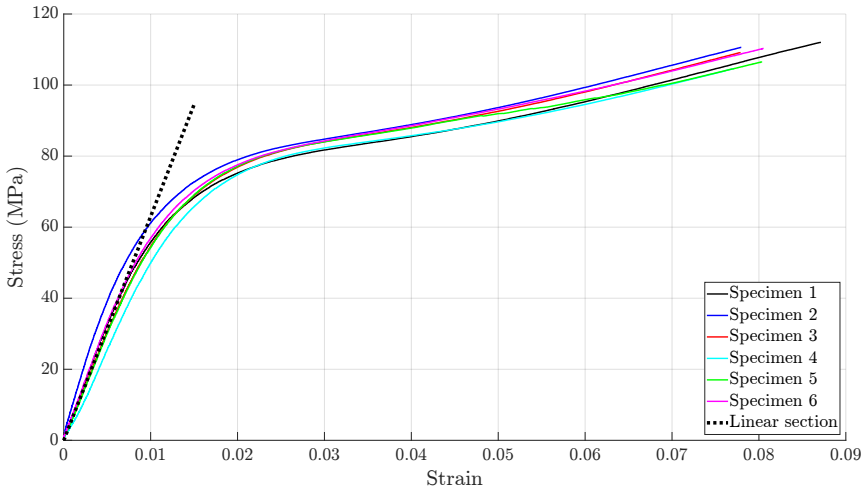

(b) Stress versus strain

Figure 4.6: GFRP tensile tests graphs for a fibre orientation of ±45°

4.2.2 Double cantilever beam tests

A series of Double Cantilever Beam (DCB) tests were conducted on GFRP specimens. These tests were conducted with S. Gabriel, a fellow researcher at BISRU, and the data was processed and analysed independently. These tests were performed to determine the mode 1 interlaminar fracture toughness (G_I).

The specimens were manufactured and tested in accordance with ASTM D5528 [84]. They were manufactured using 12 layers of 400 g m^{-2} plain weave E-glass fibre. The recommended specimen thickness should be between 3 mm and 5 mm [84], hence the specimens were manufactured to produce specimens with an average thickness of 4 mm. A release film was placed between layers six and seven to define the initial crack length of 63 mm. The specimens were nominally 160 mm long and 25 mm wide. A pair of steel hinge blocks with dimensions of 25 mm × 25 mm × 6 mm were glued to each specimen using a bonding jig and used to mount the specimen to the Zwick testing machine. The geometry of the specimens is shown in figure 4.7.

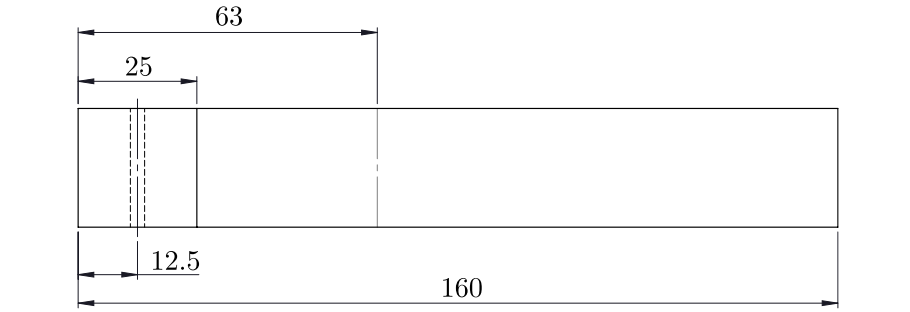

(a) Top view showing the specimen dimensions

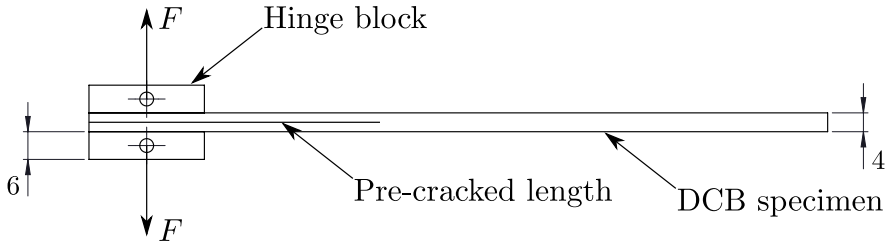

(b) Side view showing the tabs and forces during the DCB test

Figure 4.7: GFRP DCB test specimen geometry and hinge block dimensions

Specimens were manufactured and tested with two fibre orientations, namely, 0°/90° and ±45°. Five specimens were tested for each fibreglass lay-up. This was done to determine whether the fibre orientation had any effect on the Mode 1 fracture toughness. The tests were conducted using a crosshead speed of 2 mm min^{-1} in accordance with the ASTM standard [84]. A camera was used to take images of the specimen every 2 seconds during the test. The side profile of the specimen was painted white to assist with the processing of the images taken with the camera. The images were processed using MATLAB and were used to obtain the crack length versus time history for each test. The testing machine was used to measure the force and load-point displacement time history. The crack length and force were plotted against the load-point displacement and are shown in figure 4.8. Looking at the 0°/90° graph, it can be seen that the force required to propagate the crack for specimen 2 is greater than for the other four specimens.

Furthermore, the total cracked length is lower. This was due to the unstable growth of the crack in the specimen. Hence, the data from this test was excluded from the plot and calculations of the fracture toughness.

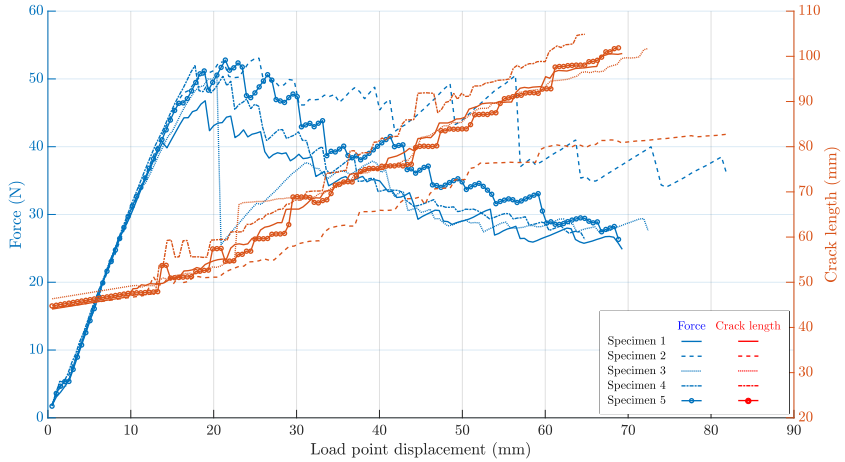

(a) Fibre orientation = 0°/90°

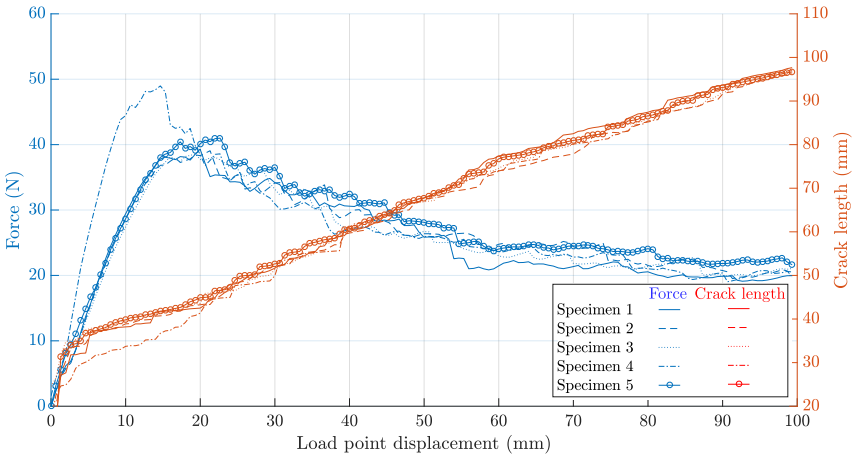

(b) Fibre orientation = ±45°

Figure 4.8: Force and crack length versus load point displacement for the DCB test specimens in the two fibre orientations

Three methods for calculating the interlaminar fracture toughness are presented in the ASTM standard [84]. It is recommended that the Modified Beam Theory (MBT) be used as it is found to yield the most conservative values of the three methods [84] when determining the energy release rate (G_I). The MBT equation for finding G_I is given in equation (4.9).

$$G_I = \frac{3P\delta}{2b(a + |\Delta|)} \tag{4.9}$$

Where, P is the load, δ is the load point displacement, b is the specimen width, and a is the delamination length. Δ is defined as the x-intercept of the least squares plot of the cube root of the compliance ($C^{1/3}$) against the delamination length (a). Figure 4.9 shows the results of the

interlaminar fracture toughness plotted against the crack length for the two fibre orientations. The initiation value for the fracture toughness ($G_{I\ init}$) was found by determining the crack length at the point of deviation from linearity in the load point displacement curves. The propagation value for the fracture toughness ($G_{I\ prop}$) was determined by finding the average value of G_I beyond the $G_{I\ init}$. The results are presented in table 4.4. The values of the propagation fracture toughness for the two fibre orientations are similar which suggests that the fibre orientation does not measurably influence the fracture toughness.

Table 4.4: Initiation and propagation fracture toughness values for the two fibre orientations

Fibre orientation	Average $G_{I\ init}$ ($\mathrm{J\,m^{-2}}$)	St. deviation ($\mathrm{J\,m^{-2}}$)	Average $G_{I\ prop}$ ($\mathrm{J\,m^{-2}}$)	St. deviation ($\mathrm{J\,m^{-2}}$)
0°/90°	1024.4	130	1024.7	102
±45°	939.8	54.1	1057.2	57.2

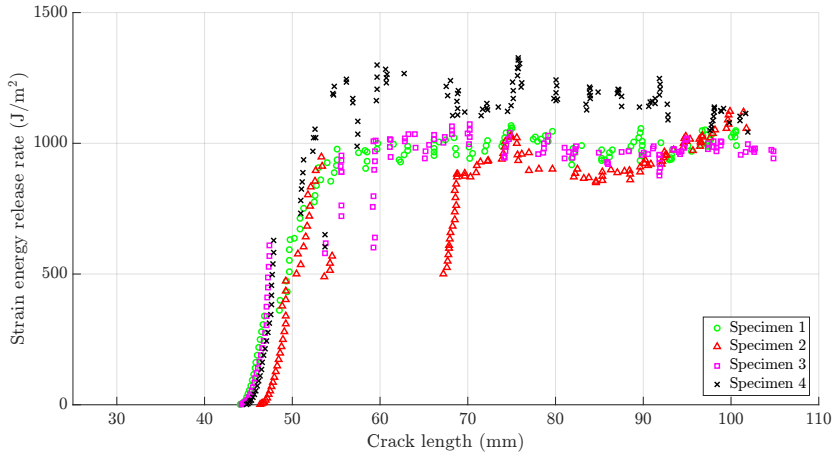

(a) Fibre orientation = 0°/90°

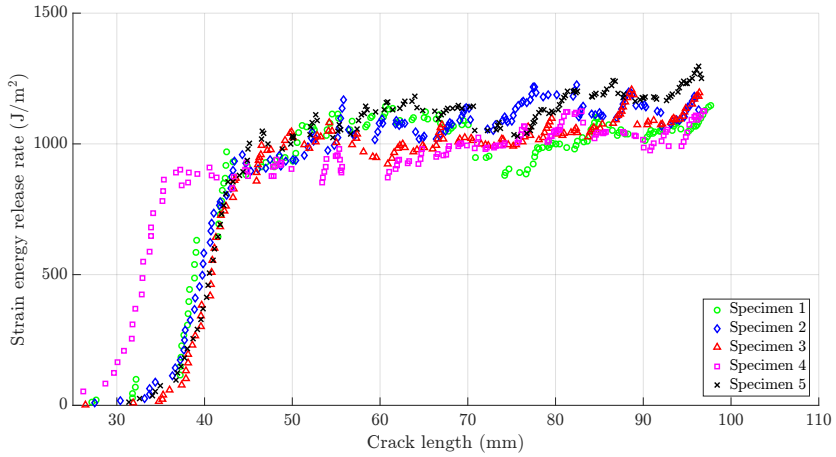

(b) Fibre orientation = ±45°

Figure 4.9: Strain energy release rate (G_I) versus crack length for the DCB test specimens in the two fibre orientations

4.3 Discussion and summary

Quasistatic tensile tests were conducted on the steel test specimens and an isotropic Johnson-Cook material model was fitted to the data. The tensile test results were found to be highly repeatable and the properties were found to closely match those found for the same material in previous studies [8, 41]. This increases the confidence in the material properties, the fitted material model, and its use when performing numerical blast simulations on the steel V-structures.

Additionally, tensile tests and DCB tests were performed on GFRP test specimens with fibre orientations of 0°/90° and ±45°. The Young's modulus, shear modulus, tensile strength and failure strain were obtained from the tensile tests, while the energy release rate was obtained from the DCB tests. The Tensile and DCB test results were also highly repeatable for the manufactured panels, which once again, increases the confidence in the model parameters that will be used in the LS-DYNA GFRP material model and a contact tiebreak model used when performing the numerical blast simulations. These results will be fitted to the material models by using implicit LS-DYNA simulations of the tensile and DCB tests.

Chapter 5

Blast testing - Experimental design

This chapter provides details of the equipment and the methodology used to conduct the blast tests, including information on the ballistic pendulums, the clamp frames and the required instrumentation. The required terminology and the chosen coordinate system are then defined. The chapter ends with a description of the blast test specimen preparation and the planned blast tests.

5.1 Ballistic pendulums

The blast experiments were performed on manufactured steel and GFRP V-structures. They were conducted using two ballistic pendulums at BISRU. Both pendulums use a laser displacement sensor to track the swing of the pendulum, which was then used to obtain the impulse transferred to the structure from the blast test.

The first pendulum, shown in figure 5.1, was designed with an I-beam structure onto which the clamp frames, target plate and counterbalance masses were attached. A backing plate with four spacers was used to separate the target plate from the body of the pendulum, while additional masses added to the sides of the pendulum helped reduce the swing of the structure when subjected to larger blast loads. The pendulum was attached to the roof with four lifting eyes and cables, that enabled it to swing axially when subjected to a blast load from an explosion. The impulse transferred to the structure could then be estimated from the pendulum swing. This pendulum was used to perform an initial set of experiments that were used to find the rupture threshold for the different types of panels that were tested.

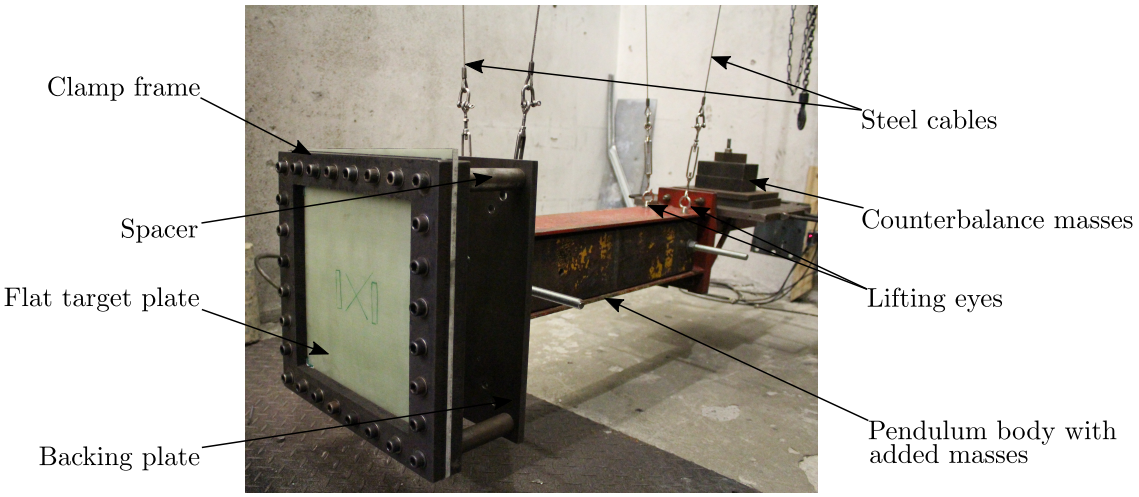

Figure 5.1: Schematic of the simple ballistic pendulum

The second pendulum used in this study is shown in figure 5.2. This pendulum is instrumented with a pair of high-speed cameras, (one shown in figure 5.3), that were mounted inside the structure, able to image the back face of the specimens during the blast test. The technical specifications of the cameras and their test arrangement has been provided in table 5.1. Again four lifting eyes and cables were also used to attach this pendulum to the roof and enabled it to swing axially. Two side shrouds were used to seal the inside of the pendulum and the instrumentation from dust and explosive gas products. Duct tape and a ratchet strap were also used to further seal the structure. This pendulum did not use a backing plate and spacer bolts, as the deformation of the rear of the target plate needed to be captured by the cameras. The cameras used were bolted onto machined aluminium bases that were then attached to an aluminium rail. This setup allowed for the cameras to be rotated and positioned appropriately in relation to the target plate. Each camera lens could then be focused on the rear of the target plate. All remaining blast tests on the steel and GFRP V-structures were performed using this pendulum so that their transient deformation behaviour could be determined.

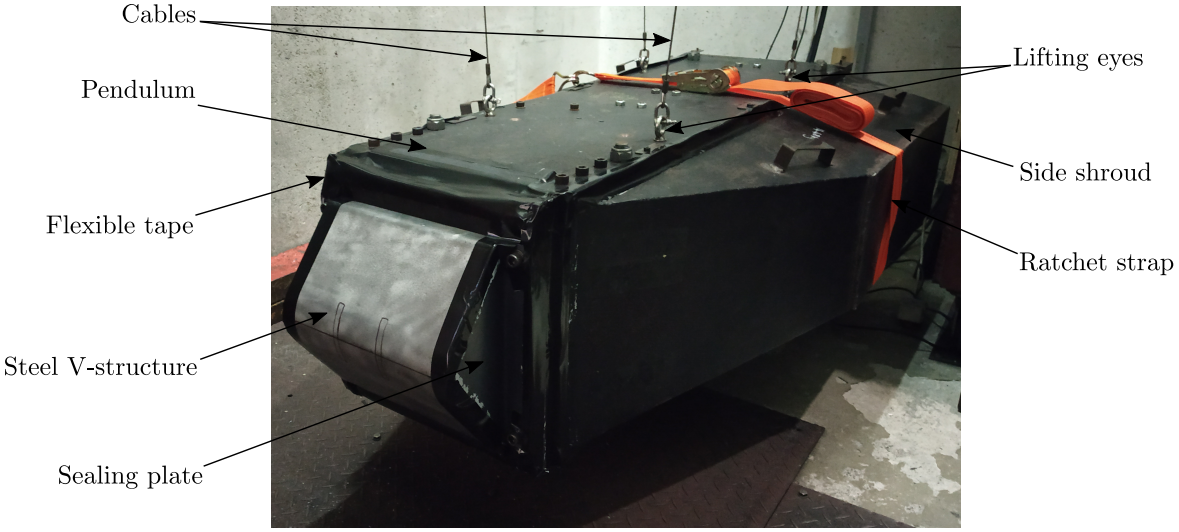

Figure 5.2: Photograph of the DIC ballistic pendulum with an attached steel V-structure

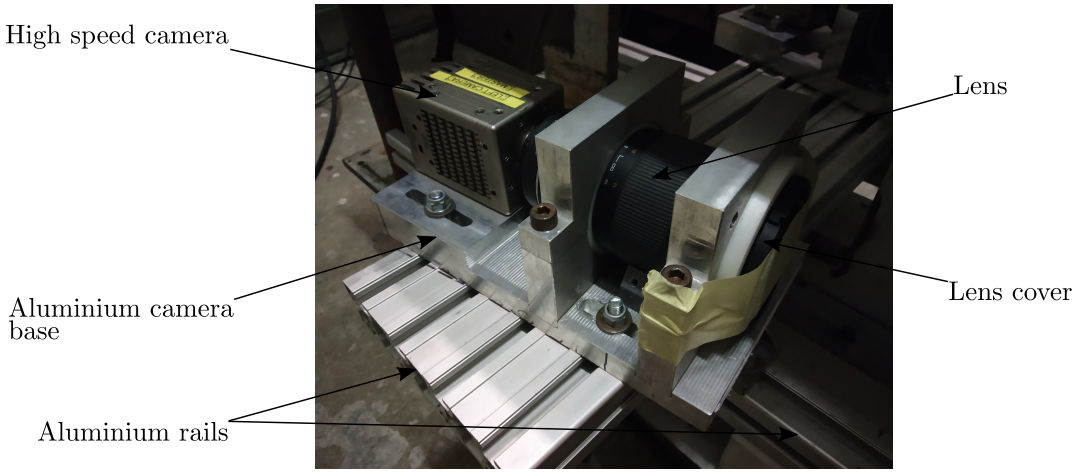

Figure 5.3: Photograph of one of the high-speed cameras used to track the motion of the plate during the blast event (Lens cover is removed prior to testing)

Table 5.1: Specifications and test arrangement of the IDT vision NR4 S3 cameras

Lenses	25 mm fixed focus	Included angle	30°	Field of view	1024x76 pixels
Frame rate	33 000 fps	Exposure	31 µs	Speckle size	0.8 mm

5.2 Clamp frame design

Figure 5.4 shows the clamp frames that were designed for mounting the V-structures to the pendulums. The modular design enabled the user to easily swap the V-structures between tests. This was done by first fitting the clamp frame side beams to the ballistic pendulum. The side frames and side clamps were then bolted onto the V-structure and then this sub-assembly was bolted to the clamp frame side beams. By splitting the components, the total mass of the sub-assembly that needed to be moved between tests was reduced, allowing for a shorter turnaround time. The V-structure was attached to the clamp frame with twelve M12 bolts and nuts, and the side frames were attached to the clamp frame side beams with four M12 bolts. The clamp frame side beams have threaded holes to simplify the assembly process. Full drawings of the clamp frames can be seen in Appendix A.

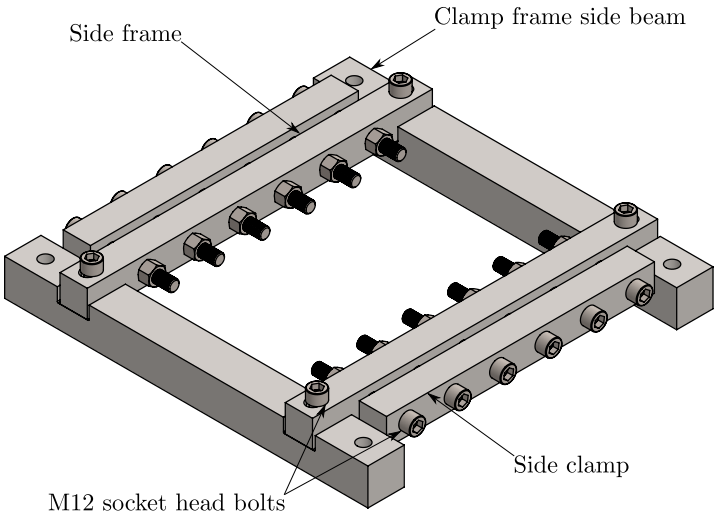

Figure 5.4: Schematic of the clamp frame designed to mount the V-structures to the pendulums

In order to test these V-structures using the instrumented pendulum, all the gaps between the outside of the enclosure and the cameras needed to be sealed. It can be seen from figure 5.5(a) that there was a large open area on either side of the V-structure. Explosive gas products, dust and other particles from the blast chamber would be able to pass through these gaps and damage the lenses fitted to the cameras. Thus, a pair of side shields were designed to seal these gaps, but not interfere with the movement of the plate during the tests. Figure 5.5(b) shows how the side shields are attached to the clamped V-structure assembly. Three pairs of side shields were designed and manufactured for each of the configurations that were to be tested. Namely, a 105° V-profile with a 32 mm tip radius, a 105° V-profile with a 62 mm tip radius,

and a 120° V-profile with a 32 mm tip radius. Each side shield was manufactured from 2.5 mm thick mild steel sheet, which was laser cut and then CNC bent into the desired profile. The shields were designed to follow the profile but not impede any movement of the V-structures. The shields are attached to the clamp frame assembly using the same M12 socket bolts that attach the side frames to the clamp frame side beams. By doing this, the existing clamp frame designs did not need to be modified.

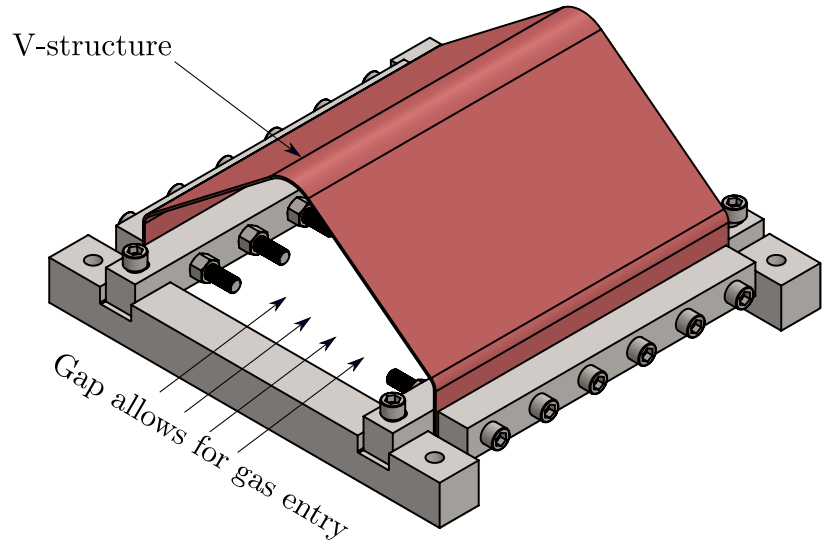

(a) Without the side shields fitted, showing the side gaps that allow for gas entry

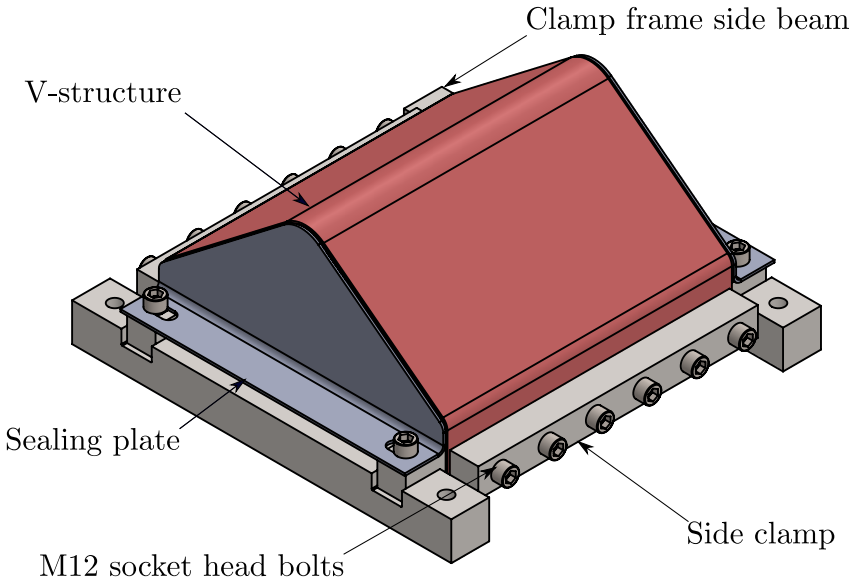

(b) With the side shields fitted, sealing the openings

Figure 5.5: Schematic of the clamp frame with a V-structure with and without the protective side shields fitted

5.3 V-structure geometry

Figure 5.6 shows a schematic of a typical V-structure used in the study with two planes running through it. The plate shape post blast is analysed along these two planes. The coordinate system used in the study is also defined here, with the positive x, y and z directions shown with the arrows. The ridge plane cuts across the top of the V-structure in the y and z directions and this profile will be called the "ridge profile". The crosscut plane cuts across the V-profile in the x and z directions and this profile will be called the "crosscut profile".

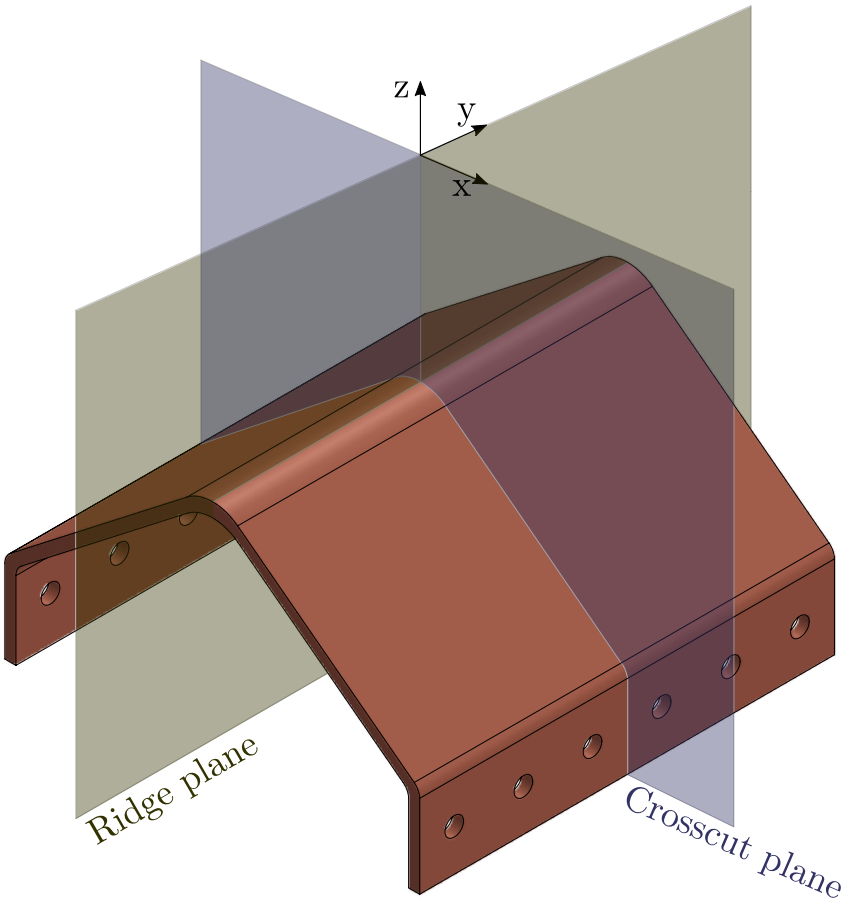

Figure 5.6: Definitions of the ridge and crosscut planes and the chosen coordinate system

5.4 Specimen preparation for high-speed imaging

The rear faces of each V-structure were painted so that their transient deformation could be tracked by the high-speed cameras. The steel panels were first lightly sandblasted to remove any mill scale and dirt present on the surface of the panels. Sandblasting also slightly roughened the surface of the V-structure, which allowed the paint to better adhere to it. The surfaces to be painted were then cleaned with acetone. Once cleaned, a layer of white high-temperature paint was applied and allowed to dry. Lastly, the panels were speckled black by controlling the force applied on the spray can nozzle. The approach followed was identical to that used by Curry [56]

in similar research performed on flat steel plates.

With all the speckled panels, the aim was to ensure an even spread of speckles with an average size of 0.8 mm [89]. A speckled DOMEX-700 MC steel V-structure is shown in figure 5.7(a), with only the central region of the V-structure along the ridge speckled. This was done because the chosen cameras were only capable of recording a strip across the target plate at the required frame rate of 33000 frames per second. This strip had dimensions of 1024 pixels × 76 pixels (260 mm × 19.3 mm), and an example of the imaged area of a plate is shown in figure 5.7(b).

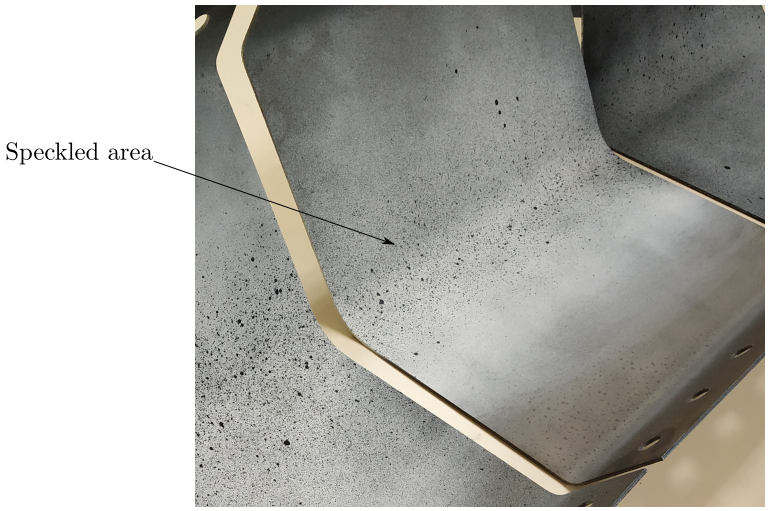

(a) Speckled area and sizes

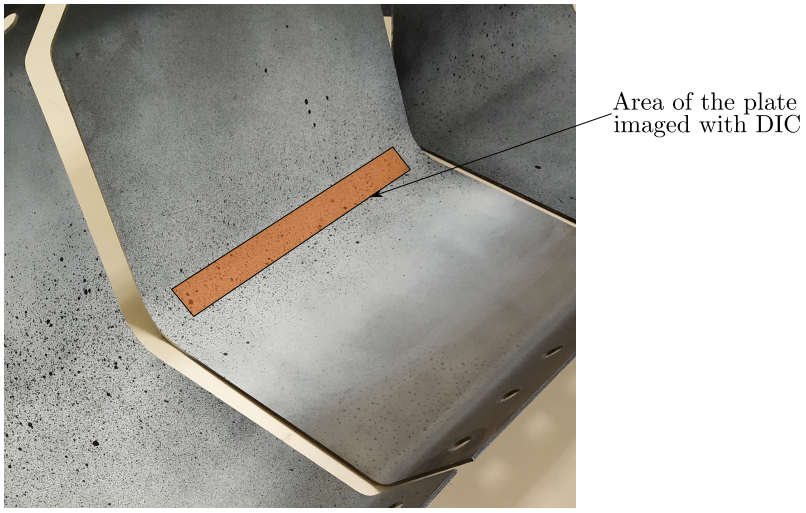

(b) Region imaged by the high-speed cameras

Figure 5.7: Photograph of a speckled DOMEX-700 MC steel V-structure

The GFRP V-structures had a resin rich area along the inside of the ridge. Initial blast tests found that resin pieces would fragment off the rear face of the V-structures during a blast test and travel towards the cameras. This was undesirable as they could potentially scratch or crack the lenses or damage the camera bodies while also obscuring the speckle pattern imaging resulting in no useful measurements. Thus, in order to reduce this effect, the resin rich area was carefully ground using a pneumatic mini grinder. Following this, the surface was roughened with

sandpaper before being cleaned with alcohol. Once dry, these panels were also painted white followed by black speckles using the same procedure used for the steel specimens.

5.5 Blast test plan

The blast test plan was developed by choosing a suitable range of charge masses and appropriate SODs. The ratio of the full-sized Casspir APC V-hull to the scaled V-structures is 8.33:1 and using this value the charge diameter was scaled down from 316 mm for a TM-57 landmine to 38 mm for the planned tests. The SOD was scaled down from the ground clearance of the Casspir APC of 410 mm and was chosen based on previous research performed on DOMEX-700 MC steel V-structures [8, 41, 42]. The charge mass range was chosen such that the rupture threshold could be determined for each type of panel and then the remaining experiments could be performed with lower charge masses (*i.e.* below the rupture threshold). The same SOD was used for the GFRP panels to ensure consistency between the blast tests performed on the two materials. The blast test plan is summarised in table 5.2. The chosen V-angles and V-tip radii for the two materials tested are also provided in the table. Further details of the manufacturing process and geometry of the blast test panels were provided in Chapter 3.

Table 5.2: Summary of the experimental blast test plan

Test configurations	Charge mass (g)	SOD (mm)	V-plates/V-angle (°)		Number of tests
			105	120	
			V-tip radii (mm)		
DOMEX-700 MC steel	10, 15, 20, 40	34, 50	32, 62	32	18
0°/90° GFRP	10, 15, 20, 40	34	34	34	13
±45° GFRP	10, 15	34	34	-	3

5.6 Discussion - Blast test design

One of the main features of this study is the use of DIC, to allow for the comparison of the transient deformation between the steel and GFRP V-structures. This data can be used to further validate the numerical blast models developed in LS-DYNA. One of the limitations of the camera setup is the small area of each panel that can be filmed. The validated numerical model can be used, with due care, to extend the experimental dataset to consider how the entire structure responds under different blast load conditions.

Chapter 6

Blast testing results - Steel

This chapter presents the blast test results for the steel flat plates and steel V-structures. A short discussion of each set of results is provided after they are presented. The impulse transferred and measured permanent mid-point deflections of the panels are presented first. This is followed by a description of the process used to optically scan the V-structures and obtain their 3D permanently deformed profiles. Next ridge and crosscut profiles obtained from the 3D scans are provided. Lastly, the transient displacement data obtained using DIC analysis of the high-speed camera images is presented. These include a selection of the mid-point deflection time histories and the ridge profiles at selected time steps.

6.1 Impulse transfer and permanent mid-point deflection results

The blast test results are split into two tables based on the Stand-Off Distance (SOD). Table 6.2 shows the impulse and permanent mid-point deflection versus charge mass data for the steel V-structures tested at a SOD of 50 mm, while table 6.1 shows the impulse and permanent mid-point deflection results for the tests carried out at a SOD of 34 mm. The impulse was determined from the swing of the ballistic pendulum. The swing of the pendulum was measured with a laser displacement sensor and an underdamped single degree-of-freedom vibration solution was fitted to the results. From the fitted curve, the initial velocity was found and multiplied with the mass of the pendulum to determine the impulse transferred [56].

In this study, four different specimen configurations were tested. Namely, flat plates, 105° V-structures with a 32 mm V-tip radius, 105° V-structures with a 62 mm V-tip radius, and 120° V-structures with a 32 mm V-tip radius. A few tests were conducted at a SOD of 50 mm to coincide with the scaled ride height of the Casspir APC, while the majority of the tests were performed at a SOD of 34 mm. This was done to allow for comparisons to be drawn with the previous studies conducted on steel V-structures [8, 41, 82]. The initial tests performed on the flat plates were performed to assist with the development of the numerical blast model in chapter 8. From the tables, it can be seen that increasing the charge mass resulted in an increase in the impulse transferred to the ballistic pendulum and the permanent mid-point deflection for all the configurations tested. Additionally, in general, tests conducted with the same charge mass of PE4 resulted in similar measured impulse and permanent mid-point deflection values. This is an important finding, as it increases the confidence in the experimental results of these blast tests.

Table 6.1: Impulse and final mid-point deflection versus charge mass for all steel specimens tested at a stand-off distance of 50 mm

Panel name	Charge mass (g)	Impulse (Ns)	Mid-point deflection (mm)
Plate type = Flat			
DOMEX_Flat_3	40	62.1	39.2
DOMEX_Flat_4	50	69.8	44.6
V-angle = 105°, Tip radius = 32 mm			
DOMEX_105_32_4	10	10.3	13.3
DOMEX_105_32_6[1]	40	29.2	-

[1] Panel ruptured in the central region.

Table 6.2: Impulse and final mid-point deflection versus charge mass for DOMEX-700 MC V-structures tested at a stand-off distance of 34 mm

Panel name	Charge mass (g)	Impulse (Ns)	Mid-point deflection (mm)
V-angle = 105°, Tip radius = 32 mm			
DOMEX_105_32_5	10	10.7	14.5
DOMEX_105_32_2	15	14.1	23.9
DOMEX_105_32_3	20	16.0	30.1
DOMEX_105_32_1	40	30.2	50.1
V-angle = 105°, Tip radius = 62 mm			
DOMEX_105_62_3	10	11.2	16.9
DOMEX_105_62_4	15	13.7	32.5
DOMEX_105_62_5	15	15.9	29.8
DOMEX_105_62_6	20	18.0	37.9
V-angle = 120°, Tip radius = 32 mm			
DOMEX_120_32_6	10	11.5	16.4
DOMEX_120_32_3	10	6.7	18.6
DOMEX_120_32_1	15	15.0	22.9
DOMEX_120_32_2	15	14.4	24.2
DOMEX_120_32_5	20	19.5	33.3
DOMEX_120_32_4	20	18.9	33.5

Following this, two graphs of the impulse and mid-point deflection versus the charge mass have been shown in figures 6.1 and 6.2. From the graphs, an increasing linear trend can be seen for both the measured impulse and the permanent mid-point deflection. These trends match the observations from previous work performed on steel V-structures [8] which further increases the confidence in the experimental blast results. Looking at the 10 g tests on the 120° V-structures with a 32 mm V-tip radius, it is clear that the measured impulse on the test panel DOMEX_120_32_3 appears to contain an error as it does not fall on the trend line.

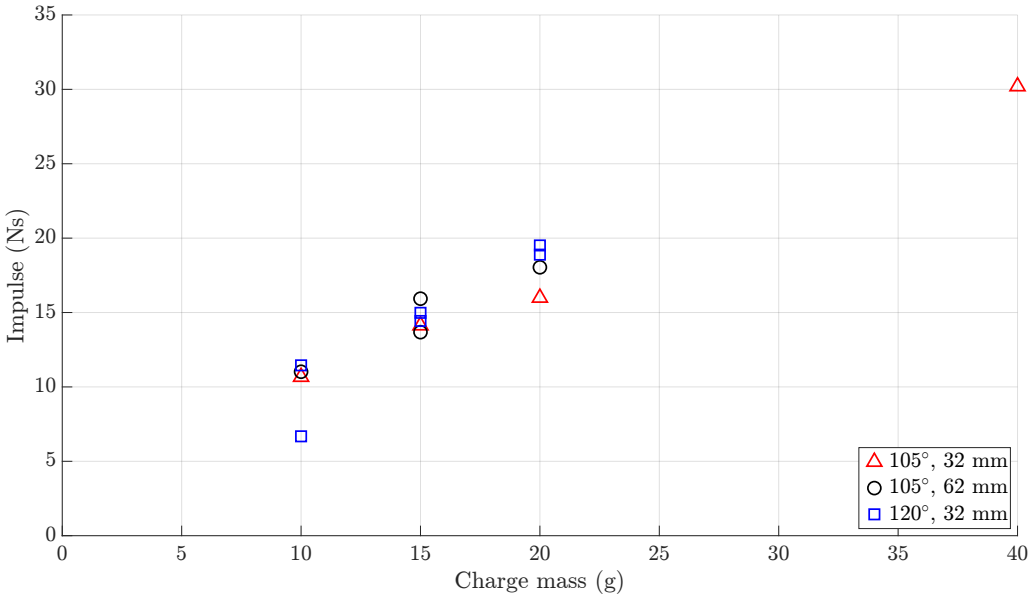

Figure 6.1: Impulse versus charge mass for the DOMEX-700 MC V-structures tested at a SOD of 34 mm

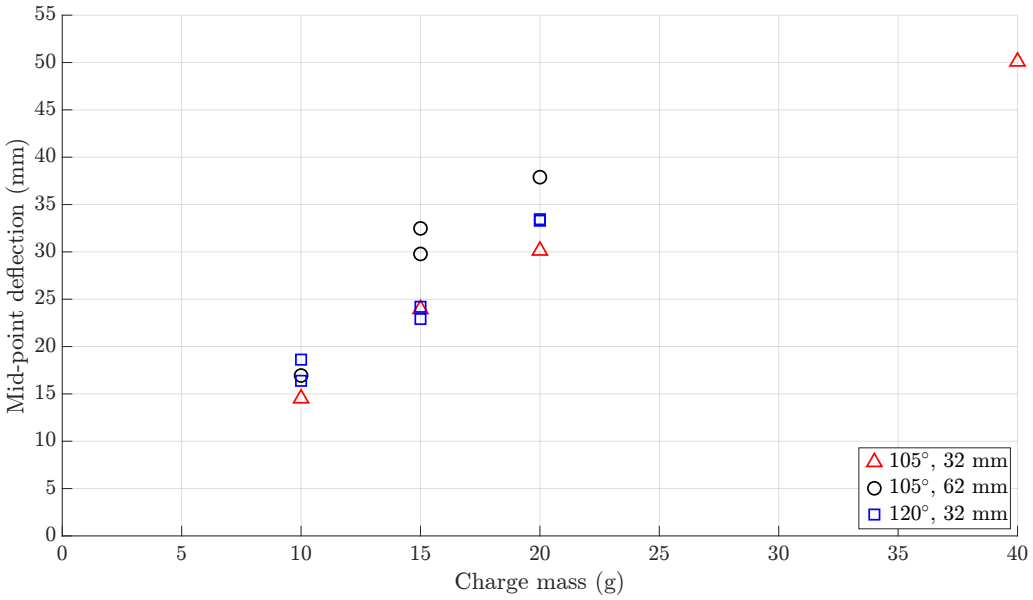

Figure 6.2: Mid-point deflection versus charge mass for the DOMEX-700 MC V-structures tested at a SOD of 34 mm

6.2 Discussion of the impulse transfer and permanent mid-point deflection results

6.2.1 Influence on the impulse transferred to the ballistic pendulum

As expected from the observations by Chung Kim Yuen *et al.* [8], an increase in the charge mass results in a nearly linear increase in the impulse transferred for all V-angles considered. Furthermore, the observed increase in impulse for a range of V-tip radii matches the findings of Langdon and Shekhar [10] in rigid V-structure simulations. For the range of V-tip radii and

charge masses tested, Langdon and Shekhar [10] observed linear trends in the measured impulse transferred. There is a large difference (4.8 Ns) in the impulse transferred between the two tests conducted on a 120° V-structure with a 10 g charge while the permanent mid-point deflection is almost identical between the two tests. This suggests a measurement error of the pendulum swing during the blast test on this V-structure.

6.2.2 Influence on the permanent mid-point deflection

An increase in permanent mid-point deflection was observed for an increase in charge mass for all the V-structure configurations investigated. A similar finding was reported in numerous studies conducted on DOMEX-700 MC V-structures [8, 41, 42, 90]. The linear trend observed for the V-structure configurations investigated increases the confidence in the blast testing method as the finding match similar studies performed on the localised blast loading of steel V-structures [8, 41].

The V-tip radii considered in this study were significantly larger than those used by Chung Kim Yuen *et al.* [8] and Hobson [82] in previous studies. This was done to enable the comparison of similar geometry GFRP and steel V-structures. The mid-point deflection of 33.3 mm was identified for a 32 mm V-tip radius in this study. Additionally, increasing the V-tip radius to 62 mm resulted in a mid-point deflection of 37.9 mm. These values are significantly higher than those reported in previous studies [8, 82]. For a 120° V-structure, tested with a 20 g charge, a mid-point deflection of 12.2 mm was reported by Hobson [82], while Chung Kim Yuen [8] observed a mid-point deflection of 17.7 mm. Both these panels had a V-tip radius of 4 mm. Thus there is a need to extend this investigation on the mid-point deflection on these V-structures with a range of V-tip radii. This analysis was performed using the numerical blast model developed in LS-DYNA and is presented in Chapter 8.

6.3 Permanent deformation profiles

6.3.1 Deformation profile analysis procedure

Figure 6.3 shows annotated photographs of two blast tested 105°, 32 mm V-tip radius DOMEX-700 MC V-structures tested at charge masses of 10 g and 40 g respectively. In figure 6.3(a), it can be seen that there is a small indentation in the V-structure, with limited deformation outside of the central region. The deformation is also greater along the ridge than along the V-profile. On the other hand, in figure 6.3(b), the V-structure has torn due to the energy transferred from the explosive load. The ridge line also appears to be bent due to the loading and the tearing of metal. These photographs show the importance of obtaining detailed 3D profiles of the blast tested plates to allow for analyses to be performed on the deformations due to changes in charge mass and V-structure geometry.

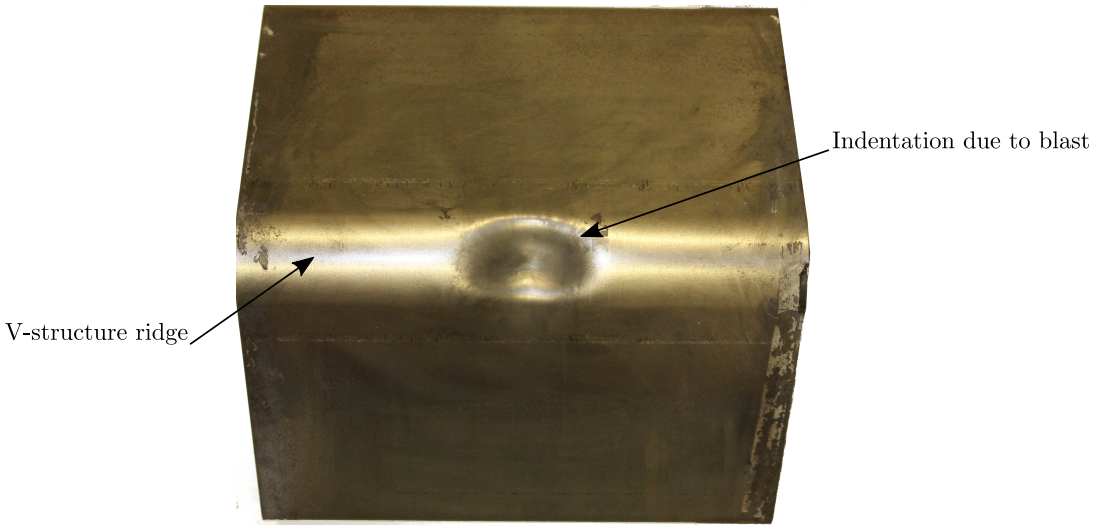

(a) Charge mass = 10 g

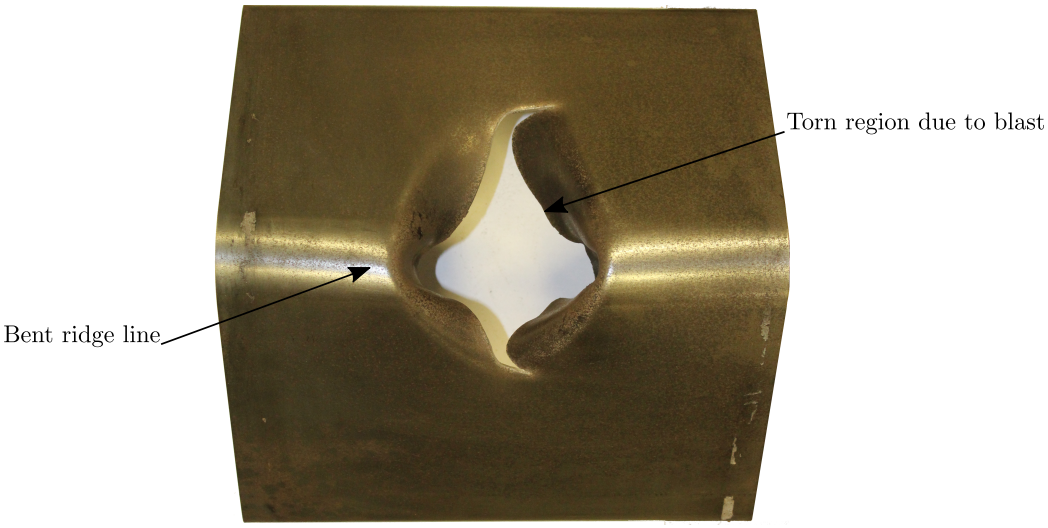

(b) Charge mass = 40 g

Figure 6.3: Photographs from the top view of two blast tested 105°, 32 mm V-tip radius DOMEX-700 MC V-structures

The outer surfaces of all the DOMEX-700 MC V-plate blast test specimens were measured using an optical 3D scanner. Each test specimen was secured in the blast test clamp frame before scanning. This was done to eliminate the effects of the elastic springback of the V-structures during the forming process and to ensure that the edge where the clamp frame meets the plate could be used to determine the boundaries of the plates. The data was exported as an OBJ file and read into MATLAB. Code was written to remove the parts of the clamp frame, centre the point cloud and extract the ridge and crosscut deformation profiles. The permanent central mid-point displacement was also measured manually using a digital height gauge and used to check the extracted profile data. The ridge and crosscut profiles were then extracted for each scanned plate.

6.3.2 3D scanned V-plates

Figure 6.4 shows the 3D profiles of the blast tested 105°, 32 mm V-tip radius V-plates tested at a SOD of 34 mm. In each, the origin is chosen to be the same point of the V-structure. The deformation is limited to the region directly beneath the explosive charge, with an ovalised indentation profile with its longitudinal axis along the ridge. Finally, the total deformed area is also observed to increase with an increasing charge mass. Additional 3D profiles of all the blast tested V-structures can be found in Appendix B.

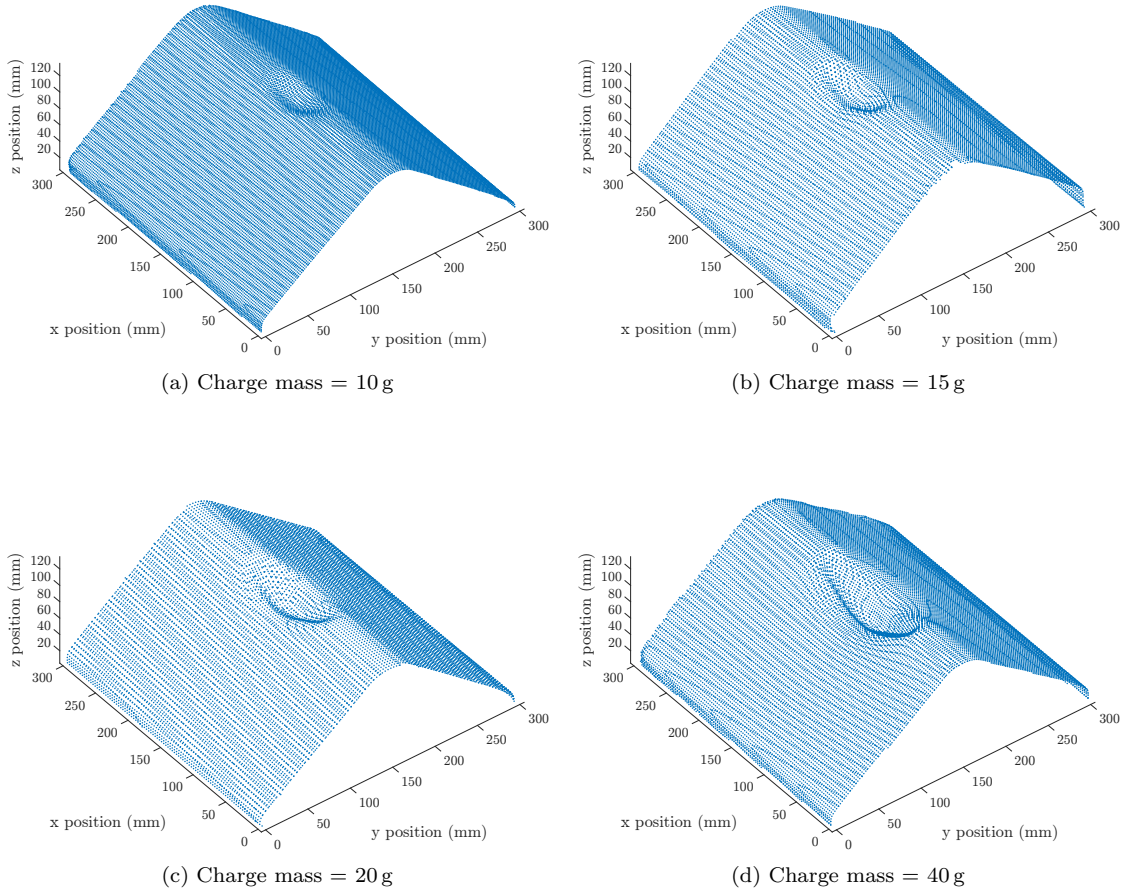

(a) Charge mass = 10 g

(b) Charge mass = 15 g

(c) Charge mass = 20 g

(d) Charge mass = 40 g

Figure 6.4: 3D Profiles of the 105°, 32 mm V-tip radius DOMEX-700 MC V-structures tested at a SOD of 34 mm

6.3.3 Ridge profiles

The increase in total deformation can be compared more easily by looking at the deformation along the ridge plane and across the mid-section of the V-structure ("crosscut plane"). The ridge profiles for the 105°, 32 mm V-tip radius DOMEX-700 MC V-structures tested a SOD of 34 mm are shown in figure 6.5. In order to allow easy comparison, the profiles are moved so that the mid-point of the V-structures is aligned with $x = 0$ mm and the profiles are shifted down such that they align with $z = 0$ mm. The ridge profiles are shown in figures 6.5 to 6.7. In general, it can be seen that increasing the charge mass results in an increase in the mid-point deflection

and an increase in the length along the ridge that gets deformed. In these figures, there is noise present in the data as seen by the jagged lines in the deformed section of each ridge profile. This is due to the noise present in the 3D scanning when the scans are fused to create the OBJ file. The data was not smoothed before generating these graphs. This was done to avoid removing the peak mid-point deformation.

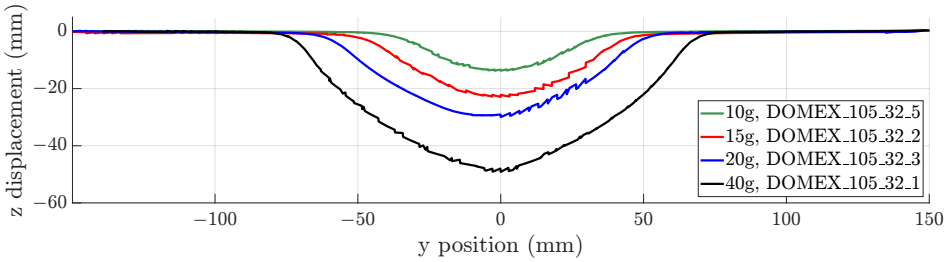

Figure 6.5: Ridge profiles of the 105°, 32 mm V-tip radius DOMEX-700 MC V-structures tested at a SOD of 34 mm

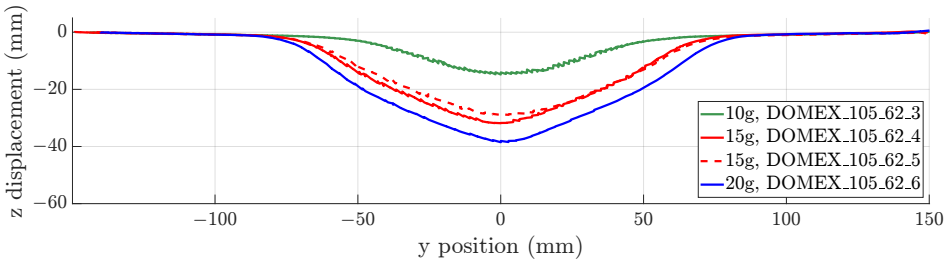

Figure 6.6: Ridge profiles of the 105°, 62 mm V-tip radius DOMEX-700 MC V-structures tested at a SOD of 34 mm

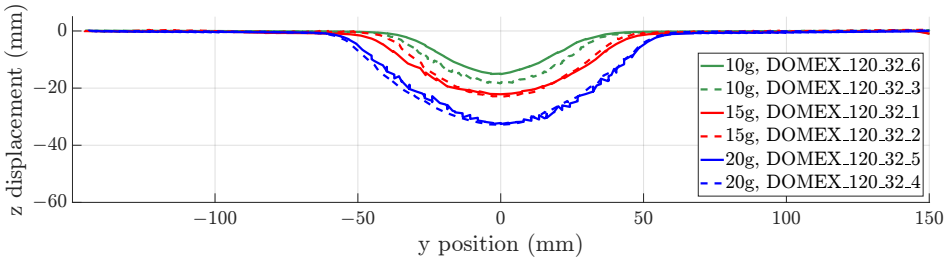

Figure 6.7: Ridge profiles of the 120°, 32 mm V-tip radius DOMEX-700 MC V-structures tested at a SOD of 34 mm

When comparing the three figures, the peak deformation of the 105°, 32 mm V-structures is lower than that of the 105°, 62 mm V-structures and the 120°, 32 mm V-structures. In figure 6.5 for a 105°, 32 mm V-structure, at a charge mass of 20 g, the deformed length along the ridge is approximately 127 mm, while for the same charge mass in figure 6.6 for a 105°, 62 mm V-structure, the deformed length along the ridge is approximately 167 mm. Similar observations can be seen for the other two charge masses tested (*i.e.* 10 g and 15 g). The deformed length along the ridge for the 120°, 32 mm V-structure tested at 20 g is approximately 124 mm. This is similar to the deformed ridge length for the 105°, 32 mm V-structure tested at the same charge mass. This suggests that increasing the V-tip radius results in an increase in the deformed length along the ridge and consequently the shape of the deformed V-structure profile.

6.3.4 Crosscut profiles

The crosscut profiles were aligned in a similar approach to the ridge profile data presented in the previous section. These profiles are shown in figures 6.8 to 6.10. Similarly to the ridge profiles, the permanent mid-point deflection is observed to increase with an increased charge mass, while the domed profile in the central region is also observed to increase in depth and width. The deformation appears to be more asymmetric for the smaller V-angles.

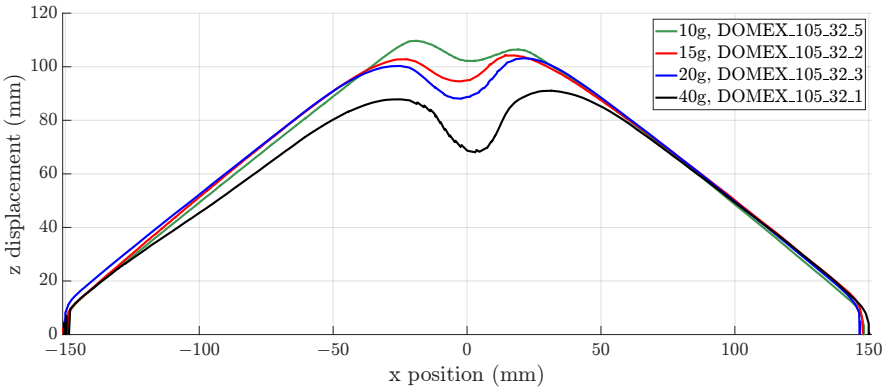

Figure 6.8: Crosscut profiles of the 105°, 32 mm V-tip radius DOMEX-700 MC V-structures tested at a SOD of 34 mm

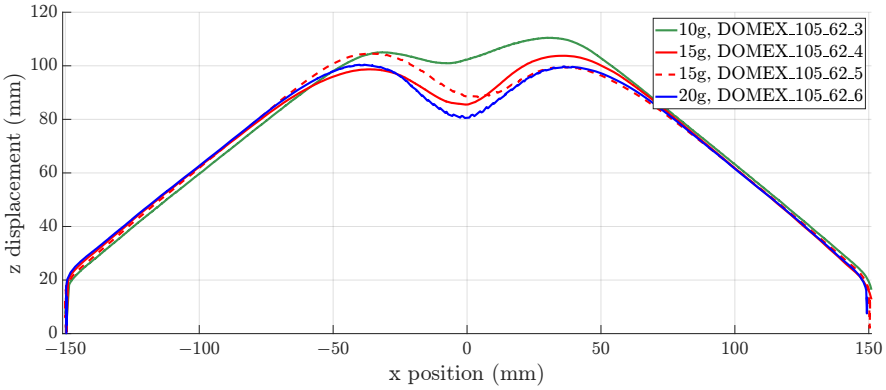

Figure 6.9: Crosscut profiles of the 105°, 62 mm V-tip radius DOMEX-700 MC V-structures tested at a SOD of 34 mm

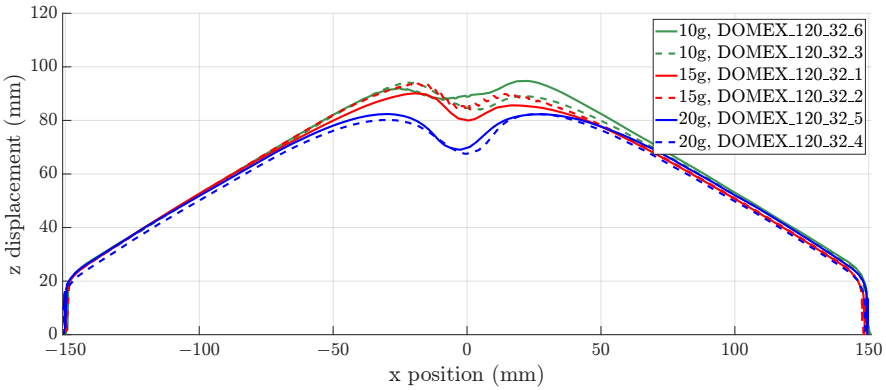

Figure 6.10: Crosscut profiles of the 120°, 32 mm V-tip radius DOMEX-700 MC V-structures tested at a SOD of 34 mm

6.4 Discussion - Permanent deformation profiles

6.4.1 Influences on the 3D plate profiles

In general, increasing the charge mass resulted in an increase in the total deformed area and the depth of the deformed area. All V-structures tested at charge masses below 40 g showed mode I failure (large inelastic deformation in the central region of the plate) [34]. Mode II*c failure (partial tearing) [36] was observed for a single V-structure specimen (105°, 32 mm) tested with a charge mass of 40 g. In previous work done on the localised blast loading on flat plates [37], a similar increase in the plastically deformed area for an increasing charge mass was observed. Additionally, Chung Kim Yuen *et al.* [8] reported similar failure modes in a study conducted on steel V-structures with sharp V-tip radii.

6.4.2 Influences on the ridge profiles

For all the V-structure geometries investigated, an increase in charge mass resulted in an increase in both the deformed length along the ridge and the depth of the permanently deformed region. Similar ridge profile plots were not published in the literature on V-structures (although the crosscut profiles were published), but the findings match the work published by Nurick and Radford [36] on circular plates and Jacob *et al.* [37] on quadrangular plates. Furthermore, the repeated test conducted on the 105°, 62 mm V-structures with a 15 g charge showed good repeatability in the experiments, with similar results for both the peak mid-point deflection and the permanently deformed ridge profile.

Increasing the V-tip radius results in an increase in the deformed length along the ridge, but there is no increase in the deformed length along the ridge when the V-angle was increased. Suggesting a link between the V-tip radius and the deformed ridge length. Qualitatively, increasing the V-tip radius results in an increase in the overall deformed area and this can likely be attributed to the reduced geometric stiffness (*i.e.* the V-structure shape) of the V-structure with large V-tip radii. Increasing the V-angle does not result in a change in the shape of the deformed area, although there is an apparent increase in the depth of the deformed area.

6.4.3 Influences on the crosscut profiles

When considering the crosscut profiles, an increase in charge mass on the 105°, 32 mm V-structures results in both the global deformation of the panel and a buckling mode at the V-tip. This response was similar to that reported by Chung Kim Yuen *et al.* [8] on the study performed on sharp V-tip structures. The inversion of the V-tip is less pronounced for the larger V-tip radii panels as confirmed by the profiles of the 105°, 62 mm. For these V-structures, the global deformation of the panels is greater but there is little inversion of the V-tip. The 120°, 32 mm V-structure profiles allow for the effect of increasing the V-angle to be considered. These profiles show a similar indentation at the V-tip to the 105°, 32 mm V-structures with an increase in the global deformation as the charge mass is increased. The inversion of the V-tip is not as evident at the charge masses of these tests.

6.5 Transient deformation results

This section details the transient deformation results on the blast tested steel V-structures. The mid-point deflection time histories and transient ridge profiles for the blast tested steel V-structures are presented below.

6.5.1 Mid-point deflection time history

The mid-point deflection time histories for a selection of the blast tested steel V-structures are presented in figures 6.11 to 6.13. The missing data in the first 300 µs is due to the motion blur in the images of the tested V-structures. The high initial velocity made it impossible to use a suitable frame rate and exposure time to eliminate the motion blur with the lighting available at the time of testing. However, the peak transient deformation and the post-blast plate vibration can still be observed in the graphs. As the camera system was mounted inside the ballistic pendulum, the purpose-built shrouding was cleaned internally and sealed to minimise particulate ingress that can affect image quality. Inevitably, however, there was often some ingress affecting the field of view for each camera. This is the most likely reason for the gaps in the transient displacement-time histories apparent in figures 6.11 to 6.13. A series of markers have also been plotted on these graphs with coloured circles corresponding to selected peaks and troughs in the displacement time histories. These timesteps will be used in the next section to plot a series of ridge profiles for each test.

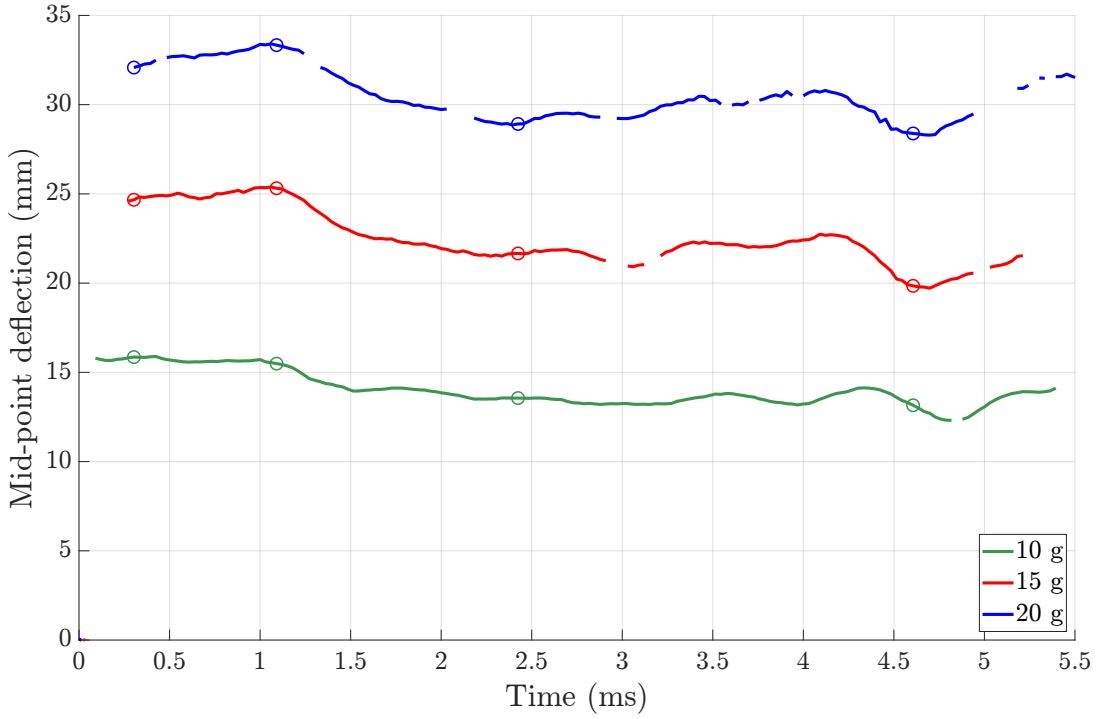

Figure 6.11: Mid-point deflection time history for the first 5.5 ms after the blast for the 105°, 32 mm V-tip radius DOMEX-700 MC V-structures tested at a SOD of 34 mm

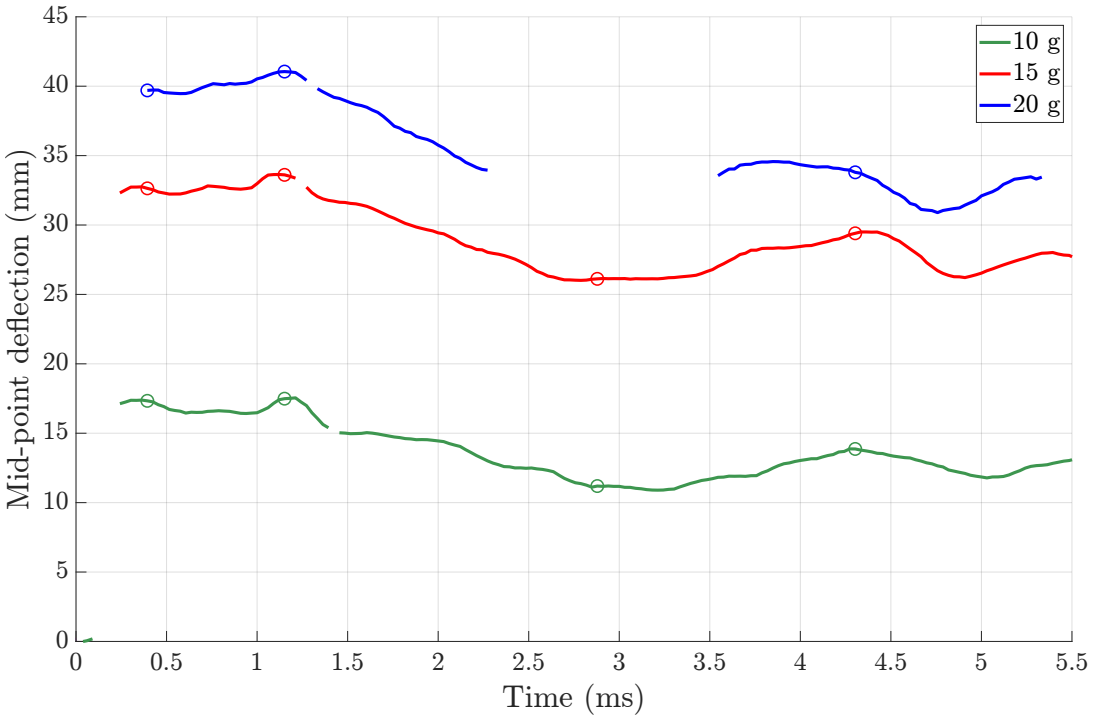

Figure 6.12: Mid-point deflection time history for the first 5.5 ms after the blast for the 105°, 62 mm V-tip radius DOMEX-700 MC V-structures tested at a SOD of 34 mm

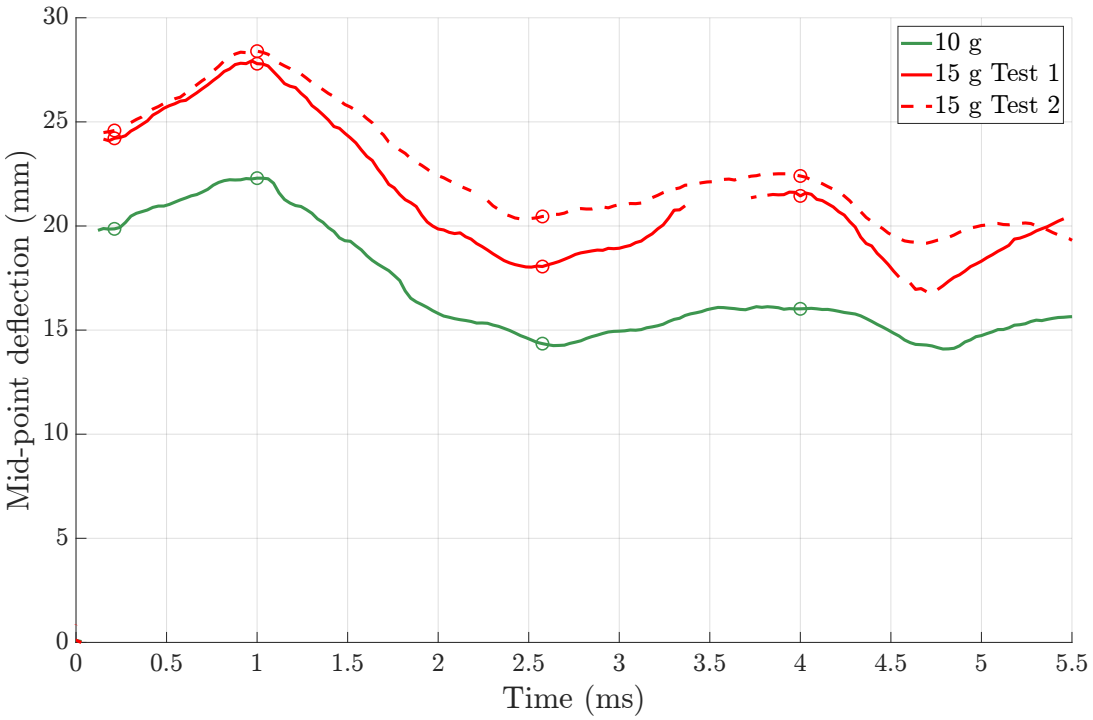

Figure 6.13: Mid-point deflection time history for the first 5.5 ms after the blast for the 120°, 32 mm V-tip radius DOMEX-700 MC V-structures tested at a SOD of 34 mm

From the figures, there appears to be about a 2 mm to 5 mm difference between the peak and the final deformation. Additionally, the V-structures do not experience a significant post-blast vibration (2 mm to 3 mm peak-to-peak vibration for all the V-structure configurations

investigated.) The differences between the peak transient mid-point deflection and the final mid-point deflection for the available tests have been summarised in table 6.3. The greatest differences between the peak and final mid-point displacements are seen for the 120° V-structures, while the differences are similar for the two 105° V-structure configurations that were investigated.

Table 6.3: Peak and final deformation versus charge mass for DOMEX-700 MC V-structures

Panel name	Charge mass (g)	Mid-point deflection (mm)		
		Peak	Final	Difference (%)
V-angle = 105°, Tip radius = 32 mm				
DOMEX_105_32_5	10	15.7	14.5	1.2 (8)
DOMEX_105_32_2	15	25.3	24.0	1.3 (5)
DOMEX_105_32_3	20	33.3	30.1	3.2 (11)
V-angle = 105°, Tip radius = 62 mm				
DOMEX_105_62_3	10	17.5	16.9	0.6 (4)
DOMEX_105_62_4	15	33.6	32.5	1.1 (3)
DOMEX_105_62_6	20	41.1	37.9	3.2 (8)
V-angle = 120°, Tip radius = 32 mm				
DOMEX_120_32_6	10	22.3	16.4	5.9 (36)
DOMEX_120_32_1	15	27.8	22.9	4.9 (21)
DOMEX_120_32_2	15	28.4	24.2	4.2 (17)

6.5.2 Ridge profiles

The transient ridge profiles for a selection of the blast tested steel V-structures are presented in this section. As with the mid-point deflection time history results presented in section 6.5.1, there are some gaps in the data at the start of each test. A selection of the results are shown in figures 6.14 to 6.16. In each figure, the final deformation is also included. The time steps were chosen to capture the earliest available data point, the first visible peak and the next trough from the mid-point displacement time histories. In each figure, it can be seen, that the majority of the central deformation has already occurred before the first recorded frame although the peak has yet to be reached. This peak deformed shape is captured at approximately 1.1 ms. After this, the entire V-structure appears to vibrate about the ridge line with a magnitude of ±2 mm to 3 mm.

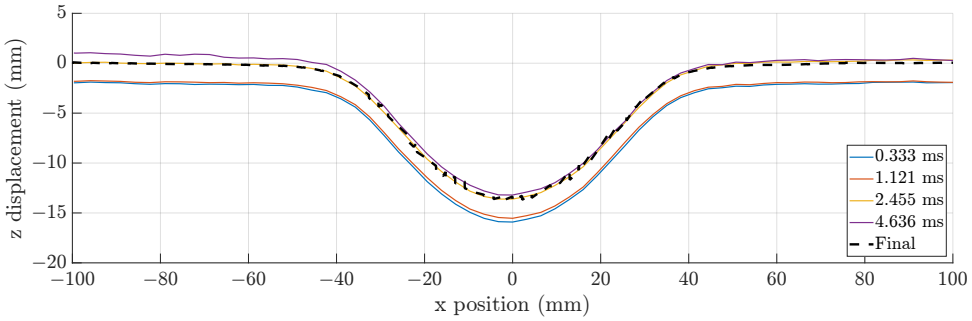

Figure 6.14: The ridge profiles for a 105°, 32 mm V-tip radius DOMEX-700 MC V-structure tested with a 10 g PE4 charge at a SOD of 34 mm

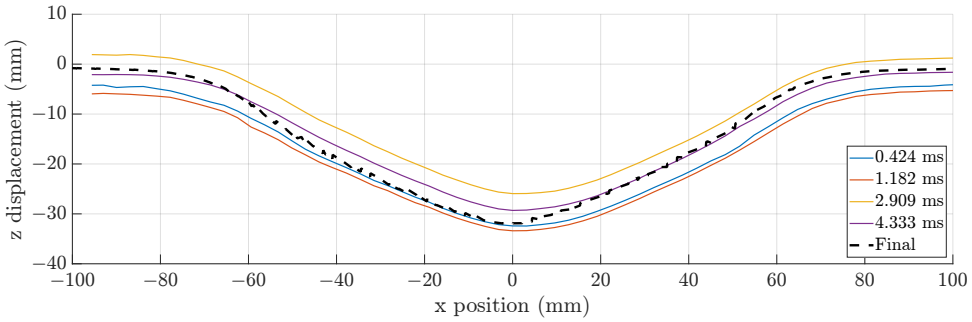

Figure 6.15: The ridge profiles for a 105°, 62 mm V-tip radius DOMEX-700 MC V-structure tested with a 15 g PE4 charge at a SOD of 34 mm

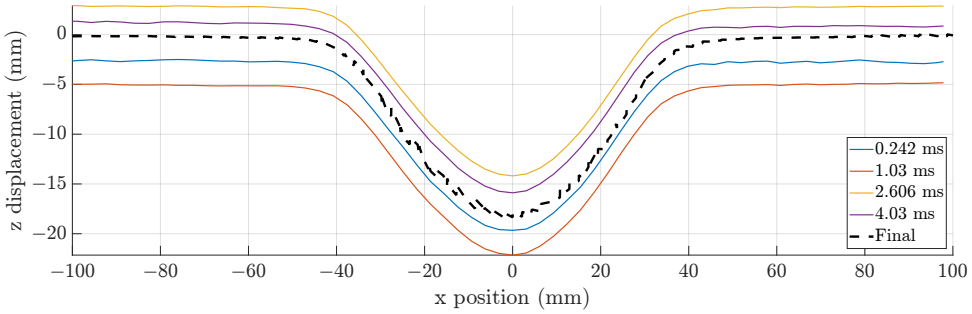

Figure 6.16: The ridge profiles for a 120°, 32 mm V-tip radius DOMEX-700 MC V-structure tested with a 10 g PE4 charge at a SOD of 34 mm

6.6 Discussion - Transient deformation results

6.6.1 Influence on the mid-point deflection time history

All the V-structures exhibited an increase in the transient peak deformation as the charge mass was increased. In general, the post-peak vibration of the V-structures is less than that observed for flat circular plates subjected to localised blast loading [56, 61]. The V-structures showed a post-peak vibration with a peak-to-peak magnitude of 2 mm to 3 mm, while in studies performed on flat steel structures [56, 61], the vibrations were found to be in the range of 10 mm. The 120° V-structures showed the largest differences between the peak and the final mid-point deflection at 5.9 mm for all the V-structure configurations investigated. This suggests that increasing the V-angle reduces the geometric stiffness of the V-structure, thus resulting in a greater peak-to-peak vibration. Although this value was still significantly lower than that observed for localised blast loaded flat plates in previous studies where the differences were found to be in the range of 10 mm [61]. This can be attributed to the additional stiffness of the V-structure geometry. The 15 g repeat tests on the 120° V-structures show good repeatability in the mid-point deflection time histories.

6.6.2 Influence on the transient ridge profiles

Due to motion blur, it was not possible to capture the initial deformation of the V-structure for any of the tests conducted but the peak deformed ridge profiles were captured. For the frames where data was available, it is evident that the central region of the plate has already

experienced the majority of the maximum deformation and after 0.3 ms the plates are mostly undergoing global vibration. By 2.5 ms, the plate vibration is observed to be close to the final ridge profile. Additionally, the peak transient deformed ridge profile appears to be similar to the final shape. This is different to the findings reported by Curry and Langdon [56] and Rigby *et al.* [91] on studies performed on circular plates. In these studies, the regions close to the clamped edge experience elastic deformation. This is likely a result of the shape of the structure being a V and the deformation mode being localised at the ridge line. As a result, a different global vibration mode of the structure was observed as the energy from the blast was transmitted through the V-structure. Additional transient ridge profile graphs are provided in Appendix B. These findings are explored further in chapter 8.

6.7 Summary

This chapter reported the blast test results for the steel V-structures. Three V-structure configurations were investigated, 105° V-structures with a 32 mm V-tip radius, 105° V-structures with a 62 mm V-tip radius, and 120° V-structures with a 32 mm V-tip radius. Charge masses ranging from 10 g to 50 g were used and tested at two SODs (34 mm and 50 mm). It was found that increasing the charge mass resulted in a nearly linear increase in the measured impulse and the final mid-point deflection. At lower charge masses, the V-angle and V-tip radius did not seem to have a significant effect on the measured impulse. These findings matched similar findings from previous studies performed on flat steel plates and steel V-structures.

For the permanently deformed V-structure ridge profiles, increasing the charge mass resulted in an increase in the deformed length along the ridge. Increasing the V-tip radius also resulted in a greater deformed length along the ridge. This deformed length did not appear to be a function of the V-angle although only two V-angles were investigated experimentally. In the permanently deformed crosscut profiles, the deformation appeared to be asymmetric at the lower charge masses tested, while the overall length and depth of the dome were observed to increase with an increase in charge mass. Due to the larger V-tip radii investigated in this study, there was no evidence of a buckling or pinching mode as reported in previous studies on sharp V-tip radius V-structures.

For all the available transient measurements, the first 300 µs of data were missing due to motion blur. It was still possible to capture the peak deformation and the post-peak vibration of the blast tested V-structures. The difference between peak and final displacement was found to be greatest for the 120° V-structures tested at 5.9 mm (36%), this was possibly due to the reduced geometric stiffness resulting from the larger V-angle. Additionally, all the V-structures showed a peak-to-peak vibration amplitude of 2 mm to 3 mm post the peak deformation. This vibration was significantly lower than that reported for flat steel plates and is likely due to the geometric stiffness of the V-structure geometry compared with that of a flat plate. The transient ridge profiles captured the peak deformed profile and the rigid post-test vibration of the V-structures as all the panels appeared to have experienced the large inelastic deformation in the first 300 µs of the test.

Chapter 7

Blast testing results - GFRP

This chapter presents the blast test results for the GFRP V-structure experiments. The impulse transferred and percentage mass change of the V-structures are presented first. A brief description of the process followed to find the resulting damage on each V-structure is then provided. Next, the total measured crack length and delaminated area of each V-structure are tabulated and discussed. Lastly, the DIC results for the GFRP V-structures are presented. These include a selection of the transient deflection time histories and the ridge profiles at selected time steps.

7.1 Impulse transfer results

Three V-structure configurations were tested. These are listed in table 7.1. These configurations were chosen to allow for the comparison of the V-angle and ply orientation effects on the blast performance of the V-structures. The impulse versus charge mass for these configurations tested at a SOD of 34 mm is shown in table 7.2. The charge mass range used for the 105° V-structures with 0°/90° ply orientation is greater than that used for the other two GFRP V-structures configurations. This GFRP V-structure configuration was chosen to compare with the equivalent mass steel V-structures and was used to determine the point of initiation of V-structure rupture. The damage propagation observed for this set of GFRP V-structures was then used to develop the 10 g to 20 g charge mass range for the other two configurations of the GFRP V-structures tested.

Table 7.1: GFRP V-structure configurations and charge mass range investigated

V-angle (°)	V-tip radius (mm)	Ply orientation (°)	Charge mass range (g)
105	34	0°/90°	10 - 40
105	34	±45°	10 - 15
120	34	0°/90°	10 - 15

From table 7.2, it can be seen that increasing the charge mass results in an increase in the impulse transferred, with the impulse increasing from 8.0 Ns to 31.3 Ns as the charge mass was increased from 10 g to 40 g.

Table 7.2: Impulse versus charge mass for GFRP V-structures tested at a stand-off distance of 34 mm

Panel name	Charge mass (g)	Impulse (Ns)
V-angle = 105°, Tip radius = 34 mm, Fibre orientation = 0°/90°		
GFRP_0-90_105_34_2	10	11.0
GFRP_0-90_105_34_6	10	10.0
GFRP_0-90_105_34_4	10	8.0
GFRP_0-90_105_34_8	12	11.4
GFRP_0-90_105_34_7	15	14.4
GFRP_0-90_105_34_1	20	17.8
GFRP_0-90_105_34_T2	30	11.5
GFRP_0-90_105_34_T4	30	24.4
GFRP_0-90_105_34_T3	35	28.6
GFRP_0-90_105_34_T1	40	31.3
V-angle = 105°, Tip radius = 34 mm, Fibre orientation = ±45°		
GFRP_45-45_105_34_2	10	8.5
GFRP_45-45_105_34_T1	10	10.2
GFRP_45-45_105_34_1	15	14.0
V-angle = 120°, Tip radius = 34 mm, Fibre orientation = 0°/90°		
GFRP_0-90_120_34_2	10	10.6
GFRP_0-90_120_34_4	10	10.7
GFRP_0-90_120_34_3	15	14.7

The impulse versus charge mass data is also plotted in figure 7.1. A near linear trend can be seen in the impulse transferred to the ballistic pendulum for an increase in the charge mass for the V-structures with a V-angle of 105° and a ply orientation of 0°/90°. It is not possible to observe a clear trend for the other two V-structure configurations as tests were only conducted at two charge masses, although the repeat tests with a 10 g show reasonable repeatability in terms of the measured impulse. Looking at the graph, the 30 g test on the V-structure, labelled GFRP_0-90_105_34_T2 and highlighted with a filled-in triangular marker, can safely be excluded from the dataset as the impulse appears to be significantly lower (12.9 Ns) than the GFRP_0-90_105_34_T4 test value, which fits on the trend line. This lower value suggests an incomplete detonation. Additionally, there was no visible damage observed in the V-structure after the blast test which further supports the suggestion that there was an incomplete detonation in this test.

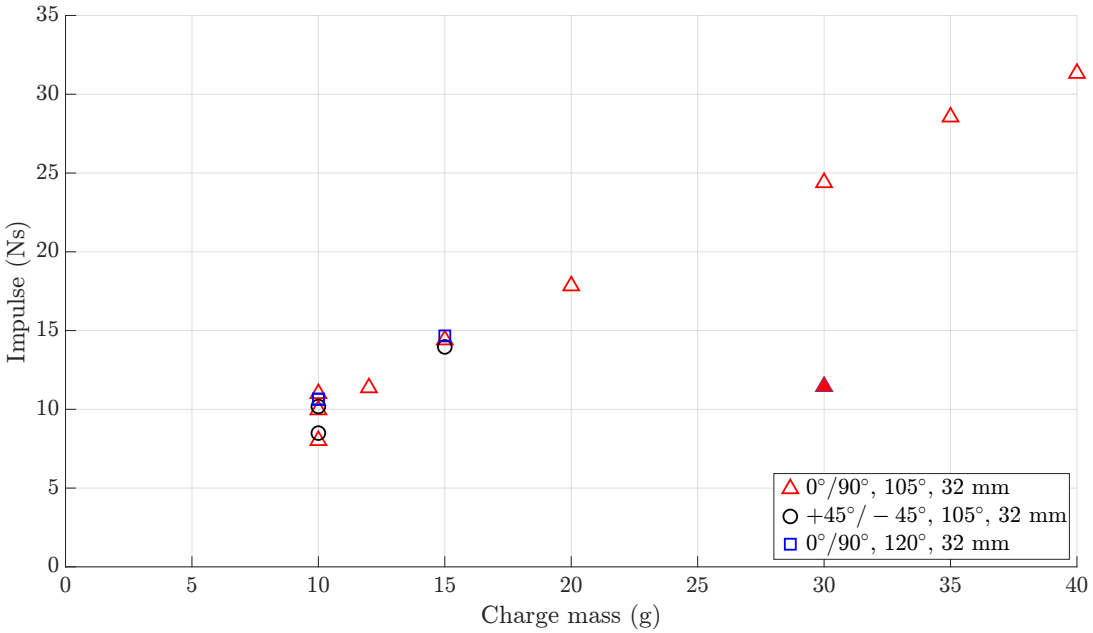

Figure 7.1: Impulse versus charge mass for the GFRP V-structures tested at a SOD of 34 mm

7.2 Discussion of the impulse transfer results

The linear trend observed for the V-structures with a V-angle of 105° and a ply orientation of 0°/90° coincides with the similar observed trends for the DOMEX-700 MC steel V-structure results presented in Chapter 6. This is likely a result of the impulse transferred to the pendulum being driven by the geometry of the V-structures rather than the materials chosen. Additionally, for the tests conducted with a charge mass of 10 g and 15 g, the measured impulse for the two ply orientations tested (0°/90° and ±45°) were in the same range. As expected, the ply orientation does not measurably affect the measured impulse, and the impulse measurements are repeatable test-to-test for a given charge mass, SOD and external V-structure geometry.

At lower charge masses (10 g to 15 g) there was no observable effect of the V-angle on the measured impulse. It is possible that for these charge masses, the V-tip radius, of 34 mm, plays a bigger role in the impulse transfer characteristics of the V-structures. As there are only two experimental data points available for this, it would be necessary to investigate this further using the numerical model before drawing any conclusions about these effects.

7.3 GFRP V-structure damage results

Following the blast testing, the painted V-structures were cleaned so that the damage could be investigated. The front and back faces of each GFRP V-structure were then photographed and the delaminated area and total crack length were measured. An example of a photograph from a blast tested V-structure is shown in figure 7.2. An open-source vector graphics editor (Inkscape) was used to measure the delaminated area for each V-structure by drawing a polygon around the area and measuring the area in pixels squared. An example of the process is shown

in figure 7.3. The length of a pixel in millimetres was found by including a ruler placed on the V-structure when photographed and using Inkscape to measure the number of pixels in a millimetre. The delaminated area was then converted to a percentage of the total projected V-structure area. With the total exposed area being the area of the inner surface of the V-structures as manufactured. Similarly, the crack length was obtained by using Inkscape to draw lines over the cracks on the front face of each V-structure and measuring this length in pixels. These post-blast test measurements are summarised in table 7.4.

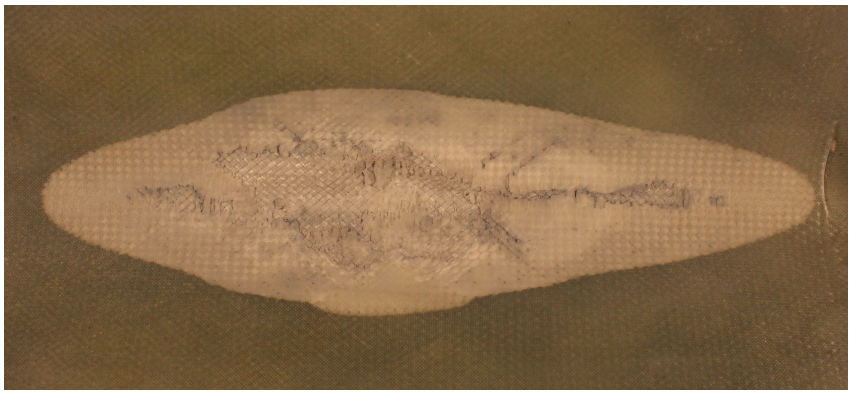

Figure 7.2: Photograph of the back face of a ±45° GFRP V-structure tested at a charge mass of 15 g and a SOD of 34 mm

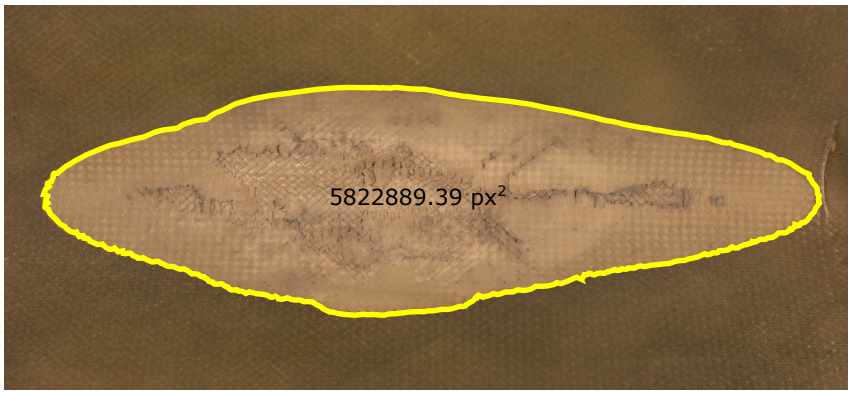

Figure 7.3: Photograph of the back face of a ±45° GFRP V-structure tested at a charge mass of 15 g and a SOD of 34 mm with the delaminated area drawn

Table 7.3 shows the chosen failure mode key with descriptions of each failure mode, while the photographs in figure 7.4 show examples of the same failure modes.

Table 7.3: Failure mode key used for the blast tested GFRP V-structures

Failure mode	Description
Delamination (DL)	The presence of white regions in the laminate, due to the separation of the layers of glass fibre
Matrix failure (MF)	Observed when the V-structures were sectioned and can be seen as the presence of missing resin with fibres intact
Fibre failure (FF)	Damaged or ruptured fibres, usually visible as cracks
Fibre failure with rupture (FFR)	Ruptured fibres through the thickness of the V-structure

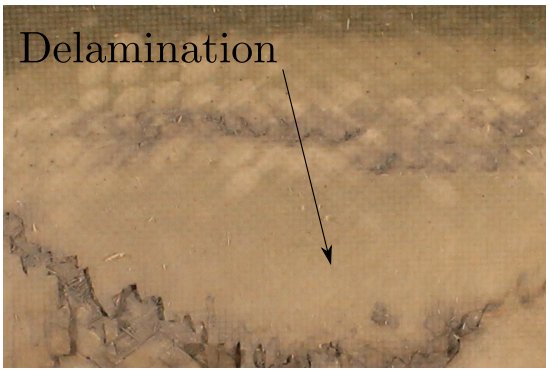

(a) Delamination (DL)

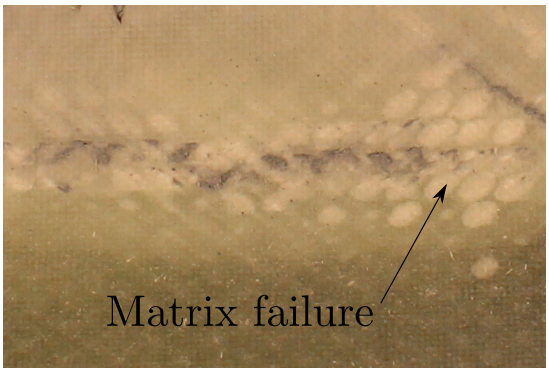

(b) Matrix failure (MF) and Delamination (DL) (Sectioned view)

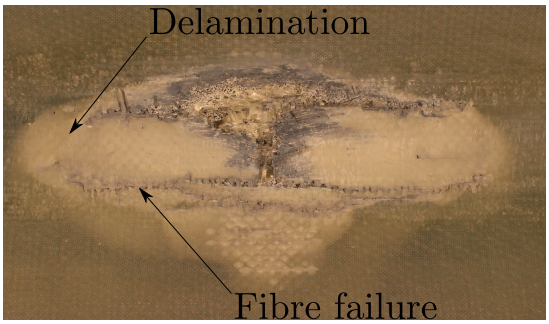

(c) Fibre failure (FF) and Delamination (DL)

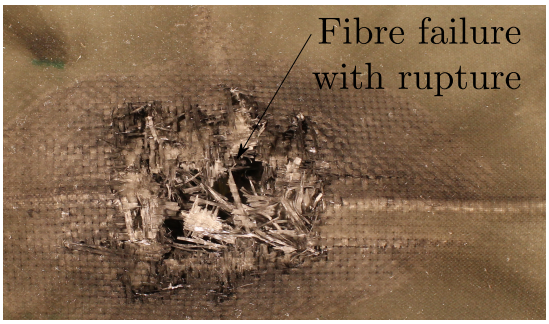

(d) Fibre failure with rupture (FFR)

Figure 7.4: Photographs of the failure modes identified for the blast tested GFRP V-structures

Delamination, fibre failure, and matrix failure were observed in every blast tested V-structure, while rupture was observed in tests with a charge mass of 20 g or more. This was an important finding, as it meant that for all tests performed with DIC, the charge mass used needed to be below 20 g to ensure that the cameras mounted inside the ballistic pendulum were not subjected to projectile impact from fragments. In general, an increase in charge mass results in an increase in the percentage delaminated area and the crack length. Looking at all three GFRP V-structure configurations, it can be seen that tests performed at the same charge mass did not result in the same total crack length and delamination. This is likely due to energy being absorbed differently by each of the failure modes observed in the blast tested V-structures.

Table 7.4: Post blast test results for all the GFRP V-structures

Specimen name	Charge mass (g)	SOD (mm)	Failure modes	Total crack length (mm)	Delaminated area (projected) (%)
GFRP_0-90_105_34_2	10	34	DL, MF, FF	39	4
GFRP_0-90_105_34_6	10	34	DL, MF, FF	243	8
GFRP_0-90_105_34_4	10	34	DL, MF, FF	242	6
GFRP_0-90_105_34_8	12	34	DL, MF, FF	203	6
GFRP_0-90_105_34_7	15	34	DL, MF, FF	256	9
GFRP_0-90_105_34_1	20	34	DL, MF, FF, FFR	-	10
GFRP_0-90_105_34_T4	30	34	DL, MF, FF, FFR	-	23
GFRP_0-90_105_34_T3	35	34	DL, MF, FF, FFR	-	20
GFRP_0-90_105_34_T1	40	34	DL, MF, FF, FFR	-	15
GFRP_45-45_105_34_2	10	34	DL, FF, MF	225	5
GFRP_45-45_105_34_T1	10	34	DL, FF, MF	198	5
GFRP_45-45_105_34_1	15	34	DL, FF, MF	230	7
GFRP_0-90_120_34_2	10	34	DL, FF, MF	117	7
GFRP_0-90_120_34_4	10	34	DL, FF, MF	228	10
GFRP_0-90_120_34_3	15	34	DL, FF, MF	408	11

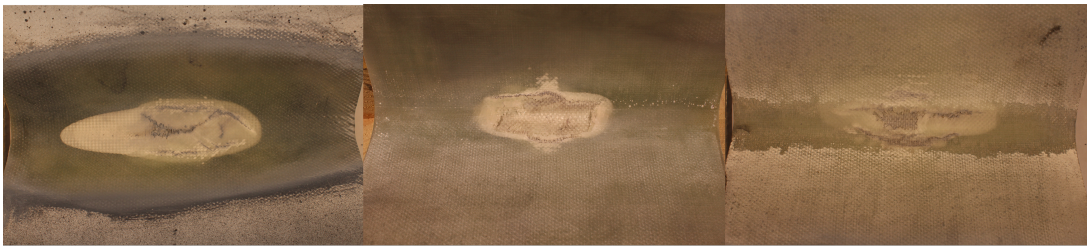

Layup ±45°, V-angle 105° Layup 0°/90°, V-angle 105° Layup 0°/90°, V-angle 120°

Figure 7.5: Photographs of the back face of three GFRP V-structures tested at a charge mass of 10 g and a SOD of 34 mm



Layup ±45°, V-angle 105° Layup 0°/90°, V-angle 105° Layup 0°/90°, V-angle 120°

Figure 7.6: Photographs of the back face of three GFRP V-structures tested at a charge mass of 15 g and a SOD of 34 mm

It was also possible to investigate the effects of the fibre orientation and the V-structure geometry on the variations in the visible delamination. Figures 7.5 and 7.6 shows the back faces of three GFRP V-structures tested at a charge masses of 10 g and 15 g respectively. The central photographs show a 0°/90° fibre orientation 105° V-structure, while the left photographs show a ±45° fibre orientation 105° V-structure, and the photographs on the right show a 0°/90° fibre

orientation 120° V-structure. From the figures, for all three V-structure configurations, an increase in charge mass results in an increase in the visible delaminated area both in terms of width along the crosscut plane and length along the ridge. Furthermore, the 0°/90° fibre orientation 105° V-structure shows the least delamination of the three V-structure configurations at both charge masses tested, while the total delaminated area is similar for the other two V-structure configurations investigated. The shape of the delaminated area for these two configurations is different though, with the ±45° fibre orientation 105° V-structure showing a large increase in delamination along the ridge line while the 0°/90° fibre orientation 120° V-structure shows a fairly even increase in delamination in both the ridge line and crosscut plane. The observed delamination in the ±45° fibre orientation 105° V-structure appears to extend further along the ridge while not covering a significantly greater area across the crosscut plane when compared to the 0°/90° fibre orientation 105° V-structures. When looking at the effect of the V-angle, an increase in the V-angle does result in an increase in the delaminated area in both the width of the delaminated area along the crosscut plane and the length along the ridge.

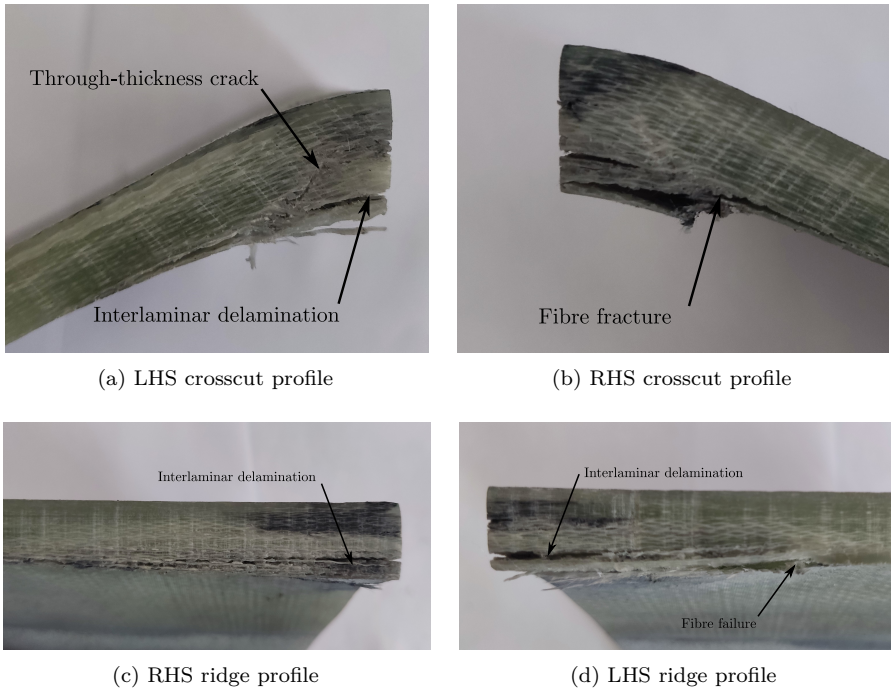

(a) LHS crosscut profile

(b) RHS crosscut profile

(c) RHS ridge profile

(d) LHS ridge profile

Figure 7.7: Photographs of a sectioned GFRP V-structure (120°, 34 mm V-tip radius) tested at an charge mass of 10 g with a SOD of 34 mm

Once the blast tested GFRP V-structures were photographed and analysed, a selection of V-structures were sectioned to investigate any through-thickness damage. The first observation was that most of the visible damage was located in the central 100 mm along the ridge of each V-structure. Figure 7.7 shows sectioned crosscut and ridge plane views of one blast tested GFRP V-structure with a V-angle of 120°, V-tip radius of 34 mm and ply orientation of 0°/90°. From figure 7.7(a), a through-thickness diagonal crack can be seen that propagates through the layers from the centre of the V-structure to the inner fibre layers. Additionally, in both figure 7.7(a) and (b), delamination can be seen in the innermost seven layers. Looking at the sectioned

ridge plane photographs in figure 7.7(c) and (d), fibre failure can be seen in the innermost layer. Delamination is visible and this is present in layers from the inner surface extending to the mid-plane of the V-structure thickness, and the amount of delamination increases towards the inside of the V-structure. Additional images for other V-structures can be found in Appendix C.

7.4 Discussion of the GFRP V-structure damage results

In general, increasing the charge mass resulted in an increase in the percentage delaminated area and the total crack length on the surface, although a linear trend could not be discerned as the GFRP response was more variable than those obtained for the steel V-structures. This is likely due to the multiple modes of failure and varying energy transfer between the modes (*i.e.* delamination, fibre failure, and matrix failure) in each blast test. This results in a distribution of the energy from the blast test amongst these failure modes. Similar findings were also observed by Sinclair [92] for flat and curved GFRP structures. This finding is important when developing the numerical blast model for the GFRP V-structures as it suggests that there might be some variations in the quantifiable measurements of failure modes observed.

When looking at the through-thickness failure, it was observed that most of the damage was limited to the central region of the V-structure, along both the ridge plane and the crosscut plane. This fits the expected response of structures subjected to localised blast loads, as most of the damage is constrained to the central region directly below the charge. This behaviour is further accentuated by the geometry of the V-structure, which deflects the blast wave around the V-structure. Additionally, most of the delamination was observed on the innermost layers of the V-structure. This behaviour is to be expected as the inner layers experience a greater tensile load when the V-structure bends in response to the blast load. Similar failure was observed for flat and curved structures tested under uniform blast loads by Sinclair [92].

7.5 Transient deformation results

In this section, the results from the DIC blast tests done on the GFRP V-structures are presented.

7.5.1 Paint spalling on the GFRP V-structures

In Chapter 5, it was explained that the resin rich area along the ridge of the GFRP V-structures was ground down to ensure a better bond with the paint. Even so, the paint was still observed to spall during the blast tests as shown in figure 7.8. This series of photographs shows the ridge during the first 0.5 ms of a blast test. In the second photograph, while the paint has not spalled yet, there is motion blur present in the central region due to the high velocity of this part of the structure. In time steps three to five, the spalling of the paint can clearly be seen. Hence, it was not possible to measure the transient deformation in the most central part of the GFRP V-structures for most of the tests conducted.

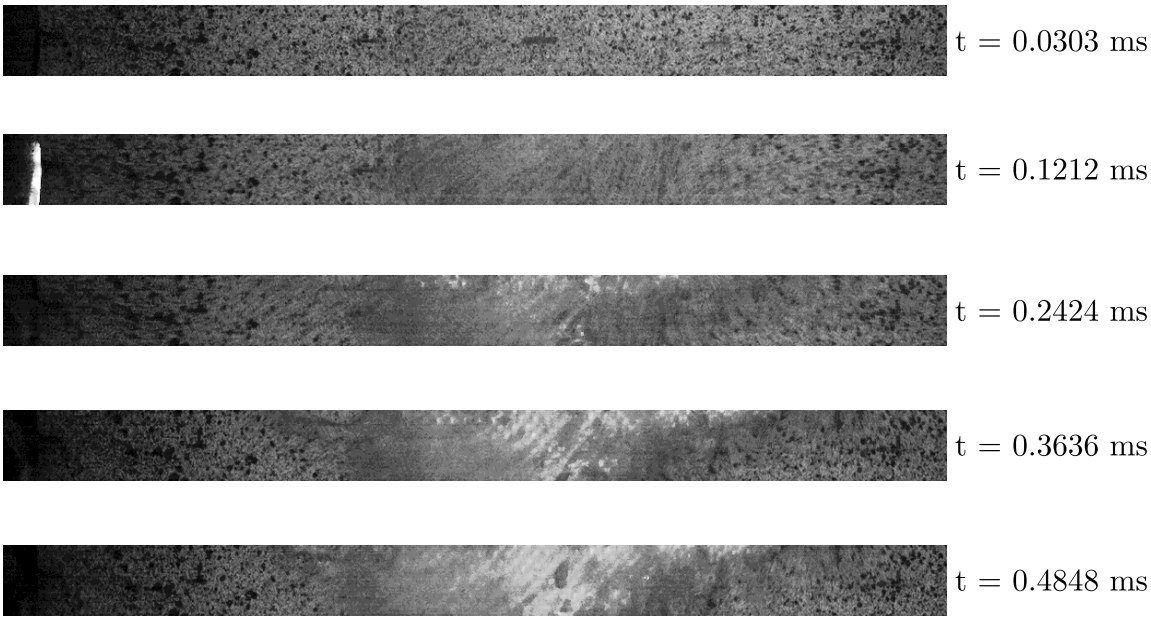

Figure 7.8: Photographs of the spalling paint during a GFRP V-structure blast test

7.5.2 Point deflection time history

Paint spalling issues affected the majority of the experiments, but two tests were conducted in which this was not an issue. These were tests conducted on 105° V-structures, with a ±45° lay-up tested at a charge mass of 10 g and a SOD of 34 mm. Hence, here it was possible to measure and track the mid-point deflection. These results are presented in figure 7.9. The missing data at the start of the test was due to motion blur due to the high initial velocity of the V-structure at the start of the test. The two lines show similar displacement histories, suggesting good repeatability of the tests. Furthermore, similar to the steel V-structures, there does not appear to be significant vibration of the mid-point after the test.

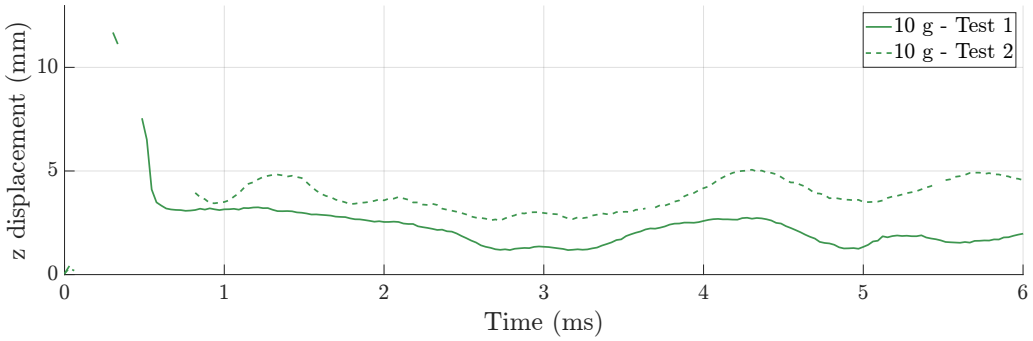

Figure 7.9: Mid-point displacement time histories for the tests done on a 105° V-structure, ±45° lay-up tested at a charge mass of 10 g and a SOD of 34 mm

Due to the motion blur and paint spalling, a point was chosen for deflection tracking located 50 mm from the centre of the V-structure as shown in figure 7.10. The mid-point deflection and the deflection at 50 mm are plotted on the same graph in figure 7.11. It can be seen that the deflection time histories follow a similar trend although the magnitude of vibration and the permanent deformation are different. The deflection-time graph for the 105° V-structures,

with a ±45° lay-up tested at a charge mass of 10 g is shown in figure 7.12 while the graph for 120° V-structures, with a 0°/90° lay-up is shown in figure 7.13. Markers have been applied as described in section 6.5.1 for the steel blast specimen. This data will prove useful for validating the numerical blast simulations and shows the V-structure response through the first 6 ms of the blast test.

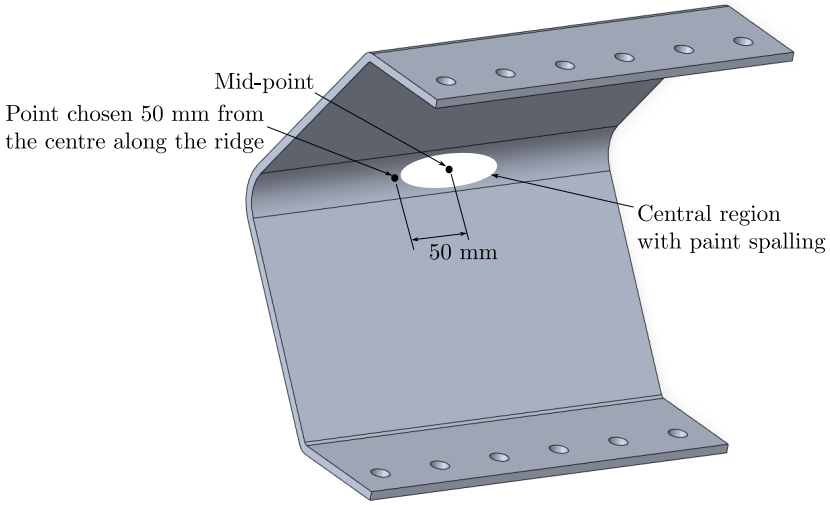

Figure 7.10: 3D profile of a V-structure showing the location of the point chosen for measuring the transient deformation of the GFRP V-structures

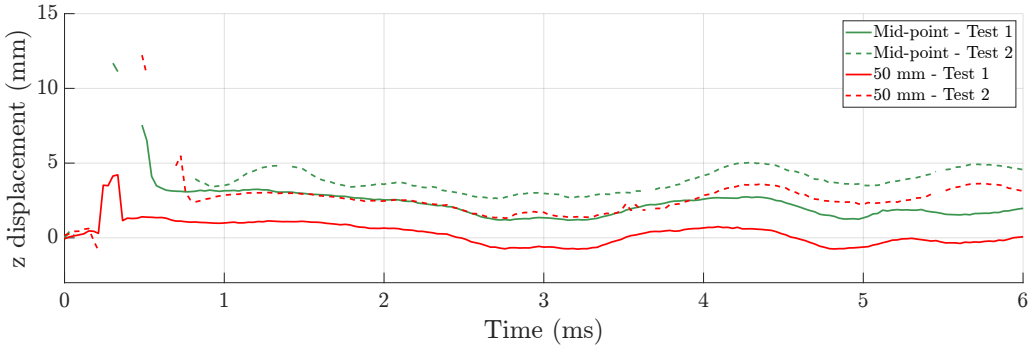

Figure 7.11: Mid-point displacement versus point displacement at 50 mm from the centre for a test performed on a 105° V-structure, ±45° lay-up tested at a charge mass of 10 g and a SOD of 34 mm

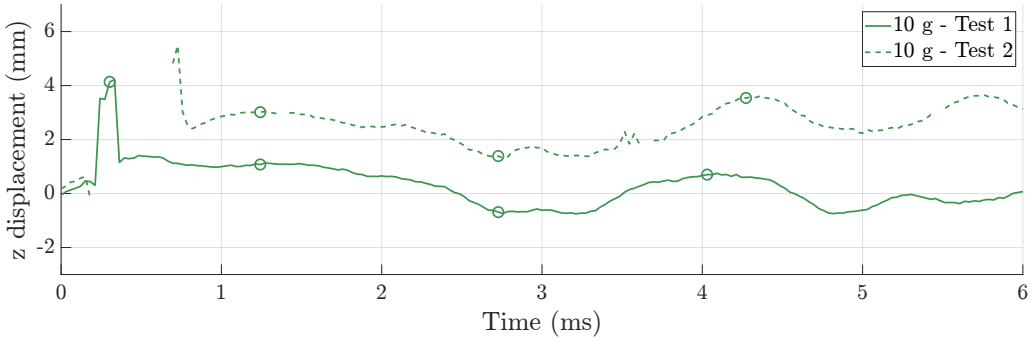

Figure 7.12: Point displacement time histories 50 mm from the centre for the tests done on a 105° V-structure, ±45° lay-up tested at a charge mass of 10 g and a SOD of 34 mm

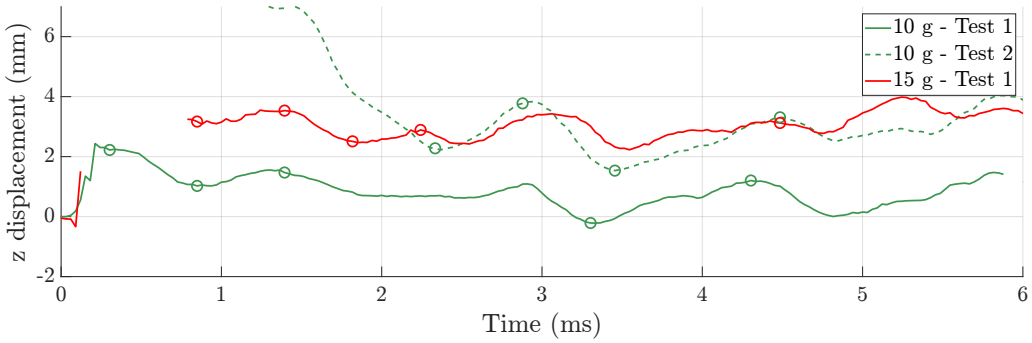

Figure 7.13: Point displacement time histories 50 mm from the centre for the tests done on a 120° V-structure, 0°/90° lay-up tested at a charge mass of 10 g and a SOD of 34 mm

For figure 7.12, as expected, the 105° V-structures with a ±45° lay-up show a lower displacement than that observed at the mid-point in figure 7.9. Furthermore, there is a peak displacement although it has a lower magnitude immediately after the blast. This finding is further supported by the results at the 50 mm point for the 120° V-structures, with a 0°/90° lay-up shown in figure 7.13. This lower peak is likely due to the location chosen for the measurements. Additionally, all the V-structures appear to be vibrating with a peak-to-peak amplitude of 1 mm. Furthermore, the displacement time histories appear to be fairly similar for the tests conducted on the same configuration of V-structure with the same charge mass. This also supports the repeatability of the blast experiments conducted and provides confidence when using these results to validate the numerical blast model for the GFRP V-structures.

7.5.3 Ridge profiles

The ridge profile transient data from selected tests are plotted in figures 7.14 and 7.15. Once again, as with the steel V-structure transient results, the ridge profiles have been flipped in the z direction and centred at 0 mm. The timesteps chosen correspond to the selected peaks and troughs in the point deflection time history graphs noted in the previous section and denoted with circles in figures 7.12 and 7.13. The final displacement was not zero for either of the tests as shown by the dashed black lines representing the top and bottom final deformed ridge profiles in figures 7.14 and 7.15. Note that the transient ridge profile measurements are taken for the inner (bottom) surface of the GFRP V-structures.

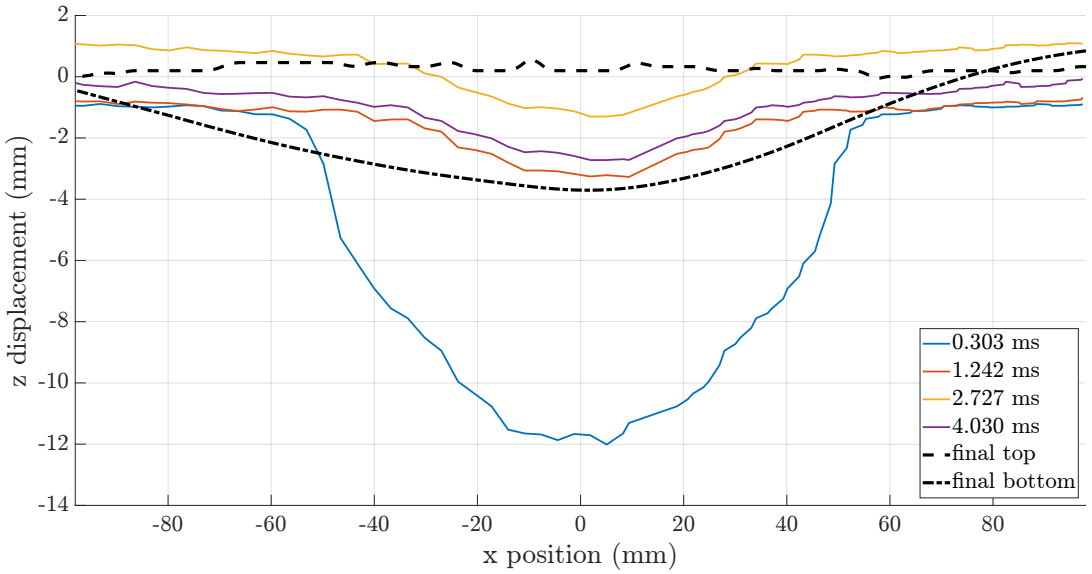

Figure 7.14: Ridge displacements for test one on a 105° V-structure, ±45° lay-up tested at a charge mass of 10 g and a SOD of 34 mm

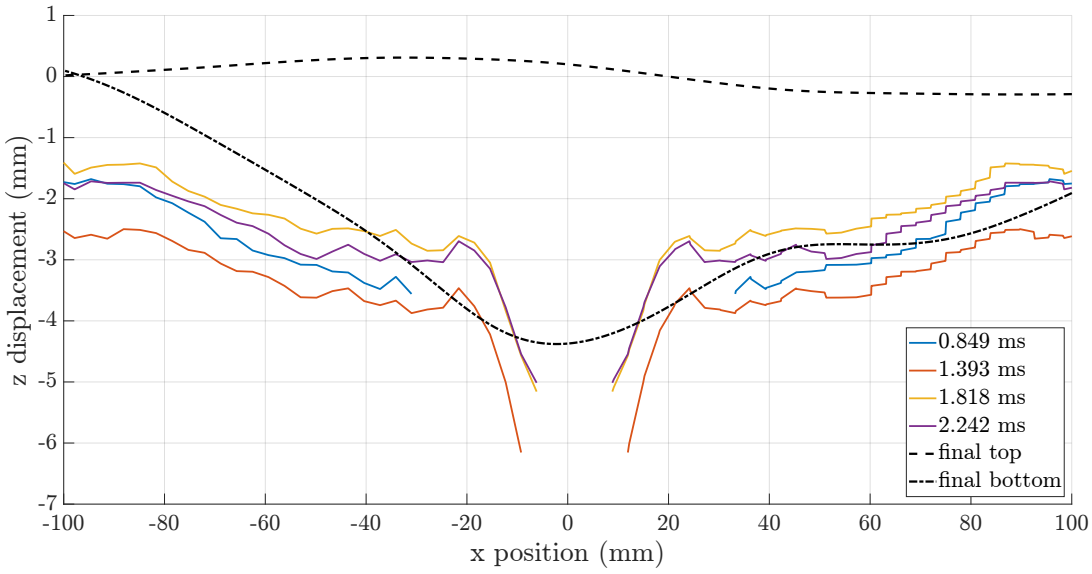

Figure 7.15: Ridge displacements for test one on a 120° V-structure, 0°/90° lay-up tested at a charge mass of 15 g and a SOD of 34 mm

In figure 7.14, showing a 105° V-structure, the large initial elastic deflection of 12 mm damps out within 1 ms and following this, the V-structure is observed to vibrate. The deformed profile is not observed to change significantly during this vibration. The two dashed lines show the ridge profiles of the top and bottom faces of the blast tested V-structure. There is no visible deformation on the top surface, while the bottom surface shows significant permanent deformation of approximately 2 mm. In figure 7.15, for a 120° V-structure, the deflection in the central region of the V-structure has not been captured for any timestep. Looking at these plots, the V-structure does show some more significant permanent deformation, due to the glass fibre layers delaminating during the blast. This can be seen in the permanent deformation profile of both the outer and inner surfaces. This delamination and permanent deformation on the

inner surface can also be seen in the sectioned photographs of these V-structures in figure 7.7. There is a small amount of permanent deformation on the outer surface, due to the multiple delamination regions through the thickness of the V-structure along the ridge line.

7.6 Discussion of the transient deformation results

There was minimal vibration in the mid-point displacement of the ±45° V-structures when tested at 10 g, possibly due to the large second moment of area (*i.e.* the thickness effects) of the V-structure. Additionally, the non-zero final mid-point displacement was attributed to the delamination and separation of the layers during the blast test. Some permanent deformation was also observed as far as 50 mm from the mid-point in the remaining figures. This is due to the delamination and layer separation along the ridge of the V-structures. The repeated tests showed good consistency in the mid-point displacement time history, increasing the confidence in the tests conducted. Similar findings were reported by Daliri *et al.* [93] for localised blast loaded flat S2 glass-fibre structures although Gabriel *et al.* [94] did not observe any noticeable final deformation for uniformly blast loaded flat E glass-fibre structures. This suggests that the final deformation observed might be a result of the localised blast loading of the GFRP V-structures and flat structures causing localised damage near the centre of the V-structure.

Ridge profile data was available for two of the tests conducted. There is a large elastic deformation immediately after the blast but this deformation quickly disappears to produce the final deformed V-structure ridge profile. This profile included a deformed central region due to the delamination and separation of the layers of glass-fibre during the blast test. Additionally, the final vibration amplitude of the profiles is around ±2 mm from the final position. As stated previously, this is likely a result of a combination of the geometric stiffness and the greater second moment of area resulting from the geometry of the thick GFRP V-structures.

7.7 Summary

A linear trend in the measured impulse for an increase in charge mass was observed for the tests on the V-structures with a V-angle of 105°, V-tip radius of 34 mm, and a ply orientation of 0°/90°. These linear trends matched observations from previous studies on flat and V-structures. The impulse results also showed good repeatability for tests conducted with the same charge mass. At the lower charge masses, there did not appear to be a significant effect of the V-angle on the measured impulse. In general, the total structure damage (*i.e.* crack length and delaminated area) increased with an increase in charge mass. This was attributed to multiple failure modes absorbing the energy of the blast load in different ways.

The transient mid-point displacement could not be obtained for most tests due to spalling of the paint in the central region of the ridge. Thus the displacement time history was taken 50 mm to the left of the mid-point of the V-structure. From these plots, the peaks and troughs were found to be within 1 mm of the final deformed position. The results were consistent for tests using the same charge mass of PE4 increasing the confidence in the results. Ridge profiles were also plotted for the tests available. The ridge of the V-structures displayed large initial elastic deformation

in the central region of 12 mm in the single test where this data was available. Following this, there was a vibration about the final deformed shape of approximately ±1 mm. This was lower than the absolute post-peak vibration behaviour observed for the steel V-structures. Most of the permanent deformation was limited to the central 100 mm along the ridge. The V-structure returned to its initial position after 1 ms with some small permanent deformation, likely due to delamination of the layers. This was expected for GFRP V-structures due to a lack of material plasticity.

Chapter 8

Numerical blast simulations - Steel

This chapter details the numerical modelling of the air-blast simulations performed on the steel V-structures. LS-DYNA was used to run all the simulations, with the pre-processing and post-processing done with LS-PrePost. The chapter starts with a description of the process followed to mesh the components used in the numerical models, including the clamp frames, bolts, and V-structures. The important keyword files and the parameters used are then listed. The impulse, mid-point deflection and ridge profiles are then compared between the blast simulations and experiments for a selection of test configurations to validate the numerical model developed herein. Once the model was validated, a series of simulations were conducted for a range of V-tip radius and charge mass combinations. These results are then presented and discussed in this chapter.

8.1 Numerical model development

8.1.1 Meshing the model components

All the blast simulations used a quarter-symmetry model to make use of the symmetry available in the experimental setup. The first step in the development of the numerical model was to generate the geometry and mesh the clamp frames and bolts. The clamp frame geometry was drawn in CAD before being sectioned based on the symmetry of the numerical model. The geometry was then imported into LS-PrePost where it was meshed and boundary conditions were applied. This meshing process is shown in figure 8.1 for one of the clamp frame components.

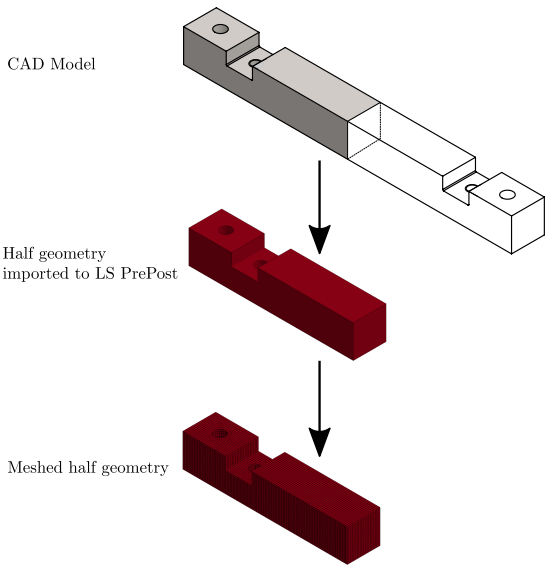

Figure 8.1: Going from a CAD model to a meshed component

8.1.2 Selection of components to model

For all the simulations, the clamp frames and bolts were included in the model. This was done for two reasons. Firstly, the exclusion of the clamp frame was found in previous studies to significantly influence the impulse [72]. Secondly, the elastic deformation of the clamp frames during the blast test simulations was found to be significant and thus if these components were not included, the measured transient deformation would not reflect the behaviour observed in the blast experiments. Figure 8.2 shows the simulated displacement time history for a node located at the centre of the clamp frame for a 105°, 32 mm steel V-structure with a charge mass of 20 g. From the graph, it can be seen that the clamp frame vibrates with a period of approximately 3.5 ms and an amplitude of approximately 2 mm. Thus, in order to ensure that the post-blast transient response of the V-structures is correctly modelled, the clamp frames need to be included in the simulations. The ballistic pendulum does not need to be included in the numerical models as it functions as a tool to measure the impulse transferred from the blast load. In the simulations this can be determined directly from the fluid-structure interaction between the explosive loading and the target structures.

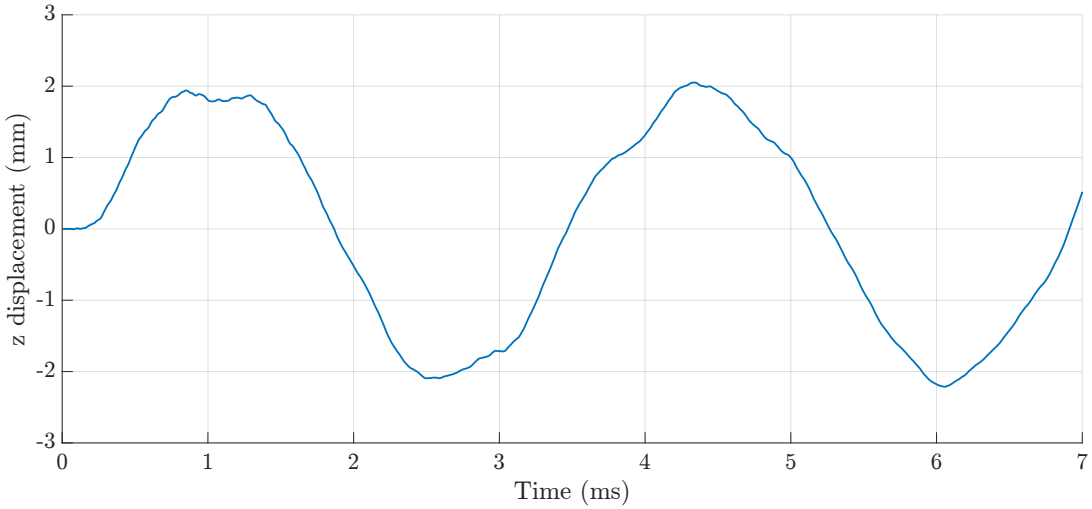

Figure 8.2: Displacement time history for a central node on the clamp frame during a blast simulation of a 105°, 32 mm steel V-structure simulation at a charge mass of 20 g

Due to the inclusion of the clamp frames and bolts, the interfacing nodes and surfaces between the clamp frames, bolts, and V-structures needed to be tied together. This was done using the CONTACT_TIED_SURFACE_TO_SURFACE and CONTACT_TIED_NODES_TO_SURFACE_OFFSET cards [95]. These two cards allowed for the forces to be transferred through the V-structure into the bolts and clamp frame components during the blast simulation. The inclusion of the additional components did result in an increase in the computational time due to the increased number of nodes and contact cards. This was deemed necessary to ensure that the model correctly captured the physics of the blast experiments and improved the accuracy of the solutions.

8.1.3 Modelling the explosive blast load

A Multi-Material Arbitrary Lagrangian-Eulerian (MMALE) formulation was used to model the air mesh, the explosive PE4 charge, and the interaction between the detonated explosive and the Lagrangian parts (*i.e.* The V-structure, clamp frames, and bolts). The air block dimensions were set at 200 mm × 200 mm × 300 mm to ensure that it covered all the Lagrangian parts. The air was modelled using a null material model (MAT_NULL) with the properties shown in table 8.1 and an ideal gas Equation of State (EOS) equation (8.1) [96], which is implemented in LS-DYNA using a linear polynomial formulation shown in equation (8.2) with constants C_4 and C_5 set to $\gamma - 1$ and the other constants set to zero [96]. The value of μ can be found from the relative volume (V) as shown in equation (8.3)

$$p = (\gamma - 1)\frac{\rho}{\rho_0}E \tag{8.1}$$

$$p = C_0 + C_1\mu + C_2\mu_2 + C_3\mu_3 + (C_4 + C_5\mu + C_6\mu_2)E \tag{8.2}$$

$$\mu = \frac{1}{V} - 1 \tag{8.3}$$

Table 8.1: Material model properties used for air in LS-DYNA [97]

ρ_0 ($\mathrm{kg\,m^{-3}}$)	E_0 ($\mathrm{kJ\,kg^{-1}}$)	γ	C_4	C_5
1.184	253.3	1.4	0.4	0.4

The cylindrical explosive disc was modelled using the INITIAL_VOLUME_FRACTION_GEOMETRY card, while the detonation point was set 1 mm from the top of the explosive charge and included in the model using the INITIAL_DETONATION card. A Jones-Wilkins-Lee (JWL) EOS (equation (8.4)) was used to model the explosive charge with a MAT_HIGH_EXPLOSIVE_BURN (MAT_008) [96]. These properties are provided in table 8.2. The properties used for the simulations were those of C4. The only difference between C4 and PE4 is the plasticisers used and thus the behaviour is known to be the same [98].

$$p = A\left(1 - \frac{\omega}{R_1V}\right)e^{-R_1V} + B\left(1 - \frac{\omega}{R_2V}\right)e^{-R_2V} + \frac{\omega E}{V} \tag{8.4}$$

Table 8.2: Material model properties used for PE4 in LS-DYNA [99]

ρ_0 ($\mathrm{kg\,m^{-3}}$)	D ($\mathrm{m\,s^{-1}}$)	P_{CJ} (GPa)	A (GPa)	B (GPa)	R_1	R_2	ω	E_0 ($\mathrm{kJ\,kg^{-1}}$)
1601	8193	28	609.77	12.95	4.5	1.4	0.25	9

From previous work performed on the blast loading on rigid V-structures [72], it was found that a termination time of 0.3 ms was sufficient for the pressure to return to atmospheric pressure at the locations furthest from the explosive detonation centre. The tracers were placed in the same locations as those used in previous research on rigid V-structure simulations [72]. This was

confirmed for a 120° V-structure with a 32 mm V-tip radius subjected to a 20 g charge as shown in figure 8.3. The pressure-time histories at the tracer locations closely matches the analytical Friedlander equation pressure-time graph. From the figure, the pressure has equalised by 0.3 ms. Hence, when modelling the blast tests, this was chosen as the termination time to switch off the MMALE formulation, remove the air mesh, and allow the Lagrangian parts to vibrate. The free vibration of these components was then allowed to run up to 7.0 ms, following which damping was added to the model to allow the final deformed V-structure profiles to be determined.

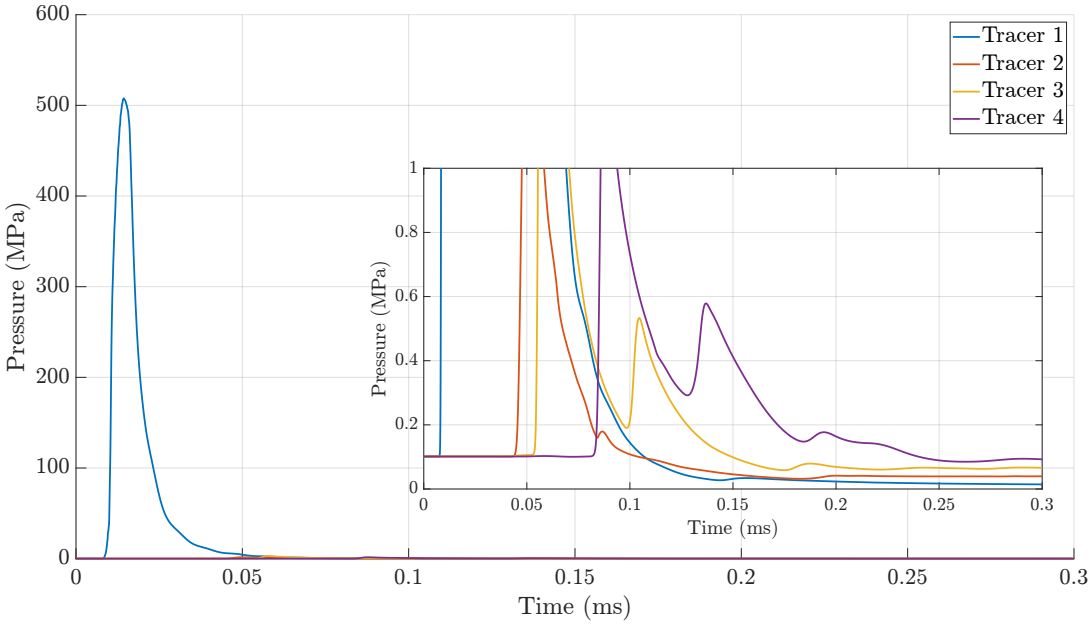

Figure 8.3: Pressure time histories at the four corners of a 120°, 32 mm V-tip radius DOMEX-700 MC V-structure simulation with a charge mass of 20 g with insert showing pressures equalising across the plate after 0.3 ms

8.1.4 Element size, type, and formulation selection

All the blast simulations utilised an explicit dynamic formulation due to the nature of the loading. In a previous study done on localised blast loaded rigid V-structures using LS-DYNA [72], it was shown that mesh convergence was observed for an Eulerian mesh size of 2.0 mm. Hence, for all blast simulations, the air mesh element size was set to 2.0 mm and this was a uniform element size across the meshed volume. Additionally, previous studies performed using LS-DYNA to model blast loaded deformable steel structures [56, 63] showed good correlation between the experimental and numerical V-structure deformation with an element size of 1.0 mm. Hence, all steel and GFRP V-structures, clamp frames, and bolts were meshed with uniform 1.0 mm elements.

Each steel V-structure was meshed with uniform four-node shell elements using a Belytschko-Tsay element formulation (ELFORM_2). Shell elements were chosen here due to the relatively low thickness of the steel V-structures (2 mm) compared to its other dimensions. The clamp frames and bolts were meshed with 8-node solid elements, with a constant stress element formulation (ELFORM_1). A Johnson-Cook material model (MAT_015) was chosen for the DOMEX-700 MC steel V-structures with the parameters obtained and presented in Chapter 4. The clamp

frames and bolts did not display any permanent deformation after all of the blast tests performed and thus were modelled using an elastic material model (MAT_001) for mild steel. A schematic of a 20°, 32 mm steel V-structure simulation with a 20 g charge is shown in figure 8.4. The symmetry of the system can be seen by the coloured portion of the image, with the geometry of the charge and the detonation points also labelled in the figure. Each blast model contained approximately 240000 solid elements for the air mesh, clamp frames, and bolts, and 38000 shell elements for the steel V-structure. The average run times were 40 h for the loading phase of 0.3 ms and 80 h for the free vibration phase.

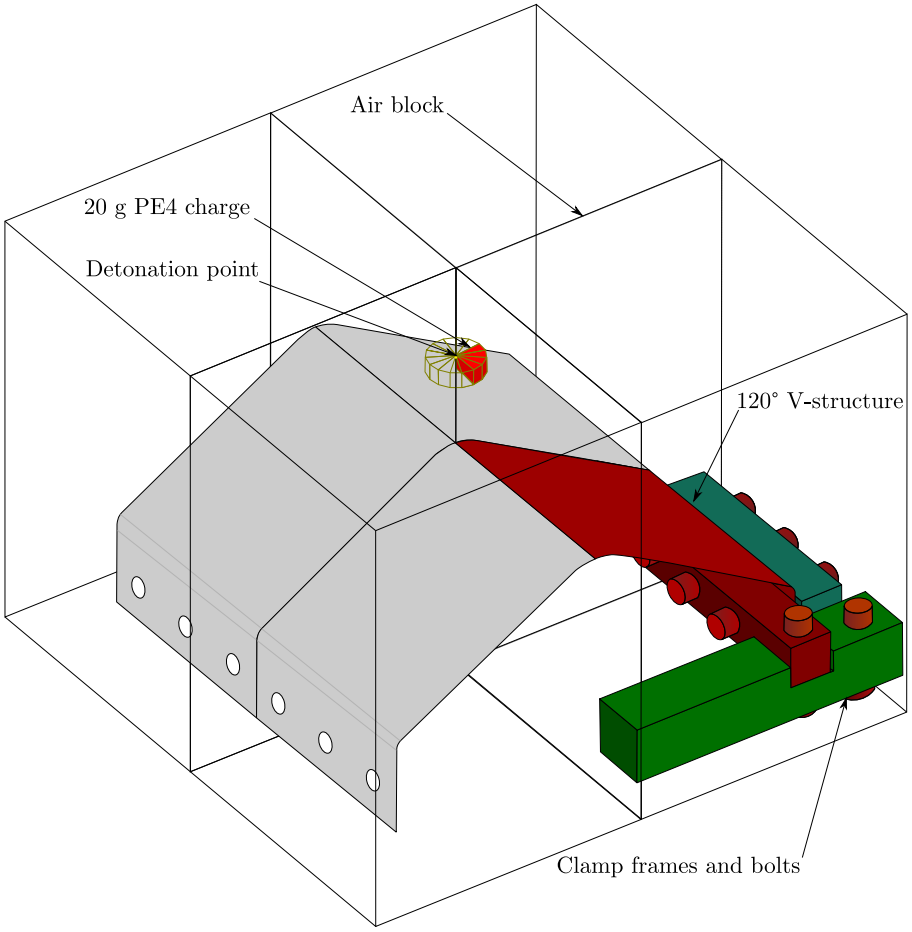

Figure 8.4: Schematic of the blast simulation of a 120°, 32 mm V-tip radius DOMEX-700 MC V-structure simulation with a charge mass of 20 g, showing the symmetry used, including the air block, the explosive charge, the clamp frames, and the bolts.

8.1.5 Deformation plot visualisations

To check that the numerical model is correctly capturing the plastic strain evolution in the V-structure, a series of plots in figure 8.5 have been shown for a 105°, 32 mm steel V-structure simulated at a charge mass of 20 g. The strain increases as the blast pressure wave interacts with the target structure and remains mostly in the central region of the V-tip. This is to be expected as the loading is localised. The peak plastic strain is seen before 0.05 ms and there is no significant evolution of the plastic strain after 0.15 ms. This supports the observations from the DIC results from the blast tested steel V-structures where the V-structures had reached

their final deformed profile before 0.3 ms.

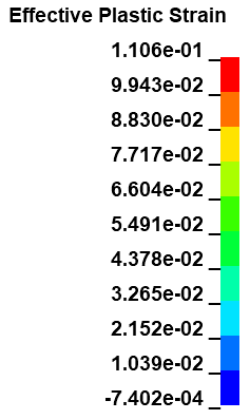

(a) Fringe levels

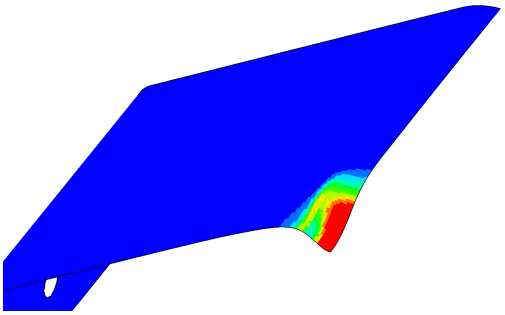

(b) t = 0.05 ms

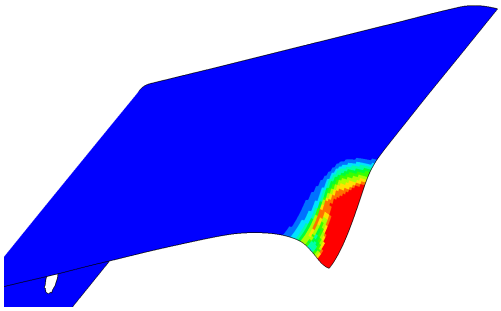

(c) t = 0.10 ms

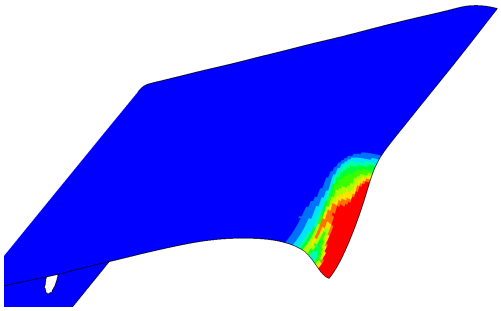

(d) t = 0.15 ms

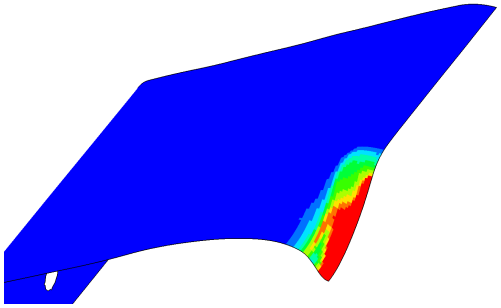

(e) t = 0.20 ms

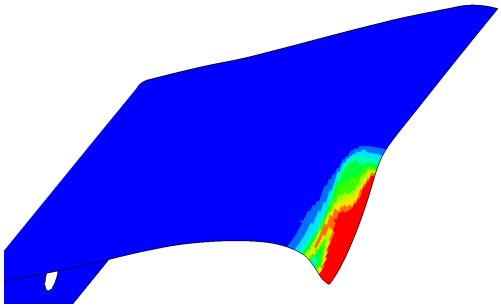

(f) t = 0.25 ms

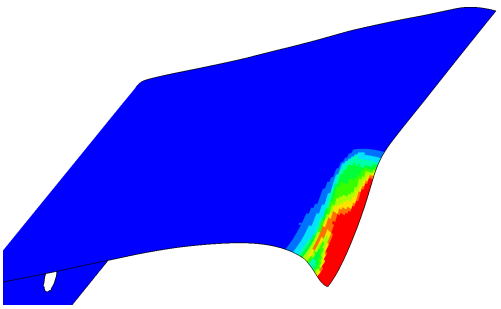

(g) t = 0.30 ms

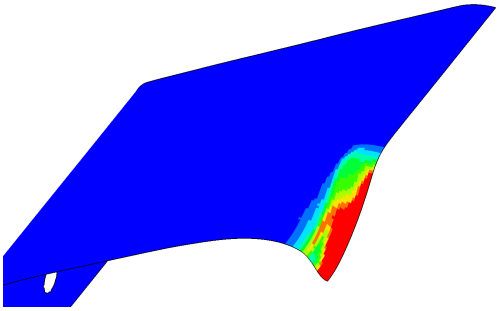

(h) t = 10.00 ms

Figure 8.5: Equivalent plastic strain evolution for a 105° steel V-structure simulation with a 32 mm V-tip radius simulated at a charge mass of 20 g

8.2 Numerical model validation - Steel

A selection of numerical results were compared to experiments to show that the model was able to accurately capture the mechanics of the blast tests. Two V-angles, two V-tip radii, and three different charge masses were chosen for the comparisons. The first comparisons were the permanent V-structure deformations in the ridge and crosscut planes. Following this, the transient responses were compared by looking at the mid-point transient deformation time histories for selected experiments. Lastly, the peak and permanent mid-point deflections and the impulse were compared. Where comparison plots are shown between the experiments and the numerical simulations, solid lines are used for the experiments while dashed lines are used for the simulations.

8.2.1 V-structure permanent deformed profiles - Ridge plane

Figure 8.6 shows the numerical and experimental permanently deformed ridge profiles for the 105°, 32 mm steel V-structure tested at a charge mass of 15 g. From the figure, the model appears to capture the correct deformed shape, although the deformed length along the ridge is slightly lower for the simulations. Additionally, the mid-point deformation is also slightly lower in the simulation. Additional ridge profile comparisons were generated and can be found in Appendix D.

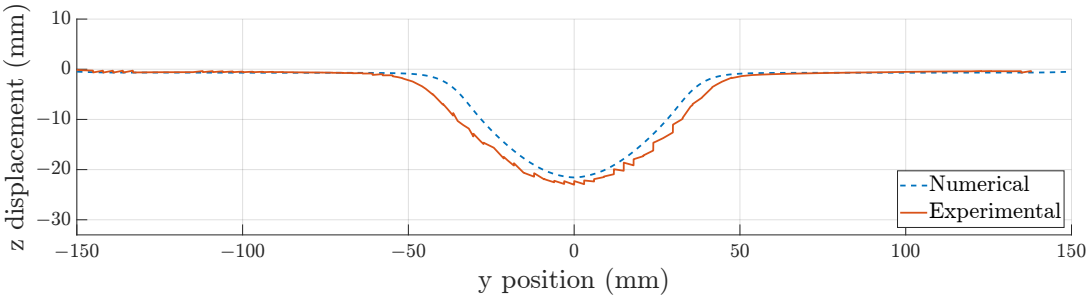

Figure 8.6: Permanently deformed ridge profiles for a 105°, 32 mm V-tip radius DOMEX-700 MC V-structure at a charge mass of 15 g (numerical versus experimental)

Figure 8.7 shows the numerical and experimental permanently deformed ridge profiles for the 105°, 62 mm steel V-structure at charge mass of 20 g. The magnitude of the displacement and the deformed length are both slightly under-predicted in the model, with similar correlations obtained at other charge masses (shown in Appendix D).

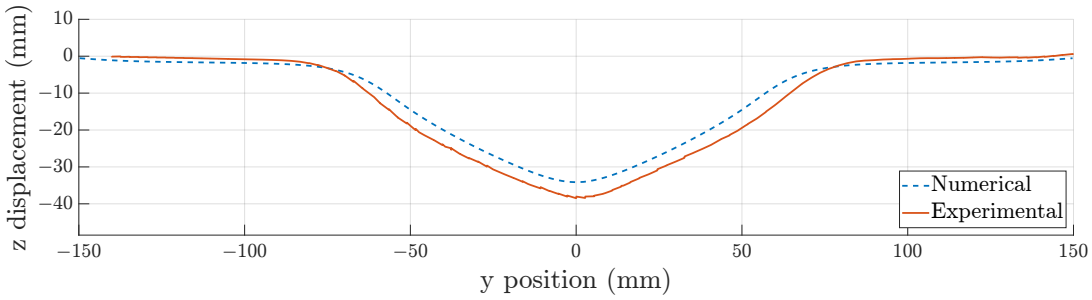

Figure 8.7: Permanently deformed ridge profiles for a 105°, 62 mm V-tip radius DOMEX-700 MC V-structure at a charge mass of 20 g (numerical versus experimental)

Figure 8.8 shows the numerical and experimental permanently deformed ridge profiles for a 120°, 32 mm steel V-structure tested at a charge mass of 20 g. Much like the other two configurations, there is good correlation between the numerical and experimental results, with the deformation along the ridge and the permanent mid-point deflection being a little lower in the test. The additional ridge profile comparisons at charge masses of 10 g and 15 g are provided in Appendix D.

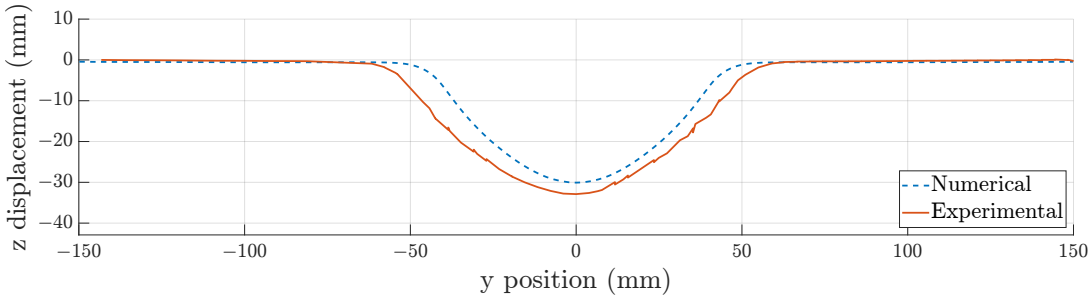

Figure 8.8: Permanently deformed ridge profiles for a 120°, 32 mm V-tip radius DOMEX-700 MC V-structure at a charge mass of 20 g (numerical versus experimental)

The simulations are able to capture the correct global deformed profile for a range of charge masses, V-tip radii, and V-angles. Importantly, in terms of developing an understanding of the structural response of these V-structures to the blast loads, the models are able to correctly predict the general shape of the deformed ridge, while also capturing the increases in deformation at the mid-point and along the ridge as the charge mass is increased.

8.2.2 V-structure permanently deformed profiles - Crosscut plane

The post-test crosscut numerical and experimental profiles were next compared in a similar manner to that done for the ridge profiles. Figure 8.9 shows the numerical and experimental permanently deformed crosscut profile for a 105°, 32 mm V-tip radius DOMEX-700 MC V-structure tested at a charge mass of 10 g. Similarly to the ridge profiles of the same V-structure configuration, the numerical model appears to capture the correct deformed shape, in terms of the indentation at the centre of the V-tip and the deformation of the regions along the V-profile. The deformed length along the V-profile is fairly similar for the 10 g test, but lower for the other two charge masses investigated, shown in figures D.7 and D.8. Additionally, much like the ridge profile comparisons, the mid-point deformation is also similar at a charge mass of 10 g but lower for the other two charge masses. Finally, The asymmetric deformation present in the

experiments was not present in the simulation results due to the model utilising the geometric symmetry of the V-structure and experimental setup to model a quarter of the geometry.

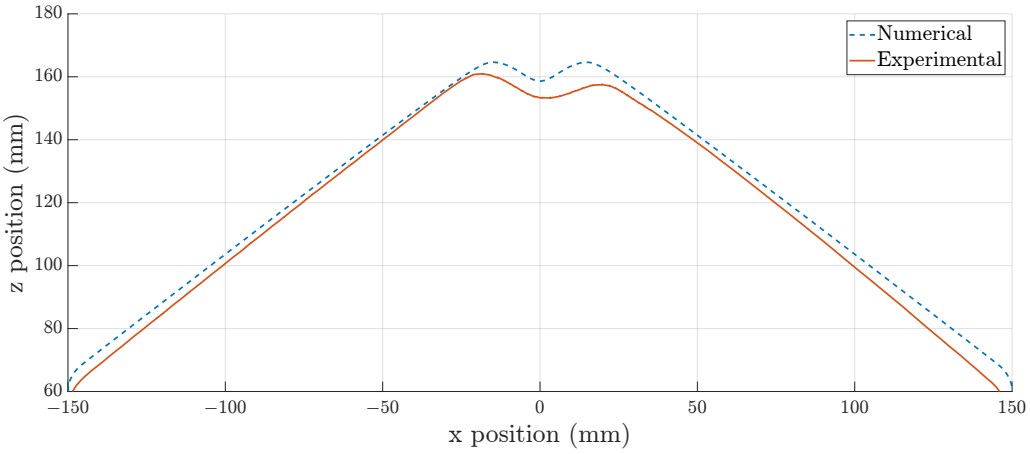

Figure 8.9: Permanently deformed crosscut profiles for a 105°, 32 mm V-tip radius DOMEX-700 MC V-structure at a charge mass of 10 g (numerical versus experimental)

Next, the numerical and experimental permanently deformed crosscut profiles for the 105°, 62 mm V-tip radius DOMEX-700 MC V-structure tested at charge masses of 20 g were compared. This is shown in figure 8.10, while additional figures can be found in Appendix D. Once again, the numerical model does appear to capture the correct deformed shape in the crosscut plane. Additionally, these model results fit the experimentally measured profiles better than those for a 32 mm V-tip radius. At a charge mass of 10 g the deformed length along the V-profile and the permanent mid-point deflection are similar to the experimentally obtained values. Similarly to the previous V-structure configuration, the asymmetry in the experimental profiles is not captured by the numerical model.

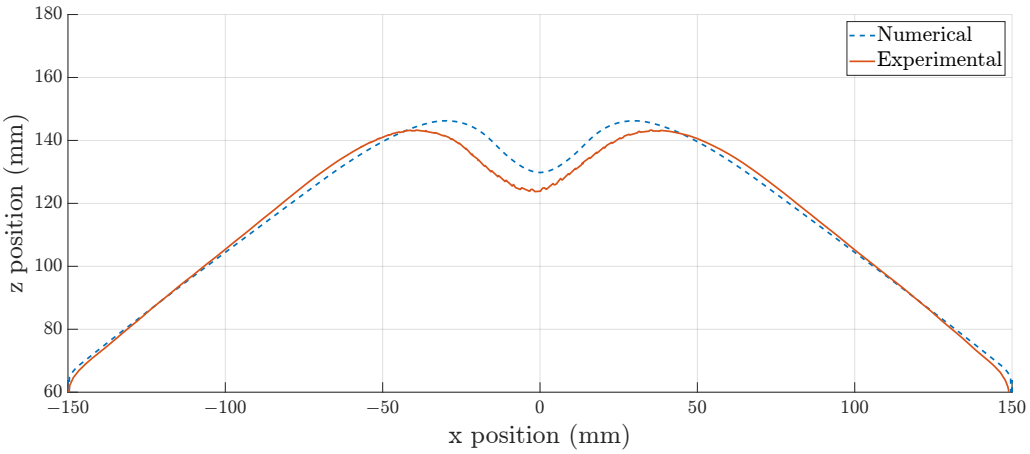

Figure 8.10: Permanently deformed crosscut profiles for a 105°, 62 mm V-tip radius DOMEX-700 MC V-structure at a charge mass of 20 g (numerical versus experimental)

The last set of comparisons was done for the 120°, 32 mm V-tip radius DOMEX-700 MC V-structures. Figure 8.11 shows the numerical and experimental permanently deformed crosscut profiles at a charge mass of 15 g. The deformed profiles from the simulations are, in general, similar to the experimental profiles with the best comparison for the 15 g test. Once again, the

asymmetry observed in the experiment is not captured by the simulations due to the use of symmetry planes in the numerical model. Additional figures can be found in Appendix D.

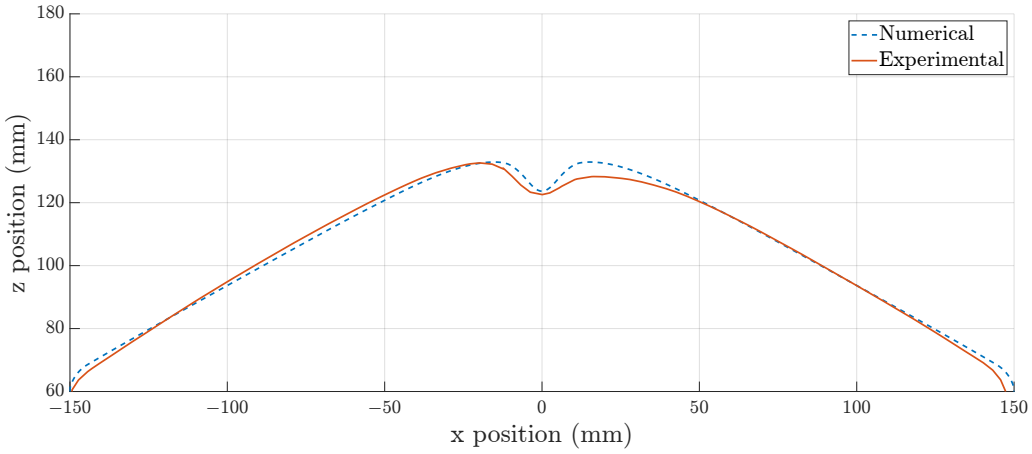

Figure 8.11: Permanently deformed crosscut profiles for a 120°, 32 mm V-tip radius DOMEX-700 MC V-structure at a charge mass of 15 g (numerical versus experimental)

Much like the ridge profiles, the general shape of the deformed crosscut profiles is similar to the experimentally obtained curves. Once again, the simulated mid-point deflection is generally lower than the experimental measurements. The trends in terms of an increase in the depth and width of the central indentation for an increase in charge mass do match the behaviour observed in the experiments, thus suggesting that the model can reasonably capture the global deformation of these V-structures with varying V-angles and V-tip radii.

8.2.3 Transient mid-point deflection

The transient mid-point displacement time histories were compared for all three V-structure configurations investigated experimentally and at three charge masses. The comparison of the mid-point displacement time histories for a 105°, 32 mm V-tip radius DOMEX-700 MC V-structure is shown for a 20 g charge in figure 8.12. As with the ridge and crosscut profiles, the response at the other charge masses is similar and thus have been provided in figures D.13 and D.14. In general, the numerical model correctly captures the mid-point displacement-time history at all three charge masses in terms of the peak displacement, the time at which this occurs, and the vibration frequency. The elastic post-test vibration amplitude appears to be higher in all three cases.

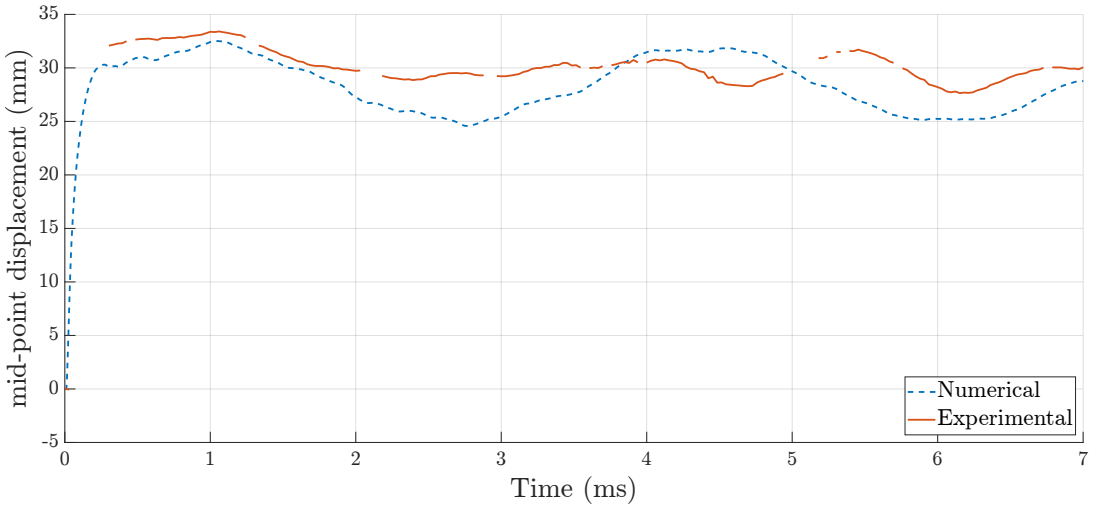

Figure 8.12: Mid-point deflection time history for a 105°, 32 mm V-tip radius DOMEX-700 MC V-structure at a charge mass of 20 g (numerical versus experimental)

The comparisons of the mid-point displacement time history for a 105°, 62 mm V-tip radius DOMEX-700 MC V-structure simulated at a charge mass of 15 g are shown in figure 8.13. The additional plots at charge masses of 10 g and 20 g are shown on page D-6. Much like the 105°, 32 mm steel V-structure simulations, the general shape of the mid-point displacement time histories from the numerical simulations closely matches that found in the experiments for all three charge masses. Additionally, the peak mid-point displacement and the time at which this occurs also closely match the experiment. At a charge mass of 15 g the numerically measured peak displacement is slightly higher than the experimental value, while at the other two charge masses, this value is slightly lower. In general, the amplitude of the elastic vibration of the V-structure simulations better matches the experimentally obtained vibration for this V-tip radius compared to the 32 mm V-tip radius simulations.

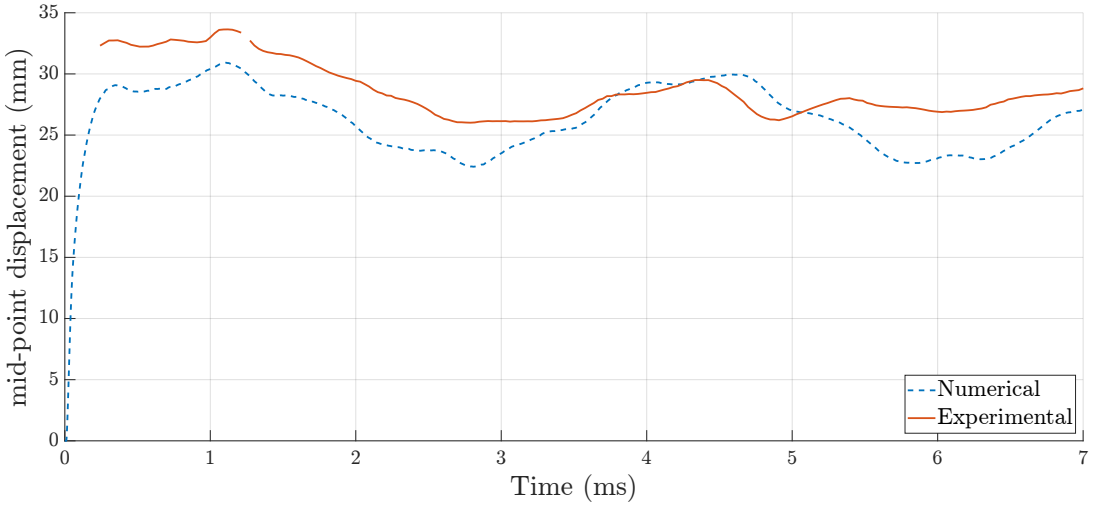

Figure 8.13: Mid-point deflection time history for a 105°, 62 mm V-tip radius DOMEX-700 MC V-structure at a charge mass of 15 g (numerical versus experimental)

The final set of comparisons of the mid-point displacement time histories for the 120°, 32 mm V-tip radius DOMEX-700 MC V-structures at a charge mass of 15 g is shown in figure 8.14.

Figure D.17 on page D-6 shows the comparison at a charge mass of 10 g. The general shape of the response from the simulations closely matched the experimental curves, with the time of the peak displacement and the vibration frequency being nearly identical between the curves. The simulation at 10 g shows a lower peak deformation than the experiments, while the peak response for the 15 g simulation is close to the experiment.

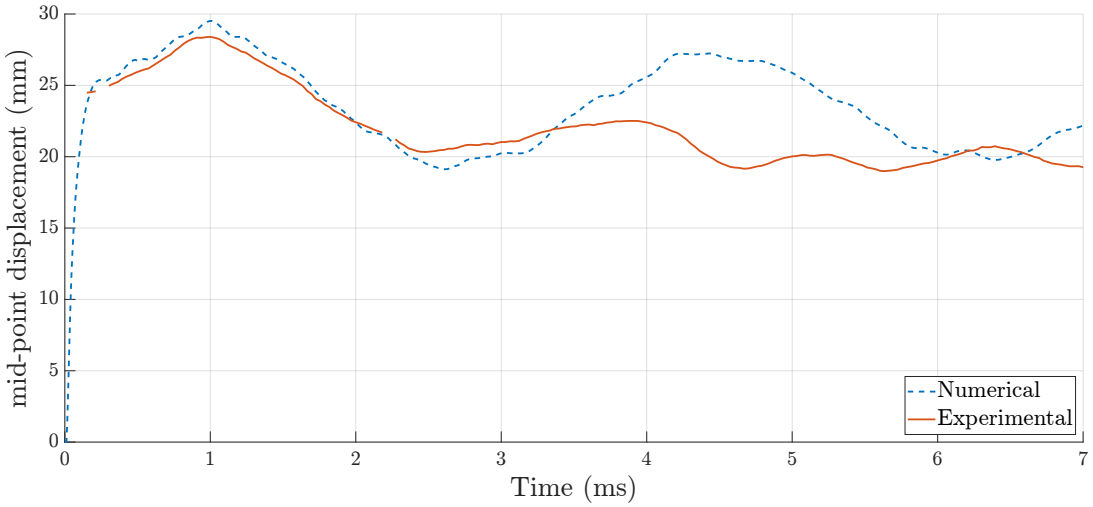

Figure 8.14: Mid-point deflection time history for a 120°, 32 mm V-tip radius DOMEX-700 MC V-structure at a charge mass of 15 g (numerical versus experimental)

In general, for all three V-structure configurations compared, the numerical simulations capture the response of the V-structures reasonably for the first 4 ms, but the simulation response becomes less representative of the experiment after that time. This is essential when attempting to determine the effects of varying the V-tip radius and the V-angle on the peak deformation and the transient blast response of the steel V-structures.

8.2.4 Permanent mid-point displacement

The next set of results are the permanent mid-point displacements, which were obtained in the simulations by allowing the V-structure velocity and acceleration to reach zero by damping out the elastic vibrations. Looking at figure 8.15, the simulations under-predict the permanent mid-point displacement, as also seen in the ridge and crosscut profile comparisons presented earlier but they are able to correctly capture the same trends as in the experiments for a change in V-angle, V-tip radius, and charge mass. Additionally, there is good correlation in the final mid-point displacement values for the 105°, 32 mm V-structures at all the charge masses considered and good correlations at selected charge masses in the other two configurations investigated. These results have been tabulated and are summarised in table D.2 on page D-7.

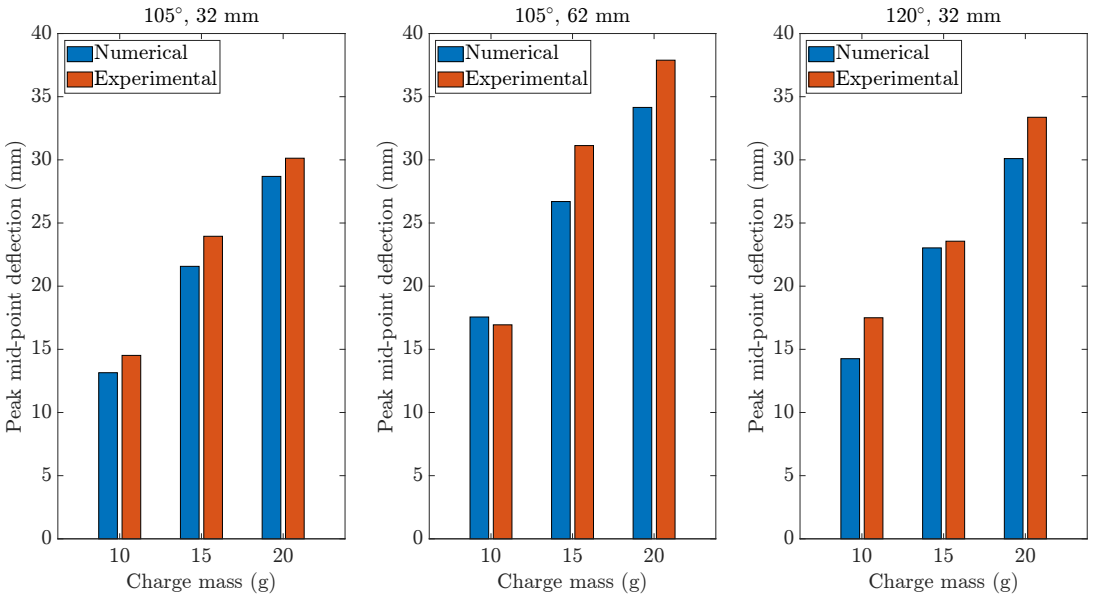

Figure 8.15: Permanent mid-point displacement versus charge mass for the numerical simulations compared with the experimentally measured values

8.2.5 Impulse transferred

The impulse from the simulations was obtained by integrating the averaged fluid-structure interaction force on all the Lagrangian components modelled (including the clamp frames and bolts). This value was compared to the measured impulse from the blast experiments. Considering figure 8.16, it can be seen that the numerical models are able to capture the trends seen in the experimental impulses when changing the charge mass, V-angle, and V-tip radius. This suggests that the model can be used to further investigate the influences of the different V-structure parameters on their blast performance. These full results have been tabulated and are summarised in table D.1 on page D-7. From the table, the numerically obtained impulse is always lower than the experimental value and this difference is approximately 1.5 Ns lower than the experimentally obtained impulse.

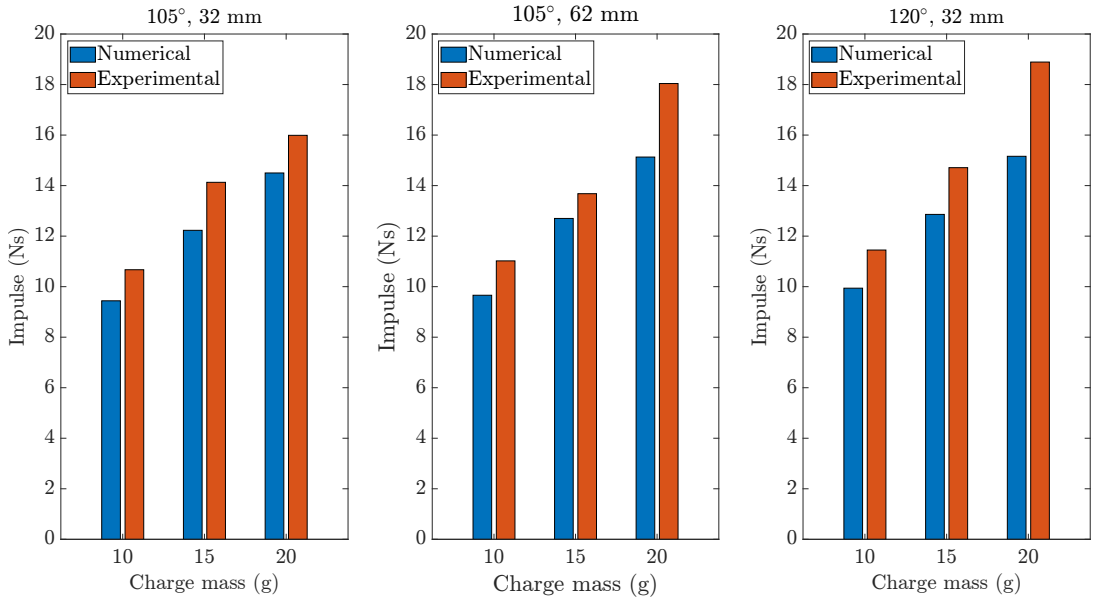

Figure 8.16: Impulse versus charge mass for the numerical simulations compared with the experimentally measured values

8.3 The influences of V-tip radius on performance metrics of the steel V-structures

8.3.1 The effect of V-tip radius on the simulated impulse

In general, an increase in the V-tip radius results in an increase in the impulse transferred to the V-structure assembly. This matches the findings found in a previous study on rigid V-structures [72]. Looking at figures 8.17 to 8.19, the impulse appears to be fairly linear across the range of V-tip radii considered for the 90° and 120° V-structures, while the results taper off above a V-tip radius of 100 mm for the 105° V-structures. Similar to the findings on rigid V-structures [72], as the V-tip radius is increased, the benefits of the V-structure shape diminish, with the influence of the V-tip radius dominating the ability of the V-structure to deflect the energy from the blast. Additionally, when looking at the increase in the impulse for an increase in V-tip radius between the three V-angles considered, the larger V-angles show a smaller increase in impulse for an increase in V-tip radius. For the 90° V-structures, the impulse increases by 2.9 Ns (34%) when the V-tip radius is increased from 20 mm to 200 mm, while for the 105° and 120° V-structures, the impulse only increases by 2 Ns (21%) and 1.9 Ns (19%) respectively over the same V-tip radius range. The percentage increases were calculated using equation (8.5).

$$\%\text{Increase} = \frac{\text{Impulse}_{200\,\text{mm}} - \text{Impulse}_{20\,\text{mm}}}{\text{Impulse}_{20\,\text{mm}}} \times 100 \tag{8.5}$$

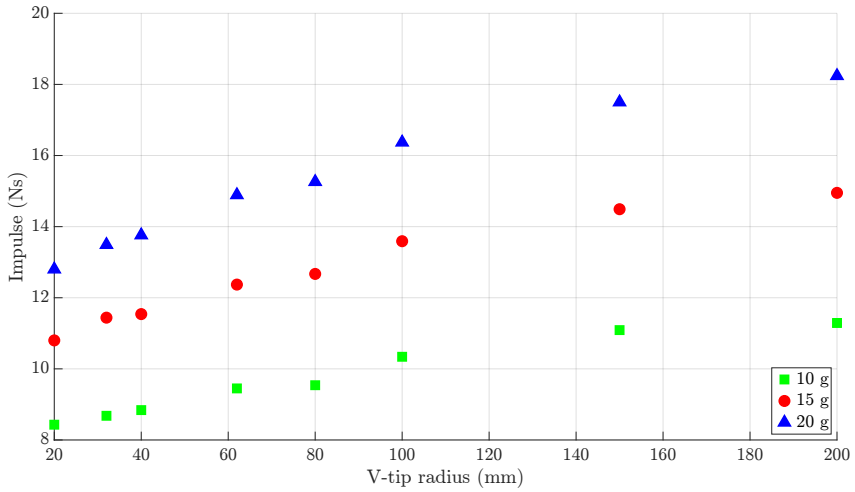

Figure 8.17: Impulse versus V-tip radius for the 90° DOMEX-700 MC V-structure simulations

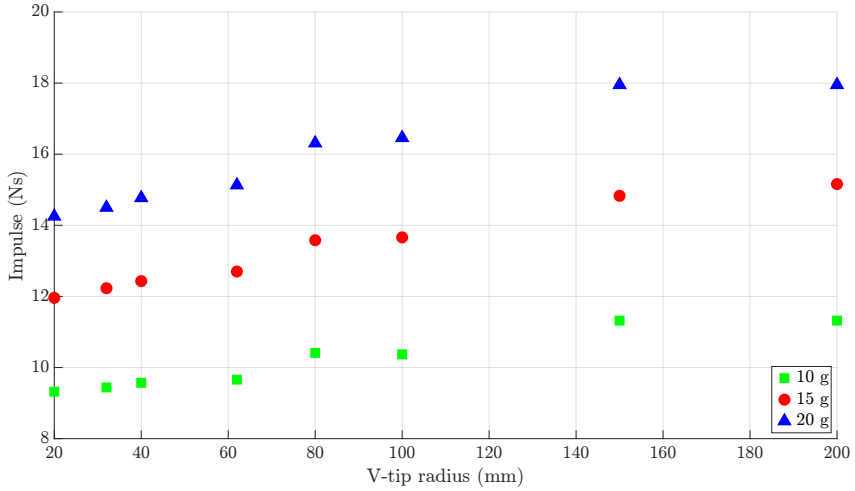

Figure 8.18: Impulse versus V-tip radius for the 105° DOMEX-700 MC V-structure simulations

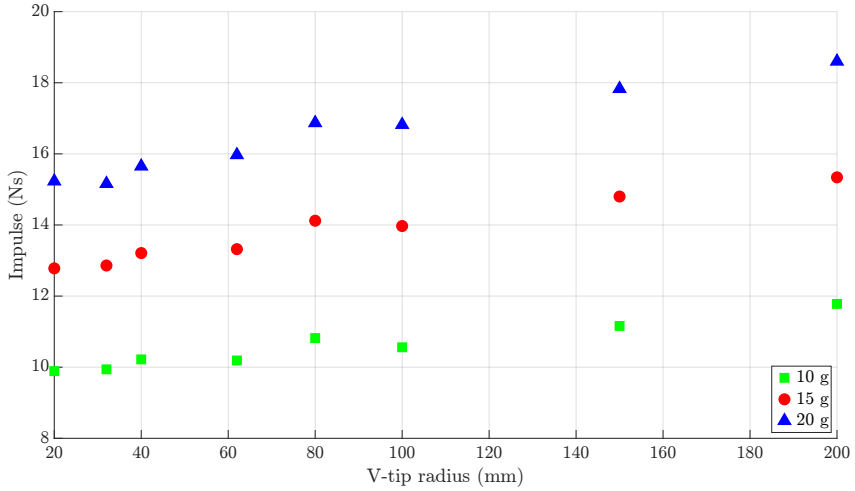

Figure 8.19: Impulse versus V-tip radius for the 120° DOMEX-700 MC V-structure simulations

8.3.2 The influence of the V-tip radius on peak transient and permanent mid-point deflection

The effect of V-tip radius on mid-point deflection for the three V-angles considered is shown in tables 8.3 to 8.5. At smaller V-angles (90°) and V-tip radii (20 mm to 40 mm), there is only a small difference between the peak and final mid-point displacements for the three charge masses investigated. This is likely due to the geometric stiffness of the V-structure shape. This beneficial feature of the V-structure design is observed to decrease as both the V-angle and V-tip radius are increased. Another observation is that regardless of the V-angle, V-tip radius, or charge mass, the time at which the peak mid-point displacement is observed is approximately 1 ms. Looking at these three tables, there are no discernable trends in the time at which this peak displacement is observed.

Table 8.3: Mid-point deflection (peak and final) versus V-tip radius for the 90° DOMEX-700 MC V-structure simulations

	Charge Mass (g)								
	10			15			20		
V-tip radius (mm)	Peak (mm)	Time (ms)	Final (mm)	Peak (mm)	Time (ms)	Final (mm)	Peak (mm)	Time (ms)	Final (mm)
20	11.03	0.93	9.86	18.02	0.93	16.81	24.02	1.03	22.51
32	13.98	1.00	13.03	22.12	1.03	20.72	29.24	1.01	27.44
40	15.88	0.93	14.77	24.60	0.97	22.94	31.65	1.24	29.52
62	19.19	0.26	16.98	28.53	1.25	25.68	36.56	1.27	32.86
80	22.35	1.24	18.70	32.05	1.26	28.06	39.79	1.27	35.45
100	23.87	0.42	19.64	33.38	0.43	29.26	40.98	0.58	36.83
150	27.91	0.82	19.86	38.33	0.86	30.17	46.32	0.89	38.43
200	29.74	1.12	19.96	41.63	1.60	30.22	50.15	1.55	38.24

Table 8.4: Mid-point deflection (peak and final) versus V-tip radius for the 105° DOMEX-700 MC V-structure simulations

	Charge Mass (g)								
	10			15			20		
V-tip radius (mm)	Peak (mm)	Time (ms)	Final (mm)	Peak (mm)	Time (ms)	Final (mm)	Peak (mm)	Time (ms)	Final (mm)
20	11.87	0.99	10.23	20.15	1.05	17.78	27.24	1.00	24.00
32	15.01	1.05	13.15	24.55	1.06	21.57	32.53	1.03	28.69
40	16.61	1.02	14.42	26.37	1.11	23.30	34.44	1.12	30.26
62	20.48	1.11	17.56	30.92	1.11	26.70	39.18	1.18	34.15
80	22.72	1.13	18.75	32.75	1.13	28.06	41.02	1.16	35.41
100	24.46	1.13	20.15	34.68	1.12	29.49	43.14	1.12	37.12
150	26.84	0.83	19.92	37.20	0.85	29.58	45.50	1.26	37.39
200	29.46	0.74	19.26	41.05	1.57	29.80	49.66	1.55	38.00

Table 8.5: Mid-point deflection (peak and final) versus V-tip radius for the 120° DOMEX-700 MC V-structure simulations

	Charge Mass (g)								
	10			15			20		
V-tip radius (mm)	Peak (mm)	Time (ms)	Final (mm)	Peak (mm)	Time (ms)	Final (mm)	Peak (mm)	Time (ms)	Final (mm)
20	14.70	0.89	10.88	25.16	0.99	19.19	34.24	0.99	26.17
32	18.56	0.98	14.26	29.51	1.00	21.57	38.56	1.08	30.1
40	19.07	1.01	14.86	30.45	1.04	23.92	39.78	1.05	31.09
62	22.68	0.97	17.62	34.20	1.08	26.68	43.58	1.17	33.87
80	24.29	1.04	18.38	35.19	1.10	27.44	44.58	1.21	35.03
100	25.84	1.07	19.55	37.18	1.07	29.04	46.85	1.28	36.72
150	27.69	1.11	20.03	39.72	1.24	29.83	49.65	1.30	37.81
200	29.36	1.42	19.03	41.27	1.42	29.02	50.73	1.45	37.31

The plots of the peak and final mid-point deflections for the three V-angles investigated in the study are shown in figures 8.20 to 8.22. The permanent mid-point displacements are shown with solid markers while the peak transient displacements are shown with hollow markers. In all three graphs, similar trends can be seen, with the curves appearing to be bilinear. There are fairly sharp slopes for V-tip radii below 100 mm, while between 100 mm to 200 mm the slopes in all three graphs are more shallow. This is also evident when looking at the change in peak displacement between 20 mm and 100 mm and then between 100 mm and 200 mm.

The increase in the V-tip radius has a more significant effect on the peak mid-point displacement for the smaller V-angles simulated. This is likely due to the reduction in the efficacy of the V-angle in terms of deflecting the blast wave as the V-tip radius is made larger. This matches the findings for the impulse results presented in the previous section.

Furthermore, at larger V-tip radii (200 mm), the peak mid-point deflections between the three V-angles investigated are also fairly similar, further suggesting that the V-tip radius dominates the structural response of the V-structure for these larger values. Unlike the peak mid-point displacement results, the final displacement appears to plateau for V-tip radii above 100 mm for all three V-angles considered. Additionally, the final mid-point displacement is also similar for all three V-angles simulated for the same charge mass and V-tip radius, when the V-tip radius is between 100 mm and 200 mm. This further supports the findings for the impulse and the peak mid-point displacement, which suggest that at larger V-tip radii, the structural response of the V-structures simulated is dominated by the effect of the curvature at the V-tip rather than the V-angle of the structure.

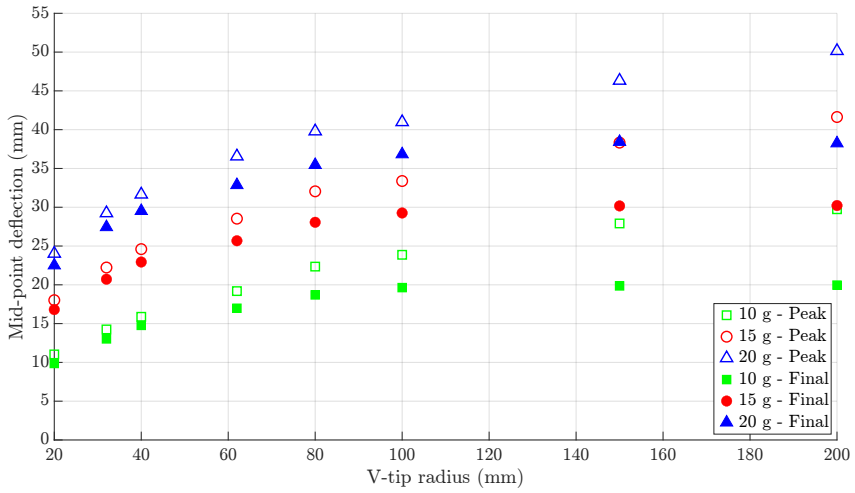

Figure 8.20: Peak and final mid-point deflection versus V-tip radius for the 90° DOMEX-700 MC V-structure simulations

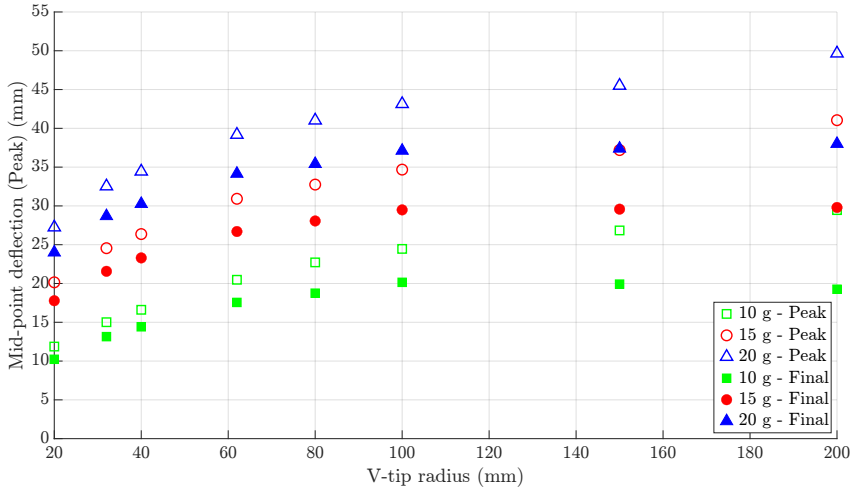

Figure 8.21: Peak and final mid-point deflection versus V-tip radius for the 105° DOMEX-700 MC V-structure simulations

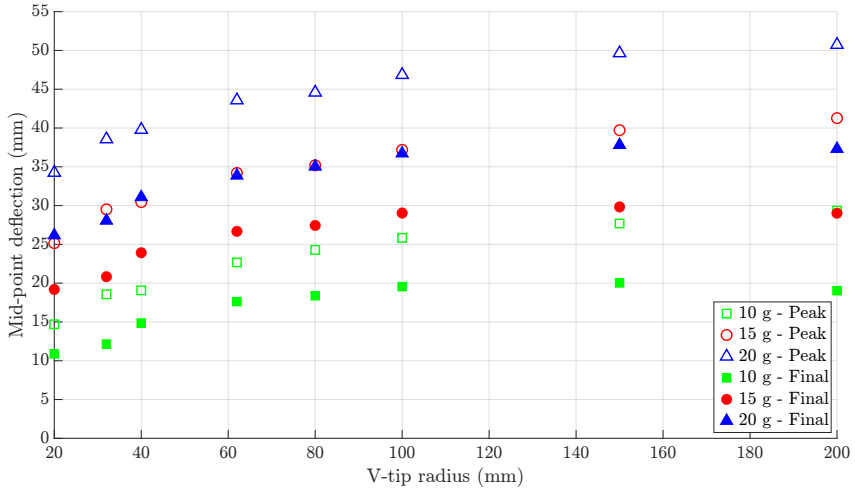

Figure 8.22: Peak and final mid-point deflection versus V-tip radius for the 120° DOMEX-700 MC V-structure simulations

8.3.3 The effects of V-tip radius on mid-point displacement time histories

The effects of the V-tip radius on the mid-point displacement time histories are presented next. These results have been separated into graphs based on the V-angle and the charge mass to enable them to be better visualised.

90° V-structures

Figure 8.23 shows the mid-point displacement time histories for a 90° DOMEX-700 MC V-structure simulation at a charge mass of 15 g. The graphs for other charge masses can be found in Appendix D. As with the comparison of the numerical and experimental results, the same trends were observed when the charge mass was increased. The only differences between the shapes of the sets of curves for each charge mass simulated are the peak amplitude and the amplitude of vibration following the blast wave interaction with the target. It can be seen that increasing the V-tip radius results in both an increase in the peak mid-point deflection, but this peak also occurs at a later time. This is likely due to the reduction in geometric stiffness of the V-structures due to the larger curvature at the V-tip.

The frequency of the post-blast elastic vibrations is also observed to decrease, with an observable increase between successive peaks and troughs as the V-tip radius is increased. Once again, this is likely due to the increased influence of the curvature at the V-tip. Finally, at extremely large V-tip radii, the amplitude of the oscillation is also observed to increase significantly. While for vibrating systems, the geometric stiffness does influence the amplitude, the increase in curvature of these V-structures does result in a decreased ability to deflect the blast pressure wave, thus increasing the energy transferred to the V-structure, which in turn would increase the amplitude of the post-blast elastic oscillations.

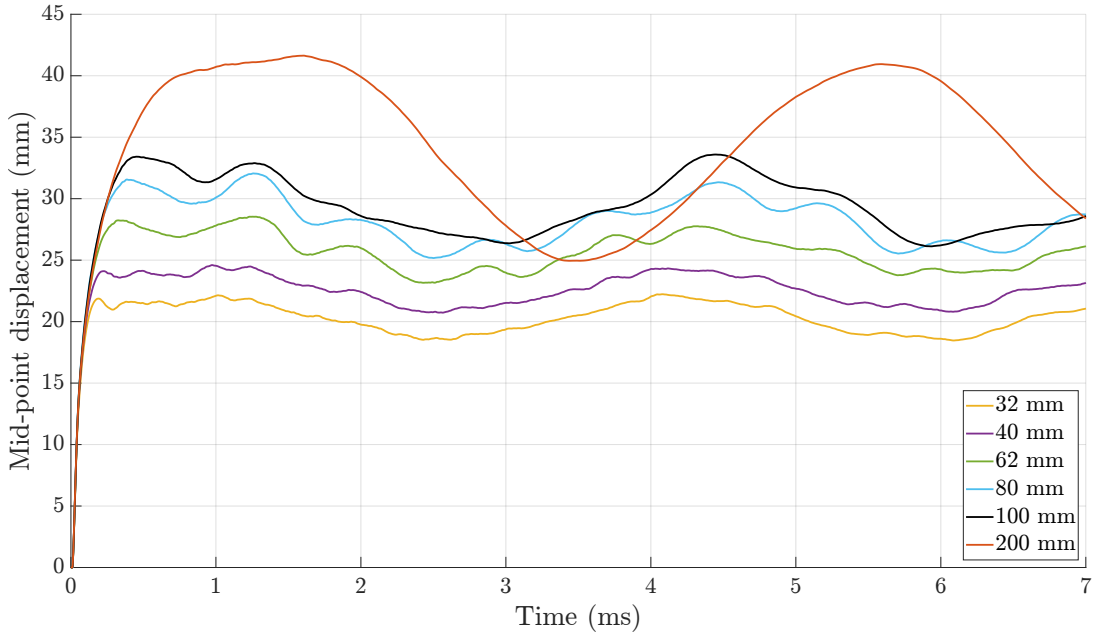

Figure 8.23: Mid-point deflection time histories for increasing V-tip radii for the 90° DOMEX-700 MC V-structure simulations at a charge mass of 15 g

105° V-structures

Figure 8.24 shows the mid-point displacement time histories for the 105° DOMEX-700 MC V-structure simulations at a charge mass of 15 g. Additional graphs are shown on pages D-9 and D-10. Similar to the 90° V-structures, the first peak displacement increases for an increase in the V-tip radius, while also occurring later in time. Additionally, a phenomenon first observed in the blast experiment results can be seen in these graphs. Namely, that the peak mid-point displacement does not occur on this first sharp rise but rather occurs closer to 1 ms. This phenomenon can be seen for V-tip radii up to 100 mm, following which the mid-point time history behaviour more closely matches that observed for flat circular steel plates [56]. Once again, the frequency of the post-blast vibration decreases and the amplitude of the oscillations increases as the V-tip radius is increased. Again, this is likely due to the same reasons suggested for the 90° V-structures.

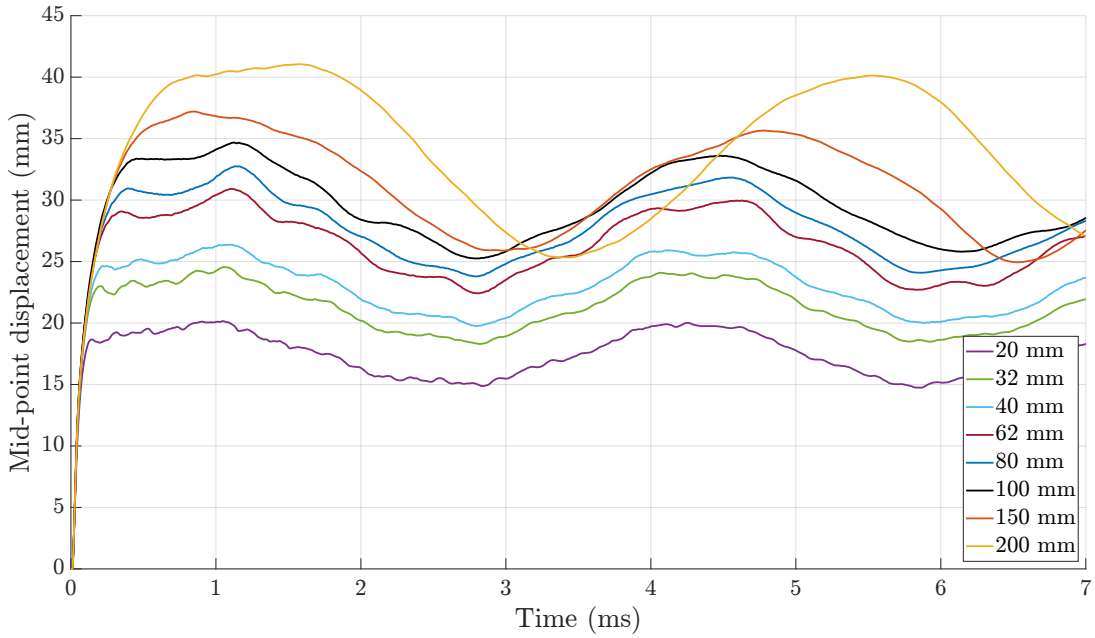

Figure 8.24: Mid-point deflection time histories for increasing V-tip radii for the 105° DOMEX-700 MC V-structure simulations at a charge mass of 15 g

120° V-structures

The mid-point displacement time histories for the 120° DOMEX-700 MC V-structure specimens simulated at charge masses of 10 g and 20 g are shown in figures 8.25 and 8.26. The graph at charge mass of 15 g is shown on page D-10. Once again, there is an increase in the magnitude and time of arrival of the first peak as the V-tip radius is increased. A similar phenomenon to that seen for the 105° V-structures can be seen in these graphs too, with the peak displacement occurring after the sharp rise in mid-point displacement with the slope of this part of the curves being greater than that seen for the 105° V-structures. This peak is visible at all V-tip radii investigated including the 200 mm V-structures and also increases in magnitude and time of arrival as the V-tip radius is increased. In a similar response to the other two V-angled V-structures investigated, the post-blast vibration frequency is observed to decrease, and the amplitude of the vibration is observed to increase for an increase in the V-tip radius.

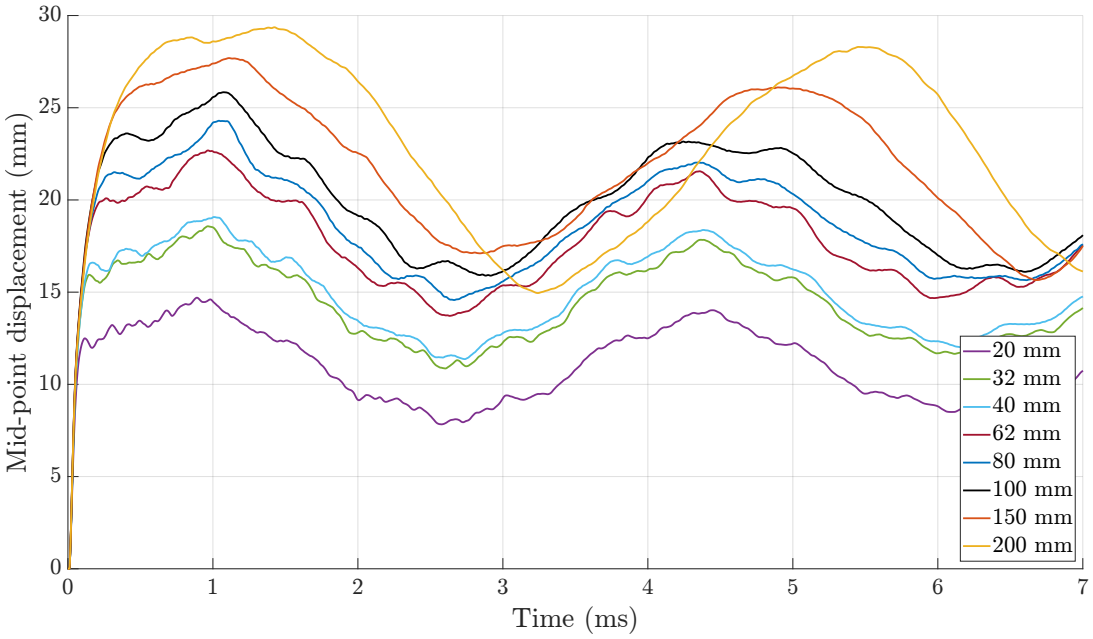

Figure 8.25: Mid-point deflection time histories for increasing V-tip radii for the 120° DOMEX-700 MC V-structure simulations at a charge mass of 10 g

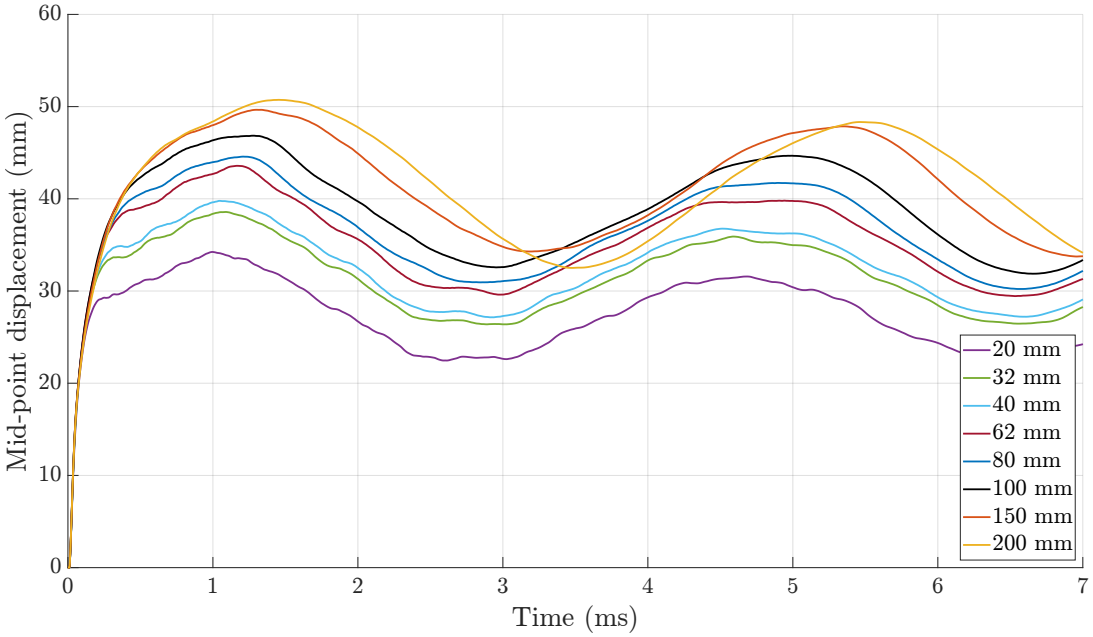

Figure 8.26: Mid-point deflection time histories for increasing V-tip radii for the 120° DOMEX-700 MC V-structure simulations at a charge mass of 20 g

8.3.4 The influences of the V-tip radius on the permanently deformed ridge profiles

The effects of the V-tip radius on the permanently deformed ridge profiles have been separated into graphs based on the V-angle and the charge mass to enable trends to be identified in the blast response of these V-structures for the different configurations. As the trends in the effects of the V-tip radius were not influenced by the charge mass, additional images for other charge masses have been provided in Appendix D.

90° V-structures

The permanently deformed ridge profiles for the 90° DOMEX-700 MC V-structure specimens of differing V-tip radii simulated at a charge mass of 15 g is shown in figure 8.27. The first observation is that increasing the V-tip radius results in an increase in the depth of the indentation at the mid-point of the V-structures. Additionally, the deformed length of the ridge is also observed to increase as the V-tip radius is increased with the entire ridge appearing to deform for V-tip radii above 80 mm. This increase in deformation as the V-tip radius is increased can be attributed to the decrease in geometric stiffness of the V-structures.

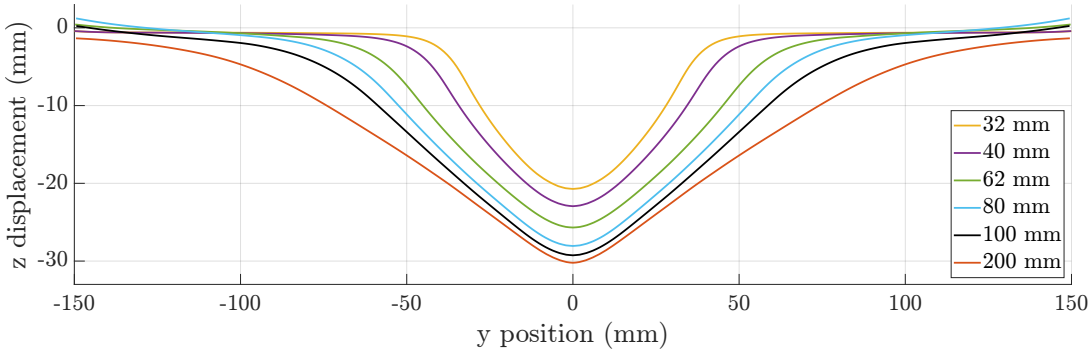

Figure 8.27: Permanently deformed ridge profiles for increasing V-tip radii for the 90° DOMEX-700 MC V-structure simulations at a charge mass of 15 g

105° V-structures

Figure 8.28 shows the permanently deformed ridge profiles for the 105° DOMEX-700 MC V-structures with a range of V-tip radii simulated at a charge mass of 10 g. Looking at the figure, the trends are similar to those seen for the 90° V-structures, with an increase in the depth of the indentation and an increase in the deformed length along the ridge for an increase in the V-tip radius. One different observation is that the final depth of the indentation is the same for the 100 mm and 150 mm V-tip radius profiles, but the deformed depth along the ridge is greater for the larger V-tip radius. Additionally, the depth of the indentation is observed to decrease for a V-tip radius of 200 mm. This was not observed for the 90° V-structures. Once again, the depth of the deformed region along the ridge can still be seen to be greater. This suggests that for this V-angle the energy distribution changes as the V-tip radius is increased and thus the deformation becomes less localised. The deformation along the entire length of the ridge line is also visible for V-tip radii above 80 mm and the deformation can be seen to become less localised with an increase in the V-tip radius.

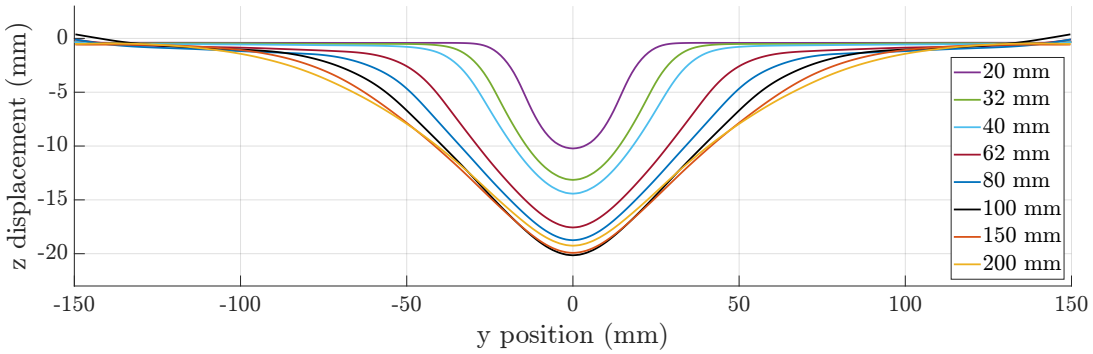

Figure 8.28: Permanently deformed ridge profiles for increasing V-tip radii for the 105° DOMEX-700 MC V-structure simulations at a charge mass of 10 g

120° V-structures

The ridge profiles in figure 8.29 show the 120° DOMEX-700 MC V-structures with differing V-tip radii simulated at a charge mass of and 20 g. Once again, the is an increase in the depth of the indentation and the deformed length along the ridge for an increase in the V-tip radius. Unlike the previous two V-angles investigated, only the V-structures with a V-tip radius of 150 mm and 200 mm show deformation along the entire ridge line. Additionally, there is a more progressive increase in the deformed length along the ridge when compared to the other two V-angles investigated. Much like the 105° V-structures, the depth of the indentation is observed to decrease for a V-tip radius of 200 mm, likely due to the loading being distributed further along the ridge. As with the other two V-angles, the deformation becomes less localised as the V-tip radius is increased.

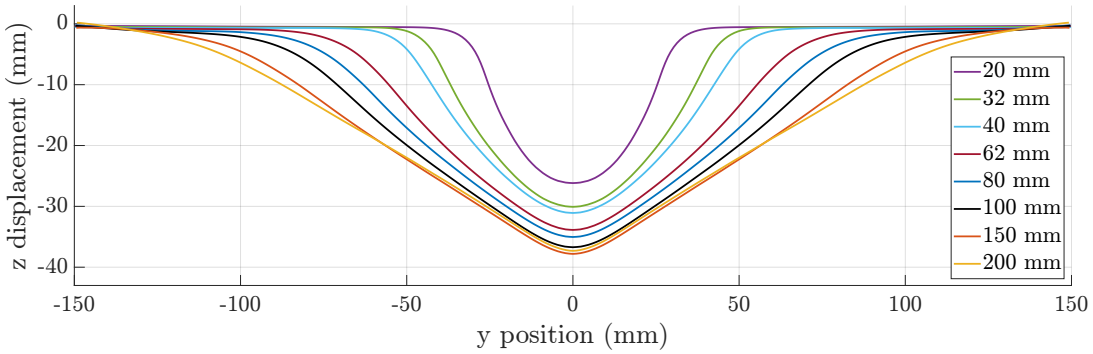

Figure 8.29: Permanently deformed ridge profiles for increasing V-tip radii for the 120° DOMEX-700 MC V-structure simulations at a charge mass of 20 g

8.3.5 The influences of the V-tip radius on permanently deformed crosscut profiles

The final set of profiles to be analysed considered the effect of the V-tip radius on the permanently deformed crosscut profiles. Once again, these results have also been separated into graphs based on the V-angle and the charge mass to allow for any trends due to the variations in the V-structure configuration to be identified. Selected graphs have been included in this section with additional graphs available in Appendix D.

90° V-structures

The permanently deformed crosscut profiles for the 90° DOMEX-700 MC V-structures with a range of V-tip radii simulated at a charge mass of 15 g are shown in figure 8.30. The shapes of these additional profiles are similar with only an increase in the magnitudes of the deformations and thus have not been included here. In general, an increase in the V-tip radius results in an increase in the width of the deformed region along the crosscut plane as the deformation becomes less localised. The inversion of the V-tip can be seen at a V-tip radius of 32 mm, but the deformation can be seen to be more distributed at the larger V-tip radii. The V-structures also start to deform outwards from the V-profile for V-tip radii above 62 mm. This can be explained by the reduced geometric stiffness of the V-structures with a larger V-tip radius.

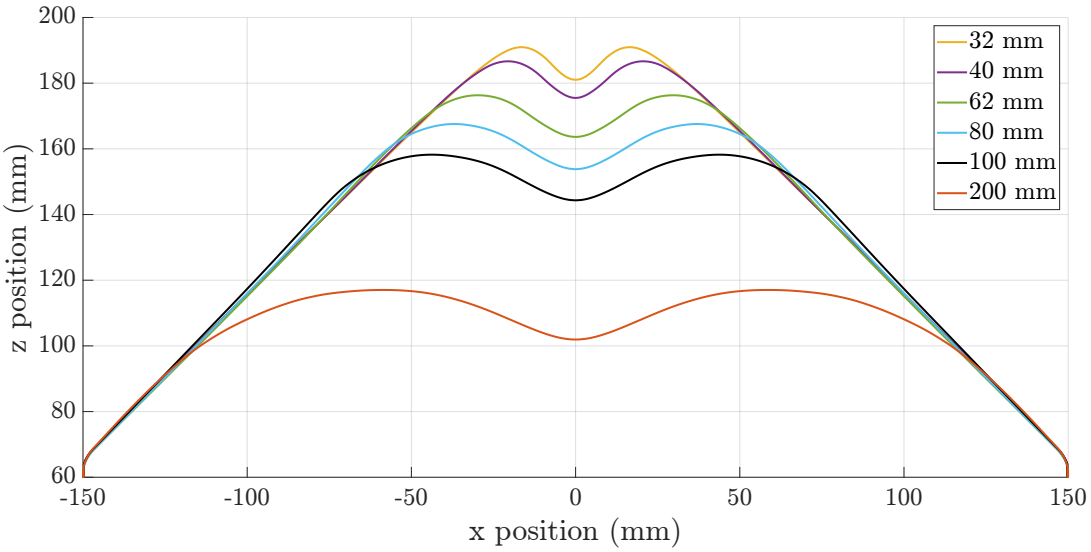

Figure 8.30: Permanently deformed crosscut profiles for increasing V-tip radii for the 90° DOMEX-700 MC V-structure simulations at a charge mass of 15 g

105° V-structures

The final crosscut profiles in figure 8.31 show the 105° DOMEX-700 MC V-structures of differing V-tip radii simulated at a charge mass of 15 g. Once again, the deformation in the crosscut plane is observed to increase with an increase in V-tip radius, with the inversion of the V-tip present at V-tip radii of 20 mm to 40 mm. The deformation gets progressively more distributed as the V-tip radius increases beyond 62 mm. Unlike the 90° V-structures, for V-tip radii above 32 mm, the V-structures are observed to bow outwards along the V-profile due to reduction of the geometric stiffness of the V-structure shape at these V-tip radii. This bowing likely starts at a smaller V-tip radius due to the reduced geometric stiffness of the 105° V-structures when compared to the 90° V-structures.

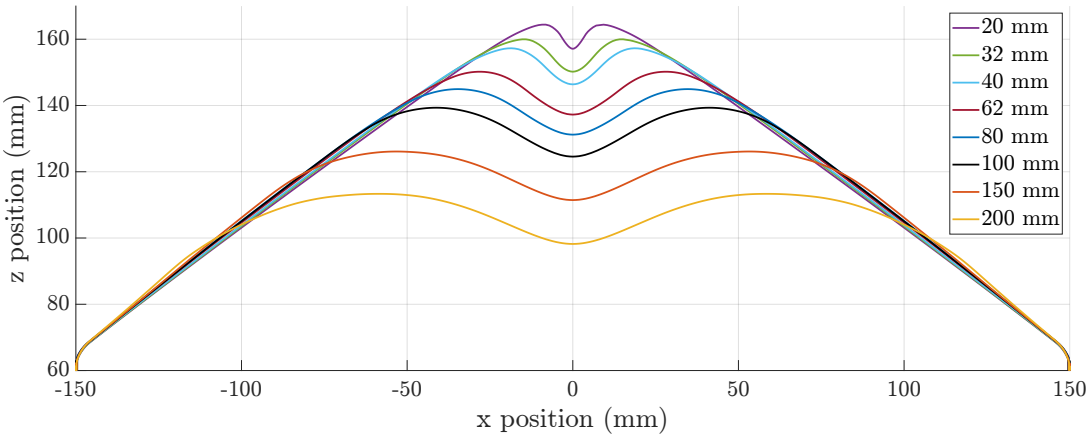

Figure 8.31: Permanently deformed crosscut profiles for increasing V-tip radii for the 105° DOMEX-700 MC V-structure simulations at a charge mass of 15 g

120° V-structures

The final set of crosscut profiles presented shown in figure 8.32 are the 120° DOMEX-700 MC V-structures with V-tip radii from 20 mm to 200 mm simulated at a charge mass of 15 g. The 120° V-structure behaviour closely matches that seen for the 105° V-structures, with the inversion of the V-tip present for a V-tip radius of 20 mm, and the bowing along the V-profile present for V-tip radii above 32 mm. Once again, this is likely due to the reduced geometric stiffness of these V-structures compared to their 90° counterparts. Due to the larger V-angle, the increase in deformation as the V-tip radius increases is lowest for the 120° V-structures when compared to the other two configurations.

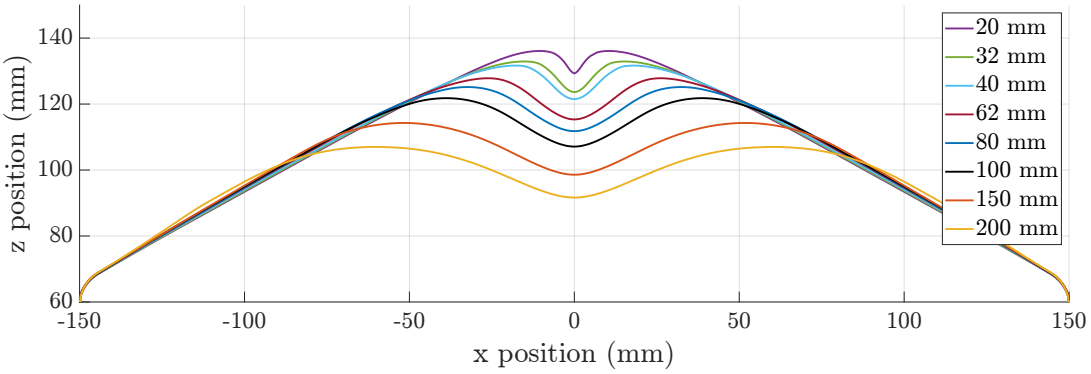

Figure 8.32: Permanently deformed crosscut profiles for increasing V-tip radii for the 120° DOMEX-700 MC V-structure simulations at a charge mass of 15 g

8.4 The influence of the V-angle on the blast performance of steel V-structures

The influences of the V-angle on the simulated impulse, mid-point deflection, mid-point deflection time history, and the ridge and crosscut profiles are presented next. Once again, selected graphs have been included here to allow for the trends to be discussed with additional plots available in Appendix D.

8.4.1 Effects of V-angle on impulse

A series of bar charts have been provided in figure 8.33. Each sub-chart shows a different V-tip radius, while the columns compare the impulse for the three V-angles and three charge masses investigated. The first observation is that, as expected, for V-tip radii below 100 mm, the V-structures with a narrower V-angle perform better in terms of the impulse transferred. Additionally, at all V-tip radii, the 120° V-structures perform the worst of the three V-angles simulated, with the highest impulse. The benefit of the sharper V-angle decreases between the 90° and 105° V-structures for V-tip radii above 62 mm, as the impulse values are fairly similar above this V-tip radius. In general, the narrower angled V-structures show the greatest increase in impulse as the V-tip radius is increased.

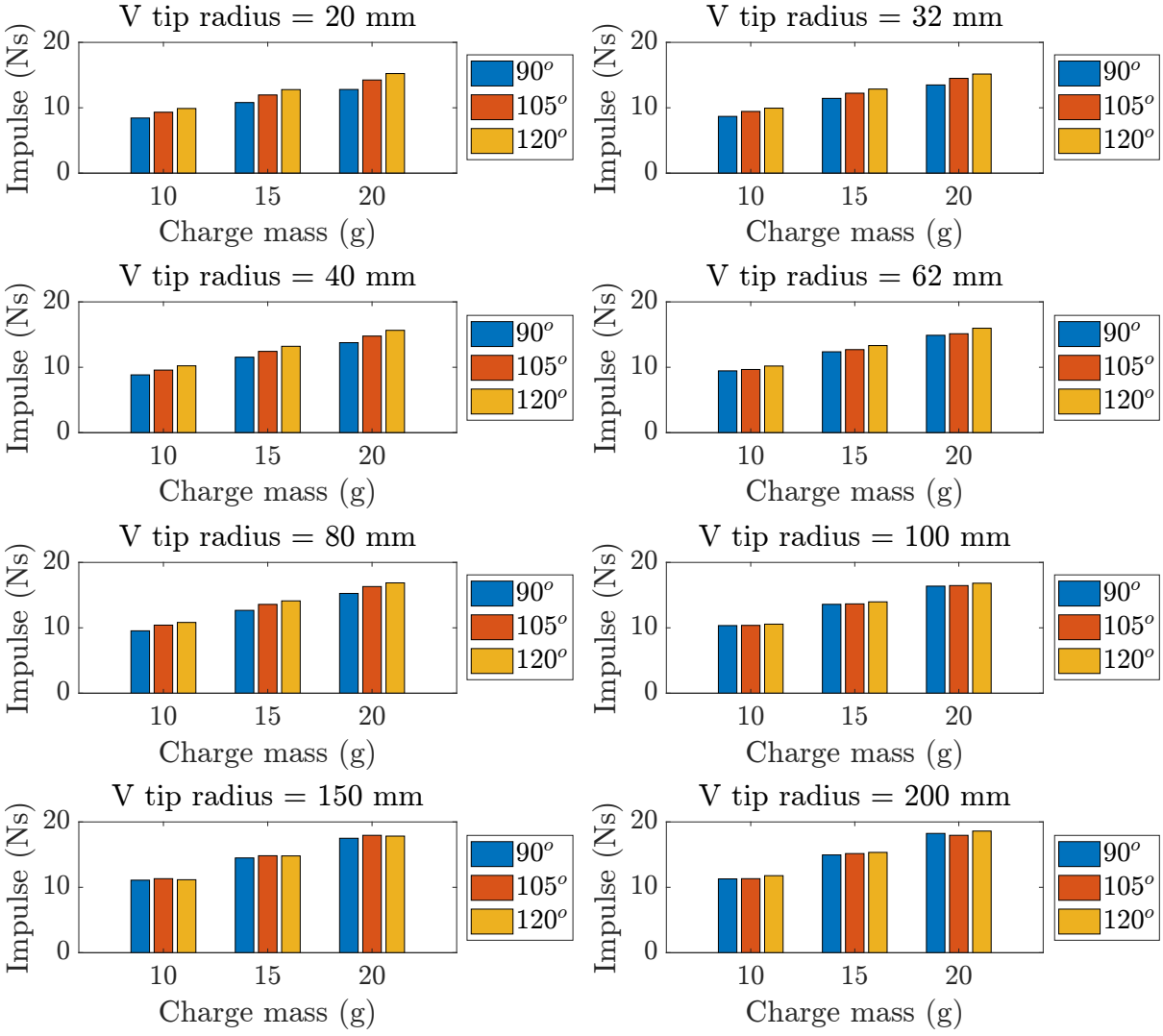

Figure 8.33: Bar charts of the impulse versus the V-angle for all V-tip radii

8.4.2 Effect of V-angle on peak transient mid-point deflection

The next series of bar graphs shown in figure 8.34 present the peak mid-point deflection at different V-tip radii. In each sub-plot, the displacements at the three V-angles and three charge masses investigated are plotted. For all V-tip radii up to 150 mm the V-structures with a

narrower V-angle perform better, with a lower peak mid-point displacement. The difference in peak displacement between the 90° and 105° V-structures reduces for V-tip radii up to 80 mm, and for a V-tip radius of 150 mm, the 105° V-structures show a lower peak displacement when compared to the 90° V-structures. In general, like for the impulse, the 90° V-structures show the greatest increase in peak mid-point displacement as the V-tip radius is increased.

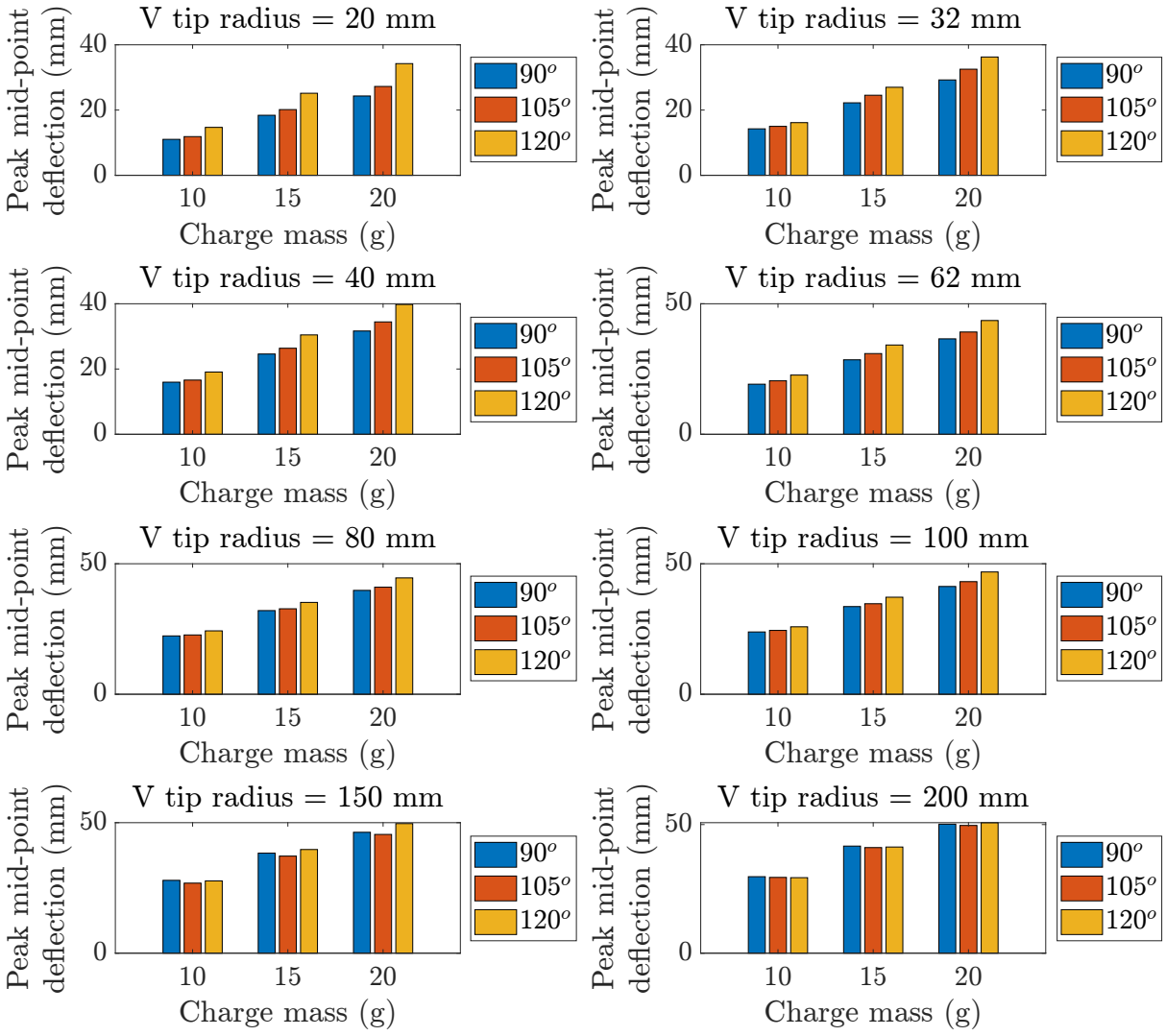

Figure 8.34: Bar charts of the peak mid-point deflection versus the V-angle for all V-tip radii

8.4.3 Effect of V-angle on permanent mid-point deflection

The final series of bar graphs show the permanent mid-point deflection at different V-tip radii in figure 8.34 where each graph shows the displacements at the three V-angles and three charge masses investigated. Unlike the peak mid-point displacement comparisons, the V-structures show similar final mid-point displacements for V-tip radii above 32 mm. Additionally, the larger V-angled V-structures appear to perform better for the larger V-tip radii considered, with lower permanent displacements observed for V-tip radii above 80 mm. This suggests that the curvature at the V-tip is the primary structural feature that drives the measured permanent mid-point displacement.

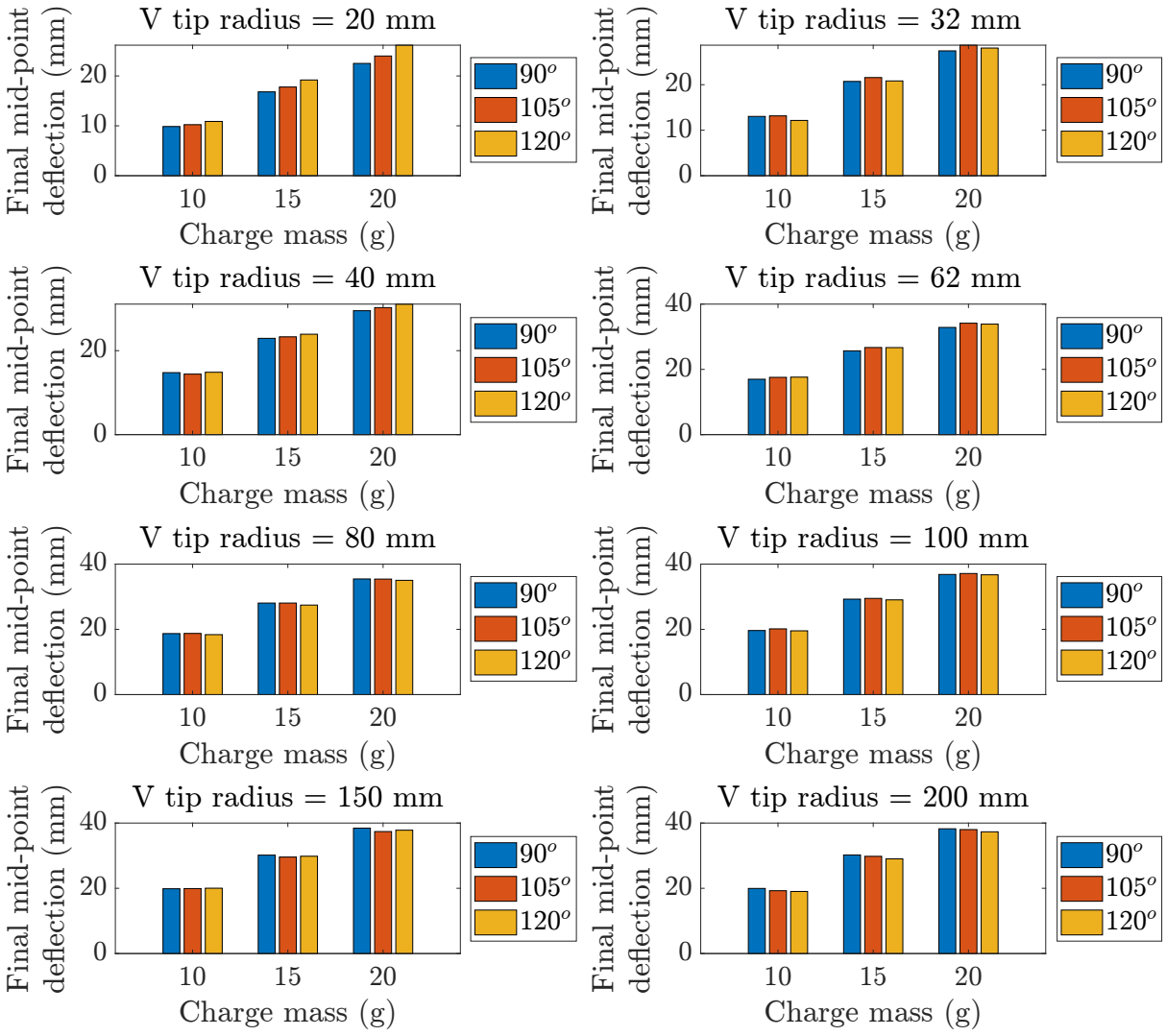

Figure 8.35: Bar charts of the final mid-point deflection versus the V-angle for all V-tip radii

8.4.4 Effect of V-angle on mid-point displacement time histories

The next sets of graphs show the mid-point displacement time histories of the V-structures simulated at a specific V-tip radius. Two figures are shown at V-tip radii of 32 mm and 200 mm. The additional figures at the other V-tip radii investigated can be found on pages D-15 and D-16.

V-tip radius of 32 mm

The mid-point displacement time histories for the 32 mm V-tip radius V-structures are shown below in figure 8.36. The first observation is that 120° V-structures display a greater peak mid-point displacement amplitude and a peak-to-peak vibration amplitude. The time of arrival of the peak mid-point displacement is also approximately the same for all three V-angles and at all three charge masses investigated. Additionally, the vibration frequency remains unchanged when the charge mass is increased for the three V-angles investigated. This suggests that the vibration frequency is primarily driven by the V-tip radius of the V-structures and not their V-angle at this V-tip radius. At the lowest charge mass investigated, the displacement time history response of the 90° and 105° V-structures is fairly similar, with only a small difference in

the peak displacement. This difference is amplified at the higher charge masses of 15 g and 20 g. One final observation is that the peak displacement for the 120° V-structure simulated at 15 g is greater than the peak displacement for the 90° V-structure simulated at 20 g although the vibration and final displacement are both significantly lower.

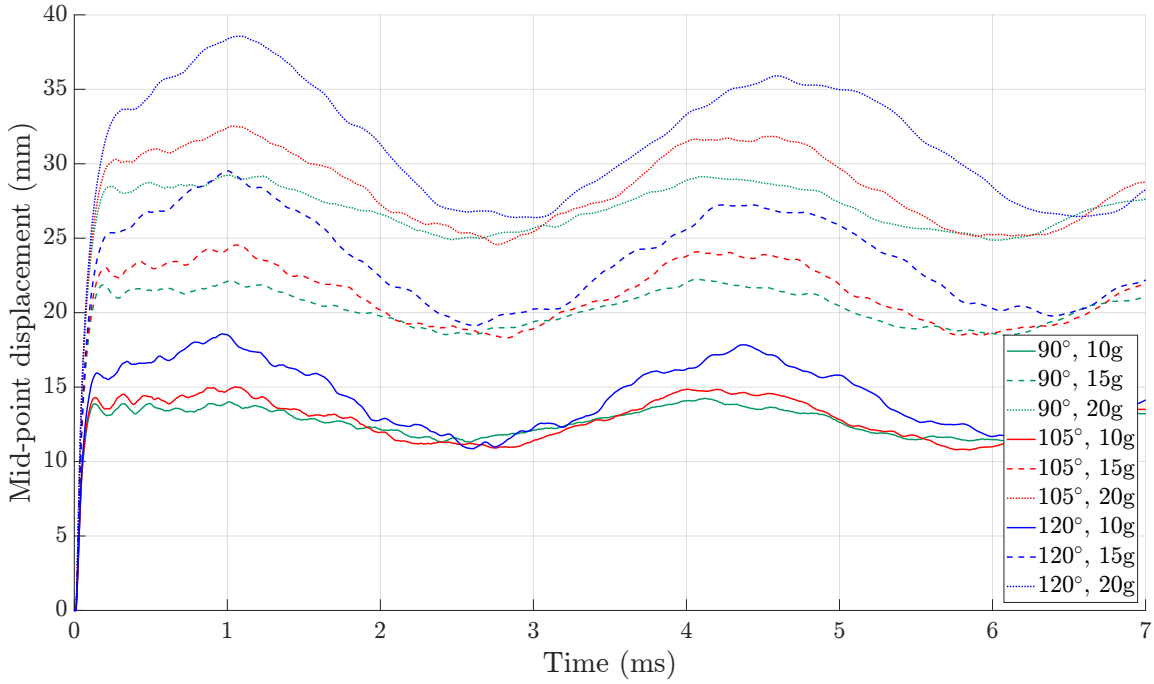

Figure 8.36: Mid-point deflection time histories versus the V-angle for a V-tip radius of 32 mm at all three charge masses investigated

V-tip radius of 200 mm

The next figure shown below figure 8.36 considers the mid-point displacement time histories for the V-structures with a 200 mm V-tip radius. The key observation here is that the curves for each V-angle appear to follow the same path, including peak mid-point displacement and peak-to-peak vibration amplitude. This confirms the observation that at larger V-tip radii, the V-tip radius dominates the blast response characteristics of the V-structures. Additionally, as with the 32 mm V-tip radius V-structures, the time of arrival of the peak displacement and the vibration frequency are the same for all three V-angles and all three charge masses. This confirms the observation that the post-blast vibration response is primarily a function of the V-tip radius which likely influences the V-structure geometric stiffness and hence the vibrating frequency response.

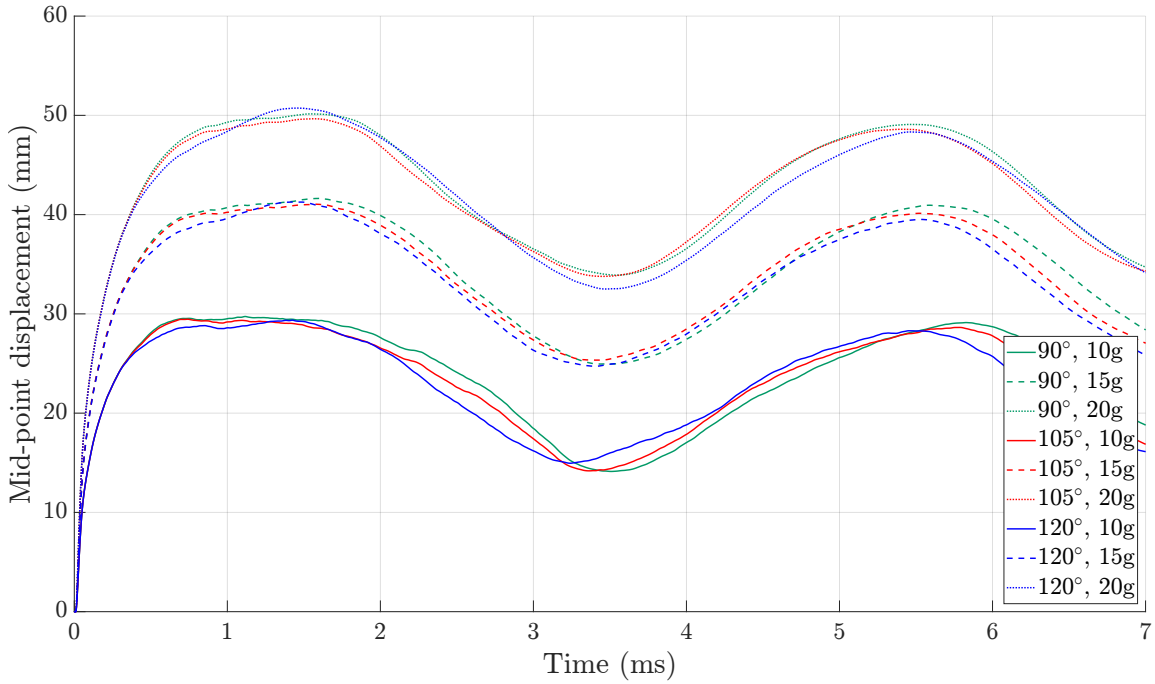

Figure 8.37: Mid-point deflection time histories versus the V-angle for a V-tip radius of 200 mm at all three charge masses investigated

8.4.5 Effect of V-angle on the permanently deformed ridge profiles

The next sets of images consider the permanently deformed ridge profiles of the V-structures at a specific V-tip radius. Presented in the following subsections are figures considering V-structures with a V-tip radius of 32 mm and 100 mm, with additional images available on pages D-16 and D-17.

V-tip radius of 32 mm

The permanently deformed ridge profiles for the 32 mm V-tip radius V-structures are shown below in figure 8.38. The shape of the deformation remains similar for all three V-angles and at all three charge masses, with an expected increase in the magnitude of the peak deflection at the larger charge masses simulated. Additionally, as expected, the V-structures with a narrower V-angle show a reduced peak mid-point deflection and a reduced deformed length along the ridge when compared to the other two V-angles investigated. Interestingly, at a charge mass of 10 g, the final ridge profiles of the 90° and 105° V-structures are fairly similar in terms of the depth of the indentation and the deformed length along the ridge. The profiles of at two V-angles are more distinct for the larger charge masses considered. Finally, the maximum deformed length along the ridge does not exceed 150 mm for the V-structures with a V-tip radius of 32 mm.

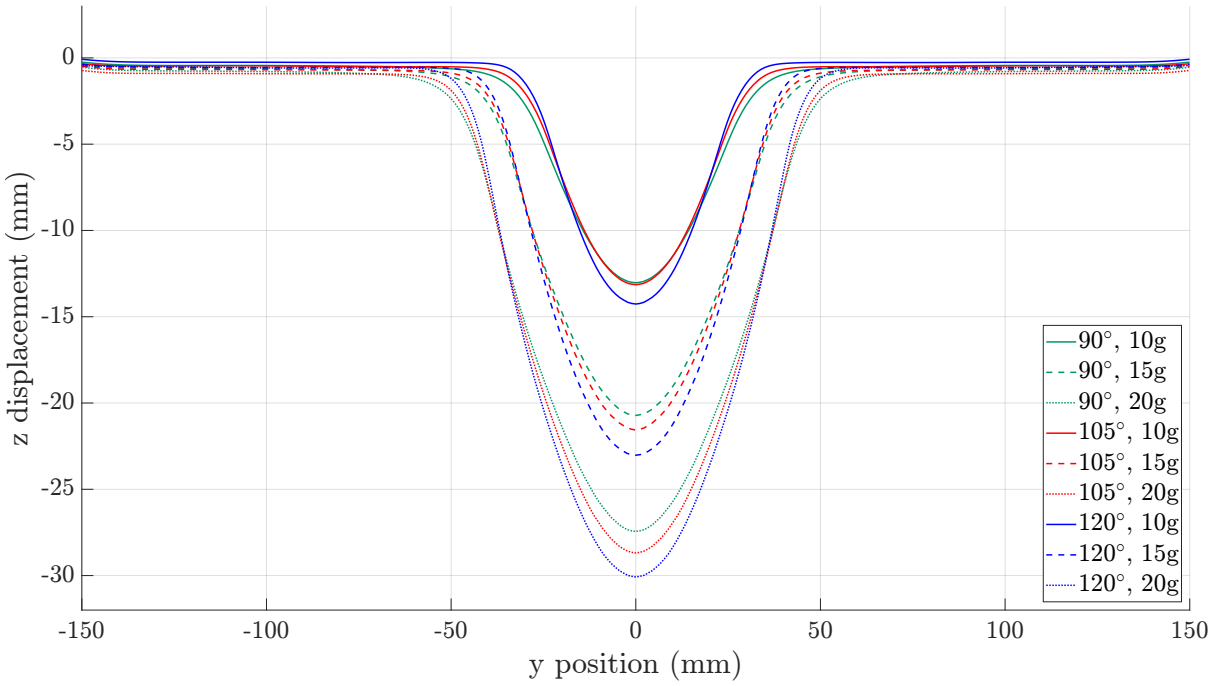

Figure 8.38: Permanently deformed ridge profiles versus the V-angle for a V-tip radius of 32 mm at all three charge masses investigated

V-tip radius of 100 mm

The ridge profiles for the V-structures with a 200 mm V-tip radius are shown in figure 8.38. At this V-tip radius, the profiles for the three V-angles have the same general shape, with the deformation covering the entire length along the ridge plane and the deformation appearing to be less localised. Additionally, the mid-point displacements appear to be fairly similar for all three V-angles and at all three charge masses. This figure supports the observation that at larger V-tip radii, the response of the V-structures is primarily driven by the curvature at the V-tip and the resulting change in the geometric stiffness and blast deflection characteristics of the structures.

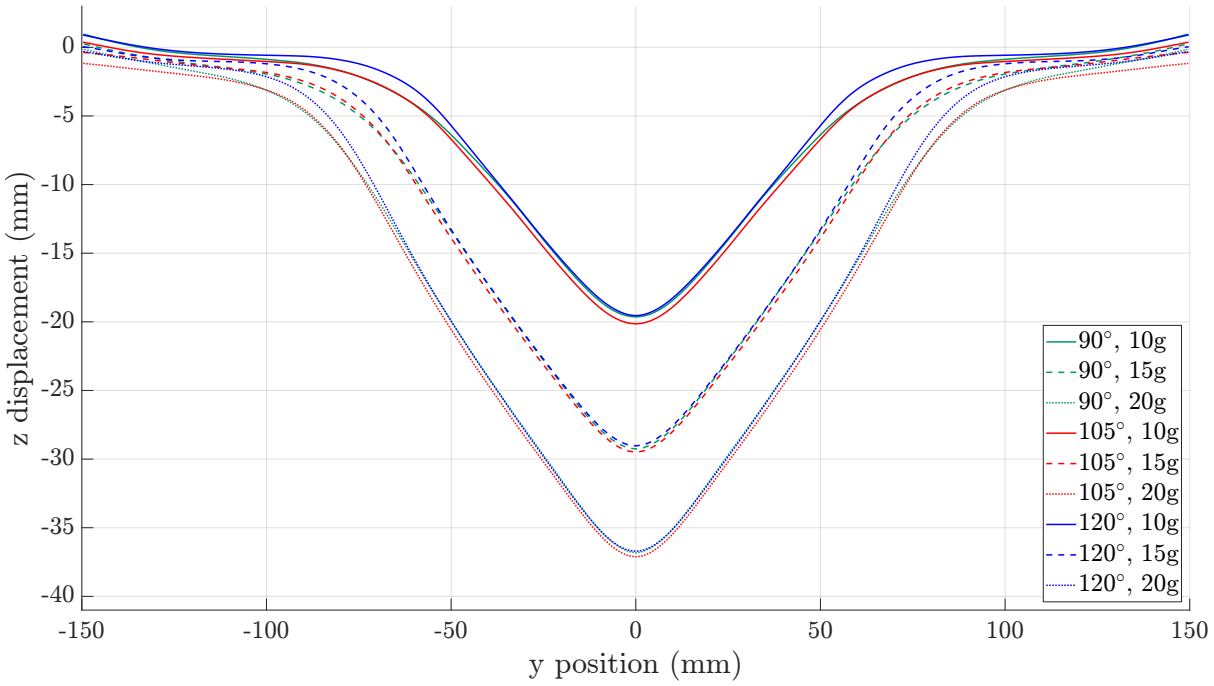

Figure 8.39: Permanently deformed ridge profiles versus V-angle for a V-tip radius of 100 mm at all three charge masses investigated

8.4.6 Effect of V-angle on the permanently deformed crosscut profiles

The final sets of images shown, look at the permanently deformed crosscut profiles of the V-structures at a specific V-tip radius. Presented in the following subsections are figures considering V-structures with a V-tip radius of 32 mm and 200 mm at selected charge masses. In general, the deformation becomes less localised as the V-tip radius was increased. Once again, the additional images at other charge masses can be found in Appendix D.

V-tip radius of 32 mm

The first set of profiles shown in figure 8.40 are the permanently deformed crosscut curves for a V-tip radius of 32 mm at a charge mass of 15 g. The three profiles appear fairly similar in terms of the shape of the indentation in the V-structures, with all three V-structures experiencing a localised deformation with minimal deformation in the crosscut plane. Once again, this supports the findings from previous sections that at this V-tip radius the permanent deformation behaviour is primarily a function of the V-tip radius rather than the V-angle of the V-structures.

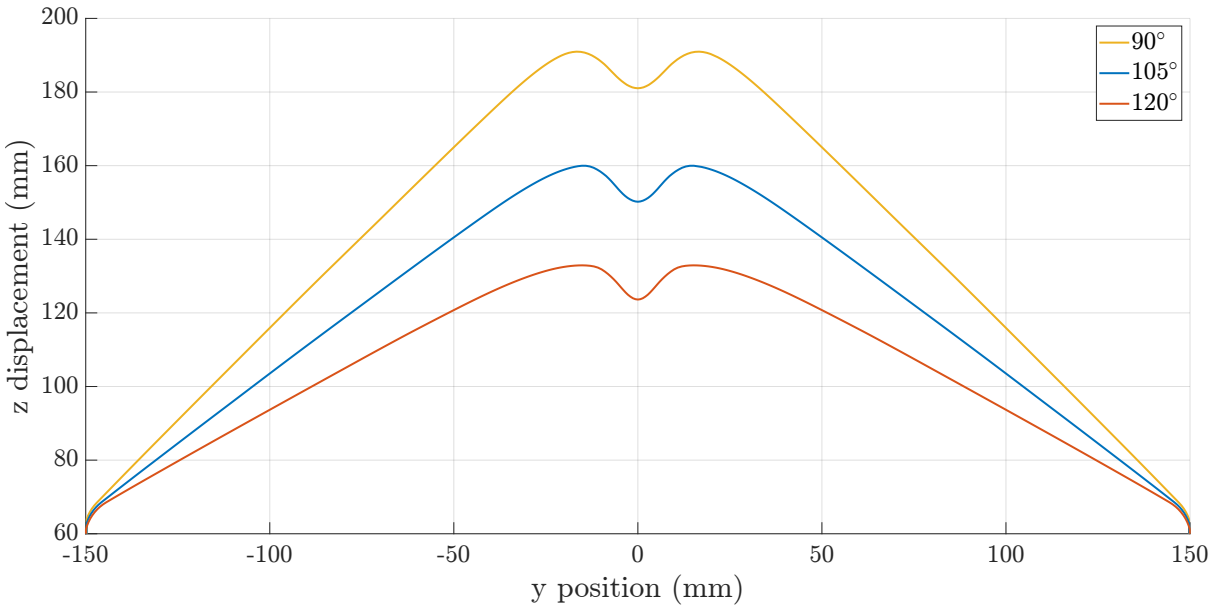

Figure 8.40: Permanently deformed crosscut profiles versus V-angle for a V-tip radius of 32 mm at a charge mass of 15 g

V-tip radius of 200 mm

The final set of crosscut profiles for a V-tip radius of 200 mm at a charge mass of 20 g are shown in figure 8.41. The deformation of the three profiles is nearly identical at this V-tip radius with a minimal variation in the height from the base and the shape of the deformed region. As expected, the deformation is the most distributed for these profiles due to the significant reduction in geometric stiffness as a result of the large V-tip radius. While the straight sides along the V-profile are fairly short, these appear to be deformed for all three V-angles investigated.

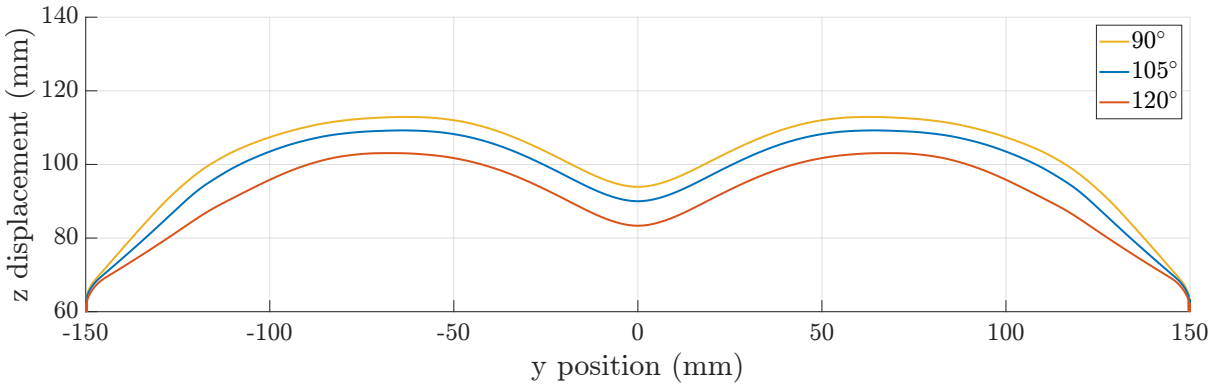

Figure 8.41: Permanently deformed ridge profiles versus the V-angle for a V-tip radius of 200 mm at a charge mass of 20 g

8.5 Summary

A numerical model was developed in LS-DYNA and validated against the set of experimental blast test results which included multiple V-angles, V-tip radii, and charge masses. This model was able to correctly capture the trends observed in the experiments and thus was deemed to be suitable for use in modelling a larger range of V-tip radii.

The V-structures showed a linear increase in the impulse for an increase in V-tip radius for all three V-angles investigated. At larger V-tip radii ($> 100\,\text{mm}$), the impulse between the three V-angles was similar. This was attributed to the increase in the influence of the V-tip radius compared to the V-angle influence.

The geometric stiffness of these V-structures was observed to decrease, as both the V-angle and V-tip radius were increased. A bilinear trend was observed for the peak mid-point displacement versus the V-tip radius, while the final mid-point displacement was observed to plateau for V-tip radii above 100 mm. At larger V-tip radii ($> 100\,\text{mm}$), both the peak and final mid-point displacements were fairly similar between the three V-angles investigated. This was due to the increase in the effect of the V-tip radius on the blast response characteristics of the V-structures.

For all three V-angles, there was an increase in the peak mid-point displacement, its time of arrival, and the post-blast peak-to-peak vibration displacement. The vibration frequency was also observed to decrease as the V-tip radius was increased. These changes were attributed to a reduction in the V-structure geometric stiffness for an increase in the V-tip radius. The ridge profiles exhibited an observed increase in the depth of the indentation and deformed length along the ridge line for an increase in V-tip radius, with the entire ridge line observed to deform for V-tip radii above 80 mm. The crosscut profiles exhibited an observed increase in the width of the deformed area along the V-profile. Bowing was present at larger V-tip radii for all three V-angles investigated.

The narrower V-angled V-structures performed better at all V-tip radii up to 100 mm. Above this V-tip radius, the response was primarily driven by the curvature at the V-tip, with the three V-angles showing similar values for the impulse and deformation. The effect of the V-angle on the mid-point displacement time histories showed, once again, that the narrower V-angles displayed superior blast performance with a reduced peak amplitude and reduced vibration amplitude for all charge masses. This benefit was diminished at the larger V-tip radii with the three V-structures showing similar vibration responses. Similar trends were observed when comparing the final ridge profiles and crosscut profiles. With the benefit of the narrower V-angle reducing as the V-tip radius was increased and the profiles of the three V-angled V-structures having the same shape.

Chapter 9

Numerical blast simulations - GFRP

This chapter presents the development of a GFRP blast model used to investigate the influence of V-structure geometry on the blast performance of GFRP V-structures. The chapter begins with the selection and parameter optimisation of suitable material models for the GFRP V-structures modelled herein followed by the validation of the numerical models against the experiments for a range of test scenarios. Finally, the trends in impulse, damage, transient mid-point deformation and transient deformation profiles are presented and discussed.

9.1 GFRP numerical blast model development

There are a number of ways to model composite laminates in LS-DYNA. The laminate can be modelled as a single structure made of solid elements. An appropriate material model enables this model to capture failure modes, such as fibre fracture and laminate rupture, although this approach is unable to capture delamination failure modes. Another approach to modelling laminates uses layers of solid or offset shell elements to model the laminate. Each layer of solid or shell elements can model a single ply or multiple plies with the fibre angle, material, and ply thicknesses controlled using the PART_COMPOSITE card in LS-DYNA. This allows for fibre fracture and rupture to be captured and this approach also allows for interlaminar delamination failure to be modelled.

MAT_ORTHOTROPIC is the simplest composite material model. It is capable of defining elastic material properties parallel and perpendicular to the fibre direction, but it cannot model fibre failure. MAT_COMPOSITE_DAMAGE is the simplest composite damage model available and is a simple brittle model that does not have a mechanism for handling compressive failure. MAT_ENHANCED_COMPOSITE_DAMAGE is an improvement on MAT_COMPOSITE_DAMAGE as it has four failure criteria that can be implemented in the model.

There are also multiple ways to model delamination in LS-DYNA. One approach to delamination modelling is to use a Cohesive Zone Element (CZE) and an associated Cohesive Zone material model, while another approach is the use of tiebreak contact cards. The use of tiebreak contacts is recommended in literature [100–102] due to the similar failure predictions in terms of capturing the delaminated area and crack growth in DCB simulations and reduced computational times when compared to the CZE approach.

9.1.1 Tensile test model and GFRP material model characterisation

LS-DYNA was used to model the material tests performed on the GFRP tensile test specimens described in Chapter 4. The tensile test specimens were modelled with a single layer of shell

elements with the properties of the individual plies included in the model with the PART_COMPOSITE card [95]. The simulation was performed using the implicit solver with a set of constrained nodes at one end and prescribed velocity boundary condition at the other end as shown in figure 9.1. MAT_ENHANCED_COMPOSITE_DAMAGE was chosen as the material model for the simulation and the properties (*i.e.* Young's modulus, failure strain and tensile failure strength) were adjusted to match the experimentally obtained stress-strain response. The fitted response is shown in figure 9.2, from these simulations, the Young's Modulus, failure strain, and tensile failure strength were determined. The density of the material was found from equation (9.1). The same volume fractions and densities of the glass-fibre and matrix found in Chapter 4 were used. Hence, the density of the manufactured panels (ρ_{eff}) was found to be $1.710\,\mathrm{g\,cm^{-3}}$. The remaining parameters were taken from literature [103]. These properties for MAT_ENHANCED_COMPOSITE_DAMAGE are summarised in table 9.1 with the properties taken from literature shown with an asterisk (*).

$$\rho_f \times v_f + \rho_m \times v_m + \rho_v \times v_v = \rho_{eff} \tag{9.1}$$

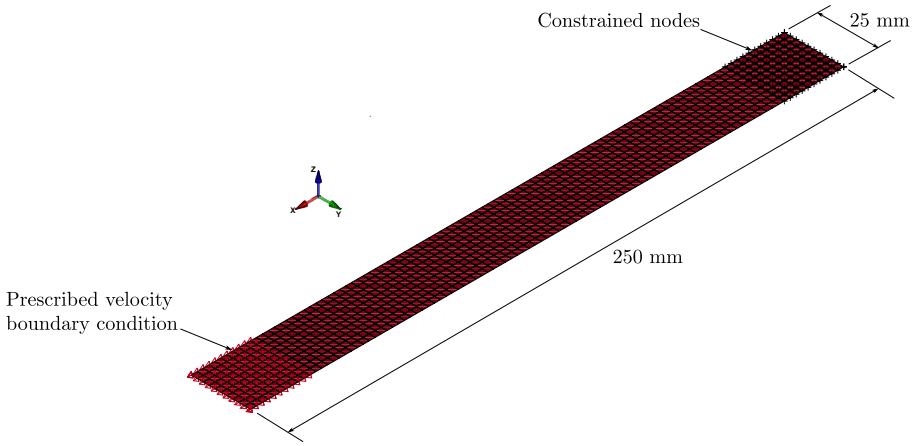

Figure 9.1: Schematic of the quasistatic tensile test model for the GFRP specimens

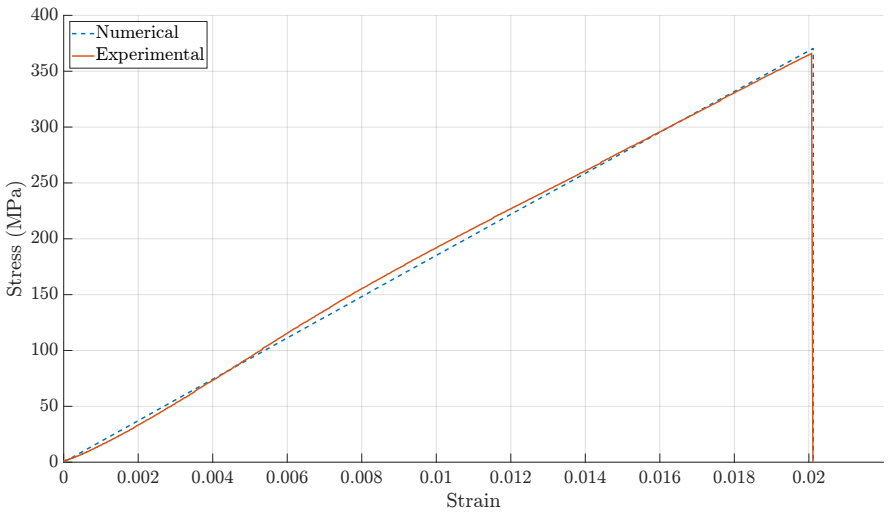

Figure 9.2: Comparisons of the stress versus strain graphs from the simulations and experiments on the quasistatic tensile tests of the 0°/90° GFRP specimens

Table 9.1: Material properties needed for MAT_ENHANCED_COMPOSITE_DAMAGE

Property name	Value	Unit
Density (ρ)	1.710	$\mathrm{g\,cm^{-3}}$
Young's modulus ($E_1,\ E_2$)	18.60	GPa
Young's modulus*[1](E_3)	9.0	GPa
Poisson's ratio*[1](ν)	0.17	
Shear modulus (G_{12})	6.18	GPa
Failure strain (μ)	0.201	
Failure stress	416	MPa

[1] Lifshitz, J. M. and Leber, H. "Response of fiber-reinforced polymers to high strain-rate loading in interlaminar tension and combined tension/shear". Composites Science and Technology 58.6 (1998), pp. 987–996. DOI: 10.1016/s0266-3538(97)00226-1

9.1.2 Delamination material model characterisation

The CONTACT_AUTOMATIC_SURFACE_TO_SURFACE_TIEBREAK card was chosen due to the anticipated layer penetration at the V-tip of the V-structures in the simulations due to the large pressures of the blast loading. The ONE_WAY contact cards only check the slave nodes for penetration through the master surface while TWO_WAY contact cards check both the slave and master nodes for penetration [95]. This approach is computationally more expensive, but it is desirable that layer penetration is prevented in the blast models [104]. OPTION 10 (Dycoss Discrete Crack Model for offset shell elements) was chosen as the failure criteria in the tiebreak card. The equation governing the tiebreak failure for this model is shown in equation (9.2), where σ_n is normal stress, σ_s is shear stress, NFLS is normal failure strength, SFLS is shear failure strength, and PARAM is the friction angle which has been set to 0° in this study, which allows the failure criteria to represent the simpler failure model available with OPTION 2 for non-offset shell elements [95].

$$\left[\frac{\max(\sigma_n, 0)}{\mathrm{NFLS}}\right]^2 + \left[\frac{\sigma_s}{\mathrm{SFLS} - \sin(\mathrm{PARAM})\min(0, \sigma_n)}\right]^2 = 1 \tag{9.2}$$

The parameters for the CONTACT_AUTOMATIC_SURFACE_TO_SURFACE_TIEBREAK card were investigated next by modelling the DCB tests performed in Chapter 4. The test specimens were modelled with two layers of shell elements, with each layer of shells modelling six composite plies. Once again, the PART_COMPOSITE card was used to include the ply information in the model with MAT_ENHANCED_COMPOSITE_DAMAGE used as the shell element material model. The geometry and boundary conditions used in the test are shown in figure 9.3. A segment set on each layer of elements was tied together using the tiebreak card and the parameters of the card were adjusted to match the response obtained in the experiments, while a prescribed velocity boundary condition was applied at a series of nodes to model the opening of the crack. The prescribed velocity boundary condition is implemented by applying a velocity function to the series of nodes across the width of the specimen in the direction of the opening of the crack as shown in figure 9.3. The delaminated area and length were obtained from the ATDOUT card, while the contact force was obtained from the RCFORC card, which

contains the resultant contact forces for tied nodes, node sets, segments, or segment sets. The fitted force and crack length curves are shown in figure 9.4. The parameters required for the contact card are summarised table 9.2. Any parameters that were not determined from the experiments or simulations were taken from literature [105, 106]. These are shown with an asterisk (*).

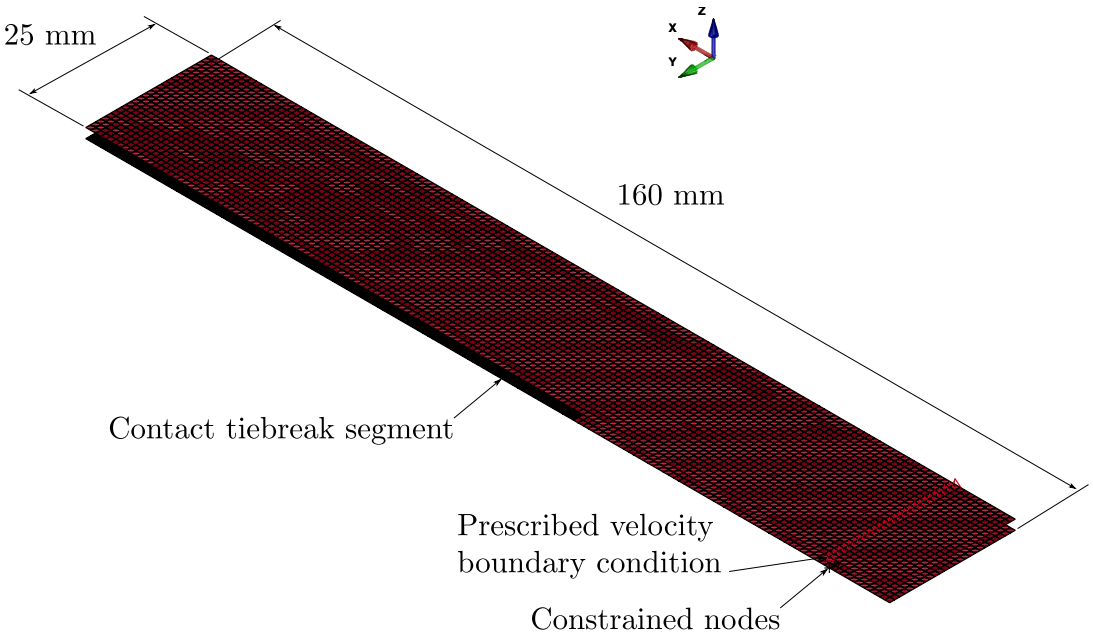

Figure 9.3: Schematic of the quasistatic DCB test model for the GFRP specimens

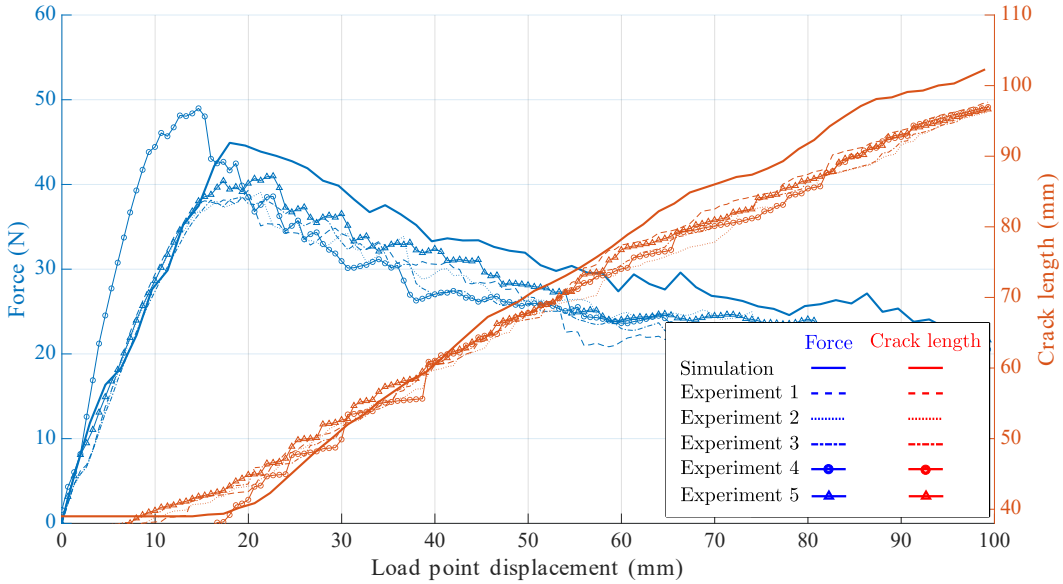

Figure 9.4: Numerical versus experimental results for the force and crack length versus load point displacement for the DCB test specimens in the ±45° fibre orientation and a crosshead speed of 2 mm min^{-1}

Table 9.2: Model parameters needed for the contact card

Property name	Value	Unit
Normal failure strength	45	MPa
Shear failure strength	45	MPa
Normal energy release rate	1020	$\mathrm{J\,m^{-2}}$
Shear energy release rate	1020	$\mathrm{J\,m^{-2}}$
Normal stiffness*[1]	5	GPa

[1] Menna, C., Asprone, D., Caprino, G., Lopresto, V., and Prota, A. "Numerical simulation of impact tests on GFRP composite laminates". International Journal of Impact Engineering 38.8-9 (2011), pp. 677–685. DOI: 10.1016/j.ijimpeng.2011.03.003

9.1.3 Inclusion of damping

It is recommended that a small amount of damping be included in blast and impact simulations. In particular, for composite structures, there are multiple sources of damping, including the matrix material, delamination failure, fibre and matrix failure, and the fibre/matrix interface. Some of these are not accounted for in the material and delamination models used and must be included to correctly model the GFRP V-structure response [107]. The damping was included in the models using the DAMPING_GLOBAL card. In order to determine the correct amount of damping required, a series of simulations were performed with increasing amounts of damping. The 50 mm point deflection time histories were compared with selected experiments to find the damping required in the model. A 105° V-structure with a ±45° fibre orientation and loaded with a charge mass of 10 g was considered for the damping study. An initial simulation was performed with no damping to determine the natural frequency of vibration of the GFRP V-structure considered. The natural frequency of the simulation vibration is $2.14\,\mathrm{rad\,s^{-1}}$. Thus, the critical damping coefficient was found to be $4.28\,\mathrm{kg\,s^{-1}}$. Figure 9.5 shows the first 1.0 ms of the simulations and the two experiments. From the figure, it can be seen that the introduction of damping significantly reduces the post-blast oscillations and the displacements more closely match the experimentally measured displacements. The peak always occurs sooner in the simulations suggesting that the model is not capturing the experiment perfectly. The optimal amount of damping can be seen to be approximately 40% of the critical damping which is in the range of the recommended damping of 20%-40% [108]. Thus, for all the remaining simulations in this study, this value will be used.

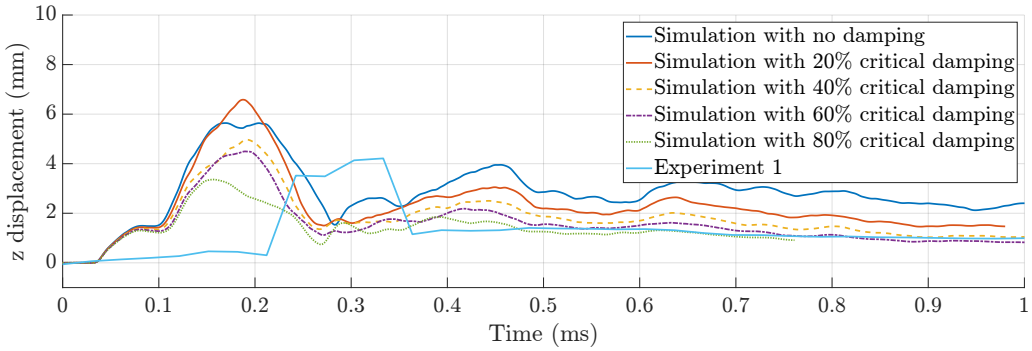

Figure 9.5: Numerical simulations with increasing amounts of damping and the experimental results for the transient response at the 50 mm point along the ridge line for a 105° 34 mm V-tip radius GFRP V-structure with a ±45° fibre orientation at a charge mass of 10 g

9.1.4 Numerical model specification

The experimentally tested GFRP V-structures were manufactured from 28 layers of plain weave E-glass with an average ply thickness of 0.32 mm as detailed in Chapter 3. An offset layered shell approach was used to model the V-structures with a factor of the total number of plies. In this study, a 14-layer offset shell model was used as it was found, in Chapter 7, that there were fewer than 13 distinct delamination sites in the sectioned blast tested V-structures. Thus, a 14-layer model would be able to capture the delamination failure seen in the blast tests. Additionally, in the blast tests, fibre failure (*i.e.* cracking) was not noted as the most significant damage mode present, thus, MAT_ORTHOTROPIC was used for the material model instead of one of the damage models. An example of the 14-layer offset shell model used for the GFRP V-structure blast simulations is shown in figure 9.6. The geometry of each layer was generated using SolidWorks and then imported into LS-PrePost as a STEP file. The edge nodes were then seeded and meshed with four-node quadrilateral elements with an approximate element size of 1.0 mm. This element size was also used for the steel V-structure blast simulations and had been shown to produce good results in similar blast simulation studies conducted on flat steel plates [56, 63].

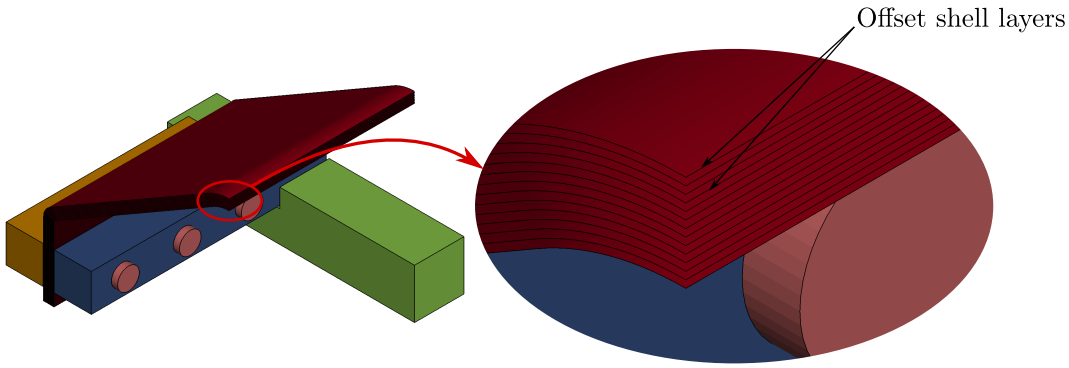

Figure 9.6: Schematic of the blast simulation of a 120°, 34 mm V-tip radius GFRP V-structure simulation showing the offset shell layers

9.2 Numerical model validation - GFRP

The GFRP V-structure models were validated against the experimental results to show that the simulations were able to capture the structural response observed in the experiments. To do this, the impulse transferred, delaminated area, and point transient displacement time histories were compared for selected test configurations. Where percentage differences are presented, these have been calculated using equation (9.3).

$$\%\text{Difference} = \frac{\text{Value}_{\text{exp}} - \text{Value}_{\text{num}}}{\text{Value}_{\text{exp}}} \times 100 \tag{9.3}$$

9.2.1 Measured impulse

The impulse was obtained by integrating the averaged fluid-structure interaction force on all the Lagrangian components modelled (including the clamp frames and bolts) and compared to the measured impulse from the blast experiments. These results have been summarised in table 9.3. The numerical simulations are able to capture the trends seen in the experimental impulses when changing the charge mass and V-angle with the model accuracy reducing for the larger charge masses investigated. There is a difference of between 7% and 18% between the simulated impulses and the experimentally measured impulses. In general, the model underpredicts the impulse for all the blast test comparisons. This matches the results obtained for the steel V-structure simulations in Chapter 8. These findings support the use of this model to investigate and extrapolate the trends in the response of GFRP V-structures to blast loads from near SOD blasts.

Table 9.3: Comparison of the impulse transferred results between the GFRP V-structures (numerical versus experimental)

		Impulse (Ns)		
Configuration	Charge mass (g)	Numerical	Experimental	Difference (%)
105°, 34 mm, 0°/90° lay-up	10	9.1	10.0	0.9 (8.6)
	15	12.1	14.4	2.3 (16.5)
	20	14.6	17.8	3.2 (18.2)
105°, 34 mm, ±45° lay-up	10	9.1	10.6	1.1 (10.5)
	15	12.0	14.7	2.0 (14.1)
120°, 34 mm, 0°/90° lay-up	10	9.9	10.6	0.7 (6.9)
	15	13.1	14.7	1.6 (11.1)

9.2.2 Delaminated area

The delaminated area in the numerical blast simulations was obtained for each contact set by taking an image of the contact layer at the end of the simulation using the CONTACT GAP visualisation option in LS-PrePost. In total, each simulation had 13 contact sets representing the delimitation sites between layers. The data was imported into MATLAB which was used to generate a map of the total projected delaminated area for each GFRP V-structure simulation which can then be compared to the photographs of the blast tested panels. These results have

been tabulated and compared with the equivalent experimental blast tests in table 9.4. There is reasonable correlation between the simulations and experiments at all the charge masses investigated although, in general, the simulations underpredict the total projected delaminated area. The average deviation across all the comparisons is approximately 12%. This difference might be due to the simulated blast load being lower across the test range, as also seen by the lower simulated impulses. While noting this difference in the simulated responses, the trends can be seen to be similar, with similar percentage increases in the delaminated areas as the charge mass was increased.

It is also beneficial to look at the shapes of the delaminated areas to determine if the simulations are able to correctly predict the shape of the regions of the V-structure that will delaminate. These comparisons are shown for selected tests in figures 9.7 to 9.12. These tests were chosen as they cover a range of V-angles, fibre orientations, and charge masses. In general, the model is able to capture the trends seen in the experiments, with greater delamination along the ridge compared with the crosscut direction. The lower delaminated areas presented in the tabulated results in table 9.4 can also be seen in the figures with the experiments displaying greater delamination in both planes. The asymmetry seen in the experiments was not captured by the model due to the quarter symmetry modelling approach used. While there is a difference in the magnitude of the delamination between the simulations and experiments, the blast model is generally able to capture the correct shape of the deformed area. This is an important observation when using the model to extrapolate trends in the response of the GFRP V-structures for a range of V-structure geometries.

Table 9.4: Comparison of the projected delaminated area (%) between the GFRP V-structures (numerical versus experimental)

		Projected delaminated area (%)		
Configuration	Charge mass (g)	Numerical	Experimental	Difference (%)
105°, 34 mm, 0°/90° lay-up	10	4.8	6.3	1.4 (23)
	15	7.0	8.7	1.7 (20)
	20	9.9	9.6	-0.3 (-3)
105°, 34 mm, ±45° lay-up	10	4.5	4.8	0.3 (6)
	15	7.1	8.1	1.0 (13)
120°, 34 mm, 0°/90° lay-up	10	5.9	7.4	1.5 (20)
	15	10.1	11.1	0.9 (9)

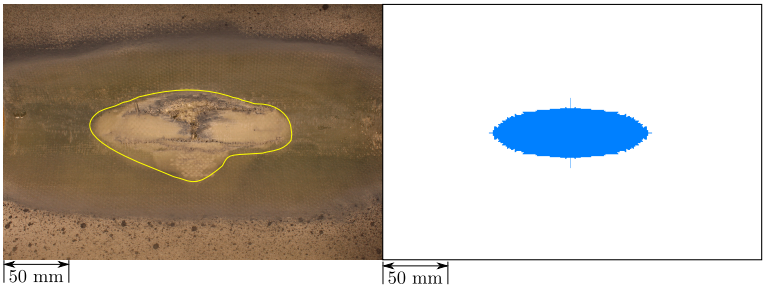

Figure 9.7: Comparison of the numerical and experimental delamination for a 105° GFRP V-structure with a V-tip radius of 34 mm and a fibre orientation of 0°/90°, tested at a charge mass of 10 g

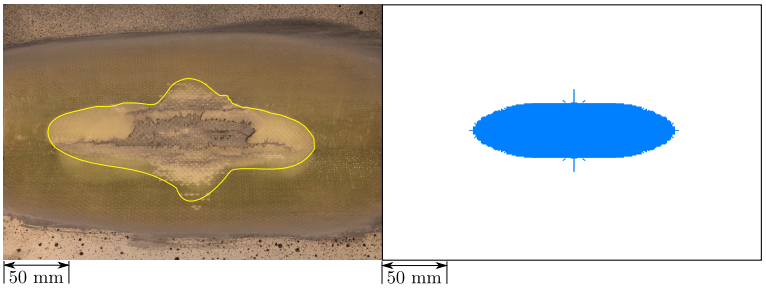

Figure 9.8: Comparison of the numerical and experimental delamination for a 105° GFRP V-structure with a V-tip radius of 34 mm and a fibre orientation of 0°/90°, at a charge mass of 15 g

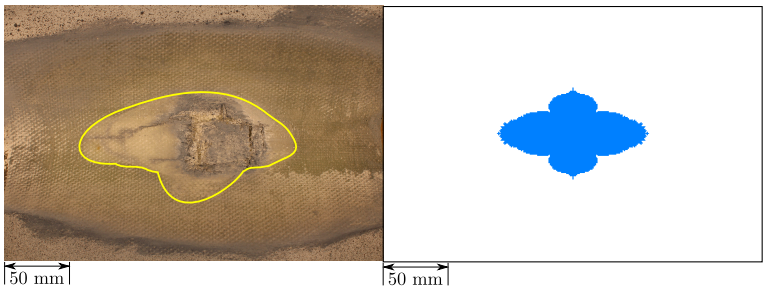

Figure 9.9: Comparison of the numerical and experimental delamination for a 120° GFRP V-structure with a V-tip radius of 34 mm and a fibre orientation of 0°/90°, tested at a charge mass of 10 g

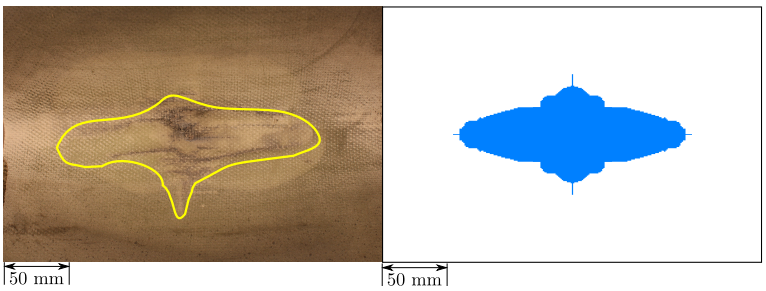

Figure 9.10: Comparison of the numerical and experimental delamination for a 120° GFRP V-structure with a V-tip radius of 34 mm and a fibre orientation of 0°/90°, at a charge mass of 15 g

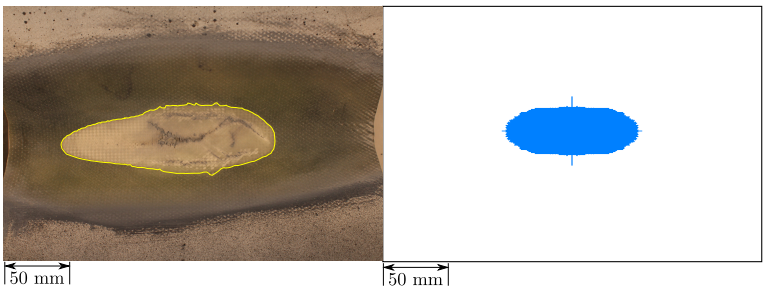

Figure 9.11: Comparison of the numerical and experimental delamination for a 105° GFRP V-structure with a V-tip radius of 34 mm and a fibre orientation of ±45°, at a charge mass of 10 g

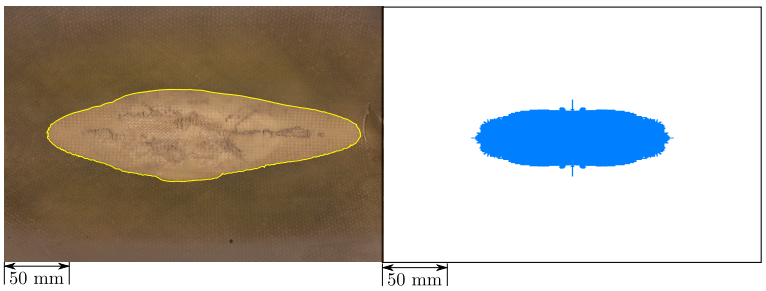

Figure 9.12: Comparison of the numerical and experimental delamination for a 105° GFRP V-structure with a V-tip radius of 34 mm and a fibre orientation of ±45°, tested at a charge mass of 15 g

9.2.3 Transient deflection

The mid-point displacement time history was available for two tests performed on the 105° GFRP V-structures with a ±45° fibre orientation tested at a charge mass of 10 g, while it also was possible to measure the transient deflection at a point located 50 mm from the mid-point for additional tests on the 120° GFRP V-structures with a 0°/90° fibre orientation tested at charge masses of 10 g and 15 g. These point displacement time histories for the numerical simulations plotted against these experiments are presented in figures 9.13 to 9.16.

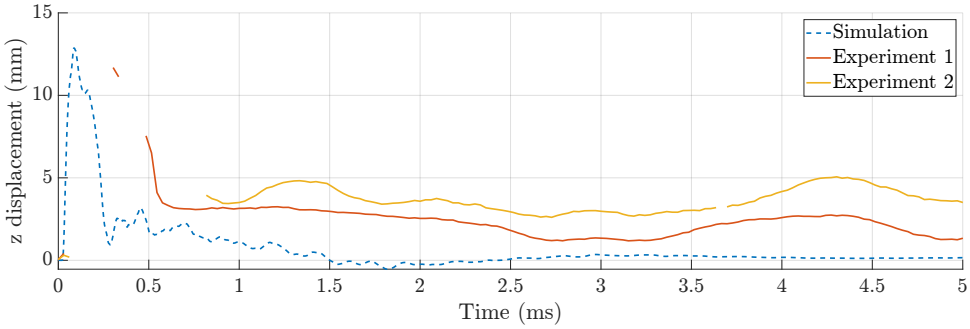

Figure 9.13: Numerical versus experimental results for the mid-point deflection time history for a 105° 34 mm V-tip radius GFRP V-structure with a ±45° fibre orientation at a charge mass of 10 g

In figure 9.13, the drop off from the first peak in the simulation is observed to occur at an earlier time than the experiment while having a similar magnitude, the post-peak oscillation is lower in magnitude and sits just above the origin. This is because the numerical simulations do not include the permanent deformation effects resulting from layer separation in the blast experiments.

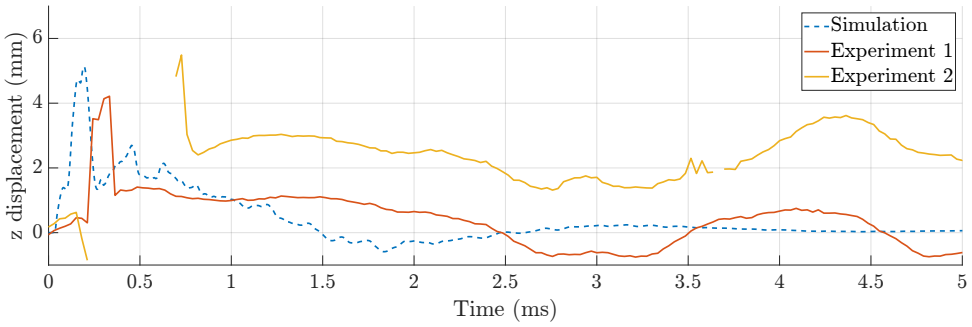

Figure 9.14: Numerical versus experimental results for the point deflection time history for a 105° 34 mm V-tip radius GFRP V-structure with a ±45° fibre orientation at a charge mass of 10 g

The earlier arrival of the peak displacement can be better observed in figure 9.14. Once again, the magnitude of the peak displacement is similar and the post-peak oscillations are lower. The peak displacement is significantly different in figure 9.15 although there is a reasonably large variation between the two experiments. In figure 9.16 there is limited data at the peak although the simulation value appears to be similar.

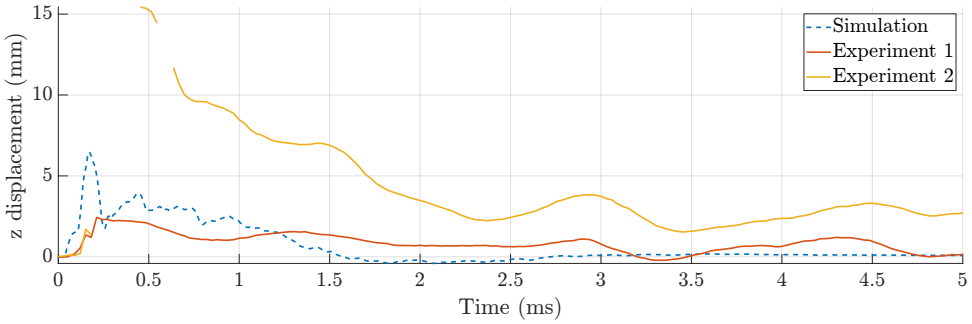

Figure 9.15: Numerical versus experimental results for the point deflection time history for a 120° 34 mm V-tip radius GFRP V-structure with a 0°/90° fibre orientation at a charge mass of 10 g

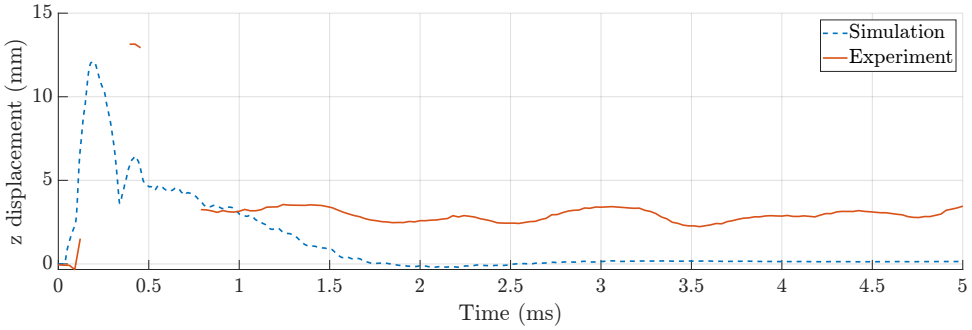

Figure 9.16: Numerical versus experimental results for the point deflection time history for a 120° 34 mm V-tip radius GFRP V-structure with a 0°/90° fibre orientation at a charge mass of 15 g

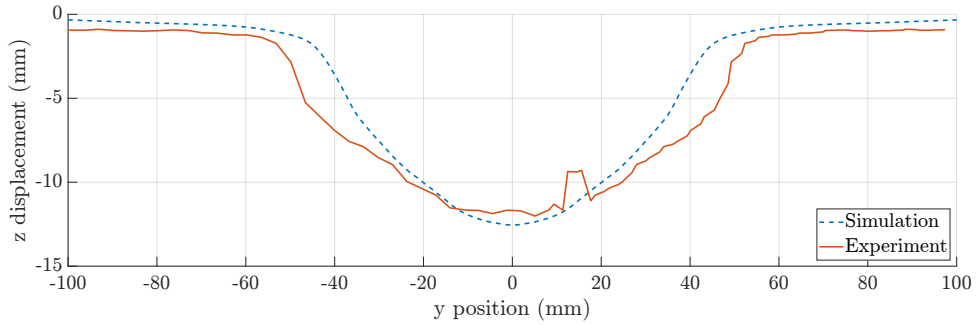

Figure 9.17: Numerical versus experimental results for the peak transient ridge profile for a 105° 34 mm V-tip radius GFRP V-structure with a ±45° fibre orientation at a charge mass of 10 g

Additionally, for a single test of a 105° GFRP with a fibre orientation of ±45° tested at a charge mass of 10 g, it was possible to extract out the peak transient ridge profile. This has been compared with the equivalent numerical simulation in figure 9.17. The numerical simulation peak is similar to the experiment with a similar deformed profile although the deformed length along the ridge is lower than the experimentally measured value. These observations suggest that the numerical simulations can be used to understand the effect of the V-structure geometry on the transient deformations, but would be unable to accurately predict the final deformation of the GFRP V-structures.

9.3 V-structure design parameters investigated

In the remainder of this chapter, the results from a numerical investigation on the blast performance of a range of V-structure design parameters have been presented. These have been chosen to extend the data sets investigated experimentally. Two V-angles were investigated numerically, namely 105° and 120°. These were chosen as they were also used for the experiments on the steel and GFRP V-structures. A 90° V-angle was not considered as these narrower V-angles are not expected to be used on MRAPs. In total, five V-tip radii were considered, ranging from 32 mm to 200 mm. The lower limit was chosen due to manufacturing limitations. It was reported in Chapter 3 that using a mould with a small V-tip radius resulted in a resin rich area at the V-tip due to difficulties for the fibre layers to bend around a tight radius. The upper limit was chosen to match the numerical simulations on the steel V-structures presented in Chapter 8. Finally, only two fibre orientations were investigated in this study, namely 0°/90°, and ±45°.

9.4 The effects of the V-structure design parameters on the impulse

The influence of the V-structure geometry was investigated in three analyses, namely, the influence of fibre orientation, V-angle, and V-tip radius. The summary of all the simulated impulse results is available in table E.1 in Appendix E. As expected, for all V-structure configurations, an increase in charge mass results in an increase in simulated impulse.

9.4.1 Fibre orientation effects

Figures 9.18 and 9.19 show the influence of the fibre orientation on the simulated impulse. Across the range of V-tip radii and V-angles investigated, the simulated impulse is nearly identical for the two fibre orientations simulated. Thus, for these fibre orientations, it can be stated that the fibre orientation does not appear to affect the impulse transferred. This is likely due to the identical geometric stiffnesses of these V-structures (*i.e.* the V-structure shape). Thus, in the remaining impulse comparisons, graphs will be shown for the 0°/90° fibre orientation, with the graphs for a ±45° fibre orientation available in Appendix E.

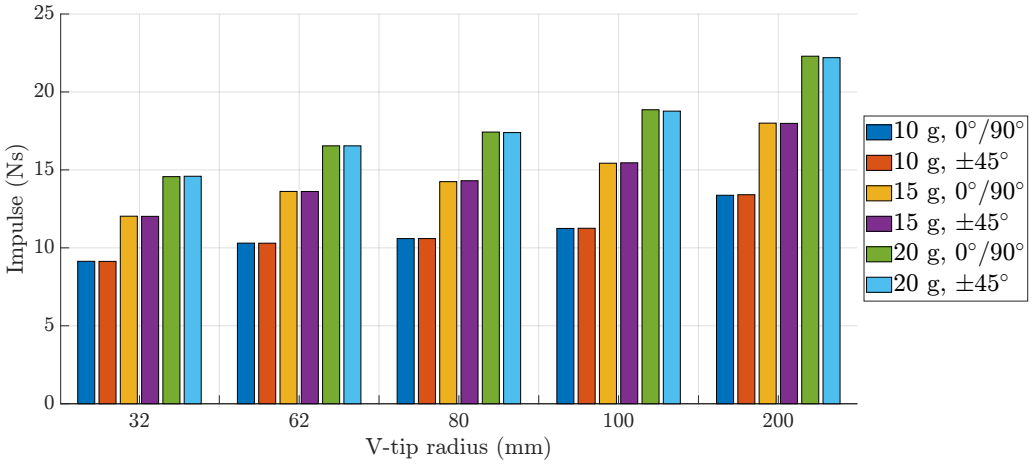

Figure 9.18: Simulated impulse versus fibre orientation for the 105° GFRP V-structures

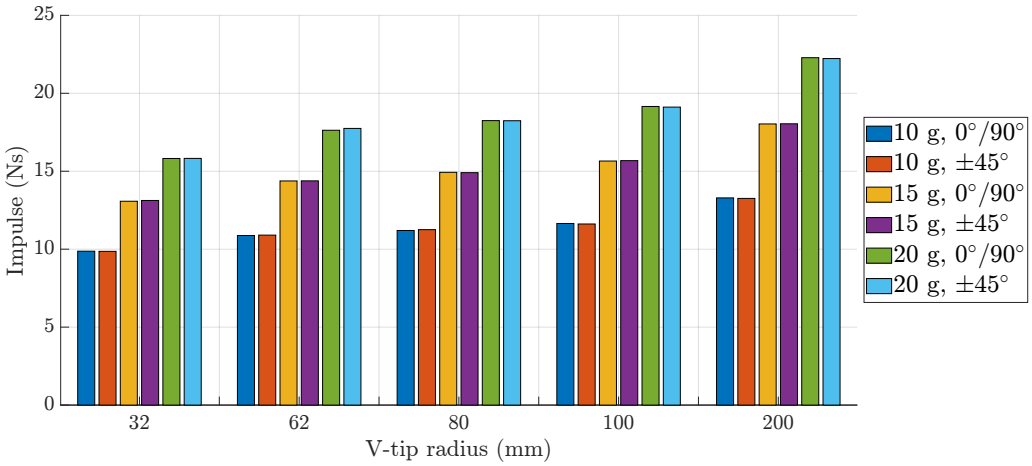

Figure 9.19: Simulated impulse versus fibre orientation for the 120° GFRP V-structures

9.4.2 V-angle effects

Next, the effect of the V-angle can be considered by looking at figure 9.20. In general, as expected, the simulated impulse is greater for the 120° V-structures. The difference in impulse between the two V-angles decreases as the V-tip radius is increased and this is true for V-tip radii up to 100 mm. For the larger V-tip radii investigated, the impulse is nearly identical for the 105° and 120° V-structures, suggesting that as with the steel V-structures, the beneficial blast deflection characteristics of the sharp V-angle are diminished at these larger V-tip radii as

the response is primarily driven by the curvature effects of the radius at the V-tip.

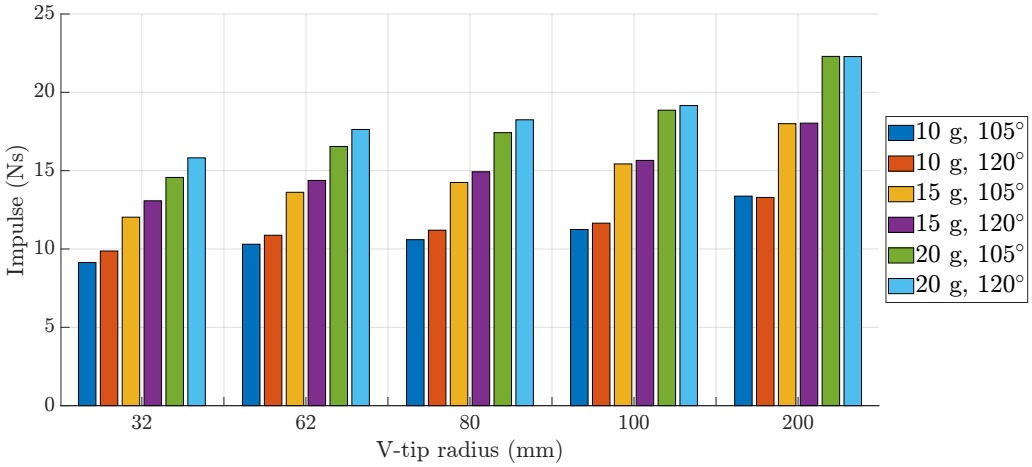

Figure 9.20: Simulated impulse versus V-angle for the GFRP V-structures with a 0°/90° fibre orientation

9.4.3 V-tip radius effects

The influence of the V-tip radius on the simulated impulse for the 0°/90° fibre orientation V-structures is shown in figures 9.21 and 9.22. Looking at the two graphs, the impulse appears to increase fairly linearly as the V-tip radius is increased for the two V-angles. For the 105° V-structures, at 10 g there is an increase of 4.2 Ns (approximately 46%) as the V-tip radius is increased from 34 mm to 200 mm, while for the 120° V-structures tested at the same charge mass, the increase is only 3.5 Ns (approximately 35%). Thus, like the steel V-structure simulation results, increasing the V-tip radius results in a greater increase in impulse transferred for the narrower V-angles tested. A similar observation can be seen at the other charge masses investigated.

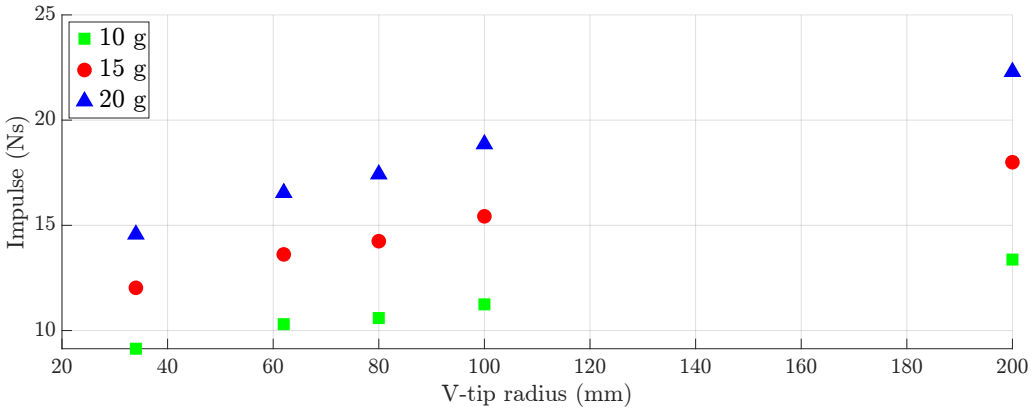

Figure 9.21: Simulated impulse versus V-tip radius for the 105° GFRP V-structures with a 0°/90° fibre orientation

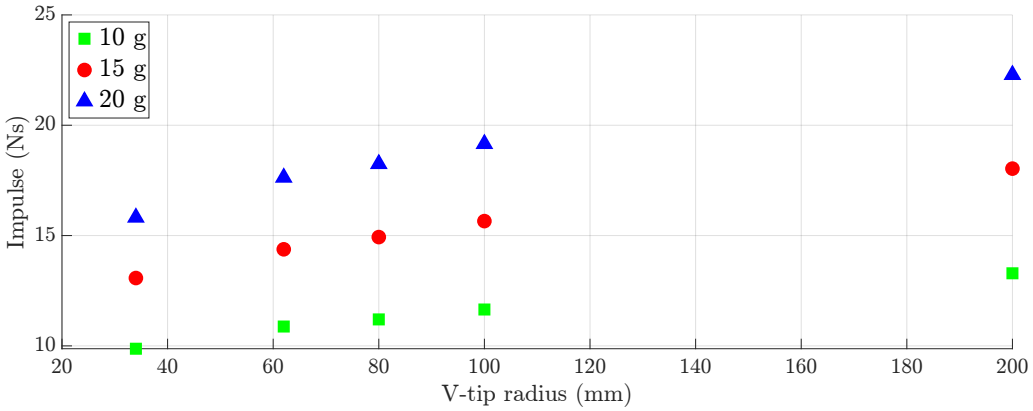

Figure 9.22: Simulated impulse versus V-tip radius for the 120° GFRP V-structures with a 0°/90° fibre orientation

9.5 The effects of the V-structure design parameters on the projected delaminated area

The projected delaminated area was calculated using the same technique presented previously in section 9.2. As with the simulated impulse, the simulated delaminated area is observed to increase as the charge mass is increased. This is to be expected as the total energy imparted to the V-structure increases. These results have been tabulated and are available in Appendix E. Once again, the analysis of the V-structure design parameter effects on delamination have been considered in three parts, namely, fibre orientation, V-angle, and V-tip radius effects.

9.5.1 Fibre orientation effects

The influence of the effect of the fibre orientation on the percentage projected delaminated area can be studied by looking at figures 9.23 and 9.24. For the 105° V-structures, the delaminated areas are fairly similar between the two fibre orientations, with some minor deviations (<2%) at a few of the configurations investigated. The differences are more significant for the 120° V-structures with up to an 8% difference between the two fibre orientations when considering a 200 mm V-tip radius tested at a charge mass of 15 g. In general, the variations between the two fibre orientations are more prominent at larger V-tip radii (> 100 mm). These differences at larger V-tip radii warrant further investigation with the use of the projected delaminated area maps.

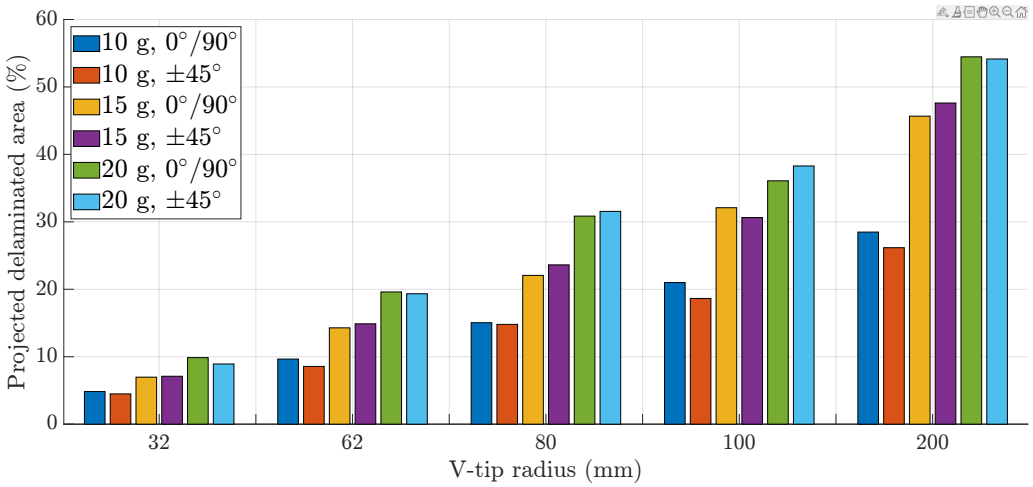

Figure 9.23: Projected delaminated area versus fibre orientation for the 105° GFRP V-structure simulations

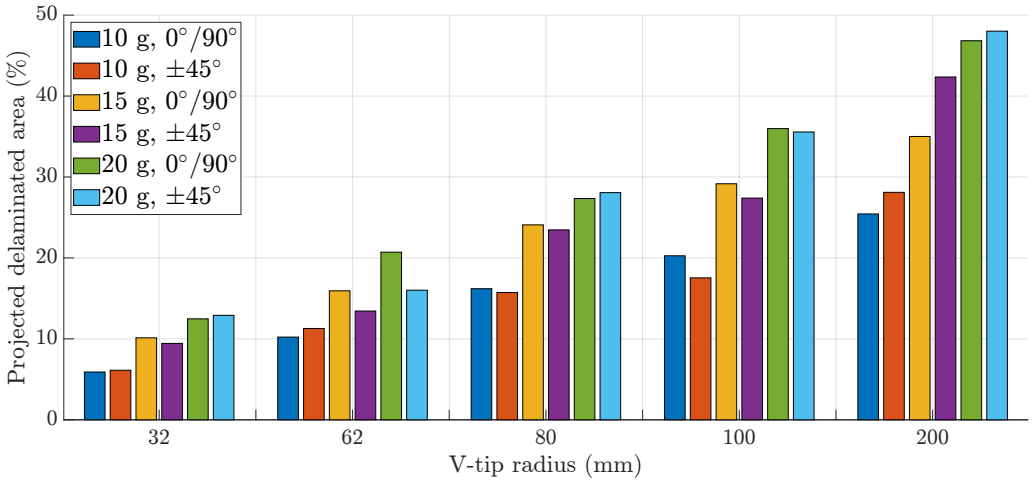

Figure 9.24: Projected delaminated area versus fibre orientation for the 120° GFRP V-structure simulations

Based on figure 9.23, the comparisons to consider are the 105° GFRP V-structures with a 100 mm and 200 mm V-tip radius simulations at a charge mass of 10 g. These delaminated area maps are shown in figure 9.25. From figure 9.25, it can be seen that the delamination extends further along the ridge plane for the V-structure with a 0°/90° fibre orientation with a similar length of delamination in the crosscut plane. Furthermore, at 100 mm, the shape of the delaminated area is fairly similar between the two fibre orientations. Finally, going from 100 mm to 200 mm the shape of the delaminated area has changed from an oval to a more circular shape for both fibre orientations although the effect is greater for the ±45° V-structure. This difference is likely due, once again, to the large curvature at a V-tip radius of 200 mm and the fibre orientation difference likely changes the way the load is transferred in the laminate plies.

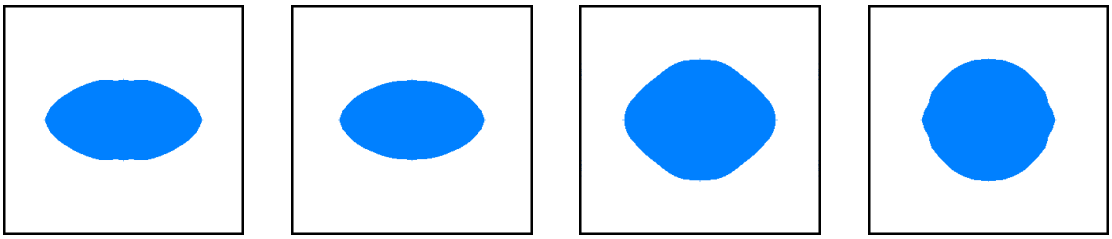

(a) 0°/90°, 100 mm | (b) ±45°, 100 mm | (c) 0°/90°, 200 mm | (d) ±45°, 200 mm

Figure 9.25: Projected total delaminated area for the 105° GFRP V-structure simulations with the two fibre orientations and V-tip radii of 100 mm or 200 mm at a charge mass of 10 g

Next, looking at the projected delaminated areas of the 120° GFRP V-structures in figure 9.24, the configurations with the largest variations in percentage delaminated area were for a V-tip radius of 62 mm at 20 g and a V-tip radius of 200 mm at 15 g. The delaminated area maps for these simulations have been provided in figure 9.26. Looking first at figure 9.26(a) and (b), the total projected delaminated area was found to be greater for the V-structures with a 0°/90° fibre orientation. This is clear from these images with greater delamination in the ridge plane and similar delamination in the crosscut plane much like the 105° V-structures. The shapes of the delaminated areas are similar although the magnitudes are lower for the ±45° V-structure. Looking at the 200 mm V-tip radius simulation results in figure 9.26(c) and (d), The trend is reversed with the ±45° V-structure showing greater delamination in the ridge plane. The source of this difference is unclear as it is only present with this configuration of V-structures at all three charge masses investigated.

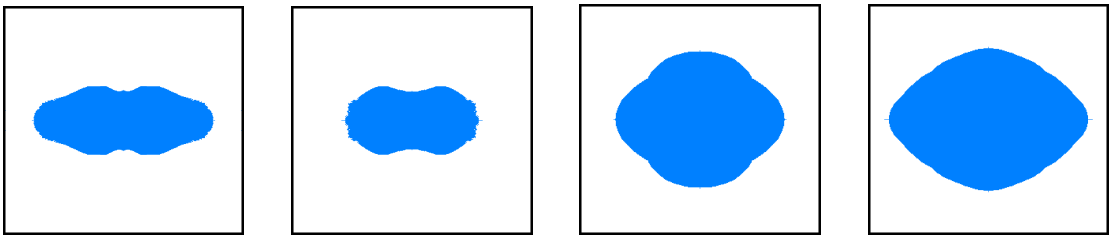

(a) 0°/90°, 62 mm | (b) ±45°, 62 mm | (c) 0°/90°, 200 mm | (d) ±45°, 200 mm

Figure 9.26: Projected total delaminated area for the 120° GFRP V-structure simulations with the two fibre orientations with V-tip radii of 62 mm or 200 mm at a charge mass of 15 g

9.5.2 V-angle effects

Figures 9.27 and 9.28 show the differences in the total projected delaminated area between the V-angles are relatively low for both fibre orientations up to a V-tip radius of 200 mm. It can be seen that at lower V-tip radii, the 105° V-structures display superior blast performance with slightly lower delaminated areas when compared to the 120° V-structures. For a fibre orientation of 0°/90°, this effect is observed to reverse for V-tip radii above 80 mm with the delamination being greater for the 105° V-structures. This transition appears to occur at a V-tip radius of

62 mm for a fibre orientation of ±45°. Once again, it is useful to look at the delaminated area maps between the two V-angled V-structures for the simulations where the greatest differences were observed. Two such cases are shown in figure 9.29. The 105° V-structures have a greater amount of delamination along the ridge and similar delamination in the crosscut plane. This is similar to the trends seen for the fibre orientation comparisons presented in the previous section.

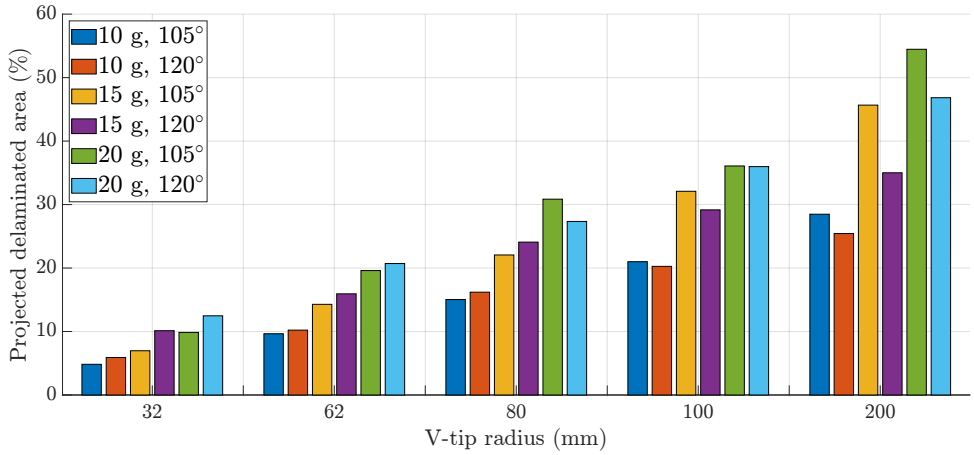

Figure 9.27: Projected delaminated area versus V-angle for the GFRP V-structure simulations with a 0°/90° fibre orientation

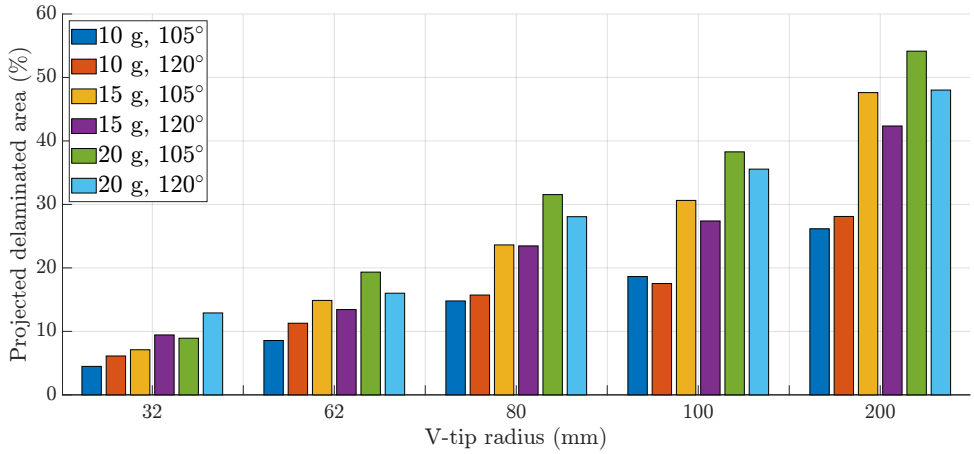

Figure 9.28: Projected delaminated area versus V-angle for the GFRP V-structure simulations with a ±45° fibre orientation

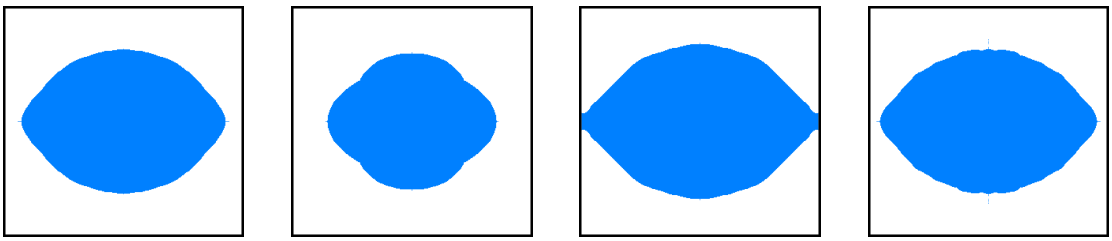

(a) 105°, 15 g (b) 120°, 15 g (c) 105°, 20 g (d) 120°, 20 g

Figure 9.29: Projected total delaminated area for the 105° and 120° GFRP V-structure simulations with a 200 mm V-tip radius and a ±45° fibre orientation and charge masses of 15 g and 20 g

9.5.3 V-tip radius effects

While there were some differences in the delaminated areas between the two fibre orientations investigated, the trends in terms of the changes with V-tip radius are similar and thus only the 0°/90° V-structure graphs are presented here with the additional graphs available in Appendix E. The projected delaminated area is observed to increase for all four V-structure configurations as the V-tip radius is increased. The trends appear to be fairly linear below a V-tip radius of 100 mm, with an apparent reduction in the slope from 100 mm to 200 mm.

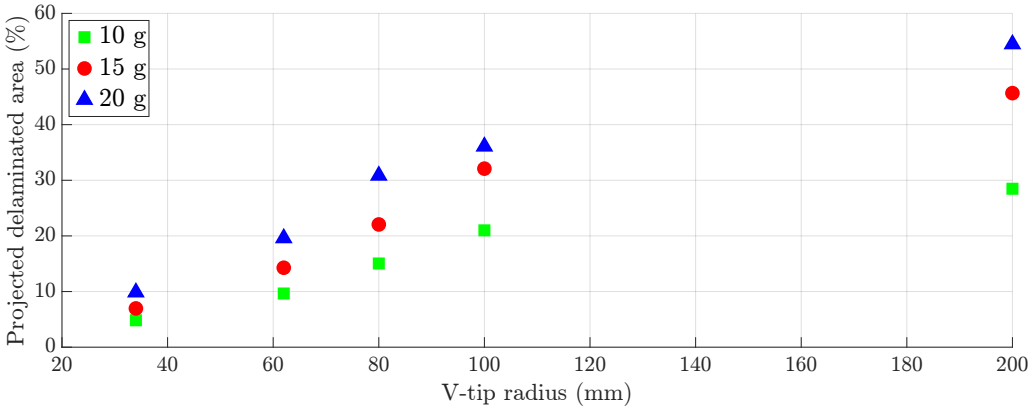

Figure 9.30: Projected delaminated area versus V-tip radius for the 105° GFRP V-structure simulations with a 0°/90° fibre orientation

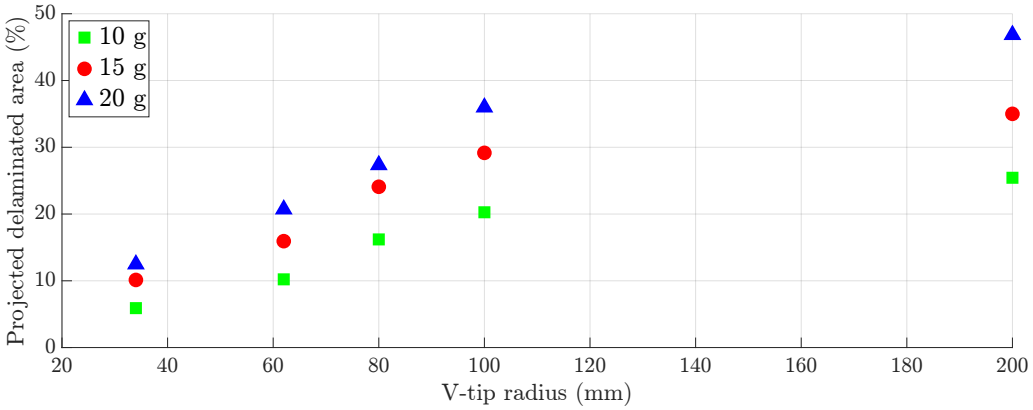

Figure 9.31: Projected delaminated area versus V-tip radius for the 120° GFRP V-structure simulations with a 0°/90° fibre orientation

9.6 The effects of V-structure design parameters on the transient response

For the GFRP V-structure simulations, it was not possible to compare final deformation profiles as material plasticity was not included in the models. The experiments showed little to no permanent deformation beyond some layer separation and thus the final deformation was not of interest. The complete table of peak transient mid-point deflection results is available in Appendix E. The influence of the fibre orientation, V-angle, and V-tip radius of the V-structure on the peak mid-point displacement, mid-point displacement time history, and peak transient

ridge profiles are presented in the following sections.

9.6.1 Fibre orientation effects

Figures 9.32 and 9.33 show the differences in the peak mid-point deflections of the 105° and 120° V-structures with the two fibre orientations investigated. In general, the peak mid-point displacement is fairly similar for the two fibre orientations although the ±45° V-structures experience slightly larger deflections for all V-tip radii and charge masses considered. There is less than a 1.0 mm (5%) difference in all the simulations considered.

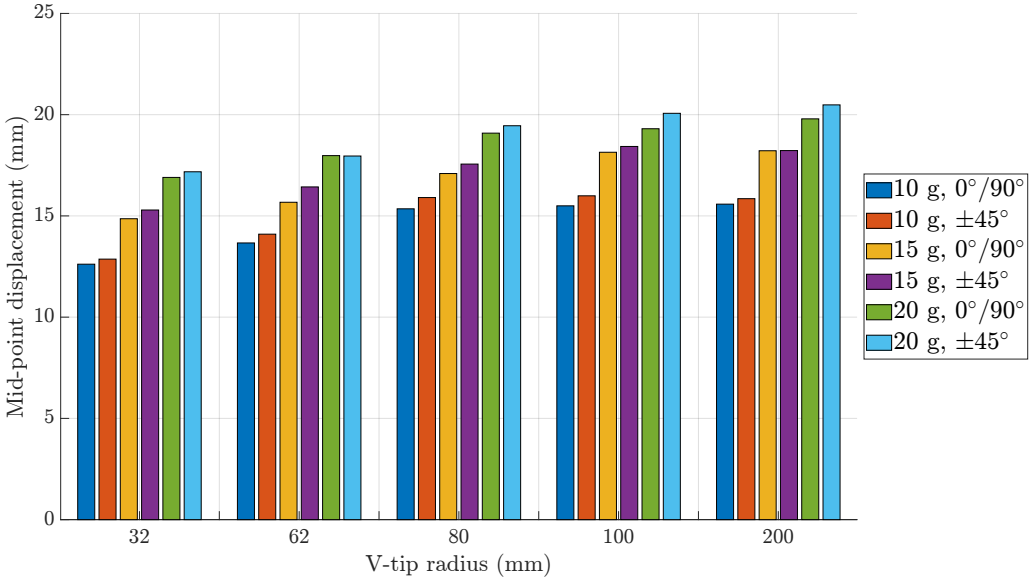

Figure 9.32: Peak mid-point displacement versus fibre orientation for the 105° GFRP V-structure simulations

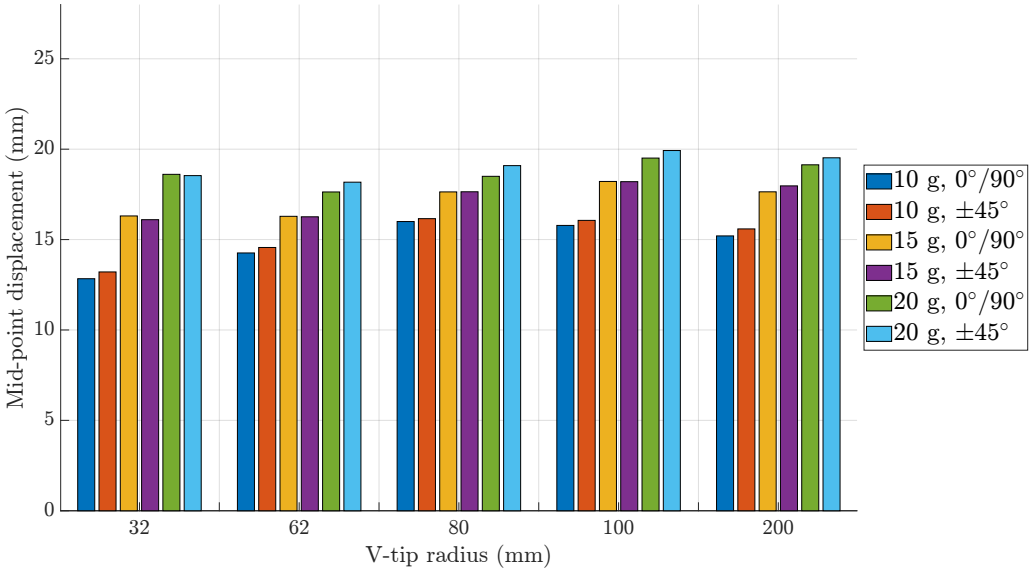

Figure 9.33: Peak mid-point displacement versus fibre orientation for the 120° GFRP V-structure simulations

It is also useful to investigate the influence of the fibre orientation on the mid-point displacement

time histories. The curves are shown in figure 9.34 for 105° V-structures with 34 mm and 200 mm V-tip radii respectively simulated at a charge mass of 10 g. These have been chosen to cover the range of V-tip radii. Additional graphs for selected tests are available in Appendix E. For a V-tip radius of 34 mm, the two curves almost lie on top of one another, while there is a small difference in the post-peak mid-point displacement time histories at a V-tip radius of 200 mm. In general, the response in terms of vibration is fairly similar between the two fibre orientations.

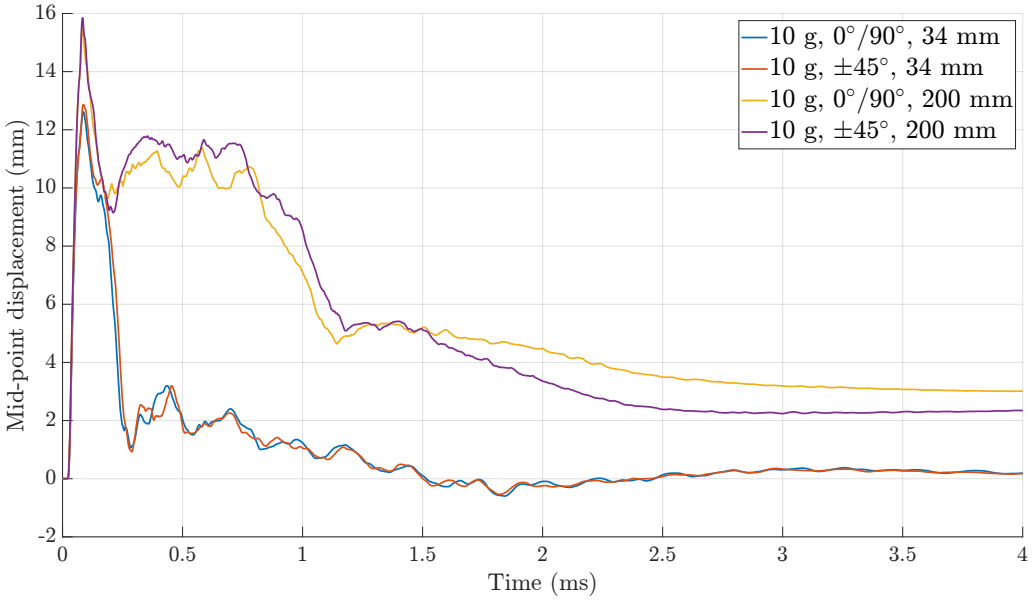

Figure 9.34: Mid-point displacement time history for the 105° GFRP V-structure with 34 mm and 200 mm V-tip radii simulated at a charge mass of 10 g with the two fibre orientations

Finally, looking at the peak transient ridge profiles for the V-structures with the two fibre orientations shown in figure 9.35 for the 105° V-structures with 34 mm and 100 mm V-tip radii respectively simulated at a charge mass of 10 g. There is almost no difference in the ridge profiles between the two fibre orientations for a V-tip radius of 34 mm while the depth of the deformation and the deformed length along the ridge are slightly greater for the ±45° V-structure at a V-tip radius of 200 mm. Thus, it can be concluded that, for the two fibre orientations considered, fibre orientation does not influence the transient displacement response of the GFRP V-structures. Hence, in the remaining comparison, figures will be provided for the V-structure simulations with a 0°/90° fibre orientation.

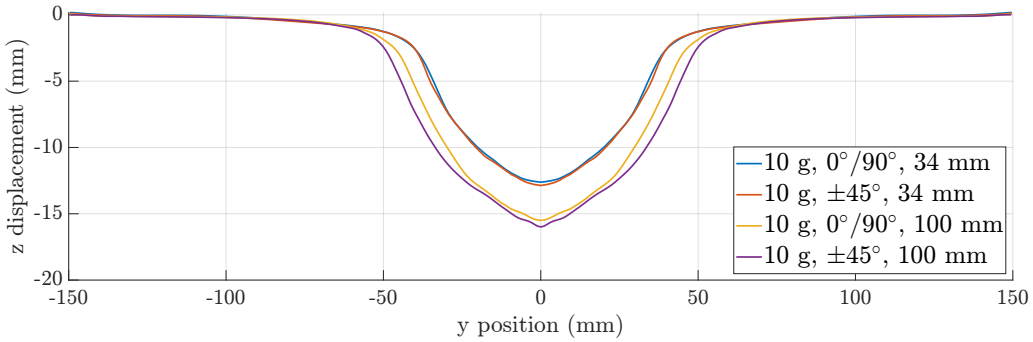

Figure 9.35: Peak transient ridge profiles for the 105° GFRP V-structure with 34 mm and 100 mm V-tip radii simulated at a charge mass of 10 g with the two fibre orientations

9.6.2 V-angle effects

The influence of the V-angle on the peak mid-point displacement is shown in figure 9.36 for the V-structure simulations with a 0°/90° fibre orientation. In general, the 105° V-structures have a lower peak mid-point displacement although the differences are relatively small (<1 mm) for most of the simulation comparisons. Similar to the delamination results, this effect is reversed at a V-tip radius of 200 mm with the 120° V-structures having a lower peak mid-point displacement although the differences are still fairly small (<1 mm).

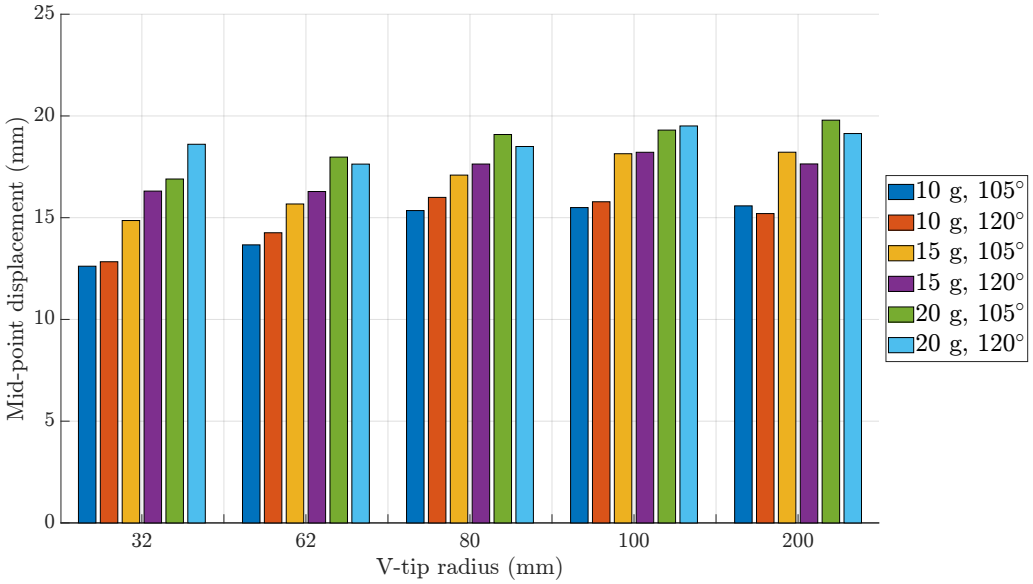

Figure 9.36: Peak mid-point displacement versus V-angle for the GFRP V-structures with a 0°/90° fibre orientation

Once again, it is worth looking at the mid-point displacement time histories for selected simulation comparisons. Figure 9.37 shows the mid-point displacement time histories for the two V-angled V-structure simulations with a 0°/90° fibre orientation and a 34 mm simulated at a charge mass of 10 g. The peak displacement and time of arrival are nearly identical for the two simulations while the post-peak blast response is slightly greater for the 120° V-structure simulation. Similar responses were seen at the other V-tip radii. Additionally, there were no significant differences in the peak transient ridge profiles at all configurations investigated. Thus, in the final analysis

on the influence of V-tip radius on transient displacement, the results presented will be based on the 105° V-structures. All the additional figures are available in Appendix E.

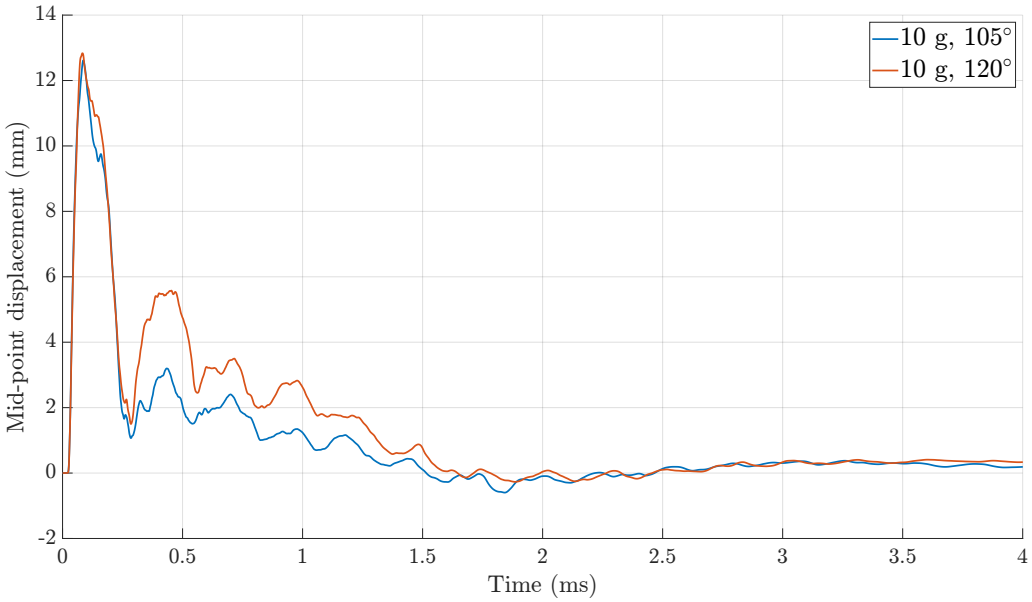

Figure 9.37: Mid-point displacement time histories for 105° and 120° GFRP V-structure simulations with a 0°/90° fibre orientation and a 34 mm V-tip radius simulated at a charge mass of 10 g

9.6.3 V-tip radius effects

The influence of the V-tip radius on the peak mid-point displacement for the 105° V-structure simulations with a 0°/90° fibre orientation is shown in figure 9.38. There is an increase up to a V-tip radius of 80 mm followed by a plateau at the charge masses of 10 g and 20 g. For the 15 g charge, the plateau is seen for V-tip radii above 100 mm. As the V-tip radius is increased there is an approximate increase in the peak mid-point displacement of 3 mm. This increase is the same for all the 105° V-structures regardless of fibre orientation or charge mass. For the 120° V-structures there is an increase in the peak mid-point displacement of approximately 2.5 mm (18%) increase at 10 g, approximately 1.5 mm (10%) increase at 15 g, and approximately 1.0 mm (5%) increase at 20 g.

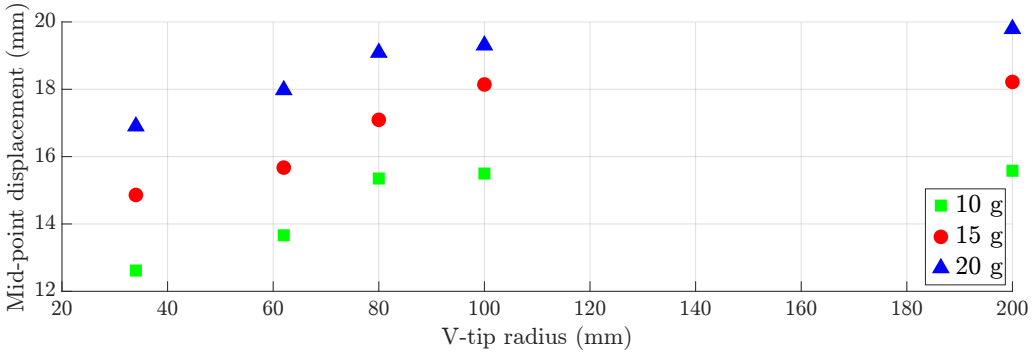

Figure 9.38: Peak mid-point displacement versus V-tip radius for the 105° GFRP V-structures with a 0°/90° fibre orientation

Looking at the mid-point displacement time histories shown in Figure 9.39, the arrival of the first peak is unaffected by the V-tip radius, with only an increase its magnitude. The post-peak behaviour is however different, with the V-structures taking a greater amount of time to return to their initial positions as the V-tip radius is increased. This might be due to the reduced geometric stiffness of the V-structure or the great amounts of delamination seen as the V-tip radius was increased. Finally, looking at the peak transient ridge profiles for an increase in V-tip radius at a charge mass of 10 g shown in figure 9.40, there is an expected increase in the depth of the indentation with an expected increase in the deformed length along the ridge. In general, however, the shape of the deformed profiles remains similar regardless of the V-tip radius of the V-structures simulated.

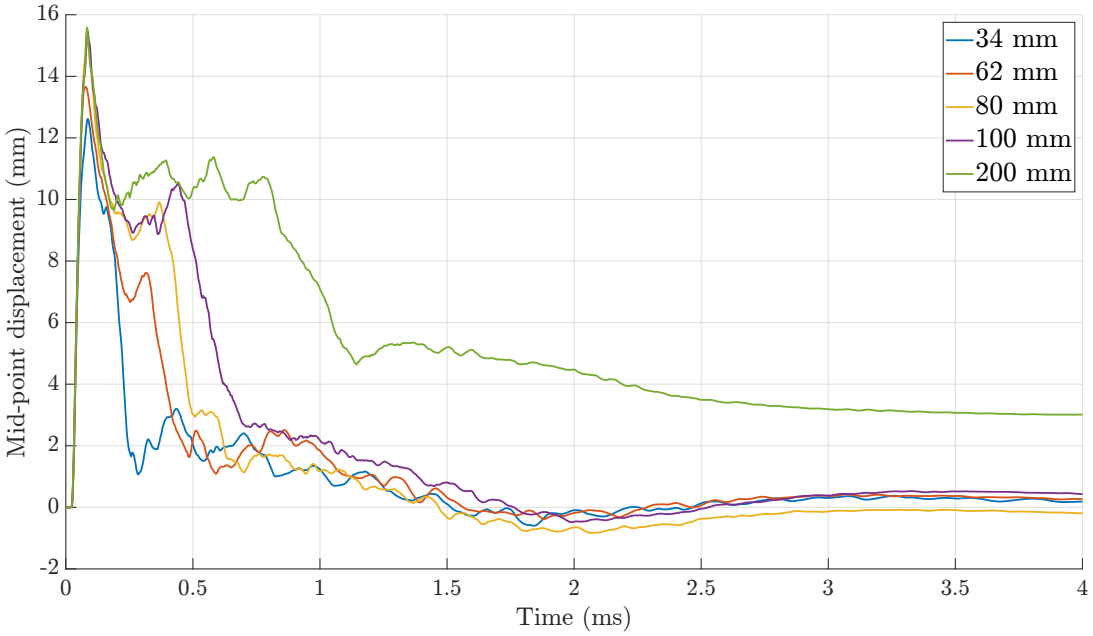

Figure 9.39: Mid-point displacement time histories for 105° GFRP V-structure simulations with a 0°/90° fibre orientation simulated at a charge mass of 10 g

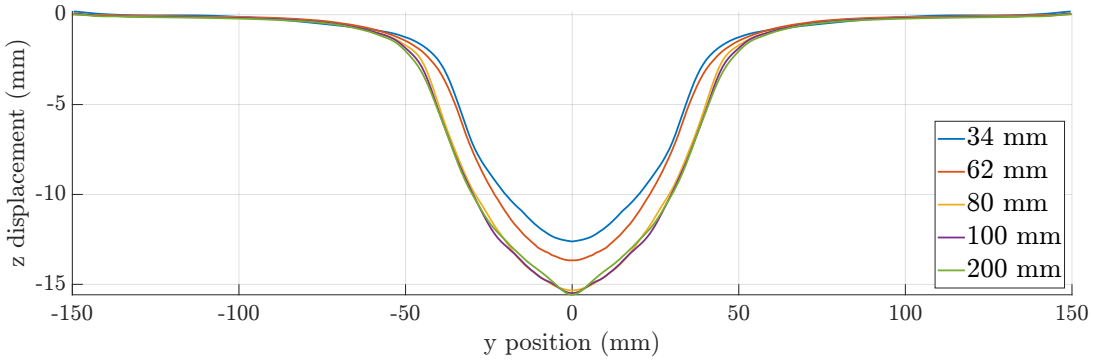

Figure 9.40: Peak transient ridge profiles for 105° GFRP V-structure simulations with a 0°/90° fibre orientation simulated at a charge mass of 10 g

9.7 Summary

The numerical blast model presented in Chapter 8 was extended to model a layered GFRP V-structure. The modelling process included the quasi-static test modelling and material model parameter selection. This model was validated against a set of experimental blast test results that included multiple V-angles, fibre orientations, and charge masses. The validation parameters included the impulse transferred, the delaminated area, and the displacement time histories. The models were able to satisfactorily capture most of the experimentally observed trends and were deemed to be suitable for modelling a larger range of V-structure geometries. The effect of the geometry and lay-up were investigated by considering two V-angles, two fibre orientations, and five V-tip radii. Additionally, three charge masses were investigated. These were chosen in accordance with the blast test experiments on the steel and GFRP V-structures.

The simulated impulse was observed to increase as the V-tip radius, V-angle, and curvature at the V-tip were all increased. This increase was also found to be lower for the larger V-angle considered. The beneficial blast deflection characteristics of the narrower V-angle were less prevalent at the larger V-tip radii investigated (*i.e.* 100 mm and 200 mm) with nearly identical simulated impulses for the V-structures with different V-angles. The fibre orientation was found to have no effect on the simulated impulse, as the impulse appears to be primarily driven by the V-structure geometry.

Considering the final projected delaminated area, similar trends to those observed for the simulated impulse were seen here although the delaminated area shape and amount did appear to be affected by the fibre orientation. The V-angle/V-tip radius combination was also found to influence the delaminated area, with the 105° V-structures showing superior blast performance at lower V-tip radii but the 120° V-structures showing superior blast performance at higher V-tip radii. Transient deflection trends were similar to those seen for the impulse and delaminated area. Blast performance of the narrower V-angled V-structures was superior for V-tip radii up to 80 mm, with the V-angle dominating the deflection characteristics, while the V-tip radius dominates the deflection response at the larger V-tip radii.

Chapter 10

Discussion - V-structure blast performance

The blast performance of the DOMEX-700 MC V-structures was investigated in Chapters 6 and 8, while the blast performance of the GFRP V-structures was investigated in Chapters 7 and 9. This chapter presents a discussion of the results of the steel and GFRP V-structures to identify trends and variations in their blast performances.

10.1 Trends in the impulse transferred

The manufactured GFRP V-structures had a V-tip radius of 34 mm while the steel V-structures had a V-tip radius of 32 mm. To determine if this difference in V-tip radius would affect the impulse transfer characteristics, a single simulation was performed on a 105° steel V-structure with a 34 mm V-tip radius at a charge mass of 20 g. The impulse was found to be 0.17 Ns higher (1.2%) for the 34 mm V-tip radius V-structure simulation when compared to the 32 mm V-tip radius V-structure simulation. Hence, it was reasonable to compare the experimental results for the two V-tip radius V-structures as the influence of this V-tip radius difference was negligible.

The measured impulse results from the blast experiments for the steel and GFRP V-structures were presented in tables 6.2 and 7.2 in Chapters 6 and 7 respectively. The impulse results from these experiments have been tabulated in table 10.1. The impulse can be compared for the 105° steel V-structures with a 32 mm V-tip radius and the 105° GFRP V-structures with a 34 mm V-tip radius for charge masses from 10 g to 40 g. In general, the measured impulse is fairly similar at all four charge masses considered. Additionally, it is also possible to compare the 120° steel V-structures with a 32 mm V-tip radius and the 120° GFRP V-structures with a 34 mm V-tip radius, although this is only possible for a smaller number of charge masses of 10 g and 15 g. Once again, the impulses between the V-structures manufactured from the two materials are fairly similar. The percentage differences in the table were calculated using equation (10.1). These results have been tabulated in table 10.1. The greatest difference is 1.8 Ns (10%) at a charge mass of 20 g for the 105° V-structures.

$$\%\text{Difference} = \frac{\text{Impulse}_{\text{GFRP}} - \text{Impulse}_{\text{steel}}}{\text{Impulse}_{\text{steel}}} \times 100 \tag{10.1}$$

Table 10.1: Comparison of the experimental impulse transferred results between the DOMEX-700 MC and GFRP V-structures

		Impulse (Ns)		
Configuration	Charge mass (g)	Steel	GFRP	Difference (%)
105°, 32 mm	10	10.7	9.7	-1.0 (-10)
	15	14.1	14.4	0.3 (2)
	20	16.0	17.8	1.8 (10)
	40	30.2	31.3	1.1 (3.5)
120°, 34 mm	10	11.5	10.6	-0.9 (-9)
	15	14.7	14.7	0.0 (0)

Further comparisons can be drawn by considering the impulse obtained from the numerical blast simulations. These results have been tabulated in table 10.2. At lower V-tip radii, the same trends observed in the experimentally measured impulse values can be seen for the simulation results. For V-tip radii below 80 mm, the GFRP V-structures provide slightly reduced blast deflection compared with their steel counterparts. The differences in simulated impulse are further increased for a V-tip radius of 200 mm. These differences are between 3 Ns and 4 Ns for a V-tip radius of 200 mm at the larger charge masses considered.

Table 10.2: Impulse (in Ns) obtained from the numerical blast simulations for the DOMEX-700 MC and GFRP V-structures

V-angle (°)	**V-tip radius (mm)**	**Charge mass (g)**								
		10			**15**			**20**		
		Steel	GFRP	% Difference	Steel	GFRP	% Difference	Steel	GFRP	% Difference
105	32	9.44	9.14	-3	12.23	12.03	-2	14.50	14.57	0
	62	9.66	10.30	6	12.70	13.62	7	15.13	16.54	9
	80	10.41	10.59	2	13.58	14.25	5	16.31	17.43	6
	100	10.37	11.25	8	13.66	15.43	11	16.46	18.86	13
	200	11.32	13.37	15	15.16	18.00	16	17.95	22.29	19
120	32	9.94	9.87	-1	12.86	13.08	2	15.16	15.82	4
	62	10.19	10.88	6	13.32	14.38	7	15.97	17.63	9
	80	10.82	11.20	3	14.12	14.93	5	16.87	18.25	8
	100	10.56	11.65	9	13.97	15.66	11	16.82	19.16	12
	200	11.78	13.29	11	15.34	18.03	15	18.60	22.28	17

In order to better understand this effect, it can be useful to overlay the plots of the cumulative impulse and transient mid-point deflection time histories. These are shown in figure 10.1 for the 105° GFRP and steel V-structures with 32 mm and 200 mm V-tip radii simulated at a charge mass of 20 g.

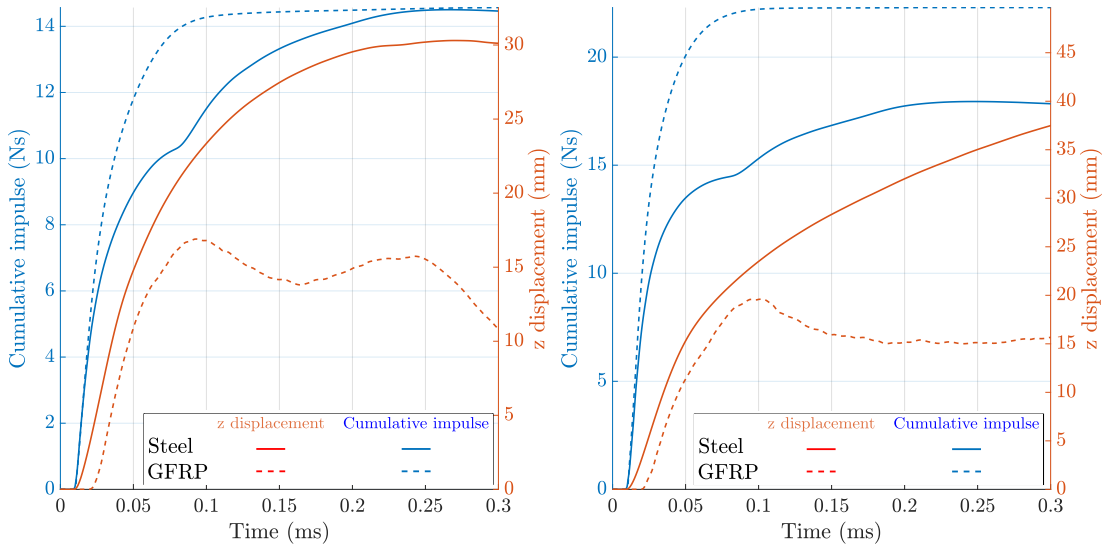

(a) V-tip radius = 32 mm (b) V-tip radius = 200 mm

Figure 10.1: Cumulative impulse and mid-point deflection for the 105° DOMEX-700 MC and GFRP V-structure simulations with 32 mm and 200 mm V-tip radii simulated at a charge mass of 20 g

First considering the cumulative impulse, for a V-tip radius of 32 mm, the total simulated impulse after 0.3 ms are nearly identical in terms of their value for the two materials, as seen by the maximum value on the blue curves in figure 10.1(a). The shapes of these cumulative impulse curves are quite different with the steel only reaching a peak value at approximately 0.25 ms, while the GFRP reaches a peak value at approximately 0.09 ms. At a V-tip radius of 200 mm, shown in figure 10.1(b), the total simulated impulse after 0.3 ms is 19% lower for the steel V-structure simulation. The cumulative impulse curves shapes are similar to those seen for a V-tip radius of 32 mm.

Figure 10.1(a) shows that the GFRP V-structure starts to deform later than the steel V-structure, due to the stress wave needing to propagate through a thicker structure but reaches peak earlier, with the peak deflection observed at 0.093 ms for the GFRP V-structure while the steel V-structure peak deflection is only observed at 0.27 ms. The peak mid-point deflection is also nearly 16 mm greater for the steel V-structure. Figure 10.1(b) shows that, at a radius of 200 mm, the steel V-structure has yet to reach its peak deformation while the total impulse transferred through the structure has reached its plateau. For both V-tip radii, the GFRP V-structure reaches its peak deflection and peak impulse more rapidly than its steel counterpart, but when the V-tip radii is large (200 mm) the slower response of the steel V-structure may have some influence on the lower impulse predicted by the model.

To allow for additional insight to be drawn, it can be useful to look at the transient ridge profiles at key times during the application of the explosive load to the V-structures. These are shown in figure 10.2 for the 105° GFRP and steel V-structures with 32 mm and 200 mm V-tip radii simulated at a charge mass of 20 g. The timesteps chosen correspond to the time of the peak deflection in the GFRP V-structure and the end of the application of the explosive loading at 0.3 ms.

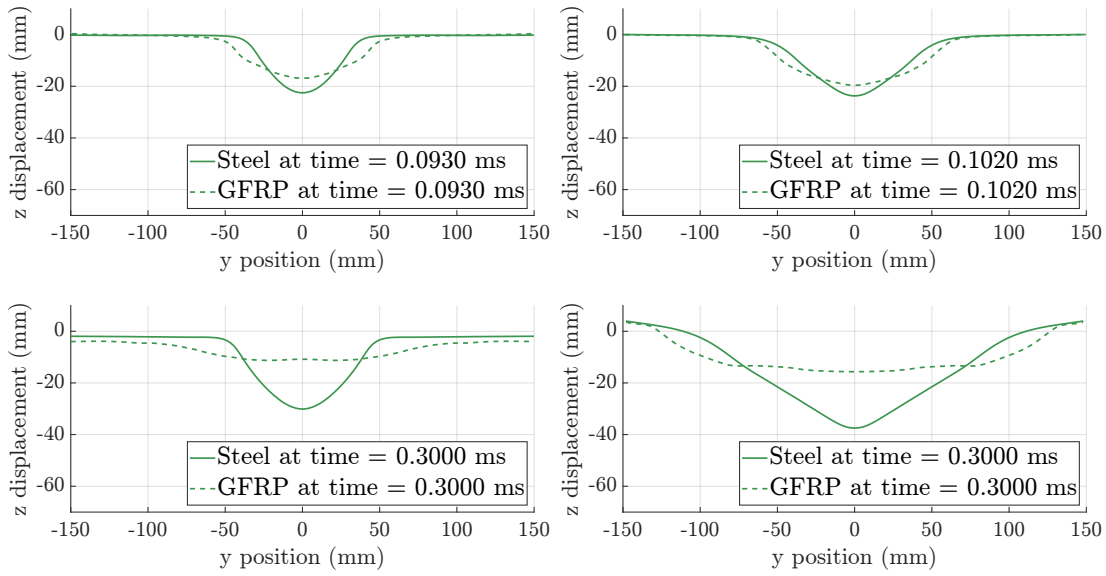

(a) V-tip radius = 32 mm (b) V-tip radius = 200 mm

Figure 10.2: Transient ridge profiles for the 105° DOMEX-700 MC and GFRP V-structure simulations with 32 mm and 200 mm V-tip radii simulated at a charge mass of 20 g

Looking at the left-hand set of profiles in figure 10.2 for a V-tip radius of 32 mm, at the time of peak deformation in the GFRP V-structure (0.0930 ms) the steel V-structure shows a greater depth of the transient ridge profile but the deformation along the ridge is lower than the equivalent GFRP V-structure. Furthermore, at the end of the impulse measurements (0.3 ms), the GFRP V-structure is already rebounding as the elastic energy is dissipated through the structure, while the steel V-structure has reached its peak deformed profile shape. Looking at the right-hand set of profiles for a V-tip radius of 200 mm, once again, at the time of peak deformation in the GFRP V-structure (0.1020 ms) the steel V-structure shows a slightly greater depth of the transient ridge profile but the deformation along the ridge is lower than the equivalent GFRP V-structure. At the end of the impulse measurement, the GFRP V-structure has begun to rebound but has not returned to the initial position with a 15 mm indentation in the V-structure ridge.

These observations suggest that the loading is not impulsive as previously suggested [72] for small SODs, with the deformation of the V-structure influencing its impulse transfer characteristics. This type of loading is considered as "dynamic" implying there may be significant load-structure interaction. It appears that the increase in plastic deformation of the V-structures with the same V-structure geometry results in a lower amount of impulse transferred through the V-structure. The differences in time taken to respond to the loading caused by the material type will influence the extent of the load-structure interaction, affecting the maximum impulse obtained. For small V-tip radii this effect is insignificant, but at larger V-tip radii the effect becomes measurable because of the slower deformation mode of the steel V-structure compared to its GFRP counterpart. The steel V-structures see a greater deformation at all V-tip radii investigated compared to their GFRP counterparts and the energy absorbed in this initial deformation likely reduces the impulse transferred through the structure.

10.2 Trends in the damage propagation

The first thing that needs to be considered is the rupture threshold of the V-structures manufactured from the two materials investigated. Noting that V-structures are used as part of the hull of an MRAP, it can be seen that rupture of the hull could result in permanent damage to any critical driveline components located inside the V-structure. This study was performed experimentally in Chapters 6 and 7 for the 105° V-structures with a 32 mm or 34 mm V-tip radius. The rupture threshold for the steel V-structures was found to be 40 g with large inelastic deformation being the primary mode of failure for charge masses below this critical value. For the GFRP V-structures, the rupture threshold was found to be 20 g. At charge masses below this critical value, the failure modes observed in the GFRP V-structures included interlaminar delamination, fibre failure, and matrix failure, with delamination being the dominant failure mode. Thus, at larger charge masses, the steel V-structures are expected to provide superior blast performance compared to the equivalent mass GFRP V-structures.

Another method of comparing the damage propagation is to look at the extent of failure along the ridge profile for the two materials investigated. This can be done by tracking the delamination progression along the ridge for the GFRP V-structures and looking at the permanent ridge profiles for the steel V-structures, for increases in charge mass and V-tip radii. Repeated below in figures 10.3 and 10.4 are the permanent ridge profiles for the 105° steel V-structures simulated at charge masses of 15 g and 20 g respectively. At 15 g, it can be seen that permanent deformation along the entire ridge length is present for a V-tip radius of 200 mm, while at 20 g, permanent deformation is present along the entire ridge length for V-tip radii above 100 mm. The equivalent GFRP V-structures are shown in figures 10.5 and 10.6. In each figure, the dimensions are 300 mm by 300 mm with the ridge plane running horizontally across the middle of each delaminated area map. From figure 10.5, the delaminated area does not extend to the edge of the ridge for any of the V-tip radii investigated at a charge mass of 15 g. Looking at figure 10.6, the delamination is far greater at a charge mass of 20 g extending along the entire ridge for V-tip radii above 100 mm. Thus, considering the 105° V-structures, the GFRP V-structures display slightly superior performance at the lower charge masses considered, while at charge masses of 20 g and above, the V-structure performance is similar in terms of permanent damage. This numerical simulation analysis does not account for panel rupture, which may affect the overall V-structure response if included in the simulations.

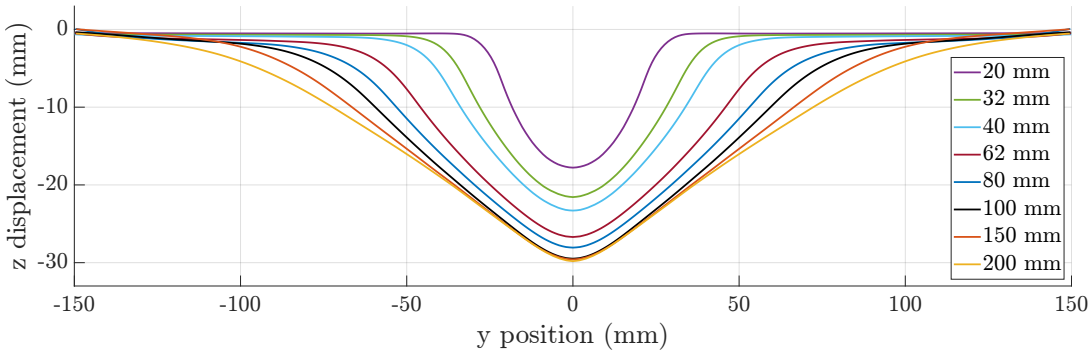

Figure 10.3: Plots of the permanent ridge profiles for increasing V-tip radii for the 105° DOMEX-700 MC V-structure simulations at a charge mass of 15 g

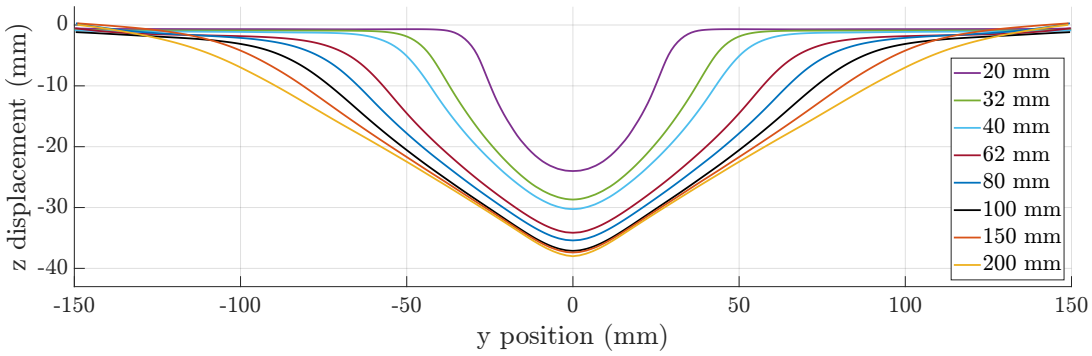

Figure 10.4: Plots of the permanent ridge profiles for increasing V-tip radii for the 105° DOMEX-700 MC V-structure simulations at a charge mass of 20 g

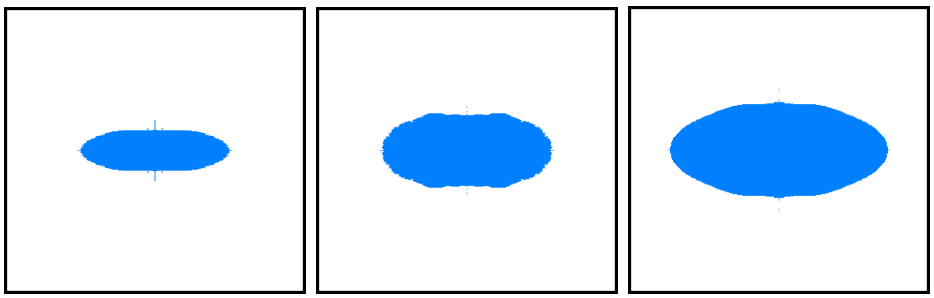

(a) 34 mm (b) 62 mm (c) 80 mm

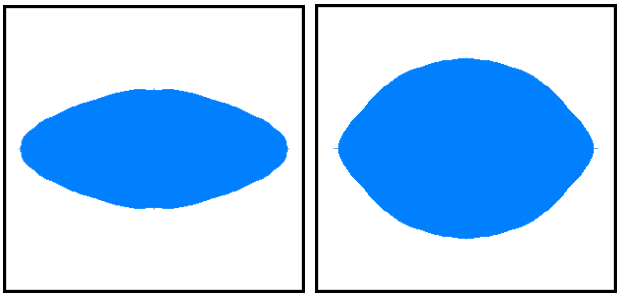

(d) 100 mm (e) 200 mm

Figure 10.5: Projected total delaminated area for the 0°/90°, 105° GFRP V-structure simulations with increasing V-tip radii for a charge mass of 15 g

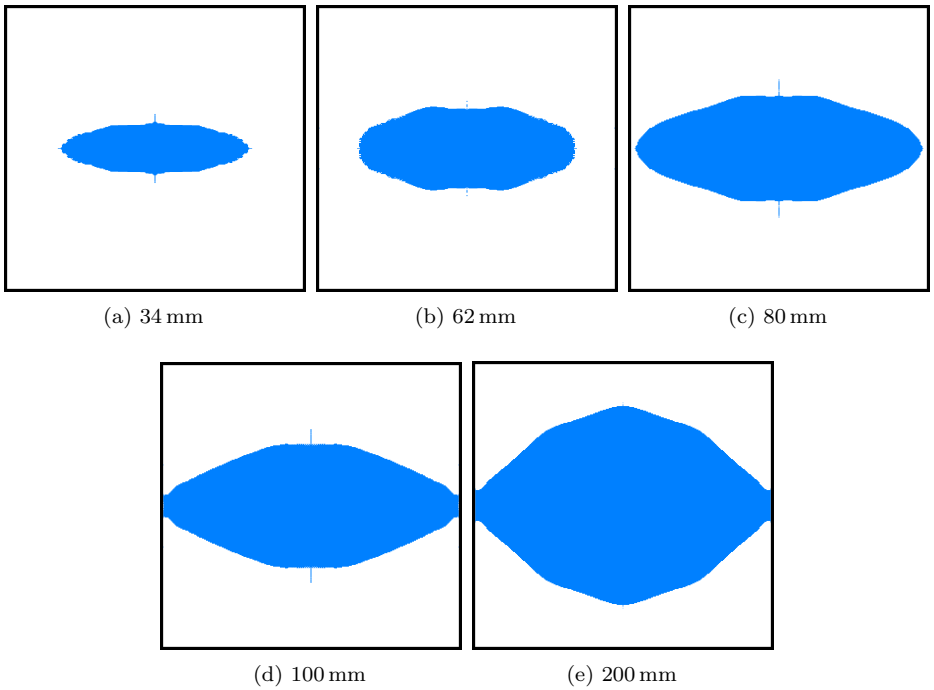

(a) 34 mm (b) 62 mm (c) 80 mm

(d) 100 mm (e) 200 mm

Figure 10.6: Projected total delaminated area for the 0°/90°, 105° GFRP V-structure simulations with increasing V-tip radii for a charge mass of 20 g

10.3 Comparison of the transient response

Due to difficulties with the paint and material spalling, the transient measurements from experiments were incomplete, so this information is supplemented by the numerical simulation results. The peak mid-point deflections obtained from the steel and GFRP simulations have been tabulated and compared in table 10.3. The differences between the peak deflections are also provided in the table.

Table 10.3: Peak mid-point deflection (in mm) obtained from the numerical blast simulations for the DOMEX-700 MC and GFRP V-structures

V-angle (°)	**V-tip radius (mm)**	**Charge mass (g)**								
		10			**15**			**20**		
		Steel	GFRP	Difference	Steel	GFRP	Difference	Steel	GFRP	Difference
105	32	15.01	12.62	2.4	24.55	14.86	9.7	32.53	16.90	15.6
	62	20.48	13.66	6.8	30.92	15.67	15.2	39.18	17.98	21.2
	80	22.72	15.35	7.4	32.75	17.09	15.7	41.02	19.09	21.9
	100	24.46	15.50	9.0	34.68	18.14	16.5	43.14	19.31	23.8
	200	29.46	15.58	13.9	41.05	18.22	22.8	49.66	19.79	29.9
120	32	18.56	12.84	5.7	29.51	16.31	13.2	38.56	18.61	20.0
	62	22.68	14.26	8.4	34.20	16.29	17.9	43.58	17.63	25.9
	80	24.29	16.00	8.3	35.19	17.64	17.6	44.58	18.50	26.1
	100	25.84	15.78	10.1	37.18	18.22	19.0	46.85	19.51	27.3
	200	29.36	15.20	14.2	41.27	17.64	23.6	50.73	19.14	31.6

Peak mid-point deflection is of particular interest because it could indicate the ingress of the V-structure into the interior of the MRAP. If these values are too large, critical components could potentially be damaged. Thus, minimizing this deflection is a key design parameter. For all configurations investigated, the peak mid-point deflection was found to be lower for the GFRP V-structures when compared to the equivalent geometry steel V-structures. In general, this difference increases with an increase in charge mass across the configurations considered. For V-tip radii between 62 mm to 100 mm there is a plateau with the differences remaining fairly consistent between the two steel and GFRP V-structures. Finally, at a V-tip radius of 200 mm the difference is approximately 14 mm for the 105° and 120° V-structures, approximately 14 mm at 10 g, and approximately 23 mm at 15 g, and approximately 30 mm at 20 g. The lower deflections observed in the GFRP V-structures can be explained by the additional second moment of area stiffness resulting from the increased thickness of the V-structure when compared to the equivalent mass steel V-structures (*i.e.* approximately 9 mm versus 2 mm). This panel thickness effect remains at all the V-tip radii investigated, which explains the consistently lower peak mid-point deflection. Thus, in terms of peak mid-point deflection, the GFRP V-structures display superior blast performance when compared to their steel counterparts.

Chapter 11

Conclusions and recommendations

11.1 Conclusions

This thesis aimed to compare equivalent mass V-structures manufactured from steel and GFRP to determine if the GFRPs were a viable alternative to armour steels for the construction of V-hulls of MRAPs. This was done with the use of blast experiments and numerical blast models developed in LS-DYNA.

Two manufacturing approaches were trialled for the GFRP V-structures both of which utilised VI. The first approach used a male mould with VI manufacture. This approach was found to produce an inconsistent radius at the V-tip of the V-structures which was not optimal when attempting to answer the research questions. A female mould was next trialled and was found to produce V-structures with a consistent V-tip radius when used with VI.

From the experimental study, the rupture threshold of the GFRP V-structures was found to be significantly lower, at 20 g, compared to their steel counterparts, at 40 g. When this was extended with the numerical simulations, the GFRP V-structures displayed lower total delamination at lower charge masses than the amount of permanent deformation seen in the steel V-structures. At larger charge masses, the two materials displayed similar performance in terms of total permanent damage. The transient deformation was lower in the GFRP V-structures for all the configurations investigated numerically. This was attributed to the greater second moment of area resulting from the thickness difference between the steel and GFRP V-structures.

When comparing the impulse transferred, a 2 mm increase in V-tip radius from 32 mm to 34 mm resulted in only a 0.17 Ns (1.2%) increase in the simulated impulse. This finding increased the confidence in the measured impulse comparison between the steel and GFRP V-structures. The impulse values were also nearly identical for the steel and GFRP V-structures up to a V-tip radius of 100 mm. At the largest V-tip radius, there was a significant deviation between the two materials investigated. When the cumulative impulse was overlaid against the mid-point deflection for a V-tip radius of 200 mm, it was seen that the GFRP V-structures experience their peak deformation earlier than the equivalent steel V-structure but the deformation was significantly lower in magnitude. The overall geometric shape of the V-structures remained mostly unchanged during the tests due to the localised blast loading. Thus, it is likely that the energy absorbed in the additional plastic deformation of steel V-structures results in a reduction in the impulse transferred while retaining the blast deflection characteristics of the V-structure shape.

The influence of the V-angle and V-tip radius on the blast performance of the V-structures was

investigated with both the experimental blast tests and numerical simulations. Firstly, looking at the steel V-structures, there was an observed linear increase in impulse for all three V-angles. Additionally, at V-tip radii above 100 mm, the impulse was found to be similar at all three V-angles. This was likely due to the increased influence of the V-tip radius and the reduction in the beneficial blast deflection characteristics of the narrower V-angles at these large V-tip radii investigated.

Looking at the peak and final mid-point deflections, for small V-tip radii and at narrower V-angles, there is only a small difference (1 mm to 2 mm) between the peak and final deflections, with this V-structure geometric stiffness decreasing with both an increase in V-angle and V-tip radius. A bilinear trend could be seen in the peak mid-point displacement for an increase in the V-tip radius, with the changeover point occurring at 80 mm. The final mid-point displacement was observed to plateau for V-tip radii above 100 mm. Much like the impulse results, the peak and final mid-point deflections were similar for all three V-angles for V-tip radii above 100 mm. This was likely due, once again, to the increased influence of the V-tip radius on the response of the V-structures. The mid-point displacement time histories revealed an increase in the time to peak displacement and an increase in the post-peak vibration amplitude for an increase in V-tip radius. The vibration frequency was also found to decrease as the V-tip radius was increased. The final ridge and the crosscut profiles saw an increase in the depth and length of the deformed region for an increase in V-tip radius. The entire ridge line was observed to permanently deform for V-tip radii above 80 mm. These trends were also attributed to the reduced geometric stiffness of the V-structure profile when the V-tip radius was increased.

Similar trends to those reported for the steel V-structures were observed in the GFRP V-structures in terms of impulse transferred. The 105° V-structures displayed superior blast performance (*i.e.* lower delamination) at lower V-tip radii but the 120° V-structures performed better at the larger V-tip radii. The transient deformation behaviour closely matched the behaviour seen for the simulated impulse and delaminated area with the narrower V-angled V-structures showing lower deflections below a V-tip radius of 80 mm and having little to no effect at the larger V-tip radii investigated.

For the GFRP V-structures, two fibre orientations were also investigated, namely, 0°/90° and ±45°, both using plain weave E-glass. In the experiments, it was found that the impulse transferred and total projected delaminated areas were nearly identical for the two layups. This finding was further confirmed in the numerical blast simulations. Where it was observed that regardless of charge mass, V-angle, or V-tip radius, the two fibre orientations considered in this study did not significantly influence the structural response and damage propagation of the GFRP V-structures. These findings suggest that the response and damage propagation for these thick GFRP V-structures is primarily driven by the geometric stiffness (*i.e.* The profile of the V-structure shape) and the second moment of area effects (*i.e.* the thickness of the GFRP V-structures).

Thus, the research questions posed at the start can be listed and answered.

How does charge mass influence impulse transfer, transient deformation and damage progression in air-blast tested GFRP and equivalent mass DOMEX-700 MC steel V-structures?

The blast tests performed on the steel and GFRP V-structures found that increasing the charge mass resulted in an increase in impulse transferred, transient deformation, and damage progression. This was found to be true in both the experiments and the extended set of numerical simulations for all the V-structure configurations investigated.

What effect does the V-tip geometry (V-angle and V-tip radius) have on impulse transfer and structural damage characteristics of GFRP and equivalent mass DOMEX-700 MC steel V-structures?

For both the steel and GFRP V-structures, for smaller V-tip radii, the narrower V-angled V-structures displayed superior blast performance in terms of impulse transferred and total damage (plastic deformation or delaminated area). However, at larger V-tip radii, the beneficial blast deflection characteristics of the narrower V-angle were diminished as the blast response appeared to be dominated by the curvature at the V-tip.

Can GFRPs be used in place of steel in the construction of V-structures without altering the protection of the V-structures?

In general, GFRP cannot be used in place of steel in the construction of V-structures due to their reduced rupture threshold. In particular, at larger charge masses and larger V-tip radii, the inability for the GFRP V-structures to plastically deform results in a reduction in their ability to absorb energy from the blast load when compared to the equivalent steel V-structures. However, at lower charge masses and V-tip radii, the GFRP V-structures do display similar impulse transfer and total damage characteristics and at larger V-tip radii, the peak deflection is significantly lower than the equivalent steel V-structure.

Finally, the hypothesis posed at the start of the research can be evaluated.

GFRP V-structures have a superior blast performance when compared to equivalent mass armoured steel V-structures, measured in terms of impulse transfer and structural response, for a range of air-blast loading scenarios.

Thus, in terms of the peak and final mid-point deformation, and cumulative damage, it can be concluded that at lower charge masses (10 g to 15 g), the GFRP V-structures have a superior blast performance when compared to equivalent mass armoured steel V-structures. It should, however, be noted that the GFRP V-structures are likely to have reduced strength post exposure to a blast in the region along the ridge where delamination and fibre fracture are present. At larger charge masses (> 20 g), the steel V-structures display superior blast performance as the GFRP V-structures would have ruptured which would result in explosive residue and material ingress into an MRAP that utilised such a V-hull.

11.2 Recommendations

It would be useful to investigate the residual strength present in such V-structures both in terms of their material properties and their blast resistance capability. This could be done by performing repeated blast loads on steel and GFRP V-structures and investigating the changes in transient deformation, variations in the amounts of each failure mode, and changes in their ability to resist impulse transfer.

This work demonstrated the significance of boundary conditions to the overall structural response. This was observed through the elastic vibrations of the clamp frames in the numerical blast model development. In future tests, the clamp frame should be speckled and its transient response measured using the same DIC techniques used on the V-structures.

It was observed that the thickness of the GFRP V-structures had a significant effect on their response compared to the material properties. Additionally, only two fibre orientations with plain weave E-glass fibres were considered in this study. Further work is recommended to ascertain to optimum lay-up and manufacturing approach for GFRP V-structures, through a combination of modelling and blast experiments on prototypes. Alternative materials could also be investigated, such as nano materials (nanoscale reinforcements such as carbon nanotubes or graphene platelets) which can be used as reinforcement in V-structures.

It would also be useful to investigate the blast performance of GFRP V-structures manufactured from fewer plies of glass fibre to investigate how the reduced second moment of area influences their structural response versus the weight reduction benefits of a thinner composite structure. The numerical modelling techniques presented herein could be applied to these reduced thickness V-structures to investigate additional configurations.

The numerical simulations performed on the steel V-structures used a Johnson-Cook material model, which was found to reasonably capture the V-structure deformation although the material model did not include rupture. In order to increase the usefulness of the model as a design tool, it would be beneficial to update the model to include tearing failure and thus characterise the failure threshold of the various steel V-structure geometries numerically. Additional material tests are recommended to determine if there are any strain rate effects on the yield strength and failure strain in the DOMEX-700MC steel and to determine the rupture threshold for the material for the damage model.

Similarly, the numerical simulations on the GFRP V-structures included delamination but utilised an orthotropic elastic material model for the glass fibre plies. This model did not include fibre rupture. It would be useful to extend the numerical models to include fibre rupture with the use of one of the composite damage models inside LS-DYNA. This model could then be used to find the rupture threshold for the various V-structure configurations studied. In order to better characterise the fibre fracture response, additional material testing is recommended to further populate the fibre damage model. Some high rate fracture tests can also be performed to better capture the delamination observed in the blast tests. This model could also be extended to consider each ply as a separate layer of shell elements.

Additional experiments with blast pressure gauges placed at similar locations to those used in the numerical model may be conducted and used as a numerical validation tool. This would help guarantee the accuracy of the modelling of the blast loading on the target V-structures. As the imaging technology and speckling techniques improves, it will become possible to film at higher frame rates, this might help with the removal of the motion blur and thus allow the initial deformation of the V-structures to be determined. This data could then be processed to obtain the strain fields across the imaged area of the V-structures and thus allow for the strain energy across the imaged region to be obtained.

It would be beneficial to investigate the influences of the noise on the 3D scanned blast tested steel V-structures. If multiple repeat tests are performed and curves are fitted to the permanently deformed ridge profile results, a study into the variance of the measured deformation could be performed. These repeat tests can also be used to determine the variance in the experimental results for impulse.

A few full-scale experiments would also be a useful way to check that the results obtained for these scaled V-structure experiments and simulations represent the blast responses and failure modes seen in V-structures used for the hulls of MRAPs.

When the results of the GFRP and steel V-structure simulations were compared, it was found that the steel V-structures displayed superior impulse transfer characteristics are the larger V-tip radii investigated. Further investigation into the cumulative impulse and the deformation-time histories revealed that the material response influences the impulse transferred even at small SODs of 34 mm. It would be useful to investigate this further both experimentally and numerically by manufacturing V-structures with larger V-tip radii and conducting similar tests.

Damage from fragmentation is a common when MRAPs are subjected to landmine or IED explosions. It would be useful to extend the research performed with bare charges on V-structures to include encased charges and charges with embedded fragments.

References

[1] Stiff, P. *Taming the Landmine*. Galago, 1986.

[2] McGrath, R. *Landmines And Unexploded Ordnance: A Resource Book*. Pluto Press, 2000. DOI: 10.2307/j.ctt18fsb7f.

[3] Wilson, C. *Improvised Explosive Devices (IEDs) in Iraq and Afghanistan: Effects and Countermeasures: CRS Report for Congress*. Tech. rep. Defense Technical Information Center (DTIC), 2006.

[4] O'Lionnain, E. *Armoured car, Army Museum Stockholm*. Online. Aug. 2008. URL: https://commons.wikimedia.org/wiki/File:Armoured_car,_Army_Museum_Stockholm.jpg.

[5] Lester, C. *Protection of Light Skinned Vehicles Against Landmines - A Review*. Tech. rep. DTIC Document, 1997.

[6] Uddin, N. *Blast Protection of Civil Infrastructures and Vehicles Using Composites*. Woodhead Publishing Series in Civil and Structural Engineering. Elsevier Science, 2010. DOI: 10.1533/9781845698034.

[7] Gibson, R. F. *Principles of Composite Material Mechanics*. 3rd ed. CRC Press, 2011. DOI: 10.1201/b14889.

[8] Chung Kim Yuen, S., Langdon, G. S., Nurick, G. N., Pickering, E. G., and Balden, V. H. "Response of V-shape Plates to Localised Blast Load: Experiments and Numerical Simulation". *International Journal of Impact Engineering* 46 (2012), pp. 97–109. DOI: 10.1016/j.ijimpeng.2012.02.007.

[9] Follett, S. "Blast Analysis Of Composite V-shaped Hulls: An Experimental And Numerical Approach". PhD thesis. Cranfield University, July 2012.

[10] Langdon, G. S. and Shekhar, V. R. "The effect of the bend radius on the impulse transfer characteristics of V-hulls: Numerical simulations". *International Journal of Protective Structures* 11.1 (June 2019), pp. 69–89. DOI: 10.1177/2041419619853292.

[11] GICHD. *Guide to Mine Action*. 5th ed. GICHD (Geneva International Centre for Humanitarian Demining), Mar. 2014.

[12] ICRC. "Anti-personnel Landmines: Friend Or Foe?: A Study of the Military Use and Effectiveness of Anti-personnel Mines". In: *International Affairs (Royal Institute of International Affairs 1944-)*. Vol. 72. ICRC publications 4. ICRC (International Committee of the Red Cross), 1996, p. 100.

[13] Youngblood IV, N. E. "The development of landmine warfare". 4.57 (2002), pp. 11–25.

[14] Keeley, R. *Understanding landmines and mine action*. Tech. rep. 9. 2003.

[15] Ramasamy, A., Masouros, S. D., Newell, N., Hill, A. M., Proud, W. G., Brown, K. A., Bull, A. M. J., and Clasper, J. C. "In-vehicle extremity injuries from improvised explosive devices: current and future foci". *Philosophical Transactions of the Royal Society B: Biological Sciences* 366.1562 (2011), pp. 160–170. DOI: 10.1098/rstb.2010.0219.

[16] Salzar, R. S. "Development of Injury Thresholds Pertaining to Under-Body Blasts". *US Army MRMC, Fort Detrick, MD* (2013).

[17] Commandeur, J., Derksen, R. J., MacDonald, D., and Breederveld, R. "Identical fracture patterns in combat vehicle blast injuries due to improvised explosive devices; a case series". *BMC emergency medicine* 12.1 (2012), pp. 1–5.

[18] Erdik, A. "Investigation of dynamic response of a mannequin in a vehicle exposed to land mine blast". *Sakarya University Journal of Science* 23.3 (2019), pp. 382–389.

[19] Cong, M., Zhou, Y.-b., Zhang, M., Sun, X.-w., Chen, C., and Ji, C. "Design and optimization of multi-V hulls of light armoured vehicles under blast loads". *Thin-Walled Structures* 168 (2021), p. 108311.

[20] Livesey, J. *The Illustrated Guide to Armoured Fighting Vehicles of the World*. Hermes House, 2006.

[21] Guardia, M. and Morshead, H. *US Army and Marine Corps MRAPs: Mine Resistant Ambush Protected Vehicles*. Vol. 1. New Vanguard 4. Bloomsbury Publishing, 2013.

[22] Pakulski, K., Johnson, J., Giffin, R., Lo, M., Wise, D., St Onge, P., Balcena, P., Fridie, M., Barrett, A., and AL, A. A. R. L. F. R. "Prevention of injury in mine resistant ambush protected (MRAP) vehicle accidents". *US Army Aeromedical Research Laboratory Report* 2013-14 (2013).

[23] Ramasamy, A., Hill, A. M., Masouros, S. D., Gordon, F., Clasper, J. C., and Bull, A. M. "Evaluating the effect of vehicle modification in reducing injuries from landmine blasts. An analysis of 2212 incidents and its application for humanitarian purposes". *Accident Analysis and Prevention* 43.5 (2011), pp. 1878–1886. DOI: 10.1016/j.aap.2011.04.030.

[24] AMISOM. *Bakaara Market, Mogadishu, Somalia - Life is returning to Bakaara Market, the key economic hub of Mogadishu, after the withdrawal of Al-Shabaab from the capital on the 6th August 2011. PRESS HANDOUT - AU/UN IST/ANTHONY HUNT*. Online. Sept. 2011. URL: https://commons.wikimedia.org/wiki/Category:Casspir#/media/File:Bakaara_Market_(6152937169).jpg.

[25] O'Malley, T. J. and Hutchins, R. *Fighting Vehicles: Armoured Personnel Carriers & Infantry Fighting Vehicles*. 1996.

[26] ASTM Standard D3878-15 (2015). *Standard Terminology for Composite Materials*. Tech. rep. West Conshohocken, PA, 2015.

[27] Hull, D., Clyne, T. W., Derek Hull, and Clyne, T. W. *An Introduction to Composite Materials*. Cambridge Solid State Science Series. Cambridge University Press, 1996. DOI: 10.1017/9781139050586.

[28] Campbell, F. C. *Structural Composite Materials*. ASM International, 2010. DOI: 10.31399/asm.tb.scm.9781627083140.

[29] Kaw, A. K. *Mechanics of Composite Materials*. 2nd ed. Mechanical and Aerospace Engineering Series. CRC Press, 2006. DOI: 10.1201/9781420058291.

[30] Gay, D., Hoa, S. V., and Tsai, S. W. *Composite Materials*. 2nd ed. Taylor & Francis, 2003. DOI: 10.1201/9781420045208.

[31] Vasiliev, V. V. and Morozov, E. *Mechanics and Analysis of Composite Materials*. Elsevier Science, 2013.

[32] Hoa, S. V. *Principles of the Manufacturing of Composite Materials*. DEStech Publications, Incorporated, 2009.

[33] Long, A. C. *Design and manufacture of textile composites*. Elsevier, 2005. DOI: 10.1533/9781845690823.

[34] Teeling-Smith, R. G. and Nurick, G. N. "The deformation and tearing of thin circular plates subjected to impulsive loads". *International Journal of Impact Engineering* 11.1 (1991), pp. 77–91. DOI: 10.1016/0734-743x(91)90032-b.

[35] Nurick, G. N., Gelman, M. E., and Marshall, N. S. "Tearing of blast loaded plates with clamped boundary conditions". *International journal of impact engineering* 18.7-8 (1996), pp. 803–827. DOI: 10.1016/s0734-743x(96)00026-7.

[36] Nurick, G. N. and Radford, A. M. "Deformation and tearing of clamped circular plates subjected to localised central blast loads". *Recent developments in computational and applied mechanics: a volume in honour of John B. Martin* (1997), pp. 276–301.

[37] Jacob, N., Chung Kim Yuen, S., Nurick, G. N., Bonorchis, D., Desai, S. A., and Tait, D. "Scaling aspects of quadrangular plates subjected to localised blast loads - Experiments and predictions". *International Journal of Impact Engineering* 30 (Sept. 2004), pp. 1179–1208. DOI: 10.1016/j.ijimpeng.2004.03.012.

[38] Nurick, G. N., Mahoi, S., and Langdon, G. S. "The response of plates subjected to loading arising from the detonation of different shapes of plastic explosive". *International Journal of Impact Engineering* 89 (2016), pp. 102–113. DOI: 10.1016/j.ijimpeng.2015.11.012.

[39] Jacob, N., Nurick, G. N., and Langdon, G. S. "The effect of stand-off distance on the failure of fully clamped circular mild steel plates subjected to blast loads". *Engineering Structures* 29.10 (2007), pp. 2723–2736. DOI: 10.1016/j.engstruct.2007.01.021.

[40] McDonald, B., Bornstein, H., Langdon, G. S., Curry, R., Daliri, A., and Orifici, A. C. "Experimental response of high strength steels to localised blast loading". *International Journal of Impact Engineering* 115.October 2017 (2018), pp. 106–119. DOI: 10.1016/j.ijimpeng.2018.01.012.

[41] Langdon, G. S., Chung Kim Yuen, S., Nurick, G. N., and Naidoo, K. "Some Insights into the Response of "Shallow V Shape" Structures to Air Blast Loading". *Proceedings of the National Academy of Sciences* (2013), pp. 695–703. DOI: 10.16943/ptinsa/2013/v79i4/48002.

[42] Langdon, G., Curry, A., and Siddiqui, A. "Improving the impulse transfer and response characteristics of explosion loaded compound angle V-plates". *Thin-Walled Structures* 148 (2020), p. 106609. DOI: 10.1016/j.tws.2020.106609.

[43] James Madison University - CISR Reference. *Landmines - Afghanistan Ordnance Identification Guide*. Online. URL: https://www.jmu.edu/cisr/_pages/research/afghanistan-oig/index.shtml.

[44] Mouritz, A. P. "Advances in understanding the response of fibre-based polymer composites to shock waves and explosive blasts". 125 (June 2019), p. 105502. DOI: 10.1016/j.compositesa.2019.105502.

[45] Comtois, J. L. R., Edwards, M. R., and Oakes, M. C. "The effect of explosives on polymer matrix composite laminates". *Composites Part A: Applied Science and Manufacturing* 30.3 (1999), pp. 181–190. DOI: 10.1016/s1359-835x(98)00172-9.

[46] Yahya, M. Y., Cantwell, W. J., Langdon, G. S., and Nurick, G. N. "The blast behavior of fiber reinforced thermoplastic laminates". *Journal of composite materials* 42.21 (2008), pp. 2275–2297. DOI: 10.1177/0021998308094968.

[47] Tekalur, S. A., Shivakumar, K., Shukla, A., Arjun, S., Shivakumar, K., and Shukla, A. "Mechanical behavior and damage evolution in E-glass vinyl ester and carbon composites subjected to static and blast loads". *Composites Part B: Engineering* 39.1 (2008), pp. 57–65. DOI: 10.1016/j.compositesb.2007.02.020.

[48] Kumar, P., Stargel, D. S., and Shukla, A. "Effect of plate curvature on blast response of carbon composite panels". *Composite Structures* 99 (2013), pp. 19–30. DOI: 10.1016/j.compstruct.2012.11.036.

[49] Gargano, A., Pingkarawat, K., Blacklock, M., Pickerd, V., and Mouritz, A. P. "Comparative assessment of the explosive blast performance of carbon and glass fibre-polymer composites used in naval ship structures". *Composite Structures* 171 (2017), pp. 306–316. DOI: 10.1016/j.compstruct.2017.03.041.

[50] Franz, T., Nurick, G. N., and Perry, M. J. "Experimental investigation into the response of chopped-strand mat glassfibre laminates to blast loading". *International Journal of Impact Engineering* 27.6 (2002), pp. 639–667. DOI: 10.1016/s0734-743x(01)00158-0.

[51] Neuberger, A., Peles, S., and Rittel, D. "Scaling the response of circular plates subjected to large and close-range spherical explosions. Part I: Air-blast loading". *International Journal of Impact Engineering* 34.5 (2007), pp. 859–873. DOI: 10.1016/j.ijimpeng.2006.04.001.

[52] Tiwari, V., Sutton, M. A., McNeill, S. R., Xu, S., Deng, X., Fourney, W. L., and Bretall, D. "Application of 3D image correlation for full-field transient plate deformation measurements during blast loading". *International Journal of Impact Engineering* 36.6 (2009), pp. 862–874. DOI: 10.1016/j.ijimpeng.2008.09.010.

[53] Zhao, X., Tiwari, V., Sutton, M. A., Deng, X., Fourney, W. L., and Leiste, U. "Deformation Scaling of Circular Plates Subjected to Dynamic Loading". 4 (2012), pp. 196–205. DOI: 10.1016/j.piutam.2012.05.021.

[54] Zhao, X., Tiwari, V., Sutton, M. A., Deng, X., Fourney, W. L., and Leiste, U. "Scaling of the deformation histories for clamped circular plates subjected to blast loading by buried charges". *International Journal of Impact Engineering* 54 (2013), pp. 31–50. DOI: 10.1016/j.ijimpeng.2012.10.016.

[55] Aune, V., Fagerholt, E., Hauge, K. O., Langseth, M., and B, T. "Experimental study on the response of thin aluminium and steel plates subjected to airblast loading". *International Journal of Impact Engineering* 90 (2016), pp. 106–121. DOI: 10.1016/j.ijimpeng.2015.11.017.

[56] Curry, R. J. and Langdon, G. S. "Transient response of steel plates subjected to close proximity explosive detonations in air". *International Journal of Impact Engineering* 102 (Apr. 2017), pp. 102–116. DOI: 10.1016/j.ijimpeng.2016.12.004.

[57] Gabriel, S., Langdon, G. S., von Klemperer, C. J., and Chung Kim Yuen, S. "Blast behaviour of fibre reinforced polymers containing sustainable constituents". *Journal of Reinforced Plastics and Composites* 41.19-20 (Feb. 2022), pp. 771–790. DOI: 10.1177/07316844211072529.

[58] Paykani, A., Khosravi, M. I., Saeimi-Sadigh, M. A., and Mahmoodi-Kaleibar, M. "Dynamic analysis and design of V-shape plates under blast loading". *Journal of Vibroengineering* 15.2 (2013), pp. 971–978.

[59] Saeimi-Sadigh, M. A., Paykani, A., Afkar, A., and Aminollah, D. "Design and energy absorption enhancement of vehicle hull under high dynamic loads". *Journal of Central South University* 21.4 (2014), pp. 1307–1312. DOI: 10.1007/s11771-014-2067-4.

[60] Longère, P., Geffroy-Grèze, A. G., Leblé, B., and Dragon, A. "Ship structure steel plate failure under near-field air-blast loading: Numerical simulations vs experiment". *International Journal of Impact Engineering* 62 (2013), pp. 88–98. DOI: 10.1016/j.ijimpeng.2013.06.009.

[61] Mehreganian, N., Louca, L. A., Langdon, G. S., Curry, R. J., and Abdul-karim, N. "The response of mild steel and armour steel plates to localised air-blast loading-comparison of numerical modelling techniques". *International Journal of Impact Engineering* 115.May 2017 (2018), pp. 81–93. DOI: 10.1016/j.ijimpeng.2018.01.010.

[62] Trajkovski, J., Kunc, R., and Prebil, I. "Blast response of centrally and eccentrically loaded flat-, U-, and V-shaped armored plates: comparative study". *Shock Waves* 27.4 (2017), pp. 583–591. DOI: 10.1007/s00193-016-0704-6.

[63] Geretto, C. "The effects of different degrees of confinement on the deformation of square plates subjected to blast loading". PhD thesis. University of Cape Town, 2012.

[64] Anderson Jr, C. E., Behner, T., and Weiss, C. E. "Mine blast loading experiments". *International Journal of Impact Engineering* 38.8-9 (2011), pp. 697–706. DOI: 10.1016/j.ijimpeng.2011.04.005.

[65] Barsotti, M. A., Puryear, J. M. H., Stevens, D. J., Alberson, R. M., and Mcmahon, P. "Modeling mine blast with SPH". In: *Proceedings of the 12th International LS-DYNA User Conference*. 1. 2012, pp. 1–12.

[66] Erdik, A., Kilic, S., Kilic, N., and Bedir, S. "Numerical simulation of armored vehicles subjected to undercarriage landmine blasts". *Shock waves* 26.4 (2016), pp. 449–464.

[67] Tabatabaei, Z. S. and Volz, J. S. "A comparison between three different blast methods in LS-DYNA: LBE, MM-ALE, Coupling of LBE and MM-ALE". In: *12th International LS-DYNA Users Conference*. 2012, pp. 1–10.

[68] Kingery, C. and Bulmash, G. "Technical report ARBRL-TR-02555: Air blast parameters from TNT spherical air burst and hemispherical burst". *AD-B082* 713 (1984).

[69] Spranghers, K., Vasilakos, I., Lecompte, D., Sol, H., and Vantomme, J. "Numerical simulation and experimental validation of the dynamic response of aluminum plates under free air explosions". *International Journal of Impact Engineering* 54 (2013), pp. 83–95. DOI: 10.1016/j.ijimpeng.2012.10.014.

[70] Markose, A. and Rao, C. L. "Mechanical response of V shaped plates under blast loading". *Thin-Walled Structures* 115.September 2016 (2017), pp. 12–20. DOI: 10.1016/j.tws.2017.02.002.

[71] Trajkovski, J., Perenda, J., and Kunc, R. "Blast response of Light Armoured Vehicles (LAVs) with flat and V-hull floor". *Thin-Walled Structures* 131 (June 2018), pp. 238–244. DOI: 10.1016/j.tws.2018.06.040.

[72] Shekhar, V. "The effect of bend radius on the impulse transfer characteristics of V-hulls". MSc Dissertation. University of Cape Town, 2015.

[73] Markose, A. and Rao, C. L. "Failure Analysis of V-shaped Plates under Blast Loading". In: *Procedia Engineering*. Vol. 173. Elsevier B.V., 2017, pp. 519–525. DOI: 10.1016/j.proeng.2016.12.080.

[74] Abdel Wahab, M., Mazek, S., Abada, M., and Abdel Shafy, M. "Blast hazard impact on V-shape composite panel performance". In: *The International Conference on Civil and Architecture Engineering*. Vol. 12. 12th International Conference on Civil and Architecture Engineering. Military Technical College. 2018, pp. 1–18.

[75] Forghani, A. and Vaziri, R. "Computational modeling of damage development in composite laminates subjected to transverse dynamic loading". *Journal of applied mechanics* 76.5 (2009). DOI: 10.1115/1.3129705.

[76] Dolce, F., Meo, M., Wright, A., French, M., and Bernabei, M. "Structural response of laminated composite plates to blast load". *Plastics, rubber and composites* 39.3-5 (2010), pp. 180–188. DOI: 10.1179/174328910x12608851832858.

[77] Giversen, S. "Blast testing and modelling of composite structures". PhD thesis. Technical University of Denmark, 2014.

[78] Balkan, D., Demir, Ö., and Arıkoğlu, A. "Dynamic analysis of a stiffened composite plate under blast load: a new model and experimental validation". *International Journal of Impact Engineering* 143 (2020), p. 103591. DOI: 10.1016/j.ijimpeng.2020.103591.

[79] Gunaryo, K., Heriana, H., Sitompul, M. R., Kuswoyo, A., and Hadi, B. K. "Experimentation and numerical modeling on the response of woven glass/epoxy composite plate under blast impact loading". *International Journal of Mechanical and Materials Engineering* 15.1 (2020), pp. 1–9. DOI: 10.1186/s40712-020-0116-3.

[80] Zhao, H., Fang, H., and Zhao, X. "Experimental and numerical investigation on dynamic behaviors of glass fiber reinforced polymer plates under explosion loadings". *International Journal of Impact Engineering* 171 (2023), p. 104362. DOI: 10.1016/j.ijimpeng.2022.104362.

[81] Gurit Composite Technologies. *Prime^{TM} 20lv*. Tech. rep., pp. 1–6.

[82] Hobson, L. "Response of Composite Panels to Blast Loading". Final year project report. University of Cape Town, 2013.

[83] ASTM Standard D3039-14 (2014). *Standard Test Method for Tensile Properties of Polymer Matrix Composite Materials*. Tech. rep. West Conshohocken, PA, 2014.

[84] ASTM Standard D5528-13 (2013). *Standard Test Method for Mode I Interlaminar Fracture Toughness of Unidirectional Fiber-Reinforced Polymer Matrix Composites*. Tech. rep. West Conshohocken, PA, 2013, pp. 1–13.

[85] ASTM Standard A370-14 (2014). *Standard Test Methods and Definitions for Mechanical Testing of Steel Products 1*. Tech. rep. West Conshohocken, PA, 2014.

[86] Volschenk, G. "Material Characterization and Blast Modelling of Multi-Layered DOMEX 550MC and 700MC Plates". Structural impact project report. University of Cape Town, 2013.

[87] Johnson, G. R. and Cook, W. H. "A constitutive model and data from metals subjected to large strains, high strain rates and high temperatures". In: *Proc. 7th Int. Symp. on Ballistics, The Hague, Netherlands*. 1983.

[88] Lundstrom, T. S., Gebart, B. R., and Lundemo, C. Y. "Void Formation in RTM". *Journal of Reinforced Plastics and Composites* 12.12 (1993), pp. 1339–1349. DOI: 10.1177/073168449301201207.

[89] Schreier, H., Orteu, J.-J., and Sutton, M. A. *Image Correlation for Shape, Motion and Deformation Measurements*. 2009. DOI: 10.1007/978-0-387-78747-3.

[90] Warncke, D. "The Design and Testing of Novel Shallow V-shape Structures". final year project report. University of Cape Town, 2013.

[91] Rigby, S. E., Akintaro, O. I., Fuller, B. J., Tyas, A., Curry, R. J., Langdon, G. S., and Pope, D. J. "Predicting the response of plates subjected to near-field explosions using an energy equivalent impulse". *International Journal of Impact Engineering* 128 (2019), pp. 24–36. DOI: 10.1016/j.ijimpeng.2019.01.014.

[92] Sinclair, G. "The response of singly curved fibre reinforced sandwich and laminate composite panels subjected to localised blast loading". MSc Dissertation. University of Cape Town, 2013.

[93] Daliri, A., Orifici, A., Curry, R., Langdon, G., Bornstein, H., and Odish, R. "Experimental response of S2-glass fibre reinforced composites subjected to localised blast loading" (2019), pp. 816–822. DOI: 10.1201/9780429426506-142.

[94] Gabriel, S., von Klemperer, C. J., Chung Kim Yuen, S., and Langdon, G. S. "Towards an Understanding of the Effect of Adding a Foam Core on the Blast Performance of Glass Fibre Reinforced Epoxy Laminate Panels". *Materials* 14.23 (Nov. 23, 2021), p. 7118. DOI: 10.3390/ma14237118.

[95] Livermore Software Technology Corporations (LSTC). *LS-DYNA Keyword User's Manual Volume I*. Vol. I. June 2022, p. 4016.

[96] Livermore Software Technology Corporations (LSTC). *LS-DYNA Keyword User's Manual Volume II*. Vol. I. June 2022, p. 2113.

[97] Kinney, G. F. and Graham, K. J. *Explosive Shocks in Air*. Springer Science & Business Media, 1985. DOI: 10.1007/978-3-642-86682-1.

[98] Bogosian, D., Yokota, M., and Rigby, S. "TNT equivalence of C-4 and PE4: A review of traditional sources and recent data". *Proceedings of the 24th military aspects of blast and shock* (2016).

[99] Dobratz, B. M. *LLNL explosives handbook - properties of chemical explosives and explosives and explosive simulants*. Tech. rep. Lawrence Livermore National Lab., CA (USA), 1981. DOI: 10.2172/6530310.

[100] Hadavinia, H., Dogan, F., Elmarakbi, A. M., and Khalili, S. M. R. "Modelling of low velocity impact of laminated composite substructures" (2011). DOI: 10.4273/ijvss.3.2.04.

[101] Sy, B. L., Fawaz, Z., and Bougherara, H. "Numerical simulation correlating the low velocity impact behaviour of flax/epoxy laminates". *Composites Part A: Applied Science and Manufacturing* 126 (2019), p. 105582. DOI: 10.1016/j.compositesa.2019.105582.

[102] Yang, C., Gao, Y., Guo, W., Yang, Y., Xu, P., and Alqahtani, M. S. "High-velocity impact behaviour of curved GFRP composites for rail vehicles: Experimental and numerical study". *Polymer Testing* 116 (2022), p. 107774. DOI: 10.1016/j.polymertesting.2022.107774.

[103] Lifshitz, J. M. and Leber, H. "Response of fiber-reinforced polymers to high strain-rate loading in interlaminar tension and combined tension/shear". *Composites Science and Technology* 58.6 (1998), pp. 987–996. DOI: 10.1016/s0266-3538(97)00226-1.

[104] *Contact Types (LS-DYNA Support)*. Accessed: 2023-01-30. URL: https://www.dynasupport.com/tutorial/contact-modeling-in-ls-dyna/contact-types.

[105] Ansari, M. T. A., Singh, K. K., and Azam, M. S. *Effect of Stacking Sequence and Fiber Volume Fraction on the Static Mechanical Properties of Woven GFRP Composite*. Springer Singapore, 2019, pp. 51–58. DOI: 10.1007/978-981-13-9016-6_6.

[106] Menna, C., Asprone, D., Caprino, G., Lopresto, V., and Prota, A. "Numerical simulation of impact tests on GFRP composite laminates". *International Journal of Impact Engineering* 38.8-9 (2011), pp. 677–685. DOI: 10.1016/j.ijimpeng.2011.03.003.

[107] Treviso, A., Van Genechten, B., Mundo, D., and Tournour, M. "Damping in composite materials: Properties and models". *Composites Part B: Engineering* 78 (2015), pp. 144–152. DOI: 10.1016/j.compositesb.2015.03.081.

[108] Becker, M. "Numerical simulation of fracture in high-velocity impact". PhD thesis. 2021.

Appendix A

CAD drawings

Table A.1: List of manufactured parts

Assembly	Drawing number	Material	Quantity
Clamp frame assembly	CF-00		1
	CF-01	Mild steel	2
	CF-02	Mild steel	2
	CF-03	Mild steel	2
	CF-04	Mild steel	2
105° male mould assembly	M-105-00		1
	M-105-01	0.9 mm Al 1050A H14	1
	M-105-02	Polystyrene	1
	M-105-03	Shutterply	1
105° female mould assembly	105-00		1
	105-01	0.9 mm Al 1050A H14	1
	105-02	Polystyrene	1
	105-03	Shutterply	1
120° female mould assembly	120-00		1
	120-01	0.9 mm Al 1050A H14	1
	120-02	Polystyrene	1
	120-03	Shutterply	1
105° 32 mm Steel V-plate	DOMEX-105-30-01	DOMEX-700 MC	6
105° 62 mm Steel V-plate	DOMEX-105-60-01	DOMEX-700 MC	6
120° 32 mm Steel V-plate	DOMEX-120-30-01	DOMEX-700 MC	6
Flat Steel V-plate	DOMEX-Flat	DOMEX-700 MC	5
DIC Sealing Plate 105° 30 mm	SP-01-01	Mild steel	2
DIC Sealing Plate 105° 60 mm	SP-02-01	Mild steel	2
DIC Sealing Plate 120° 30 mm	SP-03-01	Mild steel	2

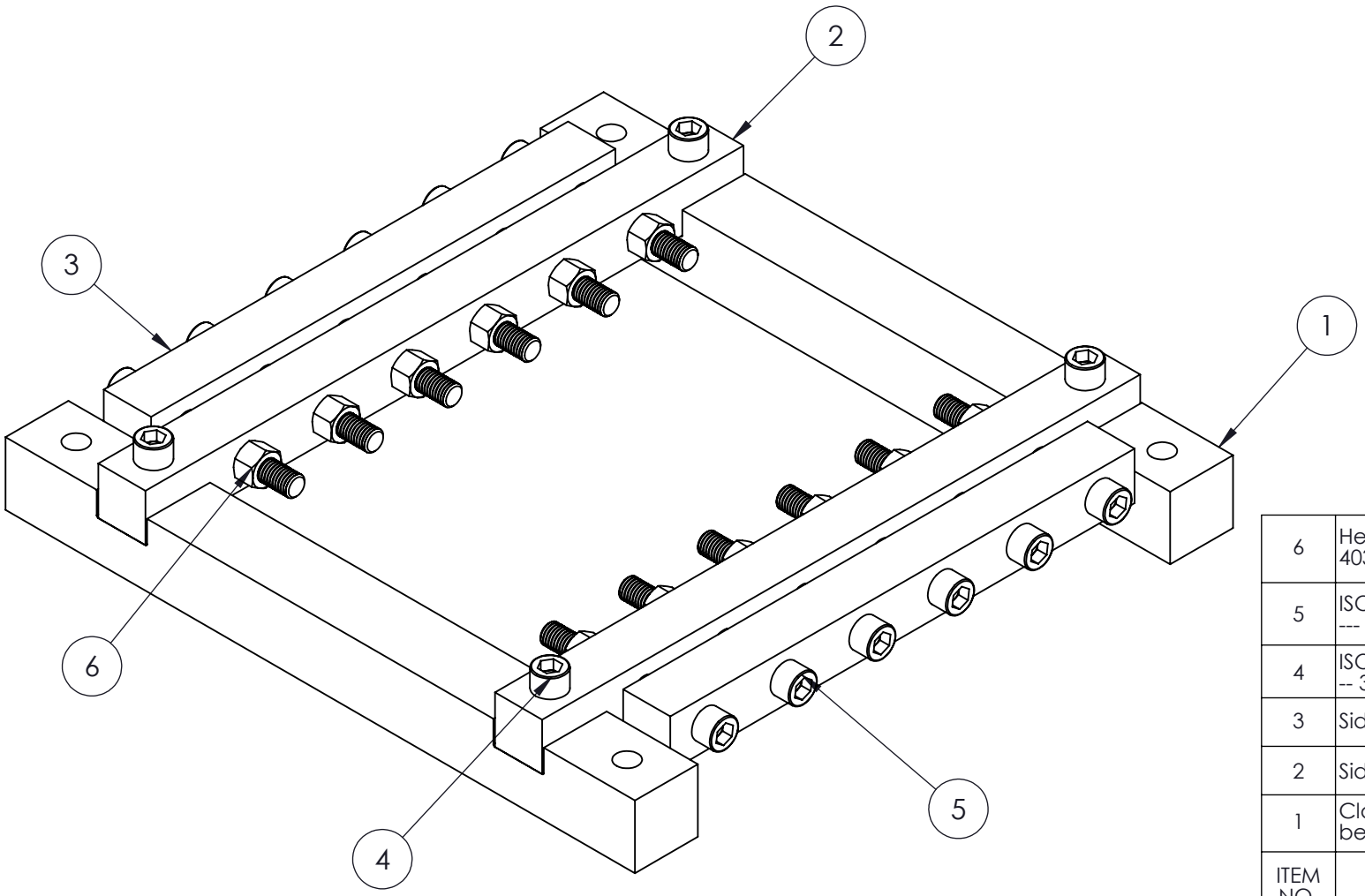

ITEM NO.	PART NUMBER	QTY.	MATERIAL
6	Hexagon Nut ISO - 4034 - M12 - S	12	
5	ISO 4762 M12 x 100 --- 36S	12	
4	ISO 4762 M12 x 60 -- 36S	4	
3	Side Clamp	2	Mild Steel
2	Side Frame	2	Mild Steel
1	Clamp frame side beam	2	Mild Steel

A4 Landscape	**University of Cape Town** **Department of Mechanical Engineering**			
	Title: Assembly drawing of Clamp Frame Assembly			
Assembly Drawing	**Scale:** 1:3	**Date:** 16/11/2016	Sheet 1	**of** 1
	Drawn By: Vinay Shekhar		**Drawing Number** CF-00	

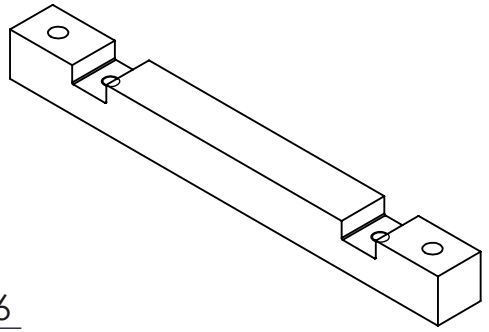

SCALE 1 : 5

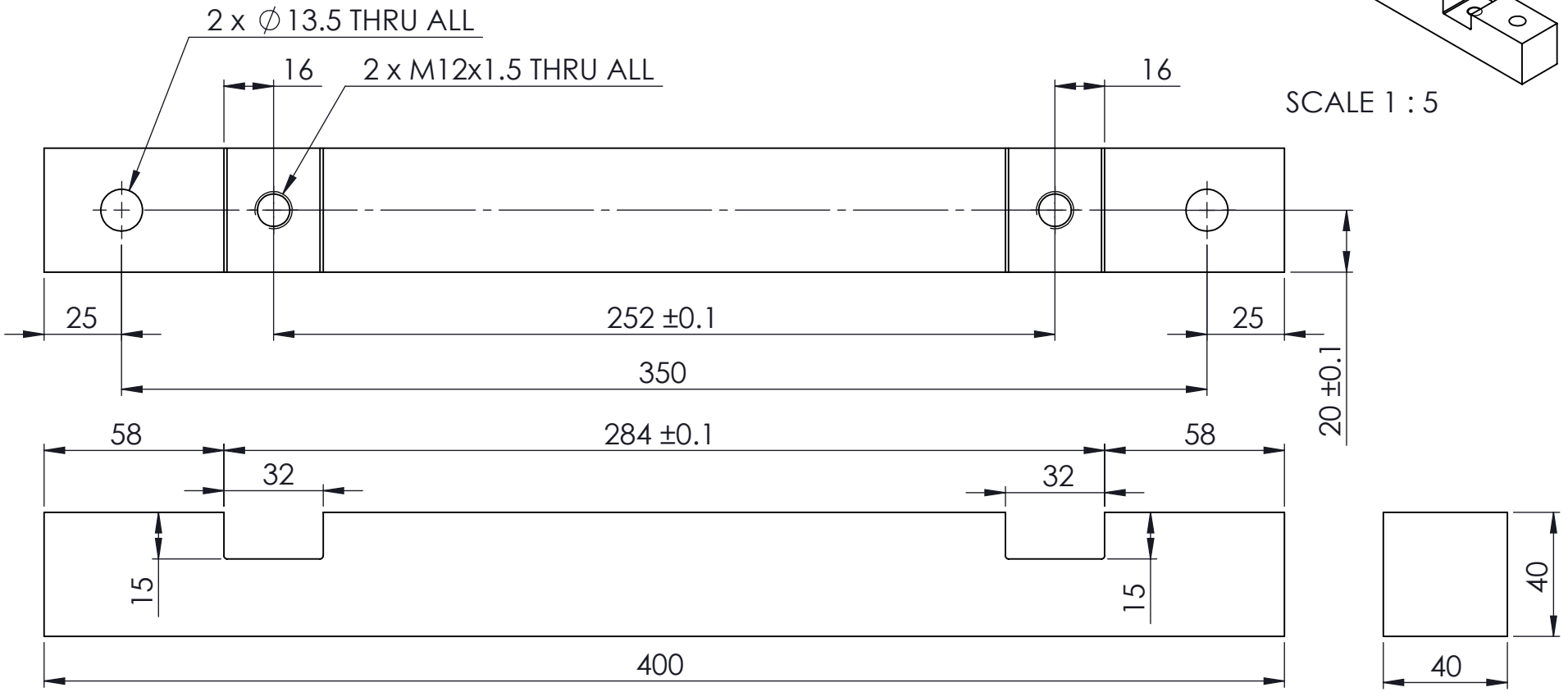

ALL ROUNDS R1 (U.O.S)

A4 Landscape	University of Cape Town Department of Mechanical Engineering			
	Title: Composite panel Clamp frame side beam			
Quantity: 2	Scale: 1:2	Date: 25/11/2016	Sheet 1	of 1
Material: Mild Steel	Drawn By: Vinay Shekhar		Drawing Number CF-01	

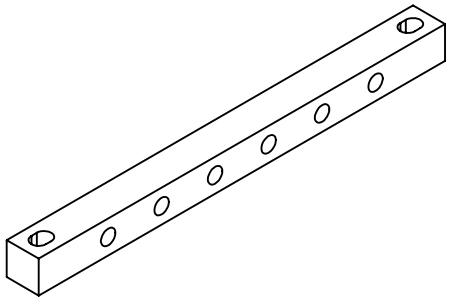

SCALE 1 : 5

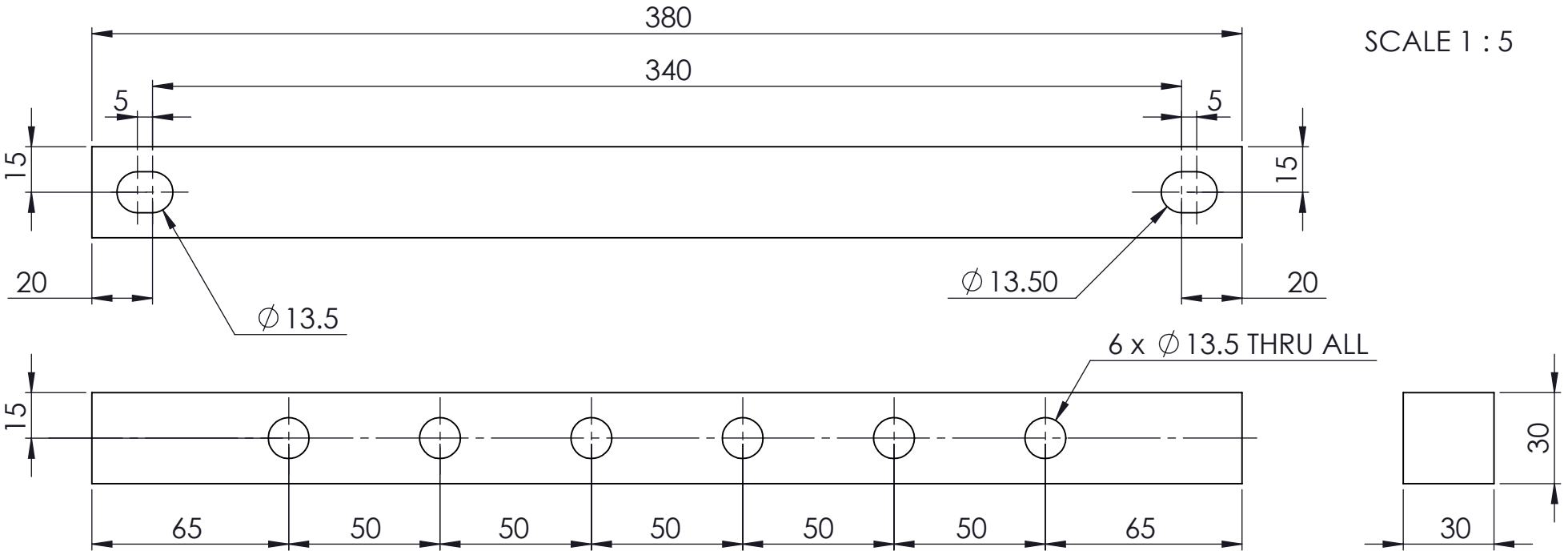

A4 Landscape	University of Cape Town Department of Mechanical Engineering			
	Title: Side Frame			
Quantity: 2	Scale: 1:2	Date: 21/11/2017	Sheet 1	of 1
Material: Mild Steel	Drawn By: Vinay Shekhar		Drawing Number CF-02	

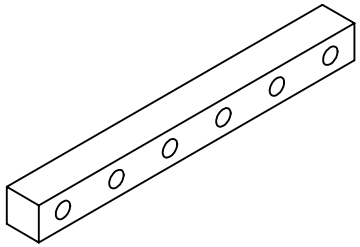

SCALE 1 : 5

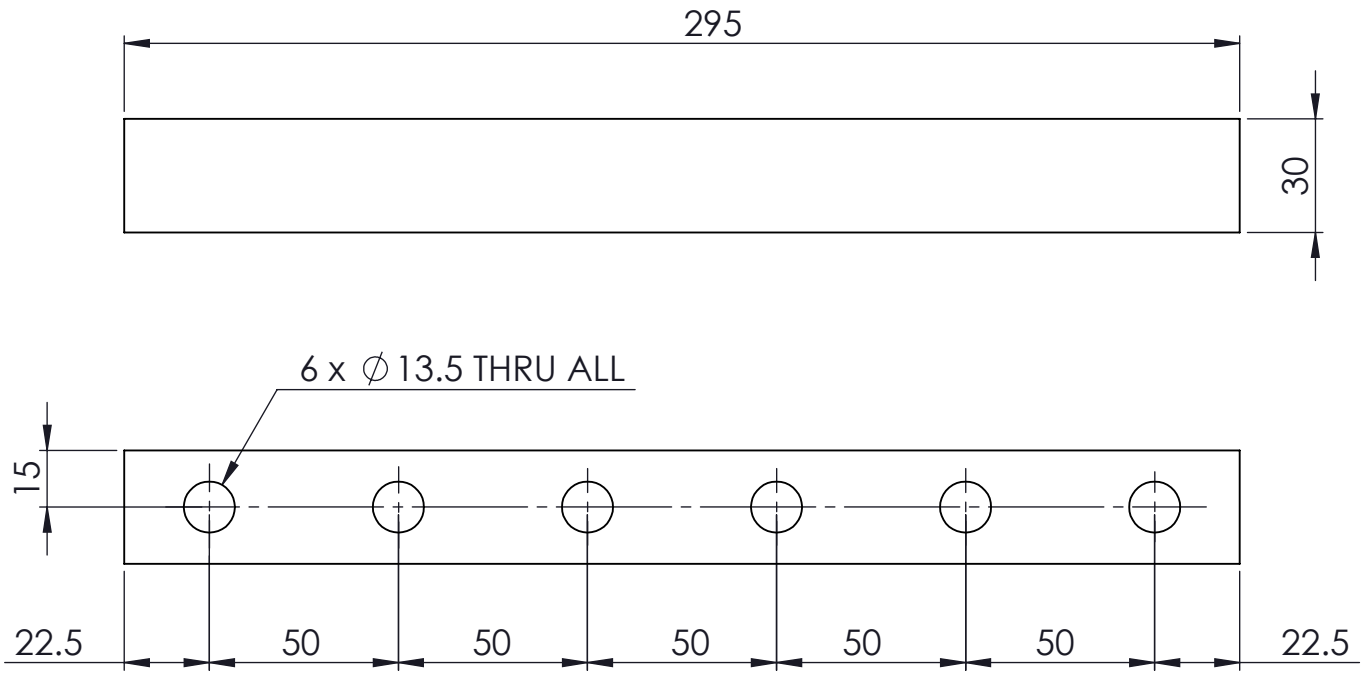

A4 Landscape	**University of Cape Town** **Department of Mechanical Engineering**			
	Title: Side Clamp			
Quantity: 2	**Scale:** 1:2	**Date:** 25/11/2016	Sheet 1	of 1
Material: Mild Steel	Drawn By: Vinay Shekhar		**Drawing Number** CF-03	

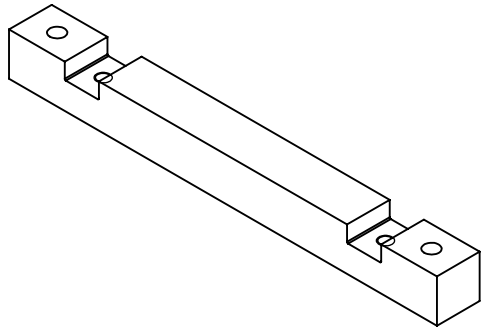

SCALE 1 : 5

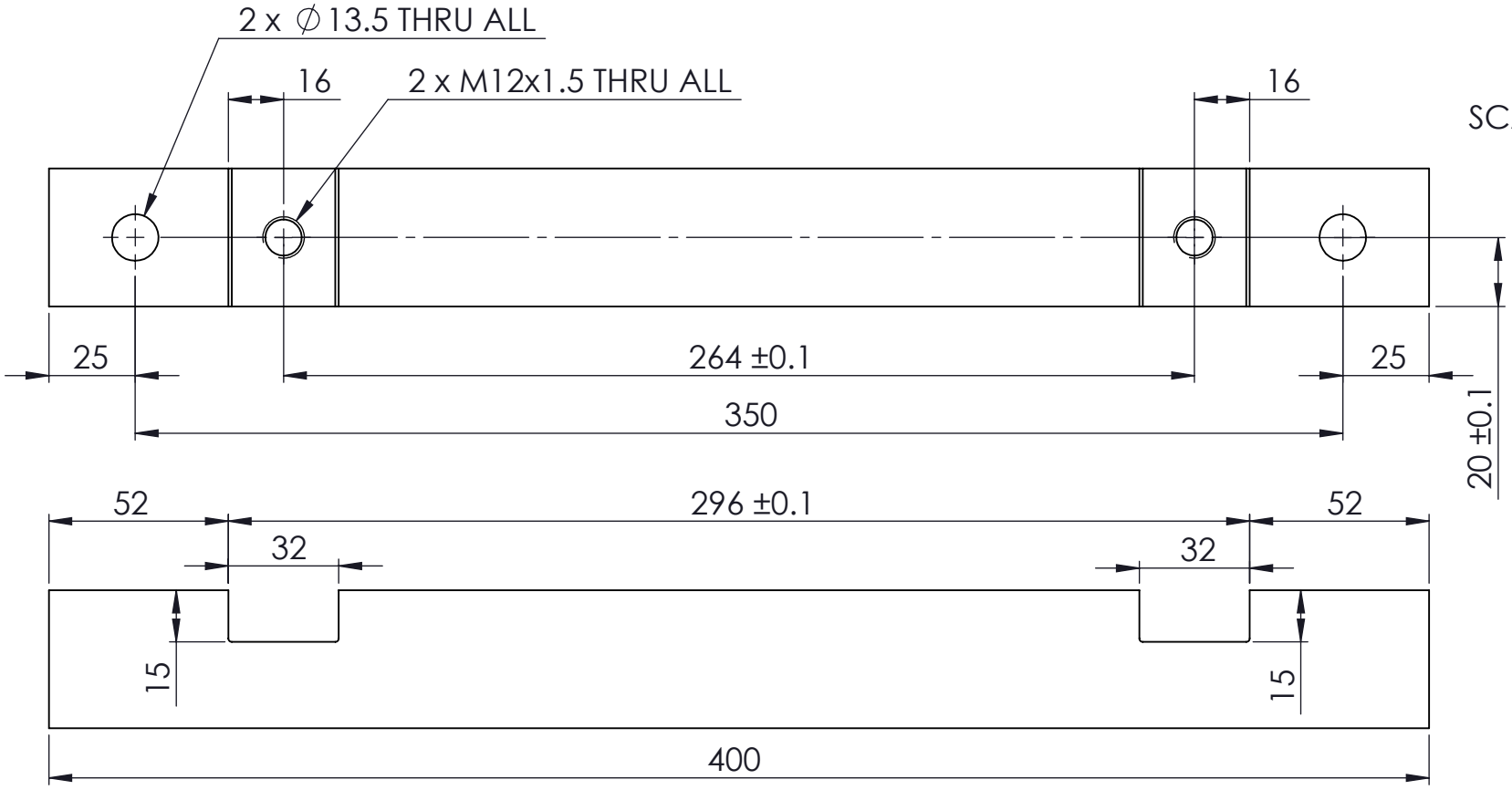

ALL ROUNDS R1 (U.O.S)

A4 Landscape	University of Cape Town Department of Mechanical Engineering			
	Title: Steel panel Clamp frame side beam			
Quantity: 2	Scale: 1:2	Date: 25/11/2016	Sheet 1	of 1
Material: Mild Steel	Drawn By: Vinay Shekhar		Drawing Number CF-04	

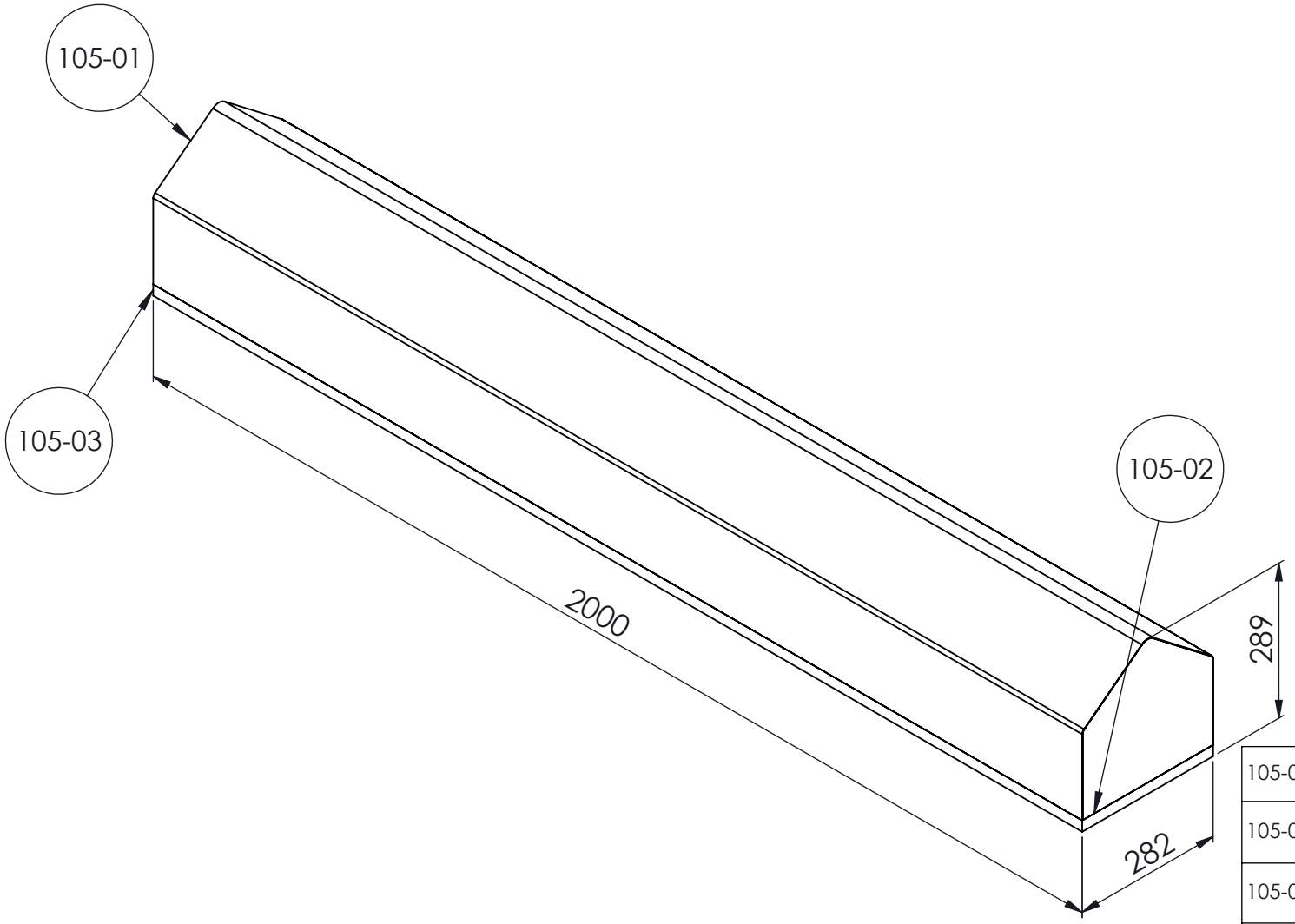

ITEM NO.	PART NUMBER	QTY.	MATERIAL
105-03	Wooden Base - 105 Degree Panel Mould	1	Shutterply
105-02	Polystyrene Structure - 105 Degree Panel Mould	1	Polystyrene
105-01	Aluminium Sheet - 105 Degree Panel Mould	1	0.9 mm Al 1050A H14

A4 Landscape	**University of Cape Town** **Department of Mechanical Engineering**			
	Title: Assembly drawing of 105 Degree Panel Mould			
Assembly Drawing	**Scale:** 1:10	**Date:** 23/11/2016	Sheet 1	of 1
	Drawn By: Vinay Shekhar		**Drawing Number** 105-00	

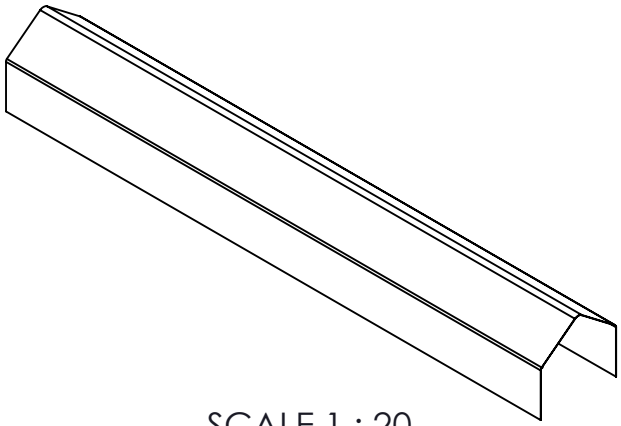

SCALE 1 : 20

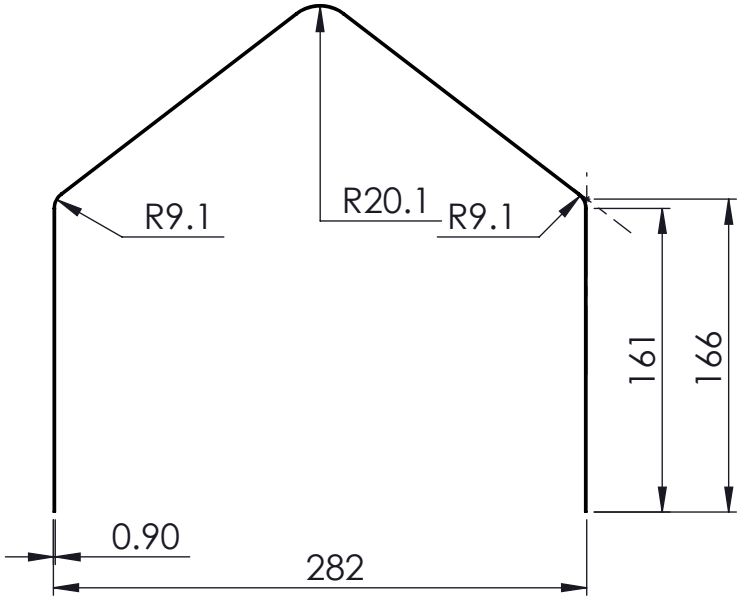

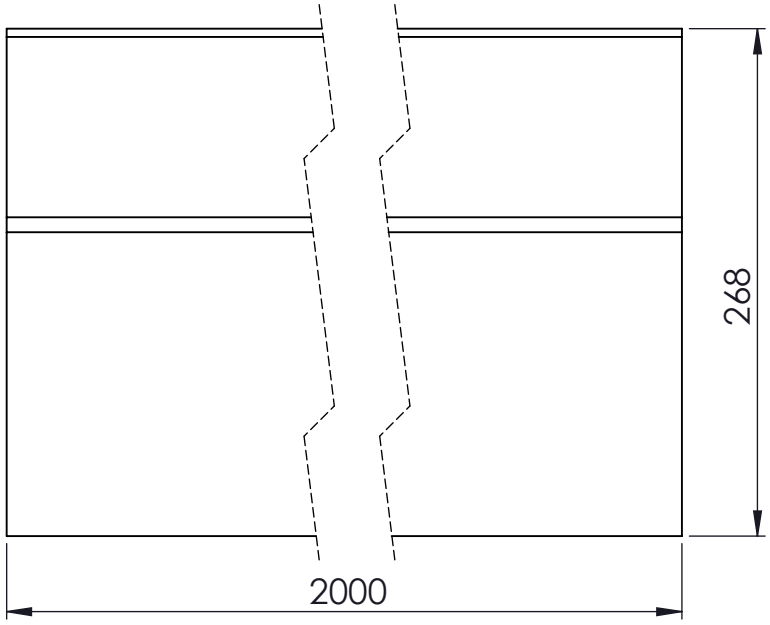

A4 Landscape	**University of Cape Town** Department of Mechanical Engineering			
	Title: Aluminium Sheet - 105 Degree Panel Mould			
Part Finish 1.6	Scale: 1:4	Date: 23/11/2016	Sheet 1	of 2
Material: 0.9 mm Al 1050 H14	Drawn By: Vinay Shekhar		Drawing Number 105-01-01	

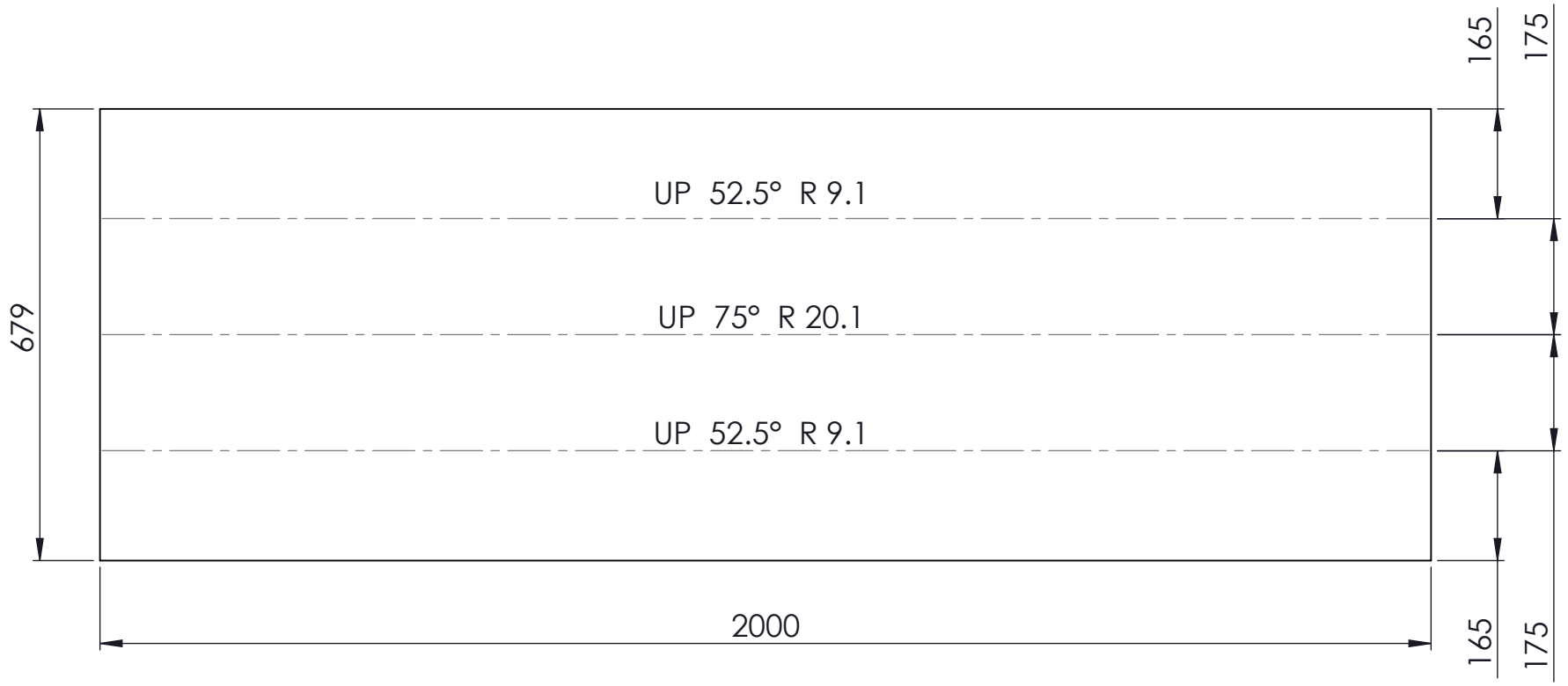

A4 Landscape	**University of Cape Town** Department of Mechanical Engineering			
	Title: Aluminium Surface - 120 Degree Panel Mould			
Part Finish 1.6	Scale: 1:10	Date: 23/11/2016	Sheet 2	of 2
Material: 0.9 mm Al 1050 H14	Drawn By: Vinay Shekhar		Drawing Number 105-01-02	

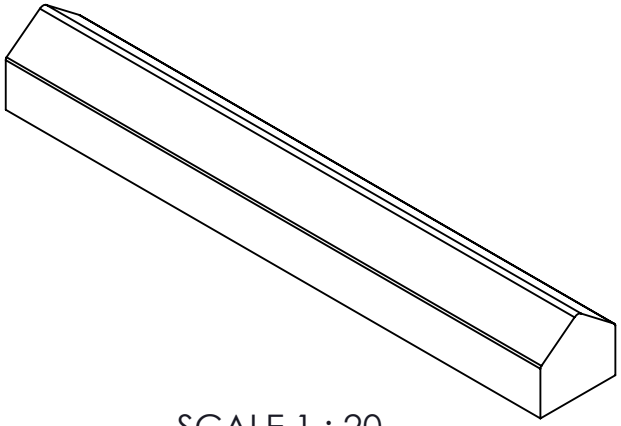

SCALE 1 : 20

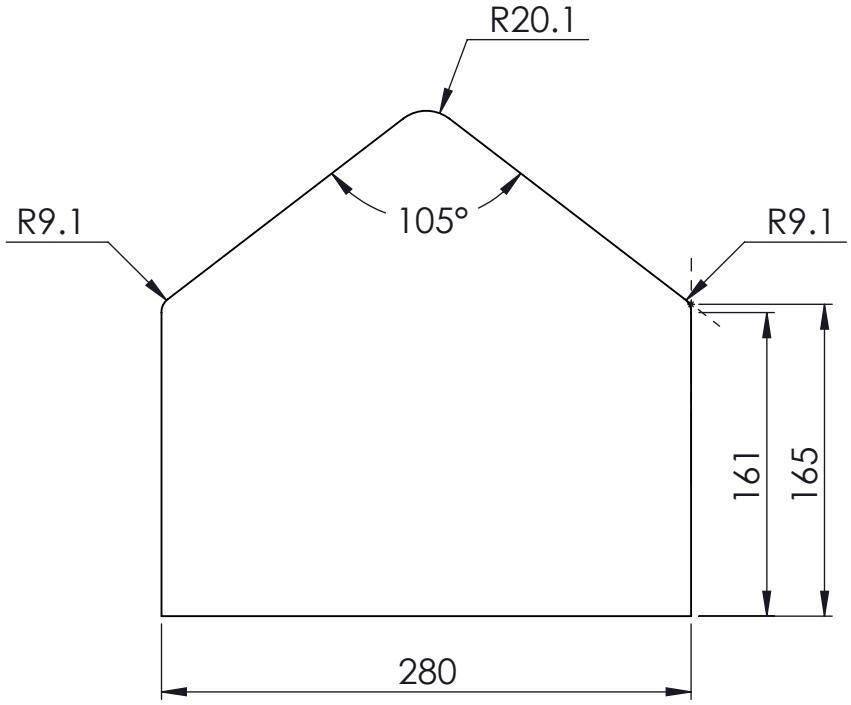

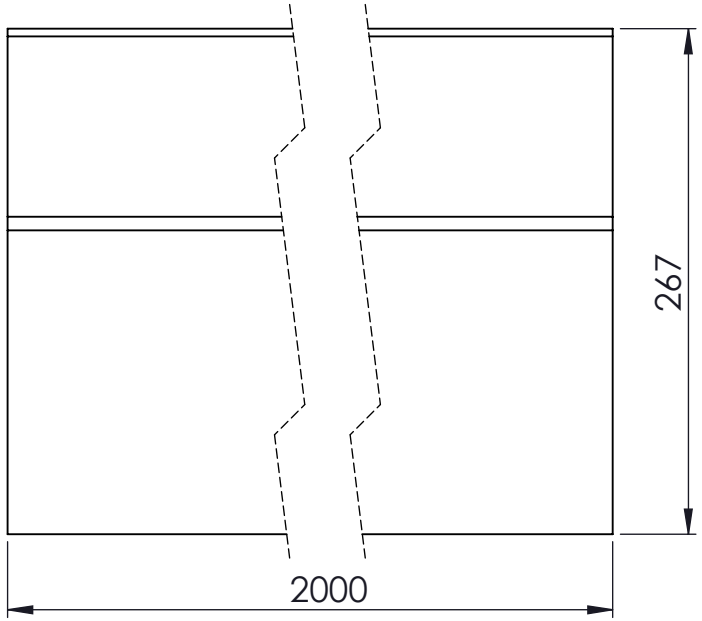

A4 Landscape	**University of Cape Town** **Department of Mechanical Engineering**			
	Title: Polystyrene Structure - 105 Degree Panel Mould			
Part Finish	**Scale:** 1:4	**Date:** 23/11/2016	Sheet 1	of 1
Material: Polystyrene	Drawn By: Vinay Shekhar		**Drawing Number** 105-02	

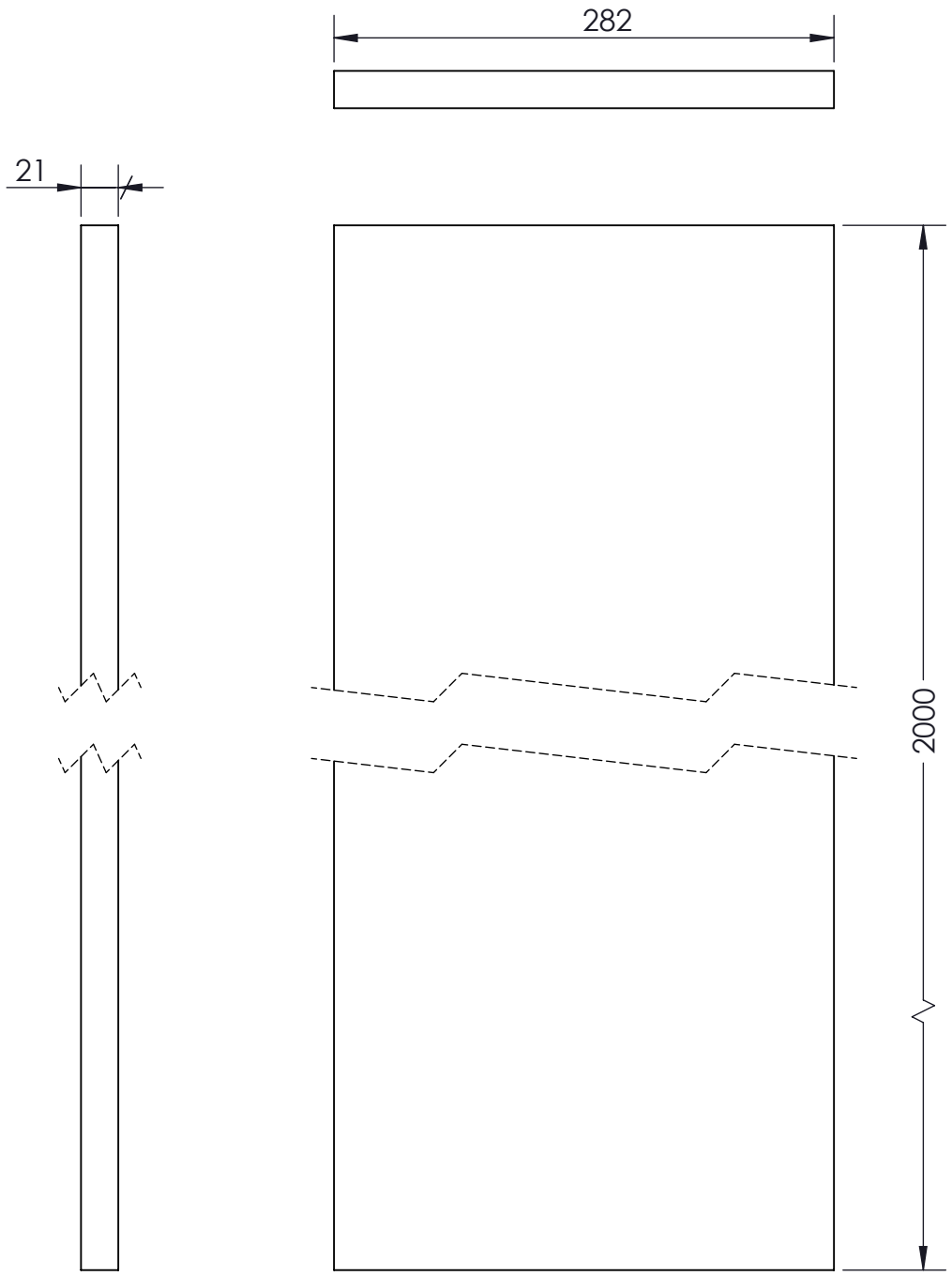

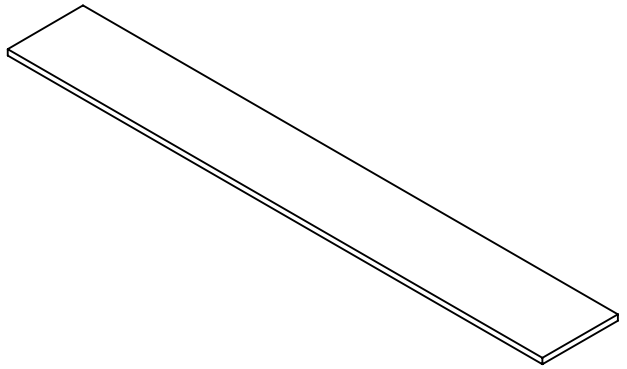

SCALE 1 : 20

A4 Landscape	University of Cape Town Department of Mechanical Engineering			
	Title: Wooden Base - 105 Degree Panel Mould			
Part Finish	Scale: 1:4	Date: 30/11/2016	Sheet 1	of 1
Material: Shutterply	Drawn By: Vinay Shekhar		Drawing Number 105-03	

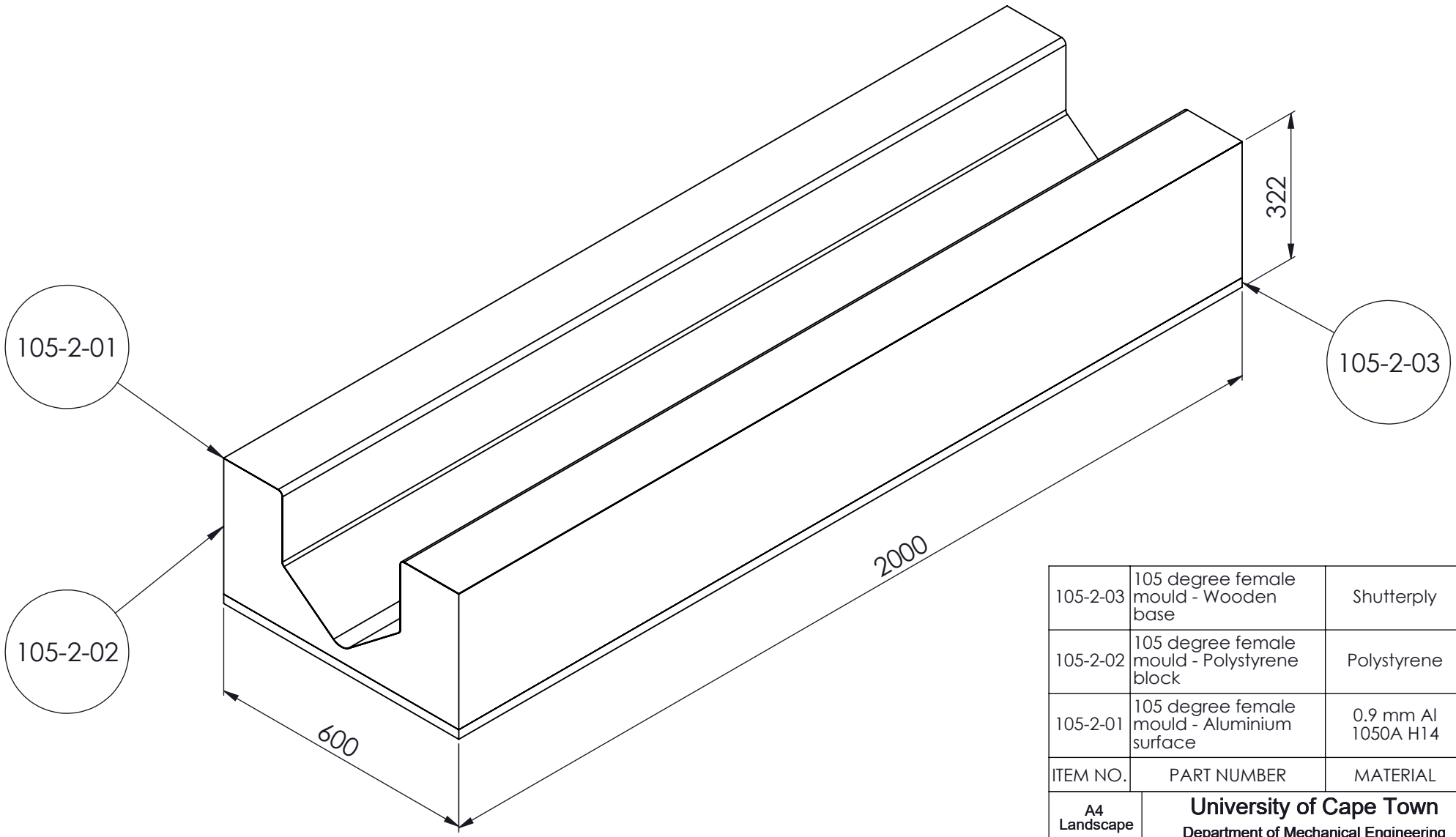

105-2-03	105 degree female mould - Wooden base	Shutterply	1
105-2-02	105 degree female mould - Polystyrene block	Polystyrene	1
105-2-01	105 degree female mould - Aluminium surface	0.9 mm Al 1050A H14	1
ITEM NO.	PART NUMBER	MATERIAL	QTY.

A4 Landscape	**University of Cape Town** **Department of Mechanical Engineering**			
	Title: Assembly drawing of 105 degree female mould			
Assembly Drawing	**Scale:** **1:10**	**Date:** **28/02/2017**	Sheet 1	**of** **1**
	Drawn By: Vinay Shekhar		**Drawing Number** 105-2-00	

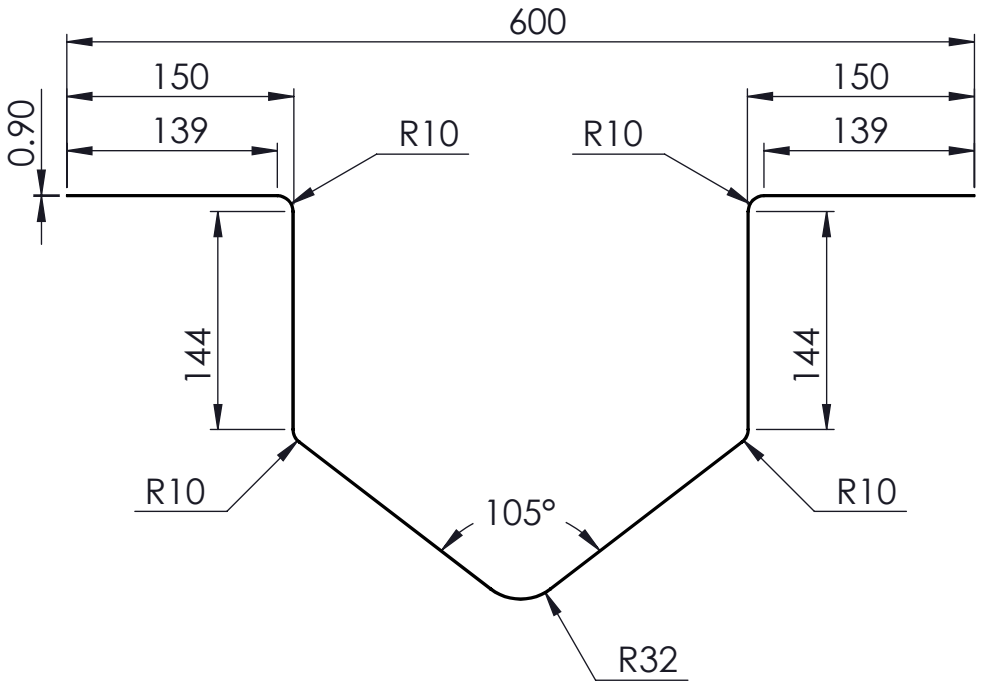

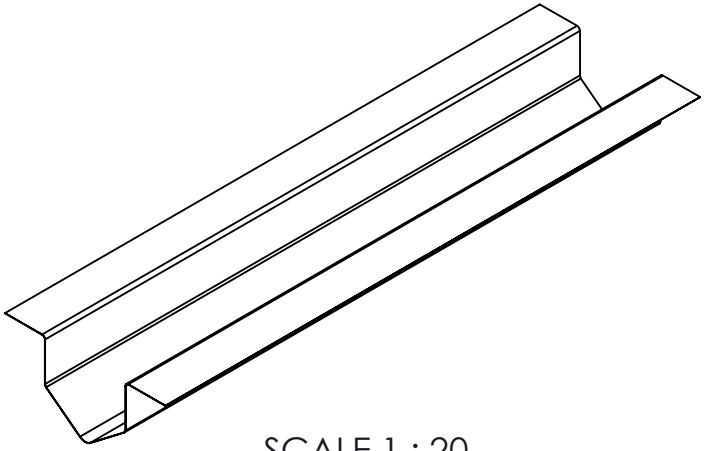

SCALE 1 : 20

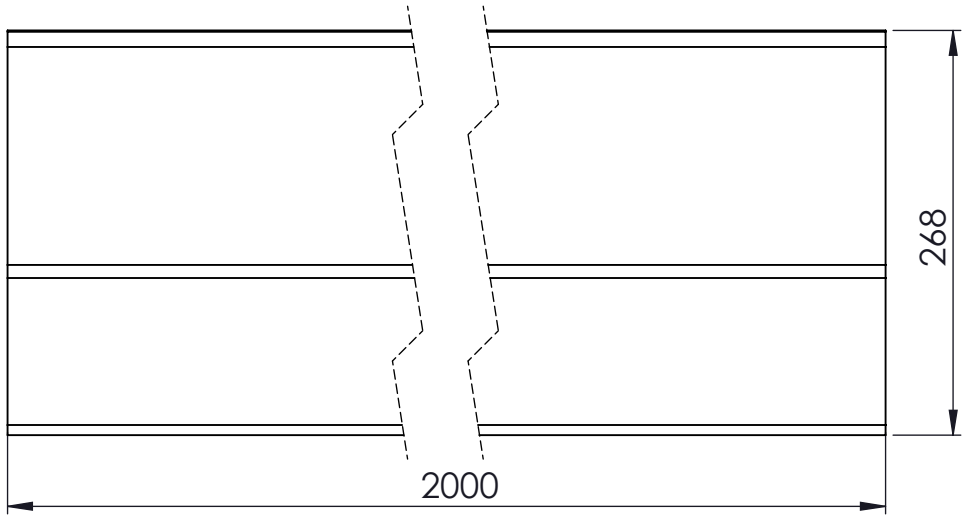

A4 Landscape	**University of Cape Town** Department of Mechanical Engineering			
	Title: Aluminium surface - 105 degree female mould			
Part Finish 1.6	Scale: 1:5	Date: 26/03/2017	Sheet 1	of 2
Material: 0.9 mm Al 1050A H14	Drawn By: Vinay Shekhar		Drawing Number 105-2-01-01	

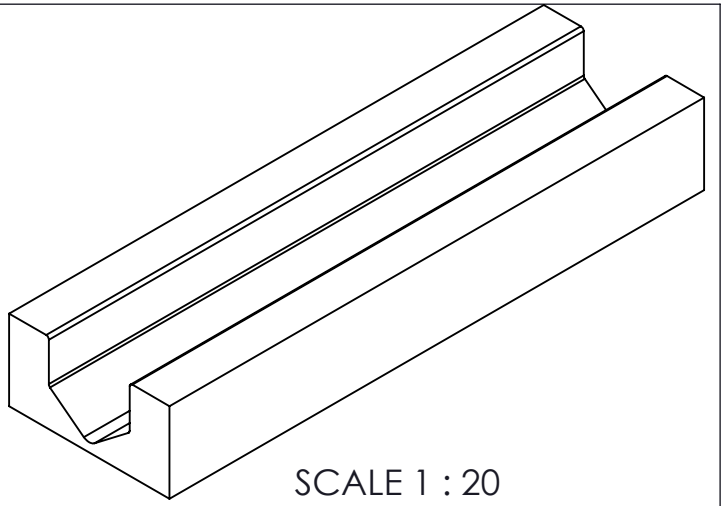

SCALE 1 : 20

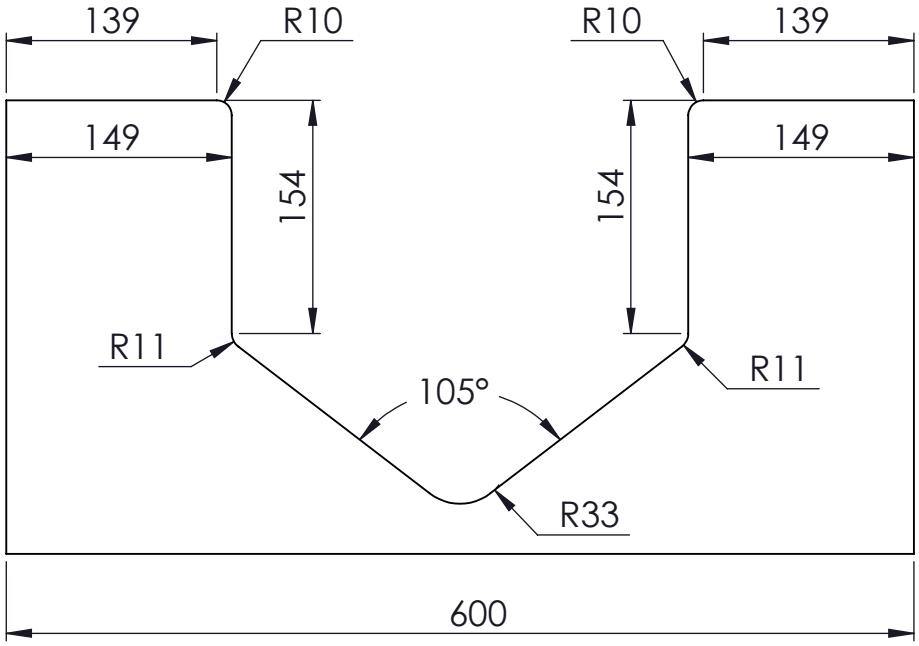

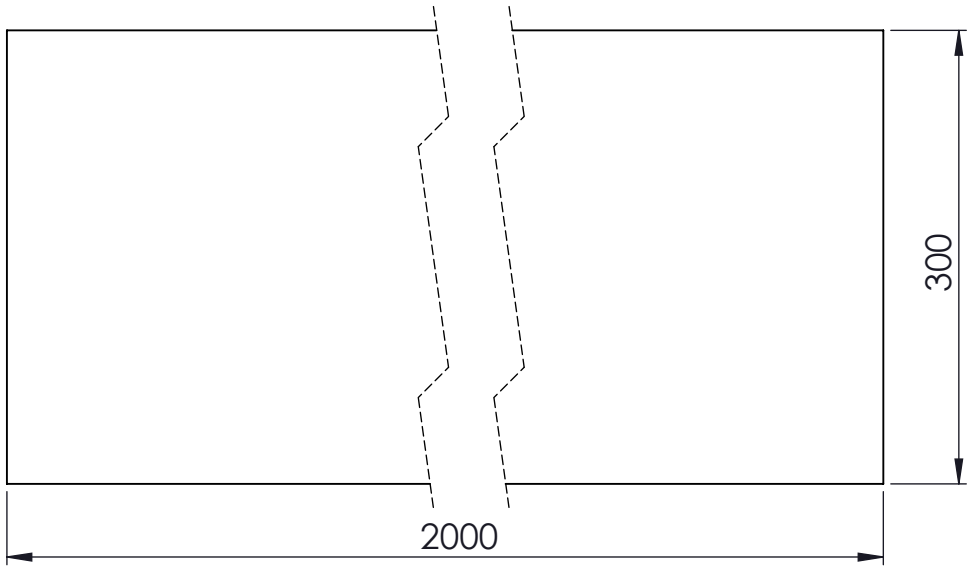

A4 Landscape	**University of Cape Town** Department of Mechanical Engineering			
	Title: Polystyrene block - 105 degree female mould			
Part Finish	Scale: 1:5	Date: 28/02/2017	Sheet 1	of 1
Material: Polystyrene	Drawn By: Vinay Shekhar		Drawing Number 105-2-02	

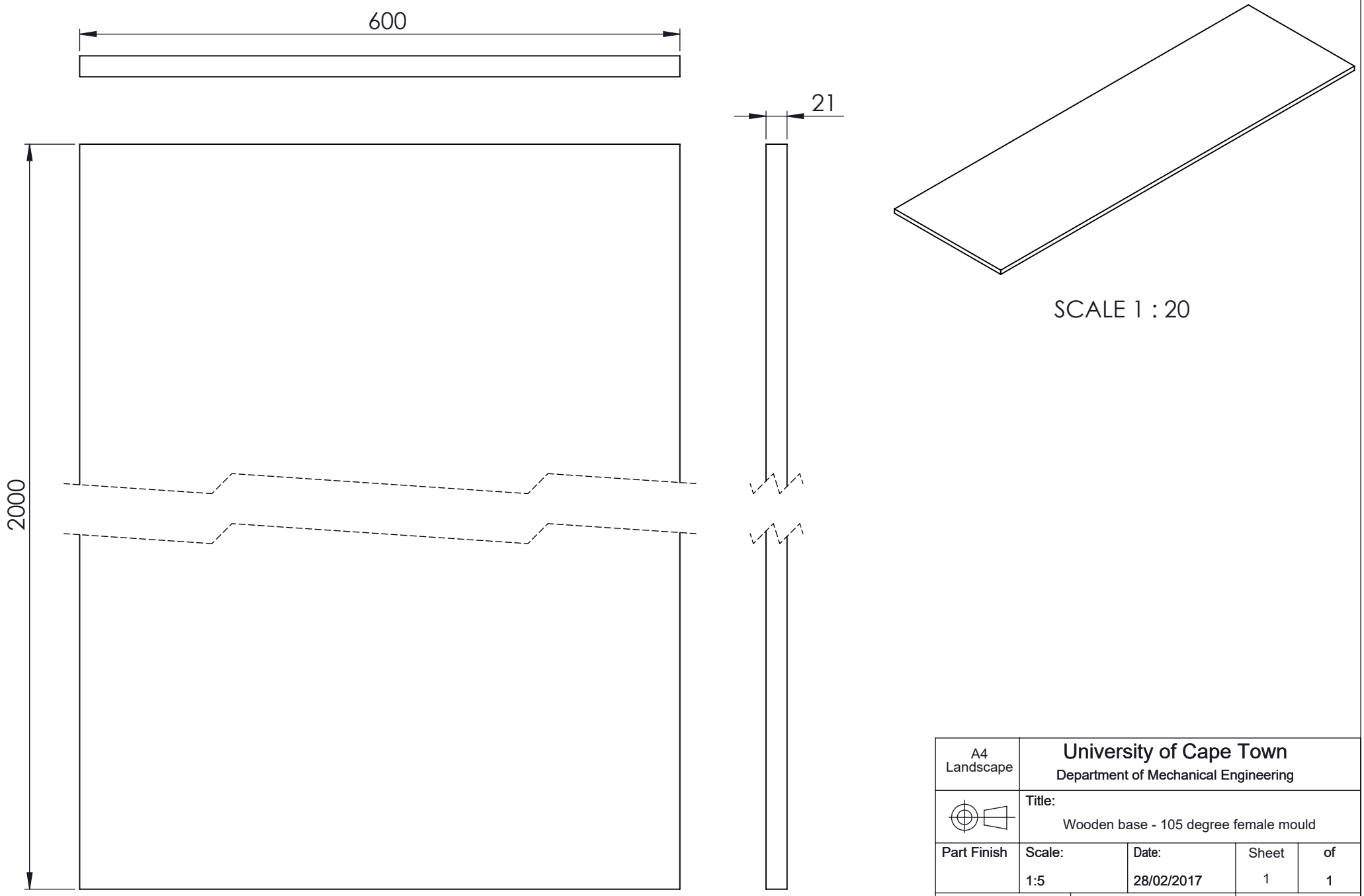

SCALE 1 : 20

A4 Landscape	University of Cape Town Department of Mechanical Engineering			
	Title: Wooden base - 105 degree female mould			
Part Finish	Scale: 1:5	Date: 28/02/2017	Sheet 1	of 1
Material: Shutterply	Drawn By: Vinay Shekhar		Drawing Number 105-2-03	

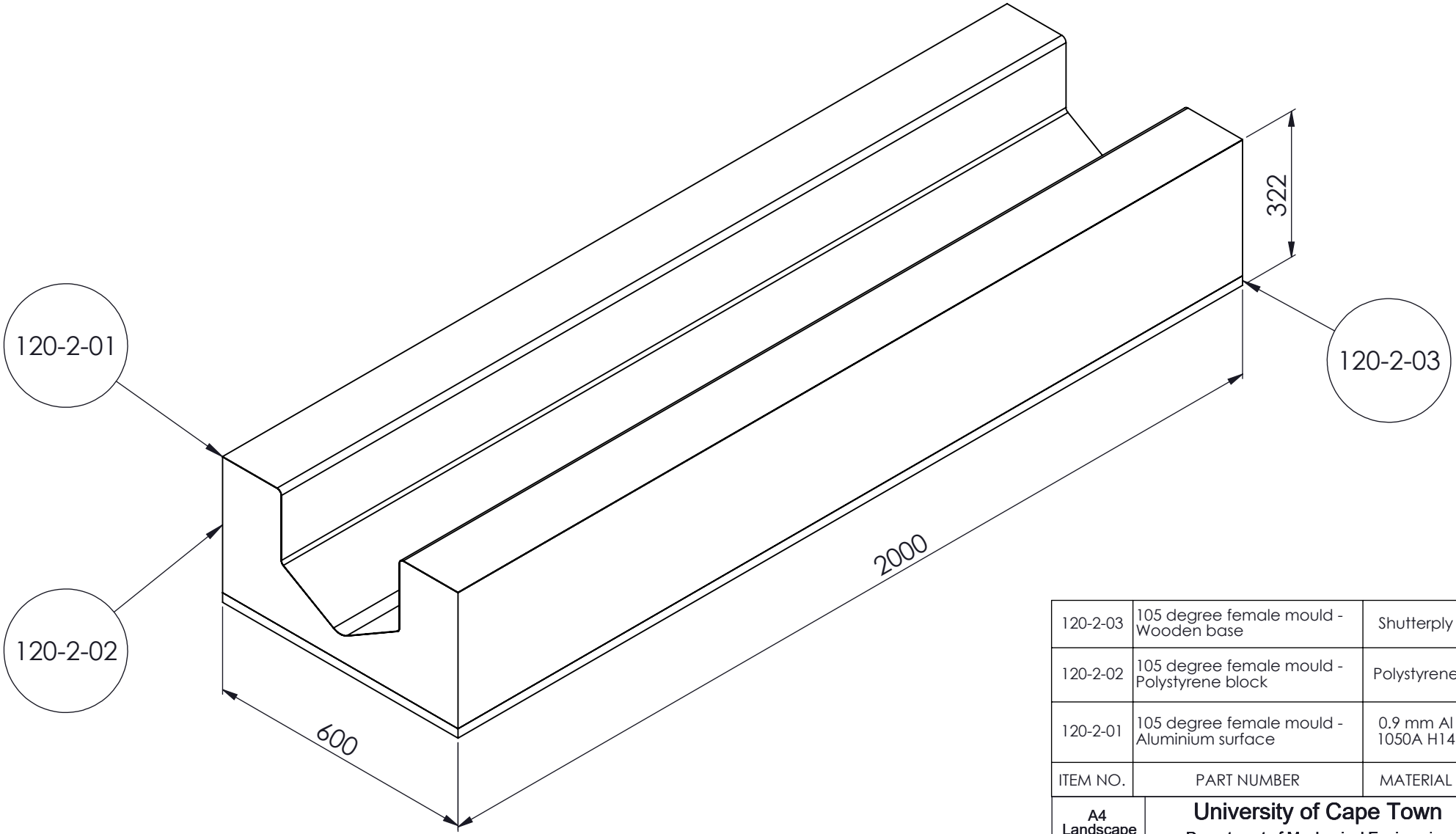

ITEM NO.	PART NUMBER	MATERIAL	QTY.
120-2-03	105 degree female mould - Wooden base	Shutterply	1
120-2-02	105 degree female mould - Polystyrene block	Polystyrene	1
120-2-01	105 degree female mould - Aluminium surface	0.9 mm Al 1050A H14	1

A4 Landscape

University of Cape Town

Department of Mechanical Engineering

Title: Assembly drawing of 120 degree female mould

Assembly Drawing

Scale:	Date:	Sheet	of
1:10	01/04/2017	1	1

Drawn By: Vinay Shekhar

Drawing Number 105-2-00

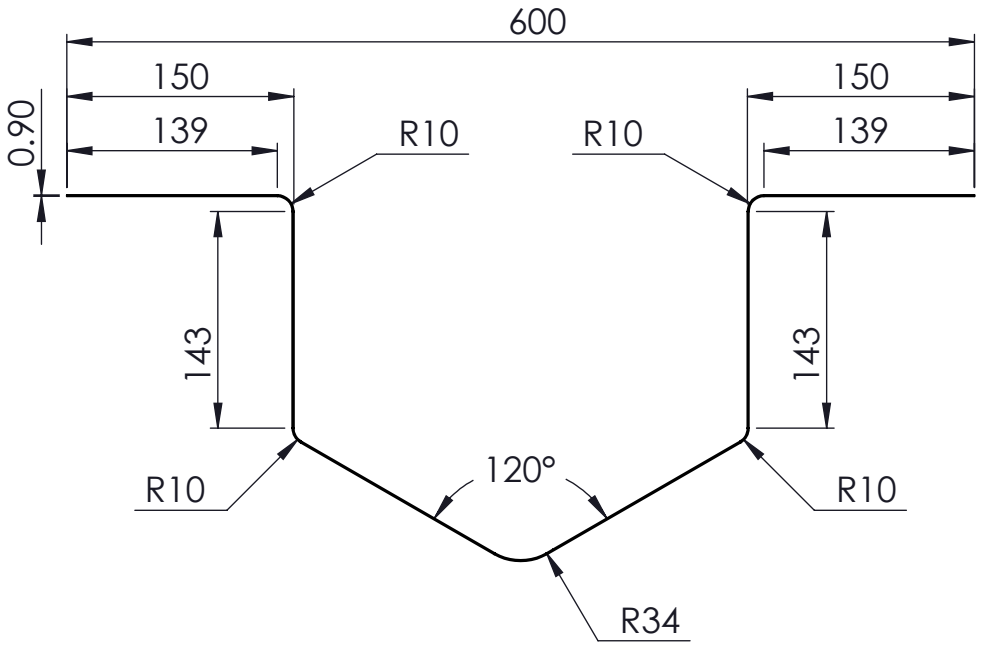

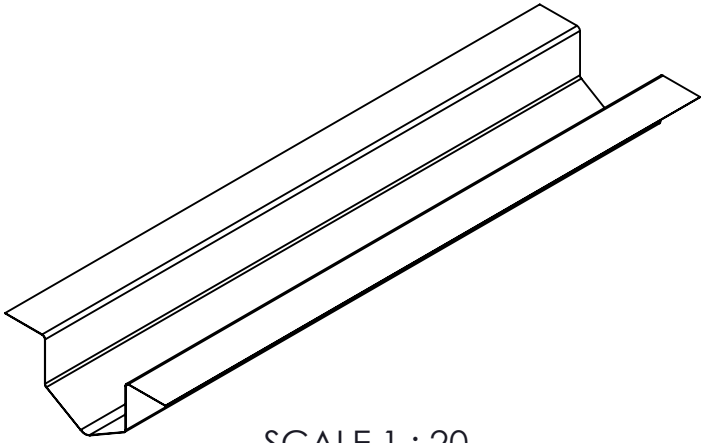

SCALE 1 : 20

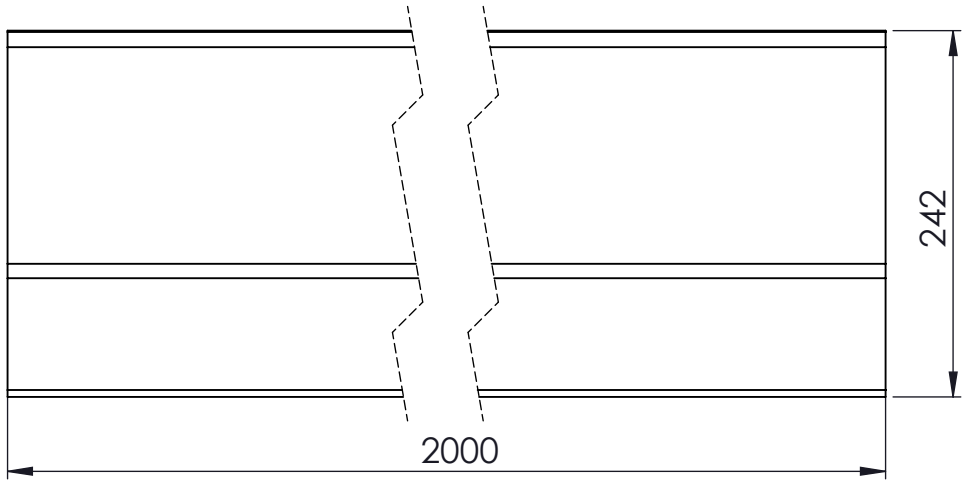

A4 Landscape	**University of Cape Town** Department of Mechanical Engineering			
	Title: Aluminium surface - 120 degree female mould			
Part Finish 1.6	Scale: 1:5	Date: 01/04/2017	Sheet 1	of 2
Material: 0.9 mm Al 1050A H14	Drawn By: Vinay Shekhar		Drawing Number 120-2-01-01	

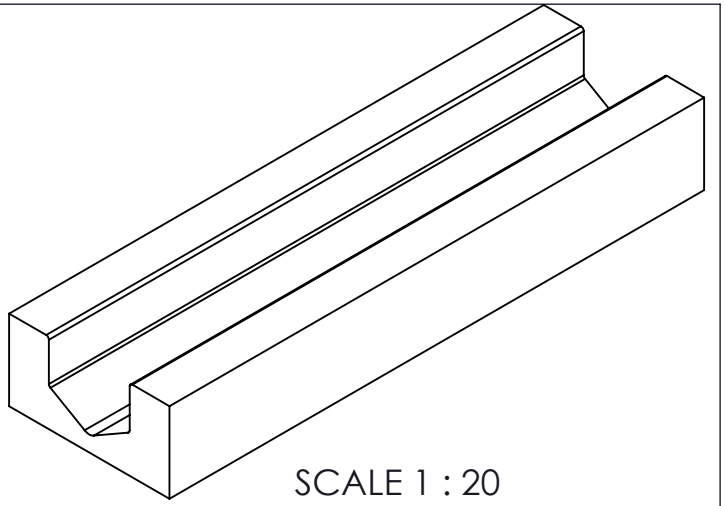

SCALE 1 : 20

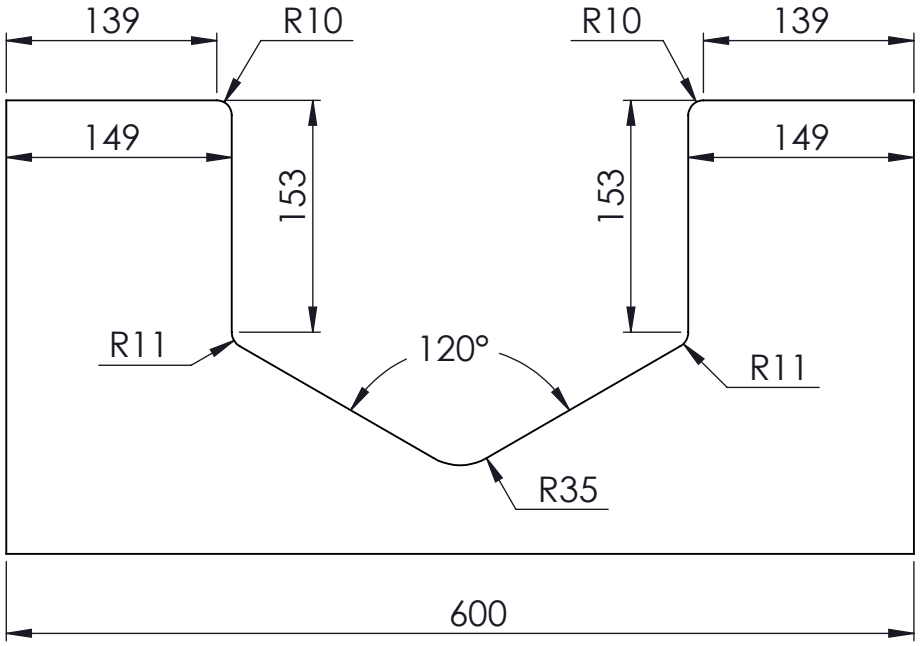

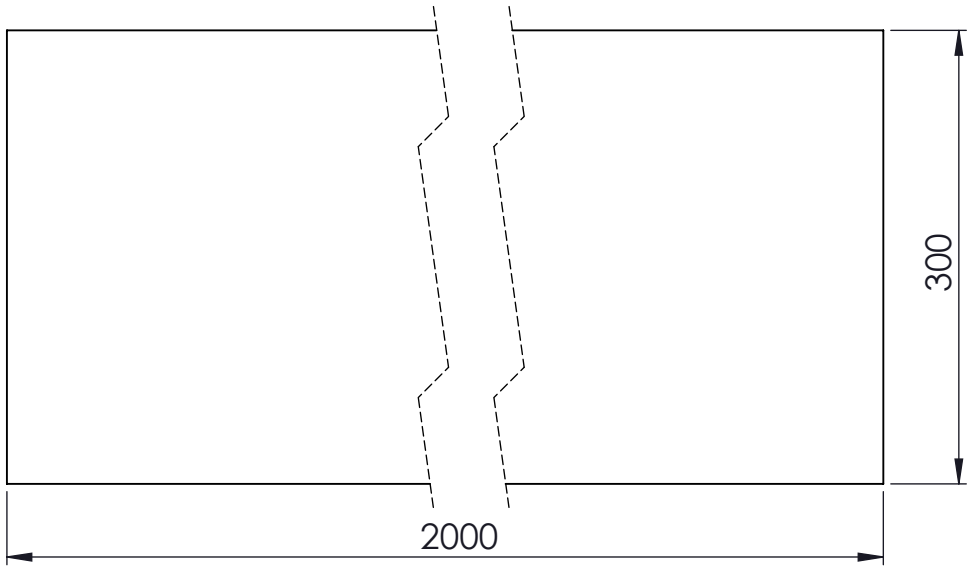

A4 Landscape	**University of Cape Town** Department of Mechanical Engineering			
	Title: Polystyrene block - 120 degree female mould			
Part Finish	Scale: 1:5	Date: 01/04/2017	Sheet 1	of 1
Material: Polystyrene	Drawn By: Vinay Shekhar		Drawing Number 120-2-02	

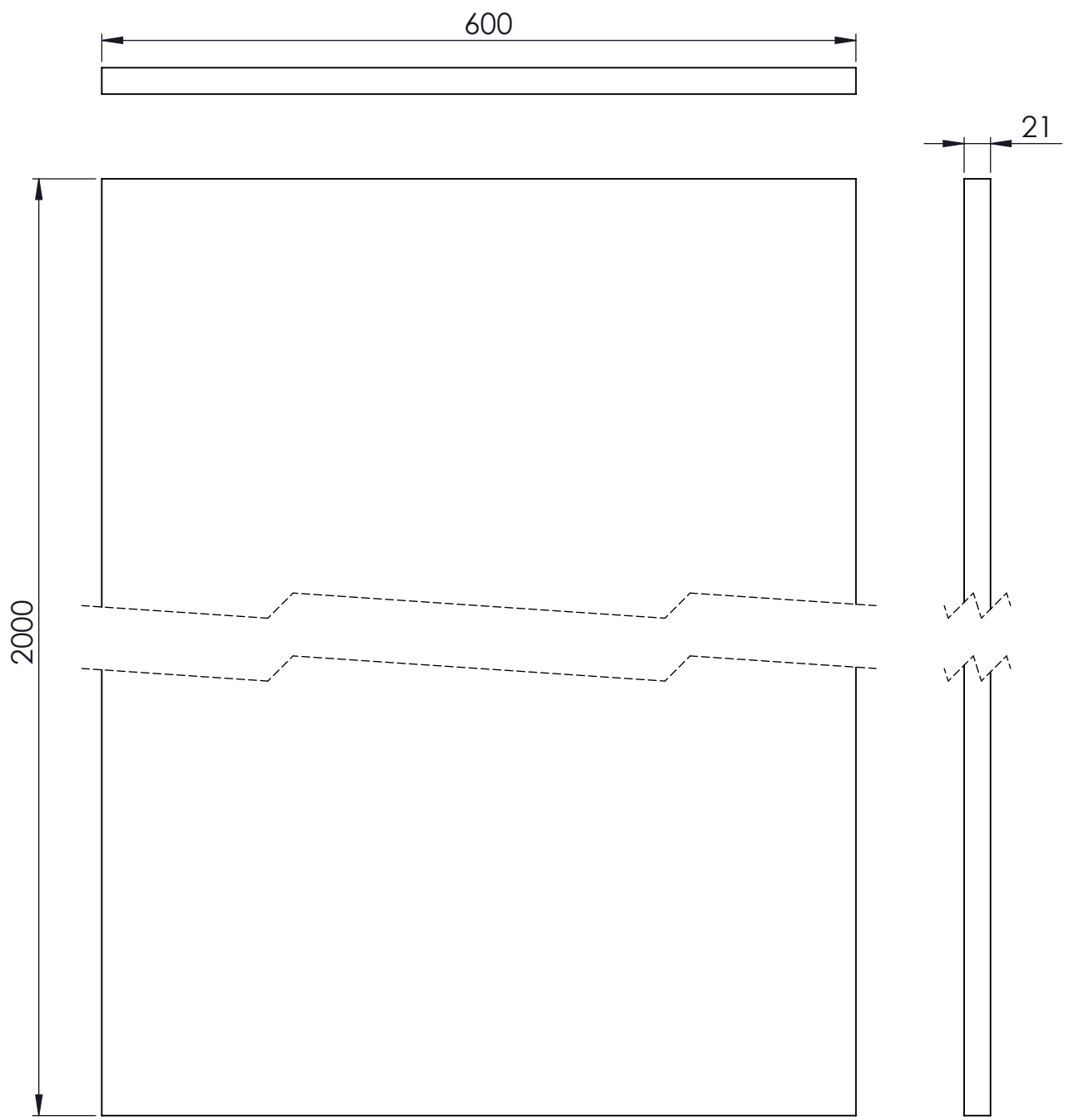

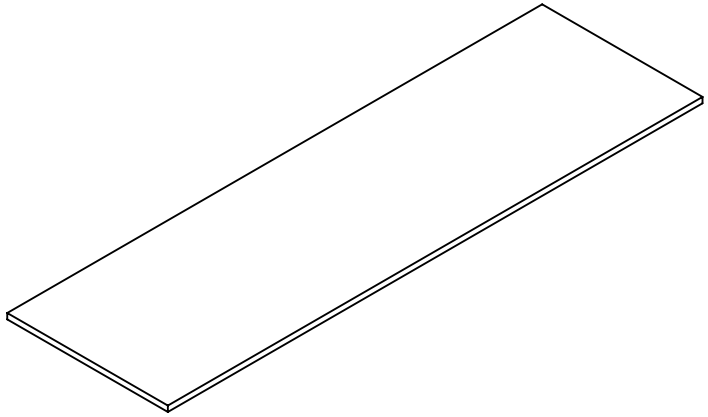

SCALE 1 : 20

A4 Landscape	University of Cape Town Department of Mechanical Engineering			
	Title: Wooden base - 120 degree female mould			
Part Finish	Scale: 1:5	Date: 01/04/2017	Sheet 1	of 1
Material: Shutterply	Drawn By: Vinay Shekhar		Drawing Number 120-2-03	

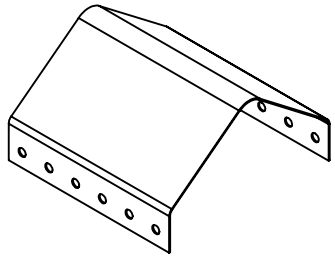

SCALE 1 : 10

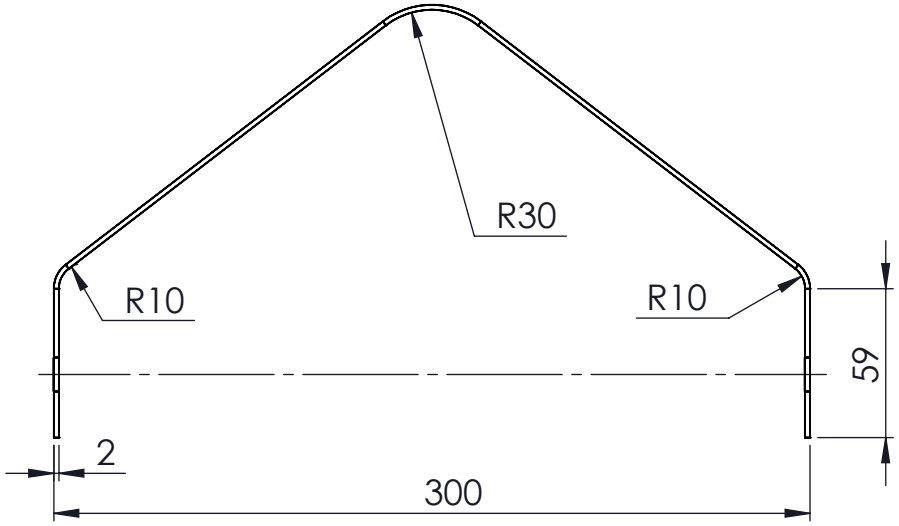

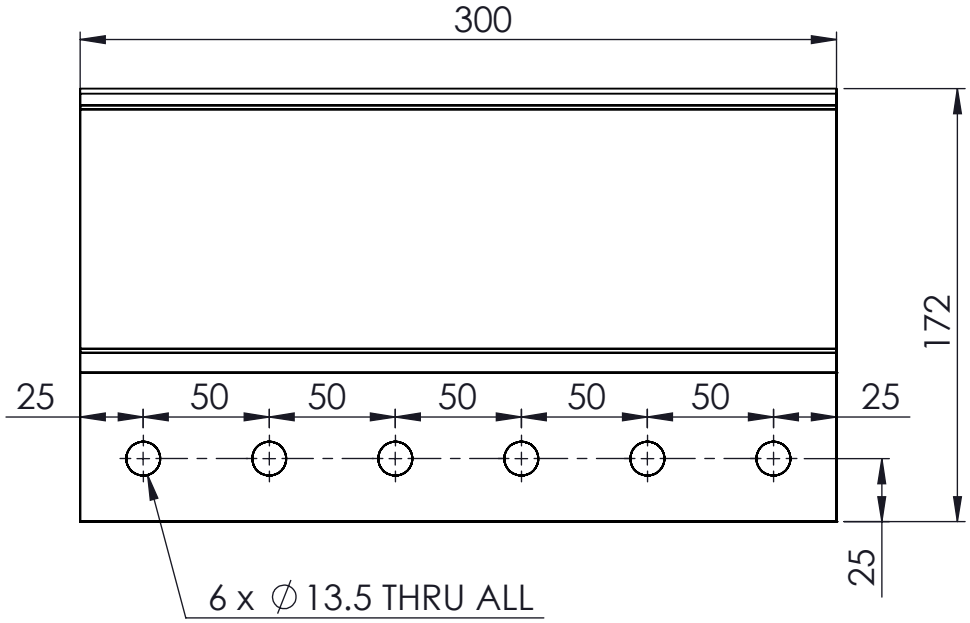

A4 Landscape	University of Cape Town Department of Mechanical Engineering			
	Title: 105 degree Steel Plate, BR 30 mm			
Quantity: 6	Scale: 1:3	Date: 05/12/2016	Sheet 1	of 2
Material: DOMEX-700MC	Drawn By: Vinay Shekhar		Drawing Number 105-30-01	

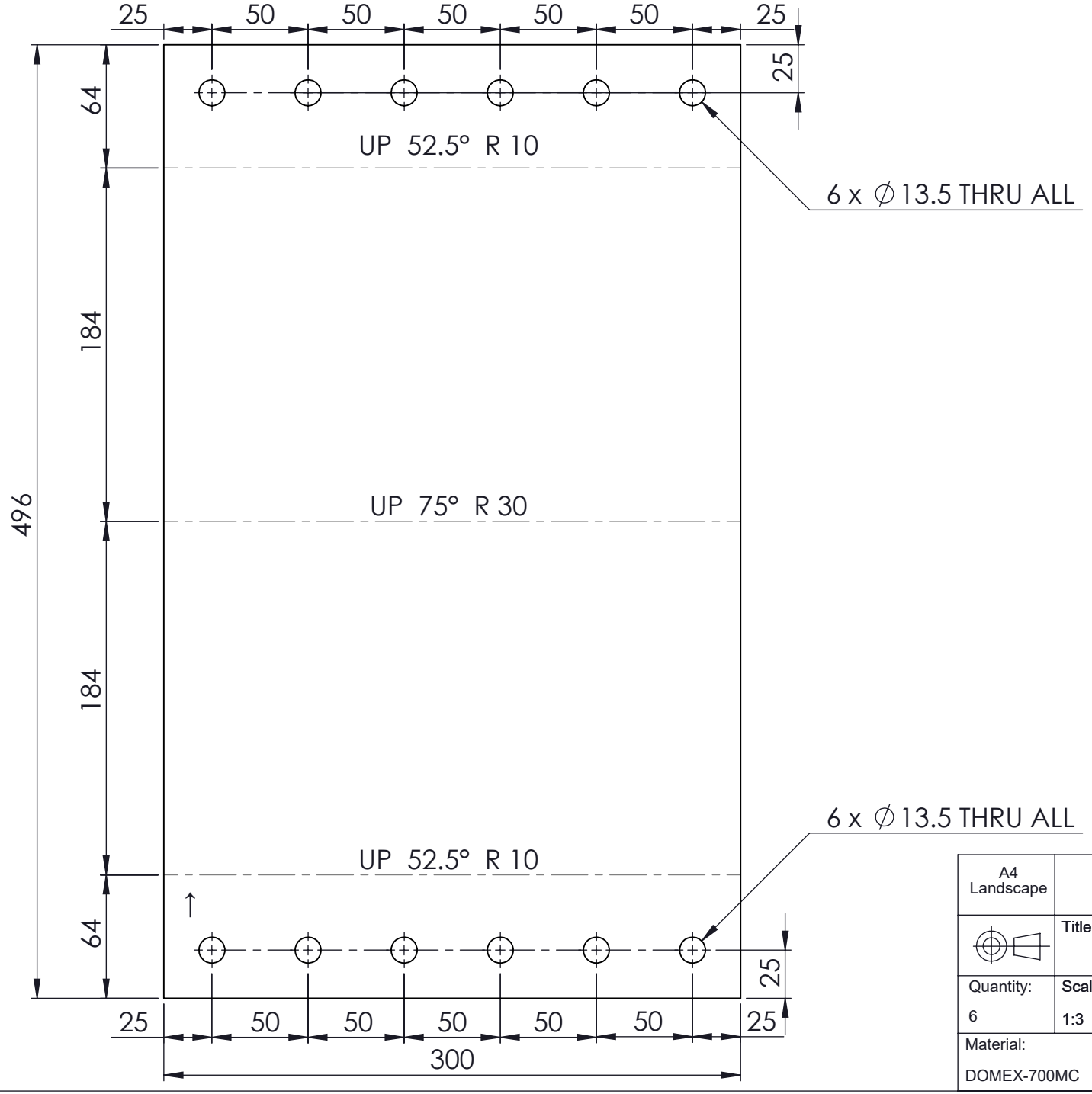

A4 Landscape	**University of Cape Town** Department of Mechanical Engineering			
	Title: 105 degree Steel Plate, BR 30 mm			
Quantity: 6	Scale: 1:3	Date: 05/12/2016	Sheet 2	of 2
Material: DOMEX-700MC	Drawn By: Vinay Shekhar		Drawing Number 105-30-02	

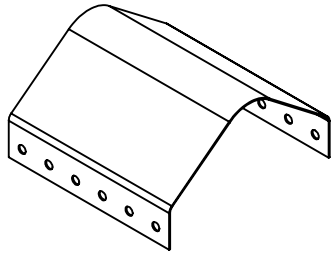

SCALE 1 : 10

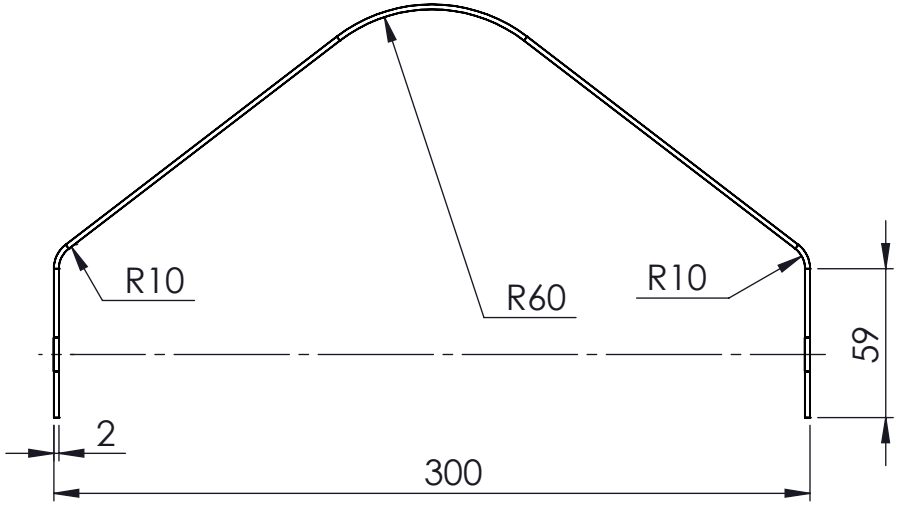

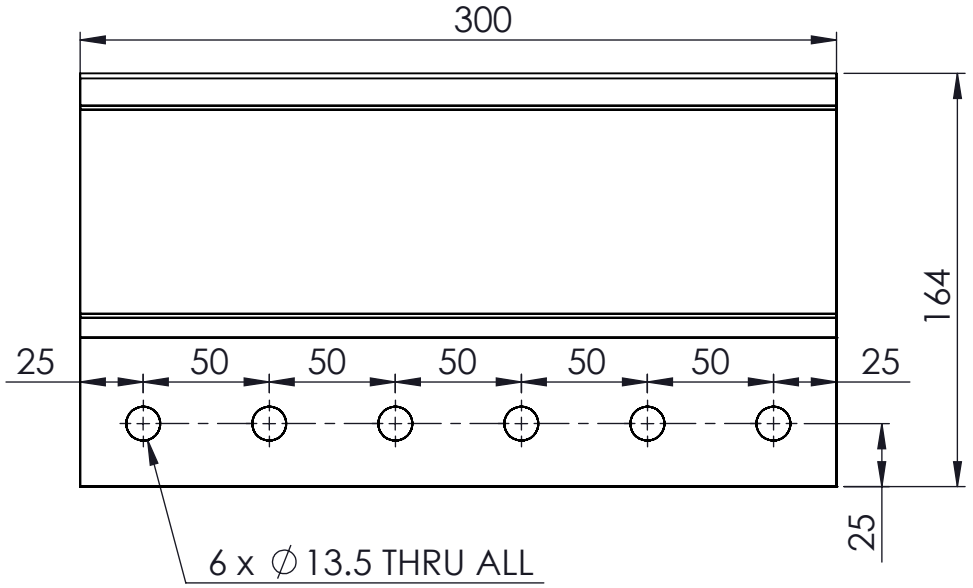

A4 Landscape	University of Cape Town Department of Mechanical Engineering			
	Title: 105 degree Steel Plate, BR 60 mm			
Quantity: 6	Scale: 1:3	Date: 04/01/2023	Sheet 1	of 2
Material: DOMEX-700MC	Drawn By: Vinay Shekhar		Drawing Number 105-60-01	

SOLIDWORKS Educational Product. For Instructional Use Only.

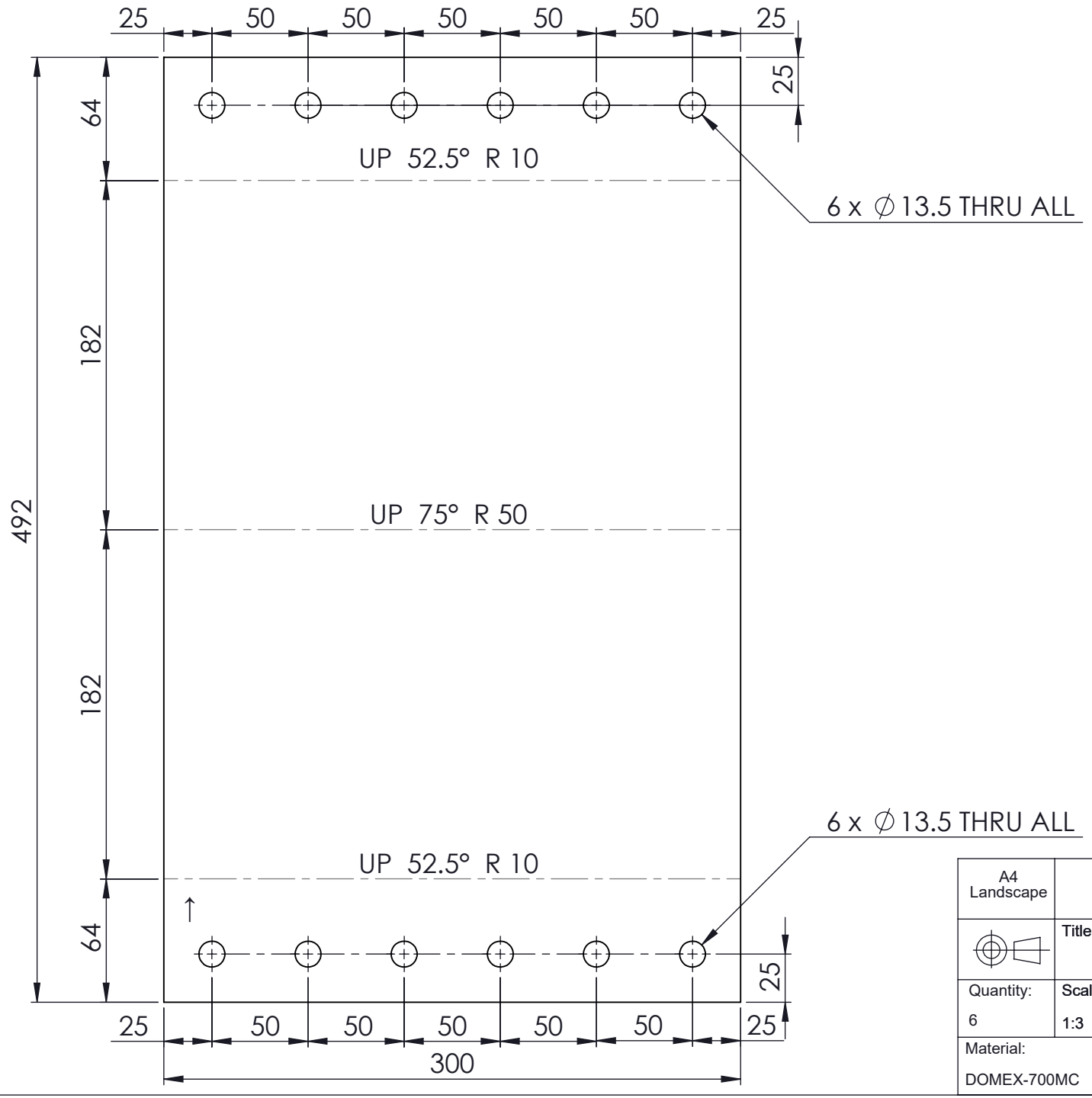

A4 Landscape	**University of Cape Town** Department of Mechanical Engineering			
	Title: 105 degree Steel Plate, BR 60 mm			
Quantity: 6	Scale: 1:3	Date: 05/12/2016	Sheet 2	of 2
Material: DOMEX-700MC	Drawn By: Vinay Shekhar		Drawing Number 105-60-02	

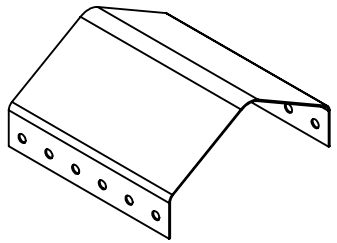

SCALE 1 : 10

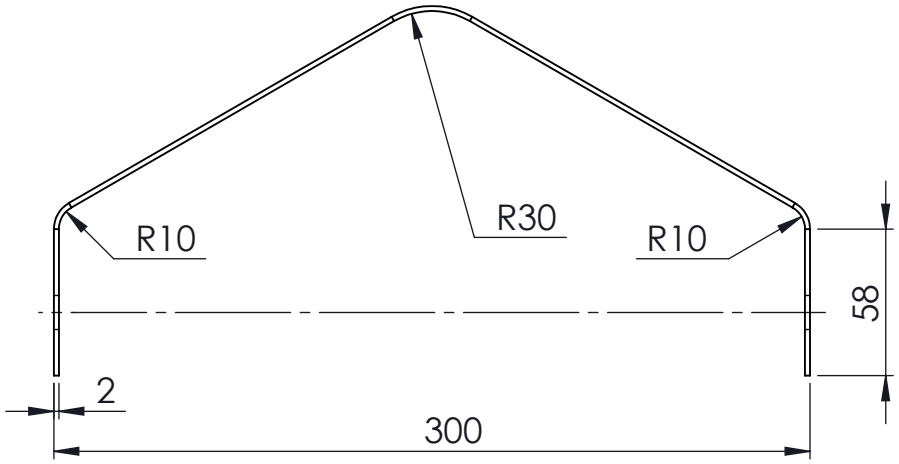

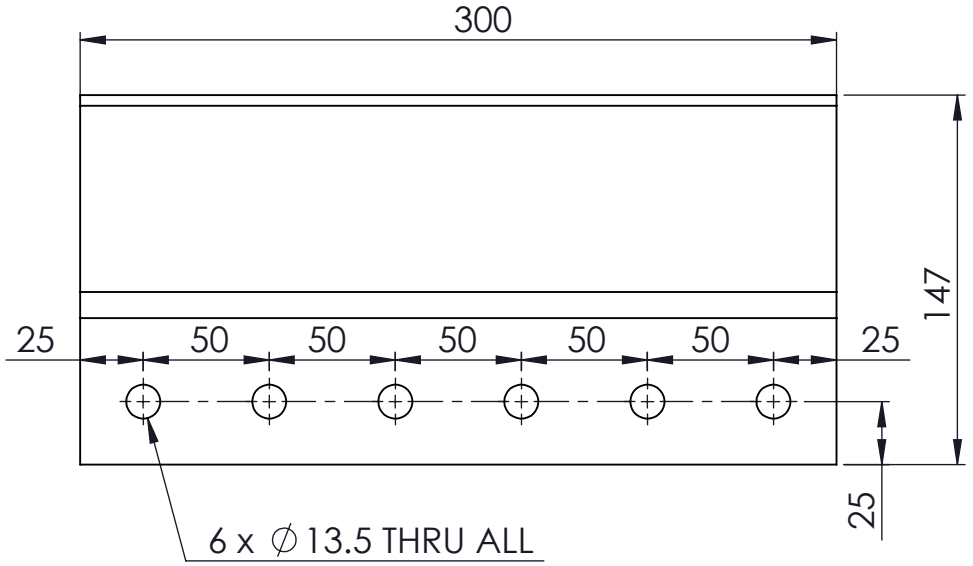

A4 Landscape	University of Cape Town Department of Mechanical Engineering			
	Title: 120 degree Steel Plate, BR 30 mm			
Quantity: 6	Scale: 1:3	Date: 05/12/2016	Sheet 1	of 2
Material: DOMEX-700MC	Drawn By: Vinay Shekhar		Drawing Number 120-30-01	

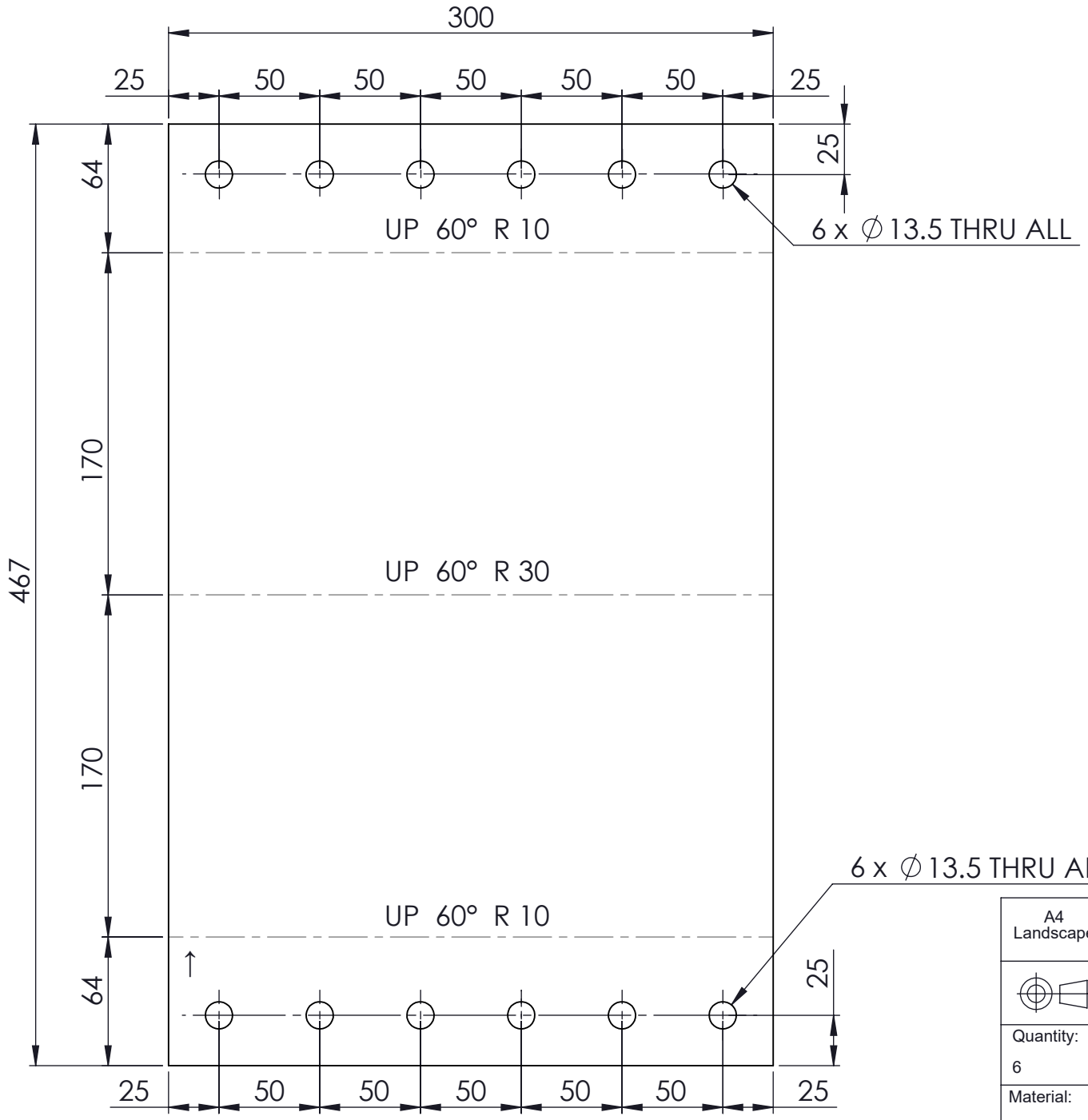

A4 Landscape	University of Cape Town Department of Mechanical Engineering			
	Title: 120 degree Steel Plate, BR 30 mm			
Quantity: 6	Scale: 1:3	Date: 05/12/2016	Sheet 2	of 2
Material: DOMEX-700MC	Drawn By: Vinay Shekhar		Drawing Number 120-30-02	

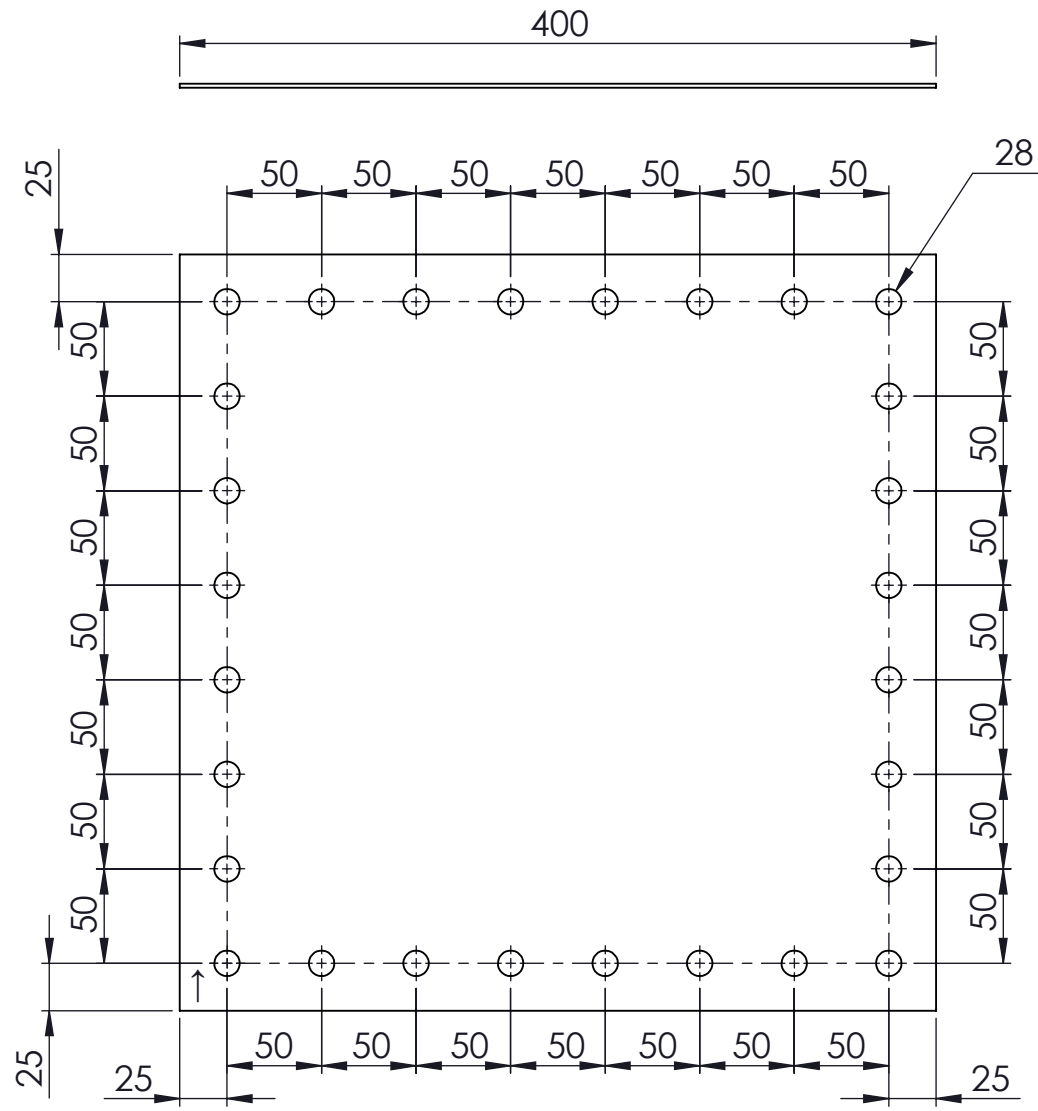

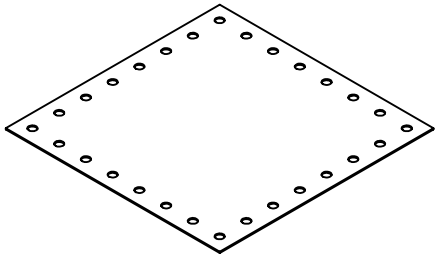

SCALE 1 : 10

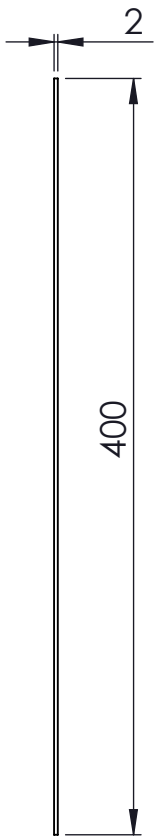

ROLL DIRECTION = ↑

A4 Landscape	University of Cape Town Department of Mechanical Engineering			
	Title: Steel flat plate			
Quantity: 5	Scale: 1:4	Date: 05/12/2016	Sheet 1	of 1
Material: DOMEX 700-MC	Drawn By: Vinay Shekhar		Drawing Number 00-01	

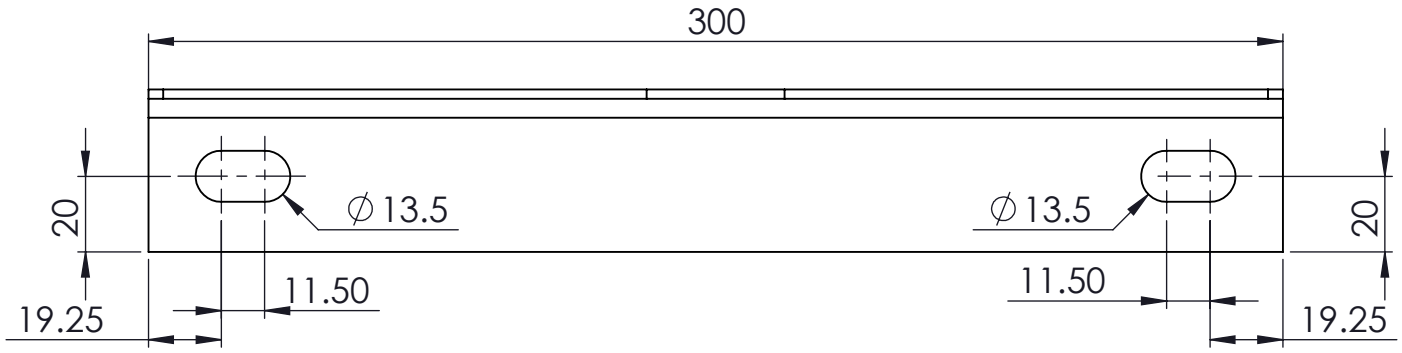

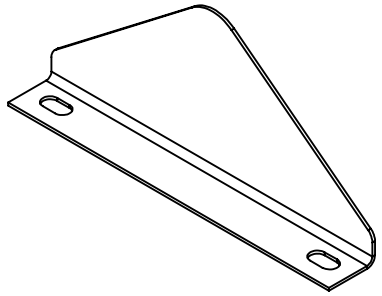

SCALE 1 : 5

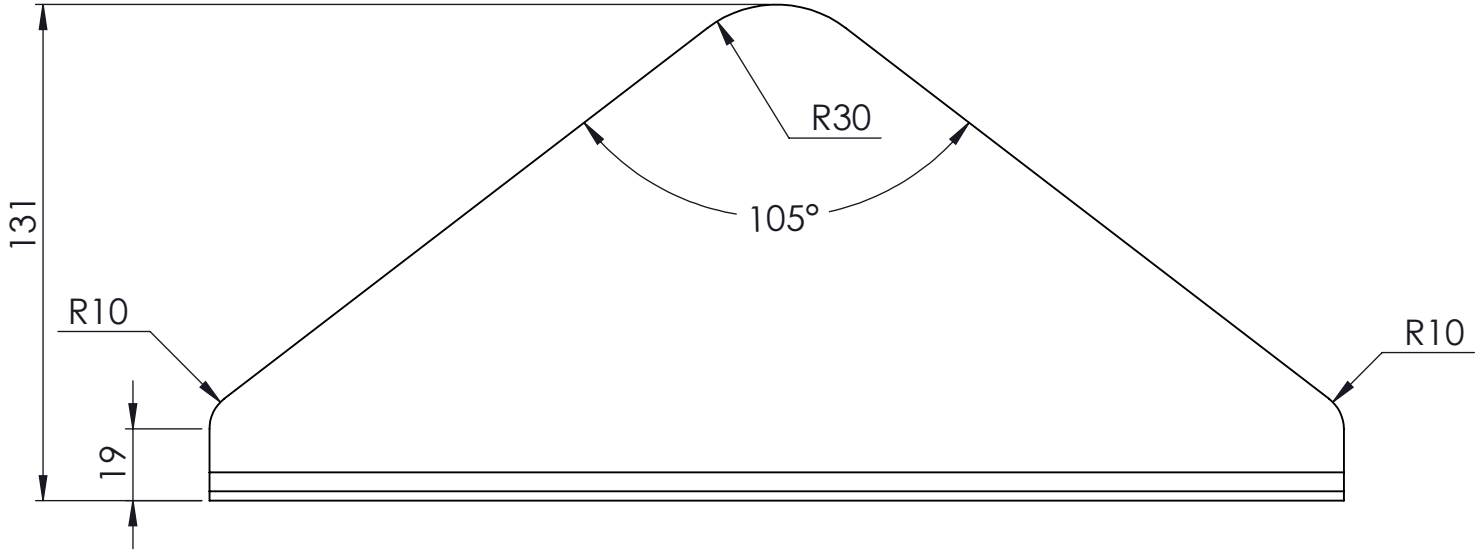

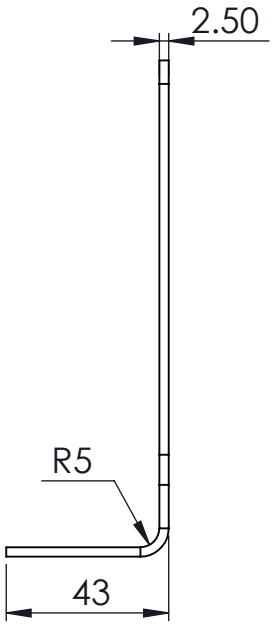

A4 Landscape	**University of Cape Town** Department of Mechanical Engineering			
	Title: DIC Sealing Plate 105 degree 30 mm			
Quantity 2	Scale: 1:2	Date: 15/01/2018	Sheet 1	of 2
Material: Mild Steel	Drawn By: Vinay Shekhar		Drawing Number SP-01-01	

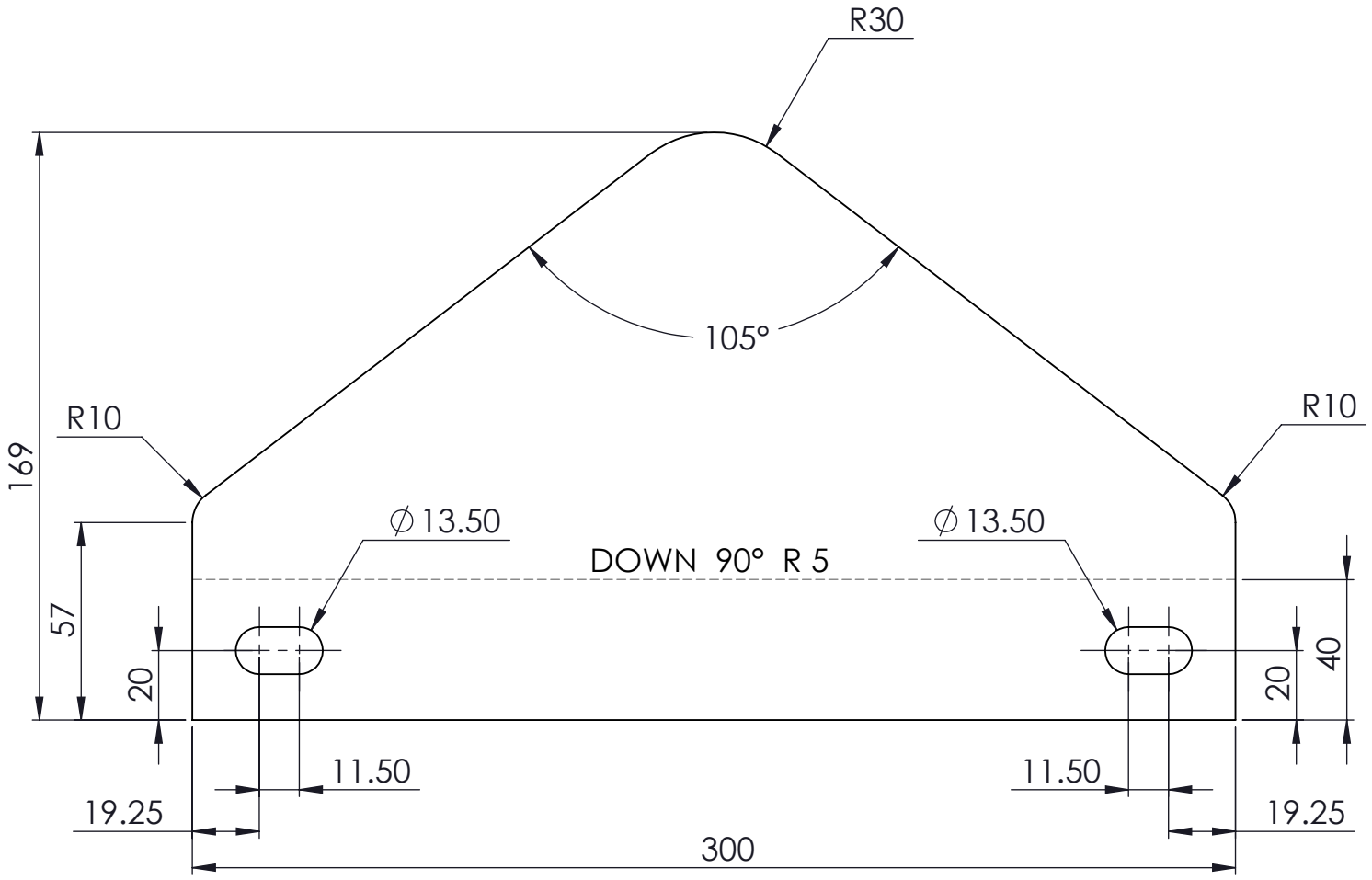

A4 Landscape	**University of Cape Town** Department of Mechanical Engineering			
	Title: DIC Sealing Plate 105 degree 30 mm			
Quantity: 2	Scale: 1:2	Date: 15/01/2018	Sheet 2	of 2
Material: Mild steel	Drawn By: Vinay Shekhar		Drawing Number SP-01-02	

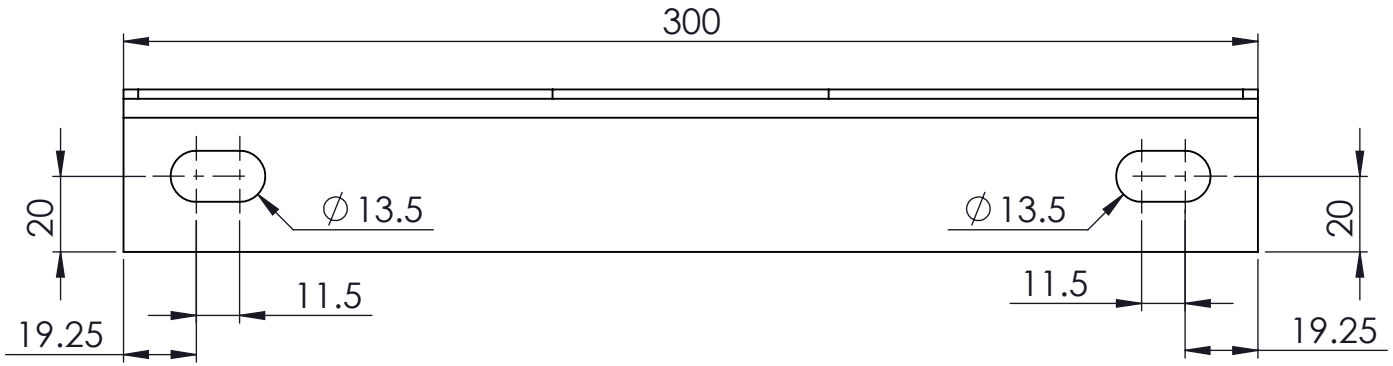

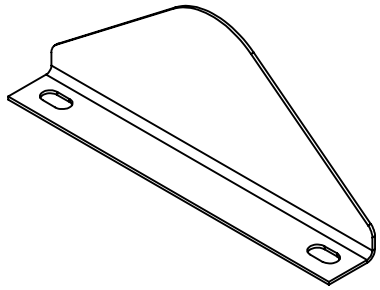

SCALE 1 : 5

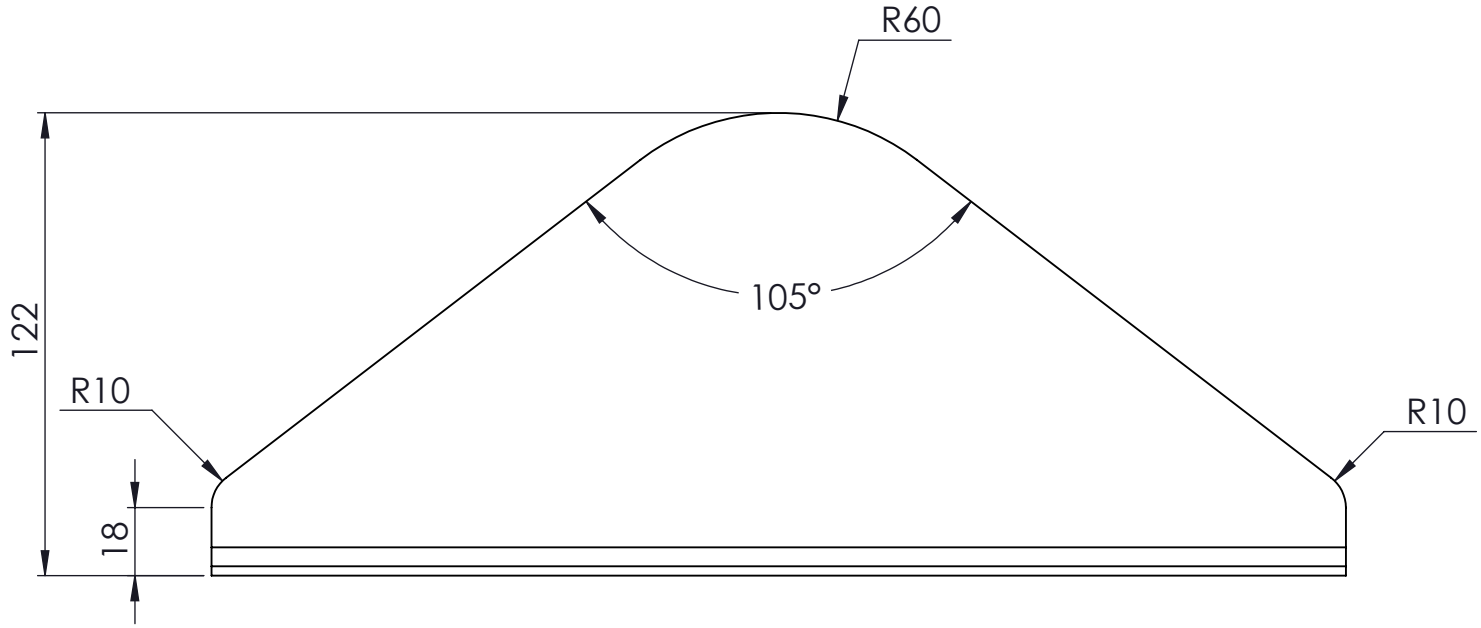

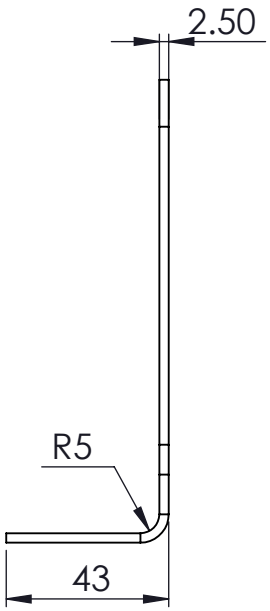

A4 Landscape	University of Cape Town Department of Mechanical Engineering			
	Title: DIC Sealing Plate 105 degree 60 mm			
Quantity 2	Scale: 1:2	Date: 15/01/2018	Sheet 1	of 2
Material: Mild Steel	Drawn By: Vinay Shekhar		Drawing Number SP-02-01	

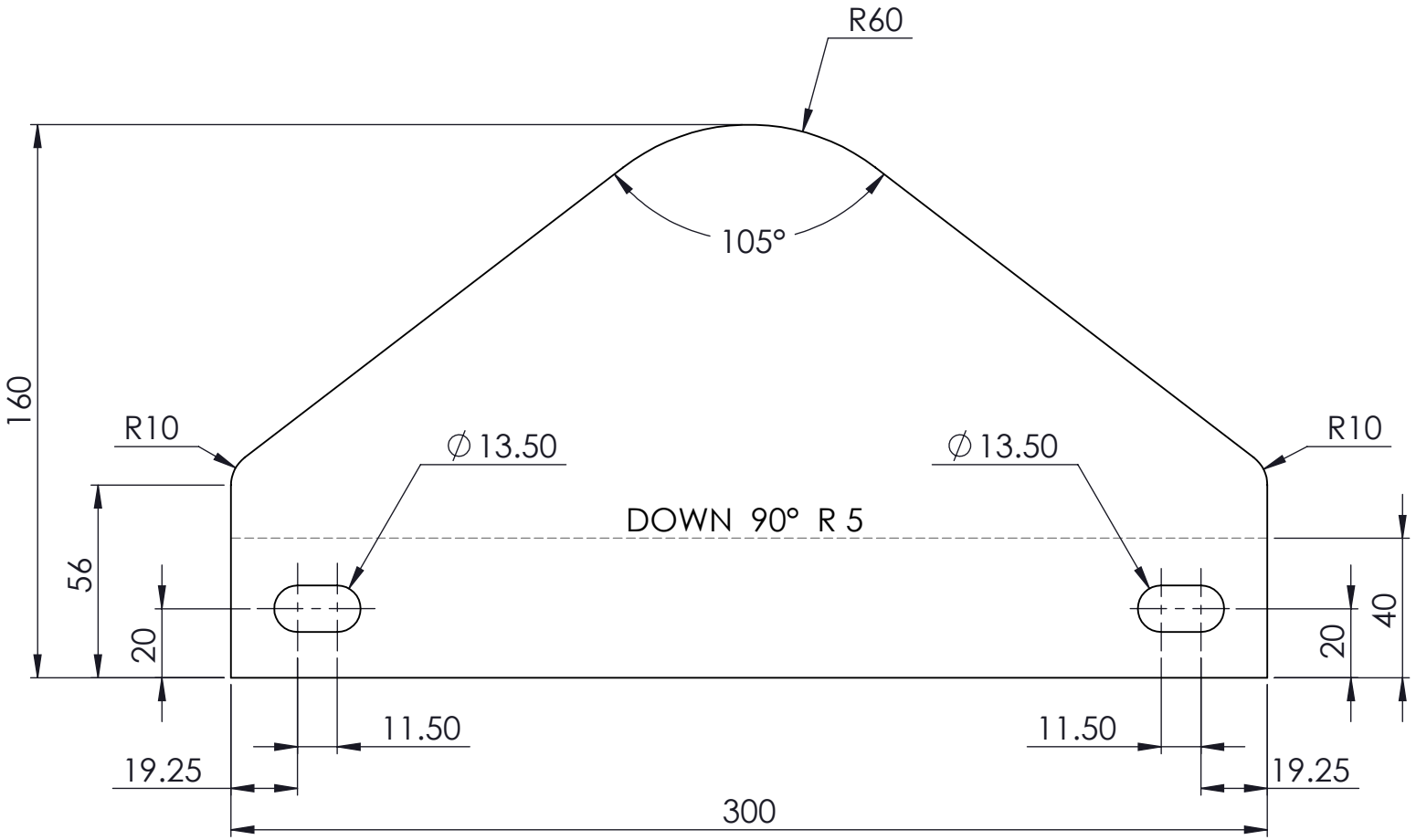

A4 Landscape	**University of Cape Town** Department of Mechanical Engineering			
	Title: DIC Sealing Plate 105 degree 60 mm			
Quantity: 2	Scale: 1:2	Date: 15/01/2018	Sheet 2	of 2
Material: Mild Steel	Drawn By: Vinay Shekhar		Drawing Number SP-02-02	

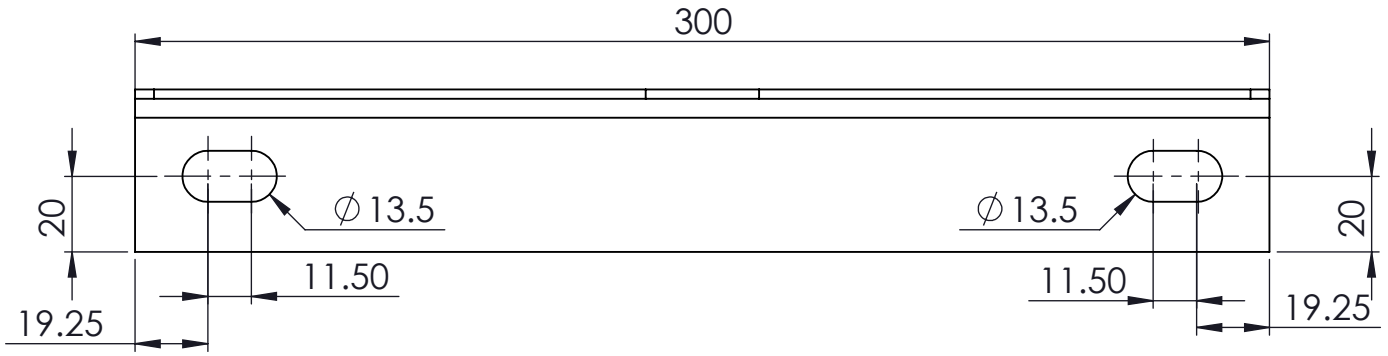

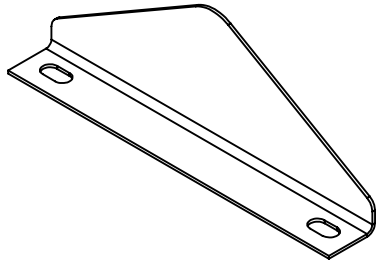

SCALE 1 : 5

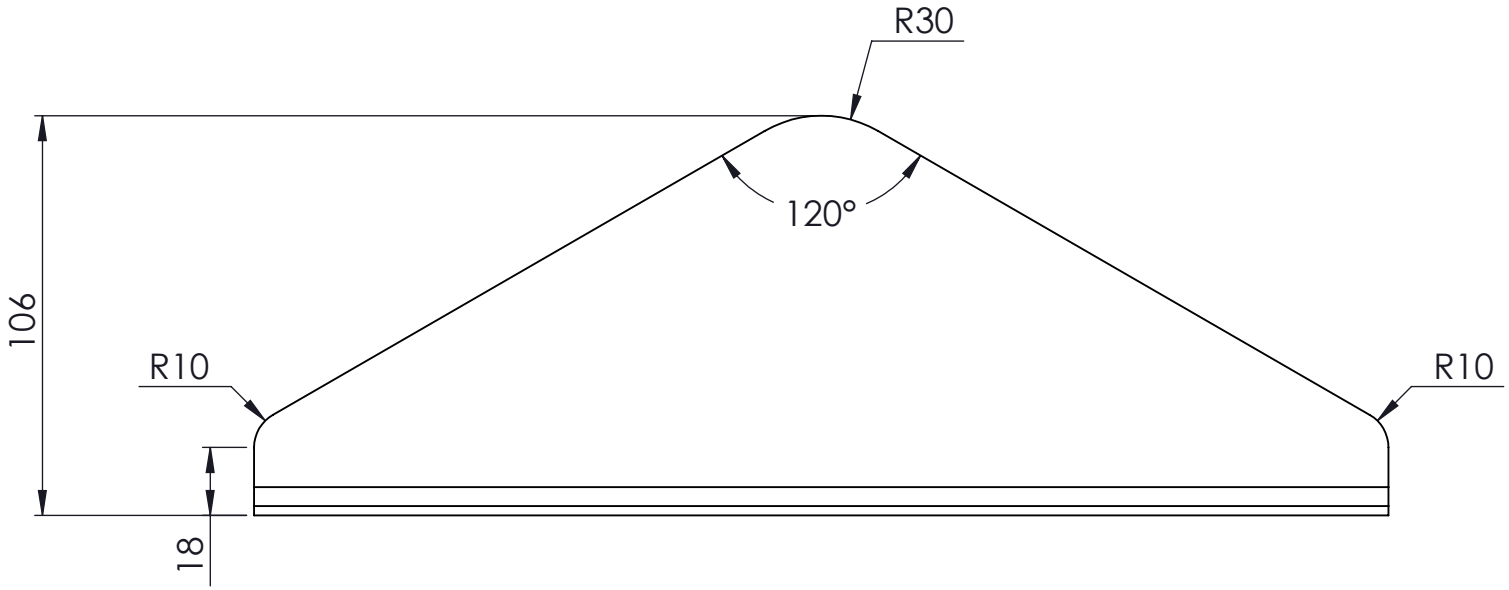

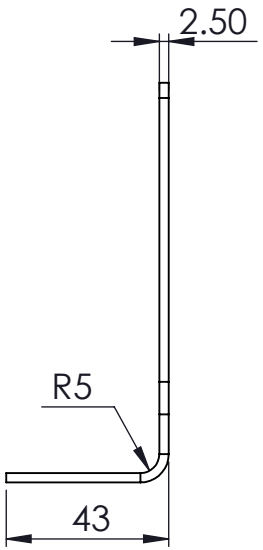

A4 Landscape	University of Cape Town Department of Mechanical Engineering			
	Title: DIC Sealing Plate 120 degree 30 mm			
Quantity 2	Scale: 1:2	Date: 15/01/2018	Sheet 1	of 2
Material: Mild Steel	Drawn By: Vinay Shekhar		Drawing Number SP-03-01	

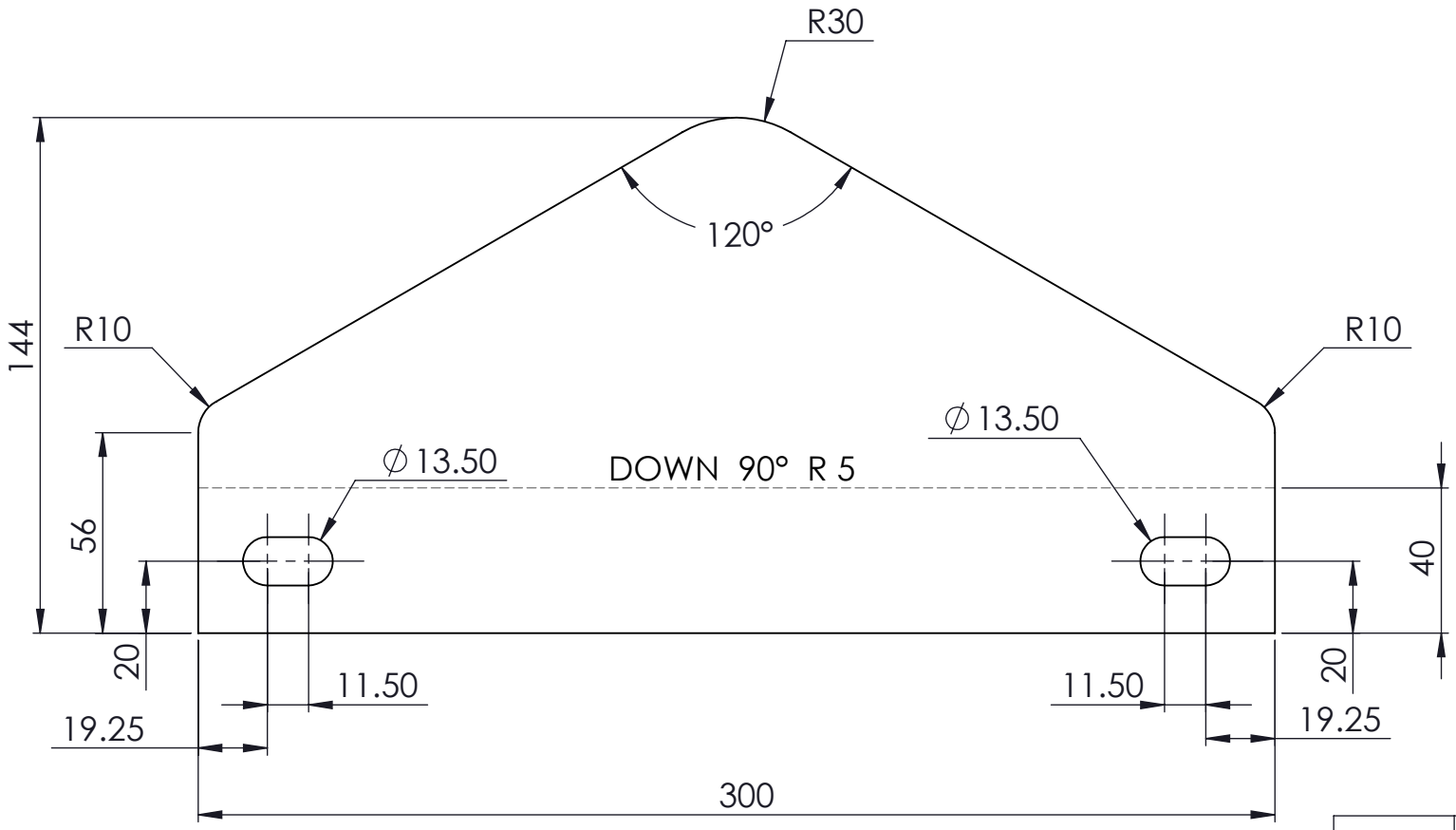

A4 Landscape	**University of Cape Town** Department of Mechanical Engineering			
	Title: DIC Sealing Plate 120 degree 30 mm			
Quantity: 2	Scale: 1:2	Date: 15/01/2018	Sheet 2	of 2
Material: Mild Steel	Drawn By: Vinay Shekhar		Drawing Number SP-03-02	

Appendix B

Blast tested steel V-structure profiles - Additional figures

This appendix contains images of the remaining optically scanned blast tested steel V-structures and the additional transient steel V-structure ridge profile plots.

B.1 Optically scanned 3D V-structure profiles

The 3D profiles have been arranged into three additional figures based on the V-angle and V-tip radius of the V-structure and the SOD of the tests. The sub-figures captions indicate the charge mass of the blast tested steel V-structure. These figures are shown below in figures B.1 to B.3

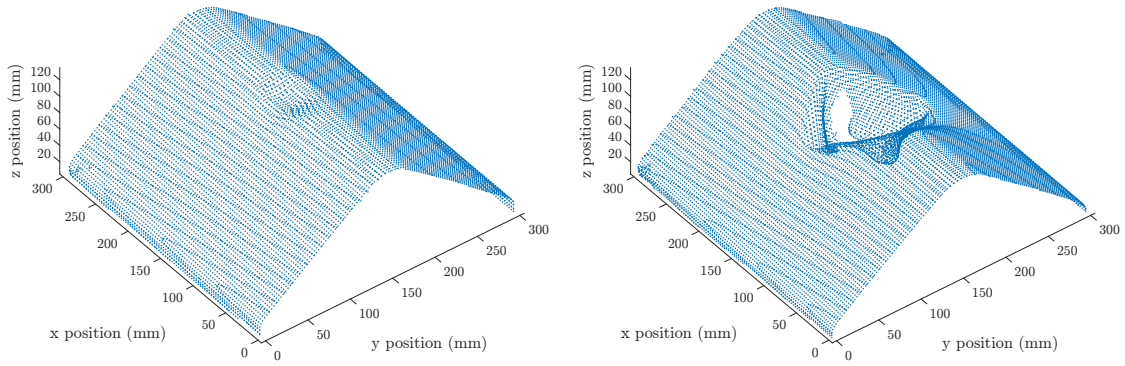

(a) Charge mass = 10 g (b) Charge mass = 40 g

Figure B.1: 3D Profiles of the 105°, 32 mm V-tip radius DOMEX-700 MC V-structures tested at a SOD of 50 mm

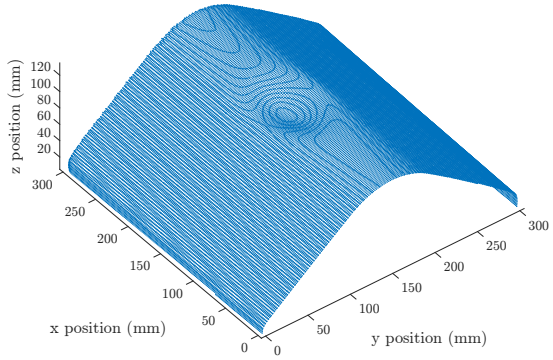

(a) Charge mass = 10 g

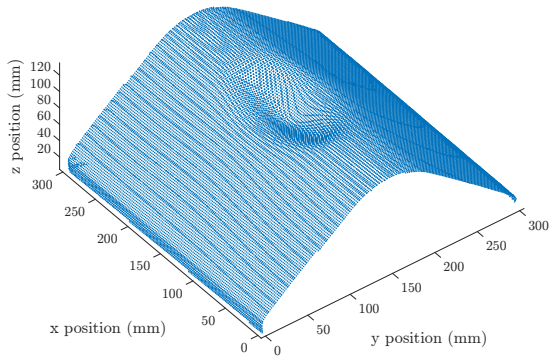

(b) Charge mass = 15 g

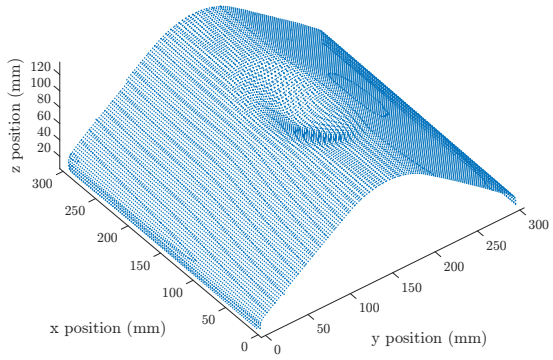

(c) Charge mass = 15 g

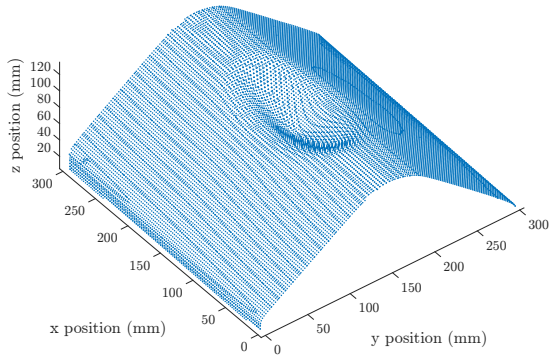

(d) Charge mass = 20 g

Figure B.2: 3D Profiles of the 105°, 62 mm V-tip radius DOMEX-700 MC V-structures tested at a SOD of 34 mm

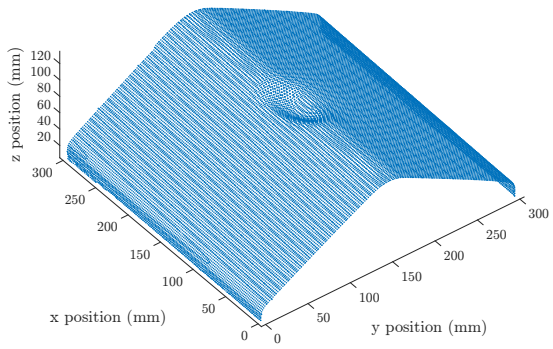

(a) Charge mass = 10 g

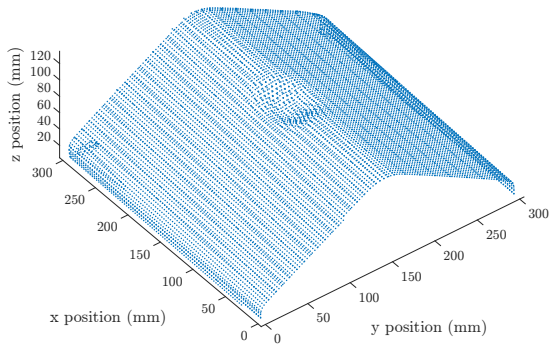

(b) Charge mass = 10 g

Figure B.3: 3D Profiles of the 120°, 32 mm V-tip radius DOMEX-700 MC V-structures tested at a SOD of 34 mm

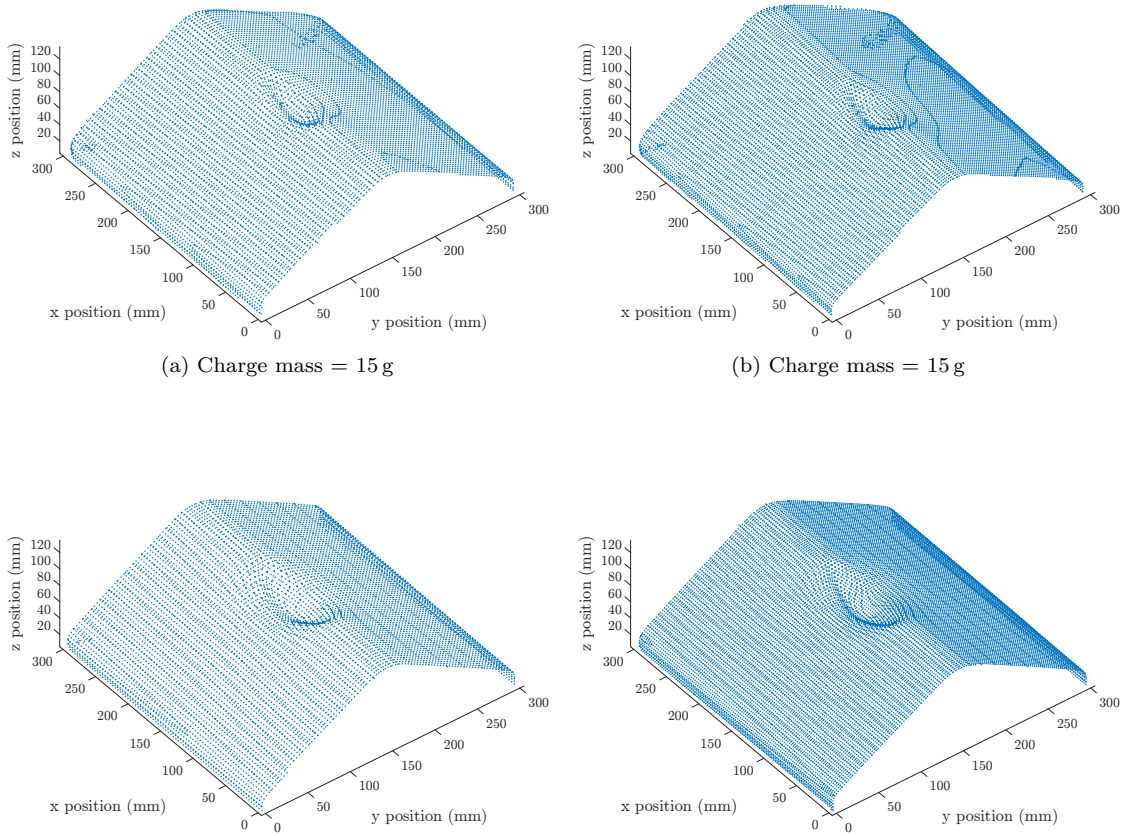

(a) Charge mass = 15 g

(b) Charge mass = 15 g

(c) Charge mass = 20 g

(d) Charge mass = 20 g

Figure B.3: 3D Profiles of the 120°, 32 mm V-tip radius DOMEX-700 MC V-structures tested at a SOD of 34 mm (cont.)

B.2 Transient ridge profile data

The additional transient ridge profiles for the blast tested steel V-structures are provided in figures B.4 to B.7. These include the final deformed ridge profile taken from the optically scanned V-structure data.

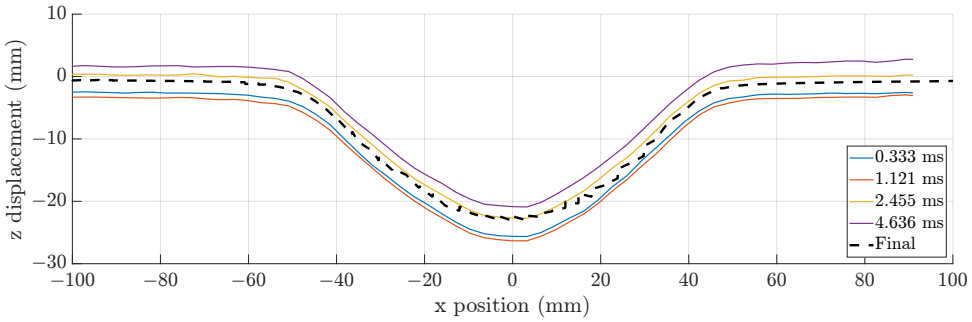

Figure B.4: The ridge profiles for a 105°, 32 mm V-tip radius DOMEX-700 MC V-structure tested with a 15 g PE4 charge at a SOD of 34 mm

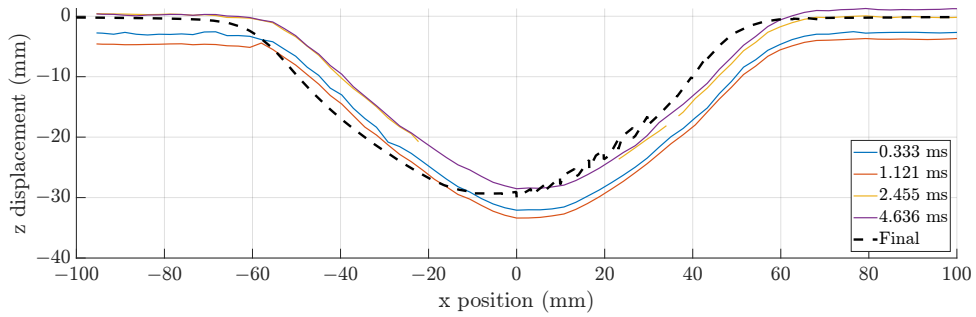

Figure B.5: The ridge profiles for a 105°, 32 mm V-tip radius DOMEX-700 MC V-structure tested with a 20 g PE4 charge at a SOD of 34 mm

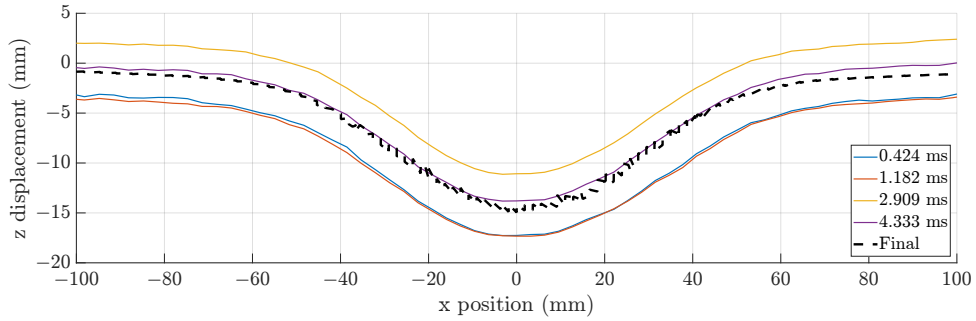

Figure B.6: The ridge profiles for a 105°, 62 mm V-tip radius DOMEX-700 MC V-structure tested with a 10 g PE4 charge at a SOD of 34 mm

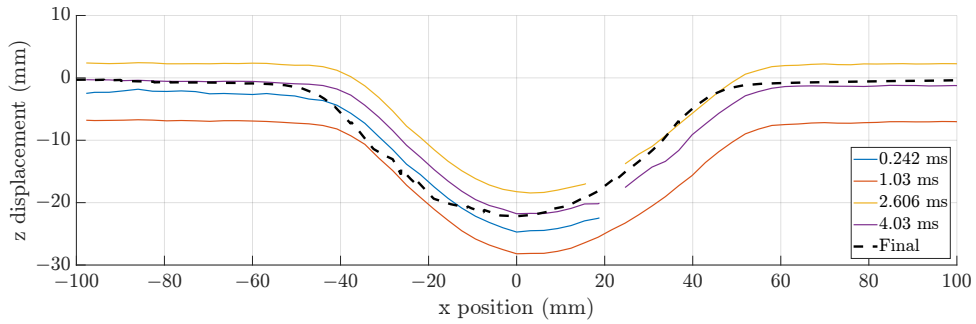

Figure B.7: The ridge profiles for a 120°, 32 mm V-tip radius DOMEX-700 MC V-structure tested with a 15 g PE4 charge at a SOD of 34 mm

Appendix C

GFRP V-structures - Supplementary photographs

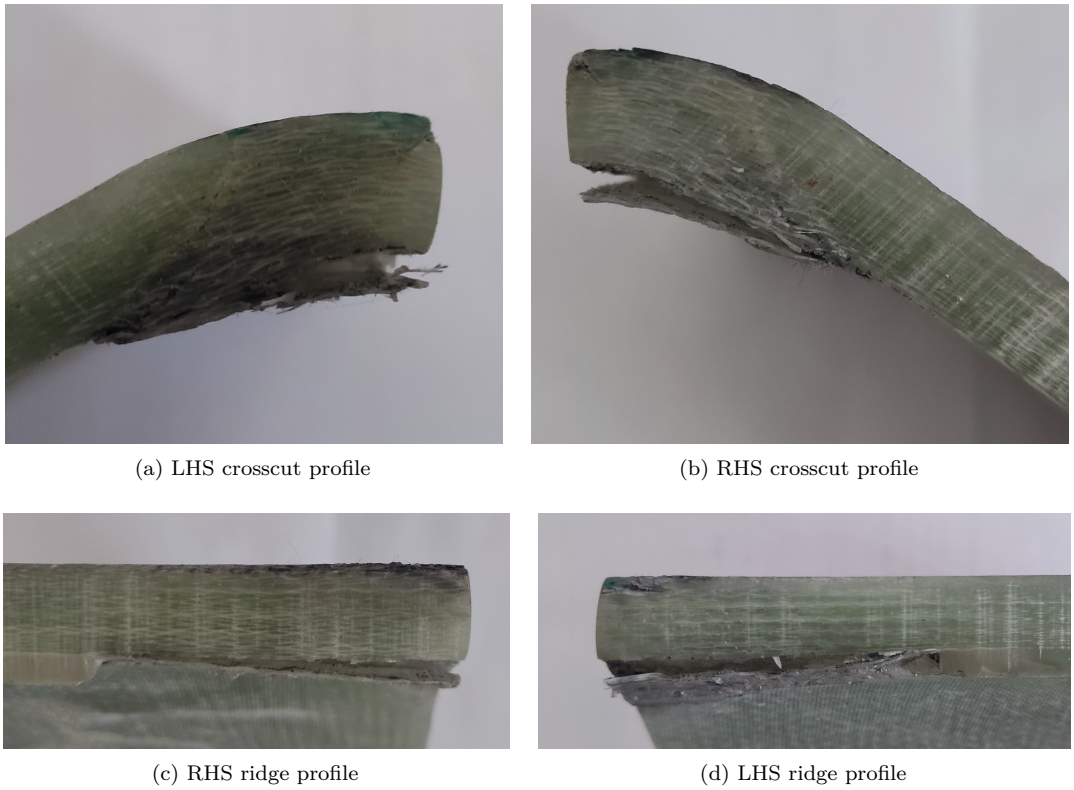

(a) LHS crosscut profile

(b) RHS crosscut profile

(c) RHS ridge profile

(d) LHS ridge profile

Figure C.1: Photographs of a sectioned GFRP V-structure (105°, 34 mm V-tip radius, 0°/90° ply orientation) tested at an charge mass of 10 g with a SOD of 34 mm

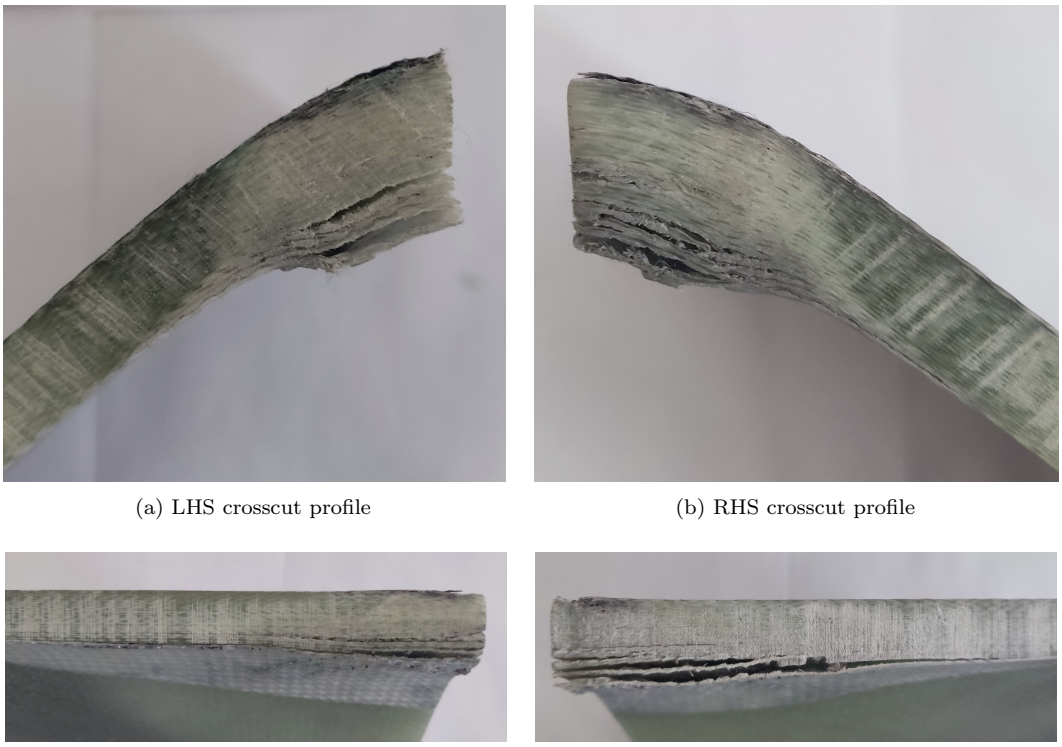

(a) LHS crosscut profile

(b) RHS crosscut profile

(c) RHS ridge profile

(d) LHS ridge profile

Figure C.2: Photographs of a sectioned GFRP V-structure (105°, 34 mm V-tip radius, ±45° ply orientation) tested at an charge mass of 15 g with a SOD of 34 mm

Appendix D

Numerical blast simulations - Steel - Supplementary figures

This appendix contains the additional figures from the numerical blast results chapter on the DOMEX-700 MC steel V-structures in chapter 8.

D.1 Experimental versus numerical results - Additional figures and tables

D.1.1 V-structure permanent deformed profiles - Ridge plane

The additional permanently deformed ridge profile comparisons are provided in figures D.1 to D.6. In each figure the dashed line represents the numerical solution while the solid line is the experimental blast test result.

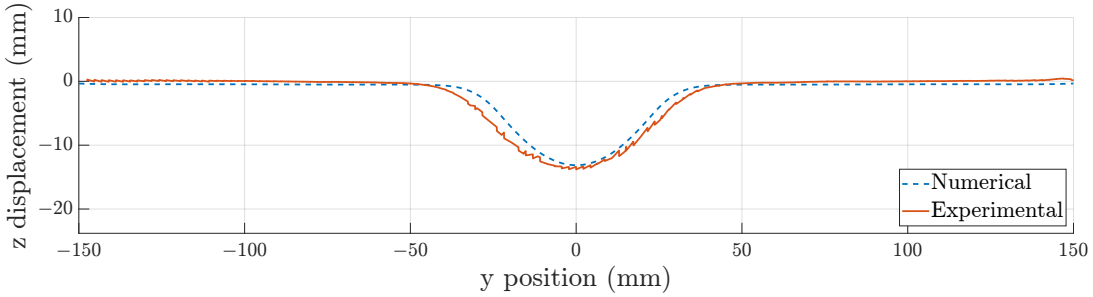

Figure D.1: Permanently deformed ridge profiles for a 105° 32 mm V-tip radius DOMEX-700 MC V-structure at a charge mass of 10 g (numerical versus experimental)

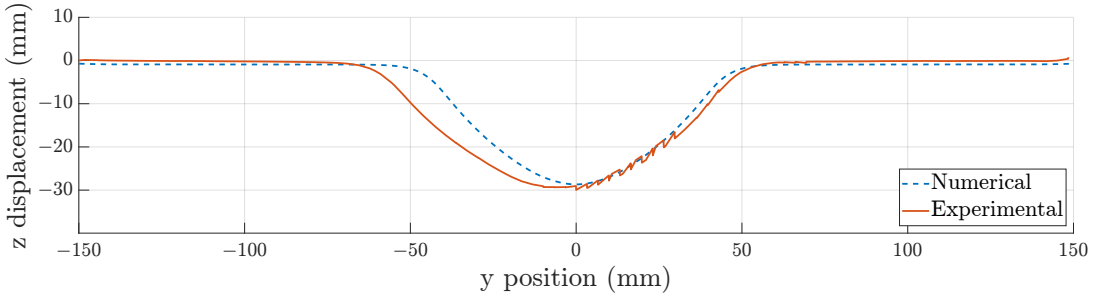

Figure D.2: Permanently deformed ridge profiles for a 105° 32 mm V-tip radius DOMEX-700 MC V-structure at a charge mass of 20 g (numerical versus experimental)

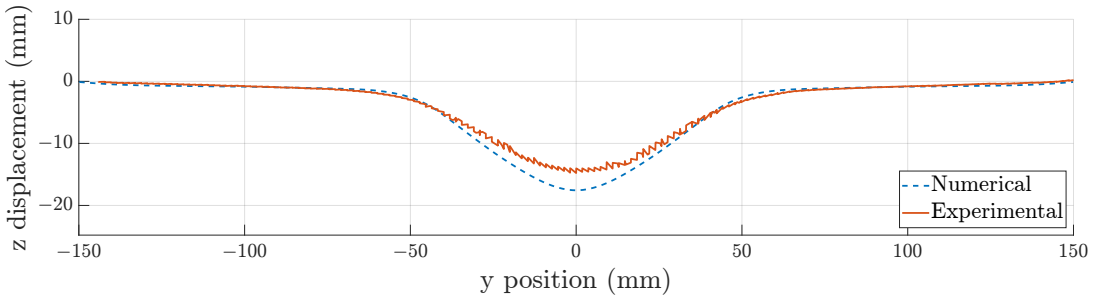

Figure D.3: Permanently deformed ridge profiles for a 105° 62 mm V-tip radius DOMEX-700 MC V-structure at a charge mass of 10 g (numerical versus experimental)

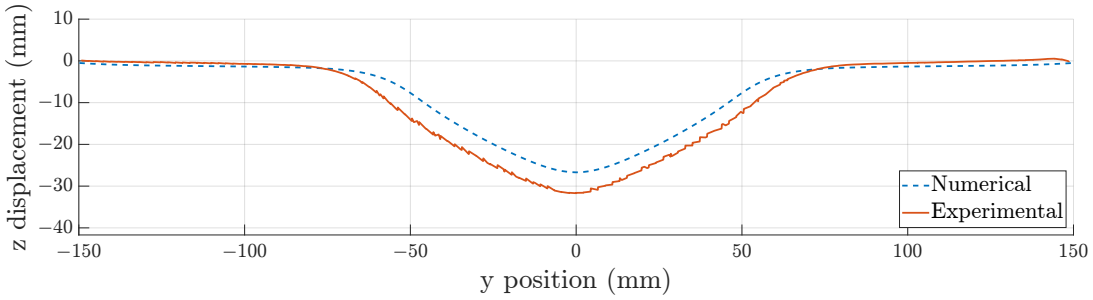

Figure D.4: Permanently deformed ridge profiles for a 105° 62 mm V-tip radius DOMEX-700 MC V-structure at a charge mass of 15 g (numerical versus experimental)

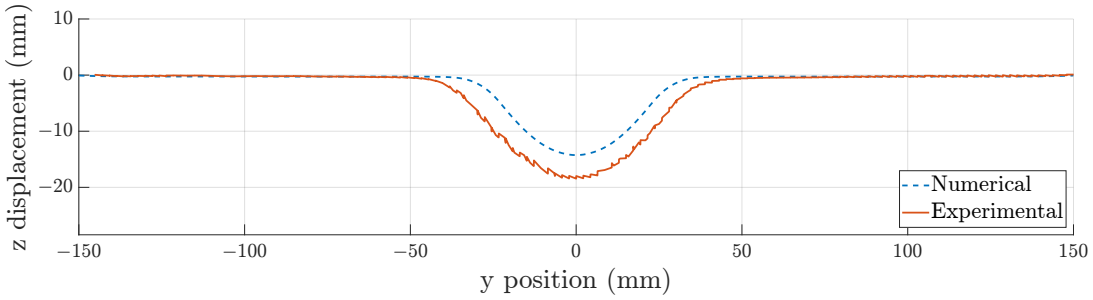

Figure D.5: Permanently deformed ridge profiles for a 120° 32 mm V-tip radius DOMEX-700 MC V-structure at a charge mass of 10 g (numerical versus experimental)

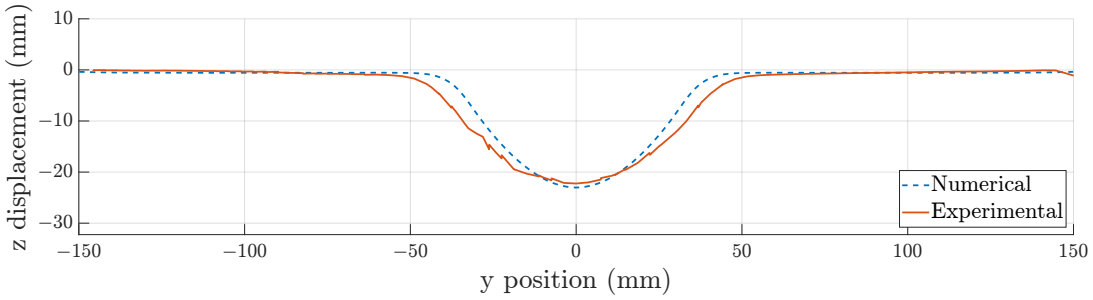

Figure D.6: Permanently deformed ridge profiles for a 120° 32 mm V-tip radius DOMEX-700 MC V-structure at a charge mass of 15 g (numerical versus experimental)

D.1.2 V-structure permanent deformed profiles - Crosscut plane

The additional permanently deformed crosscut profile comparisons are provided in figures D.7 to D.12.

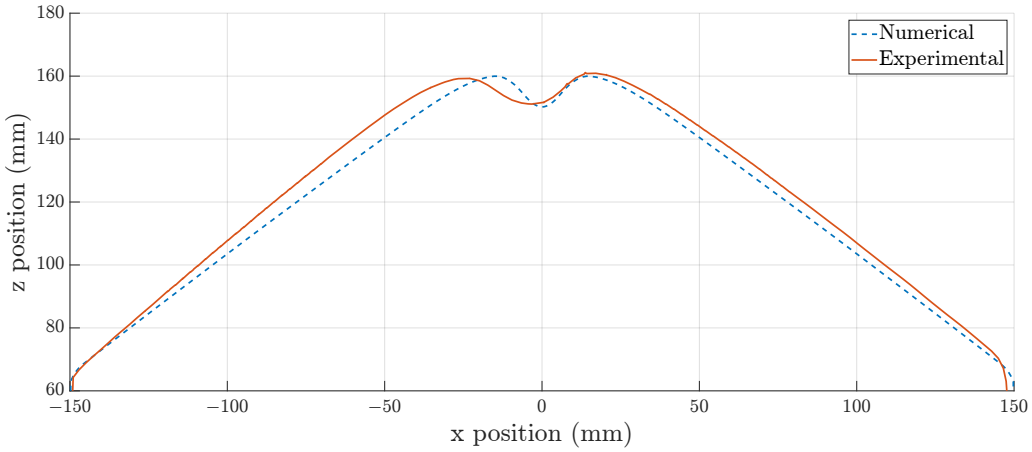

Figure D.7: Permanently deformed crosscut profiles for a 105° 32 mm V-tip radius DOMEX-700 MC V-structure at a charge mass of 15 g (numerical versus experimental)

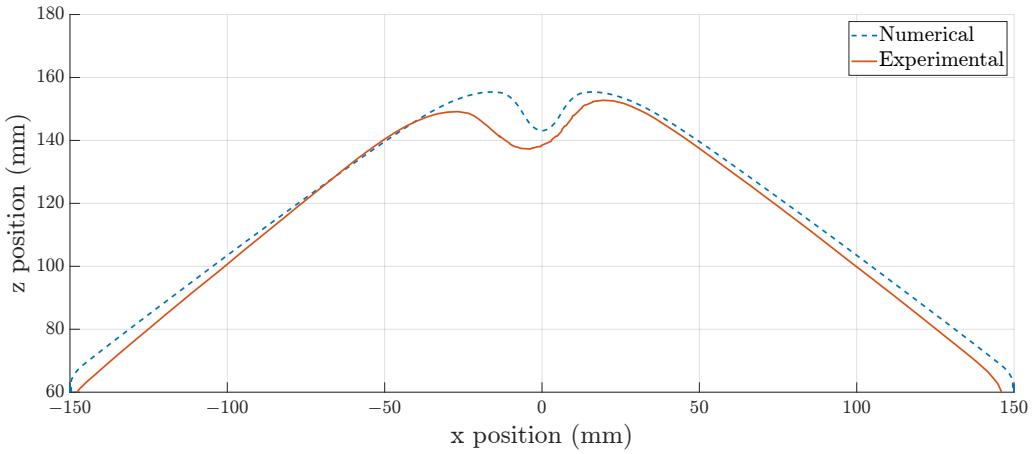

Figure D.8: Permanently deformed crosscut profiles for a 105° 32 mm V-tip radius DOMEX-700 MC V-structure at a charge mass of 20 g (numerical versus experimental)

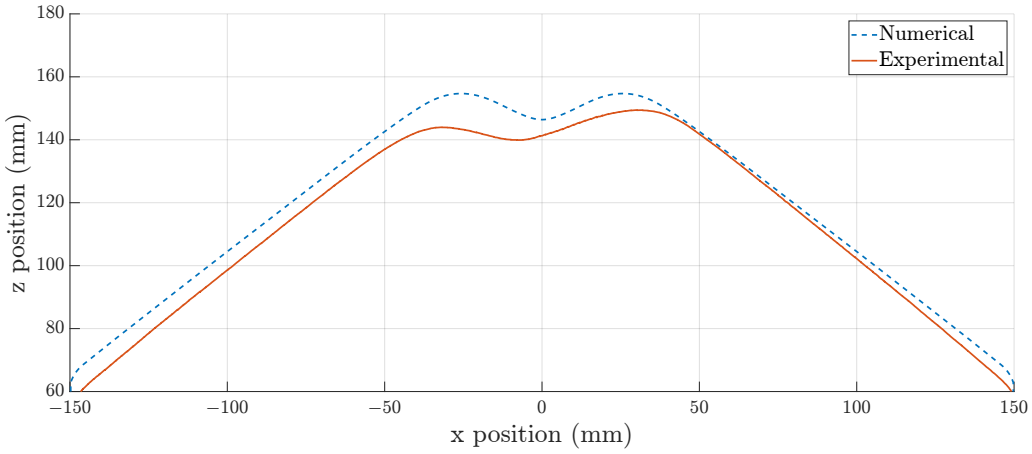

Figure D.9: Permanently deformed crosscut profiles for a 105° 62 mm V-tip radius DOMEX-700 MC V-structure at a charge mass of 10 g (numerical versus experimental)

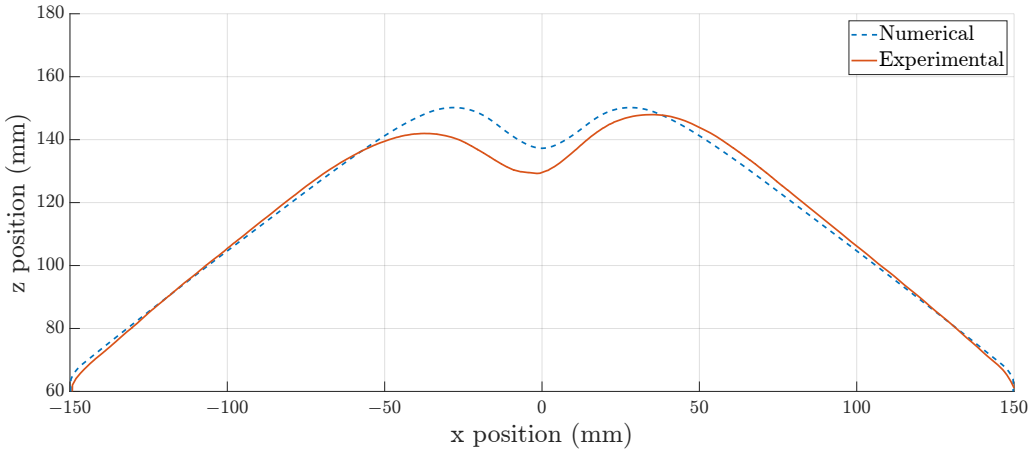

Figure D.10: Permanently deformed crosscut profiles for a 105° 62 mm V-tip radius DOMEX-700 MC V-structure at a charge mass of 15 g (numerical versus experimental)

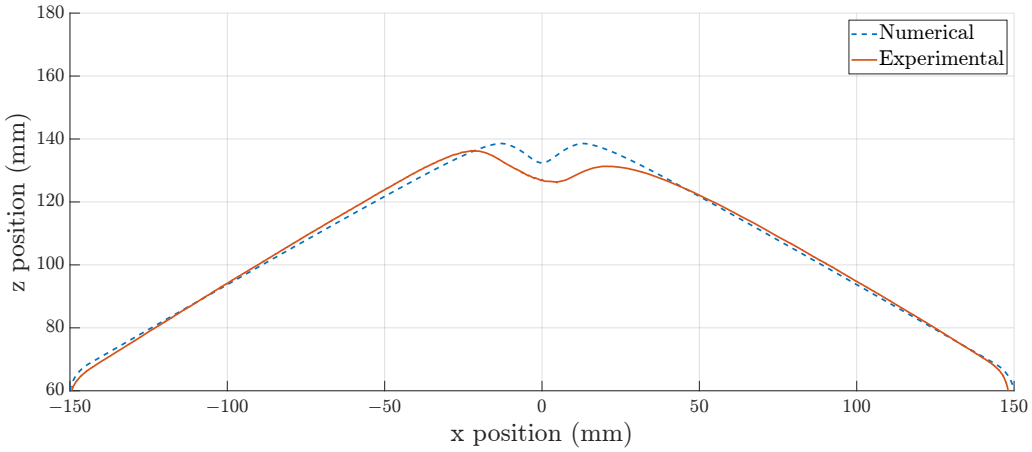

Figure D.11: Permanently deformed crosscut profiles for a 120° 32 mm V-tip radius DOMEX-700 MC V-structure at a charge mass of 10 g (numerical versus experimental)

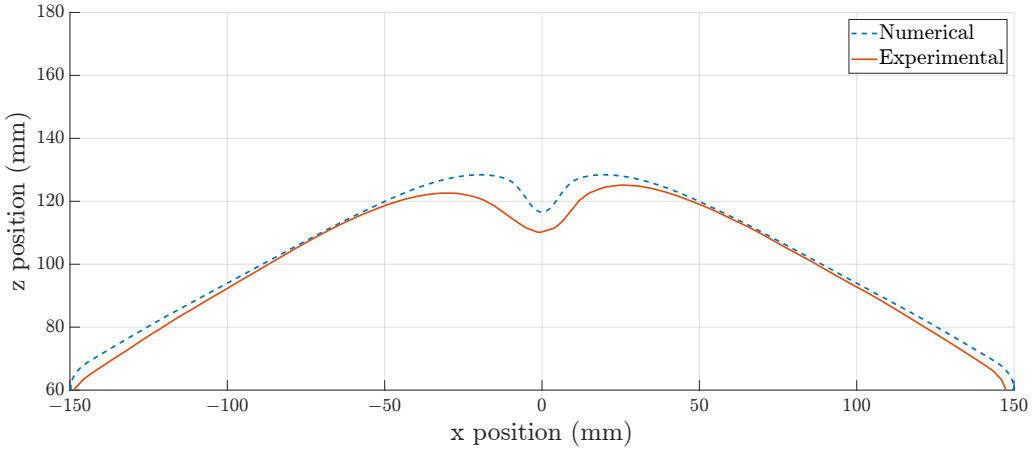

Figure D.12: Permanently deformed crosscut profiles for a 120° 32 mm V-tip radius DOMEX-700 MC V-structure at a charge mass of 20 g (numerical versus experimental)

D.1.3 Transient mid-point deflection comparisons

The additional transient mid-point deflection comparisons are provided in figures D.13 to D.17.

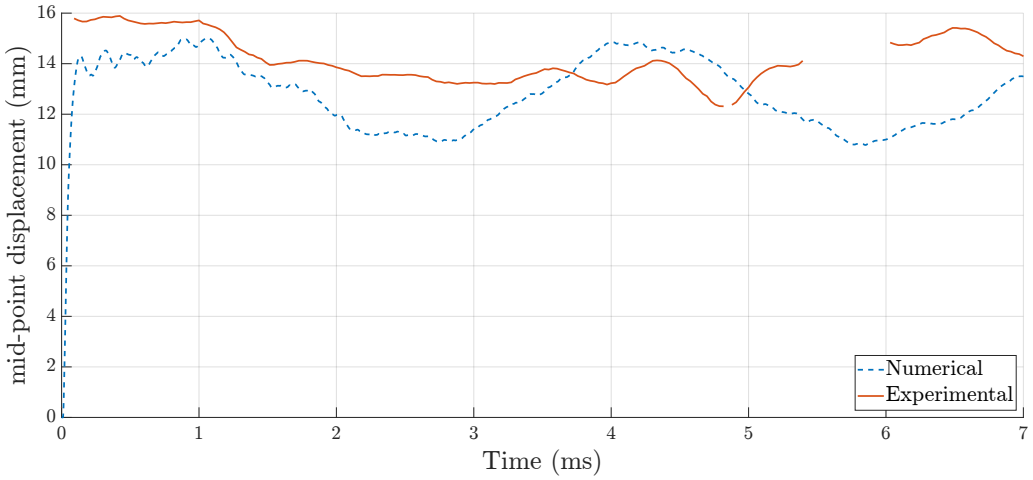

Figure D.13: Mid-point deflection time history for a 105° 32 mm V-tip radius DOMEX-700 MC V-structure at a charge mass of 10 g (numerical versus experimental)

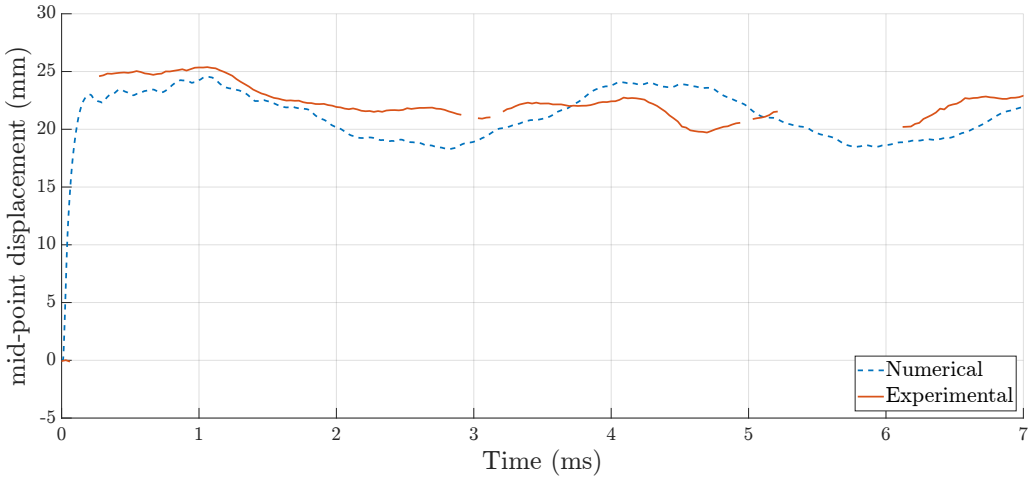

Figure D.14: Mid-point deflection time history for a 105° 32 mm V-tip radius DOMEX-700 MC V-structure at a charge mass of 15 g (numerical versus experimental)

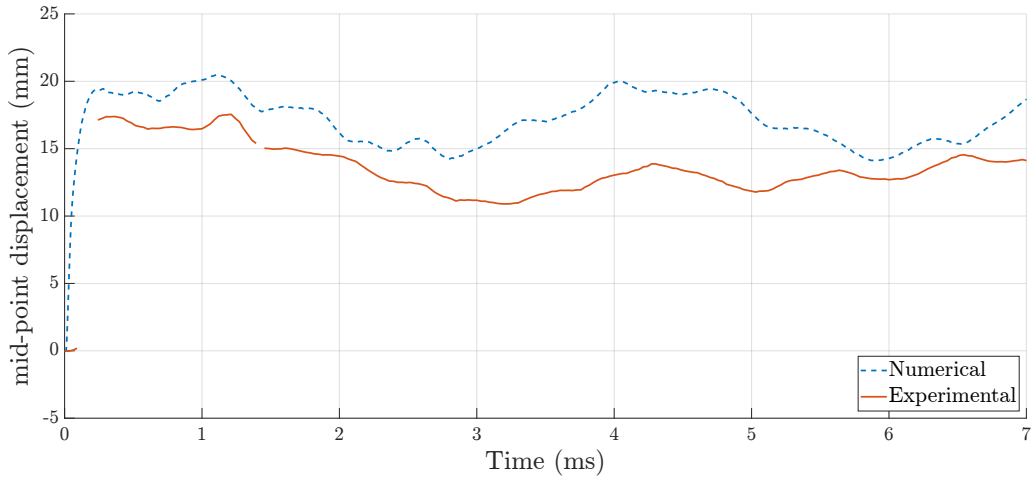

Figure D.15: Mid-point deflection time history for a 105° 62 mm V-tip radius DOMEX-700 MC V-structure at a charge mass of 10 g (numerical versus experimental)

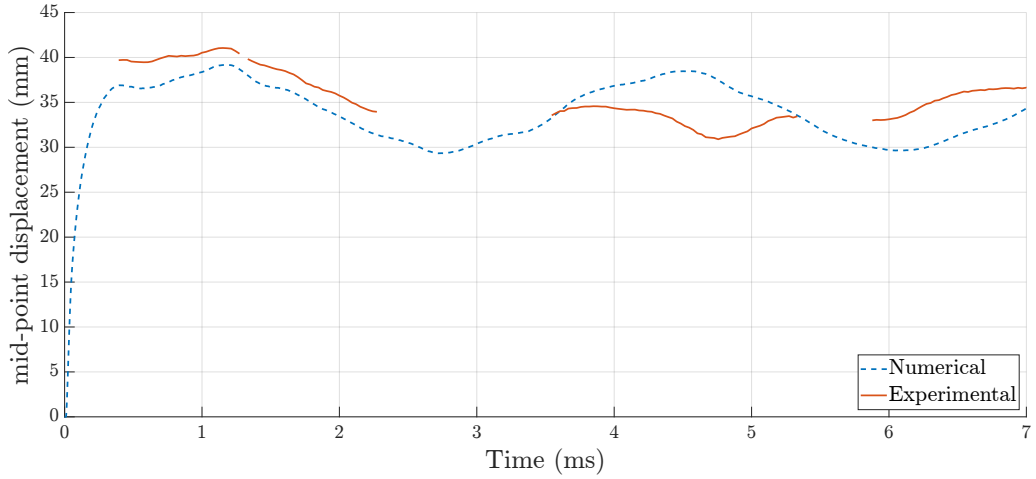

Figure D.16: Mid-point deflection time history for a 105° 62 mm V-tip radius DOMEX-700 MC V-structure at a charge mass of 20 g (numerical versus experimental)

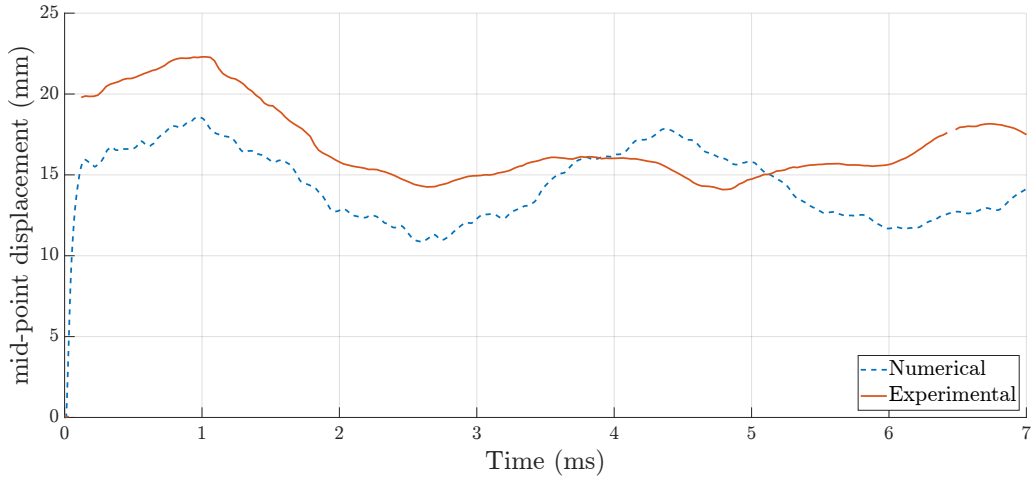

Figure D.17: Mid-point deflection time history for a 120° 32 mm V-tip radius DOMEX-700 MC V-structure at a charge mass of 10 g (numerical versus experimental)

D.1.4 Permanent mid-point displacement and impulse

Tabulated data of the permanent mid-point displacement and the impulse data are presented in tables D.1 and D.2.

Table D.1: Comparison of the impulse transferred results for selected tests (numerical versus experimental)

		Impulse (Ns)		
Configuration	Charge mass (g)	Numerical	Experimental	Difference (%)
105°, 32 mm	10	9.4	10.7	1.3 (12)
	15	12.2	14.1	1.9 (13)
	20	14.5	16.0	1.5 (9)
105°, 62 mm	10	9.7	11.0	1.3 (12)
	15	12.7	14.8	2.1 (7)
	20	15.1	18.0	2.9 (16)
120°, 32 mm	10	10.0	11.5	1.5 (13)
	15	12.9	14.7	1.9 (13)
	20	15.2	18.9	3.7 (20)

Table D.2: Comparison of the mid-point displacement results for selected tests (numerical versus experimental)

		Mid-point deflection (mm)		
Configuration	Charge mass (g)	Numerical	Experimental	Difference (%)
105°, 32 mm	10	13.2	14.5	1.4 (9)
	15	21.6	24.0	2.4 (10)
	20	28.7	30.1	1.4 (5)
105°, 62 mm	10	17.6	16.9	-0.6 (-4)
	15	26.7	31.1	4.4 (14)
	20	34.2	37.9	3.7 (10)
120°, 32 mm	10	14.3	17.5	3.2 (19)
	15	23.0	23.6	0.5 (2)
	20	30.1	33.4	3.3 (10)

D.2 The influences of V-tip radius on the blast performance of the steel V-structures - Supplementary tables and graphs

The effect of V-tip radius on impulse transfer for the three V-angles considered is shown in table D.3.

Table D.3: Simulated impulse (in Ns) versus V-tip radius for the DOMEX-700 MC V-structures

	Charge mass (g)								
	10			15			20		
	90°	105°	120°	90°	105°	120°	90°	105°	120°
V-tip radius (mm)	Impulse (Ns)			Impulse (Ns)			Impulse (Ns)		
20	8.43	9.32	9.89	10.8	11.96	12.78	12.80	14.25	15.23
32	8.68	9.44	9.94	11.44	12.23	12.86	13.49	14.50	15.16
40	8.84	9.57	10.22	11.54	12.43	13.21	13.76	14.77	15.65
62	9.45	9.66	10.19	12.37	12.70	13.32	14.89	15.13	15.97
80	9.54	10.41	10.82	12.67	13.58	14.12	15.26	16.31	16.87
100	10.34	10.37	10.56	13.59	13.66	13.97	16.37	16.46	16.82
150	11.09	11.32	11.16	14.49	14.83	14.8	17.50	17.95	17.83
200	11.29	11.32	11.78	14.95	15.16	15.34	18.24	17.95	18.60

D.2.1 V-tip radius effects on the mid-point displacement time histories

Figures D.18 and D.19 shows the mid-point displacement time histories for 90° DOMEX-700 MC V-structure simulations at charge masses of 10 g and 20 g.

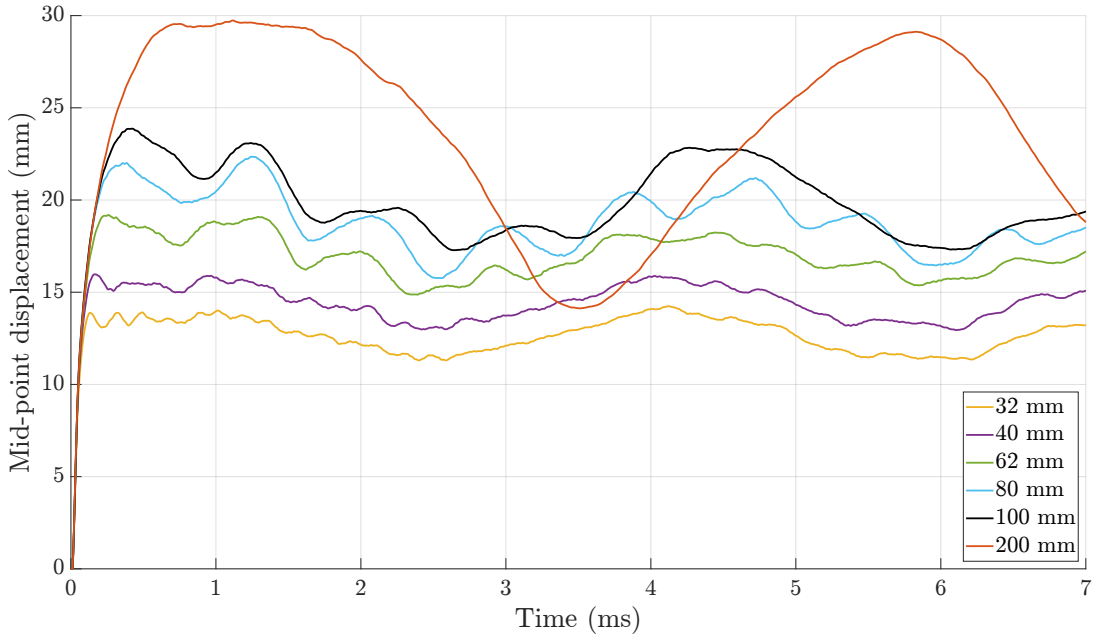

Figure D.18: Mid-point deflection time histories for increasing V-tip radii for the 90° DOMEX-700 MC V-structure simulations at a charge mass of 10 g

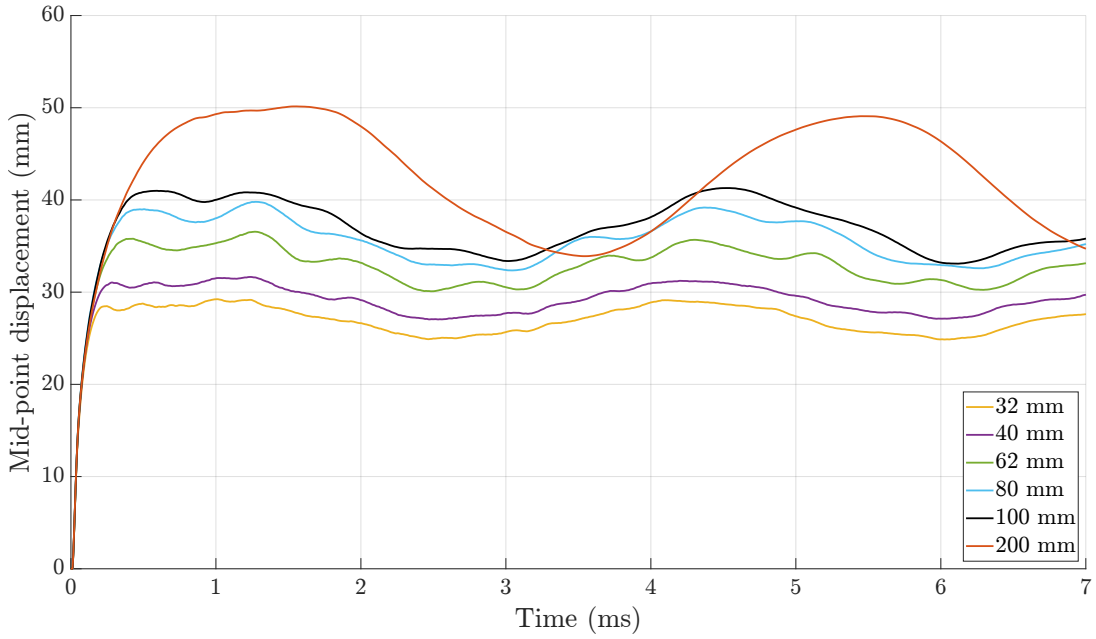

Figure D.19: Mid-point deflection time histories for increasing V-tip radii for the 90° DOMEX-700 MC V-structure simulations at a charge mass of 20 g

Figures D.20 and D.21 shows the mid-point displacement time histories for 105° DOMEX-700 MC V-structure simulations at charge masses of 10 g and 20 g.

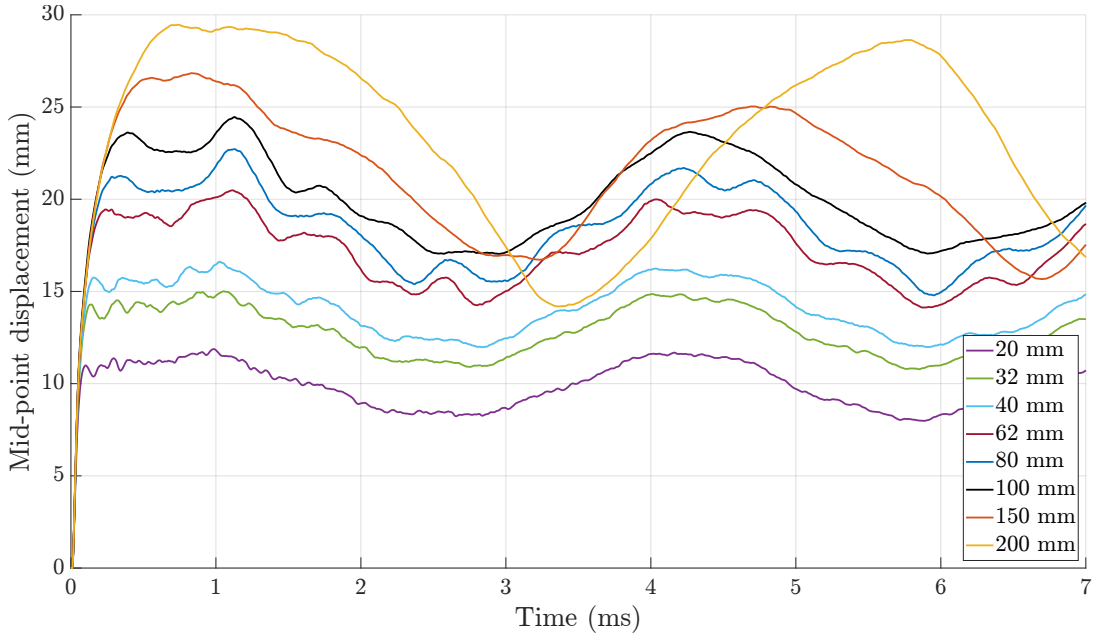

Figure D.20: Mid-point deflection time histories for increasing V-tip radii for the 105° DOMEX-700 MC V-structure simulations at a charge mass of 10 g

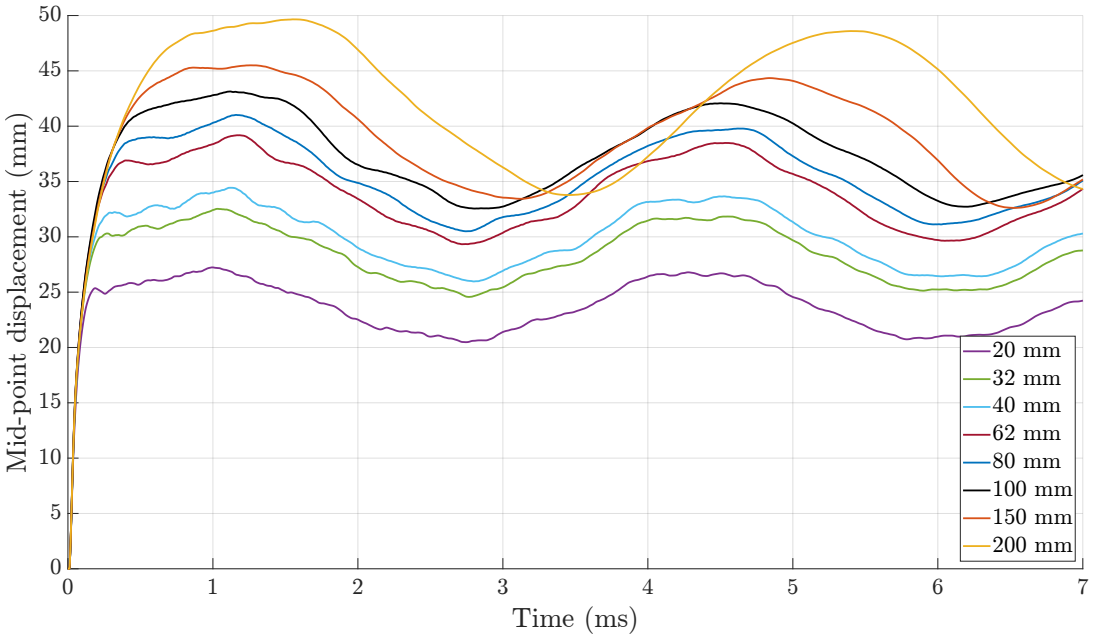

Figure D.21: Mid-point deflection time histories for increasing V-tip radii for the 105° DOMEX-700 MC V-structure simulations at a charge mass of 20 g

Figure 8.26 shows the mid-point displacement time histories for a 120° DOMEX-700 MC V-structure simulation at a charge mass of 15 g.

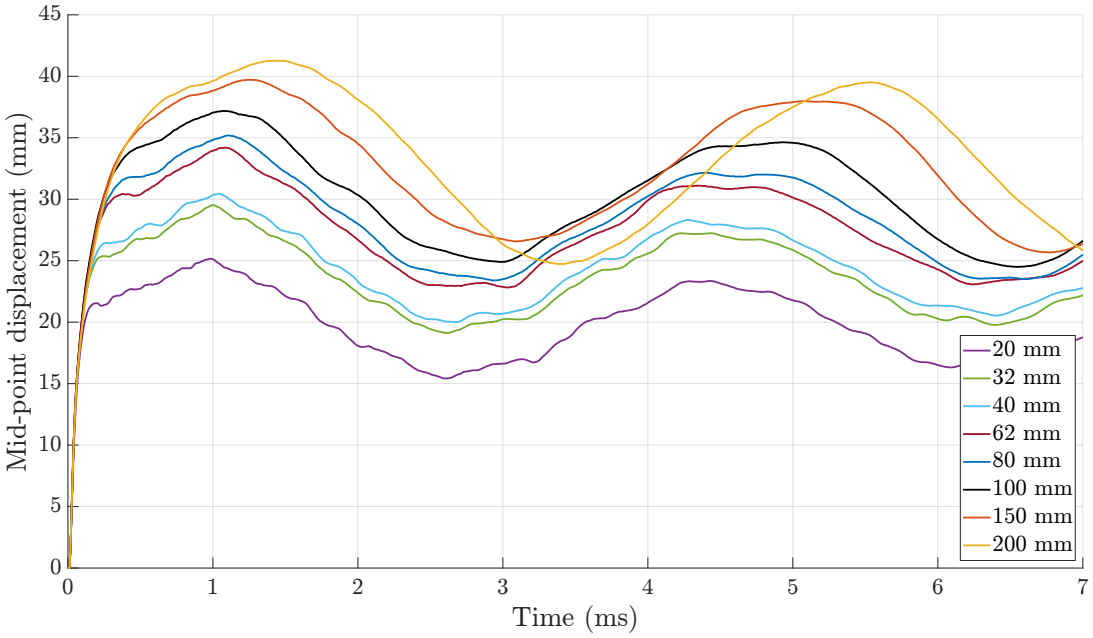

Figure D.22: Mid-point deflection time histories for increasing V-tip radii for the 120° DOMEX-700 MC V-structure simulations at a charge mass of 15 g

D.2.2 V-tip radius effects on the permanently deformed ridge profiles

The permanently deformed ridge profiles for the 90° DOMEX-700 MC V-structure specimens of differing V-tip radii simulated at charge masses of 10 g and 20 g are shown in figures D.23 and D.24.

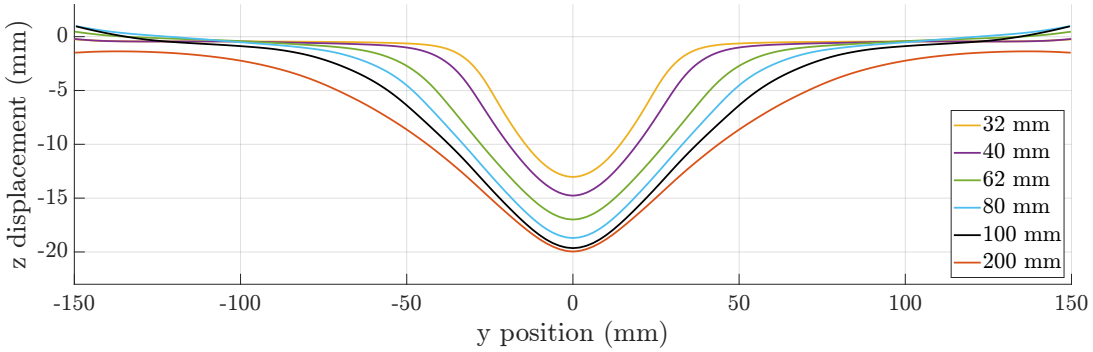

Figure D.23: Permanently deformed ridge profiles for increasing V-tip radii for the 90° DOMEX-700 MC V-structure simulation at a charge mass of 10 g

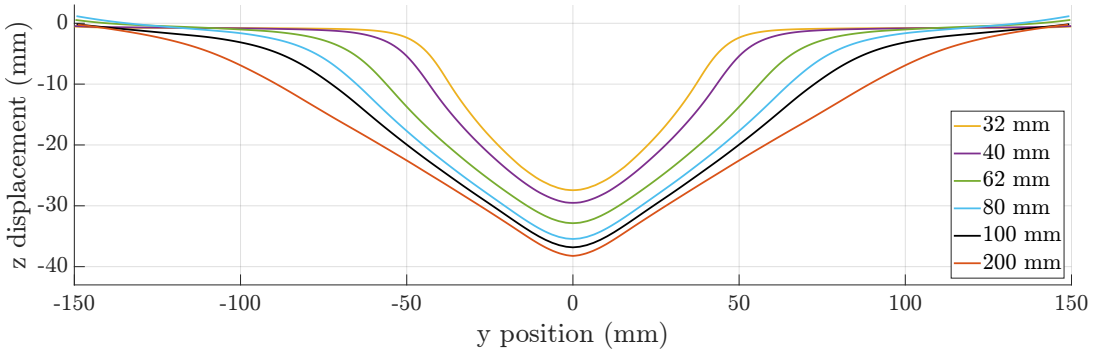

Figure D.24: Permanently deformed ridge profiles for increasing V-tip radii for the 90° DOMEX-700 MC V-structure simulation at a charge mass of 20 g

The permanently deformed ridge profiles for the 105° DOMEX-700 MC V-structure specimens of differing V-tip radii simulated at charge masses of 15 g and 20 g are shown in figures D.25 and D.26.

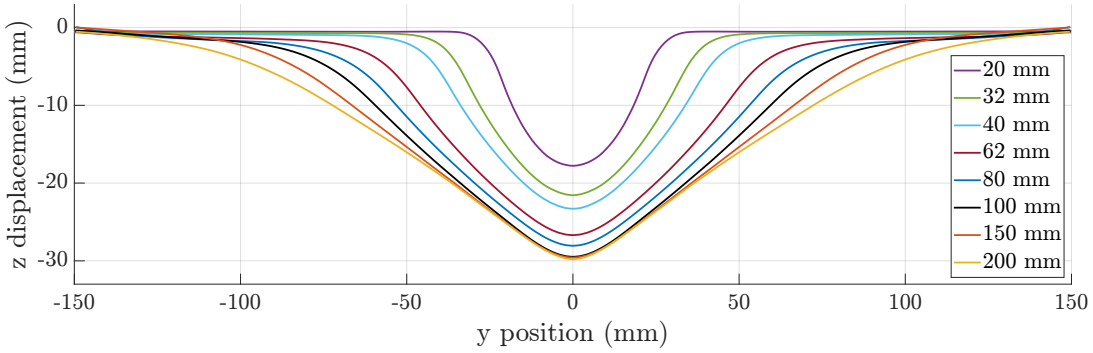

Figure D.25: Permanently deformed ridge profiles for increasing V-tip radii for the 105° DOMEX-700 MC V-structure simulation at a charge mass of 15 g

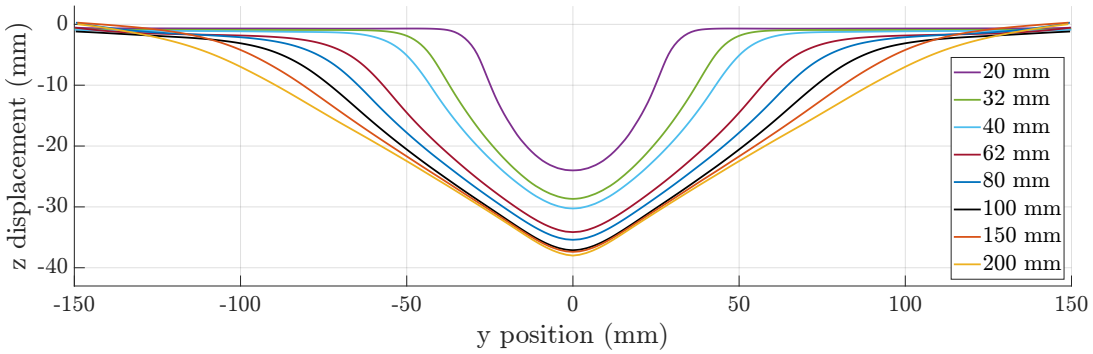

Figure D.26: Permanently deformed ridge profiles for increasing V-tip radii for the 105° DOMEX-700 MC V-structure simulation at a charge mass of 20 g

The permanently deformed ridge profiles for the 120° DOMEX-700 MC V-structure specimens of differing V-tip radii simulated at charge masses of 10 g and 15 g are shown in figures D.27 and D.28.

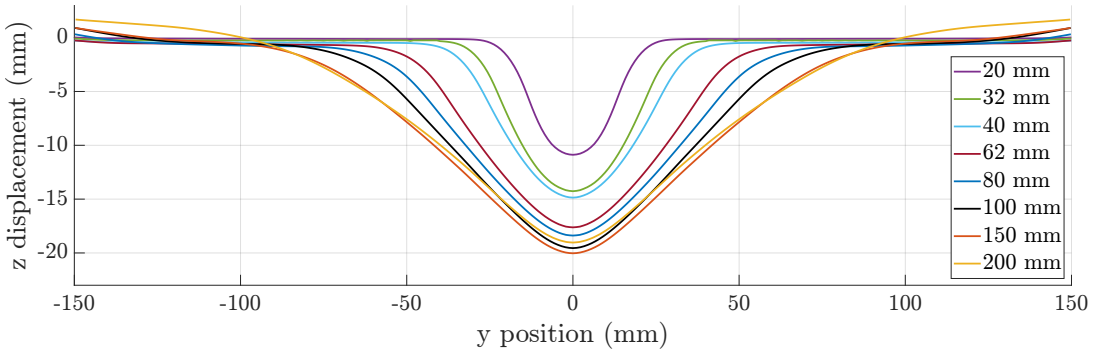

Figure D.27: Permanently deformed ridge profiles for increasing V-tip radii for the 120° DOMEX-700 MC V-structure simulation at a charge mass of 10 g

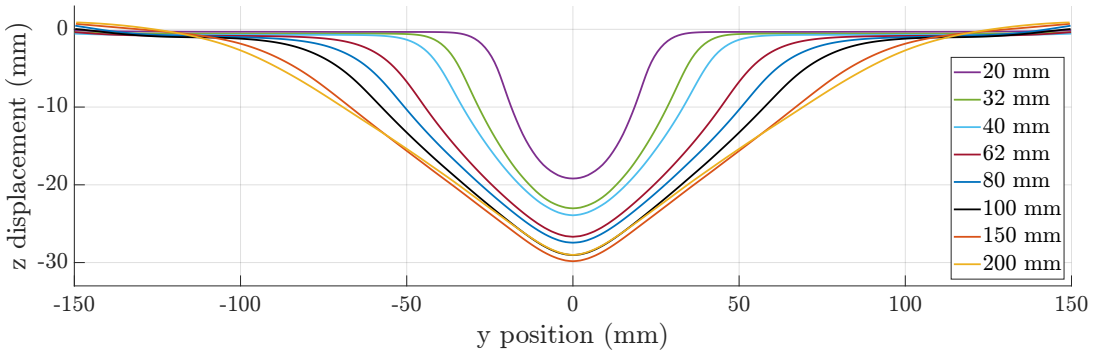

Figure D.28: Permanently deformed ridge profiles for increasing V-tip radii for the 120° DOMEX-700 MC V-structure simulation at a charge mass of 15 g

D.2.3 V-tip radius effects on the permanently deformed crosscut profiles

The permanently deformed crosscut profiles for the 90° DOMEX-700 MC V-structures with a range of V-tip radii simulated at charge masses of 10 g and 20 g are shown in figures D.29 and D.30.

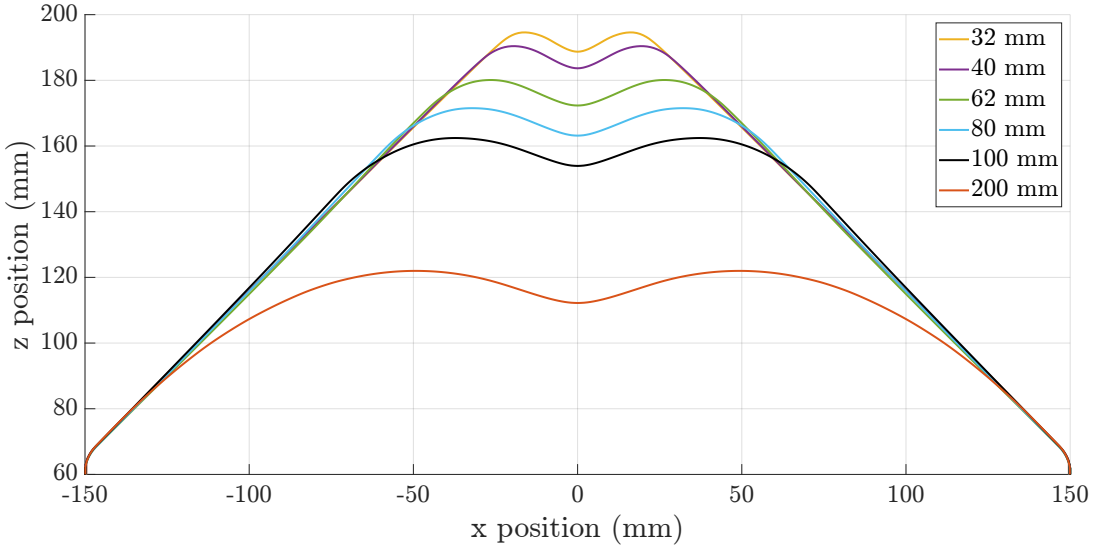

Figure D.29: Permanently deformed crosscut profiles for increasing V-tip radii for the 90° DOMEX-700 MC V-structure simulation at a charge mass of 10 g

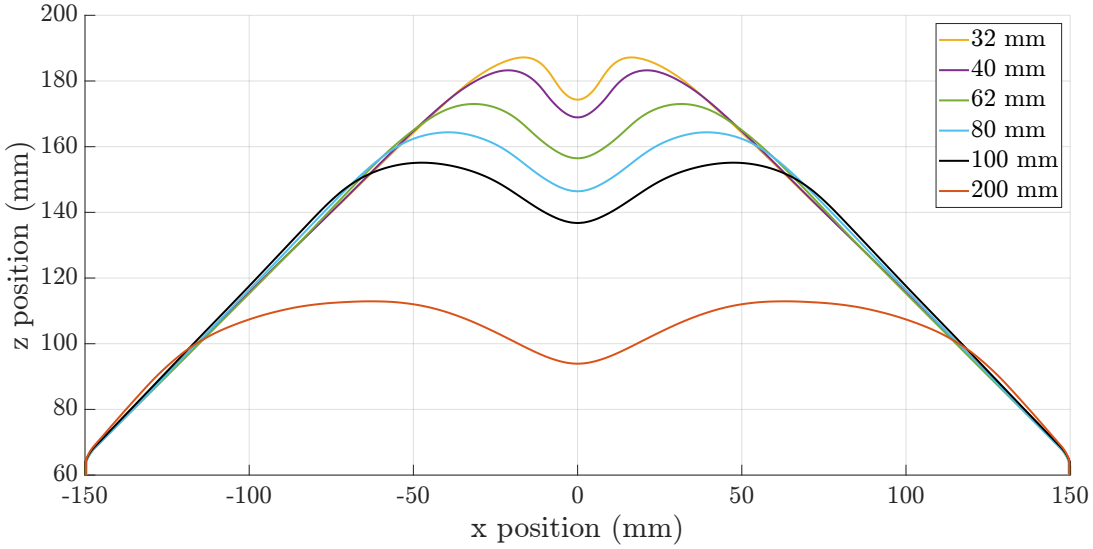

Figure D.30: Permanently deformed crosscut profiles for increasing V-tip radii for the 90° DOMEX-700 MC V-structure simulation at a charge mass of 20 g

The final crosscut profiles in figures D.31 and D.32 show the 105° DOMEX-700 MC V-structures of differing V-tip radii simulated at a charge masses of 10 g and 20 g.

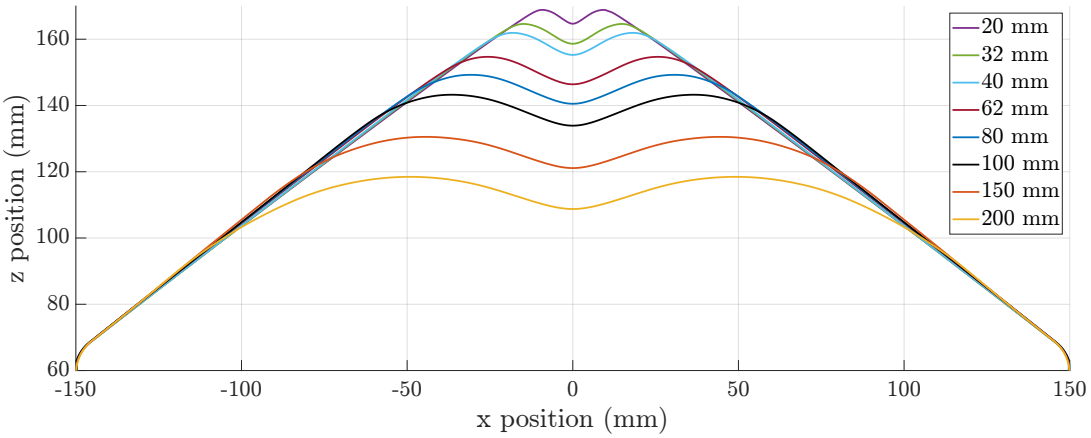

Figure D.31: Permanently deformed crosscut profiles for increasing V-tip radii for the 105° DOMEX-700 MC V-structure simulation at a charge mass of 10 g

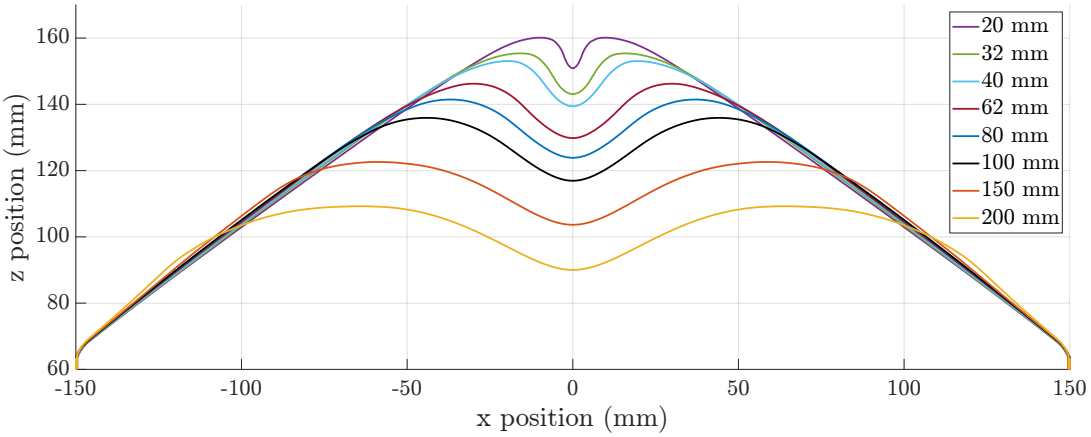

Figure D.32: Permanently deformed crosscut profiles for increasing V-tip radii for the 105° DOMEX-700 MC V-structure simulation at a charge mass of 20 g

The final set of crosscut profiles presented shown in figures D.33 and D.34 are the 120° DOMEX-700 MC V-structures with V-tip radii from 20 mm to 200 mm simulated at charge masses of 10 g and 20 g.

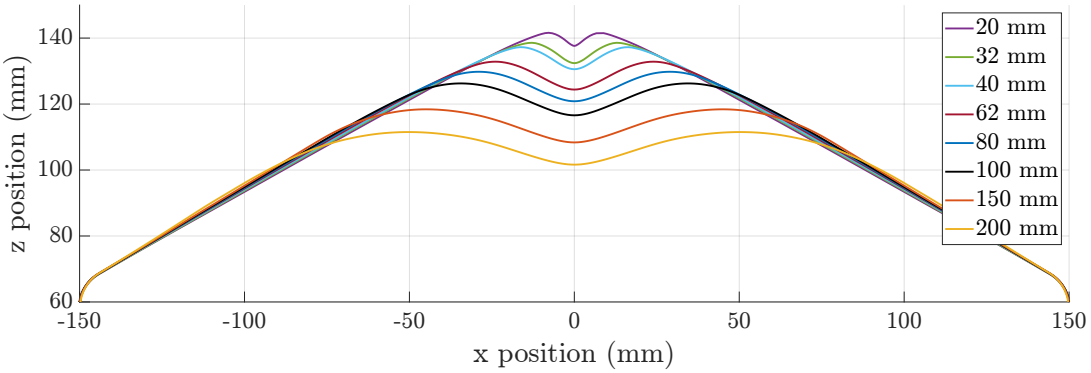

Figure D.33: Permanently deformed crosscut profiles for increasing V-tip radii for the 120° DOMEX-700 MC V-structure simulation at a charge mass of 10 g

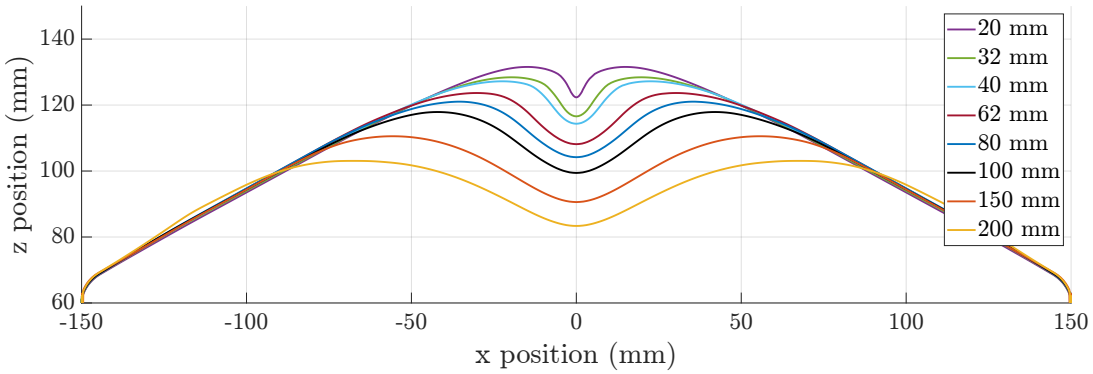

Figure D.34: Permanently deformed crosscut profiles for increasing V-tip radii for the 120° DOMEX-700 MC V-structure simulation at a charge mass of 20 g

D.3 The influences of the V-angle on the blast performance of steel V-structures - Supplementary figures

The supplementary figures showing the influence of the V-angle on the blast performance of the V-structures are presented in the graphs below.

D.3.1 Effect of V-angle on the mid-point displacement time histories

Figures D.35 and D.36 show the mid-point displacement time histories for the DOMEX-700 MC V-structure simulations with all three V-angles for a V-tip radius of 62 mm and 100 mm respectively.

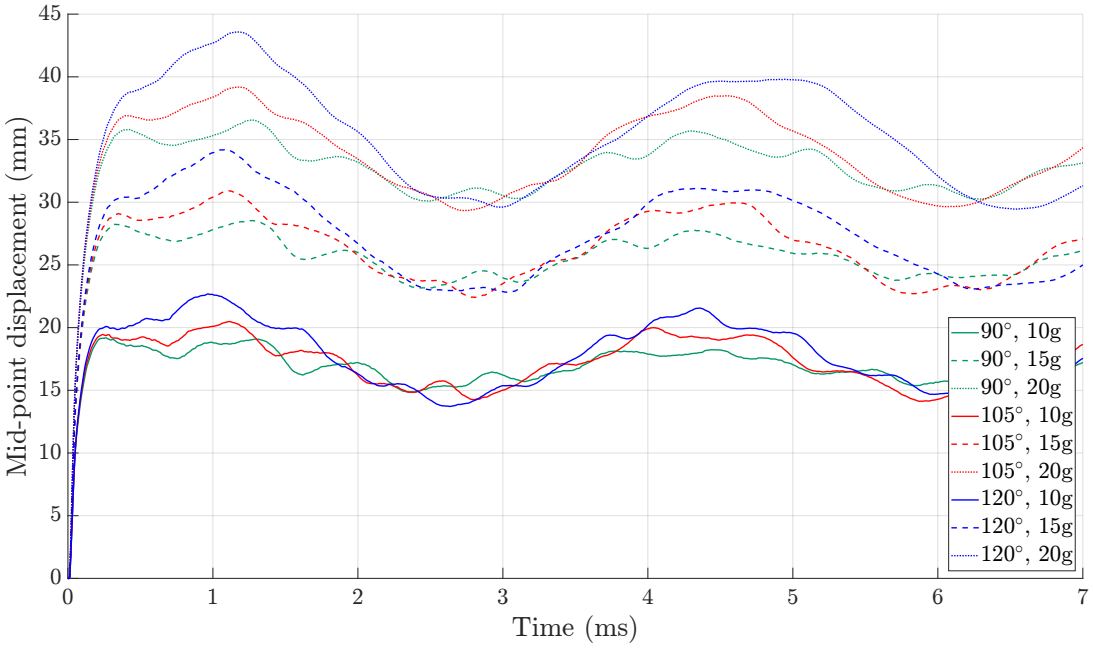

Figure D.35: Mid-point deflection time histories versus the V-angle for a V-tip radius of 62 mm at all three charge masses investigated

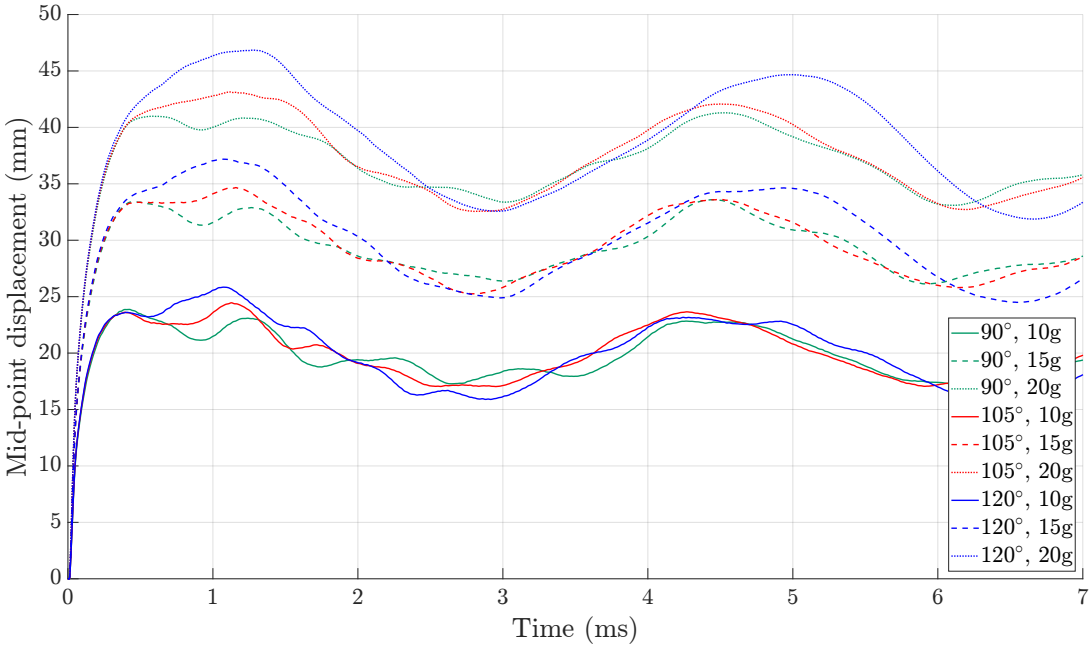

Figure D.36: Mid-point deflection time histories versus the V-angle for a V-tip radius of 100 mm at all three charge masses investigated

D.3.2 Effect of V-angle on the permanently deformed ridge profiles

Figures D.37 and D.38 show the permanently deformed ridge profiles for the DOMEX-700 MC V-structure simulations with all three V-angles for a V-tip radius of 62 mm and 200 mm respectively.

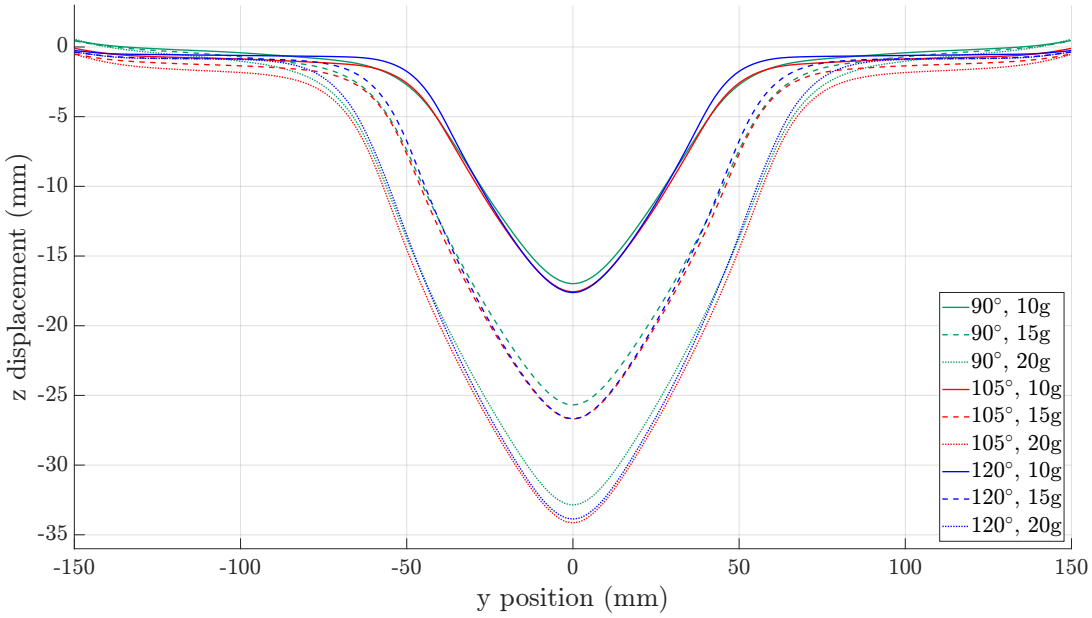

Figure D.37: Permanently deformed ridge profiles versus the V-angle for a V-tip radius of 62 mm at all three charge masses investigated

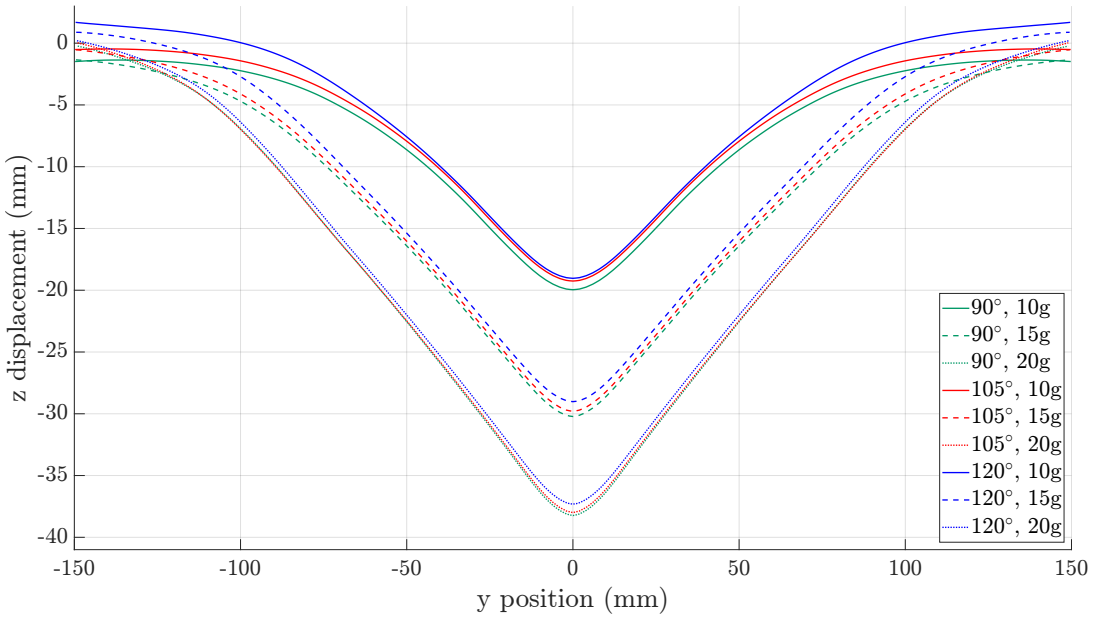

Figure D.38: Permanently deformed ridge profiles versus the V-angle for a V-tip radius of 200 mm at all three charge masses investigated

D.3.3 Effect of V-angle on the permanently deformed crosscut profiles

V-tip radius of 32 mm

The permanently deformed crosscut profiles for a V-tip radius of 32 mm and all three charge masses of 10 g and 20 g are shown in figures D.39 and D.40.

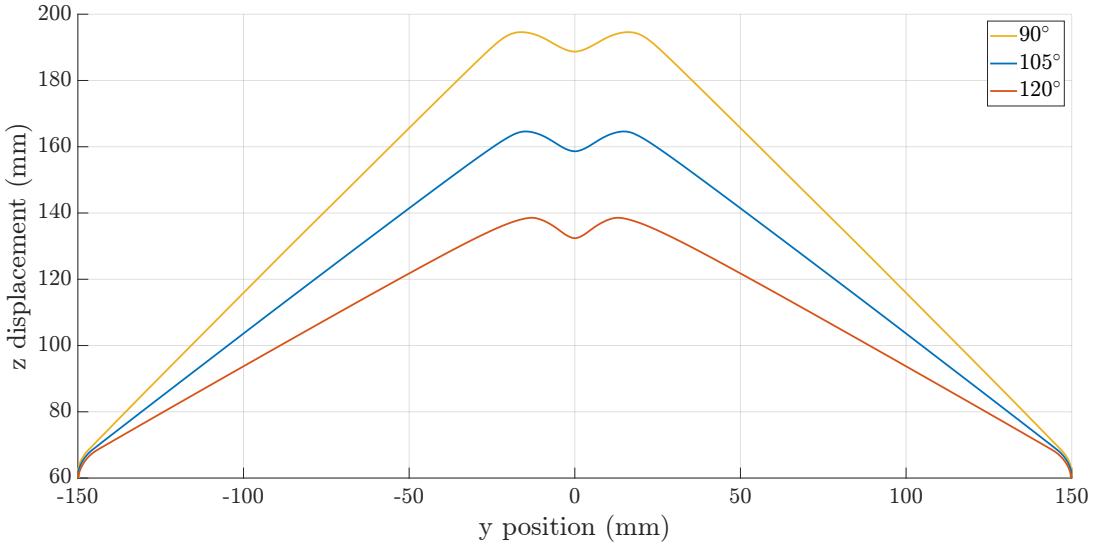

Figure D.39: Permanently deformed crosscut profiles versus the V-angle for a V-tip radius of 32 mm at a charge mass of 10 g

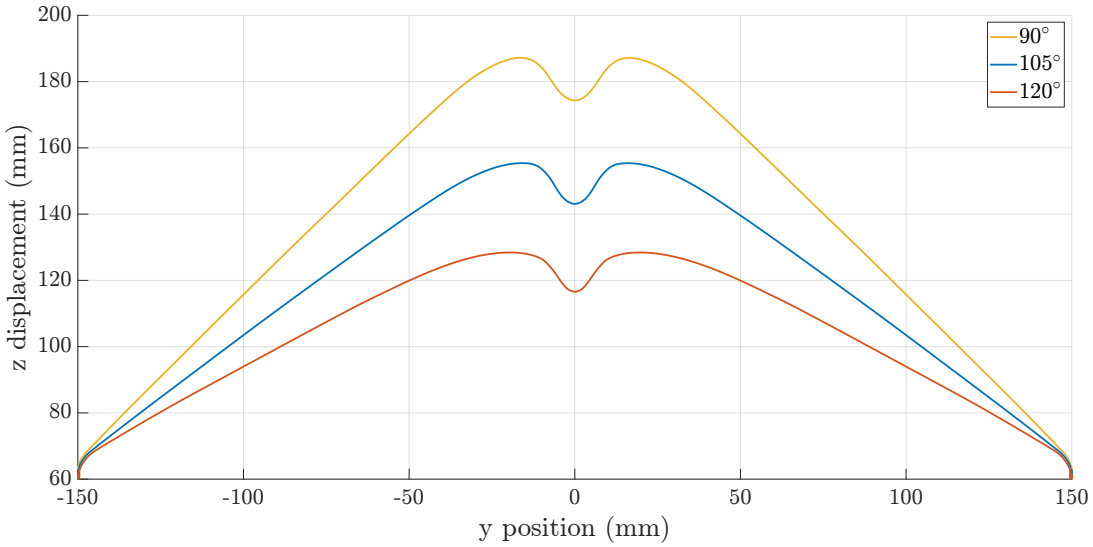

Figure D.40: Permanently deformed crosscut profiles versus the V-angle for a V-tip radius of 32 mm at a charge mass of 20 g

V-tip radius of 62 mm

The next set of profiles shown in figure D.42 are the permanently deformed crosscut curves for a V-tip radius of 62 mm at a charge mass of 15 g. Similarly to the 32 mm V-structures, the permanent deformation appears to be fairly similar for the curves at all three V-angles. Additionally, as expected, the deformation becomes less localised with the deformation extending further along the V-profile of the V-structures. Due to the reduced stiffness of the 120° V-structures, there is an apparent bowing along the V-profile, while the other two V-angled V-structure appear to be fairly undeformed. This is likely due to the reduced geometric stiffness of the larger angled V-structures.

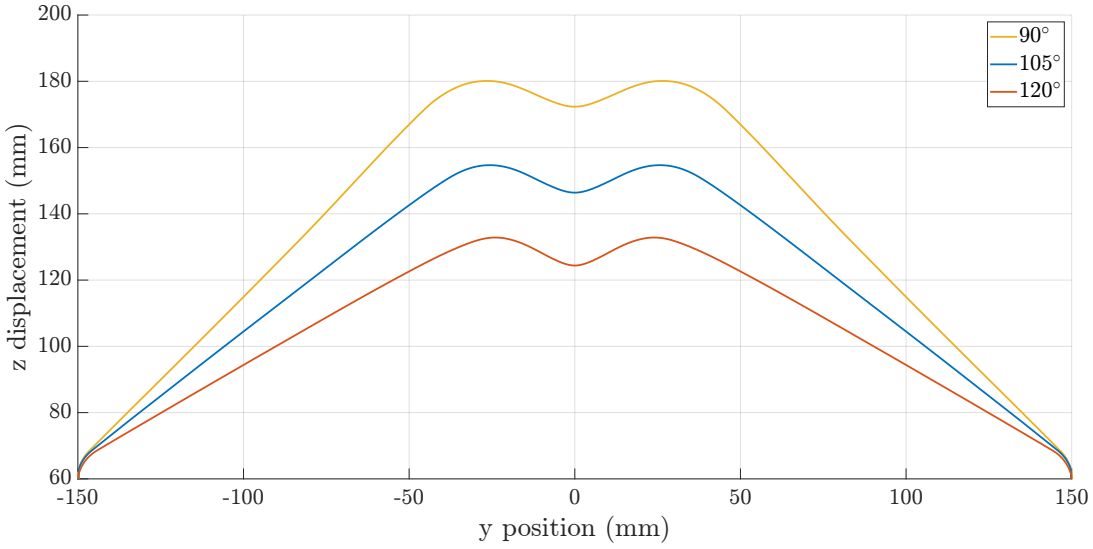

Figure D.41: Permanently deformed crosscut profiles versus the V-angle for a V-tip radius of 62 mm at a charge mass of 10 g

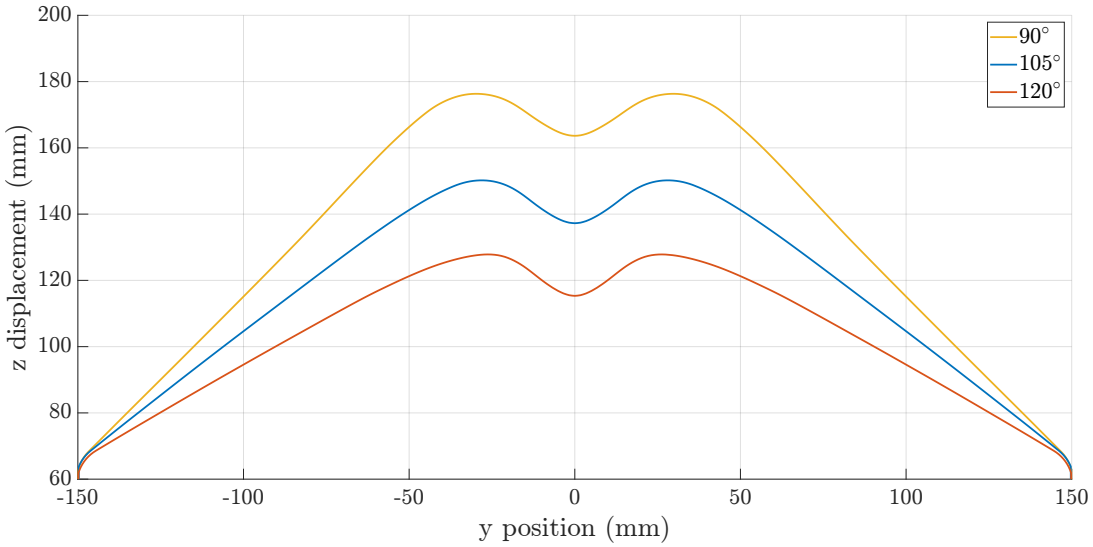

Figure D.42: Permanently deformed crosscut profiles versus the V-angle for a V-tip radius of 62 mm at a charge mass of 15 g

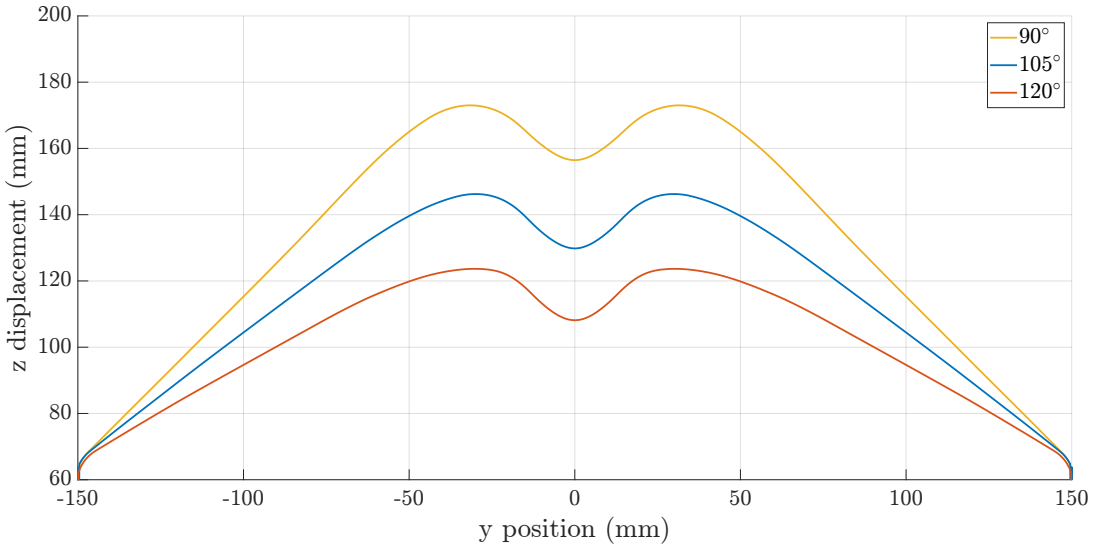

Figure D.43: Permanently deformed crosscut profiles versus the V-angle for a V-tip radius of 62 mm at a charge mass of 20 g

V-tip radius of 100 mm

The permanently deformed crosscut profiles for a V-tip radius of 100 mm and all three charge masses of 10 g, 15 g, and 20 g are shown in figures D.44 to D.46. The profiles at the three V-angles once again show a similar deformation, with an increase in the deformed length along the V-profile. Due to the larger V-tip radius, the differences in the height from the base of the V-structure for these three V-structures also starts to decrease. This would mean a reduction in the required ride height of any MRAP which would incorporate a V-hull with a large V-tip radius. At this V-tip radius, the bowing of the straight sides of the V-profile can be seen for the 105° and 120° V-structures, while the sides of the 90° V-structures still appear to be straight.

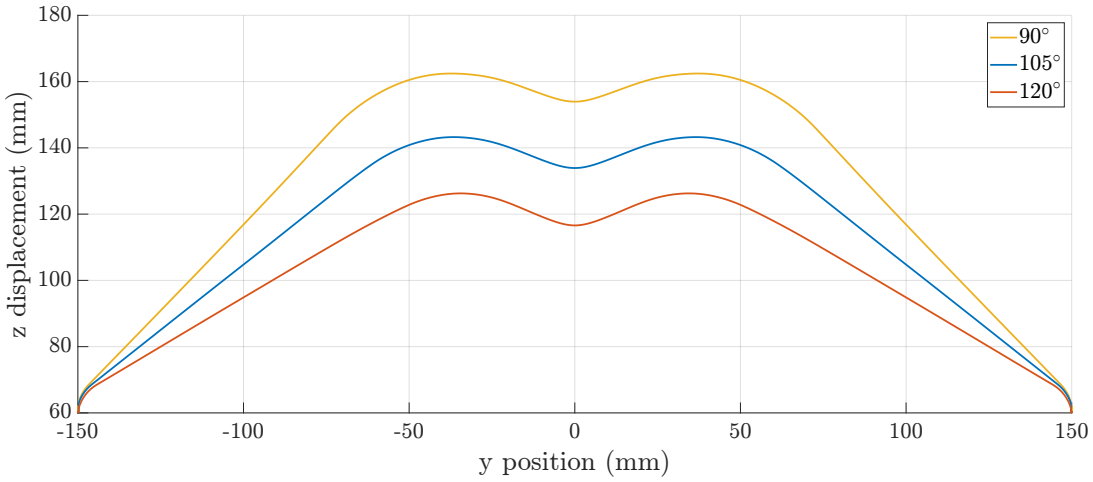

Figure D.44: Permanently deformed crosscut profiles versus the V-angle for a V-tip radius of 100 mm at a charge mass of 10 g

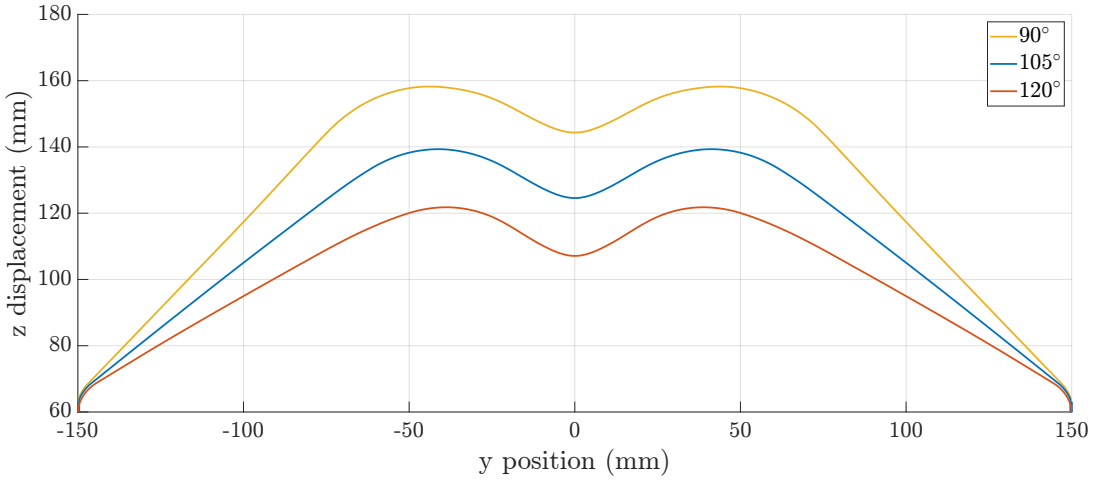

Figure D.45: Permanently deformed crosscut profiles versus the V-angle for a V-tip radius of 100 mm at a charge mass of 15 g

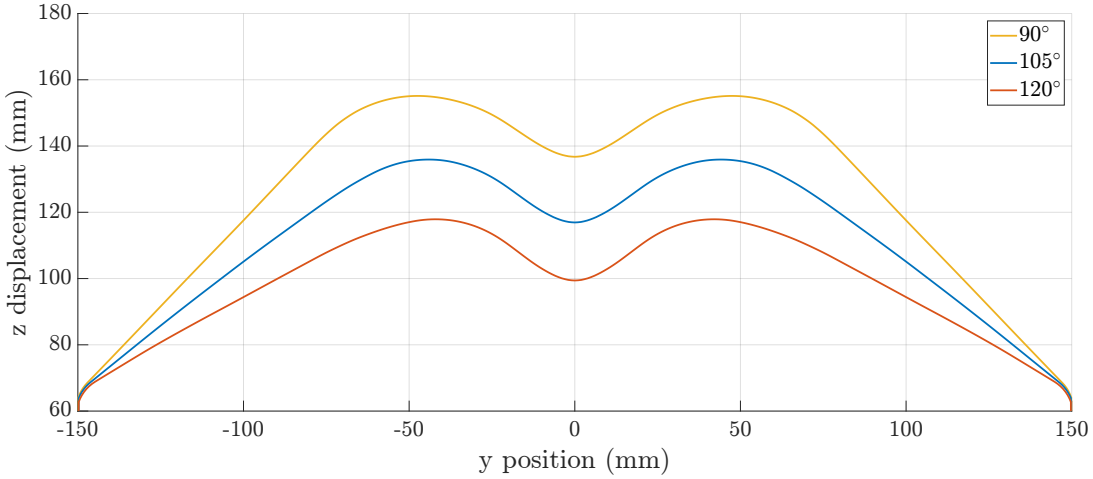

Figure D.46: Permanently deformed crosscut profiles versus the V-angle for a V-tip radius of 100 mm at a charge mass of 20 g

V-tip radius of 200 mm

The permanently deformed crosscut profiles for a V-tip radius of 200 mm and charge masses of 10 g and 15 g are shown in figures D.47 and D.48.

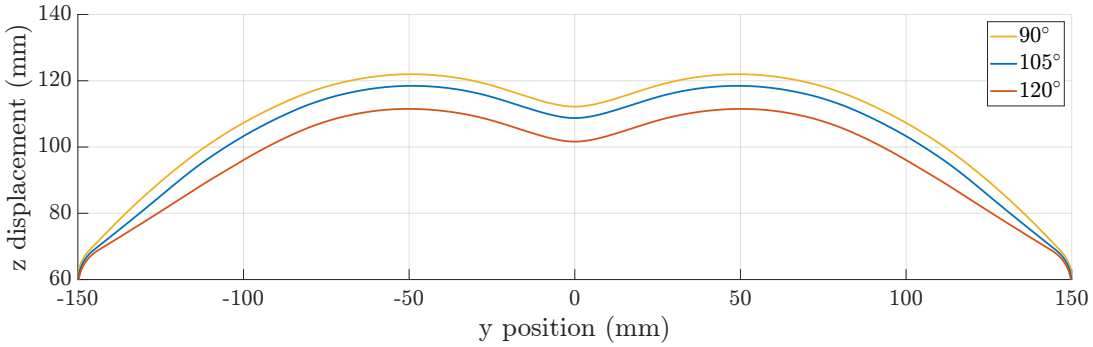

Figure D.47: Permanently deformed crosscut profiles versus the V-angle for a V-tip radius of 200 mm at a charge mass of 10 g

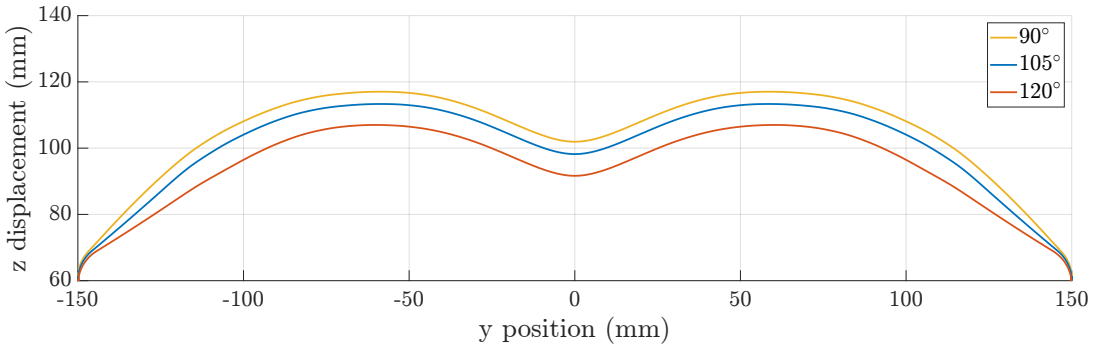

Figure D.48: Permanently deformed crosscut profiles versus the V-angle for a V-tip radius of 200 mm at a charge mass of 15 g

Appendix E

Numerical blast simulations - GFRP - Supplementary figures

This appendix contains the additional tables, graphs, and figures from the numerical blast results chapter on the GFRP V-structures. This data has been included if the reader wishes to view the additional information gathered on the numerical blast simulations on the GFRP V-structures.

E.1 The Inclusion of damping

An additional graph was generated and is shown in figure E.1. The peak displacement is similar for all values of damping but at 40% damping the response closely matches the post-peak behaviour.

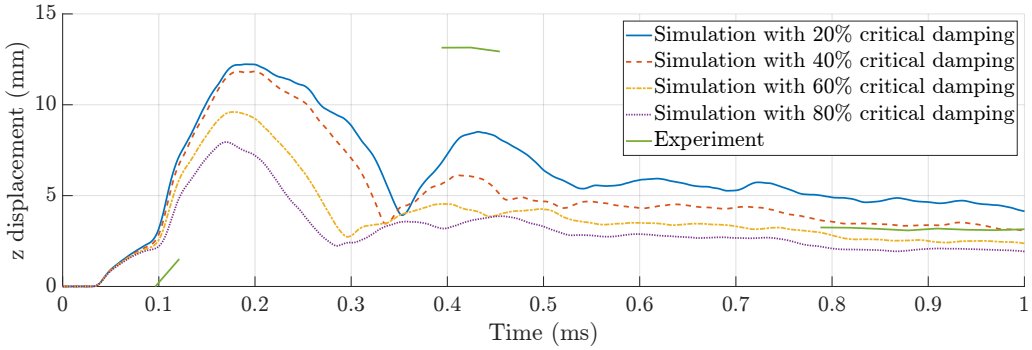

Figure E.1: Numerical simulations with increasing amounts of damping and the experimental results for the transient response at the 50 mm point along the ridge line for a 105° 34 mm V-tip radius GFRP V-structure with a ±45° fibre orientation at a charge mass of 15 g

E.2 The effects of the V-structure geometry on the impulse

Table E.1 shows the impulse transferred for all the simulations performed on the GFRP V-structures. In total, 60 simulations were performed which looked at two V-angles, five V-tip radii, two fibre orientations, and three charge masses. The SOD was held constant at 34 mm in all the simulations. The columns of the table show the simulated impulse values for the different V-angle and fibre orientation configurations investigated, while the rows show these values for an increase in V-tip radius.

Table E.1: Simulated impulse (in Ns) versus V-tip radius for the GFRP V-structures

V-tip radius (mm)	Charge mass (g)											
	10				15				20			
	105°		120°		105°		120°		105°		120°	
	0°/90°	±45°	0°/90°	±45°	0°/90°	±45°	0°/90°	±45°	0°/90°	±45°	0°/90°	±45°
	Impulse (Ns)				Impulse (Ns)				Impulse (Ns)			
34	9.14	9.13	9.87	9.86	12.03	12.02	13.08	13.13	14.57	14.59	15.82	15.82
62	10.30	10.30	10.88	10.90	13.62	13.62	14.38	14.38	16.54	16.54	17.63	17.75
80	10.59	10.59	11.20	11.25	14.25	14.31	14.93	14.91	17.43	17.39	18.25	18.24
100	11.25	11.26	11.65	11.62	15.43	15.45	15.66	15.68	18.86	18.77	19.16	19.11
200	13.37	13.41	13.29	13.26	18.00	17.98	18.03	18.04	22.29	22.20	22.28	22.23

E.2.1 V-angle effects

Figure E.2 shows the differences in the simulated impulse between the two V-angles investigated in this study for a fibre orientation of ±45°. A general increasing trend can be seen up to a V-tip radius of 100 mm with the impulses fairly similar between the two V-angles above this V-tip radius.

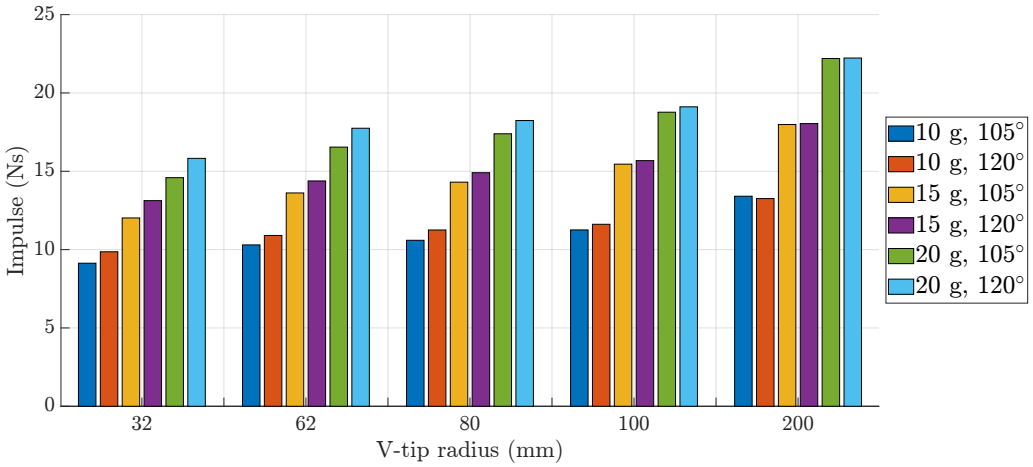

Figure E.2: Simulated impulse versus V-angle for the GFRP V-structures with a ±45° fibre orientation

E.2.2 V-tip radius effects

Figures E.3 and E.4 show the effect of increasing the V-tip radius on the measured impulse for the GFRP V-structures with a fibre orientation of ±45°. Linear trends can be seen in both graphs.

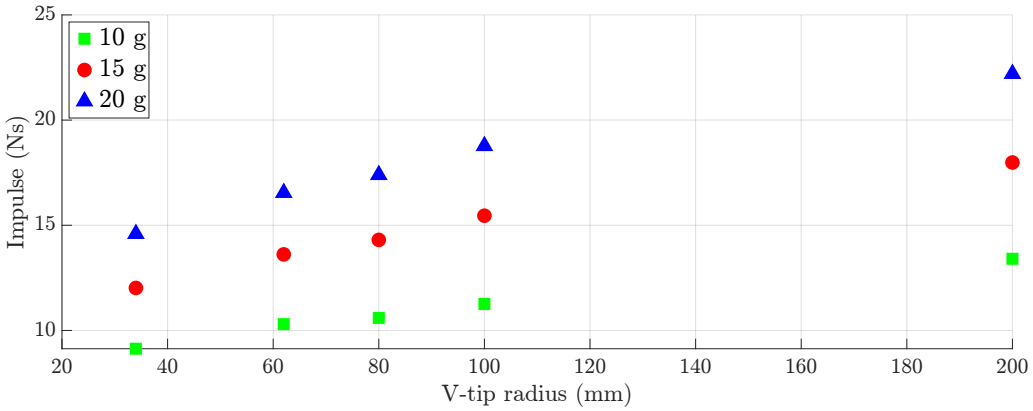

Figure E.3: Simulated impulse versus V-tip radius for the 105° GFRP V-structures with a ±45° fibre orientation

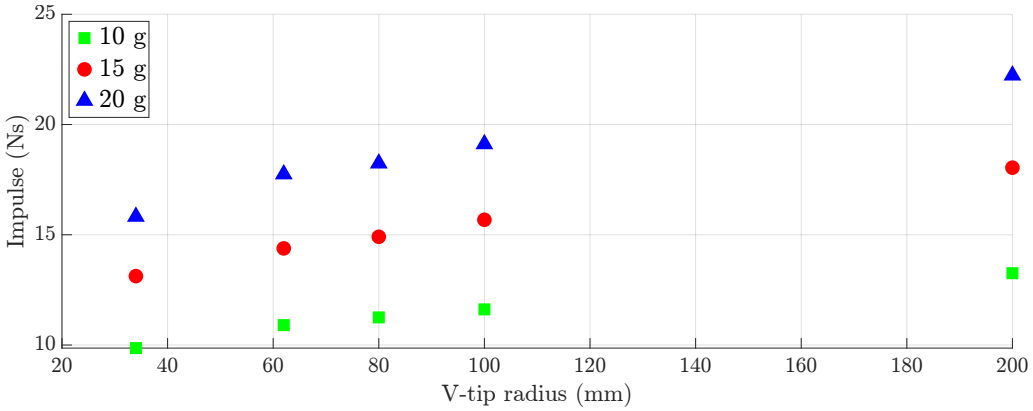

Figure E.4: Simulated impulse versus V-tip radius for the 120° GFRP V-structures with a ±45° fibre orientation

E.3 The effects of the V-structure geometry on the projected delaminated area

The projected delaminated area as a percentage of the total projected area for all the GFRP V-structure blast simulations have been tabulated in table E.2. Each column read vertically downwards shows the effect of increasing the V-tip radius, while every fourth column shows the effects of increasing the charge mass on a particular V-structure configuration. Finally, comparing selected columns allows for the effects of changing the V-angle or fibre orientation to be studied.

Table E.2: Projected delaminated area (%) versus V-tip radius for the GFRP V-structure simulations

V-tip radius (mm)	Charge mass (g)											
	10				15				20			
	105°		120°		105°		120°		105°		120°	
	0°/90°	±45°	0°/90°	±45°	0°/90°	±45°	0°/90°	±45°	0°/90°	±45°	0°/90°	±45°
	Delaminated area (%)				Delaminated area (%)				Delaminated area (%)			
34	4.8	4.5	5.9	6.1	7.0	7.1	10.1	9.4	9.9	8.9	12.5	12.9
62	9.6	8.6	10.2	11.3	14.3	14.9	15.9	13.4	19.6	19.3	20.7	16.0
80	15.0	14.8	16.2	15.7	22.1	23.6	24.1	23.5	30.8	31.5	27.3	28.1
100	21.0	18.6	20.3	17.5	32.1	30.6	29.2	27.4	36.1	38.3	36.0	35.6
200	28.5	26.2	25.4	28.1	45.7	47.6	35.0	42.4	54.5	54.1	46.8	48.0

E.3.1 V-tip radius effects

Figures E.5 and E.6 show the effect of increasing the V-tip radius on the projected delaminated area for the GFRP V-structures with a fibre orientation of ±45°. Once again, linear trends can be seen in both graphs.

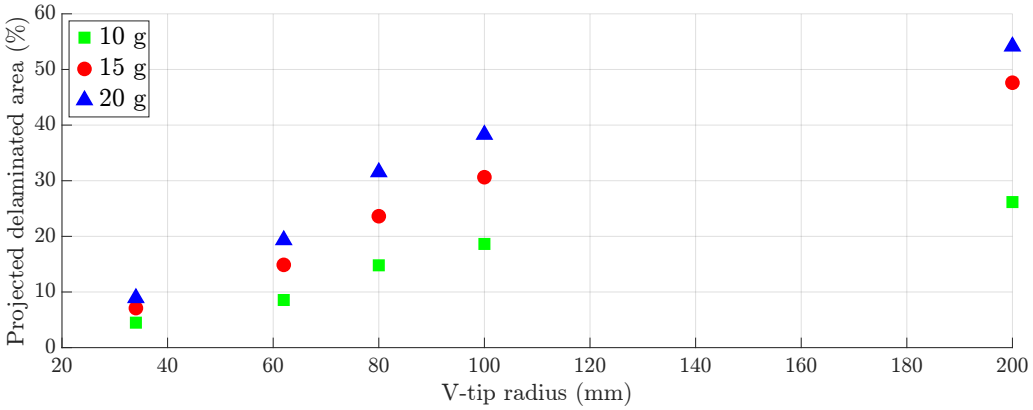

Figure E.5: Projected delaminated area versus V-tip radius for the 105° GFRP V-structures with a ±45° fibre orientation

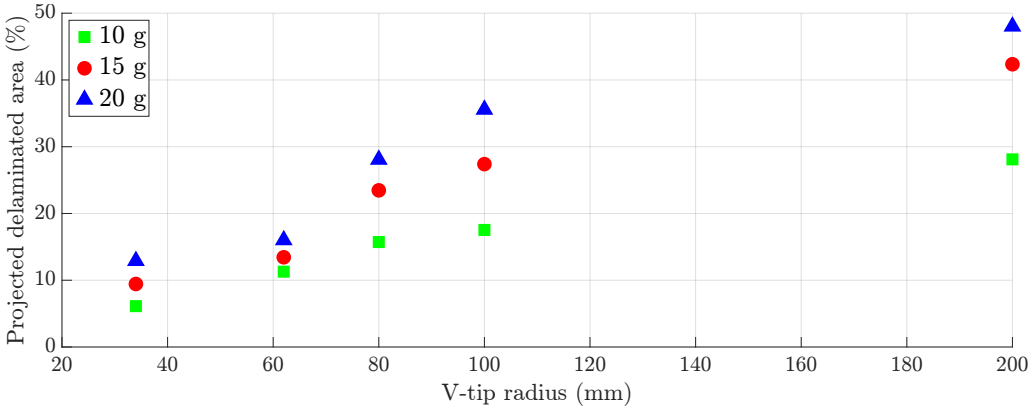

Figure E.6: Projected delaminated area versus V-tip radius for the 120° GFRP V-structures with a ±45° fibre orientation

E.3.2 Delaminated area plots - V-angle = 105°

The delaminated area maps are presented for the 105° V-structure simulations with fibre orientations of 0°/90° and ±45° in figures E.7 to E.10. As expected, increasing the V-tip radius results in an increase in the delaminated area as the V-structures experience greater levels of deformation and layer separation.

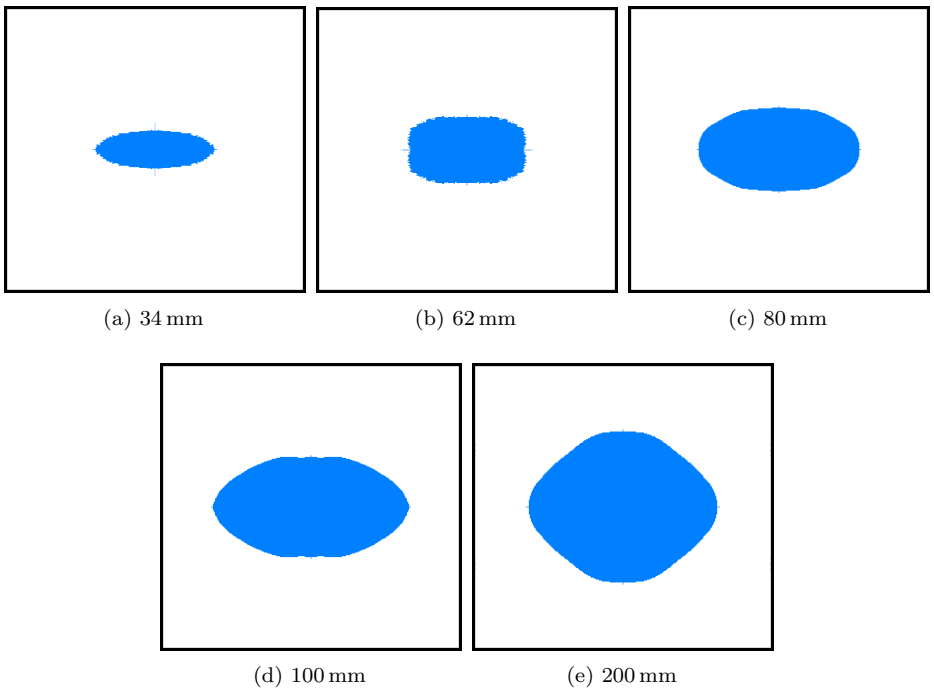

(a) 34 mm (b) 62 mm (c) 80 mm

(d) 100 mm (e) 200 mm

Figure E.7: Projected total delaminated area for the 0°/90° 105° GFRP V-structure simulations for a charge mass of 10 g

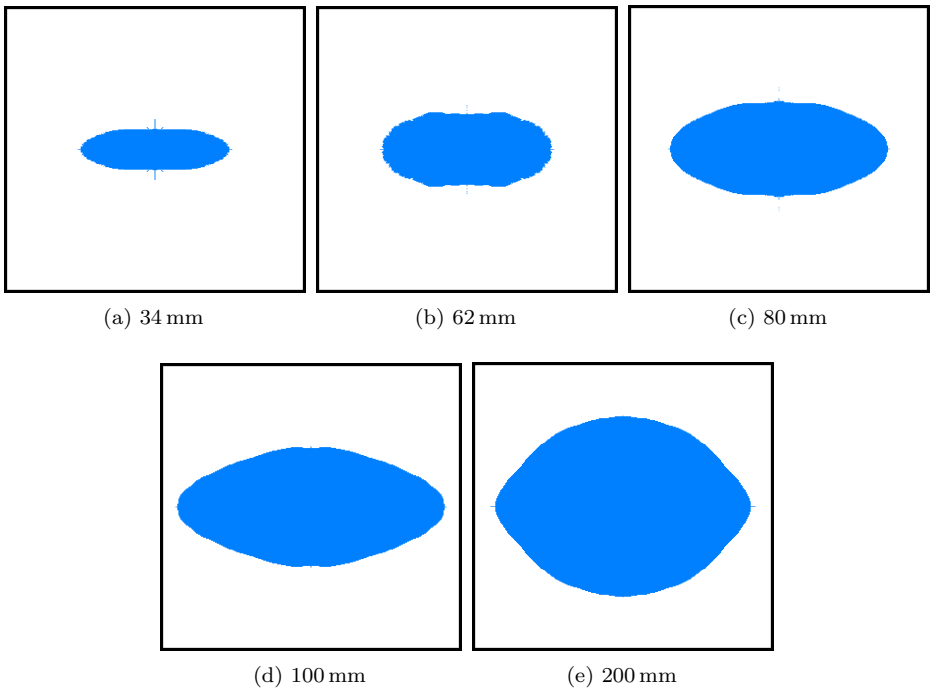

(a) 34 mm (b) 62 mm (c) 80 mm

(d) 100 mm (e) 200 mm

Figure E.8: Projected total delaminated area for the 0°/90° 105° GFRP V-structure simulations for a charge mass of 15 g

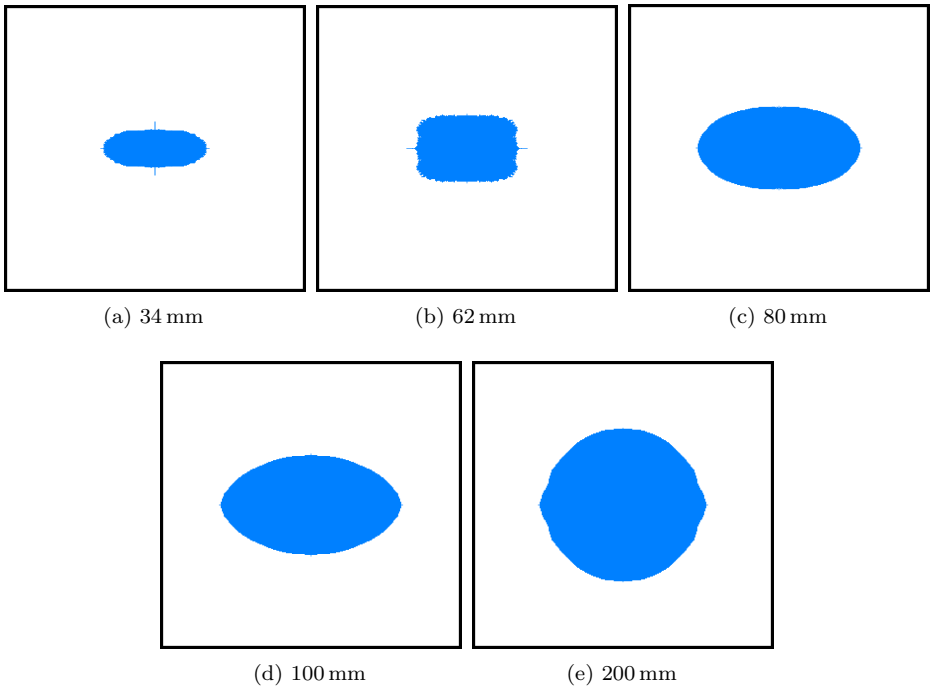

(a) 34 mm (b) 62 mm (c) 80 mm

(d) 100 mm (e) 200 mm

Figure E.9: Projected total delaminated area for the ±45° 105° GFRP V-structure simulations for a charge mass of 10 g

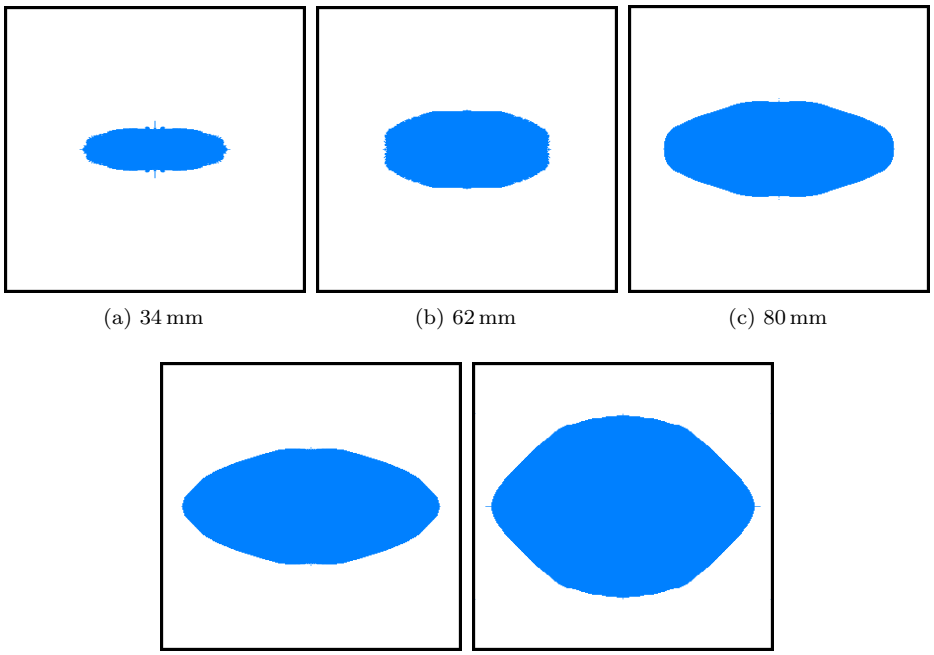

(a) 34 mm (b) 62 mm (c) 80 mm

(d) 100 mm (e) 200 mm

Figure E.10: Projected total delaminated area for the ±45° 105° GFRP V-structure simulations for a charge mass of 15 g

E.3.3 Delaminated area plots - V-angle = 120°

The delaminated area maps are presented for the 120° V-structure simulations with fibre orientations of 0°/90° and ±45° in figures E.11 to E.14. Similar trends to those seen for the 105° V-structures are observed. Below a charge mass of 20 g none of the V-structures simulated show delamination across the entire ridge line.

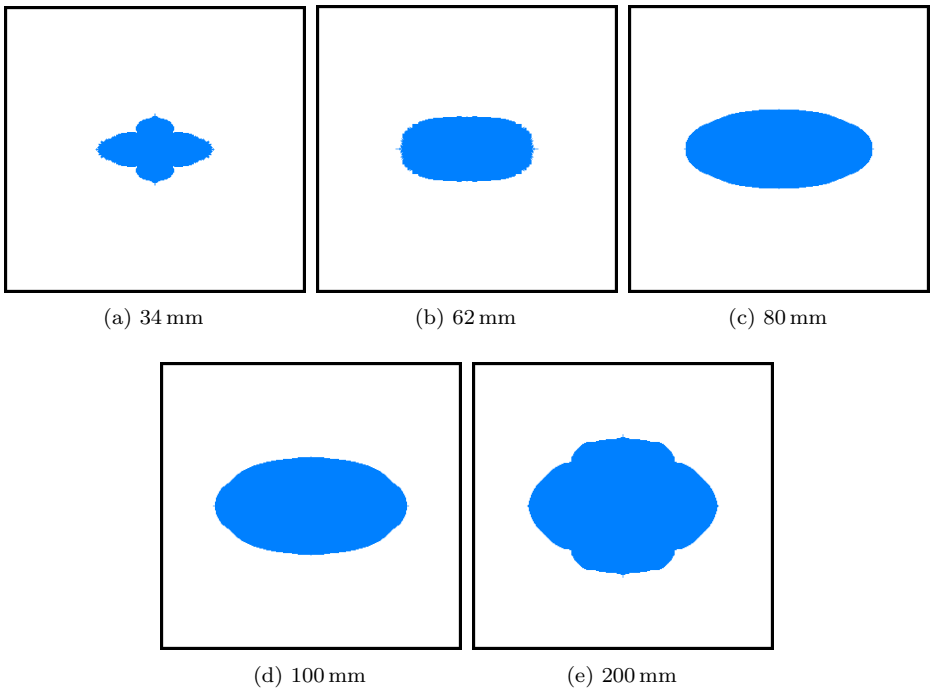

(a) 34 mm (b) 62 mm (c) 80 mm

(d) 100 mm (e) 200 mm

Figure E.11: Projected total delaminated area for the 0°/90° 120° GFRP V-structure simulations for a charge mass of 10 g

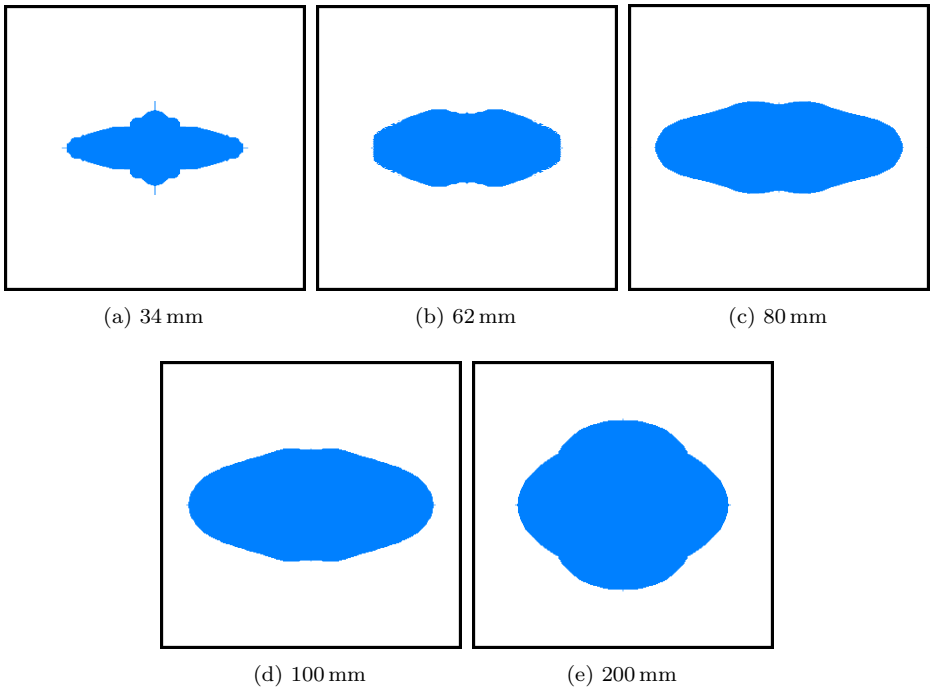

(a) 34 mm (b) 62 mm (c) 80 mm

(d) 100 mm (e) 200 mm

Figure E.12: Projected total delaminated area for the 0°/90° 120° GFRP V-structure simulations for a charge mass of 15 g

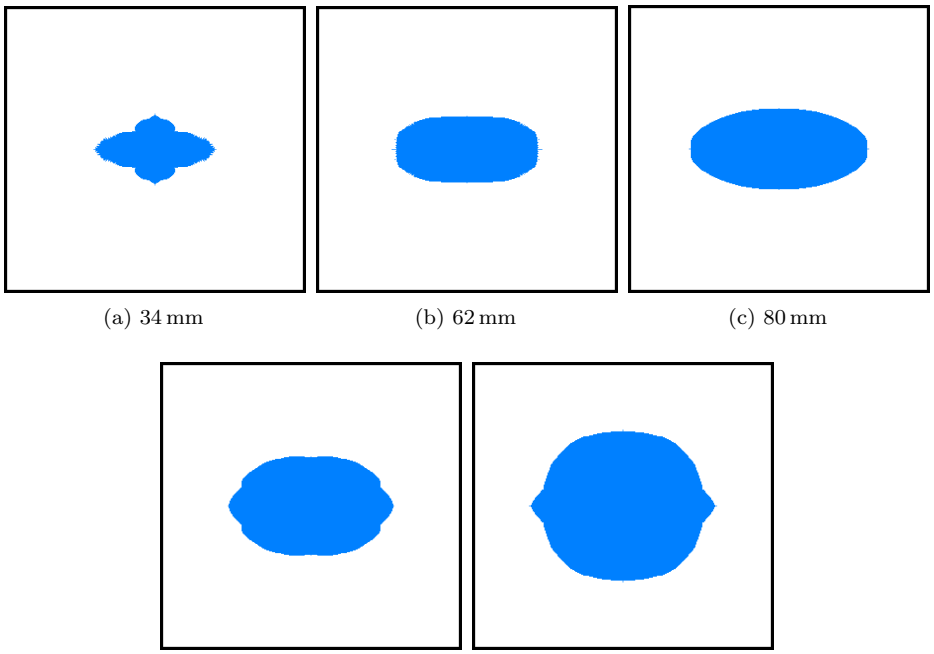

(a) 34 mm (b) 62 mm (c) 80 mm

(d) 100 mm (e) 200 mm

Figure E.13: Projected total delaminated area for the ±45° 120° GFRP V-structure simulations for a charge mass of 10 g

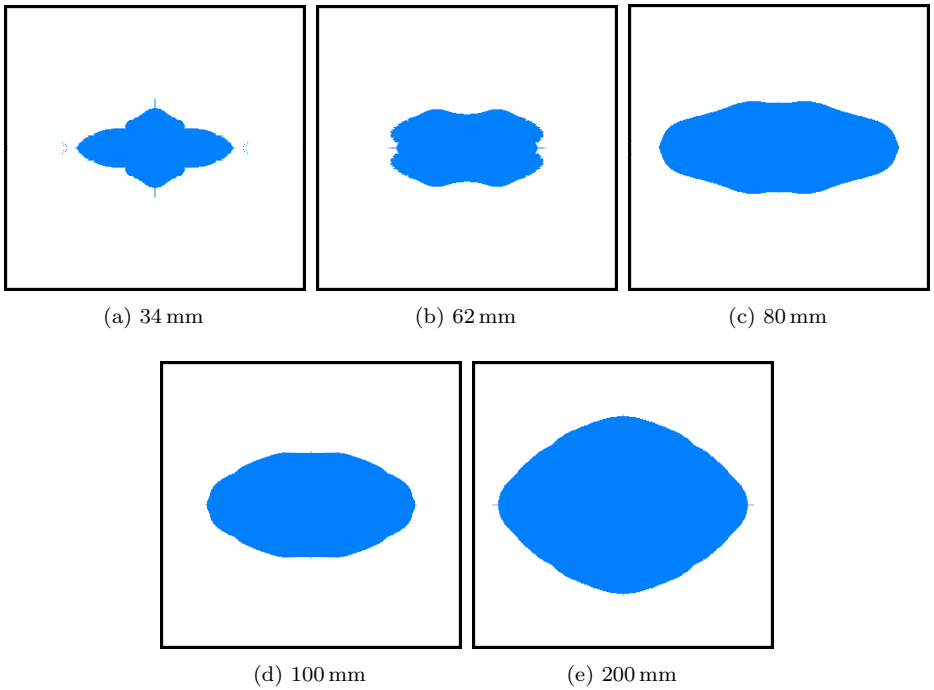

(a) 34 mm (b) 62 mm (c) 80 mm

(d) 100 mm (e) 200 mm

Figure E.14: Projected total delaminated area for the ±45° 120° GFRP V-structure simulations for a charge mass of 15 g

E.4 The effects of V-structure geometry on the transient response

Table E.3 presents the peak transient mid-point deflection results for all the simulations. Once again, as expected, the peak deflection increases with an increase in charge mass for all the V-structure configurations investigated.

Table E.3: Peak mid-point deflection (in mm) versus V-tip radius for the GFRP V-structure simulations

V-tip radius (mm)	**Charge mass (g)**											
	10				**15**				**20**			
	105°		**120°**		**105°**		**120°**		**105°**		**120°**	
	0°/90°	**±45°**	**0°/90°**	**±45°**	**0°/90°**	**±45°**	**0°/90°**	**±45°**	**0°/90°**	**±45°**	**0°/90°**	**±45°**
	Peak displacement (mm)				**Peak displacement (mm)**				**Peak displacement (mm)**			
34	12.62	12.87	12.84	13.21	14.86	15.29	16.31	16.10	16.90	17.18	18.61	18.54
62	13.66	14.10	14.26	14.56	15.67	16.43	16.29	16.26	17.98	17.96	17.63	18.18
80	15.35	15.91	16.00	16.16	17.09	17.56	17.64	17.64	19.09	19.45	18.50	19.09
100	15.50	15.99	15.78	16.06	18.14	18.43	18.22	18.20	19.31	20.07	19.51	19.93
200	15.58	15.85	15.20	15.59	18.22	18.23	17.64	17.97	19.79	20.48	19.14	19.52

E.4.1 Fibre orientation effects

Figure E.15 shows the mid-point displacement time histories for the V-structures with the two fibre orientations and V-tip radii of 34 mm and a 200 mm simulated at a charge mass of 20 g. The similar response suggests that the fibre orientation does not influence the displacement time histories of these GFRP V-structures.

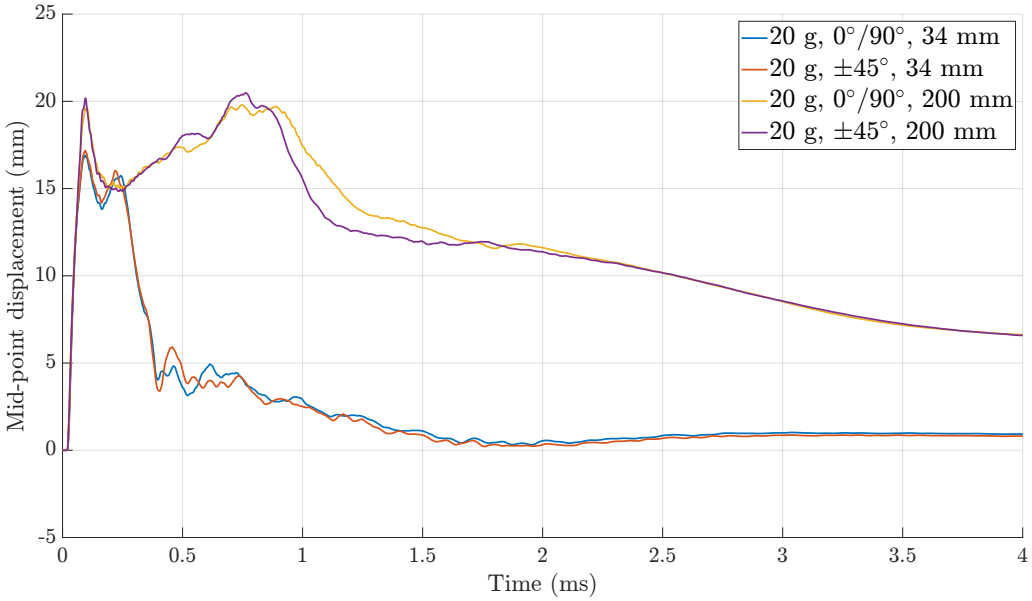

Figure E.15: Mid-point displacement time history for the 105° GFRP V-structure with 34 mm and a 200 mm V-tip radii simulated at a charge mass of 20 g with the two fibre orientations

E.4.2 V-angle effects

The influence of the V-angle on the peak mid-point deflection is shown in figure E.16. For smaller V-tip radii, the narrower angled V-structures display superior performance while this effect is reversed at larger V-tip radii.

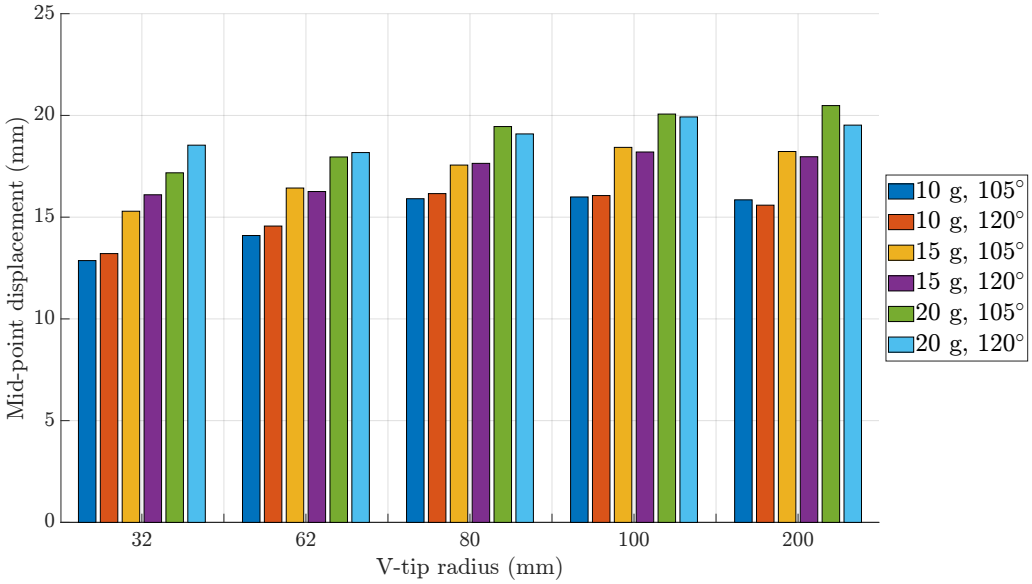

Figure E.16: Peak mid-point displacement versus V-angle for the GFRP V-structures with a ±45° fibre orientation

The influence of the V-angle on the mid-point deflection time histories is shown in figures E.17 and E.18 for V-tip radii of 100 mm and 200 mm respectively. At these V-tip radii, the response is fairly similar for the two V-angles.

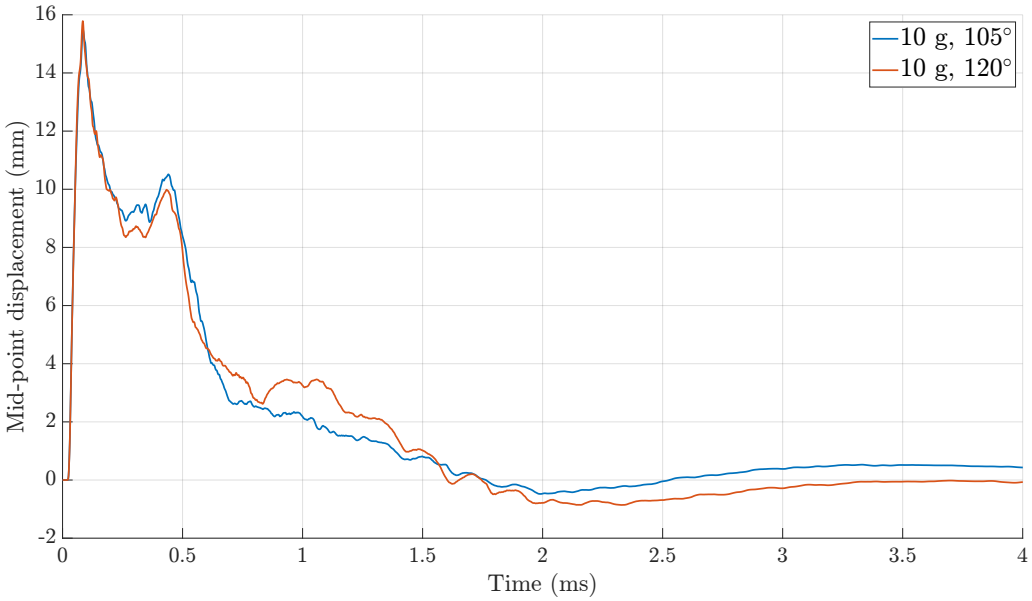

Figure E.17: Mid-point displacement time histories for 105° and 120° GFRP V-structure simulations with a 0°/90° fibre orientation and a 100 mm simulated at a charge mass of 10 g

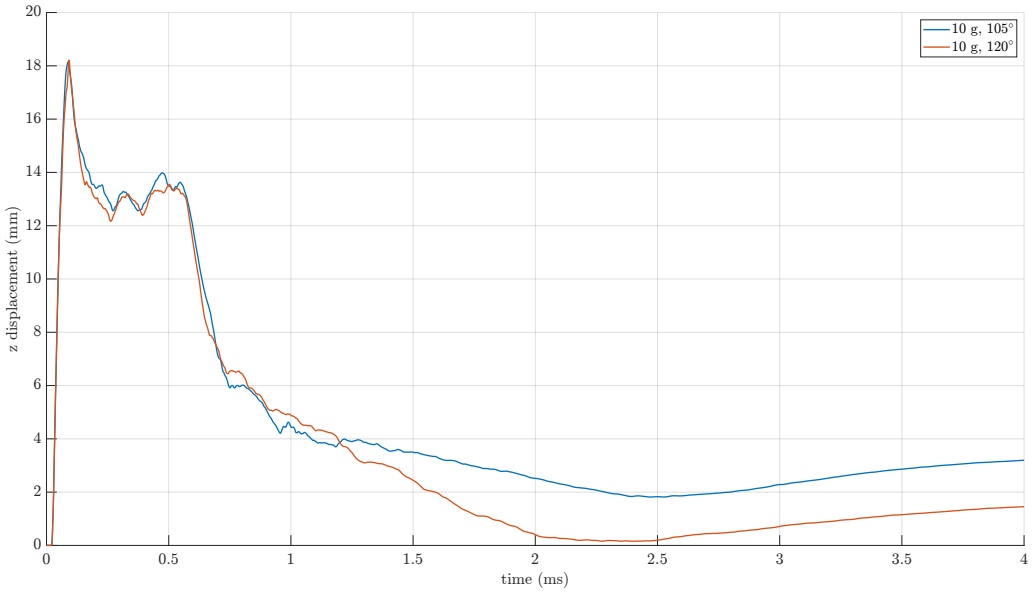

Figure E.18: Mid-point displacement time histories for 105° and 120° GFRP V-structure simulations with a 0°/90° fibre orientation and a 200 mm simulated at a charge mass of 10 g

The influence of the V-angle on the peak ridge profiles is shown in figures E.19 and E.20 for V-tip radii of 34 mm and 100 mm respectively. Once again, the response is fairly similar at these two V-tip radii with minor differences in the depth of the indentation.

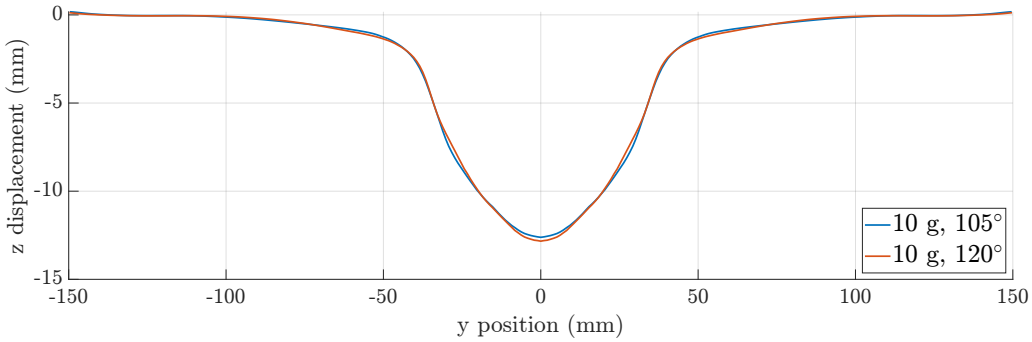

Figure E.19: Peak transient ridge profiles for 105° and 120° GFRP V-structure simulations with a 0°/90° fibre orientation and a 34 mm simulated at a charge mass of 10 g

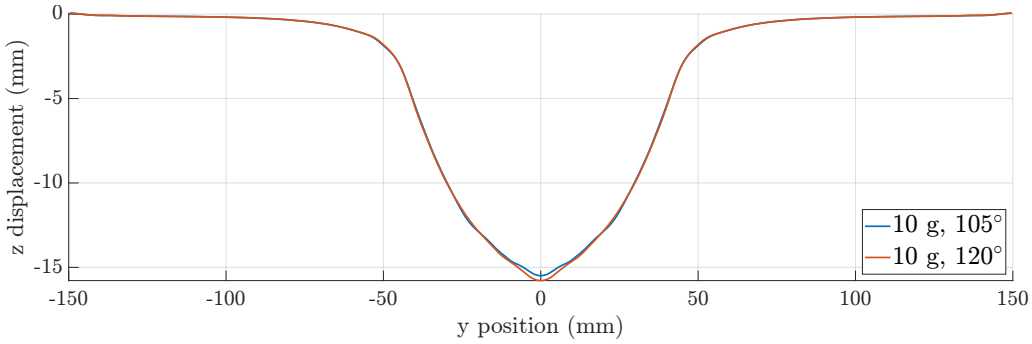

Figure E.20: Peak transient ridge profiles for 105° and 120° GFRP V-structure simulations with a 0°/90° fibre orientation and a 100 mm simulated at a charge mass of 10 g

E.4.3 V-tip radius effects

The influence of the V-tip radius on the peak mid-point deflection is shown in figures E.21 to E.23. Trend-lines cannot be drawn easily through the data points although there is a reduction in the peak mid-point deflection at a V-tip radius of 200 mm.

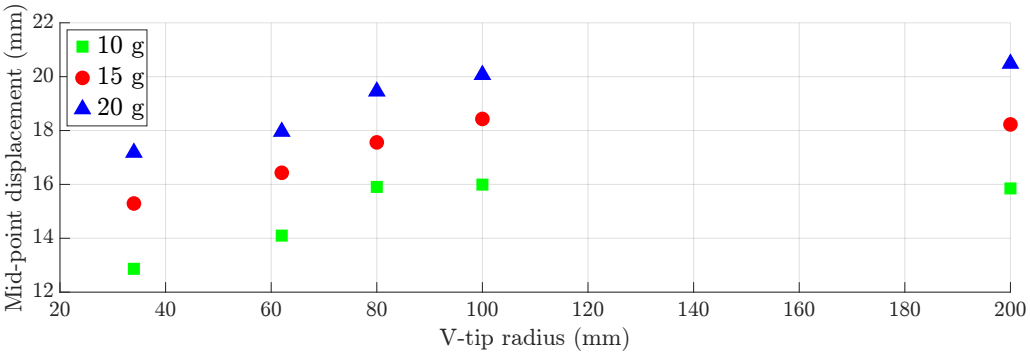

Figure E.21: Peak mid-point displacement versus V-tip radius for the 105° GFRP V-structures with a ±45° fibre orientation

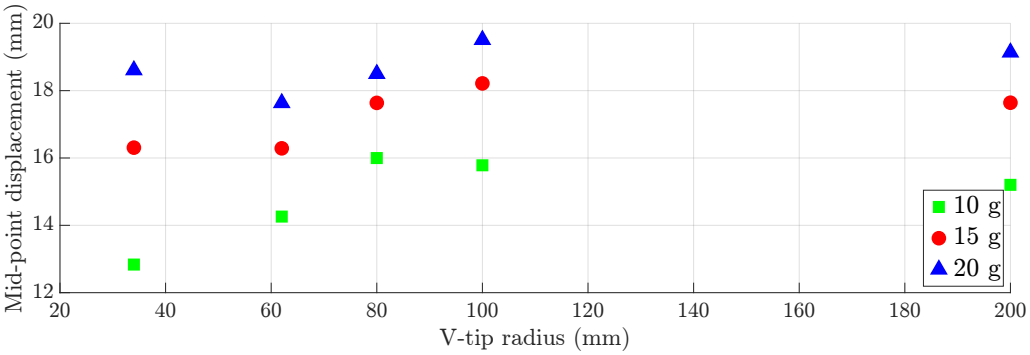

Figure E.22: Peak mid-point displacement versus V-tip radius for the 120° GFRP V-structures with a 0°/90° fibre orientation

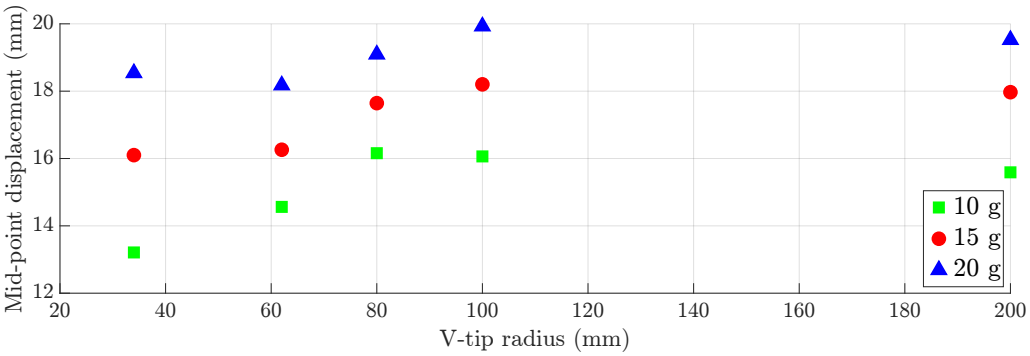

Figure E.23: Peak mid-point displacement versus V-tip radius for the 120° GFRP V-structures with a ±45° fibre orientation

The influence of the V-tip radius on the mid-point deflection time histories is shown in figures E.24 to E.26. As the V-tip radius is increased, the peak displacement increases, but the time at which it occurs remains unchanged. The post-peak vibration response is also extended with the V-structures taking longer to return to their original position.

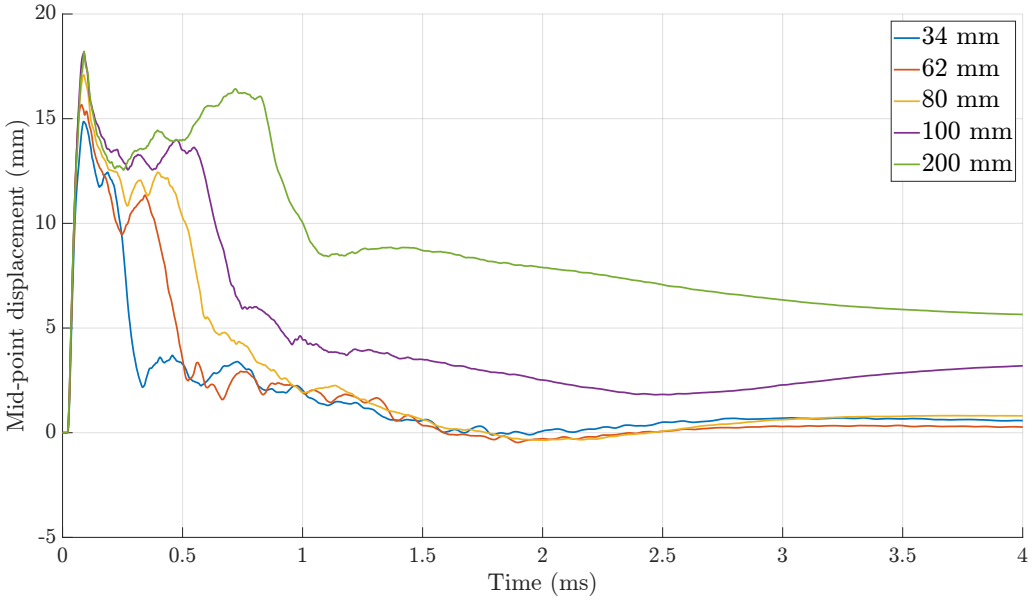

Figure E.24: Mid-point displacement time histories for 105° GFRP V-structure simulations with a 0°/90° fibre orientation simulated at a charge mass of 15 g

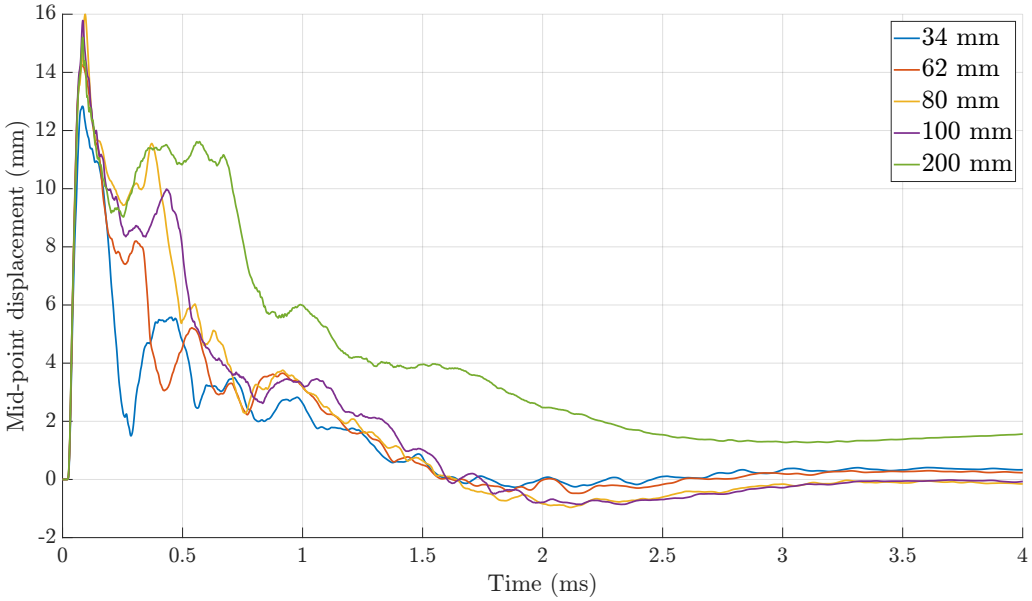

Figure E.25: Mid-point displacement time histories for 120° GFRP V-structure simulations with a 0°/90° fibre orientation simulated at a charge mass of 10 g

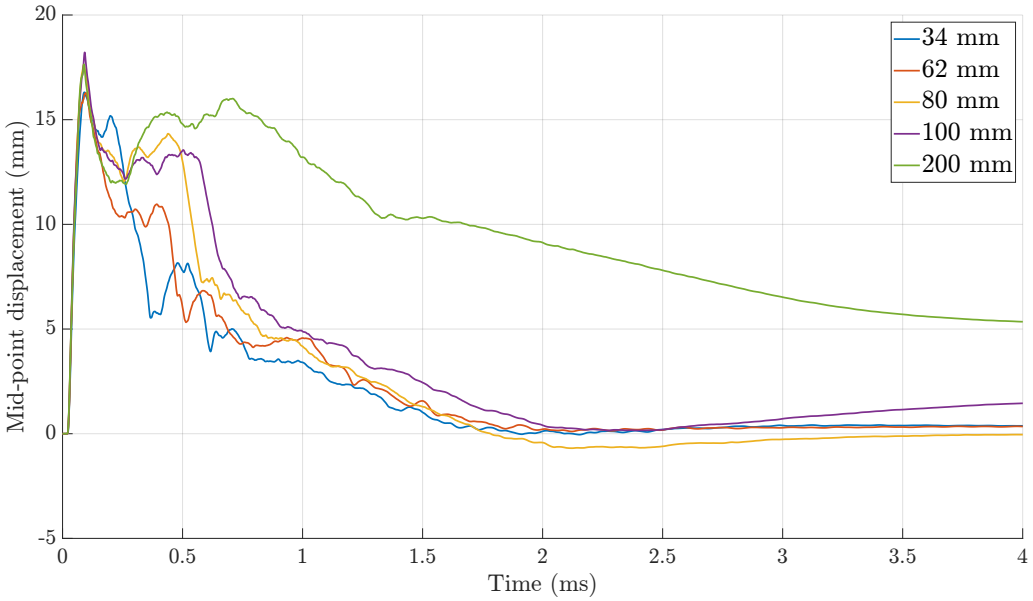

Figure E.26: Mid-point displacement time histories for 120° GFRP V-structure simulations with a 0°/90° fibre orientation simulated at a charge mass of 15 g

The influence of the V-tip radius on the peak ridge profiles is shown in figures E.27 to E.29. As the V-tip radius is increased, there are small increases in the depth of the indentation and deformed length along the ridge.

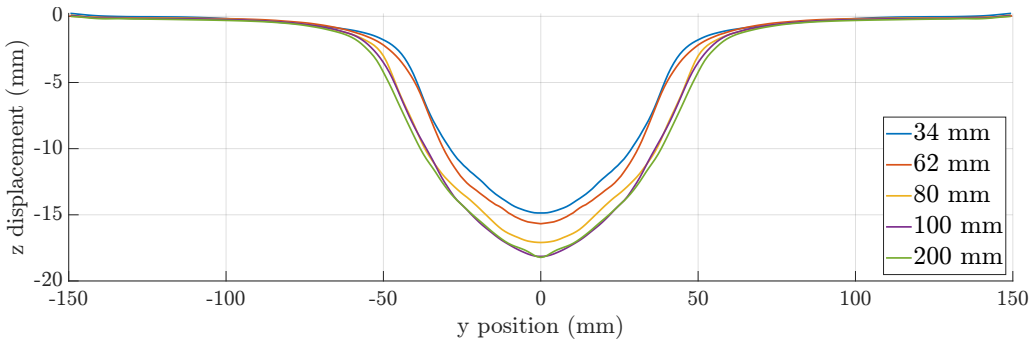

Figure E.27: Peak transient ridge profiles for 105° GFRP V-structure simulations with a 0°/90° fibre orientation simulated at a charge mass of 15 g

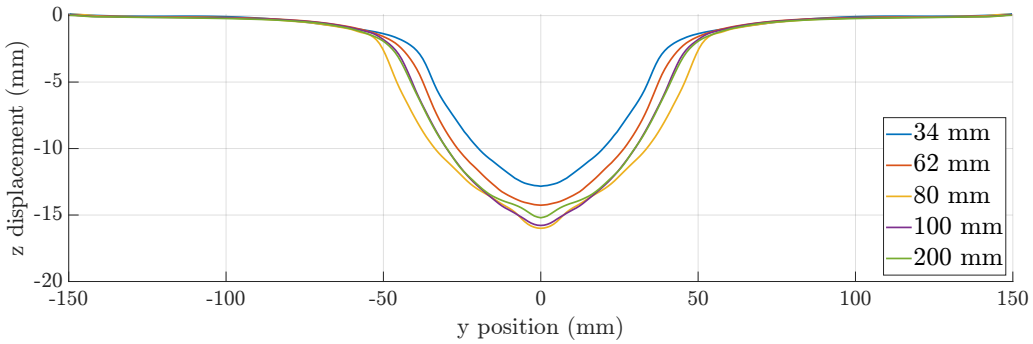

Figure E.28: Peak transient ridge profiles for 120° GFRP V-structure simulations with a 0°/90° fibre orientation simulated at a charge mass of 10 g

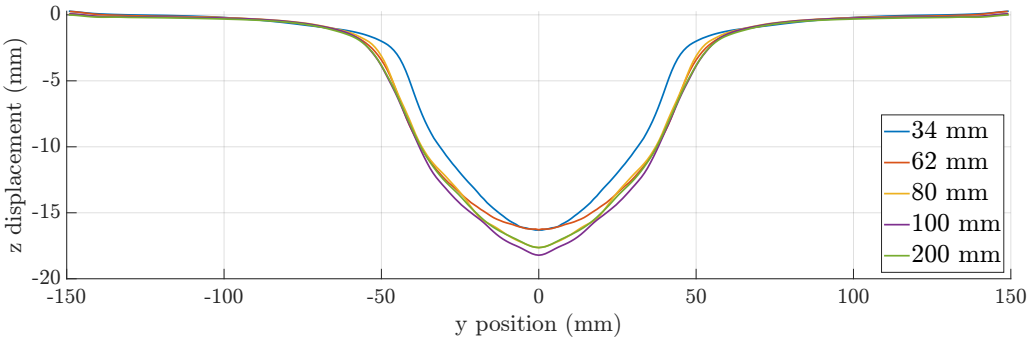

Figure E.29: Peak transient ridge profiles for 120° GFRP V-structure simulations with a 0°/90° fibre orientation simulated at a charge mass of 15 g